THE UNIVERSITY *of* EDINBURGH

This thesis has been submitted in fulfilment of the requirements for a postgraduate degree (e. g. PhD, MPhil, DClinPsychol) at the University of Edinburgh. Please note the following terms and conditions of use:

- This work is protected by copyright and other intellectual property rights, which are retained by the thesis author, unless otherwise stated.
- A copy can be downloaded for personal non-commercial research or study, without prior permission or charge.
- This thesis cannot be reproduced or quoted extensively from without first obtaining permission in writing from the author.
- The content must not be changed in any way or sold commercially in any format or medium without the formal permission of the author.
- When referring to this work, full bibliographic details including the author, title, awarding institution and date of the thesis must be given.

Ferrofluid-Gaps for Direct-Drive Wind Turbine Generators

Fergus Hall

THE UNIVERSITY *of* EDINBURGH

A thesis presented for the degree of Doctor of Philosophy

2026

Publications

A list of conference papers related to this thesis is presented below. Content from these papers is included within this thesis, however the content has been distributed throughout the thesis to provide a coherent body of interrelated work. Much of the work presented in these publications has been further refined and expanded upon since their publication.

Conference Papers:

F. P. Hall, A. S. McDonald and M. A. Mueller, "A magnetic analysis of ferrofluid-gaps for direct-drive wind turbine generators - an unconventional approach for reducing air-gap reluctance," *12th International Conference on Power Electronics, Machines and Drives (PEMD 2023)*, Brussels, Belgium, 2023, pp. 225-232, doi: 10.1049/icp.2023.2002.

F. Hall and A. McDonald, "Direct-Drive Wind Turbine Generator Vibration Induced by High-Order Air-Gap Nonuniformity," *2024 International Conference on Electrical Machines (ICEM)*, Torino, Italy, 2024, pp. 1-7, doi: 10.1109/ICEM60801.2024.10700546.

F. Hall and A. McDonald, "A Baseline Thermal Model for Liquid-Cooled Multi-Megawatt Scale Direct-Drive Permanent Magnet Wind Turbine Generators," *2024 27th International Conference on Electrical Machines and Systems (ICEMS)*, Fukuoka, Japan, 2024, pp. 1947-1954, doi: 10.23919/ICEMS60997.2024.10921260.

F. Hall, A. McDonald, M. Mueller and M. Galbraith, "Design and Fabrication of a Ferrofluid-Gap Test Rig for Radial Flux Electrical Machines," *2025 IEEE International Electric Machines & Drives Conference (IEMDC)*, Houston, TX, USA, 2025, pp. 1-8, doi: 10.1109/IEMDC60492.2025.11061175

To my parents, Alice and Derek, for all your support and encouragement.

Abstract

The commercial offering of offshore wind turbines has generally converged upon three-blade horizontal-axis designs with variable speed generators and pitch-regulated blades. Arguably, the most significant distinguishing feature is whether the powertrain has a direct-drive or geared configuration.

In a direct-drive powertrain, there is no gearbox that steps up the rotational speed and steps down the torque from the turbine rotor for input into the generator. This low-speed and high-power operation necessitates the production of immense electromagnetic torque: on the order of 20 MNm for a 15 MW wind turbine. As a result, direct-drive wind turbine generators are large, heavy, and require a substantial amount of rare earth permanent magnet material in their construction: on the order of 20 tonnes for a 15 MW wind turbine. Rare earth permanent magnets are expensive and environmentally damaging to procure, designers typically attempt to make the air-gap clearance of direct-drive wind turbine generators as small as practicably possible so that the air-gap magnetic reluctance is minimised: reducing the amount of permanent magnet material required.

This thesis investigates an unconventional approach to reducing the permanent magnet material requirements of direct-drive wind turbine generators in which the air-gap region is flooded with magnetically permeable ferrofluid such that it becomes a ‘ferrofluid-gap’.

The initial chapters of this thesis examine the design of multi-megawatt scale direct-drive wind turbine generators. A detailed design procedure is specified which is supported by an advanced thermal modelling methodology. A review of air-gap dimensioning is provided, and insights are presented that improve understanding in this area.

Subsequent chapters focus on the ferrofluid-gap concept. First, it is explained how the magnetic and mechanical behaviour of ferrofluid-gaps can be modelled according to theoretical predictions. Prior work regarding the ferrofluid-gap concept is reviewed and the opportunities for further research are highlighted.

To validate the theoretical models of ferrofluid-gap magnetic and mechanical behaviour, a novel ferrofluid-gap test rig was designed, fabricated, and tested. The

test rig dimensions were scaled such that the fluid dynamic conditions expected in multi-megawatt scale direct-drive wind turbine generators could be achieved at a laboratory scale. The resulting experimental data provides unprecedented validation of the theoretically predicted magnetic and mechanical behaviour of ferrofluid-gaps in radial-flux electrical machines.

Drawing upon the analytical models, design tools, and experimental results developed throughout this work, the feasibility of ferrofluid-gaps for direct-drive wind turbine generators is assessed. It is found that, in principle, ferrofluid-gaps can enable a reduction in permanent magnet material (~10%) without unacceptably compromising efficiency due to drag losses. It is also demonstrated that a ferrofluid-gap has the potential to enhance thermal performance. However, it can be concluded that the potential benefits of a ferrofluid-gap are outweighed by the costs and difficulties associated with their implementation in multi-megawatt scale direct-drive wind turbine generators.

Lay Summary

The offshore environment has a lot of advantages for wind energy, a key factor being that it is very windy. There is also plenty of space for construction, far away from people who might object to having a large wind turbine near their homes. In general, the overall cost of wind energy can be reduced by making turbines larger, so manufacturers have been developing increasingly big offshore wind turbines. Modern designs can be several hundred metres tall, with blades that are over one hundred metres long.

Maintaining and repairing offshore wind turbines is difficult and expensive. Offshore installations are often located far from shore and can only be accessed when weather conditions are favourable. It is therefore very important that offshore wind turbines are reliable, requiring minimal maintenance and having a low probability of failure. This has motivated the adoption of direct-drive wind turbine generators which have no gearbox. By removing the gearbox, which is one of the most failure-prone components, the turbine becomes mechanically simpler and more reliable.

For a wind turbine to produce electricity the mechanical power captured from the wind, which causes the wind turbine to rotate, must be converted into electrical power by a generator. The interaction between the turbine and the generator can be thought of as a tug of war: the blades pull one way with mechanical torque, while the generator pulls back with electromagnetic torque. For the turbine to turn at a steady speed, these opposing forces must be in balance. Because there is no gearbox, direct-drive generators must produce a very large amount of torque directly. To do this, they are made very large. This is similar in principle to using a long lever to loosen a tight bolt: the longer the handle, the easier it becomes to apply the necessary torque to loosen the bolt. In the same way, it is easier to produce more torque from a generator by making it larger.

Since direct-drive generators are very large, a lot of material is required to construct them. One of the most expensive materials is the rare earth permanent magnets that provide the generator’s magnetic field. For modern large-scale wind turbines, several tonnes of magnet material are required: as much as twenty tonnes for the largest wind turbines that are currently being installed.

A good strategy for reducing the cost of direct-drive generators is to minimise the amount of magnet material required in their construction. One of the best ways to achieve this is to make the air-gap, the clearance between the generator's rotor (the rotating part carrying the magnets) and stator (the stationary part containing the electrical windings), as small as possible.

In this thesis, an alternative approach is investigated in which the air-gap is flooded with ferrofluid, making it a 'ferrofluid-gap'. Ferrofluid is a unique material consisting of a carrier fluid, such as oil, containing suspended magnetic nanoparticles. It is easier for magnetic flux from the magnets to cross a ferrofluid-gap than an air-gap of the same size. This could potentially allow for a reduction in the amount of permanent magnet material required in wind turbine generators.

To assess how well a ferrofluid-gap would work, it is necessary to understand how it affects different aspects of generator performance, such as the magnetic field, efficiency, and temperature of the components. To do this, a range of modelling tools were developed for designing and evaluating direct-drive wind turbine generators. During the development of these tools, additional opportunities to improve the understanding of direct-drive generator design were identified and are also presented in this thesis.

To ensure that a ferrofluid-gap behaves as expected, several experiments were conducted with a purpose-built test rig. It was designed to mimic the ferrofluid-gap behaviour that would be expected in full-scale wind turbine generators. By comparing the experimental results with theoretically predicted behaviour, it is demonstrated that the ferrofluid behaves as expected.

Drawing upon the design tools and experimental results presented in this thesis, the feasibility of ferrofluid-gaps for direct-drive wind turbine generators is assessed. It was found that, in principle, a ferrofluid-gap can improve direct-drive generator performance.

Acknowledgments

First of all, I would like to thank my principal doctoral advisor Prof. Alasdair McDonald for supporting and encouraging me during my research. Our conversations were always very enjoyable and useful. I would also like to thank Prof. Markus Mueller for acting as my secondary doctoral advisor.

I would like to thank everyone who played a part in developing and maintaining the EPSRC Wind and Marine Energy Systems and Structures Centre for Doctoral Training (CDT WAMSS), and to acknowledge the funding and support I was provided (Grant Number EP/S023801/1). I am very fortunate to have received significant support which allowed me to travel to conferences in Europe, Japan, and the USA.

I am very grateful to the School of Engineering's technical staff for their advice and help in the lab, in particular Jamie Graham, Iain Gold, and Angus Spray who were always happy to lend a hand when I needed to move something heavy.

I would also like to thank Andrew Brown for recording precise measurements of the ferrofluid-gap test rig geometry. Stuart Martin for welcoming me into his chemistry lab and supporting my ferrofluid synthesis work. Prof. Konstantin Kamenev for providing me with magnetometry measurements of my ferrofluid particle samples. Dr. John Royer for providing me with viscosity measurements of my ferrofluid samples. Stephen Mitchell and Martin Singleton for facilitating and helping me with electron microscopy of my ferrofluid particles.

I am very grateful to the team at Fountain Design Ltd who enthusiastically took on the challenge of fabricating the ferrofluid-gap test rig. They delivered very quickly and with very impressive quality.

I would like to acknowledge that this work has made use of the resources provided by the Edinburgh Compute and Data Facility (ECDF).

Finally, I would like to thank my partner Ale for her support, patience, and enthusiasm during my research. I could always rely on her to distract me when needed or alternatively to provide me with an insightful technical discussion.

Table of Contents

Publications ... **ii**

Abstract ... **iv**

Lay Summary ... **vi**

Acknowledgments ... **viii**

Table of Contents ... **ix**

List of Figures ... **xiii**

List of Tables ... **xxi**

Nomenclature ... **xxii**

Chapter 1: Introduction ... **1**

1.1 Background ... 1
1.2 Aim of Thesis ... 3
1.3 Layout of Thesis ... 4
1.4 Contributions to Knowledge ... 7

Chapter 2: Design of Direct-Drive Wind Turbine Generators ... **9**

2.1 Design of Direct-Drive Wind Turbine Generators ... 9
2.1.1 Wind Turbine Aerodynamic Specification ... *10*
2.1.2 The Generator's Influence on the Overall Wind Turbine Design ... *12*
2.1.3 Initial Sizing of Generator ... *12*
2.1.4 Open-Load Magnetic Circuit ... *15*
2.1.5 Armature Inductance ... *19*
2.1.6 Armature Current and Copper Losses ... *21*
2.1.7 Stator Iron Losses ... *23*
2.1.8 Permanent Magnet Losses ... *24*
2.1.9 Converter Losses ... *26*
2.1.10 Generator Efficiency at Rated Wind Speed ... *27*
2.1.11 The Wind Turbine Power Curve ... *27*
2.1.12 Calculation of Energy Yield ... *29*
2.1.13 Specification of the Example 15 MW Outer-Rotor Generator ... *31*
2.2 Wind Turbine Generator Design Objectives ... 33
2.2.1 Minimising Material Costs ... *33*
2.2.2 Increasing Efficiency ... *35*
2.2.3 Improving Reliability ... *36*
2.2.4 Reducing Weight ... *36*
2.2.5 Reducing Volume ... *37*
2.2.6 Summary ... *38*
2.3 Approaches for Reducing the Total Permanent Magnet Cost ... 38
2.3.1 Selection of Permanent Magnet Grade ... *38*
2.3.2 Increasing the Current Loading ... *39*
2.3.3 Lowering the Magnet Temperature ... *39*
2.3.4 Reducing the Air-Gap Reluctance ... *40*
2.3.5 Summary and Motivation for the Following Chapters ... *42*
2.4 Conclusion ... 43

Chapter 3: Thermal Modelling of Direct-Drive Wind Turbine Generators 44

3.1 Thermal Management and Modelling of DD WTGs 44
3.1.1 Cooling Strategies for Direct-Drive Wind Turbine Generators 45
3.1.2 Thermal Modelling of Electrical Machines 47
3.2 Opportunities for a Refined DD WTG Thermal Model 48
3.2.1 Distributed Loss Modelling 48
3.2.2 Size Dependent Convective Heat Transfer 50
3.2.3 Comparison of Air- and Liquid-Cooling Systems 51
3.2.4 Inner- vs Outer-Rotor Topologies 51
3.2.5 Heat Exchanger Modelling 52
3.3 Thermal Modelling Methodology 52
3.3.1 Generator Topologies 52
3.3.2 Heat Sources 54
3.3.3 Convective Heat Transfer Coefficients 54
3.3.4 Water Jacket Modelling 60
3.3.5 Air Duct Modelling 62
3.3.6 Lumped Parameter Thermal Network Model 63
3.4 Heat Exchanger Design and Modelling 67
3.4.1 Liquid-to-Air Heat Exchanger Model 68
3.4.2 Air-to-Air Heat Exchanger Model 71
3.5 Thermal Model Results and Discussion 74
3.5.1 Thermal Model Parameters 74
3.5.2 Comparison of Air- and Liquid-Cooling Performance 75
3.5.3 Comparison of Inner- and Outer-Rotor DD WTG Thermal Performance 77
3.5.4 Comparison of Heat Exchanger Performance 79
3.5.5 Air-Gap Ventilation 80
3.5.6 Importance of Thermal Modelling 81
3.6 Conclusion 82

Chapter 4: Air-Gap Dimensioning of Direct-Drive Wind Turbine Generators 83

4.1 Air-Gap Dimensioning of Direct-Drive Wind Turbine Generators 83
4.2 Electromagnetic Constraints 87
4.2.1 Armature Inductance 87
4.2.2 Risk of Permanent Magnet Demagnetisation 88
4.2.3 Armature Reaction 90
4.2.4 Summary of Electromagnetic Constraints 91
4.3 Sources of Air-Gap Deformation 93
4.3.1 Centrifugal Forces 95
4.3.2 Thermal Expansion 95
4.3.3 External Loads 96
4.3.4 Manufacturing Tolerances 97
4.3.5 Magnetic Forces 97
4.3.6 Self-Weight 98
4.4 Secondary Deformation and Air-Gap Stability 98
4.4.1 Secondary Deformation 98
4.4.2 Magnetic Stiffness 101
4.4.3 Impact of Air-Gap Deformation Mode Number 104
4.4.4 Finite Element Analysis of a Disc-Rim Structure 108
4.4.5 Recommendations for a Revised Magnetic Stiffness Model 111
4.5 Vibration Induced by High-Order Air-Gap Non-uniformity 112
4.5.1 An Analytical Model for Non-uniform Air-Gap Radial Maxwell Stress Harmonics 113

4.5.2 Finite Element Method Simulation and Validation ... *116*
4.5.3 Discussion ... *119*
4.6 Conclusion ... 122
Chapter 5: Introduction to Ferrofluid-Gaps for Electrical Machines ... 124
5.1 Introduction to the Ferrofluid-Gap Concept ... 124
5.1.1 Potential for Permanent Magnet Mass Reduction ... *124*
5.1.2 Potential for Acceptable Efficiency Loss ... *126*
5.2 Overview of Ferrofluid ... 128
5.2.1 Colloidal Suspensions ... *128*
5.2.2 Colloidal Stability ... *129*
5.2.3 Ferrofluid Nanoparticles ... *130*
5.2.4 Magnetic and Hydrodynamic Volume Fraction ... *131*
5.2.5 Ferrofluid Viscosity and Density ... *132*
5.2.6 Ferrofluid Thermal Properties ... *134*
5.2.7 Particle Size and Shape Distribution ... *134*
5.2.8 Néel and Brownian Relaxation ... *135*
5.2.9 Ferrofluid Synthesis ... *137*
5.2.10 Other Types of Ferrofluid Nanoparticles ... *137*
5.3 Ferrofluid-Gap Magnetic and Mechanical Behaviour ... 138
5.3.1 Ferrofluid-Gap Magnetisation Curve ... *138*
5.3.2 Ferrofluid-Gap Temperature ... *140*
5.3.3 Ferrofluid-Gap Magnetic Behaviour ... *141*
5.3.4 Ferrohydrodynamics ... *141*
5.3.5 Magnetoviscous Effects ... *144*
5.3.6 Mechanical Wear ... *146*
5.3.7 Summary of Ferrofluid Suitability for Use in Electrical Machines ... *147*
5.4 Prior Work on Ferrofluid for Electrical Machines ... 147
5.4.1 Nethe et al. "Improving the efficiency of electric machines using ferrofluids" ... *147*
5.4.2 Andy Judge "Air Gap Elimination in Permanent Magnet Machines" ... *149*
5.4.3 Zeng et al. "Asynchronous Machine with Ferrofluid in Gap: Modelling, Simulation, and Analysis" ... *151*
5.4.4 Mateev et al. "Modelling of low-speed magnetic gear with viscose ferrofluid" .. *151*
5.4.5 Ferrofluid Cooling of Electrical Machines ... *152*
5.4.6 Opportunities for Further Research of Ferrofluid-Gaps ... *153*
5.5 Conclusion ... 153
Chapter 6: Design and Fabrication of a Ferrofluid-Gap Test Rig ... 155
6.1 Design of a Ferrofluid-Gap Test Rig ... 156
6.1.1 Scaling the Test Rig Geometry ... *157*
6.1.2 Ensuring Feasibility of the Test Rig Design ... *162*
6.2 Ferrofluid-Gap Test Rig Fabrication ... 165
6.2.1 The Full Experimental Test Set-Up ... *167*
6.2.2 Detailed Test Rig Specifications ... *169*
6.2.3 Test Rig Commissioning ... *170*
6.3 Tested Ferrofluids ... 172
6.4 Conclusion ... 174
Chapter 7: Experimental Validation of Ferrofluid-Gap Behaviour ... 175
7.1 Full Ferrofluid-Gaps ... 175
7.1.1 Ferrofluid-Gap Magnetic Behaviour in Open-Load Conditions ... *176*
7.1.2 Influence of Magnetic Field on Ferrofluid-Gap Drag ... *186*
7.1.3 Full Ferrofluid-Gap in Loaded Conditions ... *206*

7.2 Results and Discussion for Partially Filled Ferrofluid-Gaps 213
7.2.1 Partially Filled Ferrofluid-Gap Voltage Output 214
7.2.2 Partially Filled Ferrofluid-Gap Open Load Torque 221
7.2.3 Summary of Partially Filled Ferrofluid-Gap Testing 223
7.3 Conclusion 224
Chapter 8: Assessment of Ferrofluid-Gaps for Direct-Drive Wind Turbine Generators 227
8.1 Specification of Ferrofluid-Gap Material Properties 227
8.2 A Magnetic Analysis of Ferrofluid-Gaps for Direct-Drive Wind Turbine Generators . 230
8.2.1 Inter-Pole Magnetic Leakage with a Ferrofluid-Gap 231
8.2.2 An Open-Load Analysis 233
8.2.3 Additional Sources of Magnetic Circuit Reluctance 236
8.2.4 Influence on Electromagnetic Torque 238
8.2.5 Impact of Armature Reaction 239
8.2.6 Summary of Magnetic Analysis 240
8.3 Ferrofluid-Gap Drag and Impact on Efficiency 241
8.3.1 Calculation of Ferrofluid-Gap Drag 241
8.3.2 Impact of Ferrofluid-Gap Drag on Efficiency 243
8.3.3 Reduction in PM Mass vs Energy Yield 246
8.3.4 Summary of Ferrofluid-Gap Drag and Efficiency Impact 250
8.4 Thermal Performance with a Ferrofluid-Gap 251
8.4.1 Ferrofluid-Gap with No Circulation 252
8.4.2 Ferrofluid-Gap for Enhanced Cooling 255
8.4.3 Summary of Thermal Performance 261
8.5 Practical Challenges of Ferrofluid-Gaps for DD WTGs 263
8.5.1 Pressure and Volume Regulation 264
8.5.2 Sealing the Ferrofluid 265
8.5.3 Ferrofluid-Gap Longevity and Cost 271
8.6 Discussion 272
8.7 Conclusion 273
Chapter 9: Conclusion 275
9.1 Chapter Summaries 275
9.2 Discussion and Conclusions 278
9.3 Further Work 279
References 281
Appendix A: Armature Current Calculation 292
Appendix B: Magnet Losses 294
Appendix C: Magnet Grades 295
Appendix D: Thermal Resistances 297
Appendix E: In-House Ferrofluid Synthesis 304
Appendix F: Nondimensionalisation of Navier-Stokes Equation 306
Appendix G: Ferrofluid Characterisation 308
Appendix H: Large Eddy Simulation Method 313

List of Figures

Figure 1.1: Picture of a GE Vernova 12 MW Haliade-X wind turbine nacelle. The direct-drive generator is in the centre of the image [11]. 2

Figure 1.2: A simplified schematic of a pole pair within a surface mounted permanent magnet wind turbine generator [14]. 3

Figure 1.3: A basic schematic demonstrating the ferrofluid-gap concept. The air-gap region between the rotor and stator, pictured on the RHS [14], is filled with ferrofluid, pictured on the LHS [16]. 3

Figure 1.4: Overview of the thesis structure. 6

Figure 2.1: A sketch (left) and CAD model (right) of the IEA 15 MW direct-drive (DD) permanent magnet (PM) wind turbine generator (WTG) reference design [13]. 10

Figure 2.2: Blade pitch, rotor speed, generator torque, and tip speed ratio over the operational wind speed range of the International Energy Agency 15 MW reference wind turbine generator design [13]. 11

Figure 2.3: Annotated diagram showing the geometrical parameters for one slot and pole pitch (not to scale). 16

Figure 2.4: Phasor diagram of the direct-drive wind turbine generator [36]. 22

Figure 2.5: Spectrum of armature magnetomotive force (MMF) harmonics for the example 15 machine, the MMF amplitude is normalised with respect to the fundamental harmonic (order of 100). 25

Figure 2.6: Permanent magnet (PM) loss of the example 15 MW machine at rated power as a function of the number of circumferential and axial segments per pole. 26

Figure 2.7: Powertrain output power and efficiency vs wind speed for the example 15 MW machine. 29

Figure 2.8: Annual dissipation of the example 15 MW machine (MWh) plotted as a function of wind speed (m/s). 30

Figure 2.9: Proportion of annual energy loss for the example 15 MW machine. 31

Figure 2.10: Finite element method (FEM) magnetic simulation of the example 15 MW outer-rotor direct-drive wind turbine generator with dimensions to scale. 1/40th of the full design is shown (10 poles and 12 slots). 33

Figure 2.11: Proportion of material cost and mass in the example 15 MW machine. 35

Figure 2.12: Total magnet cost required for the example 15 MW machine to provide a peak fundamental air-gap flux density of 1.1 T at a temperature of $120°C$ for different grades of NeFeB permanent magnets (PMs). The cost is normalised with respect to the total cost of 33H grade PMs that would be required. 39

Figure 2.13: Magnet mass required in the example 15 MW machine to provide a peak fundamental air-gap flux density of 1.1 T for various maximum magnet temperatures. The magnet mass is normalised with respect to the mass required at a temperature of $120°C$. 40

Figure 2.14: Magnet mass required in the example 15 MW machine to provide a peak fundamental air-gap flux density of 1.1 T at a temperature of $120°C$ for various air-gap clearance factors (C_{hg}). The magnet mass is normalised with respect to the mass required for $C_{hg} = 0.001$. 41

Figure 2.15: Carter factor (C_{carter}) and normalised magnet mass of the example 15 MW machine operating with a peak fundamental air-gap flux density of 1.1 T at a magnet temperature of $120°C$ for various slot opening factors (C_{SO}). Slot opening factor is defined as the ratio between the slot opening width (w_{SO}) and the slot width (w_{slot}): a value of 1 designates an open slot. The magnet mass is normalised with respect to the mass required when ($C_{SO} = 1$). 42

Figure 3.1: Illustration of a closed-loop air cooling system for a 10+ MW direct-drive wind turbine generator taken from the Heatex website [57]. 45

Figure 3.2: Illustration of an armature coil with direct liquid cooling (a), and an inner-rotor machine with a water jacket (b) [56]. 46

Figure 3.3: Illustration (not to scale) of slot- and pole-pitch with geometrical parameters and components labelled: 1- stator structural frame, 2- water jacket wall, 3- water jacket duct, 4- stator yoke, 5- stator tooth, 6- stator tooth tip, 7- slot liner, 8 armature coil, 9- slot wedge, 10- air-gap, 11- permanent magnet, 12- rotor yoke, and 13- rotor structural frame. 53

Figure 3.4: Illustration of Taylor-Couette flow [67]. 55

Figure 3.5: Illustration of a cylinder in cross flow [71]. 58

Figure 3.6: Illustration of a spiral water jacket [56]. 60

Figure 3.7: Detailed diagram of the lumped parameter thermal network model for pole- and slot-pitch. Colour coded for improved clarity: conductive resistances (white), convective resistances (pink), negative resistances (red), radial direction (black), azimuthal direction (blue), axial direction (green). Point A represents the boundary of the internal coils and the end-windings. Points 1, 2, and 3 indicate periodic boundary conditions. 65

Figure 3.8: Simplified diagram of the lumped parameter thermal network model for pole- and slot-pitch. Colour coded for improved clarity: convective resistances (pink), negative resistances (red), lumped resistances (grey), radial direction (black), azimuthal direction (blue), axial direction (green). Point A represents the boundary of the internal coils and the end-windings. 66

Figure 3.9: Detailed (left) and simplified (right) diagrams of the lumped parameter thermal network model for the end-windings. Colour coded for improved clarity: conductive resistances (white), convective resistances (pink), negative resistances (red), lumped resistances (grey), radial direction (black), azimuthal direction (blue), axial direction (green). Point A represents the boundary of the internal coils and the end-windings. 67

Figure 3.10: Illustration of a circular tube continuous fin type heat exchanger (a), and a plate-fin heat exchanger (b) [71]. 68

Figure 3.11: Performance of the air-cooling strategy applied to the example outer-rotor 15 MW machine. Key component temperatures and the idealised power required to drive the air flow is plotted for a range of volumetric flow rates. 76

Figure 3.12: Performance of the liquid-cooling strategy applied to the example outer-rotor 15 MW machine. Key component temperatures and the idealised power required to drive the coolant flow are plotted for a range of volumetric flow rates. 77

Figure 3.13: Comparison of component temperatures in the example inner- and outer-rotor 15 MW machines over a range of specific current loading (A_1). 78

Figure 3.14: The idealised power required to drive both the closed- and open-loop flow through both the air-to-air and liquid-to-air heat exchangers is presented for various constraints on the heat exchanger volume. This is calculated for the example outer-rotor 15 MW machine with a specific current loading (A_1) of 80 kA/m. 79

Figure 3.15: Temperature rise of an air flow through the air-gap region of the air-cooled example inner-rotor 15 MW machine plotted for a range of axial velocity and inlet air temperatures. 81

Figure 3.16: Peak coil temperature and rated power factor of the example outer-rotor 15 MW machine plotted for various values of the slot height factor (C_{SH}). Slot height factor is defined as the ratio between the slot height (h_{slot}) and the slot width (w_{slot}). 82

Figure 4.1: Armature inductance (L_s) of the example 15 MW machine for a range of air-gap clearance factors (C_{hg}), the magnet height is specified such that a peak air-gap flux density of 1.1 T is achieved assuming a magnet temperature of $120°C$. NeFeB 40H and 52H grade permanent magnets (PMs) are compared. 88

Figure 4.2: Risk of permanent magnet (PM) demagnetisation (C_{demag}) in the example 15 MW machine for a range of air-gap clearance factors (C_{hg}), the magnet height is specified such that a peak air-gap flux density of 1.1 T is achieved assuming a magnet temperature of $120°C$. NeFeB 40H and 52H grade permanent magnets (PMs) are compared. A negative value of C_{demag} indicates a large risk of demagnetisation in the event of a short circuit fault. 90

Figure 4.3: Peak air-gap flux density of the rotor and stator field compared in the example 15 MW machine for a range of air-gap clearance factors (C_{hg}), the magnet height is specified such that a peak

air-gap flux density of 1.1 T is achieved assuming a magnet temperature of $120°C$. NeFeB 40H and 52H grade permanent magnets (PMs) are compared. 91

Figure 4.4: Example of air-gap non-uniformity in a large synchronous generator from the work of Palani *et al.* [88]. The measured air-gap clearance is normalised with respect to the nominal air-gap clearance. Measurements were taken along the axial length of the machine at the non-drive end (NDE), the middle of the machine, and the drive end (DE). 92

Figure 4.5: Simulation results for the spatial distribution of radial magnetic flux density in the air-gap of a 74 MW wound-rotor salient pole hydro-generator compared with air-gap clearance specified according to the design and with a nonuniform air-gap specified according to real measurements of the machine [89]. 92

Figure 4.6: Various approaches to rotor/stator structural design [93]. 94

Figure 4.7: Image of a segmented stator direct-drive (DD) wind turbine generator (WTG) design from Siemens Gamesa (a), and a photo of a GE Vernova Haliade 6 MW DD WTG rotor (b) [94]. 94

Figure 4.8: Illustration of different modes (M) of air-gap non-uniformity. The black circle represents a uniform air-gap, the blue dashed line represents a nonuniform air-gap which varies with circumferential angle (θ) according to the value of M. 95

Figure 4.9: Sketch of how the magnitude of the magnetic force and counteracting structural forces vary in the event of an air-gap deformation. 103

Figure 4.10: Stiffness factor $(\mathrm{C_K})$ plotted as a function of initial air-gap deformation (δ_{i}) for various limits imposed on the total air-gap deformation (δ_{mag}). Air-gap deformation is plotted as a percentage of the nominal air-gap clearance. 104

Figure 4.11: Illustration of a mode 0 component of radial Maxwell stress $(\Delta\sigma_{\mathrm{M0}})$ acting on a simplified rim model of an inner rotor/stator structure (a), and the resulting tension acting on a rim segment (b). 106

Figure 4.12: Illustration of a mode 2 component of radial Maxwell stress $(\Delta\sigma_{\mathrm{M2}})$ acting on a simplified rim model of an inner rotor/stator structure (a), and the resulting tension/compression and bending moments acting on a rim segment (b). 106

Figure 4.13: Illustration of unbalanced magnetic pull (UMP) acting on the wind turbine generator rotor shaft [50]. 107

Figure 4.14: Illustration of the stator geometry and the magnitude of radial deformation due to a Maxwell stress harmonic with a mode number (M) of 0-4 (not to scale). 109

Figure 4.15: Normalised peak radial displacement $(\hat{\delta}_{\mathrm{g,Mnorm}})$ of the disc-rim structure compared for a range of radial Maxwell stress mode numbers (M). A baseline case is compared against cases in which the rim or disc thickness has been doubled. The peak radial displacement is normalised with respect to the baseline peak radial displacement when $\mathrm{M} = 0$. 111

Figure 4.16: Flux density plot of entire simulation domain (LHS) with a close-up (top-right), and a close-up of the mesh (bottom-right). 117

Figure 4.17: 2D FFT spectrum of finite element method (FEM) simulation results overlaid with corresponding results from the analytical model, the harmonic sources are: MMF and stator slots $(\sigma_{\mathrm{n'l'}})$, MMF and rotor dissymmetry $(\sigma_{\mathrm{n'p'}})$, MMF and stator dissymmetry $(\sigma_{\mathrm{n'q'}})$, stator slot and rotor dissymmetry intermodulation $(\sigma_{\mathrm{n'lp}})$, stator slot and stator dissymmetry intermodulation $(\sigma_{\mathrm{n'lq}})$, and rotor dissymmetry and stator dissymmetry intermodulation $(\sigma_{\mathrm{n'pq}})$. 119

Figure 4.18: Sketch of potential air-gap radial stress harmonics assuming a non-uniform air-gap with p and q ranging from 1 to 100, the harmonic sources are: MMF and stator slots $(\sigma_{\mathrm{n'l'}})$, MMF and rotor dissymmetry $(\sigma_{\mathrm{n'p'}})$, MMF and stator dissymmetry $(\sigma_{\mathrm{n'q'}})$, stator slot and rotor dissymmetry intermodulation $(\sigma_{\mathrm{n'lp}})$, stator slot and stator dissymmetry intermodulation $(\sigma_{\mathrm{n'lq}})$, and rotor dissymmetry and stator dissymmetry intermodulation $(\sigma_{\mathrm{n'pq}})$. 120

Figure 5.1: Schematic of a 1D magnetic circuit for a pole pair. 126

Figure 5.2: Estimate for the loss in generator efficiency $(\Delta\zeta_{\mathrm{gen}})$ due to fluid flow within the air-gap region

for a range of rated input powers (P_{shaft}) and gear ratios (i_{GR}) assuming laminar flow and a dynamic viscosity (η_{FF}) of 0.1 Pa.s. 128

Figure 5.3: A ferrofluid colloid surrounded by carrier fluid molecules with random velocities [114]. ... 129

Figure 5.4: (a) Colloid with a surfactant outer layer [115]. (b) Colloid with an electrostatic outer layer [15]. 130

Figure 5.5: Depiction of multi-domain magnetorheological fluid (MRF) particles and single-domain ferrofluid particles. 131

Figure 5.6: Ferrofluid relative viscosity (η_{rel}) as a function of hydrodynamic volume fraction (ϕ_H) [127]. 133

Figure 5.7: Transmission electron microscopy (TEM) image of ferrofluid nanoparticles synthesised by Botez *et al.* (a) [131], and in-house according to the protocol provided in Appendix E (b). 135

Figure 5.8: (a) Illustration of Brownian relaxation, (b) illustration of Néel relaxation [132]. 136

Figure 5.9: Relative permeability of ferrofluid ($\mu_{r,FF}$) for a range of magnetic flux densities (B) and magnetic volume fractions (ϕ_M). 140

Figure 5.10: Picture of in-house synthesised ferrofluid exposed to a magnetic field, spikes (i.e. Rosensweig instabilities) can be observed. 142

Figure 5.11: Change in ferrofluid viscosity due to an external magnetic field for various ferrofluid purities, F1 indicates the purest sample and F5 the least pure [150]. 145

Figure 5.12: In the top image the external magnetic field is collinear with the axis of vorticity and there is no rotational viscosity, in the bottom image they are out of alignment resulting in a magnetic torque and rotational viscosity [151]. 146

Figure 5.13: 2D magnetic simulation results of A. Nethe *et al.* showing 'magnetic lines of force' at two different relative rotor-stator positions [156]. 148

Figure 5.14: Increase in induction motor efficiency due to a ferrofluid-gap for various rotational speeds and torque loads. 149

Figure 5.15: Experimental results of Andy Judge showing comparing voltage output with an air-gap and a ferrofluid-gap and a comparison with predicted values [157]. 150

Figure 6.1: Picture of the ferrofluid-gap test rig rotor (left) and stator (right). 156

Figure 6.2: Contribution to ferrofluid-gap turbulence from geometry and velocity (K_{geo}) vs wind turbine shaft power (P_{shaft}), range estimated according to parameters in Table 1 and designs referenced from literature [13], [17], [22], [27], [43], [77], [78]. Target value of test rig K_{geo} is indicated with a dashed line. 161

Figure 6.3: Contribution to ferrofluid-gap turbulence from geometry and velocity (K_{geo}) at a rotational speed of 1500 RPM as a function of test rig geometry: air-gap clearance (h_g) and rotor radius (r_r). 161

Figure 6.4: Annotated diagram of test rig rotor core geometry. 164

Figure 6.5: Current density of rotor winding (J_{RW}) vs rotor radius (r_r) for a range of rotor slot fill factors (C_{fill}) at a target K_{geo} of $2 \times 10^{-4}\ m^2/s$ for a rotational speed of 1500 RPM. 165

Figure 6.6: Key steps in fabrication of the test rig rotor: (A) The original off-the-shelf induction motor rotor prior to any modifications. (B) Original rotor core removed and custom 2-pole rotor core attached to the shaft. (C) Rotor core wound with 600 turns of 1 mm diameter copper conductor. (D) Rotor cast in epoxy. (E) Rotor after epoxy had set and mould removed. (F) Rotor after being machined. (G) Rotor being wrapped with a 0.25 mm thick carbon fibre sheet. (H) Completed test rig rotor. 166

Figure 6.7: Key steps in fabrication of the stator and final assembly of the test rig: (I) The original off-the-shelf stator. (J) Internal mould placed within the stator. (K) The stator cast in epoxy. (L) The stator after having inner bore wrapped with 0.25 mm carbon fibre sheet and with filling/draining ports added. (M) Rotor placed into stator, each end of air-gap sealed with a radial lip seal and silicone sealant. (N) Final assembly of test rig, non-drive end pictured showing the slip rings for rotor winding excitation. 167

Figure 6.8: Block diagram of the overall experimental test set-up. 168

Figure 6.9: Photos of the overall experimental test set-up in open load conditions. 168

Figure 6.10: 3D scan of a test rig stator tooth. 170

Figure 6.11: Image of a finite element method (FEM) simulation of the test rig with a rotor winding magnetomotive force (MMF) of 1500 A. 171

Figure 6.12: Comparison of test rig air-gap flux density with a rotor winding magnetomotive force (MMF) of 1500 A obtained via measurement with a gaussmeter and FEM (finite element method) simulation. 171

Figure 6.13: Time-averaged torque (1 s window) and torque harmonics measured by the torque transducer at a test rig rotational speed of 1510 RPM. 172

Figure 7.1: Change RMS Voltage measurement vs number of voltage waveform samples, rotational speed of 302 RPM and rotor winding magnetomotive force (MMF) of 1260 A. 176

Figure 7.2: Open-load air-gap normalised voltage-speed constant ($\mathrm{Z_{VAI}}$) plotted over a range of rotor winding magnetomotive force (MMF). Results are compared for when the MMF zeroing procedure is and is not followed. 178

Figure 7.3: Comparison of open-load voltage output for a rotor winding magnetomotive force (MMF) of 59 A and 1861 A. 179

Figure 7.4: RMS open-load voltage vs rotor winding magnetomotive force (MMF). A linear fit is extrapolated from rotor winding MMF values of 300-1800 A. 180

Figure 7.5: RMS open-load voltage output of each ferrofluid-gap compared against an air-gap for the same values of rotor winding magnetomotive force (MMF). 181

Figure 7.6: Coefficient of determination ($\mathrm{R^2}$) of normalised voltage-speed constant ($\mathrm{Z_{VAI}}$) obtained for each ferrofluid and an air-gap plotted over a range of rotor winding magnetomotive force (MMF). 181

Figure 7.7: Normalised open-load voltage harmonic amplitudes with an air-gap and a EFH1 ferrofluid-gap for a range of rotational speeds. The harmonic amplitudes are normalised with respect to the fundamental harmonic amplitude for each rotational speed and rotor winding magnetomotive force (MMF) value. 182

Figure 7.8: Normalised voltage-speed constant ($\mathrm{Z_{VAI}}$) plotted for a range of rotor winding magnetomotive force (MMF) for an air-gap and each tested ferrofluid-gap. 183

Figure 7.9: Comparison between the experimentally measured and simulated estimate for the increase in open-load voltage with each ferrofluid-gap compared to an air-gap. 184

Figure 7.10: Comparison between the experimentally measured and simulated change in the open-load line-to-neutral voltage waveform of the test rig due to a EFH1 ferrofluid-gap compared to an air-gap. Data is presented for a rotational speed of 1510 RPM and a rotor winding magnetomotive force of 300 and 1860 A. 185

Figure 7.11: Example of torque variation due to excitation of the rotor windings. 188

Figure 7.12: Probability density and a quantile-quantile plot of measurements of torque variation at a rotational speed of 1208 RPM and an excited rotor winding magnetomotive force (MMF) of 2400 A. 189

Figure 7.13: Combined error in the measurement of open-load magnetic torque for various rotational speeds and values of rotor winding magnetomotive force (MMF). The torque transducer measurement error ($\pm 0.0085\ \mathrm{Nm}$) is included for comparison. 189

Figure 7.14: Surface plot of open-load magnetic torque (Nm) as a function of line-to-neutral RMS voltage output (V) and rotational speed (RPM). 191

Figure 7.15: Open-load magnetic torque (Nm) measured at standstill over a range of rotor-stator relative positions (°). 191

Figure 7.16: Example of time-averaged torque history (3 s window) during a test run with a Custom ferrofluid-gap. 192

Figure 7.17: Experimentally obtained measurements for the increase in ferrofluid-gap drag due to the

test rig magnetic field in open-load conditions for a range of rotor winding magnetomotive force (MMF) and rotational speeds (RPM). 194

Figure 7.18: Estimation of ferrofluid-gap drag in the absence of a magnetic field. On the LHS the change in drag with respect to (w.r.t) a relatively low rotational speed is compared for experimental measurements and either simulation or analytical calculations. On the RHS an estimate for the total ferrofluid-gap drag is provided. 196

Figure 7.19: Experimentally measured increase in ferrofluid-gap drag due various values of rotor winding magnetomotive force (MMF) over a range of rotational speeds (RPM). 197

Figure 7.20: Analytical estimate for the increase in ferrofluid-gap drag due the rotor winding magnetomotive force (MMF). The experimentally investigated values of rotor winding MMF are highlighted. 200

Figure 7.21: Plot of ferrofluid-gap dynamic viscosity (mPa.s) overlaid on a plot of test rig flux density magnitude (T) obtained from COMSOL Multiphysics 6.1. 203

Figure 7.22: Comparison of surface-averaged shear stress (Pa) obtained from multi-physics simulations of EFH1 ferrofluid-gap flow for a rotor winding magnetomotive force (MMF) of 0 and 1800 A at rotational speeds of 604 and 1510 RPM. 204

Figure 7.23: Single-phase inductance of the test rig armature windings at standstill with an EFH1 ferrofluid-gap and an air-gap for a rotor winding magnetomotive force (MMF) of 120 A and 1800 A over a range of rotor-stator relative positions. 207

Figure 7.24: d- and q-axis single-phase inductance of the test rig armature windings with an air-gap and a EFH1 ferrofluid-gap at standstill over a range of rotor winding magnetomotive force (MMF). 208

Figure 7.25: d-axis single-phase inductance of the test rig armature windings for an air-gap and a EFH1 ferrofluid-gap over a range of rotor winding magnetomotive force (MMF) obtained from finite element method (FEM) simulation. 208

Figure 7.26: Example of torque variation due to excitation of the rotor windings with a 5.3 Ω load. .. 209

Figure 7.27: Terminal voltage (V) and torque (Nm) output of the test rig with a 5.3 Ω load for an air-gap, EFH1 ferrofluid-gap, and Custom ferrofluid-gap over a range of rotational speeds (RPM) and rotor winding magnetomotive force (MMF). 210

Figure 7.28: Comparison between the increase in terminal voltage and torque measured experimentally with an EFH1 ferrofluid-gap compared to an air-gap and estimated from finite element method (FEM) simulations over a range of rotational speeds (RPM) and for various values of rotor winding magnetomotive force (MMF). A comparison is made where iron reluctance is neglected in the simulation and when it is approximated. 211

Figure 7.29: A comparison between the experimentally measured increase in torque with an EFH1 ferrofluid-gap compared to an air-gap and estimated from finite element method (FEM) simulations. It is highlighted that an incorrect formulation for Maxwell shear stress leads to an overestimation of the increase in torque due to a ferrofluid-gap. 212

Figure 7.30: Increase in open-load voltage with a partially filled EFH1 ferrofluid-gap compared to an air-gap for a variety of rotational speeds (RPM), ferrofluid-gap fill factors ($C_{fill,FF}$), and rotor winding magnetomotive force (MMF) values. 215

Figure 7.31: Increase in open-load voltage with a partially filled Custom ferrofluid-gap compared to an air-gap for a variety of rotational speeds (RPM), ferrofluid-gap fill factors ($C_{fill,FF}$), and rotor winding magnetomotive force (MMF) values. 216

Figure 7.32: Comparison between the normalised increase in voltage due to a partially filled EFH1 and Custom ferrofluid-gap compared to an air-gap for a range of ferrofluid-gap fill factors ($C_{fill,FF}$) at a rotational speed of 302 RPM and a rotor winding magnetomotive force (MMF) of 1800 A. The increase in voltage is normalised with respect to the increase obtained with a full ferrofluid-gap. 217

Figure 7.33: Increase in open-load voltage for a partially filled EFH1 ferrofluid-gap with a fill factor of ($C_{fill,FF}$) 0.38 compared to an air-gap over a range of rotational speeds (RPM) and rotor winding magnetomotive force (MMF) values. 218

Figure 7.34: Increase in open-load voltage for a partially filled Custom ferrofluid-gap with a fill factor of

($C_{fill,FF}$) 0.38 compared to an air-gap over a range of rotational speeds (RPM) and rotor winding magnetomotive force (MMF) values. 219

Figure 7.35: Comparison between the normalised increase in voltage due to a partially filled EFH1 and Custom ferrofluid-gap compared to an air-gap for a ferrofluid-gap fill factors ($C_{fill,FF}$) of 0.38 over a range of rotational speeds (RPM) with a rotor winding magnetomotive force (MMF) of 2160 A. The increase in voltage is normalised with respect to the increase obtained with a full ferrofluid-gap. 220

Figure 7.36: Increase in terminal voltage (%) with a partially filled EFH1 ferrofluid-gap compared to an air-gap with a load of 5.3 Ω over a range of rotational speeds (RPM) and a rotor winding magnetomotive force (MMF) of 1200 and 1800 A. 220

Figure 7.37: Examples of time averaged torque history (3 s window) during test runs with a partially filled EFH1 and Custom ferrofluid-gap with $C_{fill,FF} = 0.38$ and an excited rotor winding magnetomotive force (MMF) of 2400 A. 221

Figure 7.38: Experimentally obtained measurements for the increase in torque resulting from excitation of the rotor windings with a partially filled EFH1 and Custom ferrofluid-gap with $C_{fill,FF} = 0.38$ over a range of rotational speed (RPM) and for various excited rotor winding magnetomotive force (MMF) values. 222

Figure 8.1: Positioning of cutline A (LHS) and cutline B (RHS). 232

Figure 8.2: Leakage efficiency (ζ_{leak}) for air- and ferrofluid-gap with a magnetic volume fraction (ϕ_M) of 0.2 compared for a range of magnet width factors ($C_{PM,w}$) and air-gap clearance factors (C_{hg}). 233

Figure 8.3: Increase in magnetic flux (%) due to a ferrofluid-gap with a magnetic volume fraction (ϕ_M) of 0.2 in comparison to an air-gap for a range of air-gap clearance factors (C_{hg}). Results from the 1D magnetic circuit model and the finite element method (FEM) simulation are compared. 235

Figure 8.4: Reduction in permanent magnet (PM) mass for a range of magnetic volume fractions (ϕ_M) based on an open-load condition. Various air-gap magnetic flux densities (B_g) are compared. 235

Figure 8.5: Increase in magnetic flux (%) due to a ferrofluid-gap with a magnetic volume fraction (ϕ_M) of 0.2 compared to an air-gap calculated for a range of magnet height factors ($C_{PM,h}$) estimated from a 1D magnetic circuit model and finite element method (FEM) simulations. Results are presented for a fractional slot and an integer slot direct-drive (DD) wind turbine generator (WTG) [13], [22]. 236

Figure 8.6: Increase in magnetic flux (%) due to a ferrofluid-gap with a magnetic volume fraction (ϕ_M) of 0.2 compared to an air-gap calculated for a range of normalised tooth width to slot pitch ratios (w_{tooth}/τ_{slot}). Obtained from finite element method (FEM) simulations with iron reluctance included. 237

Figure 8.7: Potential reduction in permanent magnet (PM) mass (%) achievable with a ferrofluid-gap with a magnet volume fraction (ϕ_M) of 0.2 for a range of air-gap clearance values assuming a magnet glue and reinforcement thickness of 0.1 mm and 0.5 mm respectively. 238

Figure 8.8: Average electromagnetic shear stress (kPa) developed for an air- and ferrofluid-gap with a magnetic volume fraction (ϕ_M) of 0.2 for a range of magnet heights obtained from finite element method (FEM) simulations. The potential reduction in permanent magnet (PM) mass due to the ferrofluid-gap is plotted. 239

Figure 8.9: Increase in electromagnetic torque (%) due to a ferrofluid-gap with a magnetic volume fraction (ϕ_M) of 0.2 plotted over a range of load angles (°) for linear and nonlinear iron permeability. Results are obtained from finite element method (FEM) simulations. 240

Figure 8.10: Torque coefficient (C_T) vs Reynolds number (Re) for a Taylor-Couette (TC) flow with a radius ratio of 0.998. The blue dashed line represents an analytical calculation for laminar flow, the orange squares are data points obtained from computational fluid dynamics (CFD) simulations, the black dotted line is a power law fit of the simulation data, and the pink dashed line is a constant value approximated for the region of laminar-turbulent transition. 243

Figure 8.11: Loss in efficiency (%) of the example 15 MW direct-drive (DD) wind turbine generator (WTG) resulting from ferrofluid-gap drag at rated speed and a temperature of $100°C$ for a range of magnetic volume fraction (ϕ_M). An upper- and lower-bound estimate is provided assuming turbulent and laminar flow respectively. 244

Figure 8.12: Loss in efficiency (%) of the example 15 MW direct-drive (DD) wind turbine generator (WTG) resulting from ferrofluid-gap drag at rated speed for various magnetic volume fractions (ϕ_M) and a range of ferrofluid temperatures ($°C$). 245

Figure 8.13: Loss in efficiency (%) resulting from ferrofluid-gap drag at rated speed for various direct-drive (DD) wind turbine generator (WTG) designs obtained from scaling equations subject to a range of input powers (P_{shaft}). Turbulent flow is assumed at a ferrofluid temperature of $100°C$ for various magnetic volume fractions (ϕ_M). 246

Figure 8.14: Reduction in permanent magnet (PM) mass (kg) due to a ferrofluid-gap in the example 15 MW direct-drive (DD) wind turbine generator (WTG) for a range of magnetic volume fractions (ϕ_M), and the additional annual energy losses (MWh) due to ferrofluid-gap drag for a range of ϕ_M and ferrofluid temperatures ($°C$). 248

Figure 8.15: The net cost saving taking into account the reduction in permanent magnet (PM) mass and the reduced efficiency of the example 15 MW direct-drive (DD) wind turbine generator (WTG) due to a ferrofluid-gap for a range of magnetic volume fraction (ϕ_M) and various ferrofluid-gap temperatures ($°C$). Assumed magnet cost of $29,130 per tonne and cost of energy of 152.7 $/MWh. 249

Figure 8.16: The net cost saving taking into account the reduction in permanent magnet (PM) mass and the reduced efficiency of the example 15 MW direct-drive (DD) wind turbine generator (WTG) due to a ferrofluid-gap for a range of magnetic volume fraction (ϕ_M) and various ferrofluid-gap temperatures ($°C$). Assumed magnet cost of $58,260 per tonne and cost of energy of 80.9 $/MWh. 250

Figure 8.17: Heat transfer coefficient into the air-gap region (α_g) for a ferrofluid-gap at a temperature of $100°C$ for a range of magnetic volume fractions (ϕ_M). A comparison is made with an air-gap. 252

Figure 8.18: Comparison between the thermal performance of the example 15 MW direct-drive (DD) wind turbine generator (WTG) with an air-gap and a ferrofluid-gap with a magnetic volume fraction (ϕ_M) of 0.1 with a forced-air cooling strategy. 253

Figure 8.19: Comparison between the thermal performance of the example 15 MW direct-drive (DD) wind turbine generator (WTG) with an air-gap and a ferrofluid-gap with a magnetic volume fraction (ϕ_M) of 0.1 with a liquid cooling strategy. 254

Figure 8.20: Temperature rise of ferrofluid flow through the air-gap region of the air-cooled example inner-rotor 15 MW machine with a specific current loading of 60 kA/m plotted for a range of axial velocities (m/s) and a variety of inlet temperatures ($°C$). 256

Figure 8.21: Ferrofluid axial temperature rise ($°C$) as a function of pressure drop (Pa) and idealised power required (W) to drive the axial ferrofluid flow for a variety of inlet temperatures. 258

Figure 8.22: Comparison between the thermal performance of the example 15 MW direct-drive (DD) wind turbine generator (WTG) with an air-gap and an axial ferrofluid-gap flow with a magnetic volume fraction (ϕ_M) of 0.1 with a forced-air cooling strategy. 260

Figure 8.23: Comparison between the thermal performance of the example 15 MW direct-drive (DD) wind turbine generator (WTG) with an air-gap and an axial ferrofluid-gap flow with a magnetic volume fraction (ϕ_M) of 0.1 with a liquid cooling strategy. 261

Figure 8.24: Loss in lifetime revenue (k$) of the example 15 MW direct-drive (DD) wind turbine generator (WTG) plotted against the production-based availability factor (ζ_{av}). 264

Figure 8.25: (a) Components of a ferrofluid rotary shaft seal. (b) Sketch of ferrofluid-air boundaries at the sealing interface [145]. 267

Figure 8.26: Estimate for magnetic flux density (T) required in the sealing interface of a magnetic seal applied to the IEA 15 MW reference direct-drive (DD) wind turbine generator (WTG) [13]. 269

Figure 8.27: Estimate for magnetic flux density (T) required in the sealing interface of a magnetic seal plotted as a function of air-gap diameter (m). 270

Figure 8.28: Illustration of a partially-filled ferrofluid-gap in the IEA 15 MW reference wind turbine generator design [13]. 271

List of Tables

Table 2.1: Input parameters and material properties for wind turbine generator design procedure. 13
Table 2.2: Specification of example 15 MW outer-rotor direct-drive wind turbine generator. 31
Table 2.3: Densities and specific costs of key materials. 34
Table 3.1: Heat sources in the lumped parameter thermal network model. 64
Table 3.2: Liquid-to-air heat exchanger specifications. 68
Table 3.3: Air-to-air heat exchanger specifications. 72
Table 3.4: Additional generator parameters and material properties for the thermal model. 74
Table 4.1: Direct-drive wind turbine generator air-gap clearance specification and allowable air-gap deformation in various studies. 85
Table 4.2: Summary of various sources of initial air-gap deformation. 112
Table 6.1: Range of wind turbine parameters. 159
Table 6.2: Test rig parameters for feasibility study. 165
Table 6.3: Components used in the full experimental set-up. 168
Table 6.4: Detailed test rig specifications. 169
Table 6.5: Summary of tested ferrofluid properties. 173
Table 8.1: Summary of assumed ferrofluid properties and relevant equations. 229
Table 8.2: Key parameters of the 3 MW integer-slot direct-drive wind turbine generator. 231

Nomenclature

Roman Letters

Symbol	Description	Units
A	Area	m^2
A_1	Specific current loading	$\mathrm{A/m}$
B	Magnetic flux density	T
$C_{\mathrm{fill,FF}}$	Ferrofluid-gap fill factor	–
$C_{\mathrm{PM,h}}$	Magnet height factor	–
$C_{\mathrm{PM,w}}$	Magnet width factor	–
$C_{\mathrm{rot,vis}}$	Rotational viscosity factor	–
C_{carter}	Carter factor	–
C_{demag}	Magnet demagnetisation risk parameter	–
C_{fill}	Slot fill factor	–
C_{HE}	Liquid-to-air heat exchanger scale factor	–
C_{hg}	Air-gap clearance factor	–
C_K	Stiffness factor	–
C_{leak}	Inter-pole magnetic leakage coefficient	–
C_{SH}	Slot height factor	–
C_{SO}	Slot opening factor	–
$C_{\mathcal{T}}$	Torque coefficient	–
C_{w1}	Fundamental winding factor	–
C_δ	Harmonic air-gap leakage factor	–
C_ε	Coefficient of thermal expansion	$1/\mathrm{K}$
C_ϱ	Resistivity temperature coefficient	$1/\mathrm{K}$
c_p	Specific heat capacity	$\mathrm{J/kg.K}$
Ca	Cavitation number	–
D	Diameter	m
D_h	Hydraulic diameter	m
E	Modulus of elasticity	Pa
E_p	Induced electromotive force (RMS)	V
$\mathcal{F}$	Magnetomotive force	A
f_0	Steinmetz reference frequency	Hz
f_e	Electrical frequency in Hertz	Hz
f_M	Kelvin body force	$\mathrm{N/m}^3$
g_{eff}	Effective magnetic air-gap	m
G	Mass velocity	$\mathrm{kg/s}$
Gr	Grashof number	–
H	Magnetic field strength	$\mathrm{A/m}$
h	Height	m

I	Current	A
i_{GR}	Gear ratio	$-$
j	Colburn factor	$-$
J	Current density	$\mathrm{A/m^2}$
K	Energy gradient method K parameter	$-$
K_{geo}	Contribution to turbulence due to test rig geometry and	$\mathrm{m^2/s}$
K_{mag}	Magnetic stiffness	$\mathrm{N/m}$
K_{str}	Structural stiffness	$\mathrm{N/m}$
k	Thermal conductivity	$\mathrm{W/m.K}$
l	Length	m
L	Inductance	H
$\mathcal{L}(\xi)$	Langevin function	$-$
$\mathcal{M}$	Mode of air-gap deformation	$-$
m	Magnetic moment	$\mathrm{A.m^2}$
M	Magnetisation	$\mathrm{A/m}$
m	Mass	kg
$\dot{m}$	Mass flow rate	$\mathrm{kg/s}$
M_d	Spontaneous magnetisation	$\mathrm{A/m}$
M_s	Saturation magnetisation	$\mathrm{A/m}$
$N_{\mathrm{duct,turn}}$	Number of water jacket duct turns	$-$
$N_{\mathrm{HE,tube}}$	Number of liquid-to-air HE tubes	$-$
N_{duct}	Number of air-ducts	$-$
N_{phase}	Number of phases	$-$
N_{pole}	Number of poles	$-$
N_{PP}	Number of pole pairs	$-$
N_r	Number of test rig rotor winding turns	$-$
N_{rep}	Number of measurements	$-$
N_s	Number of turns per phase	$-$
N_{sec}	Number of sectors	$-$
N_{slot}	Number of slots	$-$
N_{SPP}	Number of slots per pole per phase	$-$
N_{TC}	Number of turns per coil	$-$
$N_{\Delta t}$	Number of timesteps	$-$
$N_{\Delta\theta}$	Number of spatial samples	$-$
Nu	Nusselt number	$-$
$\mathcal{P}$	Magnetic permeance	H
p	Pressure	Pa
P	Power	W
$\dot{P}_{\mathrm{Fe,eddy}}$	Stator hysteresis loss coefficient	$\mathrm{W/kg}$
$\dot{P}_{\mathrm{Fe,hys}}$	Stator eddy loss coefficient	$\mathrm{W/kg}$
Pr	Prandl number	$-$

$\dot{Q}$	Heat flow rate	W
r	Radius	m
R	Thermal resistance	$\mathrm{K/W}$
$\mathcal{R}$	Magnetic reluctance	$1/\mathrm{H}$
Ra	Rayleigh number	$-$
Re	Reynolds number	$-$
T	Temperature	K
$\mathcal{T}$	Torque	Nm
t	Thickness	m
t	Time	s
t_B	Brownian relaxation timescale	s
t_{eff}	Effective relaxation timescale	s
t_N	Néel relaxation timescale	s
Ta	Taylor number	$-$
U_T	Overall heat transfer coefficient	$\mathrm{K/W}$
v	Velocity	$\mathrm{m/s}$
V	Volume	$\mathrm{m^3}$
$\dot{V}$	Volumetric flow rate	$\mathrm{m^3/s}$
$\mathcal{V}$	Voltage	V
w	Width	m
Z_{VAI}	Test rig voltage-speed constant normalized with respect to rotor winding current	$\mathrm{V/A.RPM}$

Greek letters

Symbol	Description	Units
ε_θ	Circumferential strain	$-$
ν	Kinematic viscosity	$\mathrm{m^2/s}$
α	Heat transfer coefficient	$\mathrm{W/m^2.K}$
β_θ	Angle between the axis of vorticity and magnetic field direction	rad
$\dot{\gamma}$	Shear rate	$1/\mathrm{s}$
$\Gamma_{\mathrm{A,V}}$	Heat transfer area/volume	$1/\mathrm{m}$
$\Gamma_{\mathrm{A,V}}$	Gas-side heat transfer area to total volume ratio	$1/\mathrm{m}$
$\Gamma_{\mathrm{FF,FA}}$	Free-flow area to frontal area ratio	$-$
$\Gamma_{\mathrm{r,s}}$	Ratio between the rotor radius, and the stator inner radius	$-$
Γ_{gen}	Generator aspect ratio	$-$
Γ_{int}	Ratio between dipole-dipole interaction and thermal energy	$-$

Γ_{TC}	Taylor-Couette aspect ratio	$-$
Γ_{TSR}	Tip speed ratio	$-$
δ	Deformation magnitude	m
ϵ_{HE}	Heat exchanger effectiveness	$-$
$\zeta_{0,\mathrm{a}}$	Surface efficiency	$-$
ζ_{aero}	Rated aerodynamic power extraction efficiency	$-$
ζ_{av}	Production-based availability factor	$-$
ζ_{conv}	Converter efficiency at rated power	$-$
ζ_{drag}	Generator efficiency with fluid in air-gap	$-$
ζ_{fin}	Fin efficiency	$-$
ζ_{gen}	Generator efficiency at full load	$-$
ζ_{leak}	Magnetic leakage factor	$-$
ζ_{PT}	Powertrain efficiency at full load	$-$
η	Dynamic viscosity	$\mathrm{Pa.s}$
η_{rel}	Relative viscosity	$-$
η_{rot}	Additional viscosity due to rotational viscosity	$\mathrm{Pa.s}$
θ	Circumferential angle	rad
κ	Magnet electrical conductivity	$\mathrm{S/m}$
μ_r	Relative permeability	$-$
ξ	Langevin parameter	$-$
ρ	Density	$\mathrm{kg/m^3}$
ϱ	Resistivity	$\Omega\mathrm{m}$
ς	Friction factor	$-$
σ_r	Radial Maxwell stress	Pa
σ_t	Tangential Maxwell Stress	Pa
τ_{pole}	Pole pitch	m
τ_{slot}	Slot pitch	m
Υ	Absolute surface roughness	m
Φ	Magnetic flux	Wb
φ	Phase angle	rad
ϕ_{H}	Hydrodynamic volume fraction	$-$
ϕ_{M}	Magnetic volume fraction	$-$
ψ_{M}	Nanoparticle specific magnetisation	$\mathrm{A.m^2/kg}$
ω	Angular velocity	$\mathrm{rad/s}$
ω_e	Angular electrical frequency	$\mathrm{rad/s}$

Physical Constants

Symbol	Description	Value	Units
μ_0	Permeability of free space	$4\pi \times 10^{-7}$	$\mathrm{H/m}$
g	Gravitational acceleration	9.81	$\mathrm{m/s^2}$
$\hbar_B$	Boltzmann constant	1.380649×10^{-23}	$\mathrm{J/K}$

Abbreviations

Abbreviation	Definition
AEP	Annual Energy Production
CAD	Computer Aided Design
CFD	Computational Fluid Dynamics
DD	Direct-Drive
DE	Drive-End
DNS	Direct Numerical Simulation
EMF	Electromotive Force
FEA	Finite Element Analysis
FEM	Finite Element Method
FF	Ferrofluid
FFT	Fast Fourier Transform
FHD	Ferrohydrodynamics
FSCW	Fractional Slot Concentrated Winding
GCD	Greatest Common Divisor
GR	Gear Ratio
HE	Heat Exchanger
IEA	International Energy Agency
IONP	Iron Oxide Nanoparticle
LCOE	Levelized Cost of Energy
LES	Large Eddy Simulation
LPTN	Lumped Parameter Thermal Network
LSS	Low Speed Shaft
MMF	Magnetomotive Force
MPPT	Maximum Power Point Tracking
MRF	Magnetorheological Fluid

NDE	Non Drive-End
NEMA	National Electrical Manufacturers Association
NPV	Net Present Value
NREL	National Renewable Energy Laboratory
NS	Navier-Stokes
NTU	Net Transfer Units
PBC	Periodic Boundary Conditions
PDF	Probability Density Function
PM	Permanent Magnet
RNA	Rotor Nacelle Assembly
TC	Taylor-Couette
TEFC	Totally Enclosed Fan Cooled
TEM	Transmission Electron Microscopy
TSR	Tip Speed Ratio
UMP	Unbalanced Magnetic Pull
VSM	Vibrating Sample Magnetometry
WJ	Water Jacket
WTG	Wind Turbine Generator

Chapter 1: Introduction

1.1 Background

Under the Paris Agreement, countries such as the UK, China, and member states of the European Union have committed to achieving net zero greenhouse gas emissions as part of international efforts to mitigate climate change [1]. Decarbonisation of energy generation is essential for achieving climate targets [2]. Offshore wind energy is expected to play a key role in enabling this transition, particularly in regions with abundant wind resources such as the UK [3].

The offshore wind energy industry has scaled up massively in the last 30 years, both in terms of installed capacity and the power capacity and sophistication of modern offshore wind turbines [4], [5]. This trend is expected to continue as global climate targets and the improving economic competitiveness of offshore installations drive further development [6].

The commercial offering of offshore wind turbines has generally converged upon three-blade horizontal-axis designs with variable speed generators and pitch regulated blades. Arguably, the most significant distinguishing feature between different designs is whether the powertrain has a direct-drive (DD) or geared architecture [7].

In a DD powertrain there is no gearbox that steps up the rotational speed and steps down the torque from the turbine rotor for input into the generator. The substantial torques that result from this low-speed and high-power operation require a very large generator design, as shown in Figure 1.1. Although DD wind turbine generators (WTGs) are very large, heavy, and expensive they are a favourable configuration offshore due to the increased reliability and efficiency that results from the elimination of the gearbox [8]. The average distance from port of offshore wind farms continues to increase which makes reliability even more crucial [9]. They are also considered to be a suitable choice of powertrain for floating offshore wind turbines which are projected to account for a large portion of future installations [10].

Figure 1.1: Picture of a GE Vernova 12 MW Haliade-X wind turbine nacelle. The direct-drive generator is in the centre of the image [11].

In modern multi-megawatt scale wind turbines, rare-earth permanent magnets (PMs) are utilised due to the increased efficiency, reliability, and reduction in weight that can be achieved in comparison to wound-rotor machines [7]. PM DD WTGs require a substantial amount of rare-earth PM material in their construction, which is both expensive and environmentally damaging to procure [12]. The PM material requirements are on the order of ~20 metric tonnes for 15 MW DD WTGs [13].

The PM material required in a DD WTG is proportional to the air-gap clearance, i.e. the spacing between the WTG's rotor on which the PMs are mounted, and the stator which contains the armature windings: a simplified schematic is provided in Figure 1.2. By making the air-gap clearance of DD WTGs as small as practicably possible the air-gap magnetic reluctance is minimised, reducing the amount of PM material required in the design. Minimising the air-gap clearance is very challenging, designers must take into consideration a variety of factors such as manufacturing tolerances, wind turbine loads, thermal expansion, magnetic forces within the generator, and the self-weight of the generator to ensure that the rotor and stator remain separated and that deviations in the air-gap clearance remain within acceptable limits.

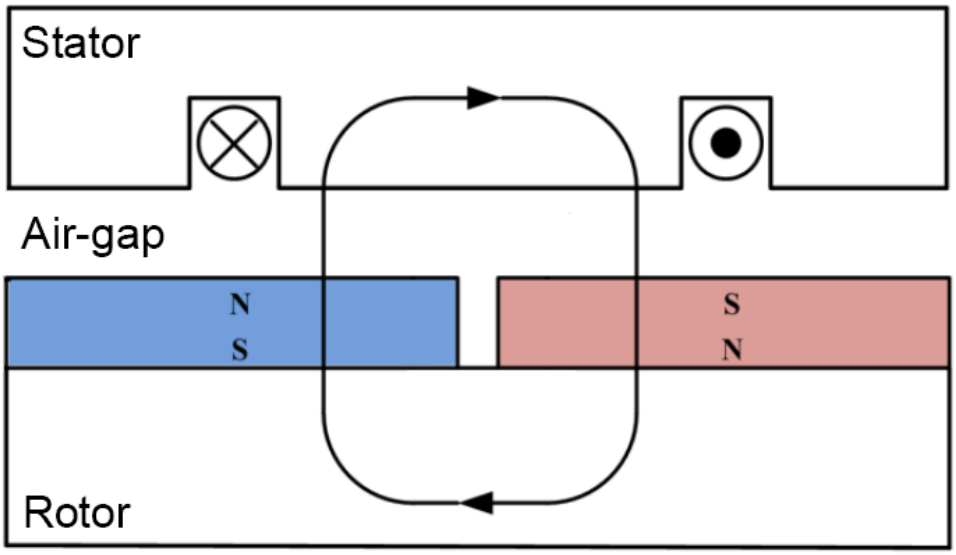

Figure 1.2: A simplified schematic of a pole pair within a surface mounted permanent magnet wind turbine generator [14].

1.2 Aim of Thesis

In this thesis, an alternative approach for reducing the PM material requirements of DD WTGs is investigated: flooding the air-gap with magnetically permeable ferrofluid such that it becomes a 'ferrofluid-gap' as depicted in Figure 1.3. Ferrofluid is a magnetic fluid, a colloidal suspension of single-domain magnetic nanoparticles, with unique properties that make it especially suitable for this application [15]. When an external magnetic field is applied to ferrofluid it becomes magnetised, yet it retains its fluidity with only a modest increase in viscosity.

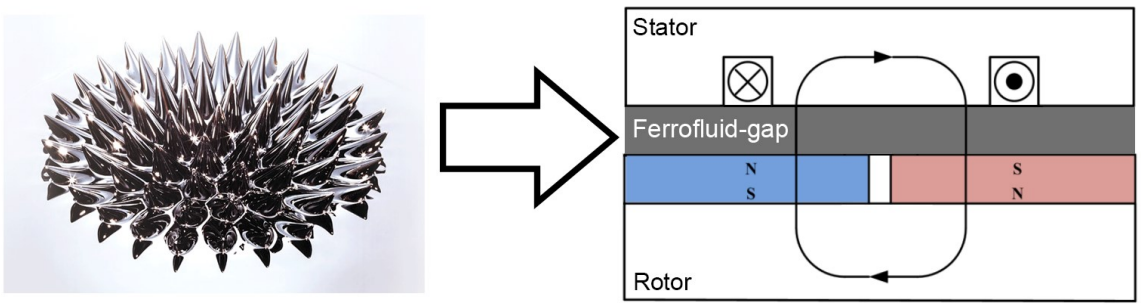

Figure 1.3: A basic schematic demonstrating the ferrofluid-gap concept. The air-gap region between the rotor and stator, pictured on the RHS [14], is filled with ferrofluid, pictured on the LHS [16].

Since a ferrofluid-gap has a larger magnetic permeability than air, the magnetic reluctance of the air-gap region can be reduced which allows for a reduction in the amount of PM material required in the DD WTG. Introducing a fluid into the air-gap region of an electrical machine will result in increased drag losses and therefore a reduction in efficiency. However, since ferrofluid retains its fluidity when magnetised the loss in efficiency may be acceptably low, especially for DD WTGs which are very large and operate at relatively low rotational speeds.

To assess the viability of the ferrofluid-gap concept for DD WTGs an assortment of design and evaluation tools have been developed such that the impact of a ferrofluid-gap on DD WTG performance could be evaluated. During the development of these tools, further opportunities to advance the understanding of DD WTG design have been identified and are also detailed in this thesis.

For this thesis, a novel ferrofluid-gap test rig was developed such that theoretical predictions of ferrofluid-gap magnetic and mechanical behaviour could be experimentally validated. By providing experimentally validated analysis methods for evaluating ferrofluid-gap performance, this work supports further investigation of the ferrofluid-gap concept for arbitrary electrical machine topologies.

Drawing upon the assortment of design and evaluation tools for DD WTGs presented in this thesis, and the experimentally validated analysis methods for ferrofluid-gap performance, the key research question is addressed:

- If the air-gap region of permanent magnet (PM) direct-drive (DD) wind turbine generators (WTG) is flooded with ferrofluid can a reduction in PM material be achieved without unacceptably compromising WTG performance?

1.3 Layout of Thesis

An overview of the thesis structure is provided in Figure 1.4. Chapters 2-4 are centred around the design of DD WTGs and the evaluation of their performance. Chapters 5-7 are focused on the ferrofluid-gap concept and detail the experimental work carried out for this thesis. Chapter 8 presents an assessment of the ferrofluid-gap concept applied to multi-megawatt scale DD WTGs which is supported by the work presented in the previous chapters.

Chapter 2 introduces a design procedure for multi-megawatt scale surface mounted PM DD WTGs with a fractional-slot concentrated winding (FSCW) topology. This serves as a review of DD WTG design and supports the assessment of DD WTG performance throughout this thesis.

Chapter 3 presents a thermal modelling methodology for multi-megawatt scale DD WTGs which expands upon existing methods and incorporates recent advancements in lumped parameter thermal network (LPTN) modelling. The performance of a forced air- and liquid-cooling strategy is compared for inner- and outer-rotor DD WTG topologies. This model is utilised later in the thesis to assess how a ferrofluid-gap influences the thermal performance of DD WTGs.

In Chapter 4, the dimensioning of DD WTG air-gap clearance is investigated. Prior work in this area is reviewed and opportunities for advancing air-gap clearance specification are highlighted. It is emphasised that the spatial distribution of air-gap deformation has a significant impact on the mechanical stability of the air-gap and the risk of vibration due to harmonic magnetic forces.

In Chapter 5, an overview of ferrofluid is provided and its applicability for use in the air-gap region of electrical machines is highlighted. It is explained how a ferrofluid-gap can be expected to behave according to theoretical predictions. A review of previous work concerned with the use of ferrofluid in electrical machines is provided and the opportunities for further research in this area are highlighted.

In Chapter 6, the design and fabrication of a ferrofluid-gap test rig is detailed. Motivated by the opportunities identified for improved experimental characterisation of ferrofluid-gap behaviour, the test rig allows for an independent evaluation of ferrofluid-gap magnetic and mechanical performance. Since DD WTGs are the application of interest, the test rig geometry was scaled such that the ferrofluid-gap turbulence and shear rates surpass what can be expected in multi-megawatt scale DD WTGs.

Chapter 7 details the various experimental investigations that were conducted with the test rig. The experimental results provide unprecedented validation of analysis methods for ferrofluid-gap magnetic and mechanical behaviour.

In Chapter 8, the impact of a ferrofluid-gap on the performance of multi-megawatt scale PM DD WTGs is investigated using the various design tools for DD WTGs and

the experimentally validated models of ferrofluid-gap behaviour provided in the previous chapters.

Chapter 9 concludes the thesis, discussing the key findings and highlighting the opportunities for further research associated with the implementation of ferrofluid-gaps in electrical machines.

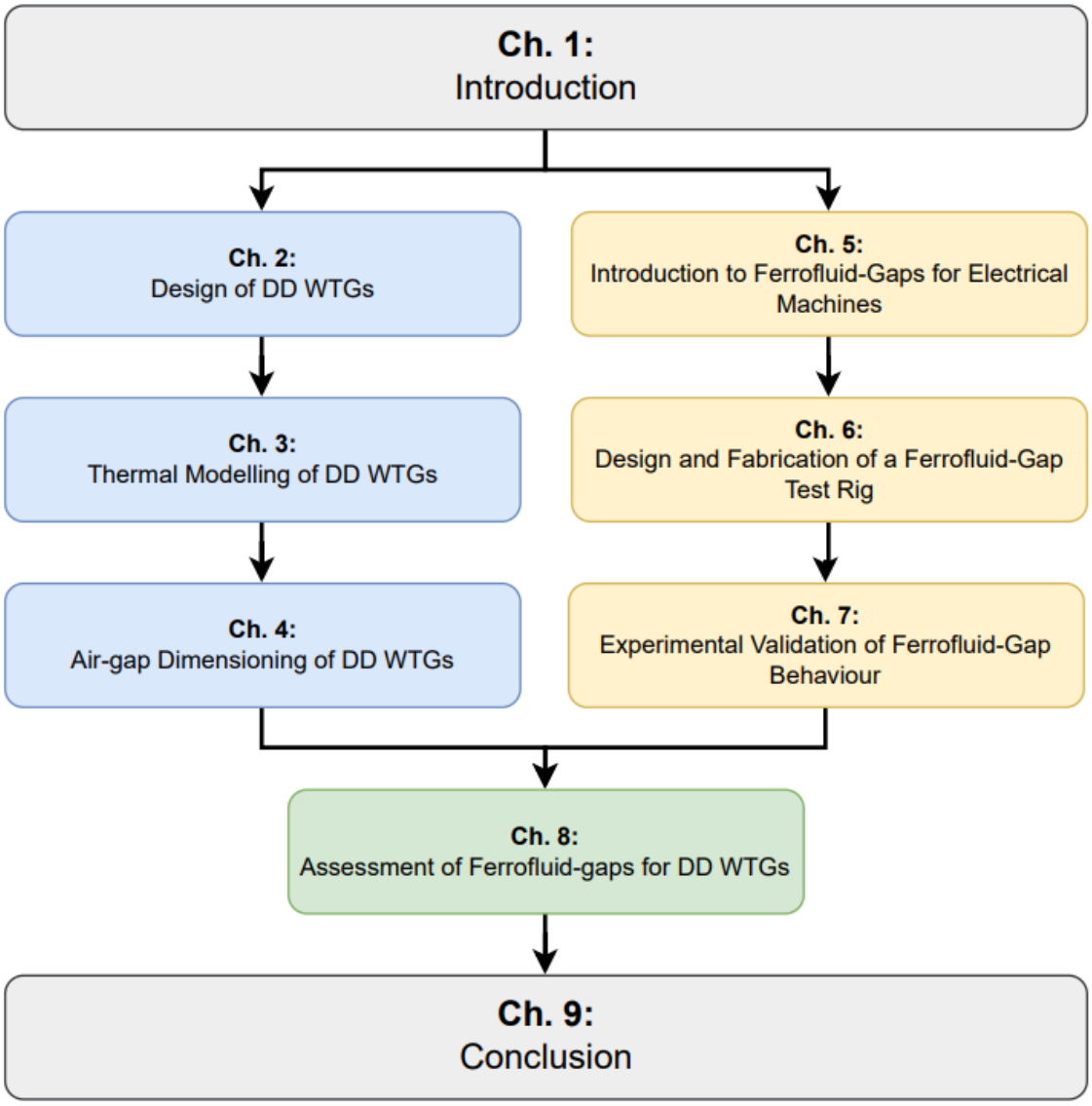

Figure 1.4: Overview of the thesis structure.

1.4 Contributions to Knowledge

The most significant contributions to knowledge in this thesis are summarised as:

1. A detailed design procedure for multi-megawatt scale fractional-slot concentrated winding (FSCW) surface mounted permanent magnet (PM) direct-drive (DD) wind turbine generators (WTGs).
2. A detailed lumped parameter thermal network (LPTN) model for surface mounted PM DD WTGs which incorporates recent advancements in distributed loss modelling and can be utilised for a range of power capacities.
3. A design procedure and analysis of air-to-air and liquid-to-air heat exchangers for DD WTGs.
4. A comparison between the thermal performance of inner- and outer-rotor DD WTGs, it is highlighted that for outer-rotor topologies exposing the external structure to the ambient air flow can significantly reduce the PM temperature.
5. A comparison between indirect air- and liquid-cooling of DD WTGs in which the improved efficiency and performance of liquid-cooling is demonstrated.
6. Recommendations for improved models of air-gap stability based on the magnetic stiffness concept, with an emphasis that the spatial distribution of air-gap non-uniformity significantly impacts the resulting secondary structural deformation of DD WTGs.
7. An analytical model for determining the wavenumber and frequency of radial Maxwell stress harmonics resulting from high-order air-gap non-uniformity.
8. An analysis of the theoretically expected magnetic and mechanical behaviour of ferrofluid-gaps for electrical machines.
9. The design and fabrication of a novel ferrofluid-gap test rig that can allow for independent evaluation of ferrofluid-gap magnetic and mechanical behaviour.
10. Experimental validation that ferrofluid-gap magnetic performance is not influenced by turbulence or shear rate for values exceeding what can be expected in multi-megawatt scale DD WTGs.
11. Experimental validation that a ferrofluid-gap can be modelled as a region with homogeneous magnetic properties with a *BH* assigned according to vibrating sample magnetometer (VSM) measurements.
12. Experimental evidence that ferrofluid-gap drag is increased by the magnetic field within a radial flux electrical machine.

13. An analytical approach and a multiphysics simulation methodology for predicting ferrofluid-gap drag in the presence of a magnetic field, supported by experimental evidence.
14. Experimental results for a partially filled ferrofluid-gap in a radial flux electrical machine demonstrating that ferrofluid can be retained above the poles by the magnetic field at significant rotational speeds.
15. Experimental results demonstrating that the magnetic field within a radial flux electrical machine has a significant impact on partially filled ferrofluid-gap drag.
16. An analysis of how a ferrofluid-gap influences the performance of multi-megawatt scale PM DD WTGs.

Chapter 2: Design of Direct-Drive Wind Turbine Generators

The following chapter introduces a design procedure for multi-megawatt scale direct-drive (DD) surface mounted permanent magnet (PM) wind turbine generators (WTGs) with double layer fractional slot concentrated windings (FSCWs). It serves as a review of DD WTG design and provides a framework for evaluating performance and cost throughout this thesis.

An example 15 MW outer-rotor DD PM WTG specification is produced according to the design procedure which aids in a discussion of the various objectives that motivate the design of DD WTGs.

This chapter is concluded by discussing various approaches in which the PM material requirements can be reduced, motivating the work that follows in this thesis.

2.1 Design of Direct-Drive Wind Turbine Generators

In this section, a detailed design methodology for multi-megawatt scale FSCW DD PM WTGs is provided, this may be of particular help to researchers who wish to produce designs similar to the IEA 15 and 22 MW reference WTGs [13], [17]. Figure 2.1 provides an illustration of the IEA 15 MW outer-rotor DD PM WTG design.

Several studies already exist that detail the step-by-step design of integer slot DD WTG topologies [18], [19]. Hebala *et al.* provide a detailed design procedure for kilowatt-scale fractional slot DD WTGs, however magnet losses are neglected, outer-rotor topologies are not considered, assumptions regarding the air-gap clearance are invalid for multi-megawatt scale WTGs, and the performance is assessed only at rated power output [20].

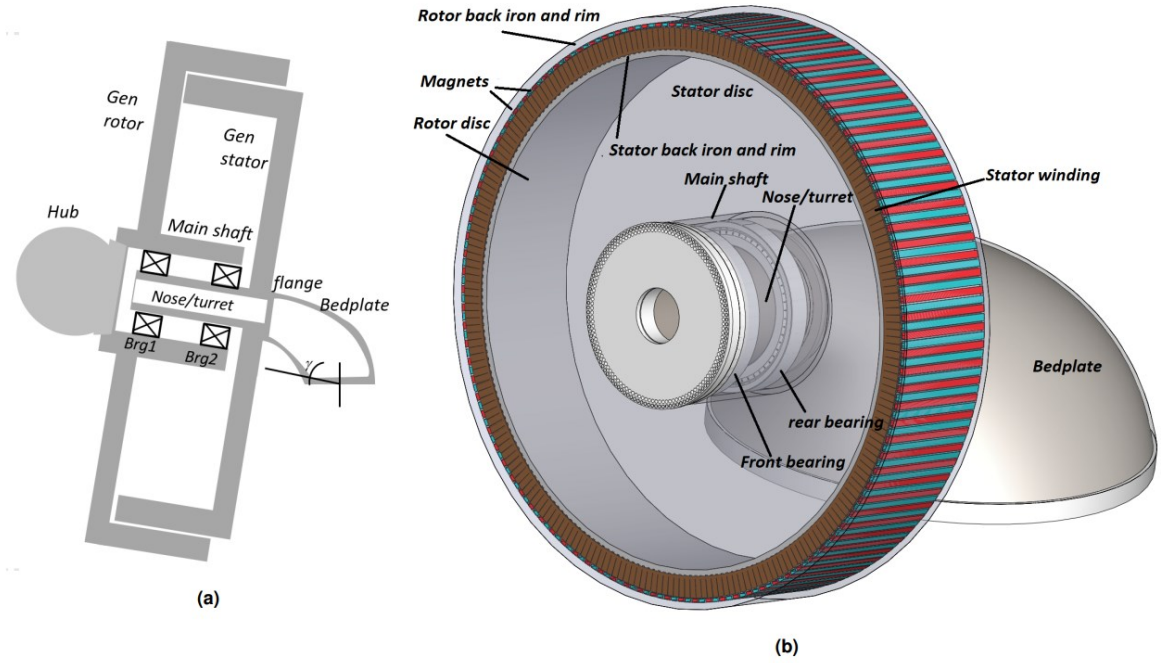

Figure 2.1: A sketch (left) and CAD model (right) of the IEA 15 MW direct-drive (DD) permanent magnet (PM) wind turbine generator (WTG) reference design [13].

2.1.1 Wind Turbine Aerodynamic Specification

To design a WTG the operational range of torque and rotational speed must be understood, this will depend on the aerodynamic design of the wind turbine and the control strategy that is utilised. Large modern wind turbines operate in a balancing act between maximising power capture and minimising loads to prevent over-engineering of the turbine design and premature component failure.

For the wind turbine to generate power the wind speed must surpass the ‘cut-in’ wind speed, the wind turbine will then operate with a maximum power point tracking (MPPT) control strategy where the optimal tip-speed ratio is maintained by adjusting the rotational speed of the blades. Once the rated wind speed is achieved the wind turbine will operate at a constant speed and the power extracted from the wind will be controlled via pitching of the turbine blades. If the wind speed exceeds the ‘cut-out’ wind speed the turbine will stop producing power: brakes will be applied, and the blades will be fully pitched out of the wind to minimise loading on the wind turbine.

For low wind speeds structural resonance should be considered, this is well illustrated in the IEA 15 MW reference wind turbine report by Gaertner *et al.* where the tip speed ratio, rotor speed, generator torque, and blade pitch are plotted over the range of operational wind speeds as shown in Figure 2.2 [13].

- Region 1 is not depicted in the plot, however this refers to the range of wind speeds below the cut-in wind speed at which the wind turbine is not operating.
- In region 1.5 the wind turbine is operating at a constant rotational speed below the rated wind speed. The tip speed ratio is initially at a value of ~20 and decreases towards a constant value as the wind speed increases. The blade pitch angle also varies with wind speed such that the power capture is maximised according to the variation in the tip speed ratio.
- In region 2 the wind turbine is operating below the rated wind speed, however the tip-speed ratio is maintained at a constant optimal value for power capture and the rotational speed increases linearly with increasing wind speed.
- In region 3 the wind turbine is operating above the rated wind speed. The rotational speed is constant, and the tip speed ratio can be seen to decrease with increasing wind speed. The blade pitch angle is increased with increasing wind speed to regulate the power capture by maintaining a constant rotational speed and torque.

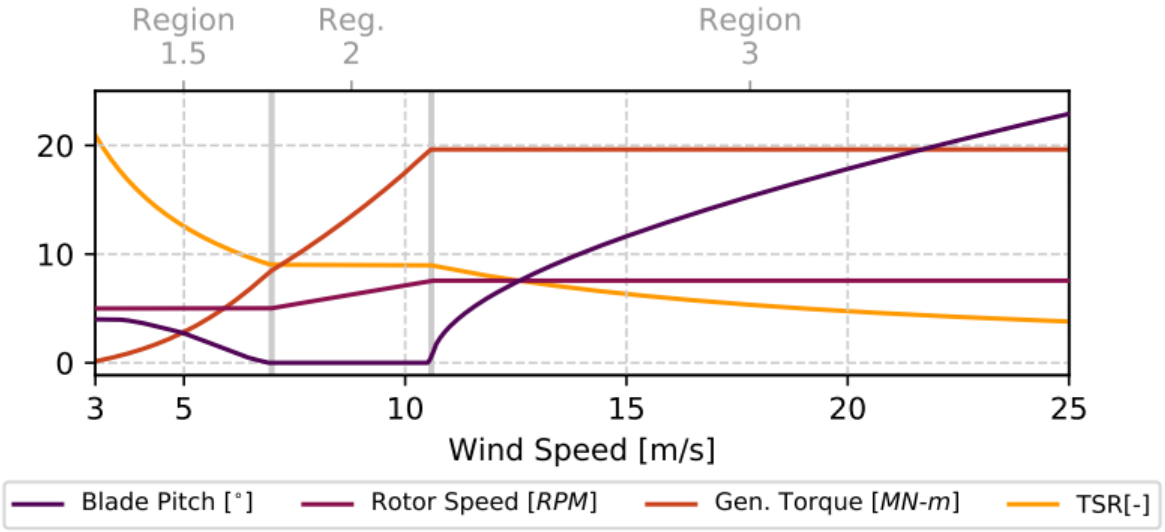

Figure 2.2: Blade pitch, rotor speed, generator torque, and tip speed ratio over the operational wind speed range of the International Energy Agency 15 MW reference wind turbine generator design [13].

Below rated wind speed the operating strategy is designed such that the optimal performance coefficient is maintained as much as possible while avoiding resonant excitation of the wind turbine's structure [21]. Operating a wind turbine at relatively low rotor speeds has the potential to excite several different wind turbine structural modes. By maintaining the rotor speed above a minimum value during operation structural resonance can be avoided at the expense of reduced energy capture. The operating

strategy is often simplified in studies regarding wind turbine generator design, resulting in a misrepresentation of WTG performance at low speeds [22], [23].

2.1.2 The Generator's Influence on the Overall Wind Turbine Design

The specification of the WTG will influence the operation and design of the entire wind turbine system: potentially influencing the rated power, rated wind speed, or required swept radius of the blades. Unless the design of the entire wind turbine system is being taken into consideration, an assumption must be made as to how the specification of the generator will influence the overall design of the wind turbine.

For this study it is assumed that the rated power and blade dimensions are fixed; the rated wind speed is adjusted such that the rated power is achieved depending on the powertrain efficiency. This assumption is made on the basis that the rated wind speed is the least consequential parameter to adjust. It is impractical to adjust the design of the blades during development; in contrast the rated wind speed can be adjusted with relative ease by modifying the wind turbine controller parameters.

Increasing the rated wind speed will increase the loading upon the wind turbine, accelerating component wear. However, consider that the power extracted from the wind is proportional to the cube of the wind speed $P_{\text{shaft}} \propto v_{\text{wind}}^3$ and the thrust loading is proportional to the square of the wind speed $F_T \propto v_{\text{wind}}^2$ [24]. Therefore, assuming that the variation in generator efficiency is relatively small between potential WTG design candidates, the variation in thrust loading will be marginal.

2.1.3 Initial Sizing of Generator

The first step in the design procedure is to size the WTG such that the required rated generator torque can be achieved. Example parameters for a 15 MW wind turbine are provided in Table 2.1, they are used to throughout this chapter unless indicated otherwise.

Since the WTG efficiency is unknown initially, an iterative approach is employed. In the first instance, an estimate is made for the rated wind speed in which powertrain losses are neglected and it is assumed that the rated shaft power (P_{shaft}) is equal to the WTG power capacity.

$$v_{\text{rated}} = \sqrt[3]{\frac{2P_{\text{shaft}}}{\pi\zeta_{\text{aero}}\rho_{\text{air}}r_{\text{swept}}^2}} \tag{2.1}$$

where ζ_{aero} is the efficiency of power extraction from the wind, ρ_{air} is the density of air, and r_{swept} is the swept radius of the wind turbine's blades.

The rated angular velocity of the turbine rotor (and generator rotor) is:

$$\omega_{\text{rated}} = \frac{\Gamma_{\text{TSR}}v_{\text{rated}}}{r_{\text{Swept}}} \tag{2.2}$$

where Γ_{TSR} is the tip speed ratio. The rated input torque into the generator is:

$$\mathcal{T}_{\text{rated}} = \frac{P_{\text{shaft}}}{\omega_{\text{rated}}} \tag{2.3}$$

Based on a specified average air-gap electromagnetic shear stress at rated power ($\bar{\sigma_t}$), the WTG rotor radius is calculated:

$$r_{\text{r}} = \sqrt[3]{\frac{\mathcal{T}_{\text{rated}}}{4\pi\Gamma_{\text{gen}}\bar{\sigma_t}}} \tag{2.4}$$

where Γ_{gen} is the aspect ratio of the generator defined as $\Gamma_{\text{gen}} = l_c/2r_r$.

Table 2.1: Input parameters and material properties for wind turbine generator design procedure.

Design Parameters	Symbol	15 MW Example Values	Units
Wind Turbine Aerodynamic Input Parameters			
Rated power	P_{rated}	15	MW
Swept rotor radius	r_{swept}	120	m
Aerodynamic power extraction efficiency	ζ_{aero}	0.5	–
Tip speed ratio	Γ_{TSR}	9	–
Cut-in Wind Speed	v_{CI}	3	m/s
Cut-out Wind Speed	v_{CO}	25	m/s
Tip speed limit	$v_{\text{tip,max}}$	100	m/s
Density of Air	ρ_{air}	1.225	kg/m^3
Direct-Drive Generator Input Parameters			
Number of phases	N_{phase}	3	–
Turns per coil	N_{TC}	4	–

Design Parameters	Symbol	15 MW Example Values	Units
Rated average electromagnetic shear stress	$\bar{\sigma}_t$	60	kPa
Generator aspect ratio	Γ_{gen}	0.21	–
Air-gap clearance factor	C_{hg}	0.001	–
Pole and slot integer	n	20	–
Magnet width factor	$C_{\mathrm{PM,w}}$	0.8	–
Magnet height factor	$C_{\mathrm{PM,h}}$	5	–
Slot height factor	C_{SH}	2	–
Slot fill factor	C_{fill}	0.65	–
Slot opening factor	C_{SO}	0.5	–
Material Properties			
Copper resistivity at $120^{\circ}\mathrm{C}$	ϱ_{Cu}	2.4×10^{-8}	Ωm
Iron saturation limit	$B_{\mathrm{Fe,max}}$	1.6	T
Magnet remanent flux density	B_{rem}	1.28	T
Magnet relative permeability	$\mu_{r,\mathrm{PM}}$	1.06	–
Magnet electrical conductivity	κ	76.9	kS/m
Stator eddy loss coefficient	$\dot{P}_{\mathrm{Fe,hys}}$	0.5	W/kg
Stator hysteresis loss coefficient	$\dot{P}_{\mathrm{Fe,eddy}}$	2	W/kg
Steinmetz reference flux density	B_0	1.5	T
Steinmetz reference frequency	f_0	50	Hz

A low aspect ratio is advantageous for maximising the amount of torque that can be produced per unit of active mass [25]. However, if Γ_{gen} is too low, the structural design of the WTG becomes increasingly challenging [26]. Constraints on the maximum allowable WTG size must also be taken into account. In line with other studies concerned with DD WTG design, in this work a value of 0.21 is considered [27], [19].

Generator core length is then:

$$l_c = 2r_{\mathrm{r}}\Gamma_{\mathrm{gen}} \tag{2.5}$$

The air-gap clearance is estimated to be a certain fraction of the rotor diameter $(D_{\mathrm{r}} = 2r_{\mathrm{r}})$ based on an air-gap clearance coefficient (C_{hg}), this is typically assumed to be 0.001 [18]:

$$h_{\mathrm{g}} = C_{\mathrm{hg}}D_{\mathrm{r}} \tag{2.6}$$

The radius of the boundary between the stator teeth and the air-gap can then be calculated:

$$r_{\mathrm{s}} = r_{\mathrm{r}} \pm h_{\mathrm{g}} \tag{2.7}$$

where h_{g} is added or subtracted in the case of an inner-rotor or outer-rotor WTG respectively.

A 12-10 slot-pole combination is utilised in this work since it is a popular choice for fractional slot concentrated winding topologies due to the relatively large fundamental winding factor (C_{w1}) of 0.933 [28]. The number of poles and slots is therefore defined to be a multiple of a positive integer n:

$$N_{\mathrm{pole}} = 10n \tag{2.8}$$

$$N_{\mathrm{slot}} = 12n \tag{2.9}$$

The pole (τ_{pole}) and slot pitch (τ_{slot}) can then be calculated:

$$\tau_{\mathrm{pole}} = \frac{2\pi r_{\mathrm{r}}}{N_{\mathrm{pole}}} \tag{2.10}$$

$$\tau_{\mathrm{slot}} = \frac{2\pi r_{\mathrm{s}}}{N_{\mathrm{slot}}} \tag{2.11}$$

The magnet width is specified to be some fraction of the pole pitch according to the magnet width factor $C_{\mathrm{PM,w}}$, this is typically limited to ~0.7-0.8 to avoid excessive inter-pole magnetic leakage which would result in an inefficient use of the expensive PM material:

$$w_{\mathrm{PM}} = C_{\mathrm{PM,w}}\tau_{\mathrm{pole}} \tag{2.12}$$

Similarly, the magnet height can be expressed in relation to the air-gap clearance by a factor $C_{\mathrm{PM,h}}$, this is typically specified to be within a range of ~4-6 so that the PM material is utilised efficiently [29]:

$$h_{\mathrm{PM}} = C_{\mathrm{PM,h}}h_{\mathrm{g}} \tag{2.13}$$

2.1.4 Open-Load Magnetic Circuit

The next step is to evaluate the open-load magnetic circuit.

In Figure 2.3 a diagram is provided for one slot and pole pitch in which the geometrical parameters used in this section are annotated.

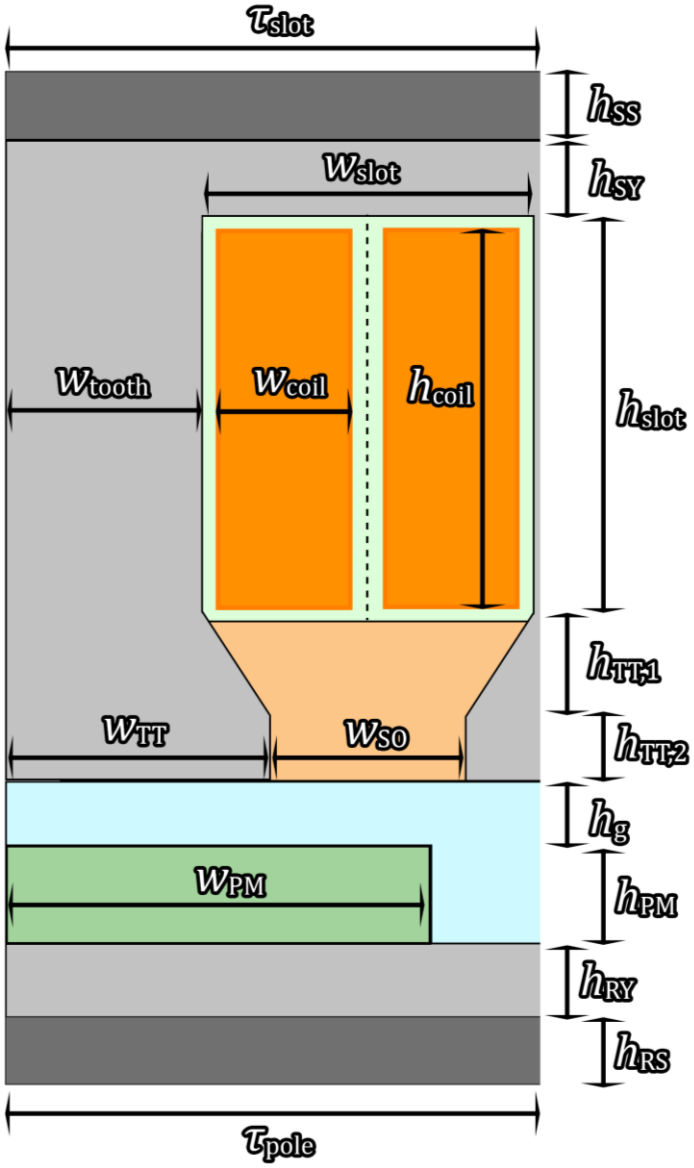

Figure 2.3: Annotated diagram showing the geometrical parameters for one slot and pole pitch (not to scale).

The Carter factor (C_{carter}) accounts for the effective increase in air-gap reluctance due to the slot openings [30]. By multiplying the air-gap clearance by the Carter factor an equivalent magnetic air-gap clearance is obtained:

$$g_{\mathrm{eff},1} = C_{\mathrm{carter}} h_{\mathrm{g}} \tag{2.14}$$

Xuan *et al.* determined that the following formulation is accurate for surface mounted PM FSCWs [31].

$$C_{\text{carter}} = \frac{\tau_{\text{slot}}}{\tau_{\text{slot}} - h_{\text{g}}\gamma_{\text{carter}}} \tag{2.15}$$

$$\gamma_{\text{carter}} = \frac{\tau_{\text{slot}}}{h_{\text{g}}}\left[\frac{w_{\text{SO}}}{\tau_{\text{slot}}} - \frac{4h_{\text{g}}}{\pi\tau_{\text{slot}}}\ln\left(1 + \frac{\pi w_{\text{SO}}}{4h_{\text{g}}}\right)\right] \tag{2.16}$$

where w_{SO} is the width of the slot opening.

Assuming that iron reluctance is negligible the total magnetic air-gap length including the PMs is:

$$g_{\text{eff,2}} = g_{\text{eff,1}} + \frac{h_{\text{PM}}}{\mu_{r,\text{PM}}} \tag{2.17}$$

where $\mu_{r,\text{PM}}$ is the relative permeability of the PMs.

The air-gap flux density above the rotor poles can then be estimated as:

$$B_g = \frac{C_{\text{leak}} B_{\text{rem}} h_{\text{PM}}}{g_{\text{eff,2}}\mu_{r,\text{PM}}} \tag{2.18}$$

where C_{leak} is a coefficient accounting for inter-pole magnetic leakage, it is estimated based on the work of Zhu *et al.* [32]:

$$C_{\text{leak}} = \frac{\left(\frac{1}{g_{\text{eff,1}}} + \frac{\mu_{r,\text{PM}}}{h_{\text{PM}}}\right)}{\left(\frac{1}{g_{\text{eff,1}}} + \frac{\mu_{r,\text{PM}}}{h_{\text{PM}}}\right) + \frac{4}{\pi w_{\text{PM}}}\ln\left(1 + \frac{\pi g_{\text{eff,1}}}{\tau_{\text{pole}} - w_{\text{PM}}}\right)} \tag{2.19}$$

Now that the air-gap flux density above the poles has been estimated, the slot (w_{slot}) and tooth width (w_{tooth}) can be determined. The tooth width is specified such that it will be close to magnetic saturation when the rotor flux is passing through it, this results in an efficient use of the electrical steel and maximises the slot width. Assuming that the electrical steel begins to saturate at $B_{\text{Fe,max}}$:

$$w_{\text{tooth}} = \frac{B_{\text{g}} w_{\text{PM}}}{B_{\text{Fe,max}}} \tag{2.20}$$

$$w_{\text{slot}} = \tau_{\text{slot}} - w_{\text{tooth}} \tag{2.21}$$

The Carter factor depends on the slot opening width, therefore if open slots are utilised, or if the slot opening is specified to be some factor of the slot width C_{SO}:

$$w_{\text{SO}} = C_{\text{SO}} w_{\text{slot}} \tag{2.22}$$

then w_{slot} can be found by first approximating its value and then iteratively solving Eq. (2.14) to Eq. (2.21) until a constant value of w_{slot} is obtained.

The slot height is specified in relation to the slot width according to a slot height factor (C_{SH}):

$$h_{\mathrm{slot}} = C_{\mathrm{SH}} w_{\mathrm{slot}} \tag{2.23}$$

If the slot height is too small the winding current density will be large, leading to elevated coil temperatures. As it increases the slot leakage inductance can become excessive, vibration can become problematic, and the armature winding material costs will increase [33].

Such as with the tooth width specification, the thickness of the rotor and stator yoke are specified so that they are close to magnetic saturation:

$$h_{\mathrm{RY}} = h_{\mathrm{SY}} = \frac{B_{\mathrm{g}} w_{\mathrm{PM}}}{2B_{Fe,max}} \tag{2.24}$$

The rated RMS fundamental open-load electro-motive force (EMF) in each phase is then calculated:

$$E_p = \sqrt{2} C_{w1} N_s \omega_{\mathrm{rated}} \widehat{B_{\mathrm{g}}} l_c r_{\mathrm{s}} \tag{2.25}$$

where $\widehat{B_{\mathrm{g}}}$ is the fundamental component of air-gap flux density:

$$\widehat{B_{\mathrm{g}}} = \frac{4}{\pi} B_{\mathrm{g}} \sin\left(\frac{\pi w_{\mathrm{PM}}}{2\tau_{\mathrm{pole}}}\right) \tag{2.26}$$

and N_s is the number of turns per phase, which for a double-layer concentrated winding layout is:

$$N_s = \frac{N_{\mathrm{slot}} N_{\mathrm{TC}}}{N_{\mathrm{phase}}} \tag{2.27}$$

where N_{TC} is the number of turns per coil, and N_{phase} is the number of phases. N_s should be specified such that the voltage level is appropriate. If the voltage level is low, the cables connecting the WTG terminals to the converter have to be very large. As the voltage level is increased the winding insulation must be made thicker resulting in a reduced slot fill factor [34]. In this work, E_p is targeted to be ~4 kV.

In loaded conditions, the induced EMF will be impacted by armature reaction, however the effect is relatively small in surface mounted PM WTGs, therefore it is neglected for the purpose of this chapter.

At this stage the geometry of the armature windings can be evaluated. The total conductor area in each slot is:

$$A_{\text{cond}} = w_{\text{slot}} h_{\text{slot}} C_{\text{fill}} \tag{2.28}$$

where C_{fill} is the slot fill factor.

For double layer windings the cross-sectional area of conductor in each coil side is:

$$A_{\text{CS}} = \frac{A_{\text{cond}}}{2} \tag{2.29}$$

The total length of conductor is:

$$l_{\text{cond}} = N_{\text{slot}}(l_c + l_{\text{EW}}) \tag{2.30}$$

where l_{EW} is the length of the end windings per slot:

$$l_{\text{EW}} = \pi \left(\frac{w_{\text{slot}}}{2} + w_{\text{tooth}} \right) \tag{2.31}$$

Note that l_{EW} is determined based on a constant cross-sectional area of A_{cond}.

The total volume of the conductor material in the WTG can then be found:

$$V_{\text{cond}} = A_{\text{cond}} l_{\text{cond}} \tag{2.32}$$

2.1.5 Armature Inductance

To evaluate the equivalent electrical circuit of the WTG the armature inductance must be calculated. The magnetic flux produced by the armature windings follows several different paths, each requiring separate consideration. Ponomarev *et al.* provide an extensive summary of analytical methods for calculating the armature inductance of FSCW PM synchronous machines which are utilised in this work [28].

The magnetising inductance refers to the fundamental component of stator flux that crosses the air-gap to the rotor. The single-phase magnetising inductance can be calculated as follows:

$$L_{m,\mathrm{sp}} = \frac{2}{\pi}\tau_{\mathrm{pole}} l_c \frac{\mu_0}{g_{\mathrm{eff},2}} \frac{4N_{\mathrm{SPP}}}{\pi} \frac{N_{\mathrm{phase}}}{N_{\mathrm{slot}}} (C_{w1}N_s)^2 \tag{2.33}$$

where N_{SPP} is the number of slots per pole per phase:

$$N_{\mathrm{SPP}} = \frac{N_{\mathrm{slot}}}{N_{\mathrm{pole}}N_{\mathrm{phase}}} \tag{2.34}$$

The total magnetising inductance can then be found:

$$L_m = \frac{N_{\mathrm{phase}}}{2} L_{m,\mathrm{sp}} \tag{2.35}$$

The harmonic leakage inductance refers to the asynchronous components of stator flux that cross the air-gap to the rotor. It can be determined from the harmonic air-gap leakage factor C_δ which is equal to 0.96 in the case of a 10-12 pole-slot concentrated winding machine:

$$L_h = C_\delta L_m \tag{2.36}$$

The slot leakage inductance refers to the stator flux that passes across the slots between neighbouring teeth:

$$L_{\mathrm{slot}} = \frac{4N_{\mathrm{phase}}}{N_{\mathrm{slot}}} \mu_0 N_s^2 l_c \lambda_{\mathrm{slot}} \tag{2.37}$$

where λ_{slot} is the slot leakage permeance factor, which for a double layer concentrated winding is given by:

$$\lambda_{\mathrm{slot}} = \lambda_{\mathrm{SL},1} \frac{h_{\mathrm{slot}} - h'}{3w_{\mathrm{slot}}} + \lambda_{\mathrm{SL},2} \left(\frac{t_{\mathrm{SL}}}{w_{\mathrm{slot}}} + \frac{h_{\mathrm{TT},2}}{w_{\mathrm{SO}}} + \frac{h_{\mathrm{TT},1}}{w_{\mathrm{slot}} - w_{\mathrm{SO}}} \ln\left(\frac{w_{\mathrm{slot}}}{w_{\mathrm{SO}}}\right) \right) + \frac{h'}{4w_{\mathrm{slot}}} \tag{2.38}$$

where the factors $\lambda_{\mathrm{SL},1} = 0.9063$ and $\lambda_{\mathrm{SL},2} = 0.8750$ for a 10-12 pole-slot machine, h' is the vertical spacing between different coils in a slot, t_{SL} is the slot liner thickness, $h_{\mathrm{TT},1}$ is the tooth tip thickness, and $h_{\mathrm{TT},2}$ is the tooth taper length.

The tooth-tip leakage inductance refers to the flux that passes between neighbouring teeth via the air-gap but without passing through the rotor. It can be calculated as follows:

$$L_{\mathrm{TT}} = \frac{4N_{\mathrm{phase}}}{N_{\mathrm{slot}}} \mu_0 N_s^2 l_c \lambda_{\mathrm{SL},2} \lambda_{\mathrm{TT}} \tag{2.39}$$

where λ_{TT} is the tooth-tip leakage permeance factor:

$$\lambda_{\mathrm{TT}} = \frac{1}{2\pi}\left\{\ln\left(\frac{g_{\mathrm{eff},3}^2}{w_{\mathrm{SO}}^2}+\frac{1}{4}\right)+\frac{4g_{\mathrm{eff},3}}{w_{\mathrm{SO}}}\tan^{-1}\left(\frac{w_{\mathrm{SO}}}{2g_{\mathrm{eff},3}}\right)\right\} \tag{2.40}$$

$$g_{\mathrm{eff},3} = h_{\mathrm{g}} + \frac{h_{\mathrm{PM}}}{\mu_{r,\mathrm{PM}}} \tag{2.41}$$

The end winding leakage inductance refers to the flux produced by the end windings. Due to the complexity of end winding geometry and the 3D geometry of the flux paths an accurate estimation requires finite element method (FEM) modelling, however since it is generally a small component of the total armature leakage inductance it is reasonable to estimate it with an analytical method:

$$L_{\mathrm{EW}} = \mu_0\mu_{r,\mathrm{env}}\frac{N_{\mathrm{slot}}}{N_{\mathrm{phase}}}\frac{\pi N_{\mathrm{TC}}^2 r_{\mathrm{EW}}^2}{h_{\mathrm{slot}}} \tag{2.42}$$

where r_{EW} is the arc radius of the end windings, which for a double layer winding with semi-circular ending windings is:

$$r_{\mathrm{EW}} = \frac{w_{\mathrm{slot}}}{4}+\frac{w_{\mathrm{tooth}}}{2} \tag{2.43}$$

and $\mu_{r,\mathrm{env}}$ considers the presence of magnetically permeable materials in proximity to the end-windings (approximated as 1.2).

The total phase inductance is therefore:

$$L_s = L_m + L_\sigma \tag{2.44}$$

where L_σ is the total leakage inductance:

$$L_\sigma = L_h + L_{\mathrm{slot}} + L_{\mathrm{TT}} + L_{\mathrm{EW}} \tag{2.45}$$

2.1.6 Armature Current and Copper Losses

Since the WTG terminals are connected to a fully rated power converter, the operating point can be chosen. Following the work of Grauers, it is assumed that reactive power is supplied by the power converter such that the magnitude of the open-load EMF (E_p) is equal to that of the terminal voltage ($\mathcal{V}_s$) [18], [35]. This approach has been utilised in several studies concerned with DD PM WTG design [19], [22], [36].

In Figure 2.4 a phasor diagram is provided, where I_s is the armature phase current, R_s is the phase resistance, and X_s is the phase reactance.

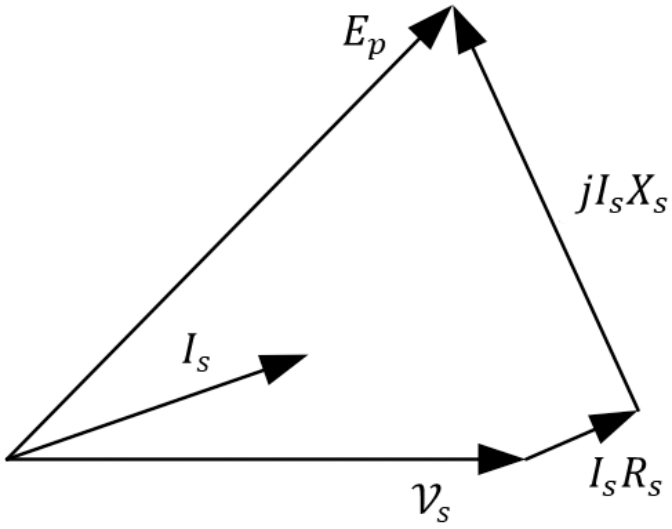

Figure 2.4: Phasor diagram of the direct-drive wind turbine generator [36].

The RMS value of the fundamental component of the armature phase current can be found as follows:

$$I_s = \sqrt{\left(\frac{P_E}{E_p N_{\text{phase}}}\right)^2 + \left(\frac{E_p - \sqrt{E_p^2 - (\omega_e L_s)^2 \left(\frac{P_E}{E_p N_{\text{phase}}}\right)^2}}{(\omega_e L_s)}\right)^2} \tag{2.46}$$

where ω_e is the electrical frequency of the fundamental harmonic at rated speed:

$$\omega_e = \frac{\omega_{\text{rated}} N_{\text{pole}}}{2} \tag{2.47}$$

a derivation of Eq. (2.46) is provided in Appendix A.

The resistive voltage drop of the armature windings is considered using an iterative approach in which the copper losses (P_{Cu}) are factored into the calculation of I_s, P_E is calculated as the sum of active power at the generator terminals and copper losses:

$$P_E = P_{\text{rated}} + P_{\text{convm}} + P_{\text{Cu}} \tag{2.48}$$

where P_{convm} is the dissipation in the converter at rated power, which is assumed to be equal to 3% of the wind turbine power capacity [22]:

$$P_{\mathrm{convm}} = 0.03P_{\mathrm{rated}} \tag{2.49}$$

In the first instance, P_E is first estimated assuming that $P_{\mathrm{Cu}} = 0$. The copper losses are then calculated assuming an average winding temperature of $120^{\circ}\mathrm{C}$:

$$P_{\mathrm{Cu}} = J_{\mathrm{RMS}}^2 V_{\mathrm{cond}} \varrho_{\mathrm{Cu}} \tag{2.50}$$

where ϱ_{Cu} is the resistivity of copper, and J_{RMS} is the RMS current density, given by:

$$J_{\mathrm{RMS}} = \frac{I_s N_{\mathrm{TC}}}{A_{\mathrm{CS}}} \tag{2.51}$$

The estimate of P_E is then updated by including the estimate for P_{Cu} and iteratively solving Eq. (2.46) to Eq. (2.51) until a constant value of P_E is obtained.

The specific current loading is determined as:

$$A_1 = \frac{6N_s I_s}{2\pi r_{\mathrm{s}}} \tag{2.52}$$

2.1.7 Stator Iron Losses

Iron loss refers to eddy current and hysteresis losses that occur within the WTG's electrical steel components due to the alternating magnetic field. Eddy current loss refers to how the alternating magnetic field induces circulating currents within the electrical steel which result in heat due to Ohmic losses. Hysteresis loss refers to how the repeated reorientation of the electrical steel's magnetic domains results in internal friction within the material which results in heat.

Iron losses in synchronous machines are often estimated using the Steinmetz equation, which is based on the extrapolation of empirically obtained material data.

$$P_{\mathrm{hys}} = 2m_{\mathrm{Fe,e}} \left(\dot{P}_{\mathrm{Fe,hys}} \left(\frac{f_e}{f_0} \right) \left(\frac{B_{\mathrm{Fe,max}}}{B_0} \right)^2 \right) \tag{2.53}$$

$$P_{\mathrm{eddy}} = 2m_{\mathrm{Fe,e}} \left(\dot{P}_{\mathrm{Fe,eddy}} \left(\frac{f_e}{f_0} \right)^2 \left(\frac{B_{\mathrm{Fe,max}}}{B_0} \right)^2 \right) \tag{2.54}$$

where $\dot{P}_{\mathrm{Fe,eddy}}$ and $\dot{P}_{\mathrm{Fe,hys}}$ are the Steinmetz coefficients for the eddy and hysteresis loss respectively, f_e and $B_{\mathrm{Fe,max}}$ is the frequency and peak flux density of the magnetic field in the electrical steel respectively, f_0 and B_0 is the reference frequency and flux density of the magnetic field of the empirical data, and $m_{\mathrm{Fe,e}}$ is the mass of the electrical steel component under consideration. As in Eq. (2.53) and (2.54), a factor of two is commonly applied to account for the iron loss resulting from the asynchronous components of flux density. For this work the iron loss parameters were taken from the work of Polinder *et al.* in which values are provided for electrical steel laminations [22].

For an outer-rotor machine, the masses of the stator yoke $(m_{\mathrm{Fe,SY}})$, teeth $(m_{\mathrm{Fe,ST}})$, and tooth tips $(m_{\mathrm{Fe,TT}})$ can be calculated as:

$$m_{\mathrm{Fe,SY}} = \rho_{\mathrm{Fe,e}} l_c \pi \left(\left(r_{\mathrm{s}} - h_{\mathrm{TT},2} - h_{\mathrm{TT},1} - h_{slot} \right)^2 - \left(r_{\mathrm{s}} - h_{\mathrm{TT},2} - h_{\mathrm{TT},1} - h_{\mathrm{slot}} - h_{\mathrm{SY}} \right)^2 \right) \quad (2.55)$$

$$m_{\mathrm{Fe,ST}} = \rho_{\mathrm{Fe,e}} N_{\mathrm{slot}} l_c h_{\mathrm{slot}} w_{\mathrm{tooth}} \quad (2.56)$$

$$m_{\mathrm{Fe,TT}} = \rho_{\mathrm{Fe,e}} N_{\mathrm{slot}} l_c \left(\left(w_{\mathrm{TT}} h_{\mathrm{TT},2} \right) + \frac{h_{\mathrm{TT},1} (w_{\mathrm{TT}} + w_{\mathrm{tooth}})}{2} \right) \quad (2.57)$$

For an inner-rotor machine, $m_{\mathrm{Fe,SY}}$ is calculated as follows:

$$m_{\mathrm{Fe,SY}} = \rho_{\mathrm{Fe,e}} l_c \pi \left(\left(r_{\mathrm{s}} + h_{\mathrm{TT},2} + h_{\mathrm{TT},1} + h_{\mathrm{slot}} + h_{\mathrm{SY}} \right)^2 - \left(r_{\mathrm{s}} + h_{\mathrm{TT},2} + h_{\mathrm{TT},1} + h_{\mathrm{slot}} \right)^2 \right) \quad (2.58)$$

Under loaded conditions, the interaction between the armature reaction field and the stator core gives rise to additional iron losses, collectively referred to as stray load losses. These losses typically represent only a small portion of the total losses and are difficult to predict accurately. In this work, they are assumed to be equal to 20% of the sum of stator hysteresis and eddy current losses [18]:

$$P_{\mathrm{add}} = 0.2 \left(P_{\mathrm{hys}} + P_{\mathrm{eddy}} \right) \quad (2.59)$$

2.1.8 Permanent Magnet Losses

In FSCW machines the armature winding magnetomotive force (MMF) contains a multitude of asynchronous harmonics which can induce iron losses in the rotor. Finite element method (FEM) simulations are often utilised to approximate rotor losses due to the complexity involved in their analytical calculation, however in this work an

analytical method presented by Ciriani *et al.* is employed to facilitate fast computation [37]. More detail on the analytical method is provided in Appendix B.

In Figure 2.5, a spectrum of armature MMF harmonics is presented for the example 15 MW machine, the MMF amplitude is normalised with respect to the fundamental harmonic (order of 100).

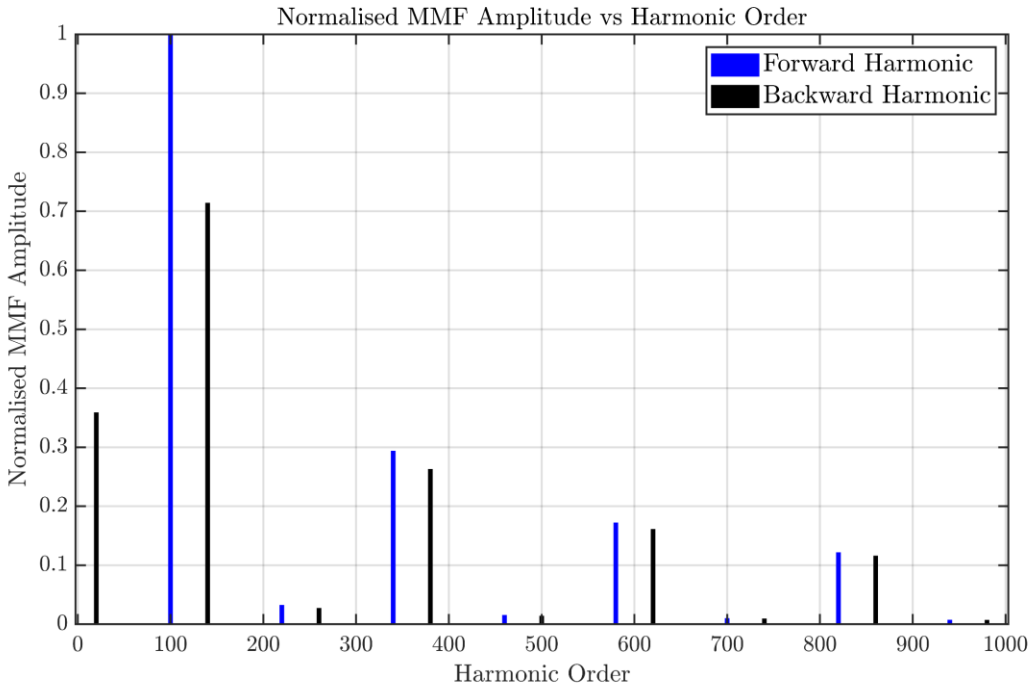

Figure 2.5: Spectrum of armature magnetomotive force (MMF) harmonics for the example 15 machine, the MMF amplitude is normalised with respect to the fundamental harmonic (order of 100).

Magnet loss can be reduced by segmenting the magnets in both the axial and circumferential directions. Since the core length of multi-megawatt scale DD WTGs is large, axial segmentation is already necessary due to practical constraints associated with PM manufacturing [38]. If the maximum axial length of a single PM is assumed to be ~100 mm, this would result in at least 21 distinct axial segmentations in the case of the example 15 MW machine. In Figure 2.6, the magnet loss of the example 15 MW machine at rated power is presented for a range of axial and circumferential segmentations. Further axial segmentation beyond the assumed practical minimum appears to have a small impact on the PM loss, however circumferential segmentation is a viable approach for further PM loss reduction. Ultimately, additional PM segmentation will be a trade-off between efficiency targets, operating temperatures, and manufacturing complexity.

Rudden *et al.* demonstrate that a solid rotor yoke can result in significant iron losses in FSCW WTGs [39]. In this work, it is assumed that the rotor yoke is comprised of a sufficient number of laminations such that the rotor yoke losses are negligible.

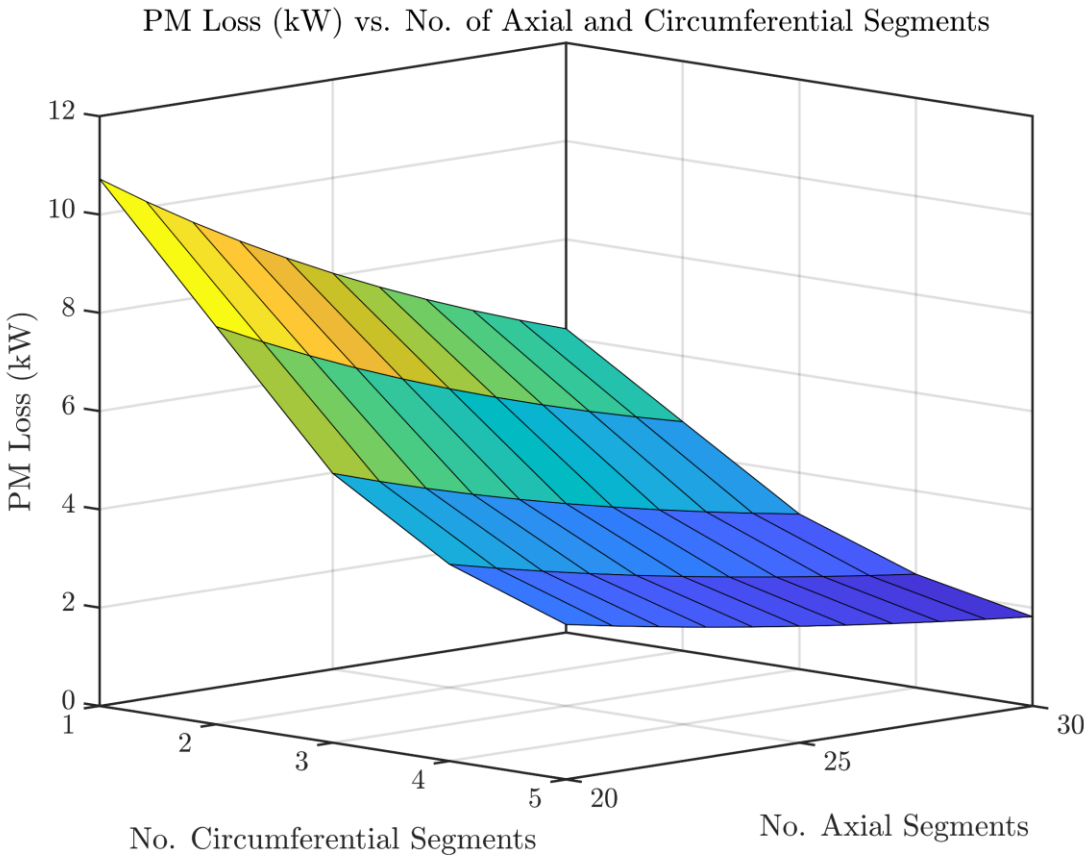

Figure 2.6: Permanent magnet (PM) loss of the example 15 MW machine at rated power as a function of the number of circumferential and axial segments per pole.

2.1.9 Converter Losses

The losses in the converter are approximated based on the work of Polinder *et al.* [22]:

$$P_{\text{conv}} = \frac{P_{\text{convm}}}{31}\left(1 + 10\frac{I_s}{I_{sm}} + 5\frac{I_s^2}{I_{sm}^2} + 10\frac{I_g}{I_{gm}} + 5\frac{I_g^2}{I_{gm}^2}\right) \tag{2.60}$$

where I_s is the generator side current, I_{sm} is the maximum generator side converter current, I_g is the grid side current, and I_{gm} is the maximum grid side converter current. The grid side current is assumed to scale with the generator active power output such that:

$$\frac{I_g}{I_{gm}} = \frac{P_E - P_{\text{Cu}}}{P_{\text{rated}} + P_{\text{convm}}} \tag{2.61}$$

2.1.10 Generator Efficiency at Rated Wind Speed

Neglecting windage, bearing, and cooling system losses, the total generator loss at rated power is:

$$P_{\text{loss}} = P_{\text{Cu}} + P_{\text{hys}} + P_{\text{eddy}} + P_{\text{add}} + P_{\text{PM}} + P_{\text{conv}} \tag{2.62}$$

The shaft power required to achieve the specified wind turbine power rating is therefore:

$$P_{\text{shaft}} = P_{\text{rated}} + P_{\text{loss}} \tag{2.63}$$

The procedure is iterated from Eq. (2.1) to Eq. (2.63) until a constant value of P_{shaft} is obtained.

The blade tip speed is monitored to ensure that it does not surpass an imposed limit:

$$\Gamma_{\text{TSR}} v_{\text{rated}} \leq v_{\text{tip,max}} \tag{2.64}$$

2.1.11 The Wind Turbine Power Curve

To generate the full wind turbine power curve, the powertrain efficiency must be evaluated over the full range of operational wind speeds since each loss component varies according to the WTG rotational speed and/or the torque output.

It is assumed that the wind turbine initially operates at a constant rotational speed until the optimal TSR is achieved:

$$\omega_0 = 0.5\omega_{\text{rated}} \tag{2.65}$$

Therefore, the torque increases with wind speed as:

$$\mathcal{T}(v_{\text{wind}}) = 0.5\pi\zeta_{\text{aero}}\rho_{\text{air}} r_{\text{swept}}^2 \frac{v_{\text{wind}}^3}{\omega_0} \tag{2.66}$$

Once an optimal tip speed ratio is achieved it is then maintained up to the rated wind speed, therefore the torque increases with wind speed as:

$$\mathcal{T}(v_{\text{wind}}) = 0.5\pi\zeta_{\text{aero}}\rho_{\text{air}} r_{\text{swept}}^3 \frac{v_{\text{wind}}^2}{\Gamma_{\text{TSR}}} \tag{2.67}$$

Once rated power is achieved, the WTG rotational speed and torque is assumed to be constant until the cut-off wind speed is reached. For simplicity, ζ_{aero} is assumed

constant throughout the operational range despite the non-optimal tip-speed ratio in the first constant speed region.

The shaft power into the generator at each wind speed is calculated as:

$$P_{\text{shaft}}(v_{\text{wind}}) = \omega(v_{\text{wind}})\mathcal{T}(v_{\text{wind}}) \tag{2.68}$$

The iron losses are evaluated for each wind speed considering the variation in electrical frequency and assuming that the flux density amplitude is constant throughout the operational range.

For below-rated operation the armature current is calculated for each wind speed assuming that:

$$P_E(v_{\text{wind}}) = P_{\text{shaft}}(v_{\text{wind}}) - P_{\text{hys}}(v_{\text{wind}}) - P_{\text{eddy}}(v_{\text{wind}}) - P_{\text{add}}(v_{\text{wind}}) - P_{\text{PM}}(v_{\text{wind}}) \tag{2.69}$$

An iterative approach is taken where $P_E(v_{\text{wind}})$ is first solved assuming that $P_{\text{PM}}(v_{\text{wind}}) = 0$. $P_{\text{PM}}(v_{\text{wind}})$ is then calculated and the value of $P_E(v_{\text{wind}})$ is updated, this process is repeated until a constant value for $P_E(v_{\text{wind}})$ is obtained. E_P and I_s are calculated taking into consideration that ω_e varies according to the wind speed.

Finally, the converter losses are calculated for the range of wind speeds using Eq. (2.60).

A power curve can then be generated for the wind turbine:

$$P_{\text{out}}(v_{\text{wind}}) = P_{\text{shaft}}(v_{\text{wind}}) - P_{\text{loss}}(v_{\text{wind}}) \tag{2.70}$$

In Figure 2.7 a power curve and an efficiency curve are presented for the example 15 MW WTG.

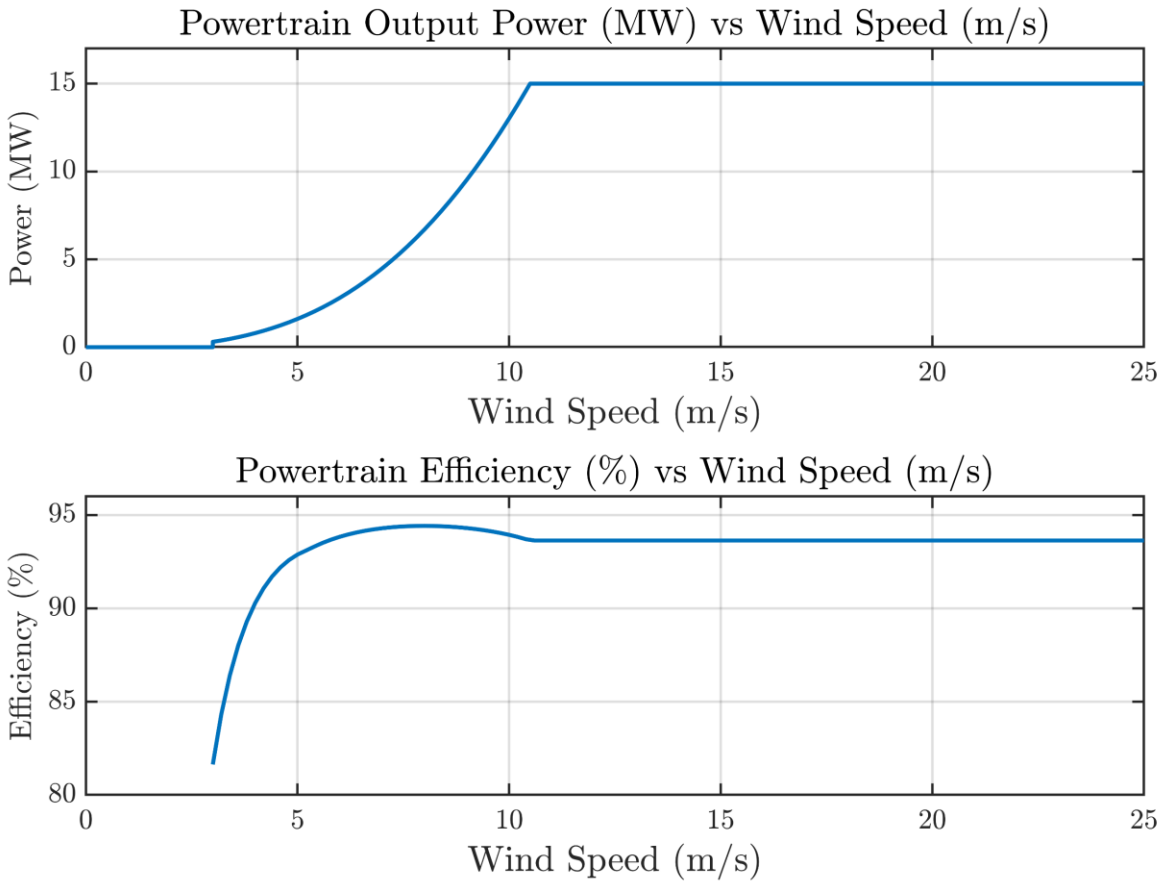

Figure 2.7: Powertrain output power and efficiency vs wind speed for the example 15 MW machine.

2.1.12 Calculation of Energy Yield

Now that a wind turbine power curve has been produced the annual energy yield of the wind turbine can be calculated based on a historical wind speed distribution which is estimated using the Weibull density distribution:

$$w(v_{\text{wind}}) = \frac{k_1}{c_1}\left(\frac{v_{\text{wind}}}{c_1}\right)^{k_1-1} \exp\left(-\left(\frac{v_{\text{wind}}}{c_1}\right)^{k_1}\right) \tag{2.71}$$

where k_1 is the shape parameter which represents wind speed variability and c_1 is the scale parameter which represents the mean wind speed at the site. The total annual energy yield is calculated by summing the incremental energy yield at each wind speed:

$$\text{AEP} = \zeta_{\text{av}} t_{\text{year}} \sum_{j=1}^{n} P_{\text{out}}(v_{\text{wind},j}) \cdot w(v_{\text{wind},j}) \Delta v_{\text{wind}} \tag{2.72}$$

where t_{year} is the number of hours in a year, and ζ_{av} is the production-based availability factor which accounts for the fact that a wind turbine will not be available for power generation all the time due to component faults, maintenance, and external circumstances such as a congested energy grid. Accurate prediction of availability is challenging as it is site specific, depending on component failure rates, weather conditions, and the availability of workers, vessels, and replacement components [40].

Figure 2.8 shows how the cumulative losses vary with wind speed assuming that $\zeta_{\text{av}} = 1$. Converter and copper losses are the most significant contributing ~46% and ~40% to the total cumulative annual loss respectively. Iron losses are also appreciable, especially at low wind speeds, contributing to ~14% of the cumulative annual loss as shown in Figure 2.9. Although it is assumed that there is no circumferential segmentation in each PM, the magnet losses were found to contribute to less than 1% of the cumulative annual loss.

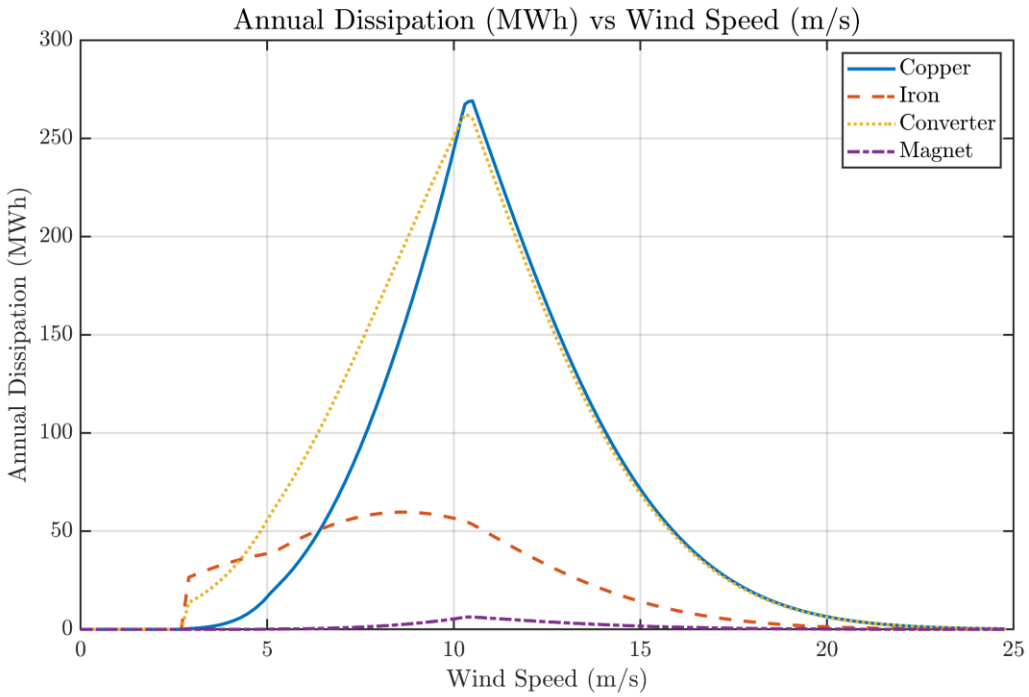

Figure 2.8: Annual dissipation of the example 15 MW machine (MWh) plotted as a function of wind speed (m/s).

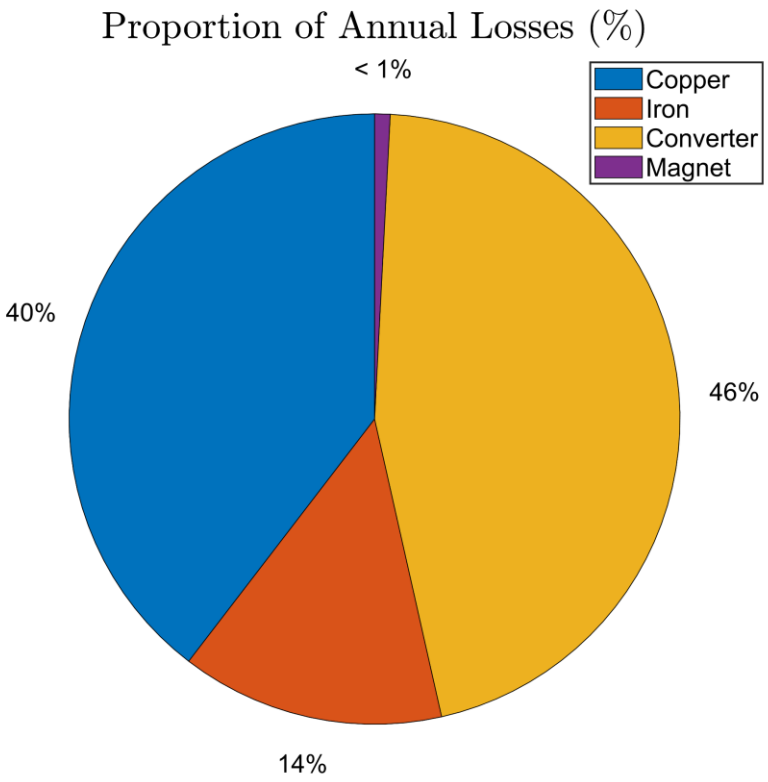

Figure 2.9: Proportion of annual energy loss for the example 15 MW machine.

2.1.13 Specification of the Example 15 MW Outer-Rotor Generator

In Table 2.2 the specification of the example 15 MW outer-rotor DD WTG is provided, calculated according to the input parameters in Table 2.1. In Figure 2.10 an image is provided from a finite element method (FEM) magnetic simulation of the example DD WTG which shows the dimensions to scale.

Table 2.2: Specification of example 15 MW outer-rotor direct-drive wind turbine generator.

Description	Symbol	Value	Units
Rated Operational Conditions			
Rated power out of the converter	P_{rated}	15	MW
Rated rotational speed	ω_{rated}	0.787	rad/s
Rated electrical frequency	$\omega_{e,\text{rated}}$	78.72	rad/s
Rated torque	$\mathcal{T}_{\text{rated}}$	20.35	MNm
Rated wind speed	v_{wind}	10.50	m/s
Rated tip speed	$\Gamma_{\text{TSR}} v_{\text{rated}}$	94.46	m/s
Electromagnetic Design			

Description	Symbol	Value	Units
Rotor radius	r_{r}	5.0465	m
Core length	l_c	2.12	m
Air-gap clearance	h_{g}	10.10	mm
Number of poles	N_{pole}	200	–
Number of slots	N_{slot}	240	–
Stator yoke thickness	h_{SY}	38.6	mm
Rotor yoke thickness	h_{RY}	38.6	mm
Pole pitch	τ_{pole}	158.5	mm
Slot pitch	τ_{slot}	131.9	mm
Slot height	h_{slot}	109.5	mm
Slot width	w_{slot}	54.7	mm
Slot opening width	w_{SO}	27.35	mm
Tooth width	w_{tooth}	77.1	mm
Tooth tip width	w_{TT}	104.55	mm
Tooth tip height	$h_{\mathrm{TT,2}}$	10.10	mm
Tooth taper height	$h_{\mathrm{TT,1}}$	20.20	mm
Magnet height	h_{PM}	50.5	mm
Magnet width	w_{PM}	126.8	mm
Rated RMS no-load voltage	E_p	4179	V
Rated RMS winding current	I_s	1418	A
Rated RMS winding current density	J_{RMS}	2.91	$\mathrm{A/mm^2}$
Specific current loading	A_1	85.7	kA/m
Stator winding turns per phase	N_s	320	–
Peak air-gap flux density	$\widehat{B_g}$	1.18	T
Generator efficiency at full load	ζ_{gen}	96.53	%
Converter efficiency at full load	ζ_{conv}	97.0	%
Powertrain efficiency at full load	ζ_{PT}	93.64	%
Magnetising inductance	L_m	3.9	mH
Leakage inductance	L_σ	29.5	mH
Key Masses			
Electrical steel mass	$m_{\mathrm{Fe,e}}$	72.58	Tonne
Structural steel mass [13]	$m_{\mathrm{Fe,s}}$	157.3	Tonne
Copper mass	m_{Cu}	20.37	Tonne
Magnet mass	m_{PM}	20.52	Tonne
Total active mass	m_{active}	113.5	Tonne
Total generator mass	m_{gen}	270.8	Tonne

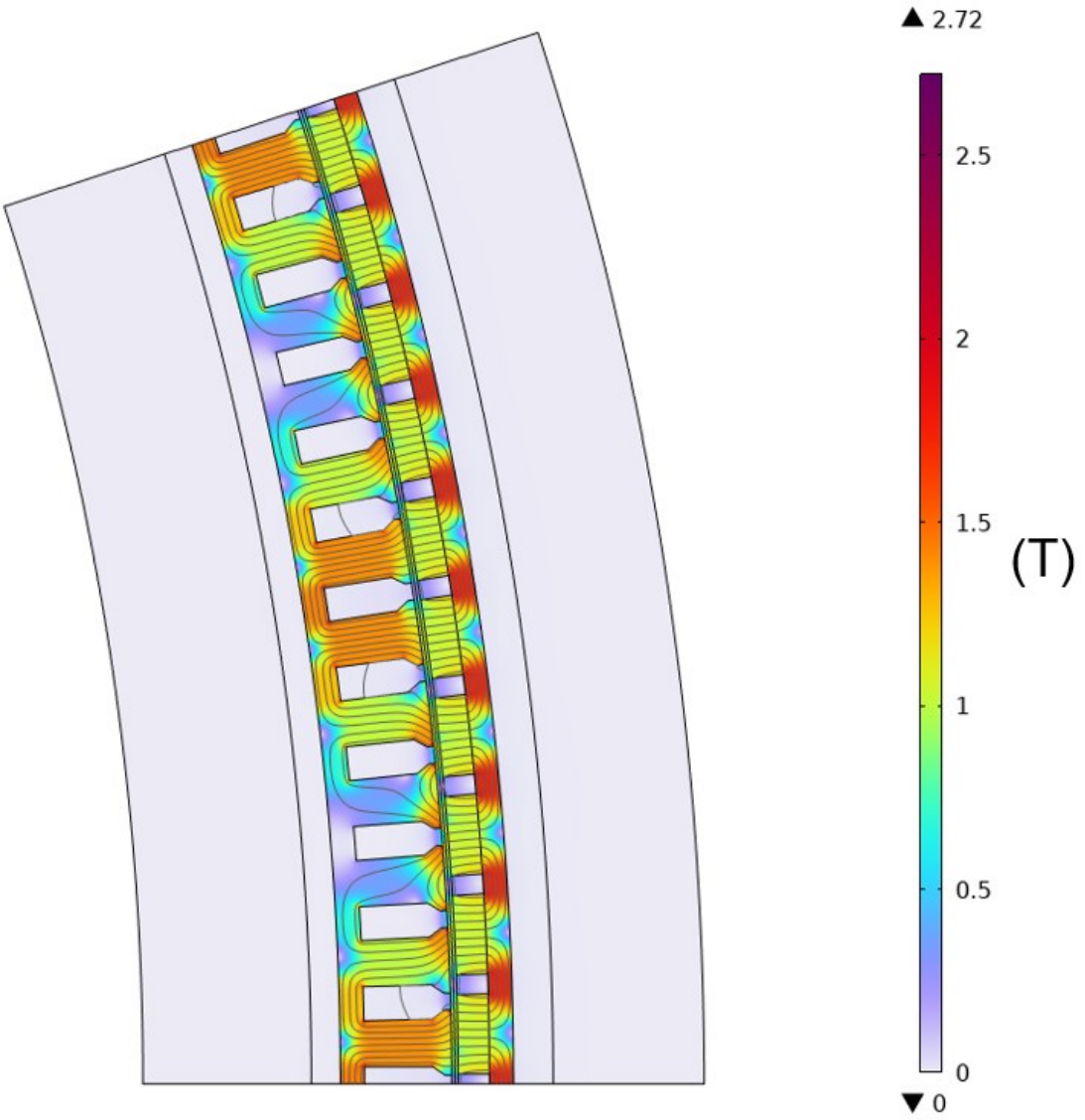

Figure 2.10: Finite element method (FEM) magnetic simulation of the example 15 MW outer-rotor direct-drive wind turbine generator with dimensions to scale. 1/40th of the full design is shown (10 poles and 12 slots).

2.2 Wind Turbine Generator Design Objectives

In the following section, various objectives behind WTG design are discussed.

2.2.1 Minimising Material Costs

The construction of multi-megawatt-scale DD WTGs requires substantial amounts of material, particularly electrical and structural steel, copper, and rare-earth permanent magnets. It is therefore desirable to utilise these materials efficiently to reduce capital expenditure, especially in the case of rare-earth permanent magnets which are both costly and subject to significant price volatility [41]. In Table 2.3 indicative costs and densities are provided for the key materials.

Table 2.3: Densities and specific costs of key materials.

Material	Density $(\mathbf{Kg/m^3})$	Specific Cost $(\$/\mathbf{Tonne})$	Source
NeFeB 52H Magnets	7600	29,130	[42]
Copper	8960	7,300	[43]
Electrical Steel	7700	4,440	[43]
Structural Steel	7850	1,560	[43]

Figure 2.11 provides a breakdown of the material costs and their corresponding mass proportions for the example 15 MW DD WTG design. Although PMs make up only ~8% of the total mass, they are the largest contributor to the total raw material cost accounting for ~45%. Between 2016 and 2024, the commodity price of neodymium fluctuated between $42,000 and $210,000 per metric tonne [44]. Under the assumption that PM cost scales with the neodymium commodity price, the proportion of total material cost attributed to the magnets would range from ~32% to ~70%, depending on when the cost was assessed during this period. Due to this volatility, a wide range of assumed PM costs can be found in literature concerning DD WTG design.

Copper and electrical steel also contribute significantly to overall material costs. It is important to avoid oversizing the slots, stator teeth, stator yoke, and rotor yoke so that their requirement is minimised.

Although structural steel has a relatively low specific cost, the structural frame of DD WTGs contributes significantly to the overall mass [45]. The estimate given here is based on the simplified disc-and-rim structure specified for the IEA 15 MW reference generator [13]. However, in practice the structure will take on a more complicated form that will utilise the structural steel more effectively [46].

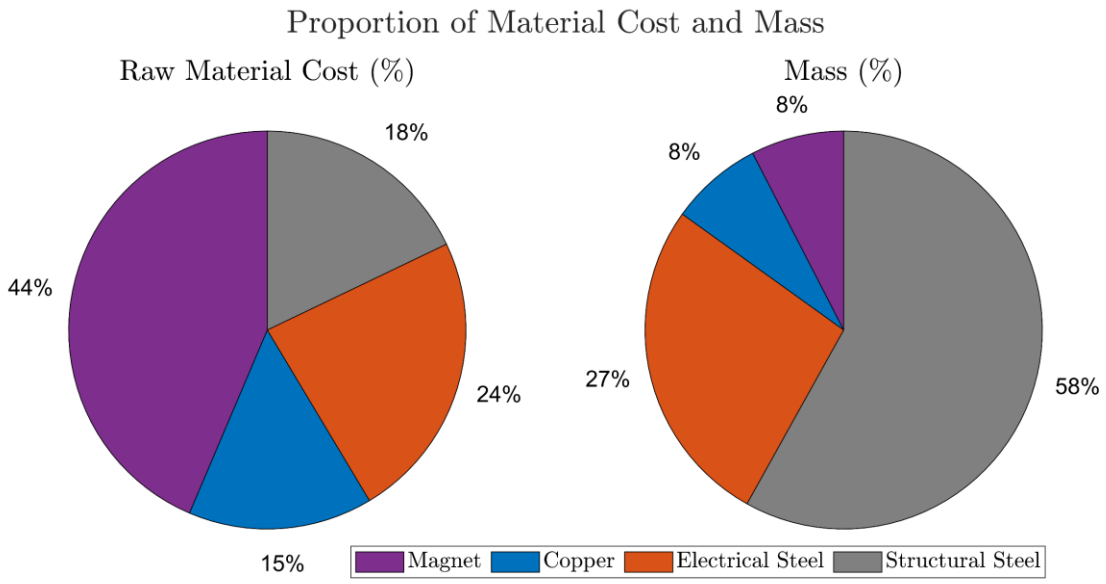

Figure 2.11: Proportion of material cost and mass in the example 15 MW machine.

2.2.2 Increasing Efficiency

Increasing the efficiency of a DD WTG design has several benefits, the most notable of which is that less energy is wasted as losses, leading to an increased energy yield and therefore revenue over the lifetime of a wind turbine.

It is also important to note that an increased efficiency will reduce the loading on the wind turbine for a given power rating, less aerodynamic torque is required to achieve rated power and the rated wind speed can be lowered (reducing the thrust loading).

The copper losses are the dominant loss mechanism within a PM DD WTG. It is challenging to reduce them assuming that the average electromagnetic shear stress ($\bar{\sigma}_t$) is kept constant:

- Increased flux linkage from the rotor field would allow for reduced current loading due to an increased EMF (E_p), however this is limited by magnetic saturation of the electrical steel in the magnetic circuit.
- An increased slot fill factor would reduce copper losses, however this is limited by the practicalities of coil manufacturing and the requirement for voltage insulation.

Improved cooling of armature windings can reduce the copper losses by lowering the copper resistivity ϱ_{Cu}, however more effective cooling strategies generally result in increased complexity of the WTG. In Chapter 3 it is demonstrated how the temperature

dependence of the copper loss can be modelled and how the WTG component temperatures can be estimated according to a thermal modelling methodology.

2.2.3 Improving Reliability

High reliability, and as a result availability, is very important for offshore wind energy installations since generator repair or replacement can result in substantial costs and a significant amount of revenue may be lost if the wind turbine is out of operation for a long time [46]. Examples of how high reliability can be designed for include:

- Maintaining sufficiently low armature winding temperature during operation to avoid premature degradation of the insulation.
- Maintaining sufficiently low PM temperatures during operation and evaluating the risk of PM demagnetisation in the event of short circuit faults such that the likelihood of PM demagnetisation is minimised.
- Avoiding complexity in auxiliary systems, e.g. utilising forced air-cooling as opposed to liquid-cooling.
- Eliminating mechanical contact where possible, e.g. eliminating slip rings by utilising permanent magnets instead of a wound rotor design.

2.2.4 Reducing Weight

The weight of the wind turbine nacelle must be carefully controlled to remain within the lifting capabilities of existing offshore installation vessels. As only a limited number of vessels are capable of installing multi-megawatt-scale turbines, excessive nacelle weight would pose significant logistical challenges [47]. A design that is more expensive or difficult to install than competing solutions would place a wind turbine supplier at a considerable commercial disadvantage.

It is often stated that WTG weight has a large impact on the structural cost of wind turbines. However, several studies indicate that for fixed-bottom multi-megawatt scale offshore wind turbines, the tower and foundation mass is mostly influenced by the thrust loading from the wind as opposed to the rotor nacelle assembly (RNA) mass.

Mendoza *et al.* present a design approach for the optimisation of offshore wind turbine structural mass [48]. They conclude that the tower and monopile design depends significantly on the rotor thrust and that the influence of RNA mass is small in comparison.

In the INNWIND.EU project it was investigated whether a cost reduction in the tower and foundations of a fixed-bottom offshore wind turbine could be achieved from a reduction in WTG mass, however it was found that there was limited potential for reducing structural costs [49]. If the tower mass was reduced significantly, they found that fatigue on the foundations would be worsened due to a change in the tower and foundation resonance frequencies.

Barter *et al.* investigate different powertrain topologies for offshore wind turbines with power capacities ranging from 15-25 MW [43]. Despite a large variation in nacelle mass between the different designs, as large as ~500 vs ~800 tonnes for the 25 MW WTGs, they present similar estimates for the required tower and monopile mass of fixed bottom wind turbines according to their structural model.

In summary, while the weight of WTGs is an important parameter, it should be treated as a practical constraint rather than a target for cost optimisation for fixed-bottom offshore wind turbines. For floating installations, minimisation of RNA mass may be more beneficial since it has a direct influence on the hydrostatic stability and motion of the wind turbine [50].

2.2.5 Reducing Volume

The size of a WTG is another logistical constraint. The nacelle must be transported from the factory to the top of a tower offshore.

The size of DD WTGs has continued to increase considerably due to the demand for large power capacities: surpassing practical limits assumed by authors such as Semken *et al.* who in the early 2010s suggested that DD WTGs should not exceed an external diameter of 6 m or a mass of 100 tonnes [33]. At the time of writing, prototype DD WTGs with power ratings of ~21.5 MW are being tested, demonstrating that the demand for increasing power capacities has outweighed the logistical issues associated with DD WTG size and mass [51].

It is difficult to directly quantify the negative impact of a large generator volume. It is often treated as a constraint in design studies, if it is left unconstrained optimisation procedures tend to produce very large generator designs since a large air-gap diameter is very beneficial for torque production.

In the early 2000s, Spooner *et al.* considered the design of a very large, air-cored PM DD WTG for multi-megawatt scale offshore installations [52]. Since the air-gap diameter is very large compared to conventional machines the required torque output can be achieved with a relatively low value of $\bar{\sigma}_t$, allowing for a lightweight and efficient design.

2.2.6 Summary

In summary, it is desirable to maximise the efficiency and reliability of DD WTGs and minimise the material costs, especially the PM material cost. While it is important to avoid an excessive WTG weight and volume, this should be treated as a practical constraint rather than a strict target for minimisation in optimisation studies.

2.3 Approaches for Reducing the Total Permanent Magnet Cost

As highlighted in the previous section, one of the most effective ways to reduce the cost of DD PM WTGs is to reduce the PM material costs. The following section will discuss various approaches for reducing the PM material cost.

2.3.1 Selection of Permanent Magnet Grade

The specific cost of PM material ($/Kg) depends on the grade selected, generally rising as the strength and the maximum allowable operating temperature of the magnet material increases. In Appendix C a summary of different grades of NeFeB PMs is provided.

Although selecting a magnet grade with a large remanent flux density increases the specific cost ($/kg) it can reduce the overall PM mass required in a DD WTG design depending on the required performance. For example, in Figure 2.12 the normalised total cost of PM material required in the example 15 MW WTG is compared for different H-grade PMs assuming that a peak fundamental flux density of 1.1 T must be achieved at their maximum operating temperature of $120^{\circ}\mathrm{C}$. Although the NeFeB 52H magnets have the highest specific cost, the total PM cost required for the DD WTG design is the lowest in this case.

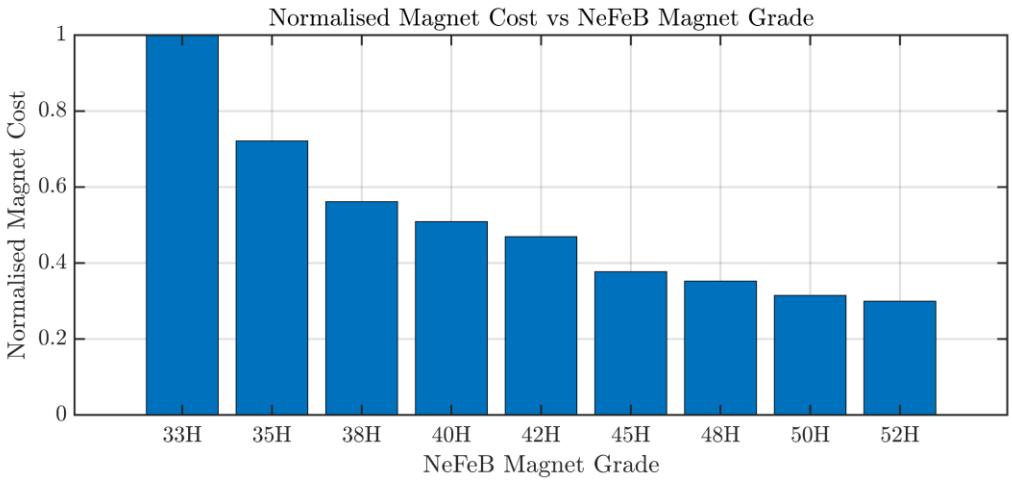

Figure 2.12: Total magnet cost required for the example 15 MW machine to provide a peak fundamental air-gap flux density of 1.1 T at a temperature of $120^{\circ}\mathrm{C}$ for different grades of NeFeB permanent magnets (PMs). The cost is normalised with respect to the total cost of 33H grade PMs that would be required.

2.3.2 Increasing the Current Loading

If the current loading of the armature windings can be increased, it would lead to an increased torque production per unit of induced EMF. The WTG could be made smaller due to the increased electromagnetic shear stress, or the volume could be maintained, and less PM material used such that the required torque is achieved at a lower value of induced EMF.

A key constraint limiting WTG current loading is the temperature limit of the PMs and the armature windings. If the generator can be cooled more effectively, then the current loading can be increased. However, an increased current loading will also reduce efficiency: negatively impacting the energy yield.

2.3.3 Lowering the Magnet Temperature

If the maximum operating temperature of the PMs can be maintained at low values, then less expensive grades of magnet can be utilised. Therefore, if the DD WTG can be cooled more effectively there is potential to significantly reduce PM costs. PM remanent flux density is also larger at lower temperatures leading to improved performance [53].

The temperature dependence of PM remanent flux density (B_{rem}) is approximately linear and can be described by the following equation [29]:

$$B_{\mathrm{rem}}(T) = B_{\mathrm{rem}}\left(T_{\mathrm{PM},0}\right)\left[1 + C_{\mathrm{PM,Temp}}\left(T_{\mathrm{PM}} - T_{\mathrm{PM},0}\right)\right] \tag{2.73}$$

where $C_{\mathrm{PM,Temp}}$ is the temperature coefficient of the PM remanent flux density, T_{PM} is the PM temperature, $T_{\mathrm{PM},0}$ is a reference temperature of the PM, and $B_{\mathrm{rem}}(T_{\mathrm{PM},0})$ is the remanent flux density of the PM at the reference temperature $T_{\mathrm{PM},0}$.

In Figure 2.13, normalised magnet mass required to achieve a peak flux density of 1.1 T is plotted for a range of PM temperatures assuming that $C_{\mathrm{PM,Temp}} = -0.00174$, $T_{\mathrm{PM},0} = 120^{\circ}\mathrm{C}$, and $B_{\mathrm{rem}}(T_{\mathrm{PM},0}) = 1.28\ \mathrm{T}$. The required magnet mass can be observed to decrease significantly as the maximum magnet operating temperature is decreased with a reduction of ~35% if it is lowered from $120^{\circ}\mathrm{C}$ to $50^{\circ}\mathrm{C}$.

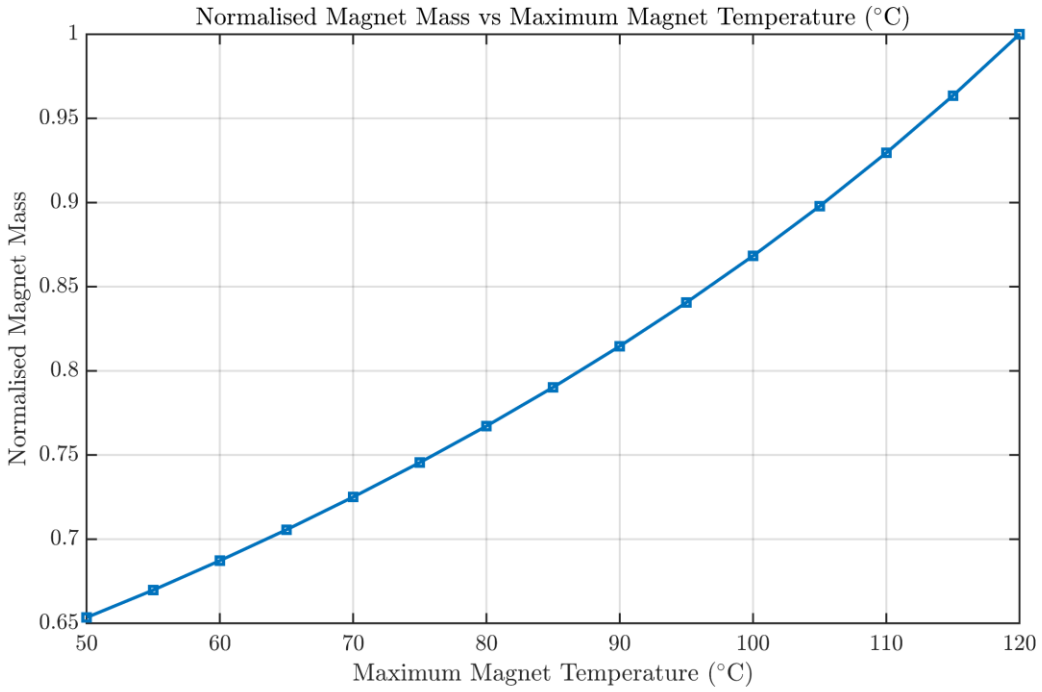

Figure 2.13: Magnet mass required in the example 15 MW machine to provide a peak fundamental air-gap flux density of 1.1 T for various maximum magnet temperatures. The magnet mass is normalised with respect to the mass required at a temperature of $120^{\circ}\mathrm{C}$.

2.3.4 Reducing the Air-Gap Reluctance

The amount of PM material required in a DD WTG design is strongly linked to the air-gap reluctance. By reducing the air-gap clearance the requirement for PM material can be significantly reduced. In Figure 2.14, normalised magnet height is plotted for a range of air-gap clearance factors (C_{hg}) for a target peak flux density of 1.1 T. If C_{hg} is increased beyond the assumed value of 0.001 the required magnet height increases non-linearly due to a significant increase in inter-pole magnetic leakage, if it is

decreased below 0.001 the required magnet height is observed to decrease in an approximately direct proportion to the air-gap clearance.

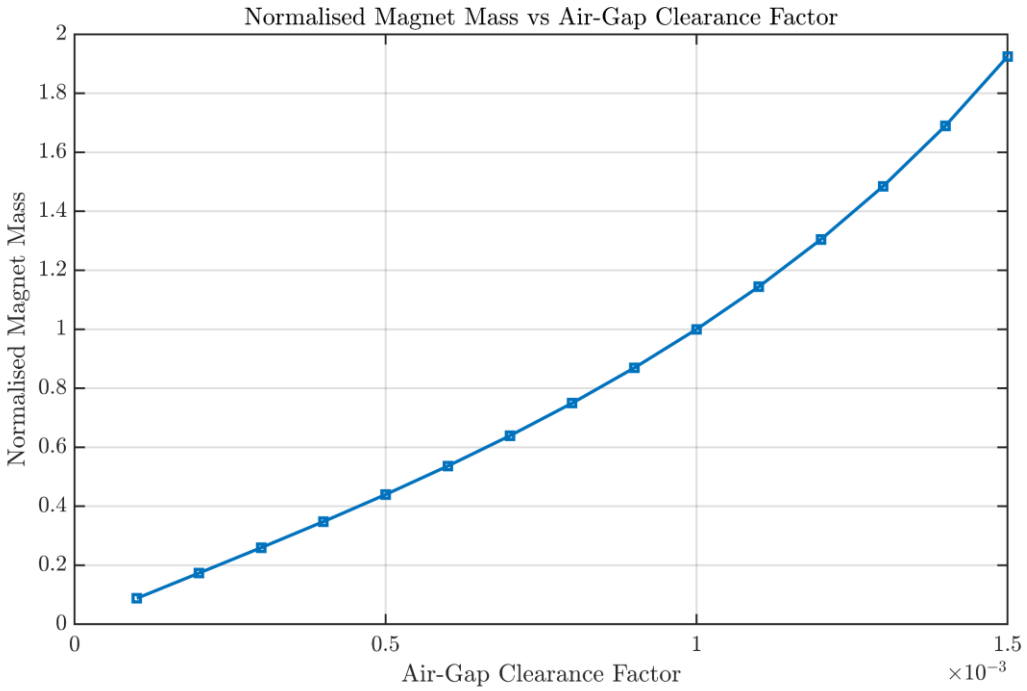

Figure 2.14: Magnet mass required in the example 15 MW machine to provide a peak fundamental air-gap flux density of 1.1 T at a temperature of $120^{\circ}\mathrm{C}$ for various air-gap clearance factors (C_{hg}). The magnet mass is normalised with respect to the mass required for $C_{\mathrm{hg}} = 0.001$.

Tooth-tips can add manufacturing complexity to large offshore wind turbine generators in comparison to open-slot designs [54]. However, an open-slot design results in a large Carter factor. The impact of tooth-tips on Carter factor and the height required of a 52H grade PM to achieve a target peak fundamental flux density of 1.1 T at an operating temperature of $120^{\circ}\mathrm{C}$ is shown in Figure 2.15. The addition of tooth-tips has a significant impact on the amount of PM material required.

The Carter factor can also be reduced by increasing the number of poles and slots. However, this will increase inter-pole magnetic leakage, slot and tooth-tip leakage inductance, and the manufacturing complexity.

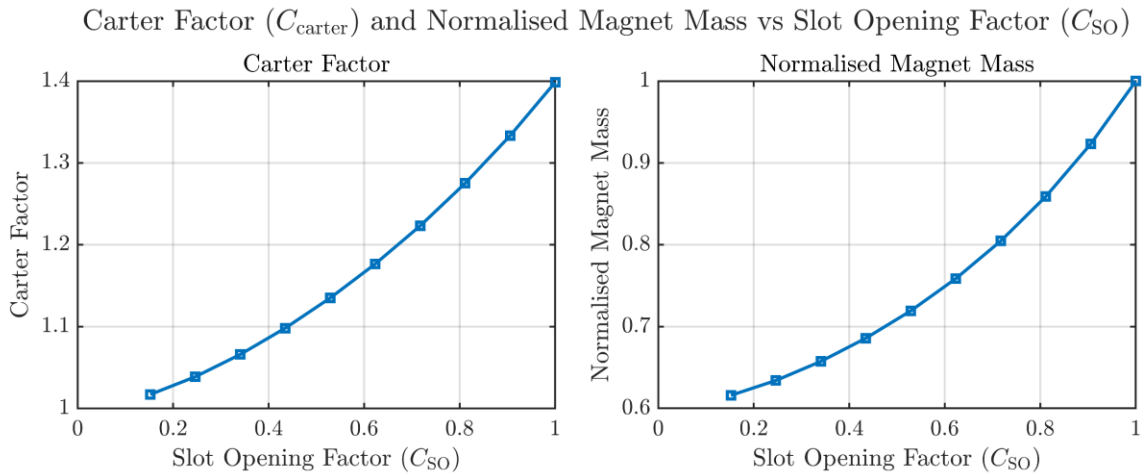

Figure 2.15: Carter factor (C_{carter}) and normalised magnet mass of the example 15 MW machine operating with a peak fundamental air-gap flux density of 1.1 T at a magnet temperature of $120^{\circ}\mathrm{C}$ for various slot opening factors (C_{SO}). Slot opening factor is defined as the ratio between the slot opening width (w_{SO}) and the slot width (w_{slot}): a value of 1 designates an open slot. The magnet mass is normalised with respect to the mass required when $C_{\mathrm{SO}} = 1$.

2.3.5 Summary and Motivation for the Following Chapters

As demonstrated in this section, the total PM magnet material cost can be reduced significantly by improving the cooling of the WTG or by reducing the air-gap reluctance.

Despite the significance of DD WTG thermal performance, studies regarding DD WTG design often elect to forgo a thermal analysis and instead assume a 'rule-of-thumb' constraint for the armature current density and current loading. There is a lack of up-to-date thermal models in literature that are relevant for modern DD WTGs. Motivated by this, Chapter 3 will introduce a revised lumped parameter thermal network (LPTN) model for DD WTGs, compare the thermal performance of an inner- and outer-rotor WTG topologies, and investigate the behaviour of a forced air- and liquid-cooling system.

Despite the strong influence of the air-gap clearance on DD WTG cost, there is little work available in literature detailing its appropriate specification. Simple 'rules-of-thumb' are widespread in literature, namely the assumption that $C_{\mathrm{hg}} = 0.001$. Chapter 4 will detail the air-gap clearance specification of DD WTGs, reviewing prior work in this area and presenting novel research.

Chapters 5-8 will detail an investigation into an unconventional approach for reducing air-gap reluctance in which the magnetic permeability of the air-gap region is increased by filling it with magnetically permeable ferrofluid: making it a 'ferrofluid-gap'.

2.4 Conclusion

In conclusion, a design procedure for multi-megawatt scale fractional slot concentrated winding (FSCW) permanent magnet (PM) direct-drive (DD) wind turbine generators (WTGs) has been introduced, serving as a review of DD WTG design and providing a resource for the following chapters.

Several simplifications have been made in the procedure: notably an absence of iron reluctance and armature reaction. Such simplifications are reasonable for a first approximation of a DD WTG design; further design refinement and optimisation would involve the application of finite element method (FEM) simulations to appropriately incorporate these effects. Extra detail could also be applied in considering how aerodynamic efficiency varies at low wind speeds, or in how component temperatures would vary during operation, influencing key parameters such as the winding resistivity and the PM residual flux density.

In this chapter, assumptions were made as to the average temperature of key WTG components such as the armature windings and the PMs. However, in the following chapter a thermal model for DD WTGs is introduced which allows for the calculation of the WTG component temperatures.

An example 15 MW outer-rotor DD WTG was specified according to the design procedure to help illustrate the opportunities for DD WTG cost reduction. It has been highlighted how PM material costs contribute significantly to the total material cost of DD WTGs due to their expensive and volatile price.

In Section 2.3 various approaches for reducing the total PM material cost required for a DD PM WTG have been summarised. It was highlighted that the PM material cost can be reduced by cooling the WTG more effectively, or by reducing the magnetic reluctance of the air-gap region: motivating the following chapters of this thesis.

Chapter 3: Thermal Modelling of Direct-Drive Wind Turbine Generators

The following chapter will discuss cooling strategies for direct-drive (DD) wind turbine generators (WTGs), approaches for thermal modelling, and prior work in literature regarding DD WTG thermal modelling. Opportunities for improved thermal modelling of DD WTGs are highlighted, motivating the development of a refined lumped parameter thermal network (LPTN) model which is detailed in Section 3.3. In Section 3.4 a design procedure is provided for a liquid-to-air and an air-to-air heat exchanger. In Section 3.5, the performance of a forced air- and liquid-cooling strategy is compared, and the influence of an inner- and outer-rotor DD WTG topology on thermal performance is investigated. The power consumption and required volume for a liquid-to-air and air-to-air heat exchanger are also examined.

3.1 Thermal Management and Modelling of DD WTGs

The thermal performance of direct-drive (DD) wind turbine generators (WTGs) is vitally important, most notably due to the temperature limits of the winding insulation and the permanent magnets (PMs): exceeding these limits can result in accelerated aging of the insulation and irreversible demagnetisation of the PMs. For example, National Electrical Manufacturers Association (NEMA) class F winding insulation has a temperature limit of $155^{\circ}\mathrm{C}$, and H-grade NeFeB PMs have a maximum operating temperature of $120^{\circ}\mathrm{C}$.

Elevated component temperatures also result in increased copper resistivity and reduced PM remanent flux density; therefore, improved WTG cooling can result in increased efficiency and can potentially allow for a reduction in PM costs. However, thermal modelling is often neglected in studies focusing on the design or optimisation of DD WTGs. Instead, constraints are imposed upon the maximum allowed armature current density and/or current loading according to established ‘rules-of-thumb’ [55]. In the work of Boldea it is stated that a specific current loading (A_1) in the range of 30-80 $\mathrm{kA/m}$ and a stator current density (J_{RMS}) of 3-6 $\mathrm{A/mm^2}$ can be accommodated using an indirect air-cooling system [56]. The large range of permissible values highlights

the difficulty of predicting the effectiveness of different cooling strategies without considering the specific design and operational context of the generator.

3.1.1 Cooling Strategies for Direct-Drive Wind Turbine Generators

As discussed by Taras *et al.* there are a variety of cooling techniques utilised for electrical machines that could in theory be applied to multi-megawatt scale DD WTGs [57]. Generally, improved cooling performance comes at the expense of increased system complexity and maintenance requirements, resulting in a compromise between the generator cost, efficiency, and wind turbine availability.

At the time of writing, closed loop forced air cooling is generally preferred in DD WTGs due to its relative simplicity compared to liquid or multi-phase cooling methods. A closed-loop cooling circuit utilises purified air to cool the generator, a second open-loop circuit is used to re-cool the air via an air-to-air heat exchanger, an illustration is provided in Figure 3.1. Taras *et al.* suggest that a closed-loop forced air cooling strategy will not be sufficient to deal with the trend of increasing wind turbine power capacity, and that quantitative analysis of alternative methods would be very valuable for assessing the viability of different cooling strategies [57]. Semken *et al.* illustrate that the efficiency of an air-cooling strategy does not scale well as armature current loading is increased beyond typical values, and that liquid cooling has potential for efficient and high-capacity cooling [33].

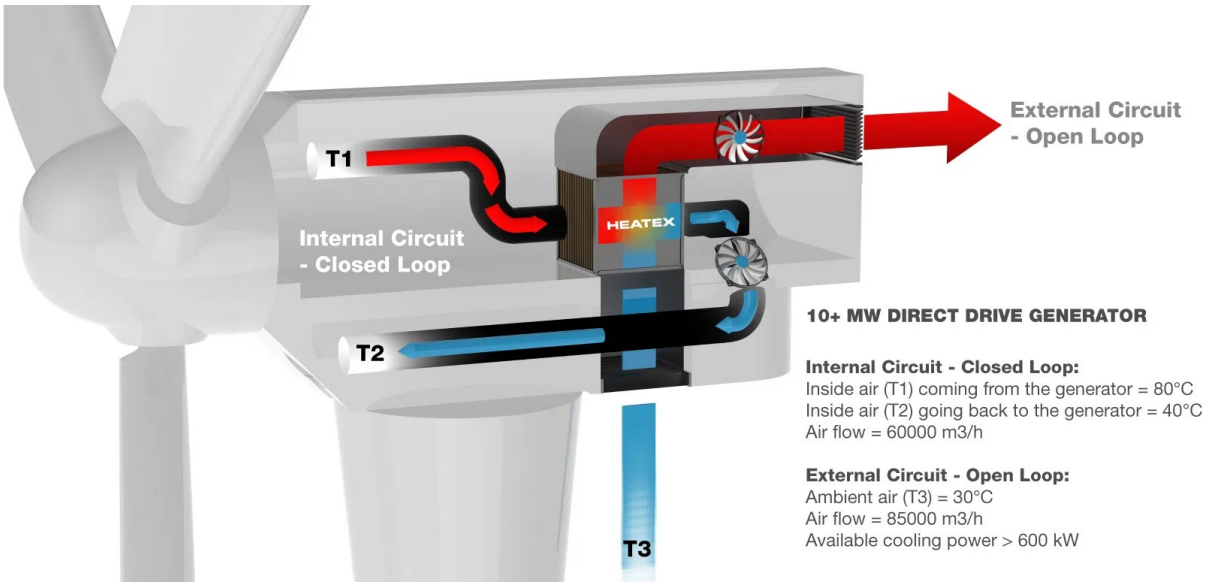

Figure 3.1: Illustration of a closed-loop air cooling system for a 10+ MW direct-drive wind turbine generator taken from the Heatex website [58].

Polikarpova *et al.* describe the design and analysis of a novel 8 MW outer-rotor DD WTG in which direct liquid cooling is utilised: coolant flows internally within the copper conductors enabling very efficient heat extraction [59]. It is claimed that an average air-gap electromagnetic shear stress of 80 kPa can be achieved, while maintaining relatively low PM and winding temperatures of $50^{\circ}\mathrm{C}$ and $80^{\circ}\mathrm{C}$ respectively without the need for excessive cooling circuit power consumption. Direct liquid cooling has been utilised successfully for high-power capacity hydro-generators, however in this case access for maintenance is relatively simple in comparison to offshore WTGs [60]. While it has yet to be established whether the performance benefits of direct-liquid cooling outweigh the associated complexity and operational risks for offshore WTGs, it is conceivable that this approach will gain appeal as power capacities continue to rise.

A less intrusive liquid cooling strategy is to implement a water jacket (WJ), such as in the Northern Power 1.5 MW DD WTG design in which a spiral WJ is positioned between the stator yoke and the stator frame [61]. In this approach the cooling performance is reduced in comparison to direct liquid-cooling, however it can be implemented in conjunction with a conventional stator design.

In Figure 3.2 an illustration is provided of an armature coil with direct liquid cooling and an inner-rotor machine with a water jacket.

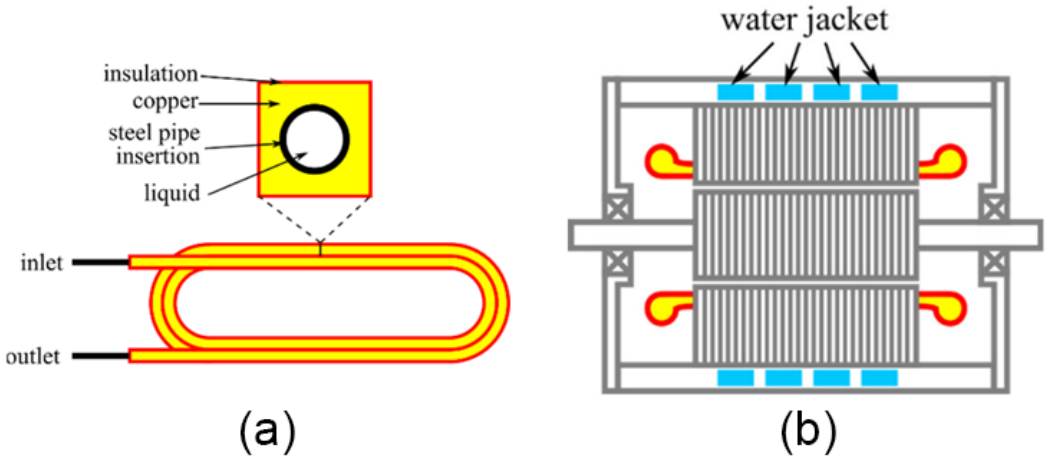

Figure 3.2: Illustration of an armature coil with direct liquid cooling (a), and an inner-rotor machine with a water jacket (b) [57].

3.1.2 Thermal Modelling of Electrical Machines

Generally, there are two favoured approaches for thermal modelling of electrical machines: lumped parameter thermal networks (LPTNs) and finite element analysis (FEA) [55].

LPTN models take an analogous form to electrical circuits, the electrical machine is discretised into a set of nodes which represent either the conductive (R_{cond}), convective (R_{conv}), or radiative (R_{rad}) heat transfer resistance (R) encountered by the flow of heat:

$$R_{\mathrm{cond}} = \frac{l_i}{k_i A_i} \quad R_{\mathrm{conv}} = \frac{1}{\alpha A_s} \quad R_{\mathrm{rad}} = \frac{1}{\alpha_{\mathrm{rad}} A_s} \tag{3.1,3.2,3.3}$$

where l_i is the path length of the heat flow through a node, k_i is the thermal conductivity of the node, A_i is the cross-sectional area of the heat flow path through a node, A_s is surface area, α is the convective heat transfer coefficient, and α_{rad} is the radiative heat transfer coefficient. The flow of heat through a node is driven by the temperature difference (ΔT) between each end according to Fourier's law:

$$\dot{Q} = \frac{\Delta T}{R} \tag{3.4}$$

Conductive and convective heat transfer are the dominant mechanisms of heat flow in electrical machines; radiative heat transfer is often ignored since it has a negligible influence at the typical surface and ambient temperatures relevant to electrical machines.

Conductive thermal resistances are estimated according to the geometry and conductivity of the machine's components. In the case of interface gaps, such as between the stator yoke and frame, a representative gap length is usually estimated assuming conduction through air.

Convective thermal resistances are more difficult to calculate since they depend on the state of flow over the surface under consideration. For simple geometries, such as flat plates, empirically derived convection correlations can be used. However, for complicated flow and/or surface geometries an accurate estimation requires the use of computational fluid dynamics (CFD) simulations which have ideally been validated using appropriately scaled experimental data.

For complicated geometries, such as the consideration of individual windings within a slot, finite element analysis (FEA) can be used to simulate the conductive heat transfer. However, although FEA simulations can be more accurate, LPTNs are popular for the thermal analysis and optimisation of electrical machine designs since they can be solved very quickly, facilitating a wide exploration of the possible design space.

Thermal analysis is often conducted assuming steady-state conditions in a worst-case scenario, e.g. maximum ambient operating temperature with maximum losses, to verify that the temperature limits for the windings and PMs will not be exceeded.

3.2 Opportunities for a Refined DD WTG Thermal Model

In his 1996 PhD thesis, Anders Grauers presents a detailed LPTN model for a forced air-cooled 0.5 MW surface mounted PM DD WTG [18]. It has been utilised by researchers concerned with the thermal behaviour of multi-megawatt scale WTGs, and inspired the methodology of similar models [53], [62].

In this thesis, a refined thermal model for DD WTGs is presented where:

- Recent advancements in LPTN modelling by Liang *et al.* are utilised, improving model accuracy [63], [64].
- Convection coefficients are calculated according to empirically derived relationships, as opposed to being designated constant values.
- Both inner- and outer-rotor DD WTG topologies are considered.
- Both forced air- and liquid-cooling are considered.
- The specification of both air-to-air and liquid-to-air heat exchangers is considered.

3.2.1 Distributed Loss Modelling

Accurate representation of heat sources in LPTN models can pose a significant challenge. For instance, if the heat generated within a stator slot is directly assigned to a single node it will result in an overestimation of the peak temperature within the slot. In this case, the heat is treated as a concentrated point source rather than being spatially distributed. If the temperature gradient within a component is small, such an approximation may be acceptable. However, when there is a significant temperature

gradient within a component, such as across the cross-section of a stator slot, this simplification can result in substantial error.

One approach to address this issue is to discretise a component into a multitude of nodes, allowing for an accurate representation of the temperature gradient. However, this increases the complexity and computational burden of a LPTN model.

A widely used solution to this problem is to introduce negative valued thermal resistances, referred to as compensation thermal resistances, which serve to correct for the spatial distribution of heat generation. This approach is based on the Poisson equation, which in one dimension (i) can be written as:

$$k_i \frac{\partial^2 T(i)}{\partial i^2} + \dot{q} = 0 \tag{3.5}$$

where k_i is thermal conductivity, T is temperature, and $\dot{q}$ is the heat generation rate per unit volume. By solving the Poisson equation, the resulting temperature profile can be used to derive an equivalent thermal resistance (R_{poisson}) that accounts for the spatially distributed heat generation without requiring discretisation into multiple nodes.

The compensation thermal resistance is essentially a correction factor: it modifies the thermal resistance of a component to match the result derived from the Poisson equation:

$$R_{\mathrm{comp}} = R_{\mathrm{poisson}} - R_{\mathrm{org}} \tag{3.6}$$

where R_{org} is the conductive thermal resistance obtained according to Eq. (3.1).

This approach is widely used in what is referred to as “T-type” LPTN models, where the heat flow in each dimension is considered independently and a corresponding compensation thermal resistance is specified according to the 1D Poisson equation.

In recent publications Liang *et al.* present an improved method for modelling distributed loss generation for multi-dimensional heat flows in LPTNs [63], [64]. For 2D and 3D heat flows, the corresponding 2D or 3D Poisson equation is solved to find the appropriate compensation thermal resistances for a multi-dimensional heat flow, resulting in improved estimation of peak and average component temperatures. By

incorporating this methodology, there is an opportunity to provide an improved LPTN model for DD WTGs.

3.2.2 Size Dependent Convective Heat Transfer

Convective heat transfer is one of the most critical yet challenging heat transfer mechanisms to model in electrical machines. The effective heat transfer coefficient depends on the fluid dynamic conditions at solid-fluid interfaces, such as between the end-windings and the internal airflow. It characterises the thermal resistance of the laminar boundary layer through which heat must first conduct before being advected by the free stream flow.

The most accurate way to determine convective coefficients is to obtain data from scaled physical experiments. This can be used to derive empirical relationships for the heat transfer coefficient and validate computational fluid dynamics (CFD) simulations. However, this approach can be prohibitively expensive and time-consuming.

Care needs to be taken when utilising empirical relationships for convective heat transfer. The convective heat transfer coefficient is defined as:

$$\alpha = \frac{\mathrm{Nu}\, k_{\mathrm{fluid}}}{l_{\mathrm{scale}}} \tag{3.7}$$

where k_{fluid} is the thermal conductivity of the fluid, l_{scale} is the characteristic length scale, and Nu is the Nusselt number. In forced convection, the Nusselt number can be correlated to Reynolds and Prandtl numbers via an algebraic expression:

$$\mathrm{Nu} = C_{\mathrm{Nu}} \mathrm{Re}^{m_1} \mathrm{Pr}^{n_1} \tag{3.8}$$

Where C_{Nu} is a coefficient, Pr is the dimensionless Prandtl number representing the ratio of momentum to thermal diffusivity of the fluid, the exponents m_1 and n_1 are typically less than unity, and Re is the Reynolds number which represents the ratio of inertial to viscous forces in a fluid flow:

$$\mathrm{Re} = \frac{\rho_{\mathrm{fluid}} v_{\mathrm{fluid}} l_{\mathrm{scale}}}{\eta_{\mathrm{fluid}}} \tag{3.9}$$

where ρ_{fluid} is the fluid density, v_{fluid} is the fluid velocity, and η_{fluid} is the dynamic viscosity. Substituting Eq. (3.8) and (3.9) into (3.7), results in the following relationship between the convective heat transfer coefficient and the characteristic length scale:

$$\alpha \propto l_{\text{scale}}^{(m_1-1)} \tag{3.10}$$

This shows that the heat transfer coefficient depends explicitly on the length scale, even if the flow velocity remains unchanged. Therefore, if an empirical correlation for $\bar{\alpha}$ is provided as a function of only velocity, it should only be applied to machines of a similar size and topology from which it was derived.

For example, according to Kylander the average heat transfer coefficient from the rotor to the internal air of an induction motor can be obtained from [65]:

$$\bar{\alpha} = 15.5(1 + 0.29v_{\text{r}}) \tag{3.11}$$

where v_{r} is the tangential velocity of the rotor at the air-gap. This relationship was used by Polikarpova *et al.* in the analysis of a multi-megawatt scale DD WTG [66].

In the thermal model presented by Grauers convective coefficients are estimated as constant values in his study of a 0.5 MW machine. However, these values have been used in the analysis of much larger machines with power capacities ranging from 6-10 MW [53].

In this work, the convective heat transfer coefficients from the various generator surfaces to air are calculated using analytical methods, drawing analogies to simplified geometries. This improves the flexibility of the model since the relevant length scales are considered explicitly in the calculations.

3.2.3 Comparison of Air- and Liquid-Cooling Systems

Other than in the work of Polikarpova *et al.* there is little work on modelling liquid-cooled DD WTGs [66]. In this work, a model is defined for both an air- and liquid-cooling approach such that a comparison can be made between the performance of both systems.

3.2.4 Inner- vs Outer-Rotor Topologies

The thermal performance of inner- and outer-rotor WTG topologies will be different due to the exposure of the external stator/rotor structure to the ambient air flow. By investigating the performance of both topologies there is an opportunity to provide a comparison of their thermal performance.

3.2.5 Heat Exchanger Modelling

The heat extracted from the WTG by a closed-loop cooling system must be exchanged to the open-loop airflow via a heat exchanger. Space is limited within and on top of a wind turbine nacelle, and an inefficient design may result in a reduced overall energy yield. In this work the design of both an air-to-air and liquid-to-air heat exchanger is specified, providing insight into the size requirements and power consumption of WTG heat exchangers.

3.3 Thermal Modelling Methodology

The following section details the methodology and assumptions employed in the thermal model used throughout this thesis.

3.3.1 Generator Topologies

Two different generator topologies are considered in this section, one that is air cooled and another that is liquid cooled. Both topologies are of a fractional slot concentrated winding (FSCW) surface mounted PM design, the key difference is that the water cooled design has a stainless steel spiral water jacket (WJ) positioned between the stator yoke and the stator structural frame with a press fit such as in the Northern Power “NW 1500 DD” generator design [61]. Similarly, for the air-cooled design it is assumed that the air flows through axial vents located between the stator yoke and frame.

It is assumed that the rotor yoke and stator yoke/teeth are constructed from electrical steel laminations that are connected to the rotor structure and WJ respectively with a press fit. The rotor and stator structures are made from structural steel. Epoxy glass fibre slot wedges are present and are assumed to be flush with the stator tooth tips. The PMs are glued to the rotor yoke and are protected by a thin layer of glass fibre reinforcement. Within the machine the coils are surrounded by an insulating slot liner, and the end windings follow a semi-circular arc around the end of each tooth. In Figure 3.3 an illustrated cross section of a pole- and slot-pitch is provided with geometrical parameters and generator components labelled.

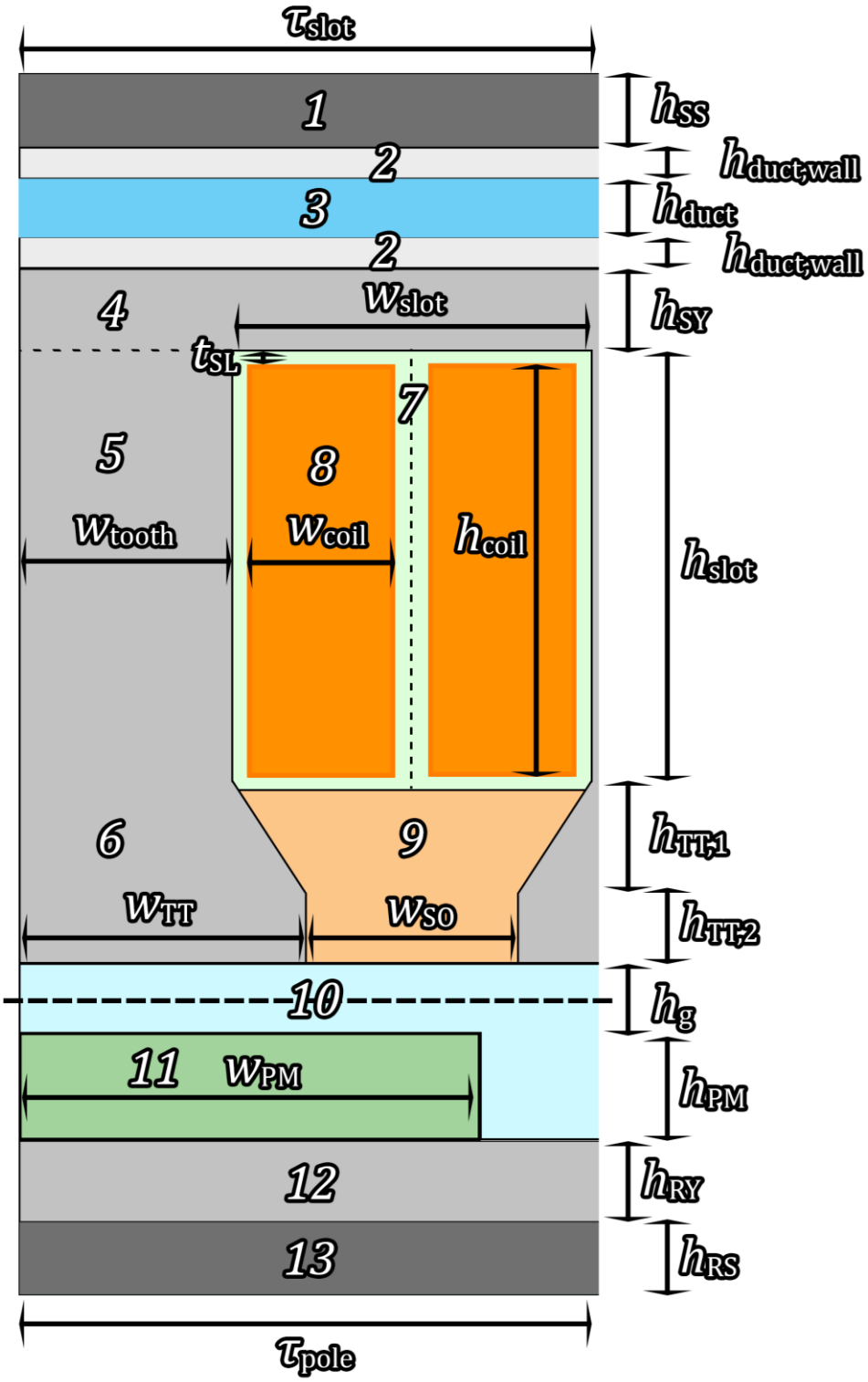

Figure 3.3: Illustration (not to scale) of slot- and pole-pitch with geometrical parameters and components labelled: 1- stator structural frame, 2- water jacket wall, 3- water jacket duct, 4- stator yoke, 5- stator tooth, 6- stator tooth tip, 7- slot liner, 8 armature coil, 9- slot wedge, 10- air-gap, 11- permanent magnet, 12- rotor yoke, and 13- rotor structural frame.

3.3.2 Heat Sources

The heat sources, i.e. the WTG losses, have already been introduced in Chapter 2. However, now that the component temperatures are directly evaluated with the thermal model the temperature dependence of the losses can be incorporated into their evaluation.

Conductor resistivity depends on temperature, it is therefore calculated according to the average winding temperature:

$$\varrho_{\mathrm{Cu}} = \varrho_0 + \varrho_0 C_\varrho (\bar{T}_{\mathrm{cond}} - T_0) \tag{3.12}$$

where ϱ_0 is the reference conductor resistivity, T_0 is the reference temperature, $\bar{T}_{\mathrm{cond}}$ is the average winding temperature, and C_ϱ is the temperature coefficient. The copper loss is calculated independently for the internal armature coils and the end windings according to their respective values of V_{cond} and ϱ_{Cu}.

The eddy current and hysteresis losses are assumed to be distributed in the stator yoke and teeth according to their respective masses. Following the work of Grauers the stray load losses are assumed to be concentrated in the stator teeth [18].

The magnet losses are assumed to be evenly distributed within the magnet volume.

Windage losses in the air-gap are assumed to be negligible.

Viscous losses in the WJ and air ducts are taken into consideration as detailed in Section 3.3.4 and 3.3.5, it is assumed that they contribute to the temperature rise of the closed-loop coolant flow.

3.3.3 Convective Heat Transfer Coefficients

The following section will detail the analytical calculation of the various convective heat transfer coefficients considered in the model. In each case the average Nusselt number ($\overline{\mathrm{Nu}}$) is calculated and the average heat transfer coefficient ($\bar{\alpha}$) is obtained using the appropriate length scale (l_{scale}) and the thermal conductivity of air (k_{air}).

These approximations provide generalisable first-order estimates; for improved accuracy, specific WTG topologies could be analysed using computational fluid dynamics and appropriately scaled physical experiments.

3.3.3.1 Air-Gap Surfaces

The average convective heat transfer coefficient in the air-gap ($\bar{\alpha}_{\mathrm{g}}$) of radial flux electrical machines is commonly estimated by approximating the air-gap flow as a Taylor-Couette (TC) system with a rotating inner cylinder and a fixed outer cylinder [67]. An illustration of a TC system is provided in Figure 3.4.

The flow state is characterised by the Taylor number:

$$\mathrm{Ta} = \mathrm{Re}_{\mathrm{g}} \left(\frac{h_{\mathrm{g}}}{r_{\mathrm{r}}} \right)^{0.5} \tag{3.13}$$

where the Reynolds number of the air-gap flow (Re_{g}) is given by:

$$\mathrm{Re}_{\mathrm{g}} = \frac{\rho_{\mathrm{air}} \omega r_{\mathrm{r}} h_{\mathrm{g}}}{\eta_{\mathrm{air}}} \tag{3.14}$$

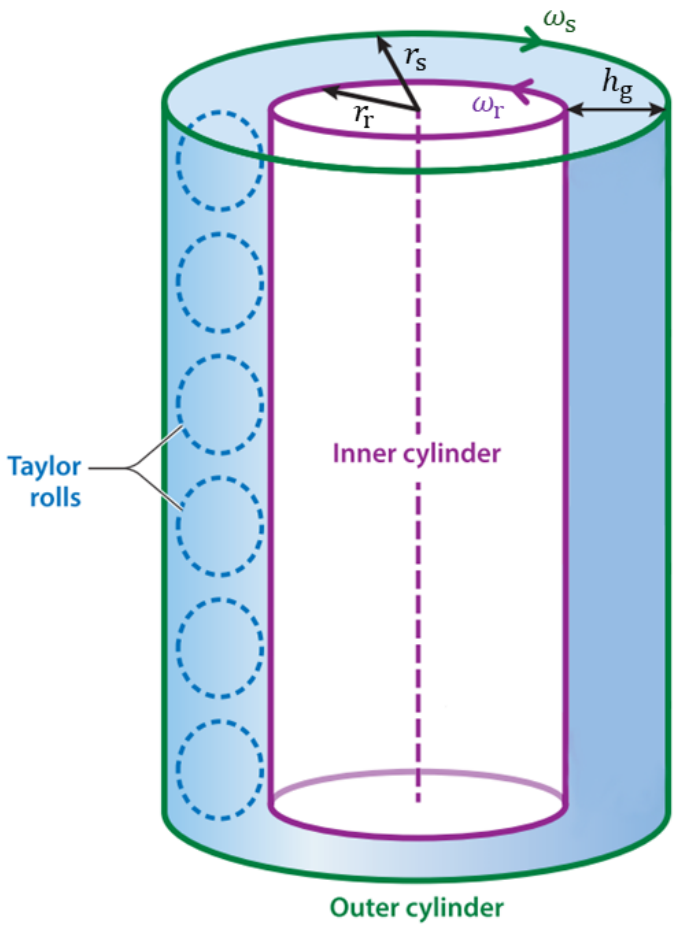

Figure 3.4: Illustration of Taylor-Couette flow [68].

The flow is laminar if $\mathrm{Ta} < 41$, Taylor vortices are then present until the flow becomes fully turbulent for $\mathrm{Ta} > 100$. The following equations can be used to find $\overline{\mathrm{Nu}}$ for each flow regime:

$$\overline{\mathrm{Nu}} = 2 \quad \mathrm{Ta} < 41 \tag{3.15}$$

$$\overline{\mathrm{Nu}} = 0.202\,\mathrm{Ta}^{0.63}\mathrm{Pr}_{\mathrm{air}}^{0.27} \quad 41 < \mathrm{Ta} < 100 \tag{3.16}$$

$$\overline{\mathrm{Nu}} = 0.386\,\mathrm{Ta}^{0.5}\mathrm{Pr}_{\mathrm{air}}^{0.27} \quad \mathrm{Ta} > 100 \tag{3.17}$$

Using Eq. (3.7), $\bar{\alpha}_{\mathrm{g}}$ can then be calculated where $l_{\mathrm{scale}} = 2h_{\mathrm{g}}$.

In the case of DD WTGs, the air-gap clearance is very small in comparison to the rotor radius, resulting in a radius ratio ($r_{\mathrm{s}}/r_{\mathrm{r}}$) that is very close to unity. For very thin-gap TC flow, the Taylor criterion is no longer strictly appropriate, and the behaviour of the flow is analogous to plane Couette flow, i.e. the flow of fluid sheared between two parallel plates [69].

For inner-rotor TC flow, the onset of turbulence can be predicted mathematically according to a linear stability analysis. This is because the onset of turbulence is driven by centrifugal instability imparted by the inner cylinder [68].

In contrast, outer-rotor TC and plane Couette flows are linearly stable. The onset of turbulence is instead triggered by finite size perturbations, e.g. from irregularities in the geometry or displacement of the system boundaries due to an external force. If the Reynolds number is sufficiently high, the turbulence can be sustained indefinitely.

According to experimental data, turbulence can be sustained in plane Couette flow beyond a Reynolds number of 370 [70]. For plane Couette flow, the Reynolds number is defined according to the average velocity and with a characteristic length equal to half of the gap, for a DD WTG air-gap this can be calculated as:

$$\mathrm{Re}_{\mathrm{g,PC}} = \frac{\rho_{\mathrm{air}}\omega r_{\mathrm{r}} h_{\mathrm{g}}}{4\eta_{\mathrm{air}}} \tag{3.18}$$

In DD WTGs, there is appreciable air-gap non-uniformity due to manufacturing/assembly tolerances and deformation of the rotor/stator from self-weight and magnetic forces. External loading can also displace the WTG rotor, perturbing the airflow. $\mathrm{Re}_{\mathrm{g,PC}}$ is relatively large due to the substantial air-gap clearance

and tangential velocity of the rotor. It is therefore reasonable to assume that the flow in the air-gap will be turbulent. The air-gap Nusselt number is therefore approximated according to Eq. 3.15, 3.16, or 3.17 for both inner- and outer-rotor WTG topologies.

In surface-mounted PM machines, the rotor has a slotted form due to the magnet spacings. Several studies have investigated the influence of slotting on heat transfer in Taylor-Couette flow [71]. The consensus is that, in comparison to a smooth rotor/stator there is a slight decrease in heat transfer for laminar flow, a slight enhancement for moderately turbulent air-gap flow, and a significant increase for Reynolds numbers beyond what could be expected in DD WTGs. For simplicity, the convective heat transfer area of the PMs is calculated according to the pole pitch, with the average heat transfer coefficient derived from a smooth rotor/stator assumption.

Due to the sensitivity of PM temperature to air-gap heat transfer, further research in this area would be very useful for improving the accuracy of DD WTG thermal analysis.

3.3.3.2 External Structure Surface

It is assumed that the external generator structure is directly exposed to wind. Analogy is made to external flow over a flat plate where the boundary layer has been ‘tripped’ at the leading edge resulting in a fully turbulent flow [72]. The average Nusselt number is given by:

$$\overline{\mathrm{Nu}} = \left(0.037\mathrm{Re}_{\mathrm{ext}}^{\frac{4}{5}} - 871\right)\mathrm{Pr}_{\mathrm{air}}^{\frac{1}{3}} \tag{3.19}$$

where $\mathrm{Re}_{\mathrm{ext}}$ is the Reynolds number at the end of the external structure, with the length scale approximated as l_c:

$$\mathrm{Re}_{\mathrm{ext}} = \frac{\rho_{\mathrm{air}} v_{\mathrm{ext}} l_c}{\eta_{\mathrm{air}}} \tag{3.20}$$

An outer-rotor structure will experience enhanced convective heat transfer due to an increased effective air velocity v_{ext} owing to its rotation:

$$v_{\mathrm{ext}} = \sqrt{v_{\mathrm{wind}}^2 + (\omega r_{\mathrm{ext}})^2} \tag{3.21}$$

where r_{ext} is the external radius of the WTG. For an inner-rotor machine $v_{\mathrm{ext}} = v_{\mathrm{wind}}$.

Using Eq. (3.7), the average external surface convective heat transfer coefficient ($\bar{\alpha}_{\mathrm{ext}}$) can then be calculated where $l_{\mathrm{scale}} = l_{\mathrm{c}}$.

3.3.3.3 Internal Structure Surface

The airflow between the internal structure and the shaft is approximated as a TC system with co-rotating cylinders or just inner cylinder rotation in the case of an inner-rotor and outer-rotor WTG respectively. The large gap between the structure's inner surface and the shaft ($h_{\mathrm{int}} = r_{\mathrm{int}} - r_{\mathrm{Shaft}}$) results in large values of Re and Ta, hence $\overline{\mathrm{Nu}}$ is calculated using Eq. (3.17) as it is assumed that the centrifugal force from the shaft dominates the flow. Using Eq. (3.7), the average internal surface convective heat transfer coefficient ($\bar{\alpha}_{\mathrm{int}}$) can then be calculated where $l_{\mathrm{scale}} = 2h_{\mathrm{Int}}$.

3.3.3.4 End Winding Surfaces

Estimating convective heat transfer from end windings into the internal air of an electrical machine is challenging due to the complex geometry and the difficulty in accurately modelling airflow over the various surfaces analytically [73]. While several empirical studies exist for small-scale machines, there is a lack of data for DD WTGs. To address this, the average end winding convective heat transfer coefficient ($\bar{\alpha}_{\mathrm{EW}}$) is estimated by approximating the end windings as cylinders in cross flow, as illustrated in Figure 3.5 [72].

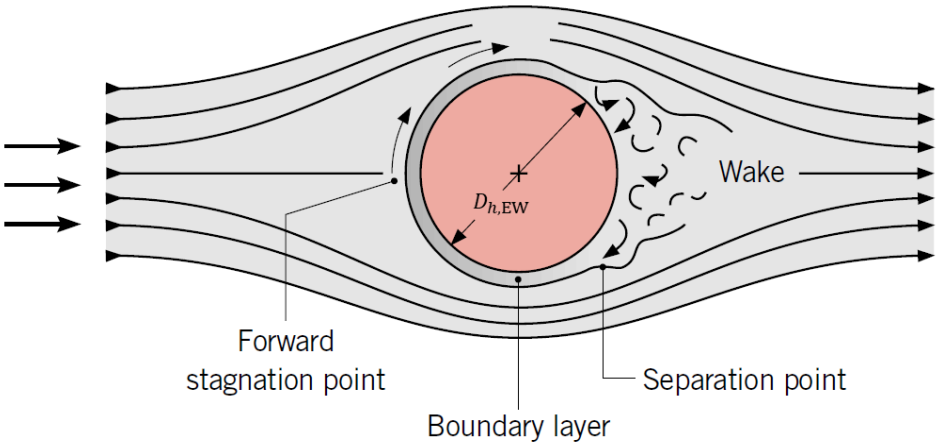

Figure 3.5: Illustration of a cylinder in cross flow [72].

The length scale is equated to the hydraulic radius of the end-winding cross section:

$$l_{\mathrm{scale}} = D_{h,\mathrm{EW}} = 2\frac{h_{\mathrm{coil}} w_{\mathrm{coil}}}{h_{\mathrm{coil}} + w_{\mathrm{coil}}} \tag{3.22}$$

Mixed convection is assumed, where the total average Nusselt number is the sum of the contributions from both free and forced convection, with the latter based on an air velocity equal to the rotor tangential velocity at the air-gap:

$$\overline{\mathrm{Nu}}_{\mathrm{T}} = \overline{\mathrm{Nu}}_{\mathrm{N}} + \overline{\mathrm{Nu}}_{\mathrm{F}} \tag{3.23}$$

The contribution from natural convection is given by:

$$\overline{\mathrm{Nu}}_{\mathrm{N}} = \left\{ 0.6 + \frac{0.387\mathrm{Ra}^{\frac{1}{6}}}{\left[1 + \left(\frac{0.559}{\mathrm{Pr}_{\mathrm{air}}}\right)^{\frac{9}{16}}\right]^{\frac{8}{27}}} \right\}^2 \tag{3.24}$$

where Ra is the Rayleigh number:

$$\mathrm{Ra} = \mathrm{Gr}\,\mathrm{Pr}_{\mathrm{air}} \tag{3.25}$$

where Gr is the Grashof number:

$$\mathrm{Gr} = \frac{g\beta_1\left(\bar{T}_{\mathrm{EW},s} - T_{\mathrm{int}}\right)l_{\mathrm{scale}}^3}{\eta_{\mathrm{air}}} \tag{3.26}$$

where β_1 is the volumetric thermal expansion coefficient of the internal air ($\beta_1 = 1/T_{\mathrm{int}}$ for an ideal gas), g is the gravitational acceleration constant, $T_{\mathrm{EW},s}$ is the average end winding surface temperature, and T_{int} is the internal air temperature. The contribution from forced convection is given by:

$$\overline{\mathrm{Nu}}_{\mathrm{F}} = 0.3 + \frac{0.62\,\mathrm{Re}_{\mathrm{EW}}^{\frac{1}{2}}\mathrm{Pr}_{\mathrm{air}}^{\frac{1}{3}}}{\left[1 + (0.4/\mathrm{Pr}_{\mathrm{air}})^{\frac{2}{3}}\right]^{\frac{1}{4}}}\left[1 + \left(\frac{\mathrm{Re}_{\mathrm{EW}}}{282000}\right)^{\frac{5}{8}}\right]^{\frac{4}{5}} \tag{3.27}$$

Where the Reynolds number of the airflow over the end windings is given by:

$$\mathrm{Re}_{\mathrm{EW}} = \frac{\rho_{\mathrm{air}}\omega r_{\mathrm{r}} D_{h,\mathrm{EW}}}{\eta_{\mathrm{air}}} \tag{3.28}$$

Using Eq. (3.7), $\bar{\alpha}_{EW}$ can then be calculated where $l_{\mathrm{scale}} = D_{h,\mathrm{EW}}$.

3.3.4 Water Jacket Modelling

Spiral WJ topologies, as depicted in Figure 3.6, have a good balance between heat transfer performance and efficiency, the behaviour of the fluid can also be estimated effectively using analytical methods [74]. The duct cross section is assumed to be rectangular: the duct height (h_{duct}) is estimated to be equal to the stator yoke height and the duct width (w_{duct}) is calculated assuming an aspect ratio of 8. The length of the WJ duct can be calculated as follows:

$$l_{\mathrm{duct}} = N_{\mathrm{duct,turn}} \sqrt{(2\pi r_{\mathrm{duct}})^2 + \left(\frac{l_c}{N_{\mathrm{duct,turn}}}\right)^2} \tag{3.29}$$

where r_{duct} is the distance between the centre of the duct and the WTG's rotational axis and $N_{\mathrm{duct,turn}}$ is the number of WJ turns assuming no clearance between adjacent ducts:

$$N_{\mathrm{duct,turn}} = \frac{l_c}{w_{\mathrm{duct}} + 2h_{\mathrm{duct,wall}}} \tag{3.30}$$

where $h_{\mathrm{duct,wall}}$ is the duct wall thickness.

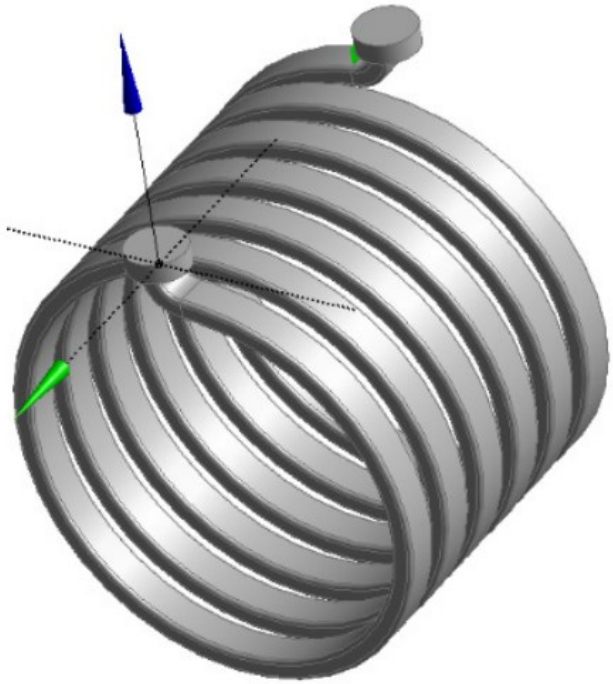

Figure 3.6: Illustration of a spiral water jacket [57].

Fully developed flow is assumed within the WJ with constant heat flux boundary conditions at the WJ walls, this means that the convection coefficient at the WJ walls (α_{cool}) is assumed to be uniform throughout the WJ. It is assumed that due to the temperature rise between the inlet and outlet of the WJ there is a corresponding axial temperature gradient within the machine. A WJ coolant velocity v_{cool} is specified from which the volumetric flow rate is calculated:

$$\dot{V}_{\mathrm{cool}} = w_{\mathrm{duct}} h_{\mathrm{duct}} v_{\mathrm{cool}} \tag{3.31}$$

The Reynolds number of the coolant flow is calculated:

$$\mathrm{Re}_{\mathrm{cool}} = \frac{\rho_{\mathrm{cool}} v_{\mathrm{cool}} D_{h,\mathrm{duct}}}{\eta_{\mathrm{cool}}} \tag{3.32}$$

where $D_{h,\mathrm{duct}}$ is the hydraulic diameter of the WJ duct which can be calculated with Eq. (3.22) by substituting in the WJ duct dimensions w_{duct} and h_{duct}. The Nusselt number of the WJ coolant can then be found:

$$\mathrm{Nu}_{\mathrm{cool}} = 0.023\ \mathrm{Re}_{\mathrm{cool}}^{0.8}\ \mathrm{Pr}_{\mathrm{cool}}^{\frac{1}{3}} \tag{3.33}$$

$\bar{\alpha}_{\mathrm{cool}}$ can then be calculated with Eq. (3.7) where $l_{\mathrm{scale}} = D_{h,\mathrm{duct}}$ and by substituting in the coolant thermal conductivity k_{cool}.

The power required to drive the coolant flow through the WJ ducts is calculated, first the Darcy friction factor (ς_d) is found by iteratively solving the Colebrook-White equation:

$$\frac{1}{\sqrt{\varsigma_d}} = -2\log\left(\frac{\Upsilon}{3.7 D_{h,\mathrm{duct}}} + \frac{2.51}{\mathrm{Re}_{\mathrm{cool}}\sqrt{\varsigma_d}}\right) \tag{3.34}$$

Where Υ is the absolute roughness coefficient of the duct. The pressure drop between the WJ inlet and outlet can then be found:

$$\Delta p = \varsigma_d \frac{l_{\mathrm{duct}} \rho_{\mathrm{cool}} v_{\mathrm{cool}}^2}{2 D_{h,\mathrm{duct}}} \tag{3.35}$$

The frictional losses in the duct are calculated:

$$P_{\mathrm{cool}} = \dot{V}_{\mathrm{cool}} \Delta p \tag{3.36}$$

In the LPTN model the WJ coolant is represented as a constant temperature source assigned as the WJ inlet temperature ($T_{\mathrm{duct,in}}$), the net heat transfer rate into the WJ coolant is obtained ($\dot{Q}_{\mathrm{duct}}$), and the temperature rise is calculated:

$$\Delta T_{\mathrm{cool}} = \frac{\dot{Q}_{\mathrm{duct}} + P_{\mathrm{cool}}}{\rho_{\mathrm{cool}} c_{p,\mathrm{cool}} \dot{V}_{\mathrm{cool}}} \tag{3.37}$$

where $c_{p,\mathrm{cool}}$ is the specific heat capacity of the coolant.

The generator component temperatures are evaluated by adding ΔT_{cool} to the values obtained from the LPTN model.

3.3.5 Air Duct Modelling

An axial cooling duct topology was selected since it has a relatively short flow length, resulting in a relatively small pressure drop. A circumferential flow was also investigated: the increased flow length was found to result in an unacceptably large pressure drop and power requirement for multi-megawatt scale DD WTG designs.

The cooling duct geometry is calculated similarly to the WJ duct. The duct height (h_{duct}) is assumed to be equal to the water jacket duct height. An aspect ratio of 8 is also assumed, therefore the number of ducts is calculated with the following equation, and by rounding the answer to the nearest integer.

$$N_{\mathrm{duct}} = \frac{2\pi r_{\mathrm{duct}}}{8 h_{\mathrm{duct}}} \tag{3.38}$$

The duct width is then:

$$w_{\mathrm{duct}} = \frac{2\pi r_{\mathrm{duct}}}{N_{\mathrm{duct}}} \tag{3.39}$$

For simplicity, the thickness of the duct walls is ignored.

The volumetric flow rate of the cooling air through a single duct can then be calculated with Eq. (3.31), the total volumetric flow rate is then found by multiplying this value by the number of ducts (N_{duct}). The rest of the procedure can then be followed as before using Eq. (3.32) to Eq. (3.37), but with the properties of air instead of liquid coolant.

3.3.6 Lumped Parameter Thermal Network Model

A steady-state lumped parameter thermal network (LPTN) model of the DD PM WTG was constructed based on several assumptions and simplifications:

- Axial heat flow is neglected other than in the armature windings [18].
- Heat generation is assumed to be spatially uniform within the associated components.
- WJ and air duct side walls are excluded from the model.
- Due to the large air-gap radius the pole- and slot-pitch geometry is approximated to have constant cross-sectional area.
- Interface gaps between the structural frames, rotor/stator yokes, and WJ are represented by an average gap thickness t_{tol}.
- The internal generator air is well mixed with nacelle air and is regulated by the nacelle cooling system (which also handles heating from other systems such as the power electronics and bearings). It is represented as a constant temperature source (T_{int}).
- The coil insulation, epoxy, and slot liner are assumed to have the same thermal conductivity (k_{SL}). The average thermal conductivity perpendicular to current flow within the coils is calculated according to the slot fill factor [75]:

$$k_{\mathrm{coil,eq}} = k_{\mathrm{SL}} \frac{(1 + C_{\mathrm{fill}})k_{\mathrm{Cu}} + (1 - C_{\mathrm{fill}})k_{\mathrm{SL}}}{(1 - C_{\mathrm{fill}})k_{\mathrm{Cu}} + (1 + C_{\mathrm{fill}})k_{\mathrm{SL}}} \tag{3.40}$$

First, a detailed thermal model was constructed, this model was then simplified using periodic boundary conditions and the lumping of series and parallel resistances where possible. With consideration that the temperature distribution is symmetric about the middle of a slot, the double layer windings were simplified to a thermally equivalent single layer winding.

The peak coil temperature is calculated at the centre of the slot. The peak PM temperature is obtained from either the PM surface or centre, depending on which is larger.

The LPTN is solved iteratively to account for the temperature dependence of the conductor resistivity, natural convection from the end winding surfaces, and the properties of air which are calculated according to the correlations provided by Zografos *et al.* [76].

The selection of convective heat transfer coefficients for the stator structure ($\bar{\alpha}_{SS}$) and rotor structure ($\bar{\alpha}_{RS}$) depends on whether the machine has an inner- or outer-rotor topology as detailed in Section 3.3.3.2 and 3.3.3.3.

The thermal resistance equations are provided in Appendix D. The heat sources are summarised in Table 3.1. In Figure 3.7 a diagram is provided for the detailed LPTN model for a slot and pole pitch. In Figure 3.8 a diagram is provided for the simplified LPTN model for a slot and pole pitch. Figure 3.9 provides a diagram for both the detailed and simplified LPTN model of the end windings.

Table 3.1: Heat sources in the lumped parameter thermal network model.

Symbol	Heat Source Location	Loss Mechanism
P_1	Water jacket	Frictional Loss
P_2	Stator yoke above tooth	Iron Loss
P_3	Stator yoke above slot	Iron Loss
P_4	Stator tooth top	Iron Loss
P_5	Simplified coil	Copper Loss
P_6	Stator tooth bottom	Iron Loss
P_7	Air-gap region	Frictional Loss
P_8	Permanent magnet	Magnet Loss
P_9	End-winding	Copper Loss

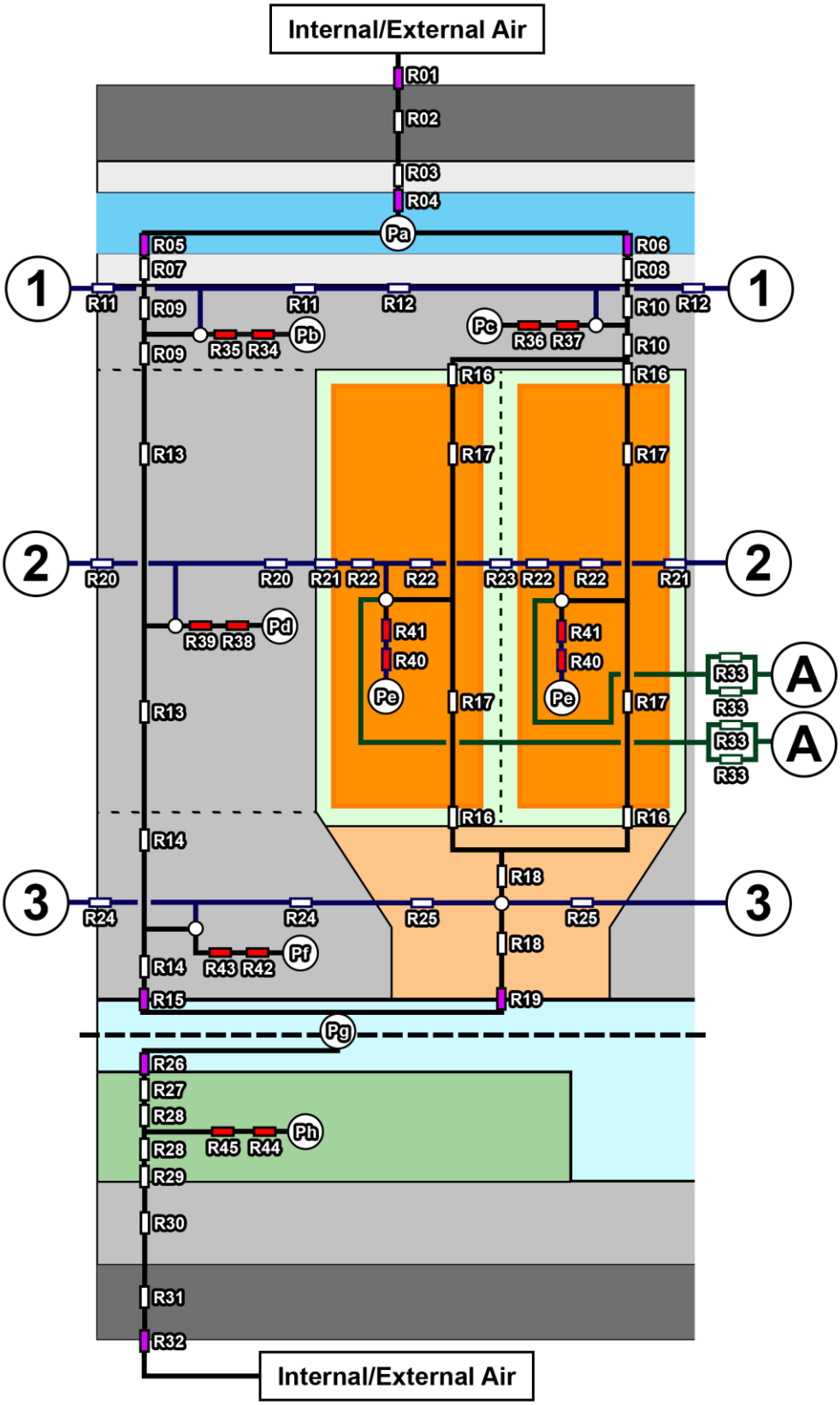

Figure 3.7: Detailed diagram of the lumped parameter thermal network model for pole- and slot-pitch. Colour coded for improved clarity: conductive resistances (white), convective resistances (pink), negative resistances (red), radial direction (black), azimuthal direction (blue), axial direction (green). Point A represents the boundary of the internal coils and the end-windings. Points 1, 2, and 3 indicate periodic boundary conditions.

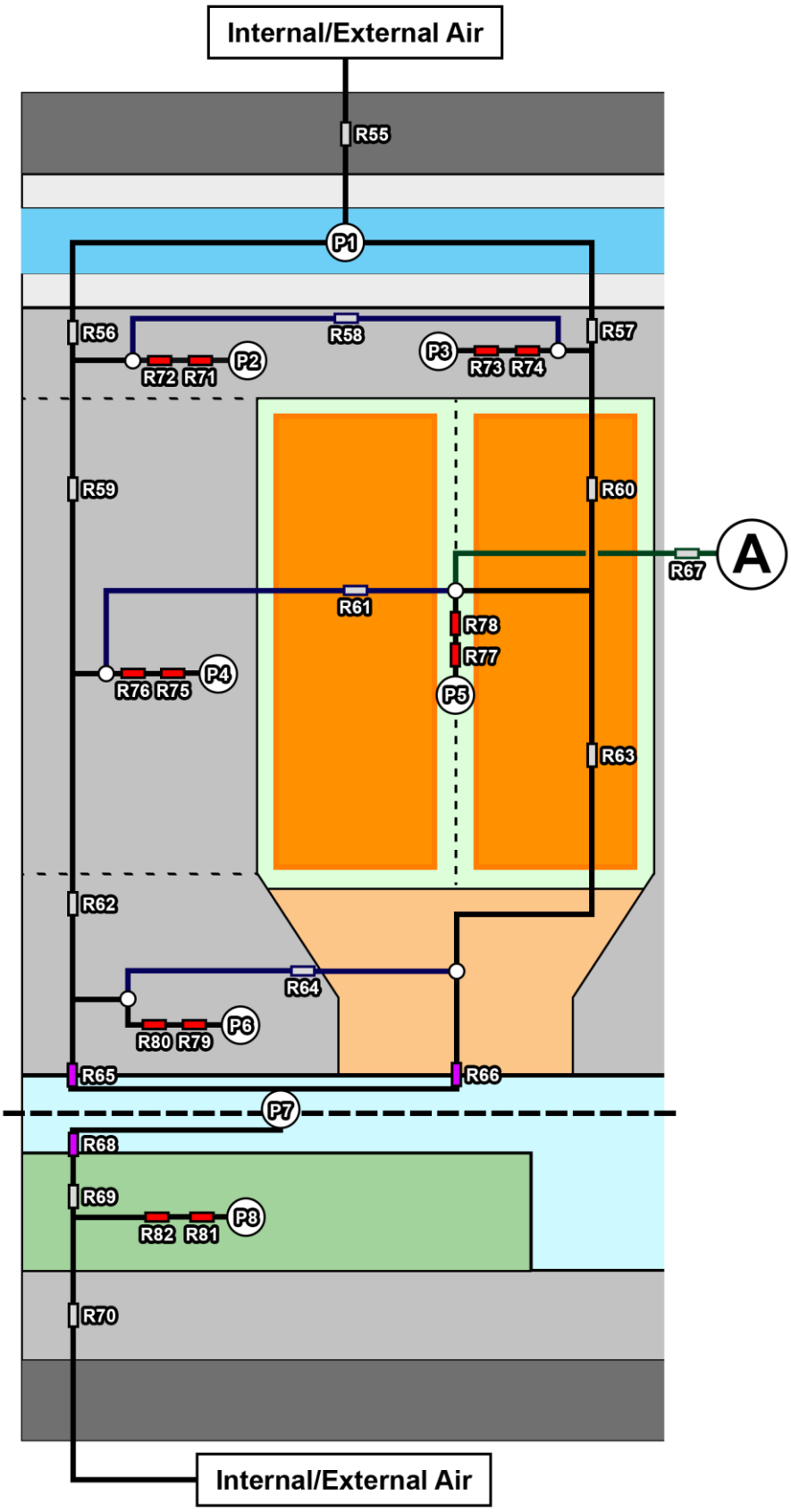

Figure 3.8: Simplified diagram of the lumped parameter thermal network model for pole- and slot-pitch. Colour coded for improved clarity: convective resistances (pink), negative resistances (red), lumped resistances (grey), radial direction (black), azimuthal direction (blue), axial direction (green). Point A represents the boundary of the internal coils and the end-windings.

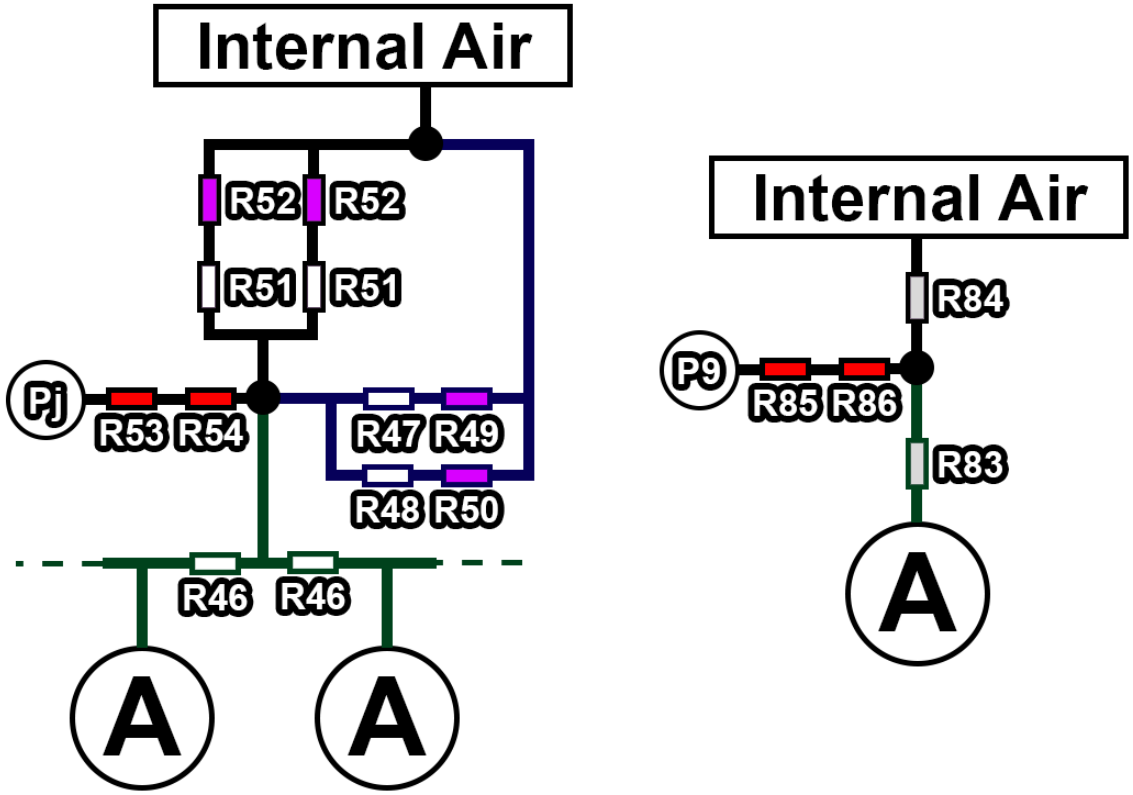

Figure 3.9: Detailed (left) and simplified (right) diagrams of the lumped parameter thermal network model for the end-windings. Colour coded for improved clarity: conductive resistances (white), convective resistances (pink), negative resistances (red), lumped resistances (grey), radial direction (black), azimuthal direction (blue), axial direction (green). Point A represents the boundary of the internal coils and the end-windings.

3.4 Heat Exchanger Design and Modelling

It is assumed that the heat extracted from the WTG by the closed loop cooling flow of liquid/air is exchanged to the ambient air via an open loop air flow via either a liquid-to-air or air-to-air heat exchanger. In the following section a design and modelling strategy is presented for both cases.

In the liquid cooled design, it is assumed that the heat extracted by a 50/50 water-glycol mixture WJ coolant is expelled to the ambient air with a circular tube continuous fin type HE which is located externally on the nacelle. In an air-to-air heat exchanger, a large gas-to-surface heat transfer area is required on both the closed- and open-loop sides due to the relatively low convective heat transfer associated with air in comparison to liquid coolant. Plate-fin HEs are therefore preferred as opposed to tube-fin type HEs such as implemented for the liquid-to-air heat exchanger. In Figure 3.10 an illustration is provided of both types of HE.

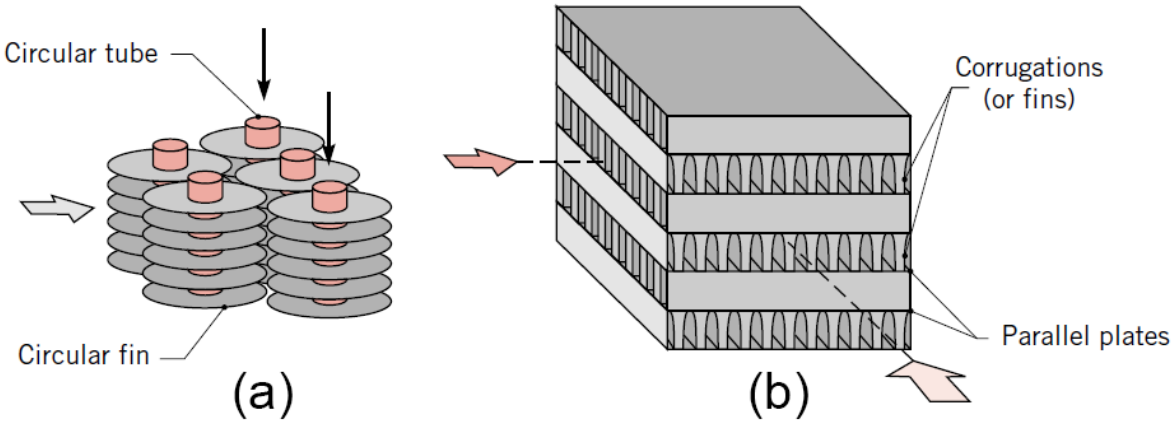

Figure 3.10: Illustration of a circular tube continuous fin type heat exchanger (a), and a plate-fin heat exchanger (b) [72].

3.4.1 Liquid-to-Air Heat Exchanger Model

Specifications for a circular tube-continuous fin type HE were taken from Kays and London (designation 8.0-3/8T), they are provided in Table 3.2 [77]. The tube wall thickness is assumed to be 1 mm.

Table 3.2: Liquid-to-air heat exchanger specifications.

Description	Units	Equation
Tube outer diameter	m	$D_{\text{tube,ext}} = 0.0102 C_{\text{HE}}$ (3.41)
Tube inner diameter	m	$D_{\text{tube,int}} = D_{\text{tube,ext}} - 0.002$ (3.42)
Gas-side flow passage hydraulic diameter	m	$D_{\text{h,ext}} = 0.00363 C_{\text{HE}}$ (3.43)
Free-flow area to frontal area ratio	–	$\Gamma_{\text{FF,FA}} = 0.534$ (3.44)
Gas-side heat transfer area to total volume ratio	m^{-1}	$\Gamma_{\text{A,V}} = \frac{587}{C_{\text{HE}}}$ (3.45)
Vertical distance between tubes	m	$h_{\text{HE,tube}} = 0.0254 C_{\text{HE}}$ (3.46)
Horizontal distance between tubes	m	$w_{\text{HE,tube}} = 0.022 C_{\text{HE}}$ (3.47)

The HE dimensions are scaled by a factor C_{HE}. By increasing C_{HE} the internal coolant pressure drop through the tubes can be reduced at the expense of HE compactness. Five tubes are specified in the vertical direction, and the total number of tubes was

determined by specifying a minimum tube internal flow Reynolds number ($\mathrm{Re}_{\mathrm{HE,tube}}$) of 10,000: ensuring that the internal coolant to tube wall heat transfer coefficient is sufficiently large. The fluid velocity through a HE tube is therefore:

$$v_{\mathrm{HE,tube}} = \frac{\mathrm{Re}_{\mathrm{HE,tube}}\eta_{\mathrm{cool}}}{\rho_{\mathrm{cool}}D_{\mathrm{tube,int}}} \tag{3.48}$$

The number of tubes can then be found via mass balance:

$$N_{\mathrm{HE,tube}} = \frac{4\dot{V}_{\mathrm{cool}}}{\pi\left(\frac{D_{\mathrm{tube,int}}}{2}\right)^2 v_{\mathrm{HE,tube}}} \tag{3.49}$$

$N_{\mathrm{HE,tube}}$ is rounded down to the nearest integer and $v_{\mathrm{HE,tube}}$ is updated with Eq. (3.48). The width of the HE active area can then be found:

$$w_{\mathrm{HE}} = \frac{N_{\mathrm{HE,tube}}w_{\mathrm{HE,tube}}}{5} + 2\left(w_{\mathrm{HE,tube}} - D_{\mathrm{tube,ext}}\right) \tag{3.50}$$

An initial guess for the HE length (l_{HE}) and an inlet velocity for the cooling air ($v_{\mathrm{HE,air}}$) is made. The mass flow rate of the airflow can then be calculated:

$$\dot{m}_{\mathrm{HE,air}} = \rho_{\mathrm{air}}v_{\mathrm{HE,air}}A_{\mathrm{HE}} \tag{3.51}$$

where A_{HE} is the HE frontal area:

$$A_{\mathrm{HE}} = w_{\mathrm{HE}}l_{\mathrm{HE}} \tag{3.52}$$

The “effectiveness-NTU” method is then used to assess the HE performance [72]. First the heat transfer capacities of the internal and external flow are calculated:

$$c_{\mathrm{ext}} = \dot{m}_{\mathrm{HE,air}}c_{p,\mathrm{air}} \tag{3.53}$$

$$c_{\mathrm{int}} = \dot{V}_{\mathrm{cool}}\rho_{\mathrm{cool}}c_{p,\mathrm{cool}} \tag{3.54}$$

The larger of the two values is designated as c_{max} and the smaller c_{min}. The outlet temperature of the air flow is calculated:

$$T_{\mathrm{HE,out}} = \frac{\dot{Q}_{\mathrm{cool}}}{\dot{m}_{\mathrm{HE,air}}c_{p,\mathrm{air}}} + T_{\infty} \tag{3.55}$$

where T_{∞} is the ambient air temperature. The ideal maximum possible heat transfer rate is then calculated:

$$\dot{Q}_{\max} = c_{\min}\left(T_{\text{duct,out}} - T_{\infty}\right) \tag{3.56}$$

where $T_{\text{duct,out}}$ is the outlet temperature of the WJ cooling duct:

$$T_{\text{duct,out}} = T_{\text{duct,in}} + \Delta T_{\text{cool}} \tag{3.57}$$

The HE effectiveness can then be calculated:

$$\epsilon_{\text{HE}} = \frac{\dot{Q}_{\text{cool}}}{\dot{Q}_{\max}} \tag{3.58}$$

In this HE configuration both fluids are unmixed, therefore the number of transfer units (NTU) is determined by iteratively solving the following equation with the Newton-Raphson method until ϵ_{HE} is obtained [72]:

$$\epsilon_{\text{HE}} = 1 - \exp\left[\left(\frac{1}{c_r}\right)(\text{NTU})^{0.22}\{\exp[-c_r(\text{NTU})^{0.78}] - 1\}\right] \tag{3.59}$$

where $c_r = c_{\min}/c_{\max}$.

The overall heat transfer coefficient of the HE is then calculated; it is assumed that the air-side heat transfer resistance dominates such that the internal convection and wall conduction heat transfer resistances can be neglected. First, the maximum mass velocity of the cooling air is found:

$$G = \frac{\dot{m}_{\text{HE,air}}}{\Gamma_{\text{FF,FA}} A_{\text{HE}}} \tag{3.60}$$

The Reynolds number of the cooling airflow over the tubes can then be found:

$$\text{Re}_{\text{HE,ext}} = \frac{G D_{\text{h,ext}}}{\eta_{\text{air}}} \tag{3.61}$$

The Colburn factor (j) and the air-side friction factor ($\varsigma_{\text{HE,ext}}$) can then be found from the empirical data provided for the HE, (valid for $400 < \text{Re}_{\text{HE,ext}} < 9000$):

$$j = -0.003 \ln\left(\text{Re}_{\text{HE,ext}}\right) + 0.0284 \tag{3.62}$$

$$\varsigma_{\text{HE,air}} = -0.006 \ln\left(\text{Re}_{\text{HE,ext}}\right) + 0.0728 \tag{3.63}$$

The total heat transfer coefficient can then be found:

$$U_T = j \frac{G c_{p,\text{air}}}{\text{Pr}_{\text{air}}} \tag{3.64}$$

The required air-side surface area of the HE tubes can then be found:

$$A_{s,\mathrm{ext}} = \frac{c_{\min}\mathrm{NTU}}{U_T} \tag{3.65}$$

The required HE volume can then be found:

$$V_{\mathrm{HE}} = \frac{A_{s,\mathrm{ext}}}{\Gamma_{\mathrm{A,V}}} \tag{3.66}$$

A new value for HE length (L_{HE}) is then determined:

$$L_{\mathrm{HE}} = \frac{V_{\mathrm{HE}}}{5h_{\mathrm{HE,tube}}w_{\mathrm{HE}}} \tag{3.67}$$

The process is then repeated iteratively from Eq. (3.51) to Eq. (3.67) until the value of L_{HE} converges to a steady value.

Neglecting changes in air density and entrance/exit effects the pressure drop of the cooling airflow can be estimated [72]:

$$\Delta p = \frac{G^2}{2\rho_{\mathrm{air}}}\left[\varsigma_{\mathrm{HE,air}}\frac{\Gamma_{\mathrm{A,V}}V_{\mathrm{HE}}}{\Gamma_{\mathrm{FF,FA}}A_{\mathrm{HE}}}\right] \tag{3.68}$$

The power required to drive the flow can be found by substituting the volumetric flow rate and pressure drop of the cooling airflow into Eq. (3.36). The pressure drop of the internal tube flow is found by assuming that viscous losses through the tube dominate and neglecting entrance/exit effects, Eq. (3.33) to Eq. (3.36) are solved to find the power required to drive the flow. The HE can then be optimised for minimum power consumption by varying C_{HE} and $v_{\mathrm{HE,air}}$ subject to size constraints and with the condition that $T_{\mathrm{HE,out}} < T_{\mathrm{duct,in}}$.

3.4.2 Air-to-Air Heat Exchanger Model

Specifications for a plate-fin type HE were taken from Kays and London (surface designation 2), they are provided in Table 3.3 [77]. The plate thickness is assumed to be 1 mm. In this case, no scale factor is introduced due to a larger uncertainty in extrapolating the performance of plate-fin HEs over different scales compared to tube-fin HEs.

Table 3.3: Air-to-air heat exchanger specifications.

Description	Symbol	Value	Units
Plate spacing	h_{plate}	19.05	mm
Plate thickness	t_{plate}	1.0	mm
Duct hydraulic diameter	$D_{\text{HE,duct}}$	14.45	mm
Fin thickness	t_{fin}	0.813	mm
Heat transfer area/volume	$\Gamma_{\text{A,V}}$	249.7	m^{-1}
Fin area/total area	$\frac{A_{\text{fin}}}{A_{\text{HE}}}$	0.606	–
Fin thermal conductivity	k_{fin}	173	W/m. K

The specification of the plate-fin type HE follows similar steps to that of the tube-fin HE, however there are some key differences:

The cross-sectional area of the HE is determined based on the target value of Reynolds number specified for the flow within each duct, first the flow velocity in each HE duct is determined:

$$v_{\text{HE,duct}} = \frac{\text{Re}_{\text{HE,duct}}\eta_{\text{air}}}{\rho_{\text{air}}D_{\text{HE,duct}}} \tag{3.69}$$

Then the required total HE free-flow area is found:

$$A_{\text{HE,FF}} = \frac{\dot{V}_{\text{cool}}}{v_{\text{HE,duct}}} \tag{3.70}$$

The ratio of free flow to frontal area for a specific HE specification can be found as follows:

$$\Gamma_{\text{FF,FA}} = \frac{h_{\text{plate}}\Gamma_{\text{A,V}}D_{\text{HE,duct}}}{8\left(h_{\text{plate}} + t_{\text{plate}}\right)} \tag{3.71}$$

The frontal area in reference to the air flow from the generator can then be found:

$$A_{\text{HE,gen}} = \frac{A_{\text{HE,FF}}}{\Gamma_{\text{FF,FA}}} \tag{3.72}$$

As with the liquid-to-air heat exchanger, an initial length is assumed such that the mass flow rate of the external air flow can be calculated, for simplicity the HE is assumed to have a square frontal cross sectional area.

$$\dot{m}_{\mathrm{HE,ext}} = \rho_{\mathrm{air}} l_{\mathrm{HE}} v_{\mathrm{HE,ext}} \Gamma_{\mathrm{FF,FA}} \sqrt{A_{\mathrm{HE,gen}}} \tag{3.73}$$

As with the liquid-to-air HE, Eq. (3.52) to Eq. (3.61) are used but with the properties of air.

The heat transfer coefficient must be determined for both sides of the HE to calculate the overall heat transfer coefficient.

For both the closed loop and open loop airflow, the Colburn factor (j) and the friction factor ($\varsigma_{\mathrm{HE,air}}$) can be found from the empirical data provided for the HE, (valid for $4000 < \mathrm{Re}_{\mathrm{HE,duct}} < 10{,}000$):

$$\varsigma_{\mathrm{HE,air}} = 0.1837 \mathrm{Re}_{\mathrm{HE,duct}}^{-0.351} \tag{3.74}$$

$$j = 0.0127 \mathrm{Re}_{\mathrm{HE,duct}}^{-0.144} \tag{3.75}$$

The heat transfer coefficient on each side is given by:

$$U_0 = j \frac{\rho_{\mathrm{air}} \dot{V}_{\mathrm{air}} c_{\mathrm{p,air}}}{A_{\mathrm{HE,FF}} \mathrm{Pr}_{air}^{\frac{2}{3}}} \tag{3.76}$$

where $\dot{V}_{\mathrm{air}}$ is the volumetric flow rate of the air flow. Note that this needs to be calculated for both the internal ($U_{0,\mathrm{int}}$) and external ($U_{0,\mathrm{ext}}$) side of the HE by substituting in the appropriate values.

The overall heat transfer coefficient is determined assuming that wall conduction has negligible heat transfer resistance and that the heat transfer area is the same on both sides of the HE:

$$\frac{1}{U_h} = \frac{1}{\zeta_{0,\mathrm{int}} U_{0,\mathrm{int}}} + \frac{1}{\zeta_{0,\mathrm{ext}} U_{0,\mathrm{ext}}} \tag{3.77}$$

where ζ_0 is the surface efficiency:

$$\zeta_0 = 1 - \frac{A_{\mathrm{fin}}}{A_{\mathrm{HE}}} (1 - \zeta_{\mathrm{fin}})) \tag{3.78}$$

Where ζ_{fin} is the fin efficiency:

$$\zeta_{\mathrm{fin}} = \frac{\tanh(m_2 l_2)}{m_2 l_2} \tag{3.79}$$

$$m_2 = \sqrt{\frac{2U_0}{k_{\mathrm{fin}} t_{\mathrm{fin}}}} \quad l_2 = \frac{t_{\mathrm{plate}}}{2} \tag{3.80,3.81}$$

The required heat transfer area can then be found as before with Eq. (3.65), and a new value for the HE length is calculated:

$$l_{\mathrm{HE}} = \frac{A_{s,\mathrm{ext}}}{A_{\mathrm{HE}} \Gamma_{\mathrm{A,V}}} \tag{3.82}$$

As before, the process is repeated iteratively until the value of l_{HE} converges to a steady value.

Neglecting changes in air density and entrance/exit effects the pressure drop of both the closed-loop and open-loop airflow can be found:

$$\Delta p = \varsigma_{\mathrm{HE,air}} \frac{G^2}{2\rho_{\mathrm{air}}} \frac{A_{\mathrm{HE}}}{A_{\mathrm{HE,FF}}} \tag{3.83}$$

As before, the power required to drive the flow on each side of the HE can be found using Eq. (3.36).

The HE can then be optimised for minimum power consumption by varying the target values of Reynolds number for both the closed-loop and open-loop airflow subject to size constraints and with the condition that $T_{\mathrm{HE,out}} < T_{\mathrm{duct,in}}$.

3.5 Thermal Model Results and Discussion

3.5.1 Thermal Model Parameters

A summary of the additional WTG parameters and material properties assumed for the thermal model is provided in Table 3.4.

Table 3.4: Additional generator parameters and material properties for the thermal model.

Description	Symbol	Value	Unit
Generator Geometrical Parameters			
Stator structure thickness [13]	h_{SS}	46.59	mm
Rotor structure thickness [13]	h_{RS}	63.69	mm
Duct wall thickness	$h_{\mathrm{duct,wall}}$	5	mm
Slot liner thickness [18]	t_{SL}	1	mm

Description	Symbol	Value	Unit
Magnet coating thickness [18]	t_{coat}	0.5	mm
Magnet glue thickness [18]	t_{glue}	0.1	mm
Structural interface gap average thickness	t_{tol}	0.1	mm
Shaft outer radius [13]	r_{shaft}	3	m
Material Properties			
Structural steel thermal conductivity	$k_{\mathrm{Fe,s}}$	45	$\mathrm{W/m.K}$
Electrical steel thermal conductivity	$k_{\mathrm{Fe,e}}$	28	$\mathrm{W/m.K}$
Copper thermal conductivity	k_{Cu}	400	$\mathrm{W/m.K}$
Magnet thermal conductivity	k_{PM}	9	$\mathrm{W/m.K}$
Liquid coolant thermal conductivity	k_{cool}	0.398	$\mathrm{W/m.K}$
Magnet glue thermal conductivity	k_{glue}	0.7	$\mathrm{W/m.K}$
Magnet coating thermal conductivity	k_{coat}	0.2	$\mathrm{W/m.K}$
Slot liner thermal conductivity	k_{SL}	0.2	$\mathrm{W/m.K}$
Slot wedge thermal conductivity	k_{wedge}	0.4	$\mathrm{W/m.K}$
Liquid coolant Prandtl number	$\mathrm{Pr}_{\mathrm{cool}}$	21.6	–
Coolant dynamic viscosity	η_{cool}	2.57	$\mathrm{mPa.s}$
Coolant density	ρ_{cool}	1069	$\mathrm{kg/m^3}$
Coolant specific heat capacity	$c_{p,\mathrm{cool}}$	3340	$\mathrm{J/kgK}$
Water jacket duct absolute roughness coefficient	Υ	0.05	mm
Copper resistivity at reference temperature (T_0) of $20°C$	ϱ_0	$1.724x10^{-8}$	$\Omega\mathrm{m}$
Copper temperature coefficient	C_{ϱ}	$3.93x10^{-3}$	$1/\mathrm{K}$

3.5.2 Comparison of Air- and Liquid-Cooling Performance

To evaluate the maximum WTG component temperatures steady-state conditions at rated wind speed are considered with $T_{\infty} = 40^{\circ}\mathrm{C}$, $T_{\mathrm{int}} = 55^{\circ}\mathrm{C}$, and $T_{\mathrm{duct,in}} = 50^{\circ}\mathrm{C}$. In Figure 3.11 and Figure 3.12, the peak magnet, coil, and end winding temperatures are presented for a range of coolant flow rates, along with the coolant temperature rise, for the air- and liquid-cooling strategies applied to the example outer-rotor 15 MW WTG presented in Chapter 2.

For both strategies, once the temperature rise of the coolant begins to converge towards a steady value, further increases in flow rate have little effect on the component temperatures.

In the air-cooling strategy, the cooling air temperature rise reaches a minimum value of $\sim 16.2^{\circ}\mathrm{C}$ at a flow rate of $\sim 36\ \mathrm{m}^3/s$ before increasing gradually with increasing flow rate, this is attributed to the significant frictional losses in the air-cooling ducts.

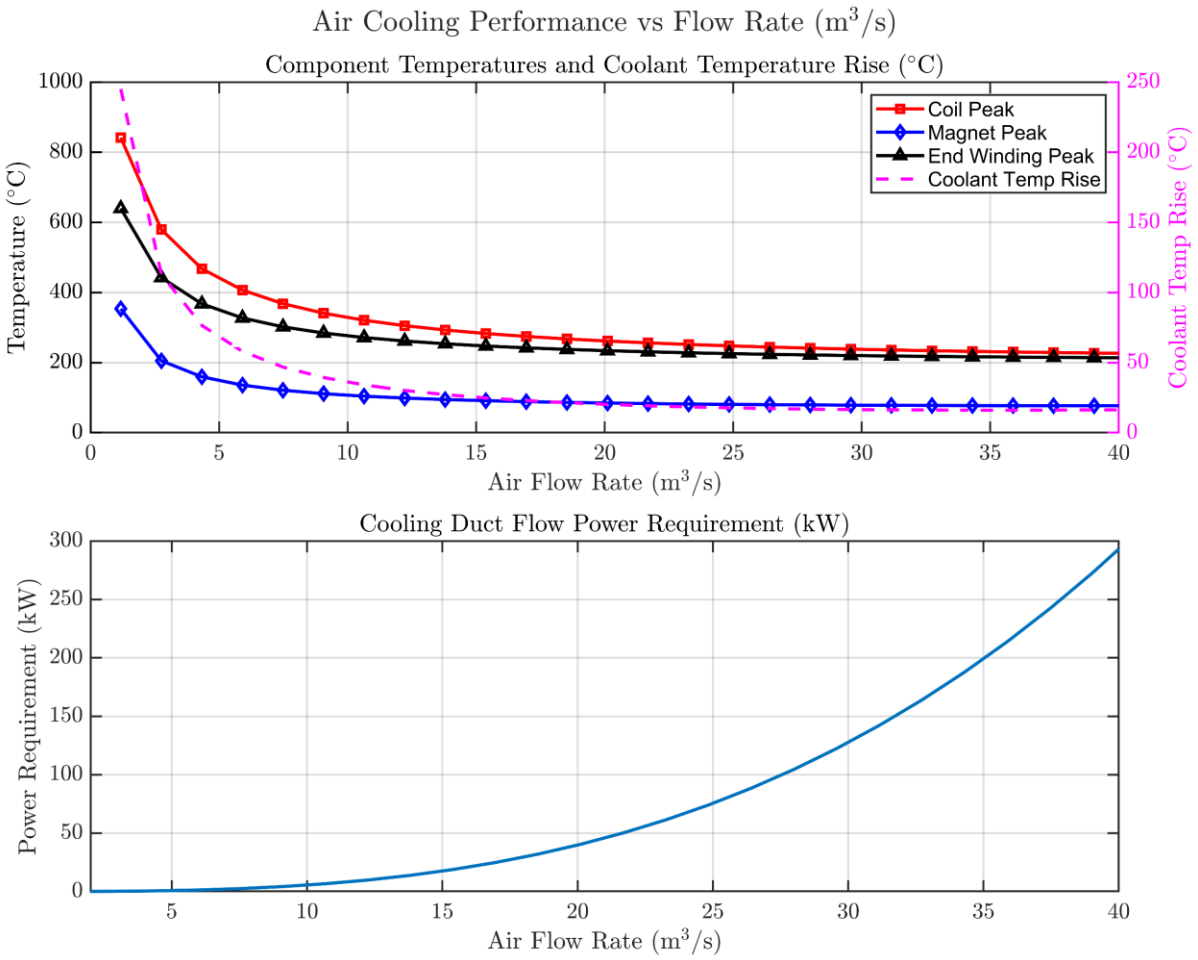

Figure 3.11: Performance of the air-cooling strategy applied to the example outer-rotor 15 MW machine. Key component temperatures and the idealised power required to drive the air flow is plotted for a range of volumetric flow rates.

In the liquid-cooling strategy, the coolant temperature rise decreases asymptotically towards $0^{\circ}\mathrm{C}$ with increasing flow rate, the frictional losses in the water jacket are very small in comparison to the mass flow rate so they have a negligible contribution to temperature rise over the presented range of flow rates.

The liquid-cooling strategy was found to outperform air-cooling, lower component temperatures are achieved and significantly less power is required to drive the coolant flow. Although the air-cooling strategy is less efficient than liquid-cooling, the power required by the cooling air flow is still reasonable in comparison to the rated power capacity of 15 MW for moderate flow rates, such as below $25\ \mathrm{m}^3/s$.

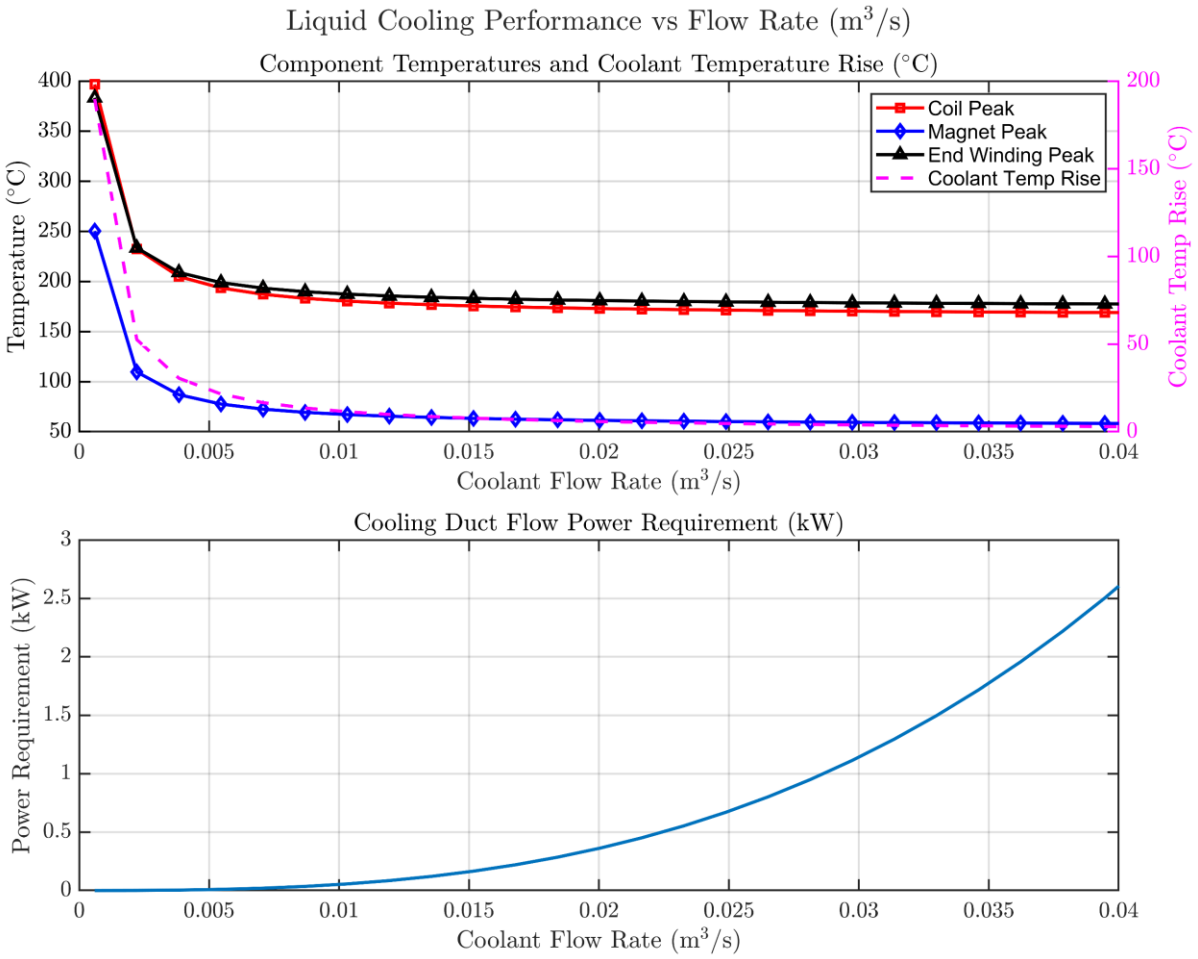

Figure 3.12: Performance of the liquid-cooling strategy applied to the example outer-rotor 15 MW machine. Key component temperatures and the idealised power required to drive the coolant flow are plotted for a range of volumetric flow rates.

3.5.3 Comparison of Inner- and Outer-Rotor DD WTG Thermal Performance

In Figure 3.13, peak magnet, coil, and end winding temperatures are presented for a range of specific current loading (A_1) for both inner- and outer-rotor DD WTGs with air- and liquid-cooling.

The geometry and iron losses within the WTG are kept constant while the current loading is changed. The inner-rotor DD WTG specification was obtained by using the same input parameters as in Table 2.1.

For the air-cooling strategy, the flow rate is kept at 25 m/s over the investigated range of current loading since, according to Figure 3.11, such a value appears to provide a reasonable trade-off between efficiency and performance. For the liquid-cooling

strategy, the coolant flow rate is adjusted for each value of current loading such that the coolant temperature rise is maintained below $5^{\circ}\mathrm{C}$.

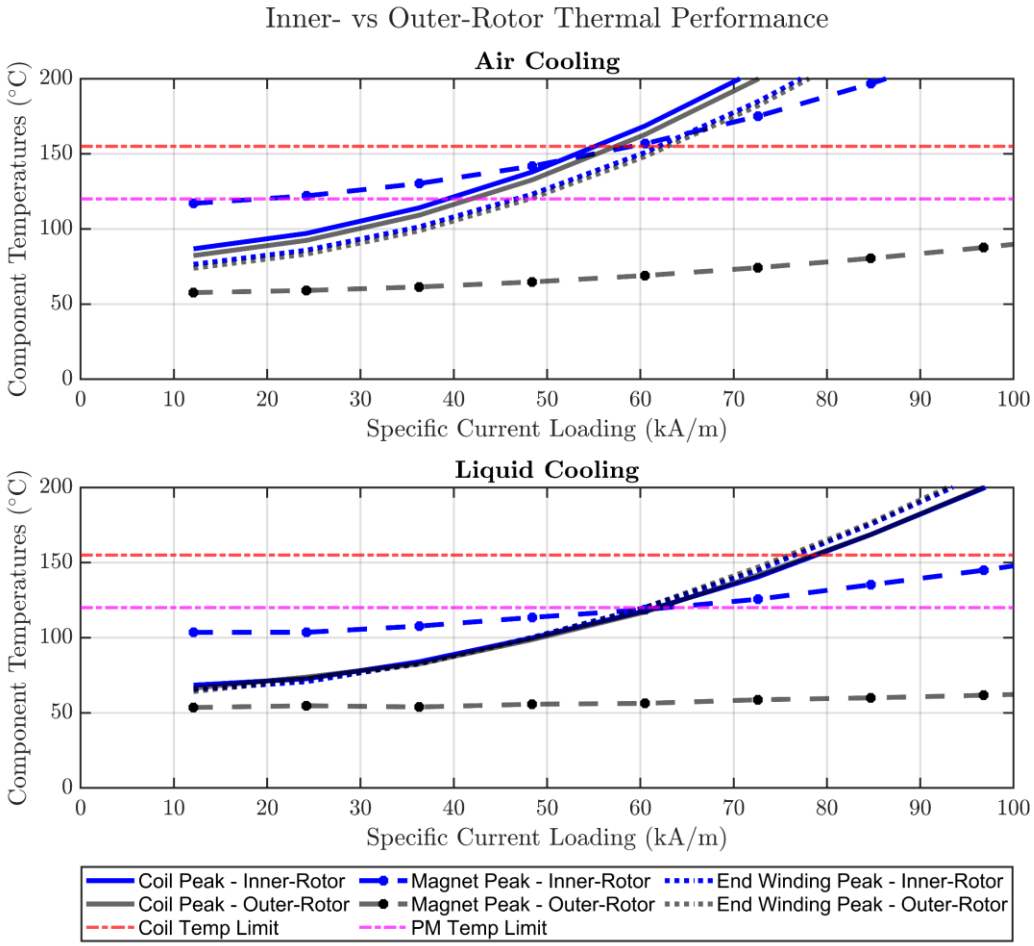

Figure 3.13: Comparison of component temperatures in the example inner- and outer-rotor 15 MW machines over a range of specific current loading (A_1).

In both cases, the outer-rotor WTG performs significantly better than the inner-rotor WTG in terms of peak magnet temperatures. In the outer-rotor topology it is assumed that the external rotor structure is exposed to the ambient airflow, leading to an enhanced convection coefficient and temperature gradient than if it were located internally. The coil and end winding temperatures were found to be very similar when comparing the inner- and outer-rotor topologies.

For the example outer-rotor WTG, the liquid-cooling strategy is capable of maintaining the critical component temperatures below their rated values up to a specific current loading of $\sim 75.9\ \mathrm{kA/m}$, in comparison the air-cooling strategy reaches the rated coil temperature at $\sim 57.4\ \mathrm{kA/m}$, resulting in a significant improvement of $\sim 32\%$.

3.5.4 Comparison of Heat Exchanger Performance

In Figure 3.14 the air-to-air and liquid-to-air heat exchanger performance is compared for the 15 MW example outer-rotor WTG with a specific current loading of $80\ \mathrm{kA/m}$. In both cases, the total power required to drive both the closed-loop and open-loop flows is presented for HE designs that are optimised subject to a volume constraint.

As the HE volume constraint is relaxed the power requirement can be seen to decrease, however for all presented designs the power requirement is negligible in comparison to the rated power capacity of 15 MW. Even when pump/fan efficiencies are considered ($\sim 70\%$).

The volume required for the liquid-to-air HE is significantly less than the air-to-air strategy, however a reasonable size can be achieved for both in the context of a 15 MW WTG nacelle. Further design refinement would likely yield HE designs that are more compact while still maintaining negligible power requirements.

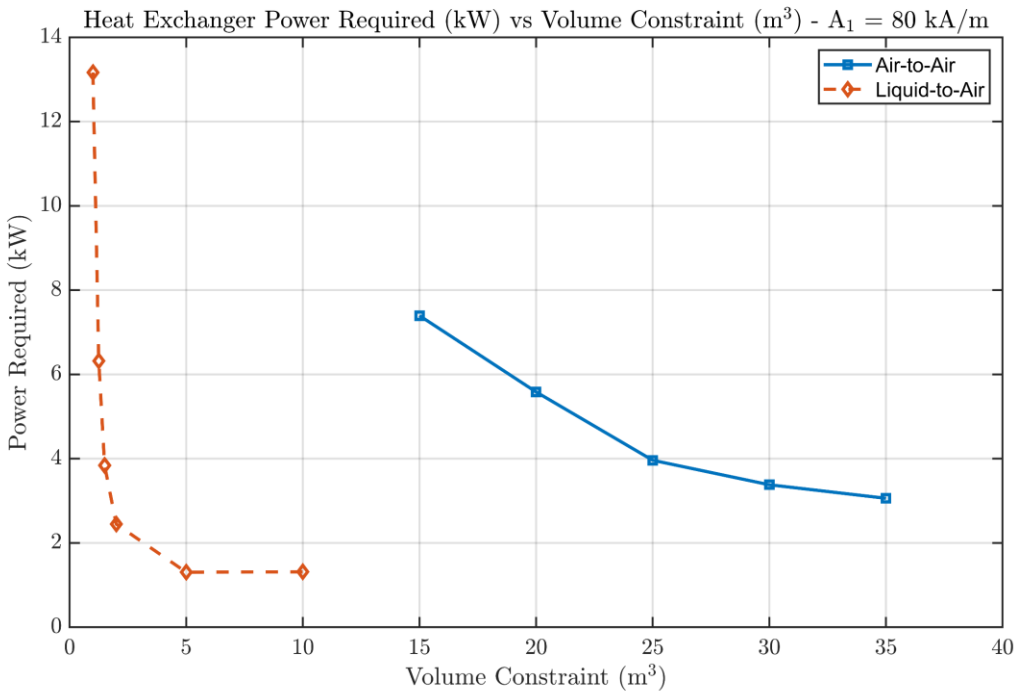

Figure 3.14: The idealised power required to drive both the closed- and open-loop flow through both the air-to-air and liquid-to-air heat exchangers is presented for various constraints on the heat exchanger volume. This is calculated for the example outer-rotor 15 MW machine with a specific current loading (A_1) of 80 kA/m.

3.5.5 Air-Gap Ventilation

In the previous section the results are presented assuming that there is no ventilation of the air-gap flow. However, the magnet temperature can be reduced considerably for the inner-rotor topologies if air-gap ventilation is implemented.

In the following section it is assumed that an axial flow is introduced into the air-gap region. Similar to how the cooling ducts are modelled, the air-gap is assigned as a constant temperature source in the LPTN model corresponding to the inlet temperature on one side. Fully developed flow is assumed within the air-gap and constant heat flux boundary conditions are assumed for the rotor and stator surfaces. The temperature rise between each end of the air-gap can then be approximated according to the axial flow rate by considering the heat flux into the air-gap region:

$$\Delta T_{\mathrm{g,axial}} = \frac{\dot{Q}_{\mathrm{g,axial}}}{\rho_{\mathrm{air}} c_{p,\mathrm{air}} \dot{V}_{\mathrm{g,axial}}} \tag{3.84}$$

The axial velocity of the air-gap flow can then be calculated by dividing the flow rate by the cross-sectional area of the air-gap region:

$$v_{\mathrm{g,axial}} = \frac{\dot{V}_{\mathrm{g,axial}}}{A_{\mathrm{g,axial}}} \tag{3.85}$$

In Figure 3.15, the air-gap temperature rise is presented for a range of axial air-gap velocities for the air-cooled inner-rotor WTG topology at a current loading of 60 $\mathrm{kA/m}$. It was found that a significant axial flow velocity is required to maintain a reasonable air-gap temperature rise. Since the axial velocity is comparable to the tangential velocity of the rotor the air-gap flow would be changed significantly, likely increasing the air-gap heat transfer coefficient considerably: resulting in a further increase in the temperature rise.

The results suggest that an outer-rotor WTG topology, in which the external structure is exposed to the ambient airflow, is very advantageous in terms of thermal performance. The ambient airflow provides effective cooling of the magnets which would otherwise need to be achieved through significant ventilation of the air-gap region. It is interesting to note that although a water jacket can provide enhanced cooling for an inner-rotor WTG topology, significant air-gap ventilation would still be required to effectively cool the magnets.

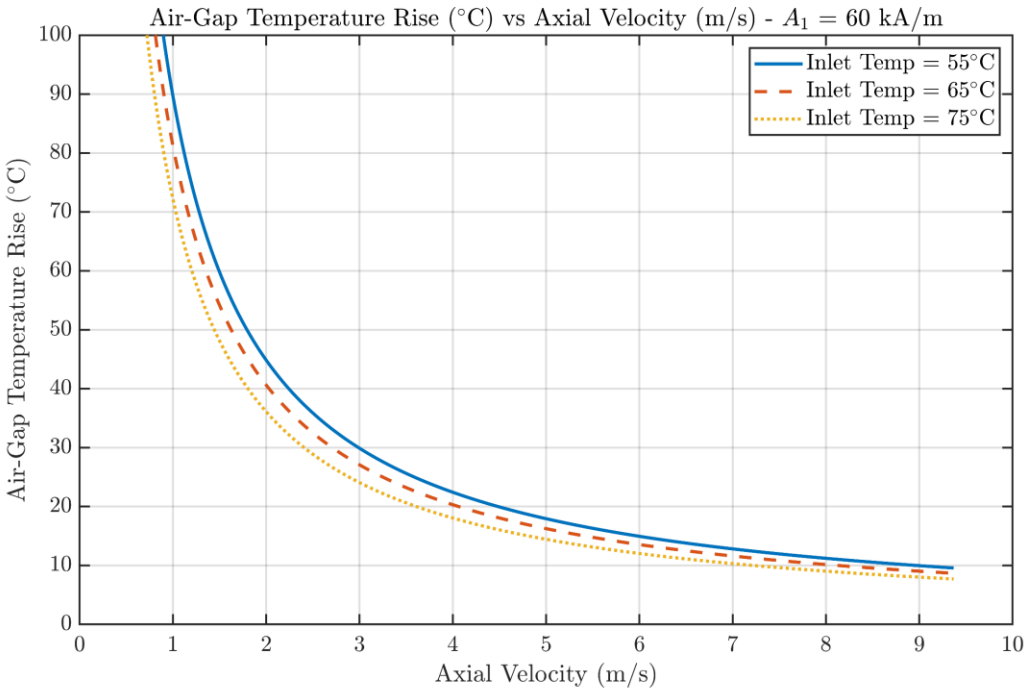

Figure 3.15: Temperature rise of an air flow through the air-gap region of the air-cooled example inner-rotor 15 MW machine plotted for a range of axial velocity and inlet air temperatures.

3.5.6 Importance of Thermal Modelling

Thermal modelling allows for informed design choices regarding critical WTG parameters.

Based on the comparison of the inner- and outer-rotor WTG topologies it appears that PMs with a relatively low temperature rating of $80^{\circ}\mathrm{C}$ could be used in the outer-rotor configuration, whereas SH grade magnets with a rating of $150^{\circ}\mathrm{C}$ would be required in the inner-rotor WTGs to allow for full utilisation of the armature windings. Based on the data provided in Appendix C, this difference in temperature rating would increase the cost of PMs by $\sim 58\%$, significantly impacting the overall cost of the WTG.

If the slot height is increased while maintaining the same specific current loading a reduction in the coil peak temperature can be achieved. However, this will result in an increased slot leakage and therefore a reduction in power factor. The increased copper volume will also increase material costs. In Figure 3.16, the peak coil temperature and the rated power factor are given for a range of slot height factors utilised in the liquid-cooled outer-rotor example 15 MW WTG. In this case the peak coil temperature can be seen to decrease considerably as the slot height factor is increased. Due to the

increased slot leakage, the rated power factor of the machine can also be seen to decrease significantly.

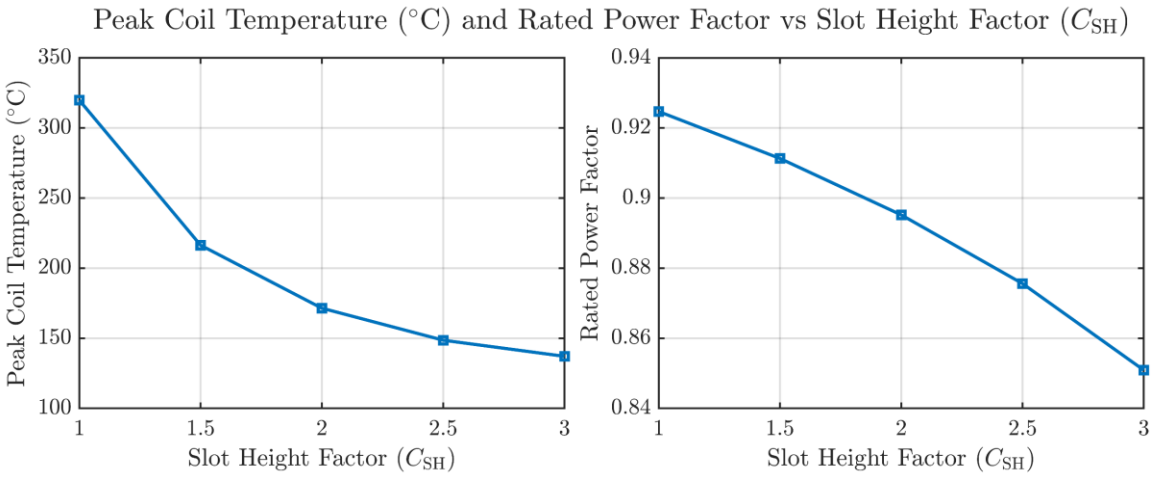

Figure 3.16: Peak coil temperature and rated power factor of the example outer-rotor 15 MW machine plotted for various values of the slot height factor (C_{SH}). Slot height factor is defined as the ratio between the slot height (h_{slot}) and the slot width (w_{slot}).

3.6 Conclusion

In this chapter a thermal model was introduced for both inner- and outer-rotor surface mounted permanent magnet (PM) direct-drive (DD) wind turbine generators (WTGs) that can be applied over a large range of power capacities.

The performance of a forced air- and liquid-cooling strategy has been compared according to the example 15 MW WTG specifications, the liquid-cooling strategy has been shown to be significantly more effective in terms of both cooling performance and efficiency. The thermal performance of an inner- and outer-rotor DD WTG topology has been compared, and it has been highlighted that exposing the outer-rotor structure to the external air flow can result in a significant reduction in the peak magnet temperature. The performance of air-to-air and a liquid-to-air heat exchanger designs has been compared; it was demonstrated that the power requirements of both designs are small in comparison to the wind turbine power capacity.

The importance of thermal modelling has been highlighted by showing how it can influence the selection of PM grades and allow designers to make appropriate decisions on key WTG geometrical parameters such as the slot height.

The thermal model will be utilised in Chapter 8 of this thesis, in which the impact of ferrofluid-gaps on the thermal performance of DD WTGs is assessed.

Chapter 4: Air-Gap Dimensioning of Direct-Drive Wind Turbine Generators

As highlighted in Chapter 2, the permanent magnet (PM) material requirements of direct-drive (DD) wind turbine generators (WTGs) can be reduced by minimising the air-gap clearance. However, despite the importance of the air-gap clearance there is a lack of work in literature detailing its appropriate specification.

The following section discusses common approaches for air-gap clearance dimensioning of DD WTGs which are used throughout literature. In Section 4.2, the constraints on air-gap clearance associated with the electromagnetic performance of surface mounted PM DD WTGs are discussed. In Section 4.3 the various sources of air-gap deformation are summarised. In Section 4.4 the concept of air-gap stability and magnetic stiffness are discussed. In Section 4.5 the link between air-gap non-uniformity and magnetically induced vibrations of DD WTGs is investigated.

4.1 Air-Gap Dimensioning of Direct-Drive Wind Turbine Generators

Determining an appropriate air-gap clearance for a DD WTG is challenging, requiring the consideration of many different factors. For a PM synchronous generator, the various objectives behind air-gap clearance dimensioning can be broadly summarised as:

- Make the air-gap clearance as small as practicably possible such that PM material requirements are minimised.
- Ensure no mechanical contact between the rotor and stator to prevent damage to the machine (taking into consideration extreme loading scenarios).
- Maintain sufficient uniformity of the air-gap during operation such that the magnitude and spatial distribution of the air-gap flux density does not deviate too far from the intended specification.
- Ensure that armature magnetising inductance does not become excessive such that power factor is significantly reduced, armature reaction becomes excessive, or the PMs are at risk of demagnetisation.

Optimal specification of the air-gap clearance therefore requires the analysis of several different aspects of generator design and depends on the context in which the machine is used.

Throughout literature concerned with the design of DD WTGs, two 'rules-of-thumb' are commonly employed when specifying the air-gap clearance, or when investigating DD WTG structural design:

- The air-gap clearance is assumed to be $1/1000^{th}$ of the air-gap diameter.
- The maximum allowable air-gap non-uniformity is limited to ~10-20% of the specified air-gap clearance.

A non-exhaustive summary of the assumed air-gap clearance and allowable air-gap deflection in literature concerned with the design of PM DD WTGs is given in Table 4.1.The same assumptions are applied to power capacities ranging from 0.5-20 MW.

Notable exceptions include:

- In the work of Barter *et al.* and Zahle *et al.* the design of very large power capacity PM DD WTGs are investigated [17], [43]. Air-gap clearances of 7 mm are specified irrespective of the air-gap diameter, resulting in a significantly lower ratio of air-gap clearance to air-gap diameter than is typically reported in literature. However, no justification is given for the relatively small air-gap clearances.
- In the work of Li *et al.* the same assumption for air-gap clearance is applied with the additional stipulation that the air-gap cannot be less than 5 mm citing mechanical stiffness and thermal expansion of the WTG structure as the main constraints [36], [78].
- The work of Bywaters *et al.* reports on the design of a real 1.5 MW prototype PM DD WTG [61]. Notably the ratio of air-gap clearance to air-gap diameter is larger than the common assumption. They specify an additional constraint for extreme load scenarios in which an air-gap deformation of up to 50% is permitted, they state that a 10% deformation limit in normal operation is for maintaining the intended WTG performance.

Table 4.1: Direct-drive wind turbine generator air-gap clearance specification and allowable air-gap deformation in various studies.

Study	Power Capacity (MW)	Air-Gap Clearance Specification (h_g)	Allowable Air-Gap Deformation
Zahle *et al.* [17]	22	$0.000735D_g$	20%
Anders Grauers [18]	0.5	$0.001D_g$	Not specified
Gaertner *et al.* [13]	15	$0.001D_g$	20%
Sethuraman *et al.* [19]	0.75-10	$0.001D_g$	Not specified
Polinder *et al.* [22]	3	$0.001D_g$	Not specified
Polinder *et al.* [27]	10	$0.001D_g$	Not specified
Jung *et al.* [79]	20	$0.001D_g$	Not specified
Sethuraman *et al.* [80]	5	$0.001D_g$	10-20%
Sethuraman *et al.* [50]	2	$0.001D_g$	10%
Bichan *et al.* [81]	15	$0.001D_g$	20%
Baseer *et al.* [82]	3.6	$0.001D_g$	Not specified
Zavvos *et al.* [83]	5	$0.001D_g$	10%
Bywaters *et al.* [61]	1.5	$0.00129D_g$	During Operation: 10% Extreme Loads: 50%
Jaen-Sola *et al.* [84]	3	5 mm, (D_g unspecified)	10%
Jaen-Sola *et al.* [85]	3	5 mm, (D_g unspecified)	10%
Li *et al.* [78]	0.75-10	At least 5 mm, otherwise $0.001D_g$	Not specified
Li *et al.* [36]	0.75-10	At least 5 mm, otherwise $0.001D_g$	Not specified
Barter *et al.* [43]	15-25	Constant, 7 mm	20%

The assumption that the air-gap clearance specification is equal to 1/1000th of the air-gap diameter is often attributed to Anders Grauers' 1996 PhD thesis in which the design of 0.5 MW surface mounted PM DD WTGs is investigated [18]. It is stated that

‘mechanical considerations’ are the limiting factor behind this assumption; however, no detail is given as to its derivation.

The second assumption concerned with allowable air-gap deflection is often attributed to the work of McDonald *et al.* in which the structural design of DD WTGs is investigated [45]. Such a limit is also stated by Hartkopf *et al.* and in the work of Boldea [86], [56]. The justification for such a limit is to avoid significant changes in the air-gap flux density which can lead to additional structural deflection, vibration, or power quality issues. However, there is a lack of evidence justifying this limit, it is a general guideline derived from experience.

It is interesting to note that in the work of Boldea a 10% air-gap deformation limit is stated for a wound rotor synchronous generator which can be expected to experience a more significant change in air-gap flux density per unit of air-gap deformation in comparison to a PM machine (since the equivalent magnetic air-gap is smaller). This highlights how such deflection limits are a rough guideline, and that an appropriate limit for air-gap deflection likely depends on the specific machine in question and the context in which it is used.

Ultimately the optimal air-gap clearance specification of commercial WTGs comes down to a trade-off between WTG capital and production costs. The achievable manufacturing and assembly tolerances and their associated costs in multi-megawatt scale DD WTG production is commercially sensitive proprietary information. Without full insight into the costs and practical issues involved in the commercial production of DD WTGs, academic studies must rely on the rules-of-thumb for air-gap clearance specification. By adhering to commonly utilised assumptions, the impact of WTG design variations can be readily compared to other works.

However, the reliance on these rules-of-thumb has resulted in a lack of research focused on the fundamental engineering behind the dimensioning of air-gap clearance for multi-megawatt scale DD WTGs. Since the cost of DD WTGs is very sensitive to the air-gap clearance, improved insight and understanding in this area has the potential to influence innovation in air-gap clearance specification and DD WTG design.

4.2 Electromagnetic Constraints

The impact that reducing the air-gap clearance has on electromagnetic performance depends on the machine in question and the context in which it is used. In the following section the impact of air-gap clearance on the electromagnetic performance of surface mounted PM WTGs is considered with reference to the example 15 MW DD WTG design introduced in Chapter 2.

4.2.1 Armature Inductance

In surface mounted PM WTGs, most of the effective air-gap reluctance is due to the PM reluctance, the magnetising inductance is therefore relatively low compared to wound rotor machines with the same air-gap clearance.

The impact of reducing the air-gap clearance factor on the total armature inductance of the example 15 MW machine was investigated by assuming that the magnet height is specified such that a peak fundamental air-gap flux density of 1.1 T is obtained at an operating temperature of $120^{\circ}\mathrm{C}$. The total armature inductance is observed to increase slowly until the air-gap clearance factor falls below 0.0005. One method of reducing the armature inductance is to use a magnet with a lower remanent flux density, resulting in a larger magnet height and therefore a larger effective air-gap. In Figure 4.1, 40 H and 52 H grade NeFeB magnets are compared.

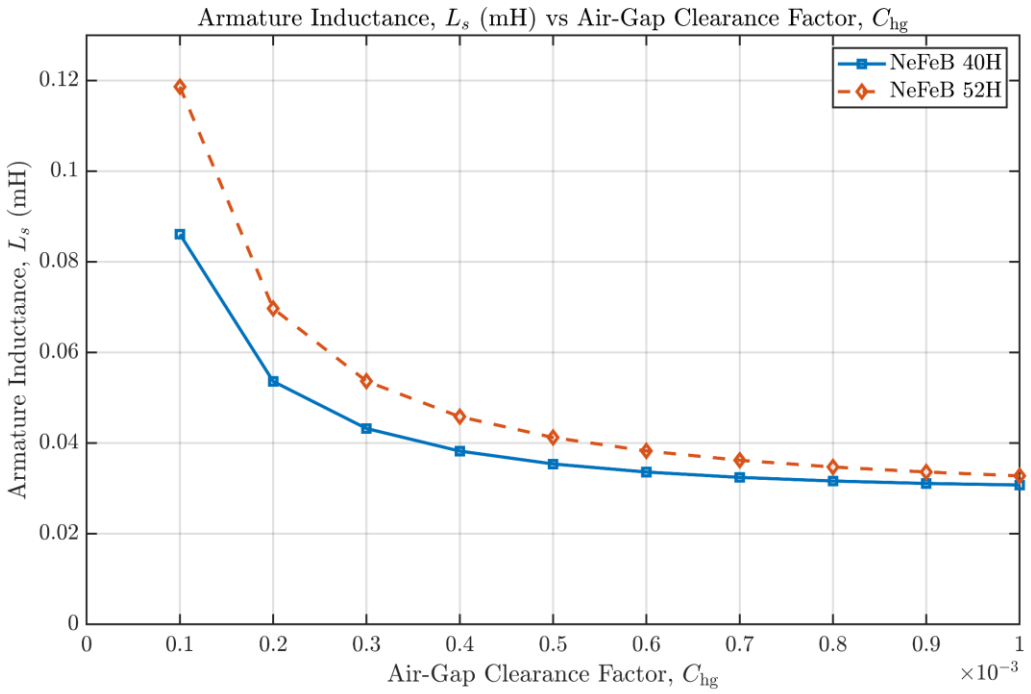

Figure 4.1: Armature inductance (L_s) of the example 15 MW machine for a range of air-gap clearance factors (C_{hg}), the magnet height is specified such that a peak air-gap flux density of 1.1 T is achieved assuming a magnet temperature of $120^{\circ}\mathrm{C}$. NeFeB 40H and 52H grade permanent magnets (PMs) are compared.

4.2.2 Risk of Permanent Magnet Demagnetisation

A short circuit fault in the armature windings can result in a significant increase in current and, consequently, a much stronger armature reaction field [87]. Depending on the specification of the machine, the armature reaction may be strong enough to partially or fully demagnetise the PMs. Therefore, for the sake of reliability, designers must ensure that the WTG will be resilient to PM demagnetisation in the event of a short circuit fault. By reducing the air-gap clearance, the armature magnetising inductance increases, which strengthens the armature reaction field and therefore raises the risk of PM demagnetisation.

A relatively large armature leakage inductance can be beneficial in the event of a short circuit fault as it will increase the impedance of the armature windings and thereby limit the magnitude of the resulting fault current. Based on a derivation by Sebastian *et al.* the following condition has been proposed for FSCW surface mounted PM machines by Chasiotis *et al.* [88], [89]:

$$\frac{L_{\mathrm{slot}} + L_{\mathrm{TT}} + L_{\mathrm{EW}}}{L_m} \geq \left(\frac{8 B_{\mathrm{rem}} h_{\mathrm{PM}} C_{\mathrm{PM,w}}}{\pi \left(B_{\mathrm{rem}} h_{\mathrm{PM}} - B_D g_{\mathrm{eff},1} \right)} \right) - 1 \tag{4.1}$$

where L_{slot} is the slot leakage inductance, L_{TT} is the tooth-tip leakage inductance, L_{EW} is the end-winding leakage inductance, L_m is the magnetising inductance, B_{rem} is the remanent flux density of the PMs, h_{PM} is the PM height, $C_{\mathrm{PM,w}}$ is the PM width factor (i.e. the ratio of PM width to pole-pitch), $g_{\mathrm{eff},1}$ is the equivalent magnetic air-gap clearance, and B_D is the flux limit of the PMs (i.e. the value of local flux density within the PM at which it becomes demagnetised). If the LHS exceeds the RHS of the equation, then the machine should be resilient to PM demagnetisation in the event of a short circuit fault.

Since the harmonic leakage inductance (L_h) of 10-12 slot pole FSCW machines is significant, i.e. the asynchronous flux density harmonics resulting from the armature winding MMF that cross the air-gap to the rotor, the criterion has been modified for this work by incorporating the harmonic leakage inductance:

$$\frac{L_{\mathrm{slot}} + L_{\mathrm{TT}} + L_{\mathrm{EW}}}{L_m + L_h} \geq \left(\frac{8 B_{\mathrm{rem}} h_{\mathrm{PM}} C_{\mathrm{PM,w}}}{\pi \left(B_{\mathrm{rem}} h_{\mathrm{PM}} - B_D g_{\mathrm{eff},1} \right)} \right) - 1 \tag{4.2}$$

This provides a more conservative estimate of the PM demagnetisation risk.

Following the same methodology as the previous section, Figure 4.2 shows how the risk of demagnetisation changes as the air-gap clearance factor is reduced assuming that $B_D = -0.4\ \mathrm{T}$. The risk of demagnetisation (C_{demag}) is represented by subtracting the RHS of Eq. (4.2) from the LHS:

$$C_{\mathrm{demag}} = \frac{L_{\mathrm{slot}} + L_{\mathrm{TT}} + L_{\mathrm{EW}}}{L_m + L_h} - \left(\frac{8 B_{\mathrm{rem}} h_{\mathrm{PM}} C_{\mathrm{PM,w}}}{\pi \left(B_{\mathrm{rem}} h_{\mathrm{PM}} - B_D g_{\mathrm{eff},1} \right)} \right) - 1 \tag{4.3}$$

A negative value therefore indicates that there is a significant risk of demagnetisation. Figure 4.2 indicates that the air-gap clearance factor can be reduced significantly from the typical value of 0.001 before there is a risk of demagnetisation. This can be attributed to the significant leakage inductance in the machine, particularly the slot leakage inductance.

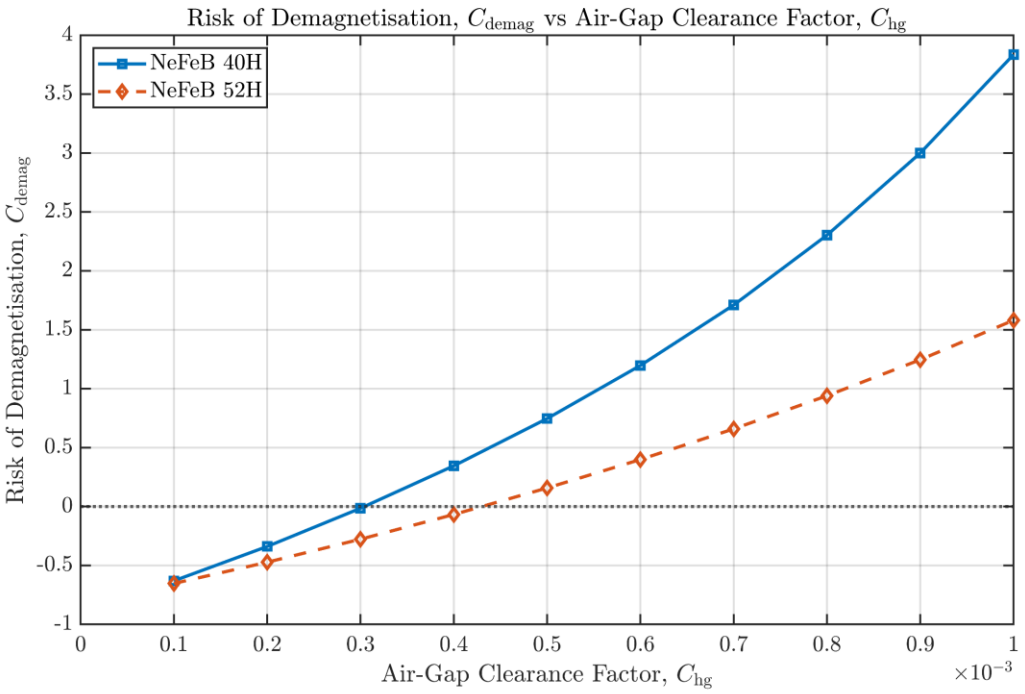

Figure 4.2: Risk of permanent magnet (PM) demagnetisation (C_{demag}) in the example 15 MW machine for a range of air-gap clearance factors (C_{hg}), the magnet height is specified such that a peak air-gap flux density of 1.1 T is achieved assuming a magnet temperature of 120°C. NeFeB 40H and 52H grade permanent magnets (PMs) are compared. A negative value of C_{demag} indicates a large risk of demagnetisation in the event of a short circuit fault.

4.2.3 Armature Reaction

A reduced air-gap clearance will lead to stronger armature reaction, weakening the net magnetic field, however for surface mounted PM machines armature reaction is generally quite weak due to the PM reluctance. In Figure 4.3, the fundamental peak flux density of the stator field is estimated for a range of air-gap clearance factors according to the following equation:

$$\widehat{B_S} = \frac{\sqrt{2} L_m I_s}{N_{\text{slot}} l_c \tau_{\text{slot}}} \tag{4.4}$$

Even as the air-gap clearance factor is reduced considerably, the peak stator air-gap flux density is observed to be very weak in comparison to the rotor field, suggesting that increased armature reaction is of little concern in the case of the example 15 MW machine.

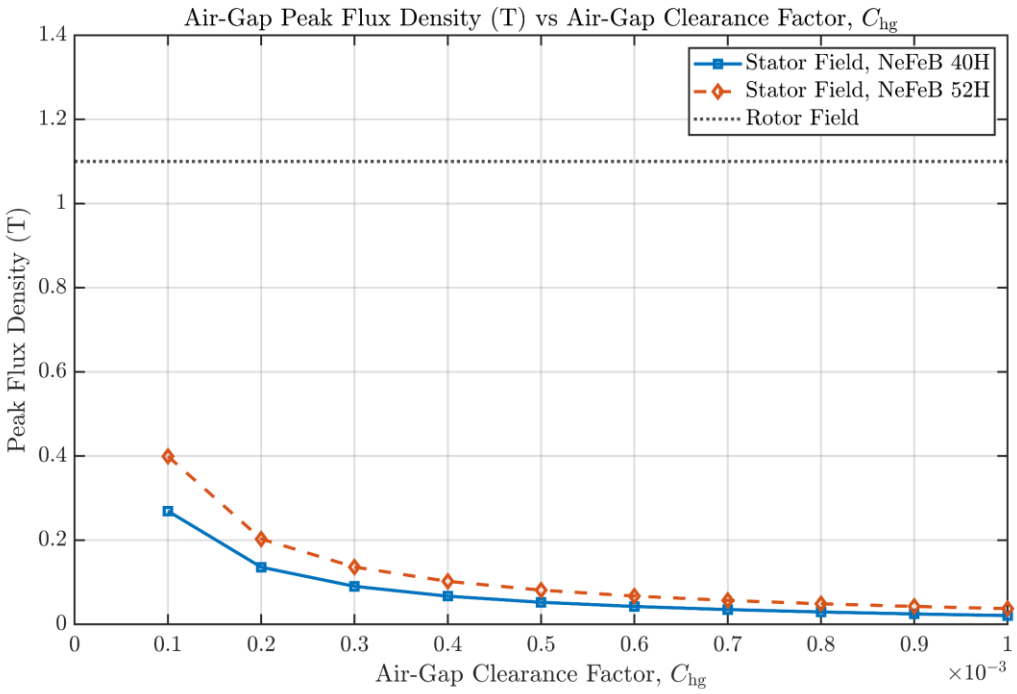

Figure 4.3: Peak air-gap flux density of the rotor and stator field compared in the example 15 MW machine for a range of air-gap clearance factors (C_{hg}), the magnet height is specified such that a peak air-gap flux density of 1.1 T is achieved assuming a magnet temperature of 120°C. NeFeB 40H and 52H grade permanent magnets (PMs) are compared.

4.2.4 Summary of Electromagnetic Constraints

As highlighted in the previous sections, under the assumption of an idealised uniform air-gap, the minimum air-gap clearance is only weakly constrained by the electromagnetic performance of surface mounted PM DD WTGs. Based on the analysis of the example 15 MW machine the air-gap clearance factor can be reduced significantly from the commonly utilised value of 0.001 before armature inductance, the risk of PM demagnetisation, and armature reaction becomes considerable. Steps can also be taken to mitigate these issues, such as using cheaper magnets with a lower remanent flux density such that the PM reluctance is increased.

In the context of electromagnetic performance, the main issue with decreasing the air-gap clearance is that non-uniformities due to manufacturing and assembly tolerances, or deformation of the WTG structure, have more of an impact on the WTG magnetic circuit. In Figure 4.4 an example of air-gap clearance measurements of a large synchronous generator is provided [90].

Non-uniformity of the air-gap results in unwanted spatial variations in the air-gap magnetic flux density which can negatively impact performance. In Figure 4.5 an

example is provided for how the spatial distribution of air-gap flux density changes in a 74 MW wound-rotor salient pole hydro-generator due to air-gap non-uniformity [91].

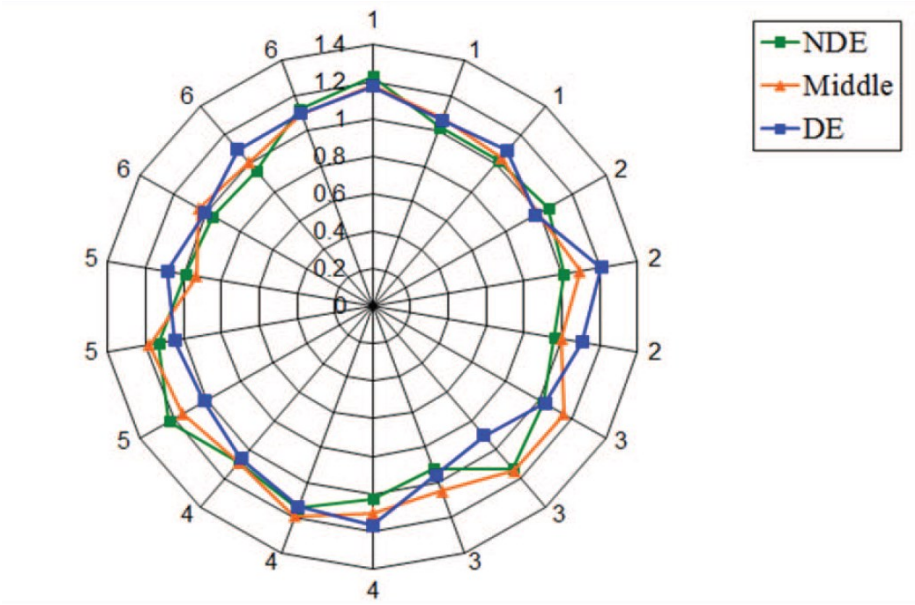

Figure 4.4: Example of air-gap non-uniformity in a large synchronous generator from the work of Palani *et al.* [90]. The measured air-gap clearance is normalised with respect to the nominal air-gap clearance. Measurements were taken along the axial length of the machine at the non-drive end (NDE), the middle of the machine, and the drive end (DE).

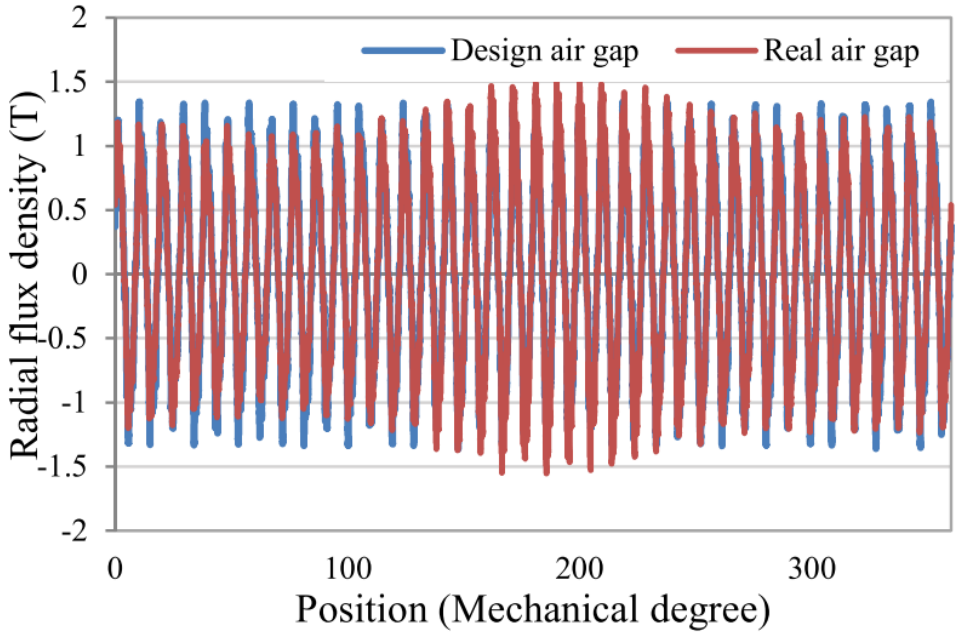

Figure 4.5: Simulation results for the spatial distribution of radial magnetic flux density in the air-gap of a 74 MW wound-rotor salient pole hydro-generator compared with air-gap clearance specified according to the design and with a nonuniform air-gap specified according to real measurements of the machine [91].

Non-uniformity of the air-gap leads to harmonic distortion of the induced EMF which reduces the output power quality of generators. In conventional power stations with directly connected synchronous generators, such harmonics are of greater concern due to their direct impact on the grid. However, in modern wind turbine generators (WTGs), which are typically interfaced to the grid via fully rated power converters, these harmonic components can be effectively filtered [92]. Therefore, power quality is less of a concern in this context.

However, the introduction of additional EMF harmonics can lead to increased torque ripple [93], [94]. This can be especially impactful if subharmonics are introduced since the resulting current harmonics will be suppressed less by the armature reactance and may have considerable magnitude. Distortion of the induced EMF can also reduce the amplitude of the working harmonic leading to a reduction in efficiency.

The additional air-gap flux density harmonics introduced by air-gap non-uniformity can also result in mechanical vibration of the WTG structure, this is investigated later in Section 4.5.

4.3 Sources of Air-Gap Deformation

As highlighted in the previous section, the key constraints behind air-gap specification of PM DD WTGs are that air-gap non-uniformity must be limited and that rotor-stator contact must be avoided. In the following section, the various sources of air-gap deformation in WTGs are summarised and discussed.

In contrast to small-scale electrical machines, which have comparatively stiff structures and generally larger ratios of air-gap clearance to air-gap diameter, mitigating air-gap deflection is a key driver in the design of DD WTG structures. The stringent requirement of maintaining such small air-gap clearances in DD WTGs in comparison to their size requires a structural design philosophy based upon minimising deflection, as opposed to stress (other than in critical areas) [45].

Generally, a DD WTG structure consists of a rim and a disc. The rim supports the rotor/stator yoke, and the disc extends down to the main shaft or turret in the case of the rotor and stator respectively. As summarised by Stander *et al.* there are many different structural topologies that can be used in DD WTGs, an illustration is provided in Figure 4.6 [95]. Commercial WTG structures are also quite complex, having been

well optimised for reduced mass, as evidenced by photos of Siemens Gamesa and GE Vernova WTG components provided in Figure 4.7 [46].

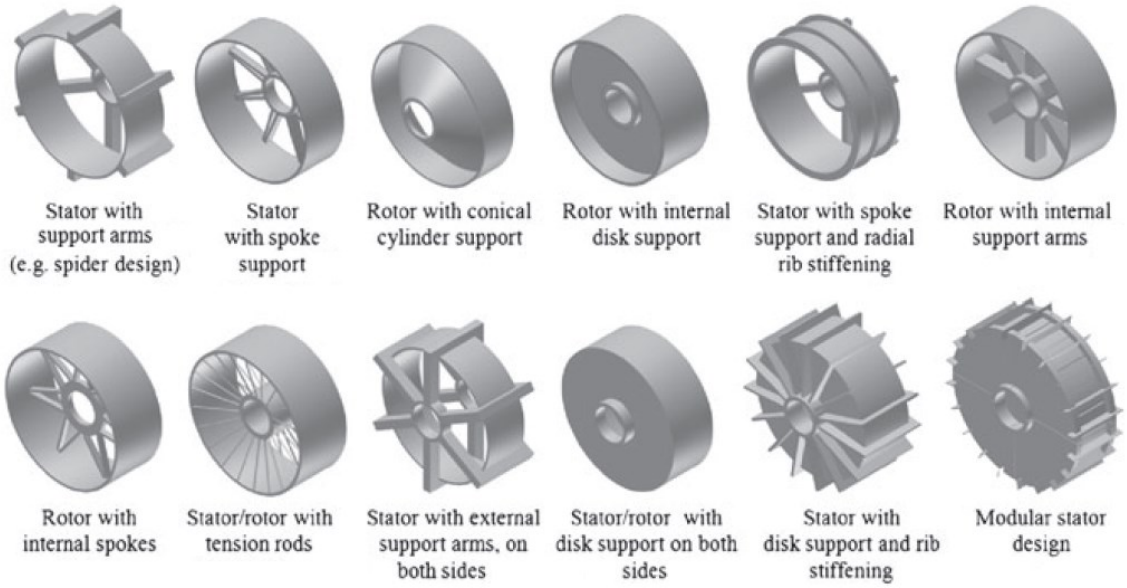

Figure 4.6: Various approaches to rotor/stator structural design [95].

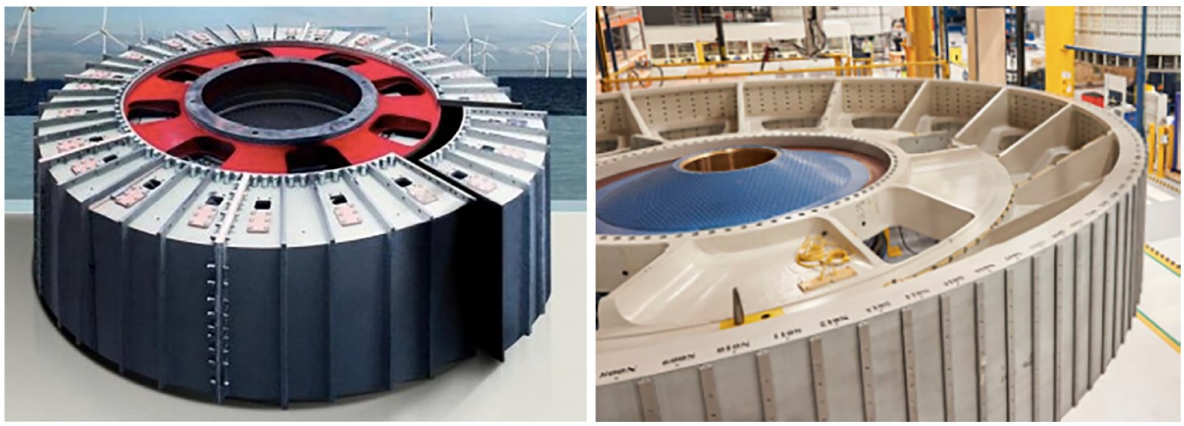

Figure 4.7: Image of a segmented stator direct-drive (DD) wind turbine generator (WTG) design from Siemens Gamesa (a), and a photo of a GE Vernova Haliade 6 MW DD WTG rotor (b) [46].

The relative importance of different sources of air-gap deformation can be distinguished by their magnitude and the way in which the air-gap deformation is distributed around the circumference of the air-gap. It is convenient to characterise different types of air-gap deformation according to the resulting mode ($\mathcal{M}$) of the air-gap non-uniformity:

$$\delta_{\mathrm{g},\mathcal{M}} = \hat{\delta}_{\mathrm{g},\mathcal{M}} \cos(\mathcal{M}\theta - \varphi_{\mathcal{M}}) \tag{4.5}$$

Where $\hat{\delta}_{g,\mathcal{M}}$ is the peak amplitude of the deformation, $\mathcal{M}$ is the mode of the deformation, θ is the circumferential angle, and $\varphi_{\mathcal{M}}$ is the offset angle with respect to other sources of air-gap non-uniformity.

In Figure 4.8 an illustration is provided of different modes of air-gap non-uniformity. A zero-order air-gap deformation ($\mathcal{M} = 0$) refers to a uniform deflection of the air-gap around the air-gap circumference. A first-order air-gap deformation ($\mathcal{M} = 1$) refers to a case in which the rotor and stator are not concentric. High-order air-gap deformations ($\mathcal{M} \geq 2$) refer to when the rotor/stator surface becomes distorted where $\mathcal{M}$ denotes the number of peaks, i.e. the wavenumber of the spatial distribution of air-gap clearance around the periphery of the air-gap.

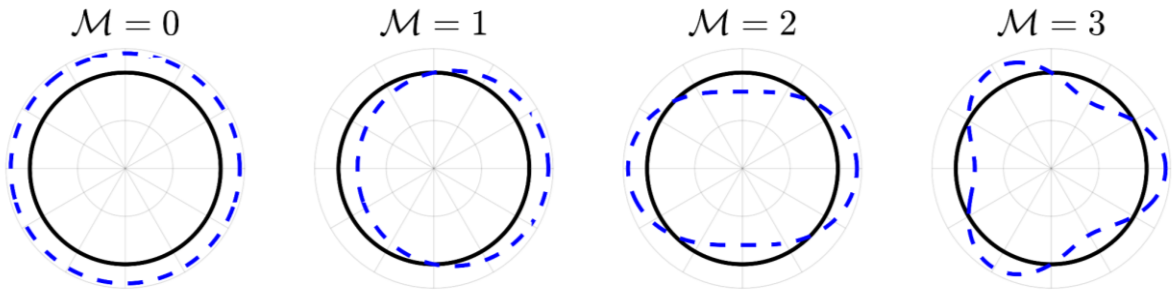

Figure 4.8: Illustration of different modes ($\mathcal{M}$) of air-gap non-uniformity. The black circle represents a uniform air-gap, the blue dashed line represents a nonuniform air-gap which varies with circumferential angle (θ) according to the value of $\mathcal{M}$.

4.3.1 Centrifugal Forces

The rotation of the WTG rotor results in centrifugal forces which act radially outward, however due to the relatively low rotational speed of DD WTGs they are negligible in comparison to other sources of air-gap deformation [45]. The small amount of deflection that does arise from centrifugal forces takes the form of a zero-order air-gap deformation ($\mathcal{M} = 0$).

4.3.2 Thermal Expansion

Thermal expansion can contribute significantly to air-gap deformation, especially when there is a large difference in temperature between the rotor and stator.

McDonald *et al.* estimate the change in rotor/stator radius of a 3 MW radial-flux WTG with a simplified analytical model [45]:

$$\Delta r = r_0 C_\varepsilon \Delta T \tag{4.6}$$

Where Δr is the change in radius of the rotor/stator, r_0 is the initial radius of the rotor/stator, C_ε is the coefficient of thermal expansion, and ΔT is the temperature rise of the rotor/stator during operation.

The air-gap deformation can then be estimated by finding the difference in the thermal expansion between the rotor (ΔR_r) and stator (ΔR_S):

$$\delta_{\mathrm{temp}} = \Delta r_{\mathrm{s}} - \Delta r_{\mathrm{r}} \tag{4.7}$$

It is important to consider the thermal expansion of both the rotor and stator such that a net change in air-gap clearance is obtained, if the rotor or stator is considered in isolation then the air-gap deflection due to thermal expansion will be overestimated [81].

Since the stator is typically at a higher temperature than the rotor, thermal expansion will act to close the air-gap in an outer-rotor WTG and open it in an inner-rotor WTG.

Thermal expansion results in a zero-order air-gap deformation ($\mathcal{M} = 0$) if the WTG has a circumferentially uniform temperature distribution. It is interesting to note that if the WTG is cooled by circumferential cooling ducts, as discussed in Section 3.3.5, this may result in a higher-order air-gap deformation due to the coolant temperature rise.

4.3.3 External Loads

Several external loads act upon WTG powertrains such as the weight of the rotor blades, horizontal and vertical wind shear, yaw error, and inertial effects [96]. These loads are counteracted by the stiffness of the wind turbine's main bearings resulting in displacement of the shaft and therefore a first-order air-gap deformation ($\mathcal{M} = 1$).

It is important to distinguish between operational conditions in which the WTG is producing power, and extreme events in which the WTG is not expected to produce power. Although less external loading can be expected during normal operation, the maximum permissible air-gap deformation will be constrained due to concerns regarding performance as detailed in Section 4.2.4. During extreme events external loads are expected to be larger, however since power production is not a concern in such cases the maximum allowable air-gap deformation can be greater. As discussed in Section 4.1, Bywaters *et al.* specify a 10% and a 50% air-gap deformation constraint in operational and extreme load scenarios respectively [61].

4.3.4 Manufacturing Tolerances

There are a variety of manufacturing and assembly tolerances which contribute towards non-uniformity of the air-gap.

In the work of Bywaters *et al.* a tolerance stack-up analysis is provided for the major sources of air-gap variation considered in the construction of a 1.5 MW inner-rotor DD WTG, they are stated to be the outer/inner diameter of the rotor/stator, the concentricity of the rotor, bearing, and shaft, and the thickness of the PMs [61].

A segmented stator construction is often utilised for modern DD WTGs with large power capacities to make assembly easier, however this can introduce additional sources of air-gap non-uniformity due to associated assembly tolerances. In partnership with Siemens Gamesa, a metrology company called Hexagon claims that advanced 3D imaging and robotic calibration tools can improve assembly tolerances associated with segmented stator assembly [97].

Increasingly stringent manufacturing/assembly tolerances may allow for a reduced air-gap clearance; however, this will generally result in increased production costs.

4.3.5 Magnetic Forces

Magnetic forces within the air-gap strain the generator structure, resulting in air-gap deflection.

The radial Maxwell stress is the main contributor to air-gap deflection, which in a cylindrical coordinate system is given by:

$$\sigma_r = \frac{B_r^2 - B_t^2}{2\mu_0} \tag{4.8}$$

where B_r and B_t are the radial and tangential magnetic flux density respectively.

The average magnetic shear stress has a significantly lower magnitude and acts tangentially to the air-gap clearance, it therefore has little impact on air-gap deformation [45].

Under the assumption of a perfectly uniform air-gap, the radial Maxwell stress results in a zero-order air-gap deformation ($\mathcal{M} = 0$). However, as discussed later in this

chapter, air-gap non-uniformity can introduce a variety of radial Maxwell stress harmonics which can result in higher-order air-gap deformations.

4.3.6 Self-Weight

Gravity can contribute significantly to air-gap deformation due to the significant mass of the WTG active components and of the structural frame itself. By analysing a disc-rim WTG structure, Bichan *et al.* demonstrate that the air-gap deformation due to self-weight can be reduced by increasing the thickness of the structural disc [81].

The air-gap deflection resulting from self-weight is three-dimensional and depends on the topology of the WTG structure. The total deflection of the rim will increase with increasing distance from the disc. It is interesting to note that the internal WTG structural rim can be supported internally by the disc, whereas the external WTG structure rim must extend over the length of the machine. Since the stator is heavier than the rotor, an outer-rotor WTG topology may allow for a reduced air-gap deflection due to self-weight.

It is important to note that there is an interplay between the self-weight deflection and that due to radial magnetic stress. If the mass of the WTG structure is increased to minimise the deflection due to the radial magnetic stress a further increase in structural mass is then required to compensate for the additional self-weight.

With respect to a circumferential coordinate system, the self-weight deflection can be approximated as a first-order air-gap deflection ($\mathcal{M} = 1$).

4.4 Secondary Deformation and Air-Gap Stability

In the following section secondary deflection and air-gap stability are discussed. The concept of magnetic stiffness is introduced and its application in prior works is examined. Based on the insights presented in this section, recommendations for a revised magnetic stiffness model for air-gap stability are made.

4.4.1 Secondary Deformation

Since the air-gap flux density depends on the air-gap reluctance, and hence the air-gap clearance, secondary deflection arises when the air-gap is deformed. If the air-gap becomes smaller, the air-gap magnetic flux density increases, therefore the radial Maxwell stress increases leading to further deflection of the generator structure.

As air-gap clearance is reduced secondary deflection becomes increasingly significant. This can be explained by considering a 1D magnetic circuit for a PM WTG in which only the air-gap and PM reluctance are considered:

$$\mathcal{R}_{\mathrm{ideal}} = 2\mathcal{R}_{\mathrm{PM}} + 2\mathcal{R}_{\mathrm{g}} \tag{4.9}$$

where $\mathcal{R}_{\mathrm{ideal}}$ is the total reluctance of the circuit, $\mathcal{R}_{\mathrm{PM}}$ is the PM reluctance ($\mu_{r,\mathrm{PM}} = 1$), and $\mathcal{R}_{\mathrm{g}}$ is the air-gap reluctance:

$$\mathcal{R}_{\mathrm{PM}} = \frac{h_{\mathrm{PM}}}{\mu_0 A_{\mathrm{PM}}}, \quad \mathcal{R}_g = \frac{h_{\mathrm{g}}}{\mu_0 A_{\mathrm{PM}}} \tag{4.10, 4.11}$$

where h_{PM} is the PM height, A_{PM} is the PM cross-sectional area in the radial direction, and h_{g} is the air-gap clearance. The air-gap flux density above the poles can then be found:

$$B_g = \frac{2\mathcal{F}_{\mathrm{ideal}}}{A_{\mathrm{PM}}\mathcal{R}_{\mathrm{ideal}}} \tag{4.12}$$

Where $\mathcal{F}_{\mathrm{ideal}}$ is the idealised magnetomotive force (MMF) from one PM:

$$\mathcal{F}_{\mathrm{ideal}} = \frac{B_{\mathrm{rem}} h_{\mathrm{PM}}}{\mu_0} \tag{4.13}$$

where B_{rem} is the remanent flux density of the PMs. If the same ratio of h_{PM} and h_{g} is maintained then B_{g} will remain approximately constant, the magnet height factor is therefore introduced:

$$C_{\mathrm{PM}} = \frac{h_{\mathrm{PM}}}{h_{\mathrm{g}}} \tag{4.14}$$

With this approach it is assumed that the intent behind reducing h_{g} is to reduce h_{PM} (and therefore WTG cost) since the scope for increasing B_{g} is limited by saturation of the rotor/stator iron. Substituting Eq. (4.14) into Eq. (4.9):

$$\mathcal{R}_{\mathrm{ideal}} = 2\mathcal{R}_{\mathrm{g}}(C_{\mathrm{PM}} + 1) \tag{4.15}$$

To introduce a change in magnetic circuit reluctance due to an air-gap deformation, it is assumed that the magnitude of the air-gap deformation (δ_{g}) does not vary significantly over the pitch of one pole-pair, this can be explained by considering that the pole pitch of DD WTGs is small in comparison to the total air-gap circumference.

Therefore, unless $\mathcal{M}$ is large, the variation in δ_{g} will be small over the pitch of one pole-pair. The change in magnetic circuit reluctance can therefore be approximated by:

$$\Delta\mathcal{R} = 2\frac{\delta_{\mathrm{g}}}{A_{\mathrm{PM}}\mu_0} \tag{4.16}$$

The maximum and minimum values of total reluctance are:

$$\mathcal{R}_{\max} = \mathcal{R}_{\mathrm{ideal}} + \Delta\mathcal{R}\,, \qquad \mathcal{R}_{\max} = \mathcal{R}_{\mathrm{ideal}} - \Delta\mathcal{R} \tag{4.17, 4.18}$$

which results in corresponding values of radial Maxwell stress:

$$\sigma_{r,\max} = \frac{2\mathcal{F}_{\mathrm{ideal}}^2}{\mu_0 A_{\mathrm{PM}}^2 \mathcal{R}_{\min}^2}\,, \qquad \sigma_{r,\min} = \frac{2\mathcal{F}_{\mathrm{ideal}}^2}{\mu_0 A_{\mathrm{PM}}^2 \mathcal{R}_{\max}^2} \tag{4.19,4.20}$$

The amplitude of the variation in radial Maxwell stress is therefore:

$$\Delta\sigma_r = \sigma_{r,\max} - \sigma_{r,\min} \tag{4.21}$$

Substituting Eq. (4.19) and (4.20) into Eq. (4.21) we arrive at:

$$\Delta\sigma_r = \frac{2B_{\mathrm{rem}}^2 C_{\mathrm{PM}}^2 h_{\mathrm{g}}^2}{\mu_0^3 A_{\mathrm{PM}}^2}\left(\frac{4\mathcal{R}_{\mathrm{ideal}}\Delta\mathcal{R}}{\left(\mathcal{R}_{\mathrm{ideal}}^2 - \Delta\mathcal{R}^2\right)^2}\right) \tag{4.22}$$

Since $\Delta\mathcal{R}$ cannot exceed $\mathcal{R}_{\mathrm{g}}$ Eq. (4.22) can be simplified by eliminating $\Delta\mathcal{R}^2$ since $\Delta\mathcal{R}^2 \ll \mathcal{R}_{\mathrm{ideal}}^2$, then substituting in Eq. (4.11), (4.15), and (4.16) we arrive at:

$$\Delta\sigma_r = 2\frac{\delta_{\mathrm{g}}}{h_{\mathrm{g}}}\frac{B_{\mathrm{rem}}^2 C_{\mathrm{PM}}^2}{\mu_0 (C_{\mathrm{PM}}+1)^3} \tag{4.23}$$

Therefore, although the radial Maxwell stress is proportional to the square of magnetic flux density, for PM machines the change in Maxwell stress due to deformation of the air-gap can be approximated as a linear function.

The impact of air-gap clearance on the sensitivity to secondary deflection is well illustrated in Eq. (4.23) by the ratio δ_{g}/h_g which must be kept sufficiently low to avoid large values of $\Delta\sigma_r$.

It is important to note that in practice magnetic saturation of the stator/rotor iron would dampen the increase in $\Delta\sigma_r$.

4.4.2 Magnetic Stiffness

The rate at which the magnetic force acting to deform the WTG structure (F_{mag}) increases due to air-gap deformation is often characterised by a 'magnetic stiffness' term:

$$K_{\mathrm{mag}} = \frac{F_{\mathrm{mag}}}{\delta_{\mathrm{g}}} \tag{4.24}$$

Since the magnetic force increases with decreasing air-gap clearance, this magnetic stiffness term is a 'negative stiffness'.

Jaen-Sola *et al.* state that the magnitude of the WTG's structural stiffness must be greater than or equal to the air-gap magnetic stiffness to ensure stability of the air-gap [98]–[100]:

$$|K_{\mathrm{str}}| \geq \left|K_{\mathrm{mag}}\right| \tag{4.25}$$

However, this criterion is only valid in idealised conditions in which manufacturing/assembly tolerances, self-weight, thermal expansion, and external loads are not considered.

Chin *et al.* take manufacturing tolerances and external wind loading into consideration in a magnetic stiffness model [101]. They introduce a stability criterion which can be stated as:

$$|K_{\mathrm{str}}\delta_{\mathrm{str}}| \geq \left|K_{\mathrm{mag}}\delta_{\mathrm{mag}}\right| \tag{4.26}$$

where:

$$\delta_{\mathrm{mag}} = \delta_{\mathrm{str}} + \delta_{\mathrm{tol}} + \delta_{\mathrm{load}} \tag{4.27}$$

where δ_{mag} is the total deformation of the air-gap, δ_{str} is the deformation of the structure, δ_{tol} is the deformation of the air-gap due to manufacturing/assembly tolerances, and δ_{load} is the deformation due to external loads. This line of reasoning can be taken further by taking into consideration air-gap deformation due to thermal expansion (δ_{temp}) and self-weight (δ_{grav}), which gives a total air-gap deformation of:

$$\delta_{\mathrm{mag}} = \delta_{\mathrm{str}} + \delta_{\mathrm{tol}} + \delta_{\mathrm{load}} + \delta_{\mathrm{temp}} + \delta_{\mathrm{grav}} \tag{4.28}$$

Which results in a structural stiffness criterion of:

$$K_{str} \geq \left| K_{mag} \frac{\delta_{\mathrm{mag}}}{\delta_{\mathrm{str}}} \right| \tag{4.29}$$

The minimum required structural stiffness can therefore be related to the magnetic stiffness by a 'stiffness factor' C_K:

$$K_{\mathrm{str}} \geq \left| C_K K_{\mathrm{mag}} \right| \tag{4.30}$$

$$C_K = \frac{\delta_{\mathrm{mag}}}{\delta_{\mathrm{str}}} \tag{4.31}$$

The key insight in this approach is that the total air-gap deformation is greater than the structural deflection, therefore the structural stiffness must be greater than the magnetic stiffness according to the stiffness factor (C_K).

Manufacturing/assembly tolerances, external loading which displaces the shaft, thermal expansion and self-weight can deform the air-gap without producing a mechanical strain, and therefore a structural elastic force, of the generator structure which acts in opposition to the magnetic forces. In the context of a spring system in which the air-gap stability is modelled, these sources of deflection can be thought of as mechanical 'play' which results in displacement without a corresponding mechanical spring force yet still produces a magnetic spring force.

In Figure 4.9 this concept is illustrated with a sketch. During the initial deformation of the air-gap (δ_i), the magnetic force increases however the structural force remains constant:

$$\delta_i = \delta_{\mathrm{tol}} + \delta_{\mathrm{load}} + \delta_{\mathrm{temp}} + \delta_{\mathrm{grav}} \tag{4.32}$$

For the structural elastic force to counteract the magnetic force, secondary deflection of the WTG structure must occur (δ_{str}). Equilibrium is achieved at some total deformation of the air-gap (δ_{mag}) assuming that the structural stiffness is sufficiently large in comparison to the magnetic stiffness. Note that the initial deformation and secondary deflection would occur at the same time, the sketch depicts a sequence of deformation for illustrative purposes. The origin of the graph depicts an initial deformation (δ_0) assuming an idealised scenario where the magnetic and structural forces are initially in equilibrium before the various sources of air-gap deformation are introduced.

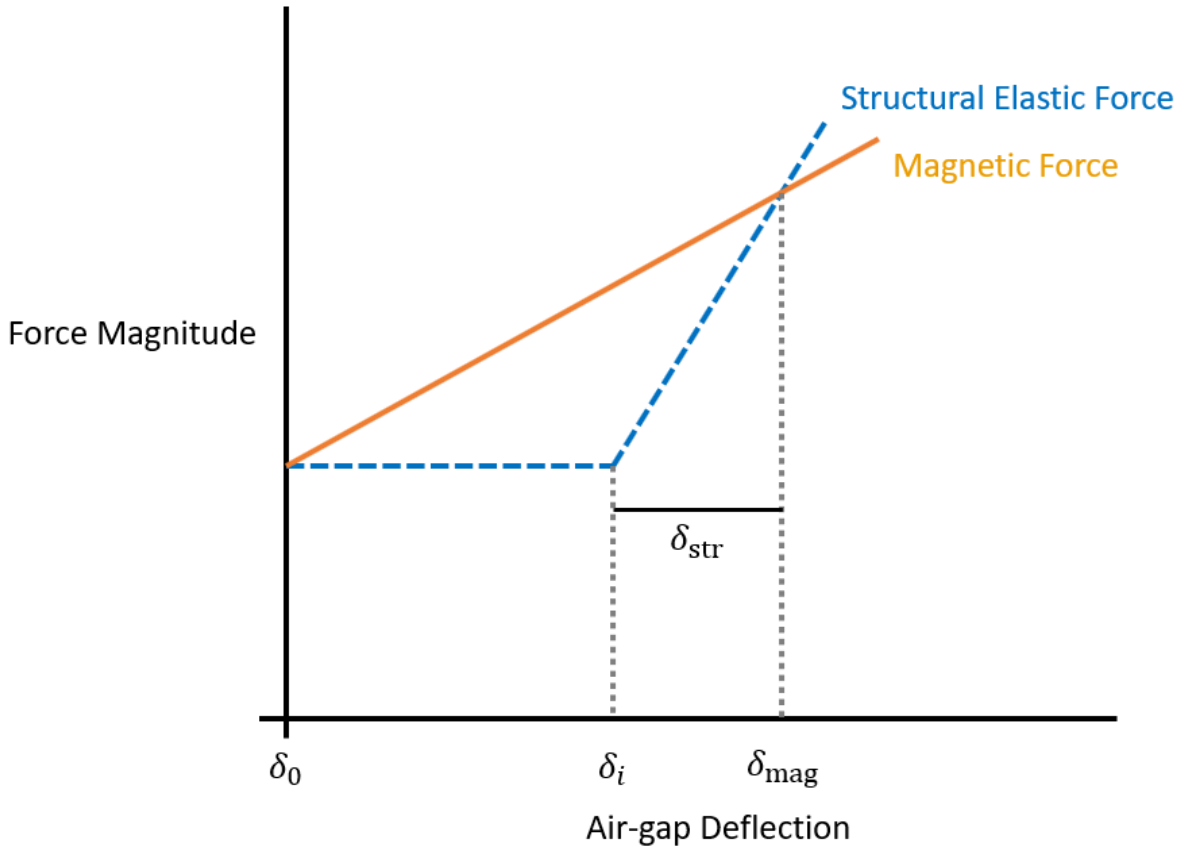

Figure 4.9: Sketch of how the magnitude of the magnetic force and counteracting structural forces vary in the event of an air-gap deformation.

According to Eq. (4.31), the stiffness factor (C_K) depends on the ratio between the total air-gap deformation (δ_{mag}) and the air-gap deformation due to the deflection of the WTG structure (δ_{str}), i.e. the secondary deflection. This has significant implications with regards to the specification of the air-gap clearance and the limits imposed on the maximum allowable air-gap deformation.

In Figure 4.10, the stiffness factor required to maintain the total air-gap deformation (δ_{mag}) within various limits is plotted for a range of initial deformation of the air-gap (δ_i). If the initial deformation of the air-gap is very close to the limit imposed on the total air-gap deformation, then the stiffness factor must be very large such that the WTG's structural elastic force can match the magnetic force with only a small amount of secondary deflection. This would require a significantly increased WTG structural mass.

Improved clarity is therefore required for limits imposed on air-gap deformation. For example, if the maximum allowable air-gap deformation is limited to 20% due to concerns regarding the electromagnetic performance as discussed in Section 4.2.4, a more stringent constraint must be applied to the maximum allowable air-gap deformation due to manufacturing/assembly tolerances, external loads, thermal expansion, and self-weight such that the required stiffness, and therefore mass, of the WTG structure is not excessive.

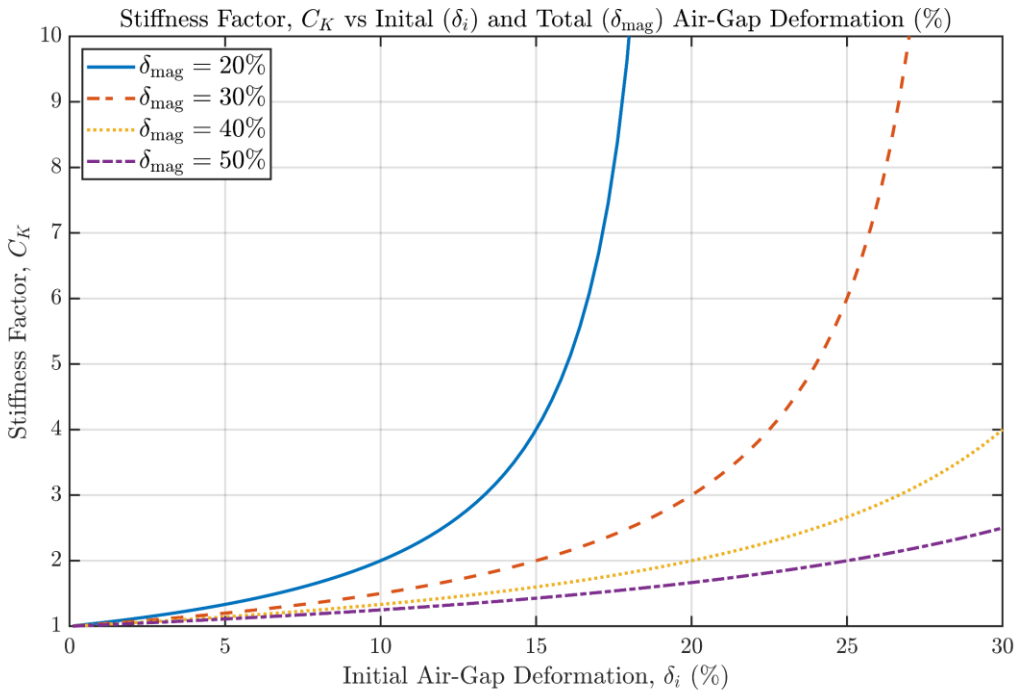

Figure 4.10: Stiffness factor (C_K) plotted as a function of initial air-gap deformation (δ_i) for various limits imposed on the total air-gap deformation (δ_{mag}). Air-gap deformation is plotted as a percentage of the nominal air-gap clearance.

4.4.3 Impact of Air-Gap Deformation Mode Number

The magnetic stiffness model introduced in the preceding section is based on a 1D assumption in which each source of air-gap deformation contributes equally to the deformation of the WTG structure due to the air-gap closing force. However, as detailed in Section 4.3, the distribution of air-gap non-uniformity can take various forms depending on the source of air-gap deformation.

By approximating the change in radial Maxwell stress as a linear function and by assuming that the elastic deformation of the WTG is linear, the total variation in the Maxwell stress around the air-gap periphery can be treated as a superposition of

various radial stress distributions from each source of air-gap deflection. It is important to note that while the net magnetic force always acts to pull the rotor and stator together, the individual components of the variation in radial Maxwell stress can act in both directions. The various components of radial Maxwell stress can be represented by substituting Eq. (4.5) into Eq. (4.23):

$$\Delta\sigma_{\mathcal{M}} = 2\frac{\hat{\delta}_{\mathrm{g},\mathcal{M}}\cos(\mathcal{M}\theta - \varphi_{AG})}{h_{\mathrm{g}}}\frac{B_{\mathrm{rem}}^2 C_{\mathrm{PM}}^2}{\mu_0(C_{\mathrm{PM}}+1)^3} \tag{4.33}$$

An air-gap deformation with a mode number $\mathcal{M}$ will therefore result in a corresponding component of radial Maxwell stress variation with the same mode number.

The mechanism in which the WTG structure deforms depends on how the radial Maxwell stress is distributed, i.e. the value of $\mathcal{M}$. By representing the WTG structure according to a simplified rim model, it can be demonstrated that the effective structural stiffness of the DD WTG depends on the value of $\mathcal{M}$.

For zero-order ($\mathcal{M} = 0$) radial stress harmonics the rim is displaced by a uniform radial displacement Δr_{rim}, and the circumference changes by $\Delta l_p = 2\pi\Delta r_{\mathrm{rim}}$, resulting in a circumferential strain:

$$\varepsilon_\theta = \frac{\Delta l_p}{l_{p,0}} = \frac{\Delta r_{\mathrm{rim}}}{r_{\mathrm{rim},0}} \tag{4.34}$$

where $l_{p,0}$ is the initial circumference of the rim, and $r_{\mathrm{rim},0}$ is the initial radius of the rim.

Based on a simplified rim model, in which the radial magnetic stress is assumed to act directly on a rim which has a small thickness in comparison to its radius, the membrane stiffness that counteracts the hoop strain can be expressed as [102]:

$$K_{\mathrm{str},0} = \frac{E t_{\mathrm{rim}}}{r_{\mathrm{rim}}^2} \tag{4.35}$$

where E is the modulus of elasticity of the rim, and t_{rim} is the rim thickness. An illustration of this scenario is provided in Figure 4.11.

For higher order ($m \geq 2$) radial stress harmonics, the rim is primary displaced by out-of-plane bending which is resisted by the bending stiffness as opposed to the membrane stiffness. An illustration of this scenario is provided in Figure 4.12.

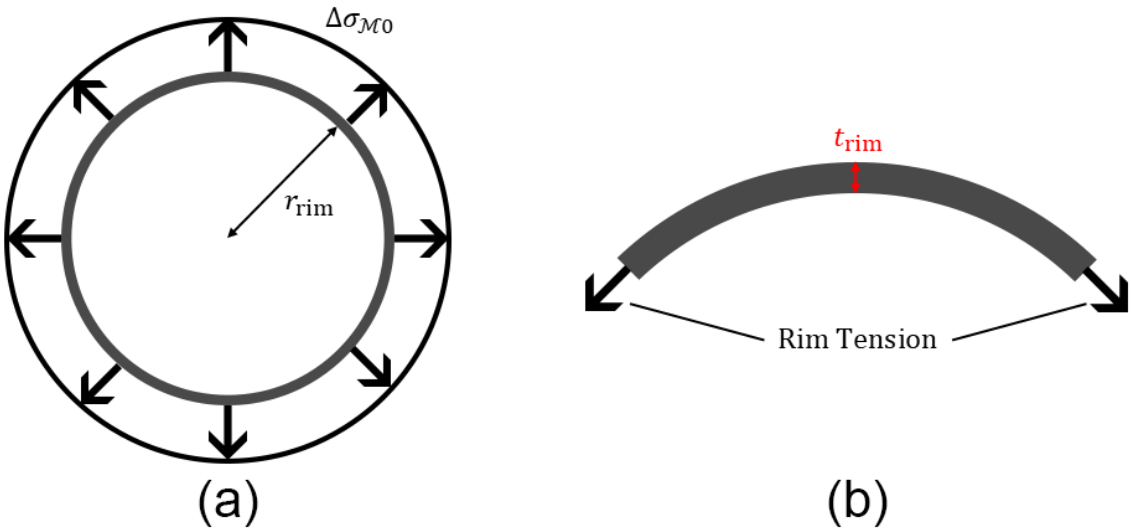

Figure 4.11: Illustration of a mode 0 component of radial Maxwell stress ($\Delta\sigma_{\mathcal{M}0}$) acting on a simplified rim model of an inner rotor/stator structure (a), and the resulting tension acting on a rim segment (b).

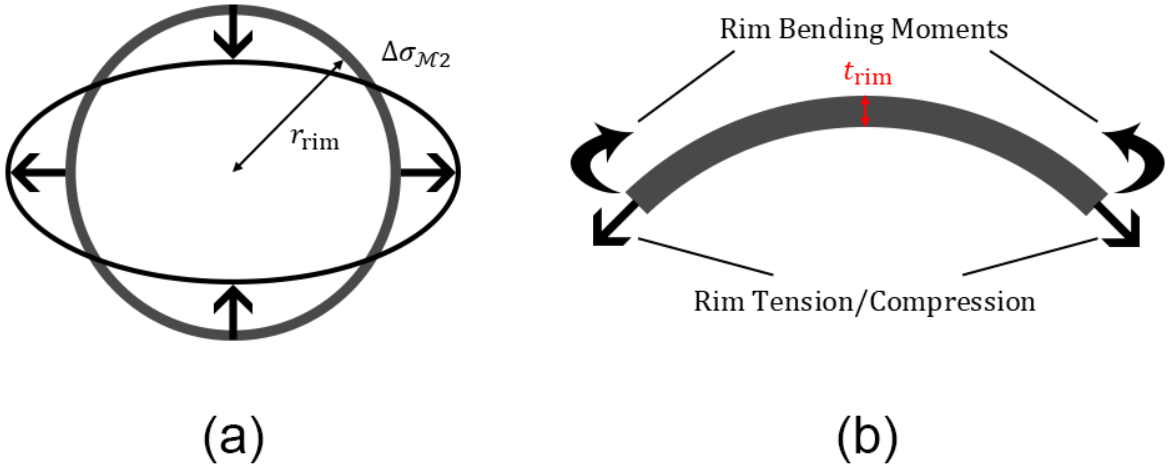

Figure 4.12: Illustration of a mode 2 component of radial Maxwell stress ($\Delta\sigma_{\mathcal{M}2}$) acting on a simplified rim model of an inner rotor/stator structure (a), and the resulting tension/compression and bending moments acting on a rim segment (b).

Based on a simplified rim model, the out-of-plane bending stiffness of the rim can be expressed as [102]:

$$K_{\mathrm{str},\mathcal{M}} = \frac{E t_{\mathrm{rim}}^3 (\mathcal{M}^2 - 1)^2}{12 r_{\mathrm{rim}}^4} \tag{4.36}$$

For a large rim with a thickness that is relatively small compared to the rim radius, such as in the case of a disc-rim type DD WTG structure, the out-of-plane bending stiffness is much lower than the membrane stiffness, this can be made clear by considering their ratio:

$$\frac{K_{\mathrm{str},0}}{K_{\mathrm{str},\mathcal{M}}} = \frac{12 r_{\mathrm{rim}}^2}{t_{\mathrm{rim}}^2 (\mathcal{M}^2 - 1)^2} \tag{4.37}$$

Since $r_{\mathrm{rim}} \gg t_{\mathrm{rim}}$, the membrane stiffness of the rim is considerably larger than the out-of-plane bending stiffness for relatively low values of $\mathcal{M}$. As $\mathcal{M}$ increases, the ratio is expected to decrease quickly according to the simplified rim model.

The spatial distribution of air-gap deformation, according to the value of $\mathcal{M}$, therefore influences the extent of the resulting secondary deflection due to the change in the radial Maxwell stress. In literature concerned with magnetically induced vibration of electrical machines, the simplified ring model is often used to explain that radial Maxwell stress harmonics with a low spatial frequency, i.e. wavenumber, are the most impactful in terms of the resulting vibration amplitudes. The deflection amplitude is assumed to decrease in proportion to $\mathcal{M}^{-4}$ for $\mathcal{M} \geq 2$ as indicated by Eq. (4.37).

First order ($\mathcal{M} = 1$) radial stress harmonics are unique in that they result in a non-zero net force on the WTG shaft. Although the variation in radial Maxwell stress changes sign around the circumference, it generally acts in the same direction with respect to a global coordinate system, this results in unbalanced magnetic pull (UMP) which is resisted by the main bearings supporting the shaft, as illustrated in Figure 4.13, and the stator supports.

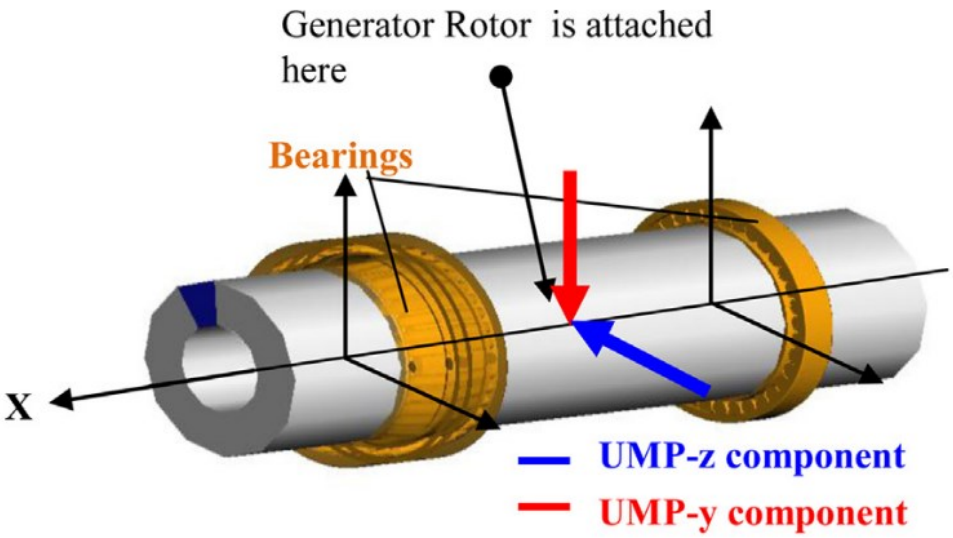

Figure 4.13: Illustration of unbalanced magnetic pull (UMP) acting on the wind turbine generator rotor shaft [50].

The impact of UMP on air-gap stability of DD WTGs has been investigated by Sethuraman *et al.* and in the PhD thesis of Kaswar Mostafa [80], [103]. In both studies it is found that the UMP has little influence on the displacement of the rotor shaft due to the large stiffness of the main bearings. However, first order air-gap deformation can still result in secondary deflection since the unbalanced magnetic forces must be transferred from the rim to the shaft resulting in structural deflection of the WTG. Since the stiffness of the structural disc has a large impact on the resulting secondary deflection, the simplified rim model fails to describe the effective stiffness of the WTG structure in this case.

4.4.4 Finite Element Analysis of a Disc-Rim Structure

A simplified rim model is useful for highlighting that the effective structural stiffness of the DD WTG depends on the order ($\mathcal{M}$) of the radial Maxwell stress. However, the role of the structural disc and 3D effects are neglected. For an improved understanding of how the distribution of the radial Maxwell stress impacts the amplitude of the structural deformation finite elment analysis (FEA) simulations of a simplified disc-rim WTG structure corresponding to the IEA 15 MW reference DD WTG stator design were conducted in COMSOL Multiphysics 6.1 [13].

A fixed constraint was applied to the interface between the structural disc and the shaft, approximating the bearing stiffness as infinite. This assumes that any deformation due to UMP is negligible.

Since the focus of this study is on how the order ($\mathcal{M}$) of the radial Maxwell stress influences the amplitude of the structural deformation, other loads such as the shear stress and self-weight were neglected.

A radial stress was applied to the rim, with the x and y components specified as:

$$\sigma_x = A_\sigma \cos(\theta)\cos(\mathcal{M}\theta) \tag{4.38}$$

$$\sigma_y = A_\sigma \sin(\theta)\cos(\mathcal{M}\theta) \tag{4.39}$$

Where A_σ is the amplitude of the radial stress harmonic. The resulting radial stress therefore represented the component of radial Maxwell stress $\Delta\sigma_{\mathcal{M}}$ of interest with a spatial distribution corresponding to $\mathcal{M}$:

$$\Delta\sigma_{\mathcal{M}} = \sqrt{\sigma_x^2 + \sigma_y^2} \tag{4.40}$$

For each simulation the peak radial deflection of the rim was determined:

$$\hat{\delta}_{\mathrm{g},\mathcal{M}} = \max\left(\sqrt{\delta_x^2 + \delta_y^2}\right) \tag{4.41}$$

where δ_x and δ_y represent the local deflection of the rim in the x and y direction respectively. The function $\max$ indicates that the maximum value was determined using the postprocessing tools in COMSOL.

Various simulations were conducted in which A_σ was kept constant and $\mathcal{M}$ was varied. In Figure 4.14 an illustration is provided of the stator geometry and the distortion of the structure due to radial Maxwell stress harmonics with various values of $\mathcal{M}$.

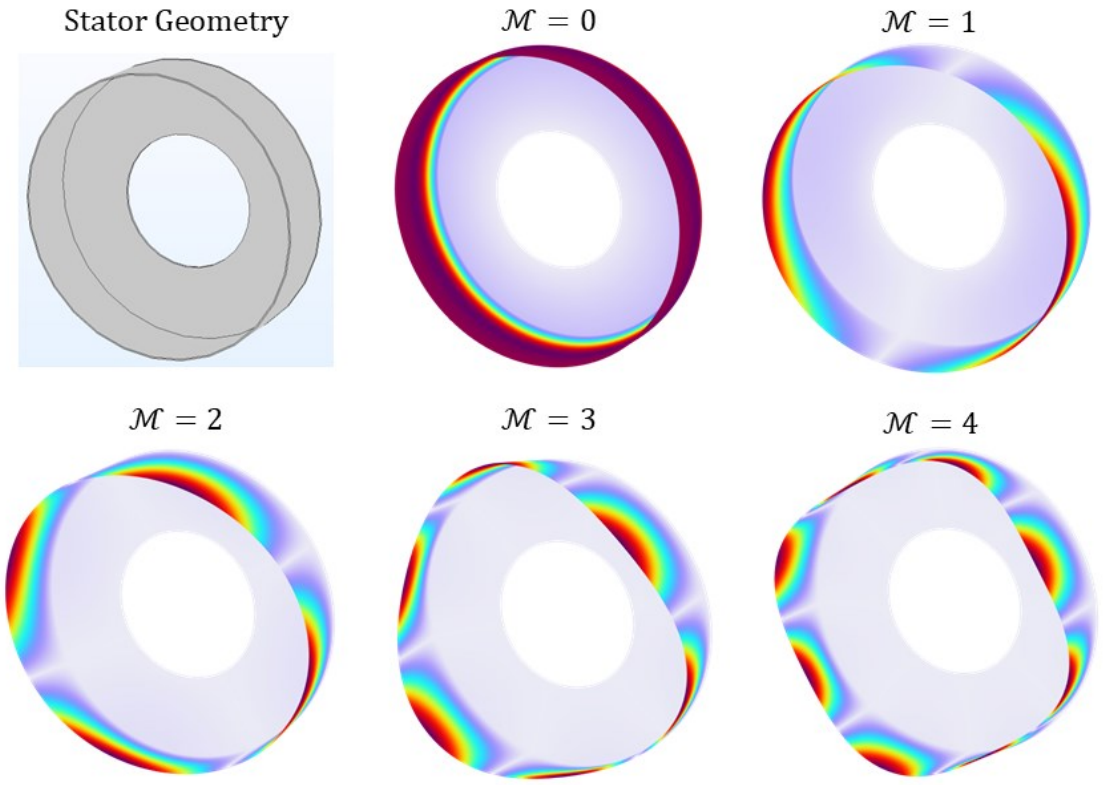

Figure 4.14: Illustration of the stator geometry and the magnitude of radial deformation due to a Maxwell stress harmonic with a mode number ($\mathcal{M}$) of 0-4 (not to scale).

To compare the relative amplitude of the peak radial deformation between the different simulations $\hat{\delta}_{\mathrm{g},\mathcal{M}}$ was normalised with respect to the peak radial deflection when $\mathcal{M} = 0$:

$$\hat{\delta}_{\mathrm{g},\mathcal{M}\mathrm{norm}} = \frac{\hat{\delta}_{\mathrm{g},\mathcal{M}}}{\hat{\delta}_{\mathrm{g},\mathcal{M}0}} \tag{4.42}$$

To understand how the rim and disc thickness influence the resulting structural deflection, additional sets of simulations were carried out in which the rim thickness and disc thickness were doubled in relation to the baseline case (corresponding to the IEA 15 MW DD WTG specifications). The peak deformation obtained in these cases was normalised with respect to the baseline case where $\mathcal{M} = 0$.

In Figure 4.15 the normalised peak radial deformation amplitude is plotted for the various values of $\mathcal{M}$. It was found that the mode number of the radial stress distribution had a very large influence on the amplitude of the resulting radial deformation.

It was found that for $\mathcal{M}$ = 0, the resulting deformation was very small in comparison to the higher order radial stress harmonics. For the baseline case it was found that the peak deformation was ~46 times larger when $\mathcal{M} = 1$, and ~530 times larger for $\mathcal{M} = 2$.

By doubling the thickness of the rim, the $\mathcal{M} = 0$ deformation was reduced by ~50%, which corresponds to the simplified rim model prediction given by Eq. (4.35). Increasing the disc thickness was found to have a negligible impact.

For $\mathcal{M} = 1$, it was found that an increase in both the rim and the disc thickness reduced the peak deformation. However, increasing the disc thickness had more of an impact.

For $\mathcal{M} = 2$, increasing both the rim and the disc thickness reduced the peak deformation.

As $\mathcal{M}$ was increased further it was found that the impact of increasing the disk thickness became negligible, however increasing the rim thickness resulted in a significant reduction in the deformation amplitude.

For $\mathcal{M} \geq 2$, the trend of deformation amplitude vs $\mathcal{M}$ number was found to decrease gradually in comparison to the $\mathcal{M}^{-4}$ dependence suggested by the simplified rim model.

In summary, the value of $\mathcal{M}$ is demonstrated to have a significant impact on the resulting deformation of the WTG structure due to the radial Maxwell stress. The FEA results agree with the predictions of the simplified rim model for $\mathcal{M} = 0$, demonstrating

that the membrane stiffness is the dominant mechanism behind the structural deformation. As $\mathcal{M}$ is increased the peak radial deformation of the structure is increased considerably for the same value of A_σ. It is shown that the disc thickness plays a significant role in mitigating deformation due to radial Maxwell stress harmonics with $\mathcal{M} = 1 - 4$. It is highlighted that although the simplified rim model is useful for explaining how $\mathcal{M}$ impacts the resulting structural deformation, it fails to capture the full complexity of DD WTG structural behaviour.

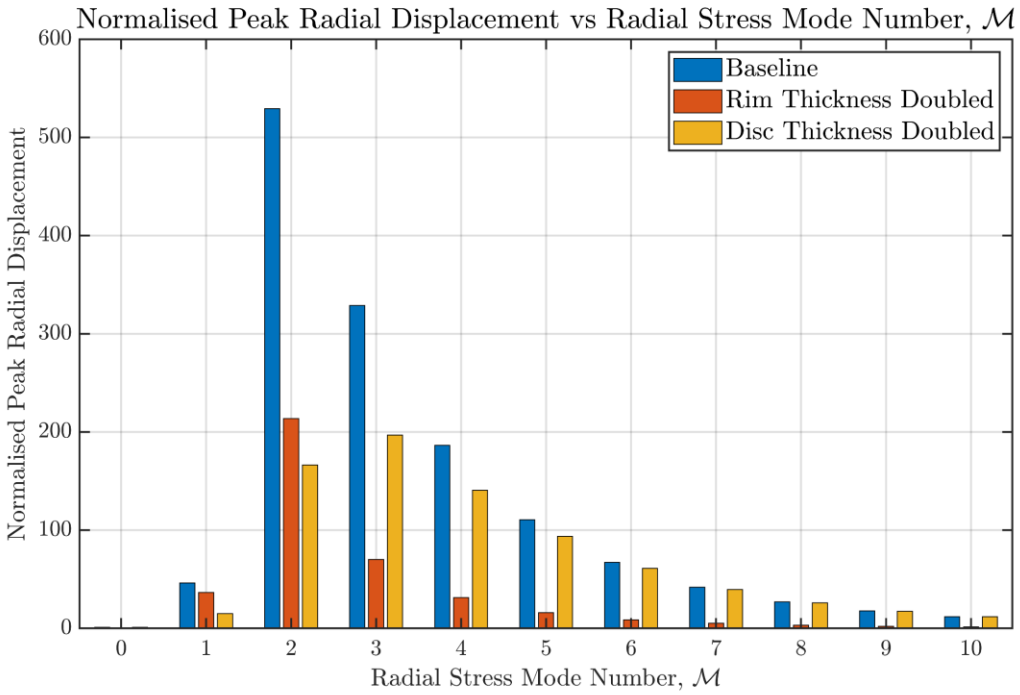

Figure 4.15: Normalised peak radial displacement ($\hat{\delta}_{g,\mathcal{M}\text{norm}}$) of the disc-rim structure compared for a range of radial Maxwell stress mode numbers ($\mathcal{M}$). A baseline case is compared against cases in which the rim or disc thickness has been doubled. The peak radial displacement is normalised with respect to the baseline peak radial displacement when $\mathcal{M} = 0$.

4.4.5 Recommendations for a Revised Magnetic Stiffness Model

It has been demonstrated that the mode number ($\mathcal{M}$) of air-gap deformation has a significant impact on the amplitude of the secondary deflection that results from the change in the radial magnetic stress.

It was found that air-gap deformations of $\mathcal{M} = 0$ are the least impactful in terms of secondary deflection, this suggests that per-unit of air-gap deformation the secondary deformation due to thermal expansion and centrifugal forces is insignificant.

By comparison air-gap deformations of $\mathcal{M} = 1$ result in significantly more secondary deflection per-unit of air-gap deformation. This includes displacement of the shaft due to external loads, eccentricity due to manufacturing/assembly tolerances, and self-weight of the WTG.

Higher-order air-gap deformations ($\mathcal{M} \geq 2$) are especially impactful, resulting in significantly more secondary deflection per-unit of air-gap deformation. Such mode numbers are less likely to occur than modes 0 and 1, however they can arise due to manufacturing tolerances concerned with the outer/inner diameter of the rotor/stator and assembly tolerances of modular machine structures.

Air-gap stability models based upon the magnetic stiffness concept, such as detailed in Section 4.4.2, should therefore account for the relative importance of the various sources of air-gap deformation with respect to their mode number. In Table 4.2 a summary is provided of the various sources of initial air-gap deformation and their relative impact on air-gap stability.

Table 4.2: Summary of various sources of initial air-gap deformation.

Air-Gap Deformation Mode ($\mathcal{M}$)	**Sources of Initial Air-Gap Deformation**	**Relative Impact on Air-Gap Stability (per unit of deformation)**
0	- Thermal expansion. - Fundamental component of air-gap radial Maxwell stress. - Centrifugal forces. - Stator/rotor manufacturing tolerances.	Low
1	- External loading. - Self-weight. - Concentricity tolerances of rotor, bearing, and shaft. - Stator/rotor manufacturing tolerances.	Moderate
2+	- Stator/rotor manufacturing tolerances. - Segmented stator assembly tolerances.	High*

*The relative impact of high-order deformations on air-gap stability decreases with increasing $\mathcal{M}$.

4.5 Vibration Induced by High-Order Air-Gap Non-uniformity

In Section 4.2.4, it was mentioned that non-uniformity of the air-gap can result in magnetically induced vibration of DD WTGs. In the following section, the mechanism in which this happens is explored using an analytical model which is then validated using finite elment method (FEM) magnetic simulations.

Due to their large size, high number of poles, and low rotational speed DD PM WTGs differ in behaviour from what is commonly assumed for smaller high-speed machines with fewer poles. Available vibration analysis of large low-speed machines is generally limited to either first-order approximations (in which perfect symmetry is assumed) or low-order air-gap non-uniformities [101], [104]–[108].

4.5.1 An Analytical Model for Non-uniform Air-Gap Radial Maxwell Stress Harmonics

In the following section an analytical model for the radial Maxwell stress harmonics produced in the nonuniform air-gap of a DD PM WTG is introduced, several simplifying assumptions are made:

- PM relative permeability $\mu_{r,\mathrm{PM}} = 1$.
- The air-gap magnetic flux density (B_g) is purely radial in direction.
- The iron components of the magnetic circuit have infinite permeability with no saturation.
- Open-load conditions are assumed for the armature windings.
- No axial variation of machine geometry, e.g. skewing of stator slots, shaping of PMs, or end effects.

A stationary cylindrical coordinate system is used with reference to the middle of the air-gap, a polar coordinate θ designates the circumferential angle. Air-gap flux density is given by:

$$B_\mathrm{g} = \mathcal{F}\mathcal{P} \tag{4.43}$$

where $\mathcal{F}$ is the magneto-motive force (MMF) from the PMs, and $\mathcal{P}$ is the magnetic circuit permeance. During operation B_g varies both spatially and temporally: $\mathcal{F}$ varies circumferentially due to the alternating polarity of the PMs and the spacing between them, $\mathcal{P}$ varies due to the stator slots, stator dissymmetry, and rotor dissymmetry. $\mathcal{F}$ can be approximated as a square wave:

$$\mathcal{F} = \sum_{n=1,3,5,\dots}^{\infty} K_n \cos\big(nN_\mathrm{PP}(\theta - \omega t)\big) \tag{4.44}$$

where K_n is the amplitude of the n^{th} harmonic of the MMF wave, n is a positive odd integer, N_{PP} is the number of pole pairs, ω is the angular velocity and t is time. The stator slots produce a permeance wave of the form:

$$\mathcal{P}_{\mathrm{slots}} = \sum_{l=1}^{\infty} \mathcal{P}_l \cos(l N_{\mathrm{slot}} \theta) \tag{4.45}$$

where $\mathcal{P}_l$ is the amplitude of the l^{th} harmonic of permeance variation, N_{slot} is the number of stator slots. Stator dissymmetry produces a permeance wave of the form:

$$\mathcal{P}_{\mathrm{stator}} = \sum_{q=1}^{\infty} \bar{\mathcal{P}}_q \cos\left(q\theta - \varphi_{sq}\right) \tag{4.46}$$

where $\bar{\mathcal{P}}_q$ is the amplitude of the q^{th} harmonic of permeance variation caused by the stator dissymmetry, q is the order of stator radius variation, and φ_{sq} is the phase angle with reference to the lowest value of q. Rotor dissymmetry produces a permeance wave of the form:

$$\mathcal{P}_{\mathrm{rotor}} = \sum_{p=1}^{\infty} \bar{\mathcal{P}}_p \cos\left(p(\theta - \omega t) - \varphi_{rp}\right) \tag{4.47}$$

where $\bar{\mathcal{P}}_p$ is the amplitude of the p^{th} harmonic of permeance variation caused by rotor dissymmetry, p is the order of rotor radius dissymmetry, and φ_{rp} is the phase angle with reference to the lowest value of p. The resultant air-gap flux density harmonics can then be found by substituting in a summation of the permeance waves, Eq. (4.45), (4.46), and (4.47) along with the MMF wave Eq. (4.44) into (4.43), which yields three flux density waves:

$$B_{nl} = \sum_{n,l} K_{nl} \cos\left((nN_{\mathrm{PP}} \pm lS_s)\theta - nN_{\mathrm{PP}}\omega t\right) \tag{4.48}$$

$$B_{nq} = \sum_{n,q} K_{nq} \cos\left((nN_{\mathrm{PP}} \pm q)\theta - nN_{\mathrm{PP}}\omega t - \varphi_{sq}\right) \tag{4.49}$$

$$B_{np} = \sum_{n,p} K_{np} \cos\left((nN_{\mathrm{PP}} \pm p)\theta - (nN_{\mathrm{PP}} \pm p)\omega t - \varphi_{rp}\right) \tag{4.50}$$

where B_{nl} results from the multiplication of Eq. (4.44) and (4.45), K_{nl} is the amplitude of the n^{th}, l^{th} flux density harmonic. B_{nq} results from the multiplication of Eq. (4.44) and (4.46), K_{nq} is the amplitude of the n^{th}, q^{th} flux density harmonic. B_{np} results from the multiplication of Eq. (4.44) and (4.47), K_{np} is the amplitude of the n^{th}, p^{th} flux density harmonic. The radial Maxwell stress in 1D is:

$$\sigma_r = \frac{B_g^2}{2\mu_0} \tag{4.51}$$

where μ_0 is the permeability of free space. By substituting in the summation of Eq. (4.48), (4.49), and (4.50) into Eq. (4.51) we arrive at six terms that describe the various harmonics of the air-gap radial Maxwell stress:

1. Harmonics due to the interaction of MMF and stator slots, where n' is an integer which can be odd or even, and $l' = l_i \pm l_j$.

$$\sigma_{n'l'} = \sum_{n',l'} K'_{n'l'} \cos\left((2n'N_{\mathrm{PP}} \pm l'S_s)\theta - 2n'N_{\mathrm{PP}}\omega t\right) \tag{4.52}$$

2. Harmonics due to the interaction of MMF and rotor dissymmetry, where $p' = p_i \pm p_j$ and $\varphi'_{rp} = \varphi_i \pm \varphi_j$.

$$\sigma_{n'p'} = \sum_{n',p'} K'_{n'p'} \cos\left(\left(2n'N_{\mathrm{PP}} \mathbin{\widehat{\pm}} p'\right)\theta - \left(2n'N_{\mathrm{PP}} \mathbin{\widehat{\pm}} p'\right)\omega t - \varphi_{rp}{}'\right) \tag{4.53}$$

3. Harmonics due to the interaction of MMF and stator dissymmetry, where $q' = q_i \pm q_j$ and $\varphi'_{sq} = \varphi_i \pm \varphi_j$.

$$\sigma_{n'q'} = \sum_{n',q'} K'_{n'q'} \cos\left((2n'N_{\mathrm{PP}} \pm q')\theta - 2n'N_{\mathrm{PP}}\omega t - \varphi_{sq}{}'\right) \tag{4.54}$$

4. Intermodulation of stator slot and rotor dissymmetry harmonics.

$$\sigma_{n'lp} = \sum_{n',l,p} K'_{n'lp} \cos\left(\left(2n'N_{\mathrm{PP}} \pm lS_s \mathbin{\widehat{\pm}} p\right)\theta - \left(2n'N_{\mathrm{PP}} \mathbin{\widehat{\pm}} p\right)\omega t \pm \varphi_{rp}\right) \tag{4.55}$$

5. Intermodulation of stator slot and stator dissymmetry harmonics.

$$\sigma_{n'lq} = \sum_{n',l,q} K'_{n'lq} \cos\left((2n'N_{\mathrm{PP}} \pm lS_s \pm q)\theta - 2n'N_{\mathrm{PP}}\omega t \pm \varphi_{sq}\right) \tag{4.56}$$

6. Intermodulation of rotor and stator dissymmetry harmonics.

$$\sigma_{n'pq} = \sum_{n',l,q} K'_{n'pq} \cos\left(\left(2n'N_{\mathrm{PP}} \,\widehat{\pm}\, p \pm q\right)\theta - \left(2n'N_{\mathrm{PP}} \,\widehat{\pm}\, p\right)\omega t - \left(\varphi_{rp} \pm \varphi_{sq}\right)\right) \tag{4.57}$$

Where K' represents the amplitudes of the various radial stress harmonics, A plus-minus sign with a hat ($\widehat{\pm}$) indicates that both in the equation must always be of the same sign, whereas ($\pm$) is independent, and the subscripts i and j denote the order of the flux density harmonics which result in the stress harmonic (note that i can equal j).

The preceding approach based on permeance waves is convenient for determining the wavenumbers and frequencies of the various air-gap radial stress harmonics, however the amplitude terms are ambiguously defined.

4.5.2 Finite Element Method Simulation and Validation

A finite element method (FEM) simulation of the IEA 15MW reference wind turbine generator was conducted with COMSOL Multiphysics 6.1, as depicted in Figure 4.16. The generator parameters are available in the IEA report [13]. Parametric curves were used to define the boundaries of the PMs and the rotor/stator at the air-gap interface, e.g. the following equations define the x and y coordinates of the stator outer diameter:

$$x = r_s \cos(\theta) + \sum_q \hat{\delta}_q \cos\left((q+1)\theta - \varphi_{sq}\right) \tag{4.58}$$

$$y = r_s \sin(\theta) + \sum_q \hat{\delta}_q \sin\left((q+1)\theta - \varphi_{sq}\right) \tag{4.59}$$

where r_s is the stator outer radius, $\hat{\delta}_q$ is the peak deflection amplitude of the q^{th} mode of non-uniformity.

Typically, when applying FEM to large electrical machines, symmetry is exploited using periodic boundary conditions (PBC). However, in this case the entire cross section of the machine had to be simulated. Furthermore, an entire 360-degree angular displacement of the rotor had to be captured to obtain the full transient behaviour of

the system. The NREL 15 MW design has a periodicity of 40, therefore 40 times the domain size and number of timesteps ($N_{\Delta t}$) were required compared to a symmetric case with the same spatial and temporal resolution. Magnetostatic simulations are sufficient to capture the frequency and wavenumber of the radial Maxwell stress waves in the air-gap, the computational workload is therefore 'perfectly parallelizable' in that each simulation can be performed independently: this allows for a manageable wall clock time assuming sufficient computational resources are available, The University of Edinburgh's 'Eddie Mark 3' compute cluster was utilised for this work.

A sliding mesh was used with a circular rotor-stator interface directly in the middle of the air-gap, this approach reduces computational expense as it avoids the generation of a unique mesh for each timestep. The mesh consisted of just over 422,000 elements giving 10,000 spatial samples (N_θ) around the circumference of the air-gap with circumferential resolution (Δl_θ) of ~3.2 mm in the centre of the air-gap. 3600 timesteps ($N_{\Delta t}$) were run with the rotor angular displacement stepped by 0.1 degrees for each timestep, this equates to a timestep length (Δt) of ~22 ms assuming the machine is operating at its rated-speed of 0.792 rad/s.

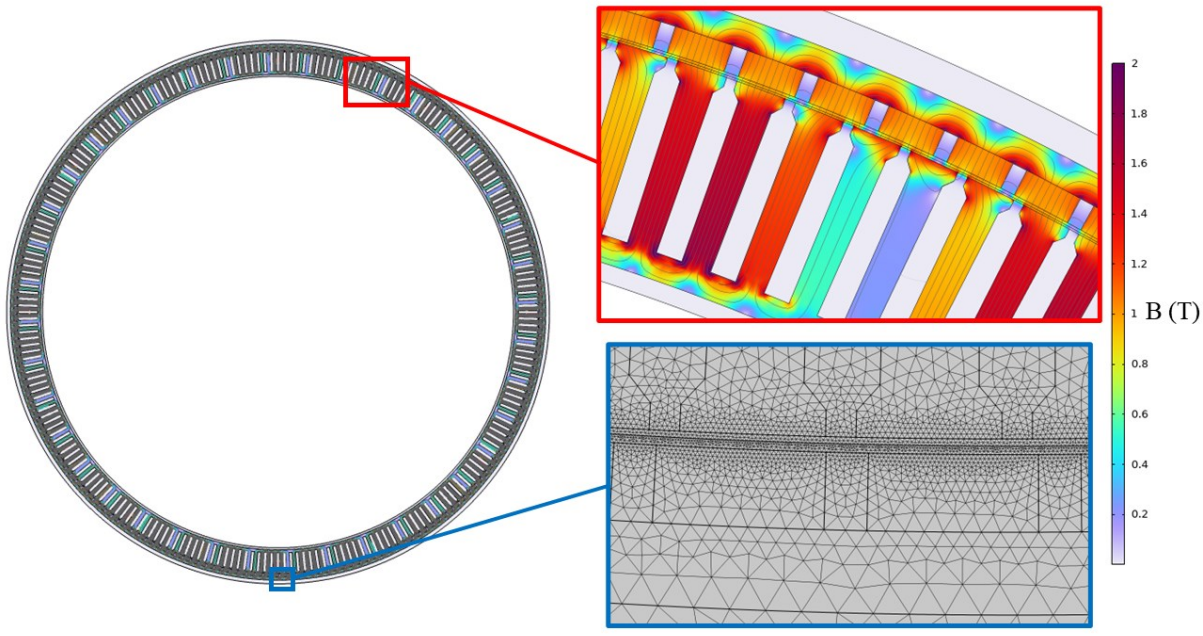

Figure 4.16: Flux density plot of entire simulation domain (LHS) with a close-up (top-right), and a close-up of the mesh (bottom-right).

The 2D radial Maxwell stress was calculated for each timestep at a circular boundary that was stationary with respect to the stator, it had a diameter (D_σ) equal to 5.079 m locating it 1 mm from the sliding mesh boundary to reduce numerical noise.

MATLAB was used to process the 3600 timesteps of circumferential radial Maxwell stress distribution with a 2D fast Fourier transform (FFT) giving wavenumbers and temporal frequencies of the constituent harmonics. The wavenumber and frequency resolution can be calculated as follows:

$$\Delta\mathcal{K} = \frac{\pi D_\sigma}{N_\theta \Delta l_\theta} = 1\,, \qquad \Delta f = \frac{1}{N_{\Delta t}\Delta t} = 0.126\ Hz \tag{4.60, 4.61}$$

where D_σ is the diameter of the circular boundary on which the radial stress was computed. A spline interpolation of the radial stress distribution was made for each timestep such that equally spaced spatial sampling could be provided for the 2D FFT. In Figure 4.17 a section of the 2D FFT spectrum obtained from a FEM simulation with rotor dissymmetry of order $p = 12, 15$ with a peak amplitude of $\hat{\delta}_p = 1.5, 1$ mm respectively, stator dissymmetry $q = 7, 10$ with a peak amplitude of $\hat{\delta}_q = 1.5, 1$ mm respectively, φ_{rp} and φ_{sq} of $\pi/7$ is compared against the analytical model. The wavenumbers and frequencies obtained from each term of the analytical model are overlaid using various symbols. There is agreement on the wavenumber and frequency of each radial stress harmonic.

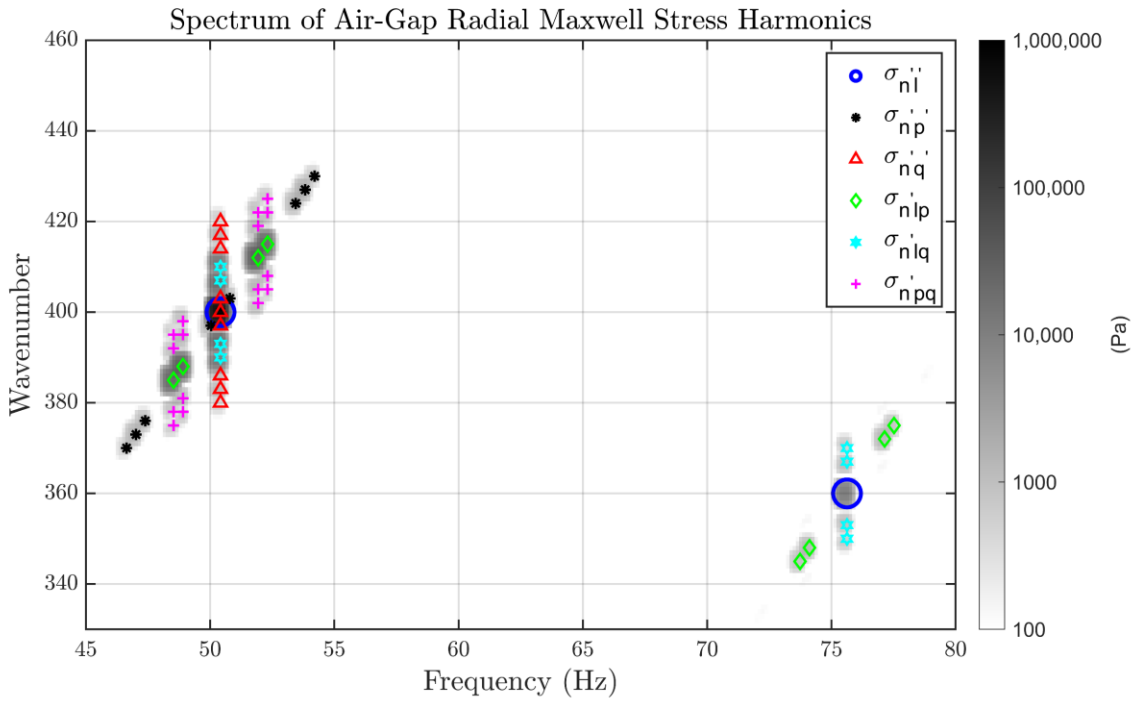

Figure 4.17: 2D FFT spectrum of finite element method (FEM) simulation results overlaid with corresponding results from the analytical model, the harmonic sources are: MMF and stator slots ($\sigma_{n'l'}$), MMF and rotor dissymmetry ($\sigma_{n'p'}$), MMF and stator dissymmetry ($\sigma_{n'q'}$), stator slot and rotor dissymmetry intermodulation ($\sigma_{n'lp}$), stator slot and stator dissymmetry intermodulation ($\sigma_{n'lq}$), and rotor dissymmetry and stator dissymmetry intermodulation ($\sigma_{n'pq}$).

4.5.3 Discussion

To illustrate the potential extent of additional air-gap radial Maxwell stress harmonics due to air-gap non-uniformity a sketch can be constructed using the relationships obtained from the analytical model. In Figure 4.18 such a sketch is provided for rated-speed of the IEA 15 MW machine. The range of p and q is limited to N_{PP} (100) as it is assumed that the analytical model will break down once the wavelength of permeance variations are of a similar scale to the pitch of a pole-pair. It is important to consider that due to the variable speed operation of the wind turbine the rotational speed varies from approximately half- up to rated-speed: resulting in a large range of possible frequencies for each radial stress harmonic.

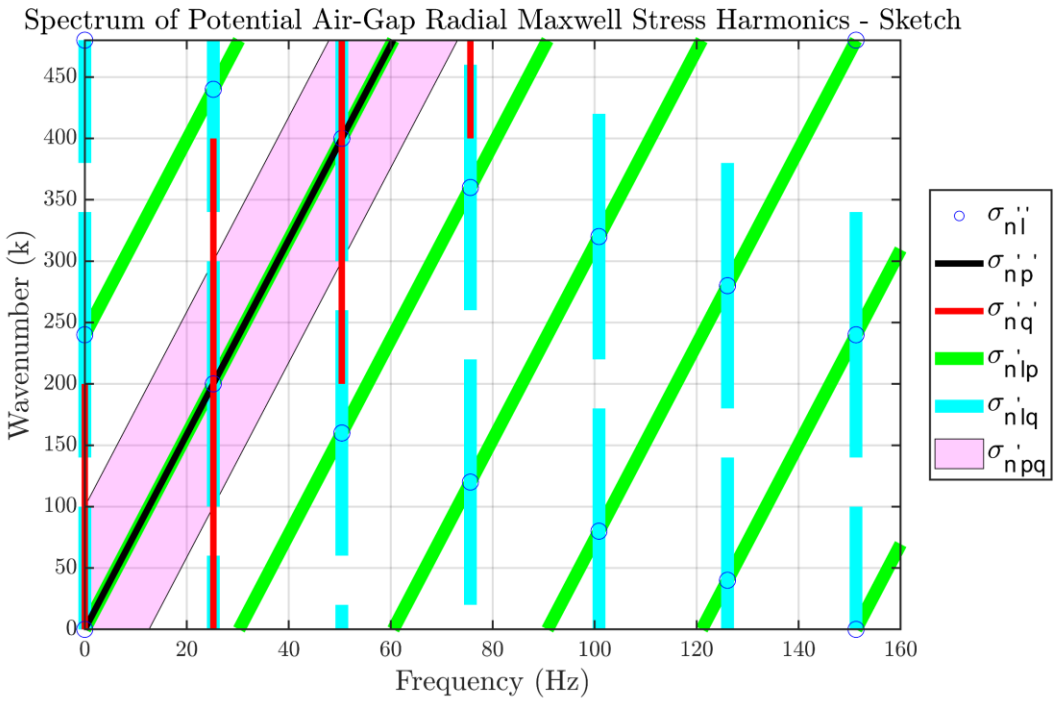

Figure 4.18: Sketch of potential air-gap radial stress harmonics assuming a non-uniform air-gap with p and q ranging from 1 to 100, the harmonic sources are: MMF and stator slots ($\sigma_{n'l'}$), MMF and rotor dissymmetry ($\sigma_{n'p'}$), MMF and stator dissymmetry ($\sigma_{n'q'}$), stator slot and rotor dissymmetry intermodulation ($\sigma_{n'lp}$), stator slot and stator dissymmetry intermodulation ($\sigma_{n'lq}$), and rotor dissymmetry and stator dissymmetry intermodulation ($\sigma_{n'pq}$).

The harmonics $\sigma_{n'p'}$ and $\sigma_{n'q'}$ deviate the most from their corresponding baseline values (when p' and $q' = 0$), however their amplitudes are relatively low. The $\sigma_{n'pq}$ harmonics have the potential to achieve a wide variety of frequencies and wavenumbers. The lS_s term present in the $\sigma_{n'lp}$ and $\sigma_{n'lq}$ harmonics also give them the potential for a wide range of frequencies and wavenumbers.

If the wavenumber and frequency of a radial stress harmonic are close to those of a generator's vibrational mode, then resonance can occur. The dynamic deflection amplitude (Y_d) is larger than the static deflection amplitude (Y_s) according to an amplification factor (C_Y) which reaches a maximum when the frequency of the radial stress harmonic and the generator's vibrational mode is the same [102]:

$$Y_d = C_Y Y_s \tag{4.62}$$

Mechanical deflections are therefore significantly enhanced by resonance.

Stress harmonics with low wavenumber are generally considered to be the most impactful since the static deflection amplitude tends to decrease with increasing wavenumber as discussed in Section 4.4.3.

Multi-megawatt scale DD WTGs have a very large number of poles, on the order of ~50-200. This means that most of the air-gap radial Maxwell stress harmonics have a large wavenumber compared to smaller high-speed machines with pole counts starting from 2. For a symmetrical case, the lowest non-zero wavenumber air-gap stress harmonic can be found by calculating the greatest common divisor (GCD) of the number of stator slots and poles. In DD WTGs the GCD can be relatively large, e.g. the IEA 15 MW machine has a value of 40 [13]. In this section, it has been demonstrated that high-order air-gap non-uniformity can introduce air-gap radial Maxwell stress harmonics with lower non-zero wavenumbers than the GCD with a variety of frequencies.

For small machines it is commonly assumed that the rotor structure and the end caps are sufficiently stiff such that any vibration is negligible, only the stator is assumed to experience appreciable vibration due to its hollow cylindrical structure. In a DD WTG the structure of both the rotor and stator takes a hollow cylindrical form so the vibration of both must be considered. Sampling of the radial Maxwell stress harmonics by the stator teeth adds complication to vibration analysis of the stator: if the wavenumber of the air-gap radial stress harmonic is greater than $N_{\mathrm{slot}}/2$ (120 for the IEA 15 MW machine) then the wavenumber of stress transmitted to the stator structure will be modulated to a value less than or equal to $N_{\mathrm{slot}}/2$ [109]. In the case of the IEA 15 MW machine, there are many radial stress harmonics with wavenumber greater than $N_{\mathrm{slot}}/2$ that would be modulated to a lower wavenumber by the stator teeth. Interestingly, since there are no rotor teeth in surface mounted PM DD WTGs the rotor may be less susceptible to vibration than the stator due to the lack of radial Maxwell stress harmonic wavenumber modulation.

DD WTGs are stiffly connected to the wind turbine nacelle—vibration can be readily transmitted to other wind turbine components. Non-uniformity of the air-gap can also result in unbalanced magnetic pull (UMP), cogging torque, and torque ripple harmonics that can be transmitted by the shaft [90]. A designer must therefore consider

more than just stator vibration as is typical for a conventional electrical machine vibration analysis.

4.6 Conclusion

The PM material requirement of DD PM WTGs is very sensitive to the air-gap clearance. Despite the importance of this parameter its appropriate specification is poorly understood. As highlighted in the introduction, simplified rules-of-thumb for air-gap clearance specification are used throughout literature concerned with DD WTG design. The air-gap clearance is commonly assumed to be 1/1000th of the air-gap diameter, and the allowable air-gap deformation is limited to ~10-20% of the air-gap clearance. A better understanding of air-gap clearance dimensioning and its implications would be very beneficial for advancing DD WTG design.

In Section 4.2 it was demonstrated that the air-gap clearance of the example 15 MW surface mounted PM DD WTG can be reduced significantly without a considerable increase in magnetising inductance, PM demagnetisation risk, or armature reaction. It was highlighted that performance issues stemming from air-gap non-uniformity are the main constraint in terms of electromagnetic performance.

In Section 4.3 the various sources of air-gap non-uniformity were summarised, and it was highlighted that different sources of air-gap deformation can result in various spatial distributions of air-gap non-uniformity which can be characterised by a mode number ($\mathcal{M}$). The mode number describes how the air-gap clearance varies around the periphery of the WTG air-gap.

In Section 4.4 the concept of air-gap stability and magnetic stiffness was discussed. It was highlighted that the structural stiffness of the WTG must exceed the magnetic stiffness according to a stiffness factor (C_K) since air-gap deformation due to manufacturing/assembly tolerances, external loads, thermal expansion, and self-weight does not result in a structural elastic force that counteracts the magnetic force. The structural stiffness must therefore exceed the magnetic stiffness by such an amount that a force equilibrium can be achieved due to secondary deformation of the WTG structure while limiting the extent of the total air-gap deformation such that the WTG performance is not compromised.

The influence of the air-gap deformation mode number ($\mathcal{M}$) on air-gap stability was discussed, based on a simplified rim model and a set of structural finite elment analysis (FEA) simulations it was demonstrated that the effective stiffness of the WTG structure depends on the value of $\mathcal{M}$. It was recommended that for improved modelling of air-gap stability, the relative impact of different sources of air-gap deformation on air-gap stability should be considered.

In Section 4.5 an analytical model for predicting the air-gap radial stress harmonic wavenumbers and frequencies associated with high-order air-gap non-uniformity was introduced and validated through full-scale 2D FEM analysis of the IEA 15 MW reference WTG. It was demonstrated that high-order air-gap non-uniformity can result in additional air-gap radial Maxwell stress harmonics with low wavenumbers and a range of frequencies which increase the risk of vibration.

In conclusion, it has been demonstrated that the spatial distribution of air-gap deformation, i.e. the air-gap deformation mode number ($\mathcal{M}$), has a significant impact on the extent of secondary deformation and the risk of vibration due to the resulting radial Maxwell stress within the air-gap region. As discussed in Section 4.4.5 it is recommended that instead of applying a single limit of ~10-20% for the peak air-gap deformation, different limits should be specified for each source of air-gap deformation according to the associated value of $\mathcal{M}$. For example, it may be beneficial to specify a more relaxed deformation limit for thermal expansion ($\mathcal{M} = 0$) in comparison to the displacement of the shaft due to external loads ($\mathcal{M} = 1$).

Additionally, as discussed in Section 4.4.2, designers should impose specific limits for both the initial air-gap deformation and for the maximum allowable air-gap deformation that occurs due to secondary structural deflection. The required mechanical stiffness of the DD WTG structure is linked to these two quantities by the stiffness factor (C_K) defined in Eq. (4.31).

Chapter 5: Introduction to Ferrofluid-Gaps for Electrical Machines

As highlighted in Chapter 2, the permanent magnet (PM) material requirements of direct-drive (DD) wind turbine generators (WTGs) constitute a large proportion of their total cost. Conventionally, the PM material requirements are minimised by making the air-gap clearance as small as possible, however as detailed in Chapter 4 there are several factors that limit the reduction of the air-gap clearance. In the following chapters an unconventional approach for reducing the air-gap reluctance is investigated in which the air-gap region is flooded with magnetically permeable ferrofluid, making it a 'ferrofluid-gap'.

Ferrofluid, a colloidal suspension of single-domain magnetic nanoparticles, is a unique material which is especially suited for this application. In the following section a brief introduction to the ferrofluid-gap concept is provided. In Section 5.2 an overview of ferrofluid is provided with a focus towards its use in the air-gap region of electrical machines. In Section 5.3, it is explained how the magnetic and mechanical behaviour of a ferrofluid-gap can be modelled according to theoretical predictions. In Section 5.4 previous work investigating the use of ferrofluid in electrical machines is reviewed and several opportunities for further research of the ferrofluid-gap concept are highlighted, motivating the following chapters of this thesis.

5.1 Introduction to the Ferrofluid-Gap Concept

In the following section the concept of ferrofluid-gaps for PM DD WTGs is introduced.

5.1.1 Potential for Permanent Magnet Mass Reduction

Based on a 1D magnetic circuit analysis it can be demonstrated that a small increase in the relative permeability of the air-gap region $\mu_{r,\mathrm{g}}$ may allow for a significant reduction in PM material requirements. A schematic for a 1D magnetic circuit of a pole pair is provided in Figure 5.1. The PM magnetomotive force can be given by:

$$\mathcal{F}_{\mathrm{PM}} = \frac{B_{\mathrm{rem}} h_{\mathrm{PM}}}{\mu_0 \mu_{r,\mathrm{PM}}} \tag{5.1}$$

the PM reluctance by:

$$\mathcal{R}_{\mathrm{PM}} = \frac{h_{\mathrm{PM}}}{\mu_0 \mu_{r,\mathrm{PM}} A_{\mathrm{PM}}} \tag{5.2}$$

and the air-gap region reluctance by:

$$\mathcal{R}_{\mathrm{g}} = \frac{h_{\mathrm{g}}}{\mu_0 \mu_{r,\mathrm{g}} A_{\mathrm{PM}}} \tag{5.3}$$

where B_{rem} is the remanent flux density of the PM, h_{PM} is the height of the PM, μ_0 is the permeability of free space, $\mu_{r,\mathrm{PM}}$ is the relative permeability of the PM, A_{PM} is the cross-sectional area of the PM normal to the magnetic flux, h_{g} is the clearance of the air-gap region, and $\mu_{r,\mathrm{g}}$ is the relative permeability of the air-gap region.

The magnetic flux can be calculated as:

$$\Phi = \frac{2\mathcal{F}_{\mathrm{PM}}}{2\mathcal{R}_{\mathrm{PM}} + 2\mathcal{R}_{\mathrm{g}}} \tag{5.4}$$

The magnetic flux density above the PMs can be calculated as:

$$B_{\mathrm{g}} = \frac{\Phi}{A_{\mathrm{PM}}} = \frac{B_{\mathrm{rem}} h_{\mathrm{PM}}}{\frac{\mu_{r,\mathrm{PM}} h_{\mathrm{g}}}{\mu_{r,\mathrm{g}}} + h_{\mathrm{PM}}} \tag{5.5}$$

Rearranging for h_{PM} we arrive at:

$$h_{\mathrm{PM}} = \frac{\mu_{r,\mathrm{PM}} h_{\mathrm{g}} B_{\mathrm{g}}}{\mu_{r,\mathrm{g}} \left(B_{\mathrm{rem}} - B_{\mathrm{g}}\right)} \tag{5.6}$$

Assuming constant values of $\mu_{r,\mathrm{PM}}$, h_{g}, B_{g}, and B_{rem} it can be shown that h_{PM} is inversely proportional to the relative permeability of the air-gap region:

$$h_{\mathrm{PM}} \propto \frac{1}{\mu_{r,\mathrm{g}}} \tag{5.7}$$

Increasing the relative permeability of the air-gap region has a compounding effect on the total magnetic circuit reluctance. Reducing $\mathcal{R}_{\mathrm{g}}$ allows for a reduction in h_{PM}, a reduction in h_{PM} results in a reduction in $\mathcal{R}_{\mathrm{PM}}$, therefore a small increase in $\mu_{r,\mathrm{g}}$ can allow for a significant reduction in the total magnetic circuit reluctance and consequently the amount of PM material required.

This 1D magnetic circuit analysis does not consider the magnetic reluctance of the electrical steel components, inter-pole magnetic leakage, or the Carter factor. However, a detailed magnetic analysis of the ferrofluid-gap concept is provided in Chapter 8, Section 8.2.

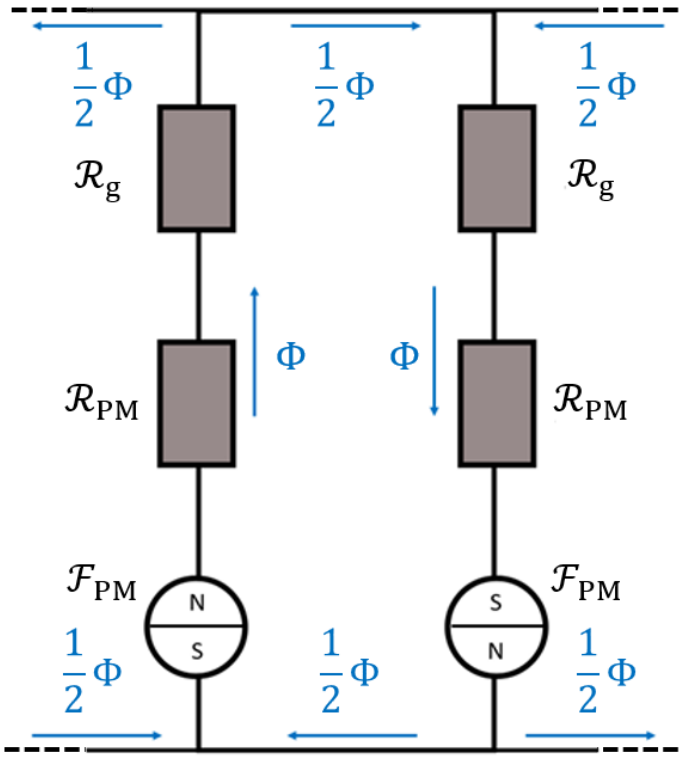

Figure 5.1: Schematic of a 1D magnetic circuit for a pole pair.

5.1.2 Potential for Acceptable Efficiency Loss

Introducing a fluid into the air-gap region will reduce the efficiency due to the increased losses resulting from the fluid drag, i.e. the windage losses will be increased. However, DD WTGs differ from conventional electrical machines in that they have very low rotational speeds and large air-gap clearances, this results in a relatively minor loss in efficiency due to drag in the air-gap in comparison to smaller scale and faster rotating machines.

For a first approximation of efficiency loss the flow in the air-gap region of a DD WTG can be approximated as a laminar inner-rotor thin-gap Taylor-Couette (TC) flow, where the power loss due to viscous drag can be calculated as [110]:

$$P_{\text{drag}} = 4\pi\eta_{\text{FF}}\omega^2 l_c \left(\frac{r_\text{r}^2 r_\text{s}^2}{r_\text{s}^2 - r_\text{r}^2}\right) \tag{5.8}$$

where η_{FF} is the dynamic viscosity of the ferrofluid, ω is the angular velocity of the DD WTG, l_c is the core length, r_{r} is the rotor radius, and r_{s} is the stator radius.

Neglecting other generator losses, the loss in generator efficiency can be approximated as:

$$\Delta\zeta_{\mathrm{gen}} = \zeta_{\mathrm{gen,ideal}} - \zeta_{\mathrm{drag}} = \frac{P_{\mathrm{drag}}}{P_{\mathrm{shaft}}} \tag{5.9}$$

where $\zeta_{\mathrm{gen,ideal}}$ is an idealised WTG efficiency equal to 1, and ζ_{drag} is the WTG efficiency with laminar viscous drag acting on the rotor.

The geometry of DD WTGs can be estimated according to the sizing equations presented in Section 2.1.3. For comparison, the geometry of WTGs driven by a gearbox is approximated by including a gear ratio in the equation for WTG angular velocity:

$$\omega = \frac{i_{\mathrm{GR}} \Gamma_{\mathrm{TSR}} v_{\mathrm{wind,rated}}}{r_{\mathrm{swept}}} \tag{5.10}$$

where i_{GR} the gear ratio (equal to 1 for DD WTGs), Γ_{TSR} is the tip-speed ratio, $v_{\mathrm{wind,rated}}$ is the rated wind speed, and r_{swept} is the wind turbine swept radius.

An estimate of $\Delta\zeta_{\mathrm{gen}}$ at rated power is presented in Figure 5.2 for various values of i_{GR} assuming a moderate ferrofluid viscosity of $\eta_{\mathrm{FF}} = 0.1\ \mathrm{Pa.s}$. Although the assumption of laminar flow underestimates viscous drag for states of turbulent flow, it is clear the DD powertrain experiences a significantly smaller reduction in efficiency compared to geared generators (which appear to suffer prohibitively large losses). In Chapter 8, Section 8.3 a more detailed analysis of ferrofluid-gap drag is presented in which turbulence and the influence of the magnetic field on ferrofluid viscosity are considered.

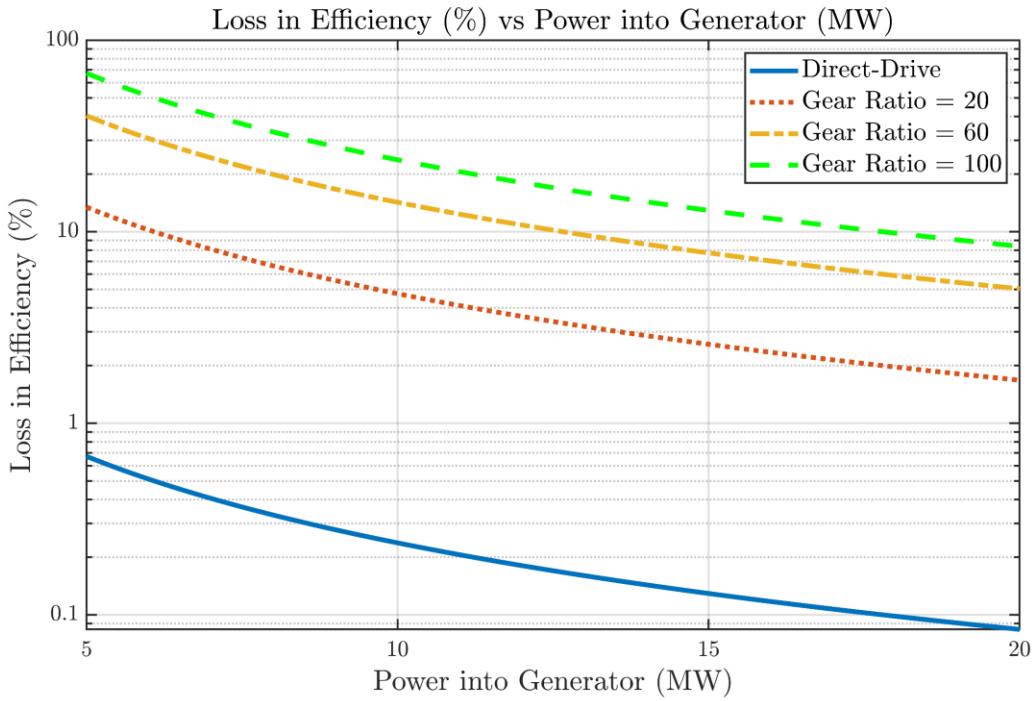

Figure 5.2: Estimate for the loss in generator efficiency ($\Delta\zeta_{\mathrm{gen}}$) due to fluid flow within the air-gap region for a range of rated input powers (P_{shaft}) and gear ratios (i_{GR}) assuming laminar flow and a dynamic viscosity (η_{FF}) of 0.1 Pa.s.

5.2 Overview of Ferrofluid

In the following section, an overview of ferrofluid is provided, detailing the key aspects of its behaviour and explaining why its unique characteristics make it particularly suitable for use in electrical machines.

5.2.1 Colloidal Suspensions

Ferrofluid is a colloidal suspension of single-domain magnetic nanoparticles.

A colloidal suspension consists of insoluble particles with diameters ranging from ~1-1000 nm (named colloids) which are dispersed within a carrier fluid. Common examples of colloidal suspensions include blood, milk, and paint. In the case of ferrofluid, the colloids are iron oxide nanoparticles with a magnetic diameter typically ranging from ~5-15 nm [15].

The bulk rheology of a colloidal suspension is governed by the complex microscale dynamics of the colloids [111]. Ferrofluid colloids are of a similar scale to the carrier fluid molecules, as depicted in Figure 5.3, therefore they experience stochastic Brownian motion. However, due to the extremely small length- and time-scales involved in colloidal dynamics, and the vast number of colloids that interact within a

ferrofluid sample, it is valid to consider ferrofluid as a continuum with bulk fluid properties when analysing its behaviour at length scales relevant to electrical machines. For example, a millilitre of ferrofluid may contain on the order of 10^{17} colloids [112]. Essentially, the complex behaviour at the nanoscale averages out to consistent behaviour at larger length- and time-scales.

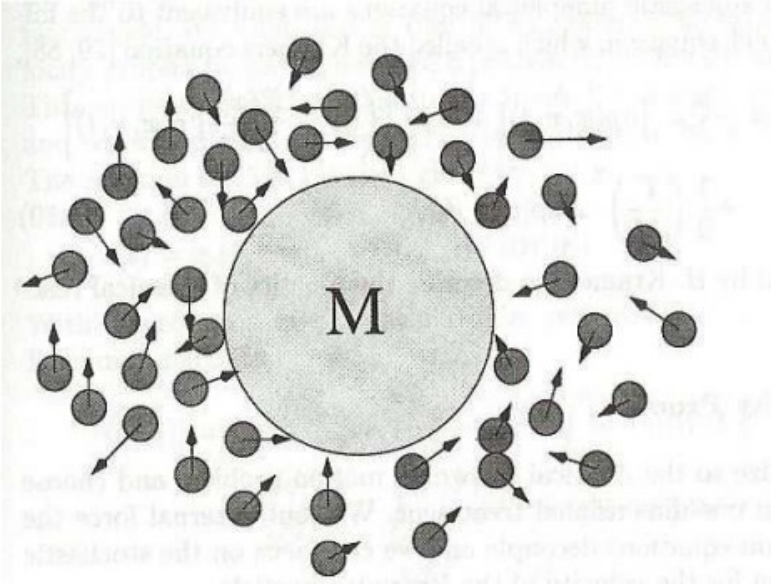

Figure 5.3: A ferrofluid colloid surrounded by carrier fluid molecules with random velocities [113].

5.2.2 Colloidal Stability

A repulsive inter-colloidal force is required to maintain the stability of a colloidal suspension. If the attractive interaction energy between colloids exceeds the thermal energy present in the system they will tend to clump together, this is often referred to as agglomeration or aggregation [15].

Ferrofluid colloids can be stabilised via the introduction of an electrical double layer which provides an inter-colloidal electrostatic repulsive force. Another method is to introduce steric repulsion between colloids through the addition of a surfactant coating: a physical barrier is added to the colloids that prevents them from getting too close, this can be thought of as the introduction of a spring force between colloids at close separations.

The stabilisation mechanism determines which carrier fluids are compatible with the colloids, steric repulsion requires a non-polar carrier fluid such as oil while electrostatic

repulsion requires a polar carrier fluid such as water. Figure 5.4 depicts both methods of stabilisation.

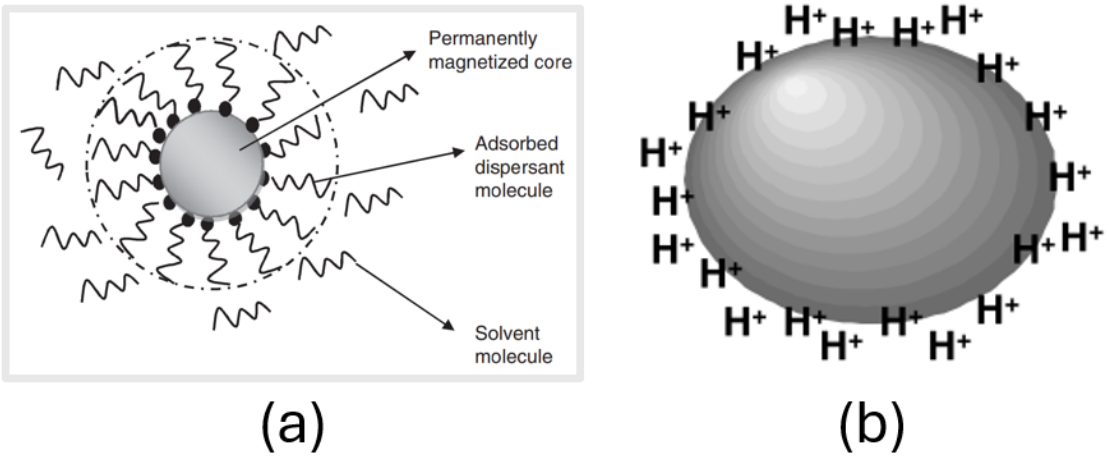

Figure 5.4: (a) Colloid with a surfactant outer layer [114]. (b) Colloid with an electrostatic outer layer [15].

5.2.3 Ferrofluid Nanoparticles

In a ferrofluid the colloids are single-domain magnetic particles, typically iron oxide nanoparticles (IONPs) with a magnetic diameter ranging from ~5-15 nm [114].

Ferrofluid nanoparticles are of such a small scale that they can only host a single magnetic domain. In the presence of an external magnetic field the magnetic dipoles of the colloids will align resulting in a net magnetisation of the ferrofluid. In this scenario the attractive inter-colloidal magnetic dipole-dipole interactions will influence the colloidal stability. The following equation gives the ratio between the dipole-dipole interaction and thermal energy [115]:

$$\Gamma_{\mathrm{int}} = \frac{\pi \mu_0 \phi_{\mathrm{M}} D_{\mathrm{M}}^3 M_s^2}{6 \hbar_B T} \tag{5.11}$$

where ϕ_{M} is the ferrofluid magnetic volume fraction, D_{M} is the magnetic diameter of the colloid, M_s is the saturation magnetisation of the ferrofluid, $\hbar_B$ is the Boltzmann constant, and T the temperature in Kelvin.

The magnetic diameter of ferrofluid colloids is sufficiently small such that $\Gamma_{int} < 1$, this means that the suspension remains dispersed and stable when a strong external magnetic field is applied.

Ferrofluid is often confused with magnetorheological fluid (MRF), the key difference being the size of the magnetic particles. MRF particles are much larger with a typical magnetic diameter of ~1-10 μm and therefore $\Gamma_{\mathrm{int}} \gg 1$, this results in intense particle clustering when a magnetic field is applied [116]. This leads to very strong non-Newtonian behaviour and up to 1000-fold increases in viscosity compared to when no magnetic field is present. In some cases, a phase change from liquid to solid is observed in the presence of a magnetic field. The particles are also large enough to host multiple magnetic domains as depicted in Figure 5.5.

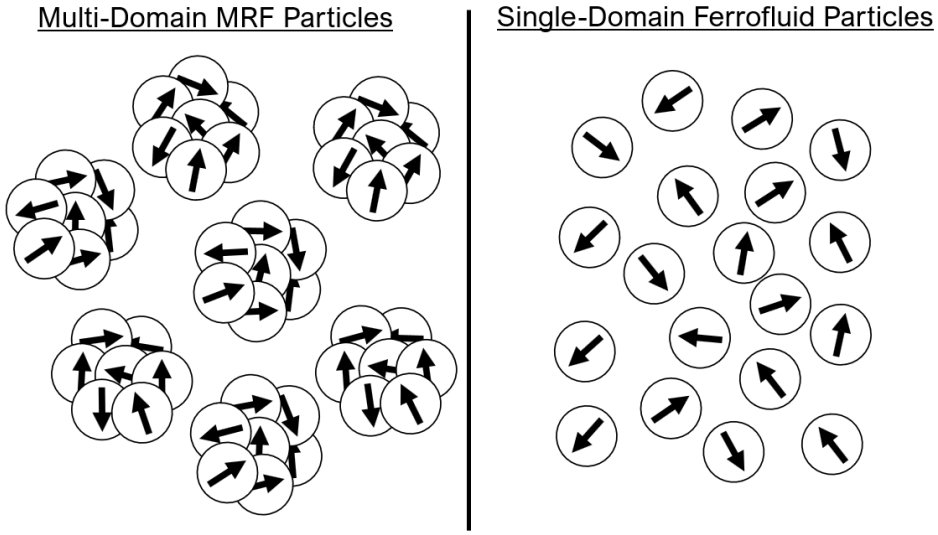

Figure 5.5: Depiction of multi-domain magnetorheological fluid (MRF) particles and single-domain ferrofluid particles.

Due to partial surface oxidation IONPs have an outer layer of maghemite (y-Fe2O3) which has a lower magnetic susceptibility compared to their magnetite (Fe3O4) core. As particle size decreases the surface layer occupies an increasing portion of the total nanoparticle volume: lowering the net spontaneous magnetisation of the IONPs [117]–[121]. There is therefore a trade-off between the achievable saturation magnetisation of the ferrofluid and its colloidal stability which must be balanced, resulting in colloid magnetic diameters that typically range between ~5-15 nm.

5.2.4 Magnetic and Hydrodynamic Volume Fraction

Volume fraction is a key metric in which the composition of a colloidal suspension is characterised based on the proportion of space occupied by a constituent material in relation to the total volume of the mixture. In ferrofluid there are two types of volume fraction to consider: the magnetic (ϕ_{M}) and the hydrodynamic volume fraction (ϕ_{H}).

The magnetic volume fraction is the volume of magnetic material in the ferrofluid divided by the total volume of the ferrofluid. As the magnetic volume fraction of the ferrofluid is increased, the saturation magnetisation increases.

The hydrodynamic volume fraction is the volume of both the magnetic material and the stabilising layer divided by the total volume of the ferrofluid. If the thickness of the stabilising layer is known, then the hydrodynamic volume fraction can be estimated according to the magnetic volume fraction.

Assuming spherical colloids, the magnetic volume of a single colloid is:

$$V_{\mathrm{M}} = \frac{4}{3}\pi r_{\mathrm{M}}^3 \tag{5.12}$$

where r_{M} is the radius of the colloid magnetic material.

The hydrodynamic volume of a single colloid can be approximated as:

$$V_{\mathrm{H}} = \frac{4}{3}\pi (r_{\mathrm{M}} + t_{\mathrm{stab}})^3 \tag{5.13}$$

where t_{stab} is the thickness of the stabilising layer.

The hydrodynamic volume fraction is therefore:

$$\phi_{\mathrm{H}} = \frac{V_{\mathrm{H}}}{V_{\mathrm{M}}}\phi_{\mathrm{M}} \tag{5.14}$$

Susan-Resiga *et al.* demonstrate that ferrofluid hydrodynamic volume fractions of ~0.65 can be achieved, which corresponds to the upper limit for random packing of spheres [122], [123]. For oil based ferrofluids, the stabilising surfactant layer is ~2 nm thick, resulting in a $V_{\mathrm{H}}/V_{\mathrm{M}}$ ratio of ~2.74 [124], [125]. The magnetic volume fraction of oil based ferrofluid is therefore limited to ~0.24, although such high values are seldom reported.

5.2.5 Ferrofluid Viscosity and Density

As the magnetic and hydrodynamic volume fraction is increased, the viscosity of the ferrofluid will increase in comparison to the carrier fluid. The viscosity of colloidal suspensions can be characterised by a relative viscosity η_{rel} which is the ratio of the suspension viscosity η_{sus} compared to the carrier fluid without colloids η_0:

$$\eta_{\mathrm{rel}} = \frac{\eta_{\mathrm{sus}}}{\eta_0} \tag{5.15}$$

With increasing volume fraction, the relative viscosity increases non-linearly, as demonstrated in Figure 5.6 [126]:

$$\eta_{\mathrm{rel}} = \left\{ \exp\left(\frac{2.5\phi_{\mathrm{H}}}{1-\phi_{\mathrm{H}}}\right) + \frac{A_{\mathrm{vis}}\phi_{\mathrm{H}}^2}{1 - A_{\mathrm{vis}}\phi_{\mathrm{H}}^2\phi_{\mathrm{M}}} \right\} \tag{5.16}$$

where A_{vis} is a parameter from Chow's model for the viscosity of concentrated dispersions, the theoretical value of 4.67 agrees well with the empirical data [127].

The density of a ferrofluid will also increase according to the magnetic volume fraction, it can be estimated according to a rule of mixtures where the relative proportions of the magnetic material and the carrier fluid are considered:

$$\rho_{\mathrm{FF}} = (1-\phi_{\mathrm{M}})\rho_0 + \phi_{\mathrm{M}}\rho_{\mathrm{M}} \tag{5.17}$$

where ρ_0 is the density of the carrier fluid, and ρ_{M} is the density of the magnetic nanoparticles. The stabilising layer is neglected in this estimation because it does not form a distinct solid phase. Instead, the surfactant molecules create a diffuse interfacial region that is partially occupied by carrier fluid molecules. As a result, the effective density is similar to that of the carrier fluid.

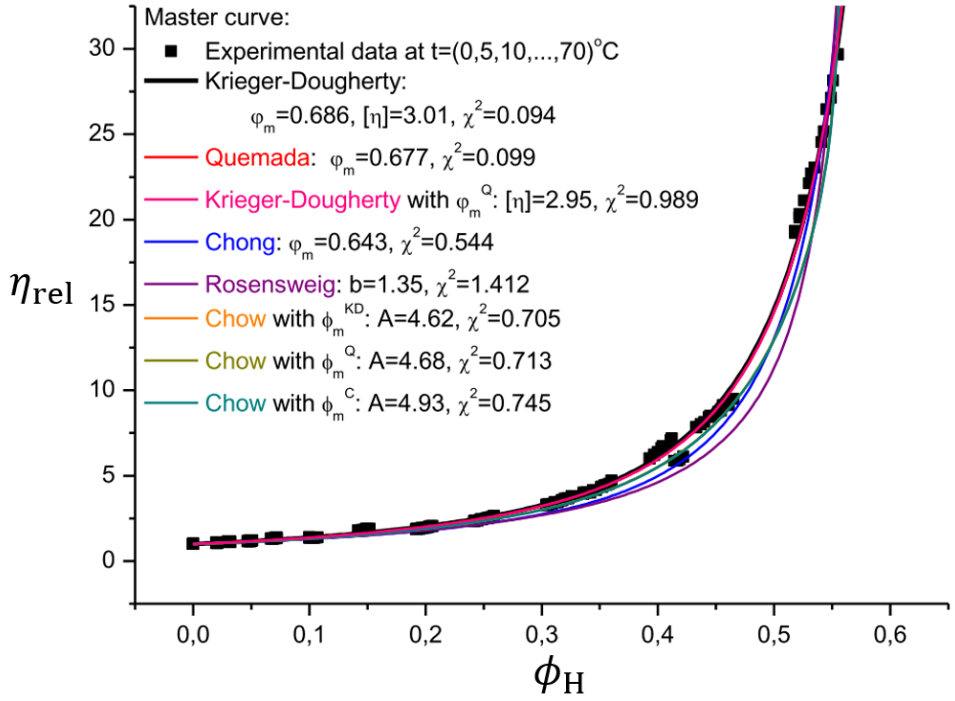

Figure 5.6: Ferrofluid relative viscosity (η_{rel}) as a function of hydrodynamic volume fraction (ϕ_{H}) [126].

5.2.6 Ferrofluid Thermal Properties

The thermal properties of ferrofluid also depend on the magnetic volume fraction. The ferrofluid thermal conductivity can be approximated by [128]:

$$k_{\mathrm{FF}} = \frac{1 + 2\beta_k \phi_{\mathrm{M}}}{1 - \beta_k \phi_{\mathrm{M}}} k_0 \tag{5.18}$$

$$\beta_k = \frac{k_{\mathrm{M}} - k_0}{k_{\mathrm{M}} + 2k_0} \tag{5.19}$$

Where k_0 is the thermal conductivity of the carrier fluid, and k_{M} is the thermal conductivity of the colloid magnetic material. This expression neglects the effects of particle clustering and chain formation, which can enhance heat transfer. However, it provides a reasonable approximation for ferrofluids under shear in which chain formation is suppressed, such as in a ferrofluid-gap.

Similar to the calculation of density, the specific heat capacity can be approximated by a rule of mixtures [129]:

$$c_{p,\mathrm{FF}} = \frac{(1 - \phi_{\mathrm{M}})\rho_0 c_{p,0} + \phi_{\mathrm{M}} \rho_{\mathrm{M}} c_{p,\mathrm{M}}}{(1 - \phi_{\mathrm{M}})\rho_0 + \phi_{\mathrm{M}} \rho_{\mathrm{M}}} \tag{5.20}$$

where $c_{p,0}$ is the specific heat capacity of the carrier fluid, and $c_{p,\mathrm{M}}$ is the specific heat capacity of the magnetic nanoparticles.

5.2.7 Particle Size and Shape Distribution

For simplicity it is common to assume that a ferrofluid is monodisperse with spherical colloids, i.e. each colloid is of the same size and has an idealised spherical geometry. In practice, ferrofluids are polydisperse and the colloid geometry will vary within a sample, resulting in variations in behaviour between samples with the same magnetic and/or hydrodynamic volume fractions. It is therefore important to empirically characterise a specific sample if precise material properties are required.

In Figure 5.7, a transmission electron microscopy (TEM) image is provided of ferrofluid nanoparticles synthesised in-house according to the protocol provided in Appendix E, and those produced by Botez *et al.* [130]. For the in-house synthesised ferrofluid particles a large variation in particle size and shape is observed, whereas the particles

produced by Botez *et al.* have a consistent spherical shape and size which is a marker of high-quality ferrofluid synthesis.

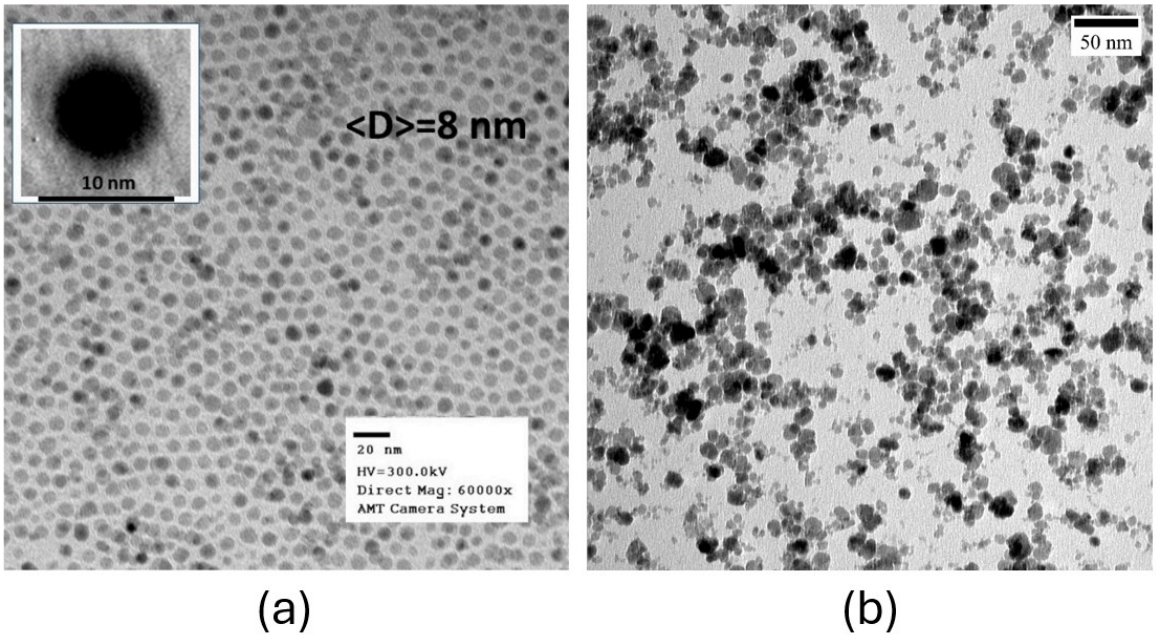

Figure 5.7: Transmission electron microscopy (TEM) image of ferrofluid nanoparticles synthesised by Botez *et al.* (a) [130], and in-house according to the protocol provided in Appendix E (b).

5.2.8 Néel and Brownian Relaxation

When an external magnetic field is applied to a ferrofluid, the magnetic dipoles of the colloidal particles tend to align with the field, resulting in a magnetisation of the ferrofluid. The timescale of this alignment is governed by two magnetic relaxation mechanisms: Néel and Brownian relaxation. The volume of the ferrofluid colloids determines the timescale and mechanism of magnetic relaxation [15].

If the colloid volume is relatively large Brownian relaxation dominates: the entire colloid will rotate so that its magnetic moment is aligned with the external field, the timescale is given by:

$$t_B = \frac{3V_{\mathrm{H}}\eta_0}{k_B T} \tag{5.21}$$

where V_{H} is the hydrodynamic volume of a nanoparticle, η_0 is the dynamic viscosity of the carrier fluid, k_B is the Boltzmann constant, and T the temperature in Kelvin.

If the colloid volume is relatively small Néel relaxation dominates: the magnetic moment of the colloid can change orientation independent of the particle orientation, the timescale is given by:

$$t_N = \frac{1}{f_N} exp\left(\frac{KV_M}{k_B T}\right) \tag{5.22}$$

where f_N is the Larmor frequency (approximately 10^9 Hz), and K is the anisotropy constant of the colloid magnetic material (approximately 1.1×10^4 J/m^3).

Both mechanisms can be incorporated into an effective relaxation time:

$$t_{\text{eff}} = \frac{t_N t_B}{(t_N + t_B)} \tag{5.23}$$

The timescale of magnetic relaxation for a ferrofluid colloid is very small, ranging from on the order of 10^{-9} to 10^{-5} seconds. In Figure 5.8 the two relaxation mechanisms are illustrated.

Unless the applied magnetic field has a frequency in the gigahertz range it is generally valid to assume instantaneous magnetic relaxation and that the ferrofluid magnetisation and external magnetic field strength vectors are collinear: resulting in negligible hysteresis effects and facilitating a quasistatic magnetic field approximation even when the ferrofluid is in motion.

In the context of ferrofluid-gaps for electrical machines this means that the fluid dynamics of the ferrofluid, namely the shear rate and the extent of turbulence, should in theory not influence the magnetic behaviour of the ferrofluid and hence the electromagnetic performance of the machine.

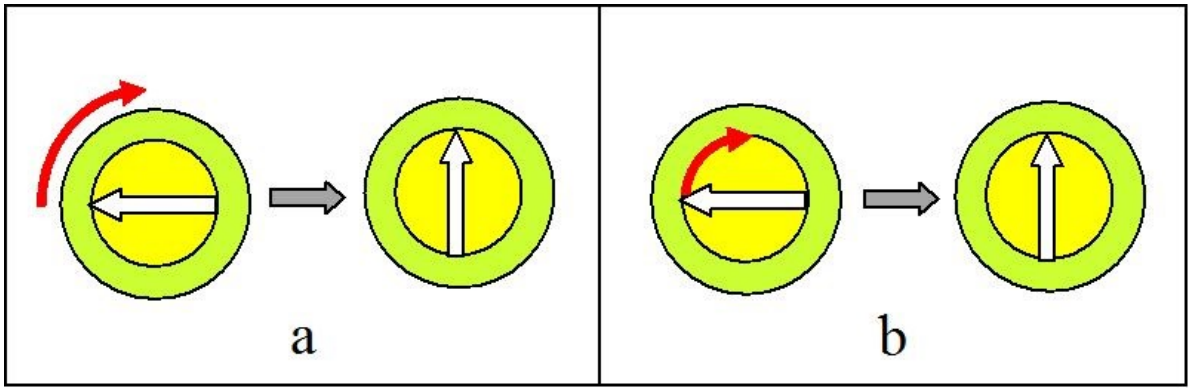

Figure 5.8: (a) Illustration of Brownian relaxation, (b) illustration of Néel relaxation [131].

5.2.9 Ferrofluid Synthesis

Ferrofluid was first synthesised at NASA by Stephen Papell by extensively ball milling iron oxide powder until nanoscopic particle sizes were achieved [132]. This method is very time-consuming, energy-intensive, and results in relatively poor quality non-spherical nanoparticles [133].

Chemical co-precipitation is currently the most popular method for synthesising ferrofluid nanoparticles [134]. It is a comparatively fast process, resulting in a high yield of quality nanoparticles. An example of a chemical co-precipitation protocol is detailed in Appendix E.

Conventionally, ferrofluid is manufactured at a relatively low scale since most applications only require small volumes. However, there has been increasing interest in scaling up ferrofluid production and utilising it in high-volume applications. A company called Liquisort are developing a magnetic waste separation system which requires significant volumes of ferrofluid [135]. There are also several potential medical applications of ferrofluid which have motivated research into high-throughput production [136].

The raw materials required for the synthesis of iron oxide based ferrofluid are relatively cheap and abundant, it is conceivable that a low unit cost ($/litre) is achievable through large-scale production.

5.2.10 Other Types of Ferrofluid Nanoparticles

The discussion so far has been centred on ferrofluids consisting of iron oxide (Fe_3O_4) nanoparticles (IONPs). However, the magnetic properties of a ferrofluid can be modified by employing alternative magnetic nanoparticle materials [15], [114], [133].

The temperature sensitivity of ferrofluid magnetisation can be enhanced by using a composition such as $Mn_{0.5}Zn_{0.5}Fe_2O_4$, such ferrofluids are referred to as temperature sensitive magnetic fluids (TSMFs) [137]. A high temperature sensitivity is particularly advantageous in heat transfer applications that exploit the thermomagnetic convection effect to enhance cooling from a hot surface [138]. In this process, the colder and more strongly magnetised ferrofluid is drawn into regions of high magnetic field strength, displacing the hotter and less magnetic fluid and thereby producing a passive

convective flow. This phenomenon can also be harnessed in ferrofluid pumps, which achieve fluid circulation without any moving parts [139].

The saturation magnetisation can be increased by incorporating metallic or alloy nanoparticles with higher magnetic moments; however, such materials are generally less stable and more prone to oxidation than iron oxides [134].

Other than in heat transfer applications, IONPs remain the most common choice because they combine a relatively high saturation magnetisation with excellent chemical stability, low toxicity, and straightforward synthesis from abundant iron salts.

5.3 Ferrofluid-Gap Magnetic and Mechanical Behaviour

In the following section it is explained how ferrofluid-gap magnetic and mechanical behaviour can be modelled according to theoretical predictions.

5.3.1 Ferrofluid-Gap Magnetisation Curve

A relatively simple yet effective approach for modelling the magnetisation curve of ferrofluids is to assume a Brownian suspension of monodisperse (uniform-sized) non-interacting spherical colloids, this is known as the Langevin model [125].

Although polydispersity, magnetic dipole-dipole interactions, irregular colloid shapes, and colloid chain formation are neglected this approach is suitable for modelling ferrofluid at magnetic field strengths sufficient to magnetically saturate it. This is a valid assumption for the majority of a typical electrical machine's air-gap region.

The ferrofluid magnetisation can be given by:

$$M_{\mathrm{FF}} = M_S \mathcal{L}(\xi) \tag{5.24}$$

where M_S is the saturation magnetisation and $\mathcal{L}(\xi)$ is the Langevin Function:

$$\mathcal{L}(\xi) = \coth(\xi) - \frac{1}{\xi} \tag{5.25}$$

With the Langevin parameter ξ given by:

$$\xi = \frac{\mu_0 m H}{k_B T} \tag{5.26}$$

where m is the colloid magnetic moment.

The saturation magnetisation M_S will depend on the spontaneous magnetisation M_d of the iron oxide nanoparticles and the magnetic volume fraction of the ferrofluid ϕ_{M}:

$$M_S = M_d \phi_{\mathrm{M}} \tag{5.27}$$

$$M_d = \psi_{\mathrm{M}} \rho_{\mathrm{M}} \tag{5.28}$$

where ψ_{M} is the specific magnetisation of the colloid magnetic material.

The specific magnetisation of bulk magnetite is between 92-100 emu/g, however IONPs have a lower value due to unwanted surface oxidation as discussed in Section 5.2.3 [140]. Therefore ψ_{M} depends on the quality of IONP synthesis.

The magnetic moment of a ferrofluid nanoparticle can be determined as follows:

$$m = \psi_{\mathrm{M}} \rho_{\mathrm{M}} V_{\mathrm{M}} \tag{5.29}$$

It is important to note that specific magnetisation (ψ_{M}) is reported in electromagnetic units of magnetic moment per unit mass (emu/g). It must be multiplied by density in units of kg/m^3 to give magnetisation in units of A/m.

To provide a reasonable approximation of the ferrofluid-gap spontaneous magnetisation for various magnetic volume fractions, an appropriate value for ψ_{M} was estimated using ferrofluid datasheets published by the company 'FerroTec' [141]. By comparing ϕ_{M} against M_S for five of their products (EMG 901/905/909 and PBG 450/900) a value for M_d can be obtained. Assuming a ρ_{M} of 5150 kg/m^3, such as bulk magnetite, ψ_{M} of 86.53 emu/g was obtained, indicating high quality IONPs as expected from an industrial ferrofluid supplier. FerroTec states that the nominal particle diameter is 10 nm which is typical.

The *BH* curve can then be obtained (for SI units):

$$B = \mu_0 (H + M_{\mathrm{FF}}) \tag{5.30}$$

The ferrofluid relative permeability for various flux densities can also be determined:

$$\mu_{r,\mathrm{FF}} = \frac{B}{\mu_0 H} \tag{5.31}$$

In Figure 5.9 the relative permeability of ferrofluid ($\mu_{r,\mathrm{FF}}$) is presented for various magnetic volume fractions (ϕ_{M}) over a range of magnetic flux density (B) assuming a nominal particle diameter of 10 nm and a specific magnetisation (ψ_{M}) of 86.53 emu/g.

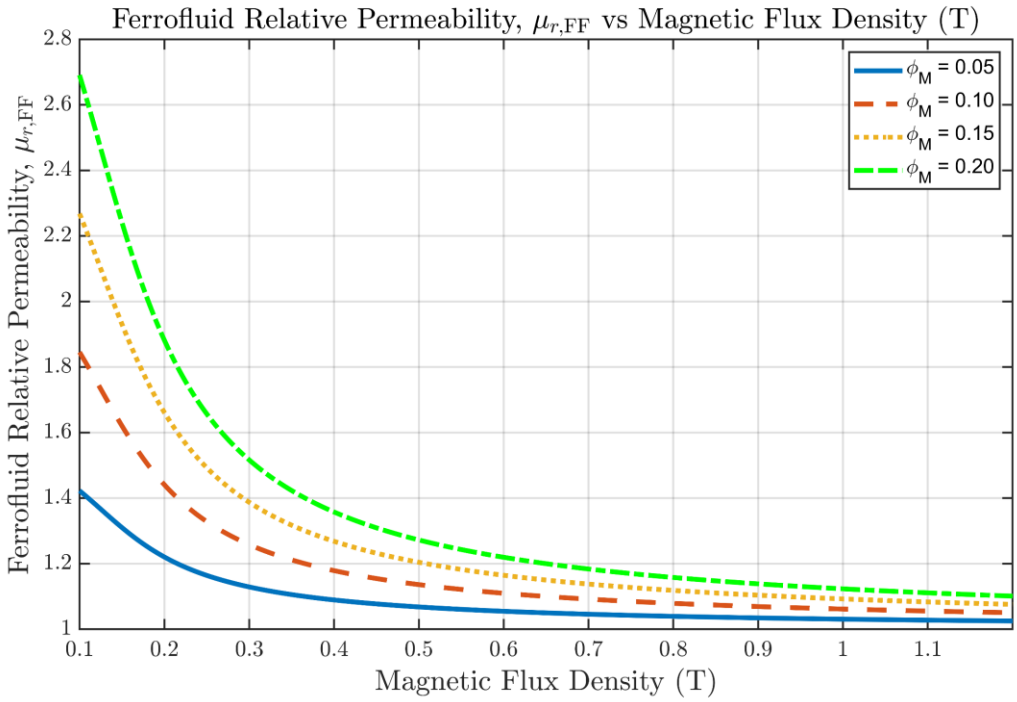

Figure 5.9: Relative permeability of ferrofluid ($\mu_{r,\mathrm{FF}}$) for a range of magnetic flux densities (B) and magnetic volume fractions (ϕ_{M}).

5.3.2 Ferrofluid-Gap Temperature

The spontaneous magnetisation of ferrofluid nanoparticles decreases with increasing temperature. If the temperature exceeds a certain threshold the magnetisation will drop to zero, this is known as the Curie temperature. The magnetic susceptibility of ferrofluid is also temperature dependent, as indicated by the Langevin parameter, Eq. (5.26), which describes how readily the ferrofluid becomes magnetised in response to an external magnetic field. It should be noted that while susceptibility characterises the ease of magnetisation under a given field, it does not determine the saturation magnetisation, which is governed by the spontaneous magnetisation of the nanoparticles.

The Curie temperature of ferrofluid nanoparticles is typically similar to that of the corresponding bulk material [134]. For iron oxide (magnetite), the Curie temperature is $\sim 577^{\circ}\mathrm{C}$ [142]. Consequently, the Curie temperature of an iron oxide based ferrofluid is considerably higher than the boiling point of its carrier fluid [143]. The spontaneous

magnetisation of iron oxide does not change significantly until the Curie temperature is approached, at this point a sharp drop in magnetisation can be observed [144].

As detailed in Chapter 3, the peak temperature of DD WTG armature windings, which is typically the hottest region of an electrical machine, is typically limited to $155^{\circ}\mathrm{C}$. Iron oxide based ferrofluid can therefore be expected to withstand the temperatures expected in DD WTGs without a significant impact on the ferrofluid-gap magnetic performance, assuming that the carrier fluid boiling point is sufficiently high.

5.3.3 Ferrofluid-Gap Magnetic Behaviour

As mentioned in Section 5.2.8, for magnetic field frequencies relevant to electrical machines the colloids can be assumed to align instantaneously to the direction of the magnetic field. It is therefore reasonable to expect that:

- Collinearity of the ferrofluid magnetisation and external magnetic field strength vectors can be assumed in a ferrofluid-gap, fluid dynamic conditions such as shear rate or turbulence will have no influence on the ferrofluid's magnetic properties.
- A ferrofluid-gap has negligible magnetic hysteresis.

Oil based ferrofluids are not electrically conductive, it is therefore reasonable to assume that there will be no eddy currents in a ferrofluid-gap.

In the presence of a stationary magnetic field ferrofluid colloids will drift towards the region with the largest field strength and, given sufficient time, an appreciable concentration gradient can be observed: this results in a non-uniformity of ferrofluid magnetic properties [145]. However, due to the large time-scale of particle drift it is reasonable to assume homogeneous magnetic properties throughout a ferrofluid-gap due to the relatively fast rotation of the magnetic field and high shear rate due to the movement of the rotor [146].

5.3.4 Ferrohydrodynamics

The motion of a ferrofluid can be influenced by external magnetic fields, a phenomenon studied within the field of ferrohydrodynamics (FHD). This is very apparent when the ferrofluid has a free surface, i.e. is unconstrained by solid boundaries. Famously, application of an external magnetic field can cause

Rosensweig instability, also known as a normal field instability, in which the ferrofluid develops a pattern of spikes as demonstrated in Figure 5.10 for an in-house synthesised sample.

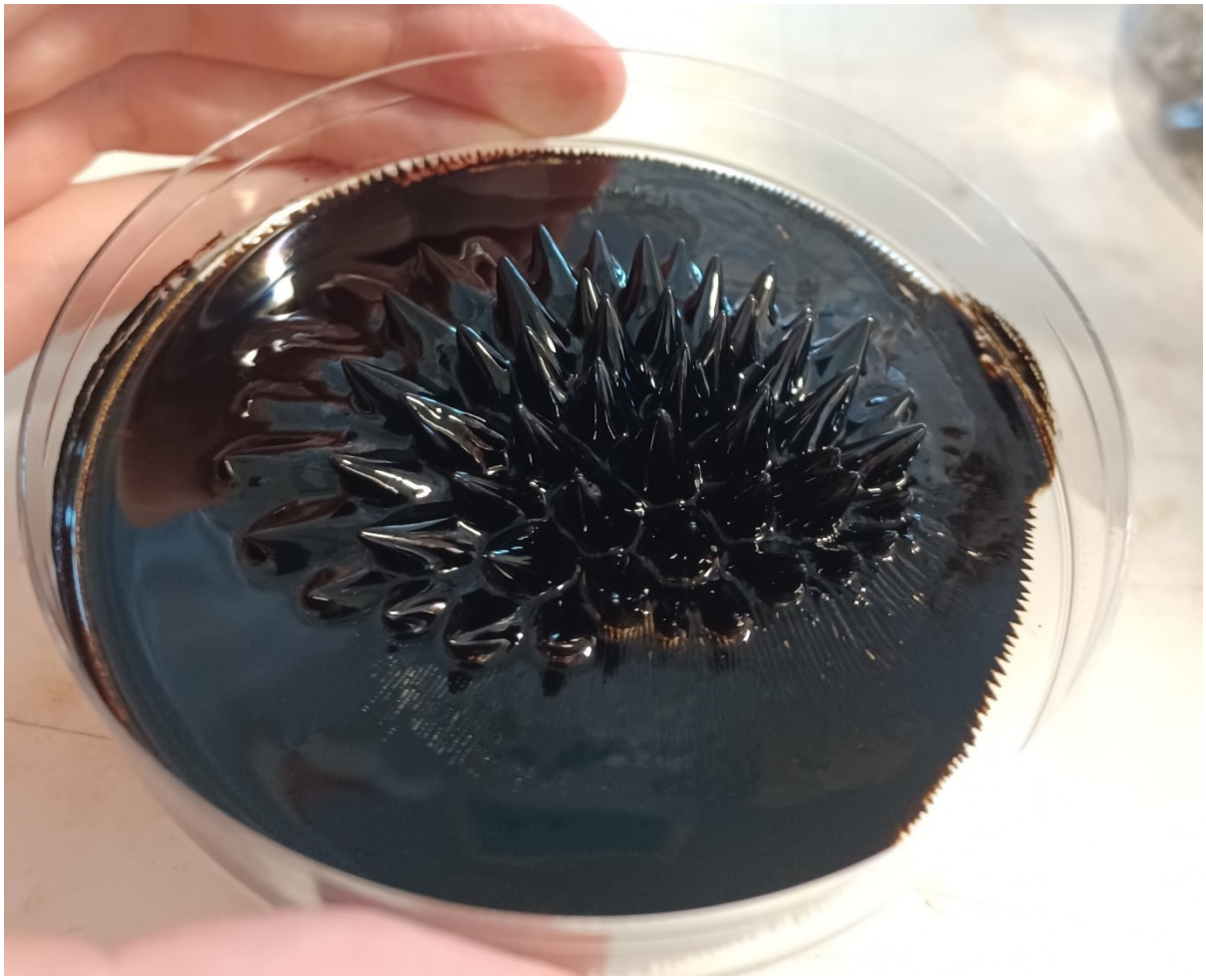

Figure 5.10: Picture of in-house synthesised ferrofluid exposed to a magnetic field, spikes (i.e. Rosensweig instabilities) can be observed.

In a non-uniform magnetic field, ferrofluid will experience a body force in the direction of increasing magnetic field strength, this is known as the Kelvin body force:

$$\mathbf{f}_M = \mu_0 M \boldsymbol{\nabla} \boldsymbol{H} \tag{5.32}$$

In the case of a ferrofluid enclosed by solid boundaries, such as in an entirely filled ferrofluid-gap, the influence of external magnetic fields on the ferrofluid dynamics is nuanced. In his seminal work Rosensweig derives equations of motion for ferrofluid flow for a variety of conditions [144]. For an isothermal flow field with no free surface, the Kelvin body force term in the ferrohydrodynamic Navier-Stokes (NS) equation is

cancelled out by the magnetic pressure gradient (Δp_M), reducing the NS equation to the same form as for a conventional incompressible enclosed fluid flow.

The ferrohydrodynamic equation of motion can be expressed as:

$$\rho \frac{\mathrm{D}\boldsymbol{v}}{\mathrm{D}t} = -\boldsymbol{\nabla}(p + p_M) + \mu_0 M \boldsymbol{\nabla} \boldsymbol{H} + \eta \boldsymbol{\nabla}^2 \boldsymbol{v} + \rho \boldsymbol{g} \tag{5.33}$$

where p_M is the fluid-magnetic pressure.

$$p_M = \mu_0 \bar{M} H \tag{5.34}$$

For an isothermal flow, it can be assumed that there is no spatial variation in ferrofluid magnetic susceptibility or saturation magnetisation, therefore:

$$|\boldsymbol{\nabla} p_M| = |\mathbf{f}_M| = |\mu_0 M \boldsymbol{\nabla} \boldsymbol{H}| \tag{5.35}$$

Eq. (5.33), can therefore be reduced to:

$$\rho \frac{\mathrm{D}\boldsymbol{v}}{\mathrm{D}t} = -\boldsymbol{\nabla} p + \eta \boldsymbol{\nabla}^2 \boldsymbol{v} + \rho \boldsymbol{g} \tag{5.36}$$

Which corresponds to the conventional Navier-Stokes equation of fluid mechanics for an incompressible flow.

If a temperature gradient exists within the enclosed ferrofluid volume such that there is a spatial variation in the ferrofluid magnetic properties, then thermomagnetic convection can take place since the Kelvin body force is no longer directly counteracted by the magnetic pressure gradient. Nondimensionalization of the NS equation can help inform the expected behaviour of thermomagnetic convection in the case of a shear flow, such as a ferrofluid-gap, a derivation is provided in Appendix F. As illustrated by the non-dimensional term for the Kelvin body force, as the inertial force within the flow increases due to increased rotational speed, the relative influence of thermomagnetic convection will become progressively less significant:

$$\frac{\mu_0 M_s H_g}{\rho v_r^2} \boldsymbol{M}^* \boldsymbol{\nabla}^* \boldsymbol{H}^* \tag{5.37}$$

It is also important to consider that turbulence within a ferrofluid-gap will distribute heat, suppressing the development of temperature gradients other than in the laminar boundary layers at the solid-fluid boundaries.

For high-frequency magnetic fields, misalignment of the ferrofluid magnetisation and external magnetic field strength vectors can introduce an additional body force component into the NS equations [147]:

$$\mathbf{f}_{\text{spin}} = \frac{1}{2}\boldsymbol{\nabla} \times (\boldsymbol{M} \times \boldsymbol{H}) \tag{5.38}$$

However, for magnetic field frequencies relevant to electrical machine air-gaps, in which the collinearity of M and H is assumed, the term vanishes since the cross product of M and H is equal to zero [134].

In summary, according to ferrohydrodynamic theory, for a totally enclosed ferrofluid flow under high rates of shear, such as in the air-gap of an electrical machine, a reasonable prediction of the flow behaviour should be possible by using the standard NS equations for an incompressible fluid.

5.3.5 Magnetoviscous Effects

A ferrofluid's viscosity can be influenced by the strength and orientation of an external magnetic field.

At low shear rates the magnetic particles may be observed to clump together and form chains, this can result in a large increase in viscosity. This effect has been observed to follow non-Newtonian shear thinning behaviour since chain formation is suppressed as shear rate is increased [148]. It has also been demonstrated that this behaviour is highly dependent on the presence of unwanted large particles that act as nucleation sites for particle clustering, improved ferrofluid purity reduces this effect significantly, as observed in Figure 5.11 [149].

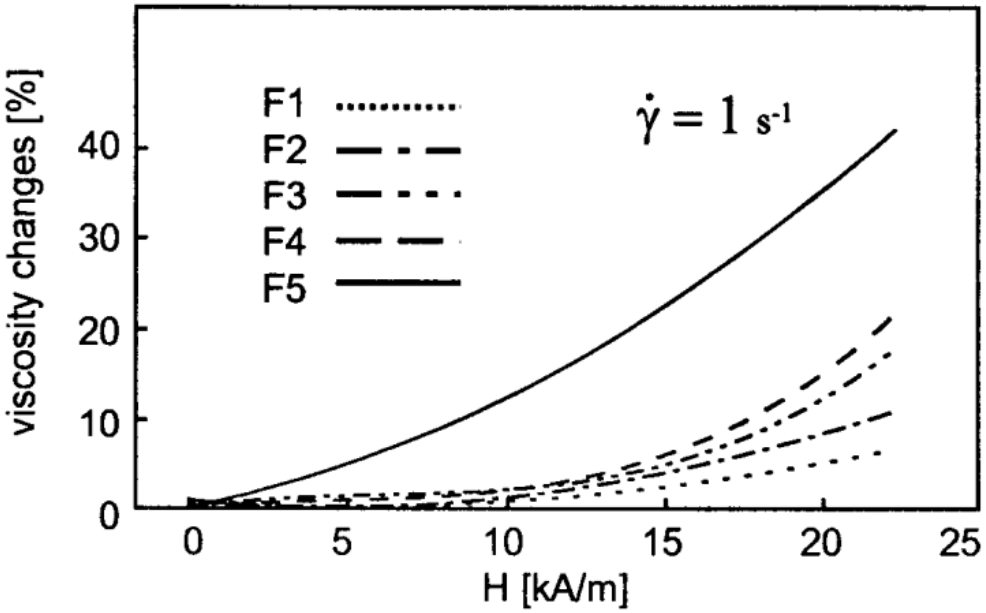

Figure 5.11: Change in ferrofluid viscosity due to an external magnetic field for various ferrofluid purities, F1 indicates the purest sample and F5 the least pure [149].

Another mechanism in which a magnetic field can increase ferrofluid viscosity is referred to as 'rotational viscosity'. If the external magnetic field's orientation is not collinear with the axis of vorticity in shear flow, then the torque incident on the colloids from the flow will be counteracted by the magnetic torque between the colloid dipoles and the external field, as illustrated in Figure 5.12. This results in less of a viscosity increase than the formation of microstructures. It is theorised that there is no rotational viscosity if all the colloids are sufficiently small for Néel relaxation since the rotation of the colloid dipole and structure are uncoupled.

The additional component of rotational viscosity is given by [150]:

$$\eta_{\mathrm{rot}} = \frac{3}{2}\phi_{\mathrm{H}}\eta_{\mathrm{FF},0}\frac{\xi - \tanh\xi}{\xi + \tanh\xi} < \sin^2\beta_\theta > \tag{5.39}$$

where $\eta_{\mathrm{FF},0}$ denotes the viscosity of the ferrofluid in the absence of a magnetic field, and β_θ is the angle between the axis of vorticity and field direction (< ... > denotes the spatial average).

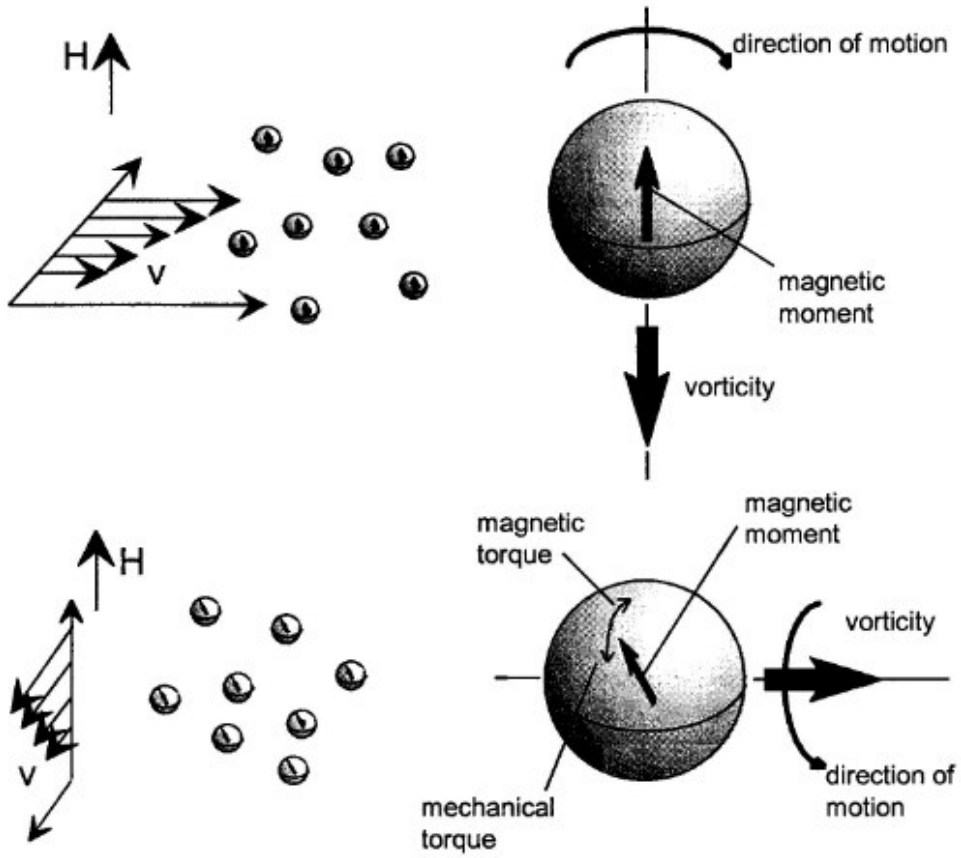

Figure 5.12: In the top image the external magnetic field is collinear with the axis of vorticity and there is no rotational viscosity, in the bottom image they are out of alignment resulting in a magnetic torque and rotational viscosity [150].

5.3.6 Mechanical Wear

Ferrofluid can be used to great effect as a lubricant, as evidenced by applications such as ferrofluid bearings and seals [151], [133]. Miyake *et al.* present friction and wear tests for cylindrical permanent magnet specimens, highlighting the lubricating properties of ferrofluid [152].

However, the stability of the colloidal suspension is critical. If the magnetic nanoparticles agglomerate, they can form larger clusters that may lead to abrasive wear. Maintaining colloidal stability is therefore essential to prevent any wear due to a ferrofluid-gap. The colloidal stability of ferrofluids was investigated by van Silfhout *et al.* for flux densities of 10 T and gradients of 100 T/m, they confirmed theoretical expectations of ferrofluid colloidal stability [153]. Susan-Resiga *et al.* demonstrate long-term stability of ferrofluid by presenting a sample that has remained stable for over 39 years in a non-uniform magnetic field [126].

5.3.7 Summary of Ferrofluid Suitability for Use in Electrical Machines

In summary, ferrofluid exhibits several properties that make it suitable for use in the air-gap of electrical machines. Its low viscosity minimises drag on the rotor, supporting efficient operation, while its high magnetic susceptibility enhances the air-gap flux density. Oil-based ferrofluids are electrically insulating, preventing short circuits and resulting in no eddy current loss; they also exhibit negligible magnetic hysteresis due to essentially instantaneous magnetic relaxation at magnetic field frequencies relevant to electrical machines. Ferrofluid offers favourable thermal properties, with the ability to withstand the temperatures typically encountered in electrical machines and the potential for enhanced heat extraction from the air-gap region. Importantly, it is non-abrasive and can act as a lubricant, reducing the risk of damage to sensitive components such as the magnets and windings. Ferrofluid has been shown to remain stable for decades even in the presence of strong magnetic gradients, and it has the potential to be produced at a low unit cost ($/litre).

5.4 Prior Work on Ferrofluid for Electrical Machines

The concept of utilising ferrofluid to improve electrical machine performance is not new, however there is little work published on the topic and there are several opportunities for improving understanding in this area. A patent application was filed by Schlumberger Technology Corp in 2009 which depicts the ferrofluid-gap concept applied to a radial flux electrical machine, however it was later abandoned [154].

The following section will review prior work in which the ferrofluid-gap concept was investigated and highlight other instances in which the application of ferrofluid for enhanced cooling of electrical machines was studied. The section is concluded by highlighting opportunities for further research of the ferrofluid-gap concept, motivating the following chapters of this thesis.

5.4.1 Nethe *et al.* “Improving the efficiency of electric machines using ferrofluids”

In their 2006 paper, Nethe *et al.* introduce the concept of a ferrofluid-gap as a means of improving the efficiency of induction motors [155]. Due to the increased permeability of the air-gap region it is proposed that less input current would be required per unit of output torque.

A basic magnetic circuit analysis is presented which neglects the nonlinearity of the ferrofluid *BH* curve and magnetic leakage. A constant relative permeability of 2 is assigned to the ferrofluid in their model. This would only be realistic for low magnetic field strengths, as indicated in Figure 5.9 a value in the range of 1-1.2 would be representative of what could be expected in a practical electrical machine.

They present a 2D magnetic analysis, an image of their simulation results is presented in Figure 5.13. They claim that an iterative numerical method is used to account for the non-linearity of the ferrofluid *BH* curve, however no information is given on the method or on the *BH* curve used. The geometry is not representative of a real electrical machine with one non-symmetric pole pair on the rotor and a single non-symmetric coil loop on the stator. The rotor and stator are also assumed to be perfectly circular so there is no accounting for stator teeth or saliency of the rotor poles.

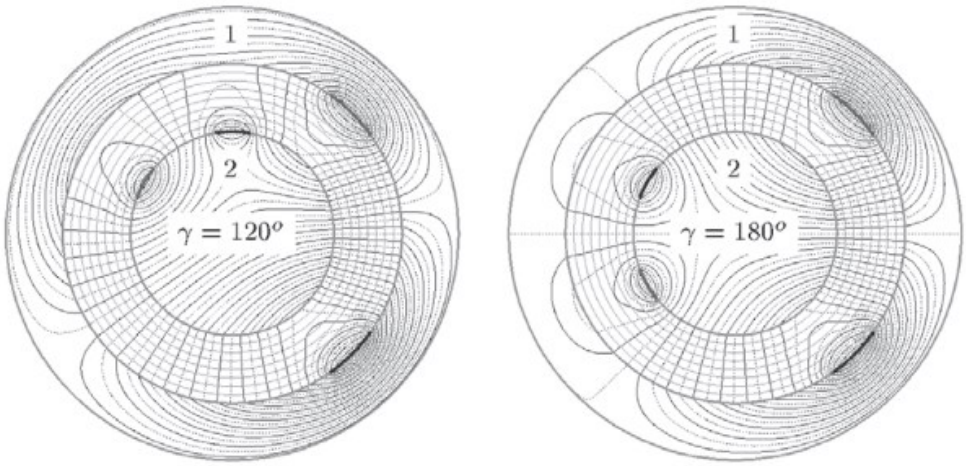

Figure 5.13: 2D magnetic simulation results of A. Nethe *et al.* showing 'magnetic lines of force' at two different relative rotor-stator positions [155].

They estimate the drag loss within an electrical machine by assuming laminar Taylor-Couette flow, they note that the assumption is invalid for rotational speeds at which the flow is turbulent. There is no consideration of the influence of the magnetic fields upon the ferrofluid flow.

A brief analysis is given on the thermal behaviour of an electrical machine with a ferrofluid-gap, however only conductive heat transfer is considered.

Experimental work is presented in which ferrofluid is introduced into the air-gap region of an induction motor. Little information is given on the specification of the experimental set-up and the properties of the ferrofluid that is used. The output torque of the

modified motor is recorded for various saturation magnetisations of ferrofluid for a variety of rotational speeds and torque loads. An increase in efficiency is observed at low rotational speeds, however the viscous drag at higher speeds appears to dominate and cause a net efficiency loss as shown in Figure 5.14.

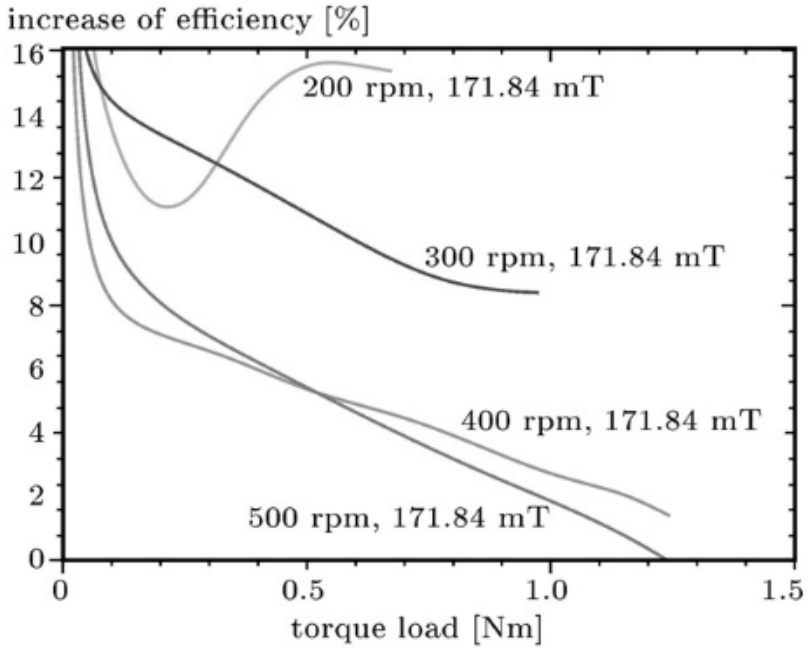

Figure 5.14: Increase in induction motor efficiency due to a ferrofluid-gap for various rotational speeds and torque loads.

A decrease in efficiency is also observed as the torque load is increased, this is not explained in the paper but is likely due to magnetic saturation of the ferrofluid-gap.

Since the test was performed with a motor with output torque measured, the positive magnetic influence of the ferrofluid cannot be distinguished from the detrimental fluid-drag that it incurs, only the net effect can be observed.

The paper lacks a rigorous comparison between their modelling techniques and the presented experimental data.

5.4.2 Andy Judge “Air Gap Elimination in Permanent Magnet Machines”

In his 2012 PhD thesis, Andy Judge investigates the ferrofluid-gap concept for various small scale electrical machines with the motivation of improving efficiency [156].

A magnetic circuit is presented with a single node representing the leakage between the poles. As in the work of A. Nethe *et al.* the ferrofluid is assigned a constant value

of relative permeability, non-linearity of the ferrofluid *BH* curve and magnetic saturation of the iron components is not accounted for.

Viscous drag of the ferrofluid is modelled using an empirical drag correlation based on a spinning disk, it is claimed that a term is added to the drag calculation to account for magnetoviscous effects, however a value for this term is not provided.

A finite element method (FEM) analysis of magnetic leakage is conducted for an arbitrary 'C-Channel' magnetic circuit which is not representative of realistic electrical machine geometries.

The performance of a small-scale off-the-shelf permanent magnet (PM) motor is compared when it is immersed in a ferrofluid and in an oil of similar viscosity, it is shown that immersion in the ferrofluid results in improved performance when compared to the oil.

A custom PM axial flux generator with a ferrofluid-gap is tested, an increase in open-load voltage output is observed compared to baseline testing with a conventional air-gap, as shown in Figure 5.15. The increase appears to coincide with values obtained from FEM simulations of the generator, however the error is significant and the trend of voltage vs rotational speed appears to be nonlinear.

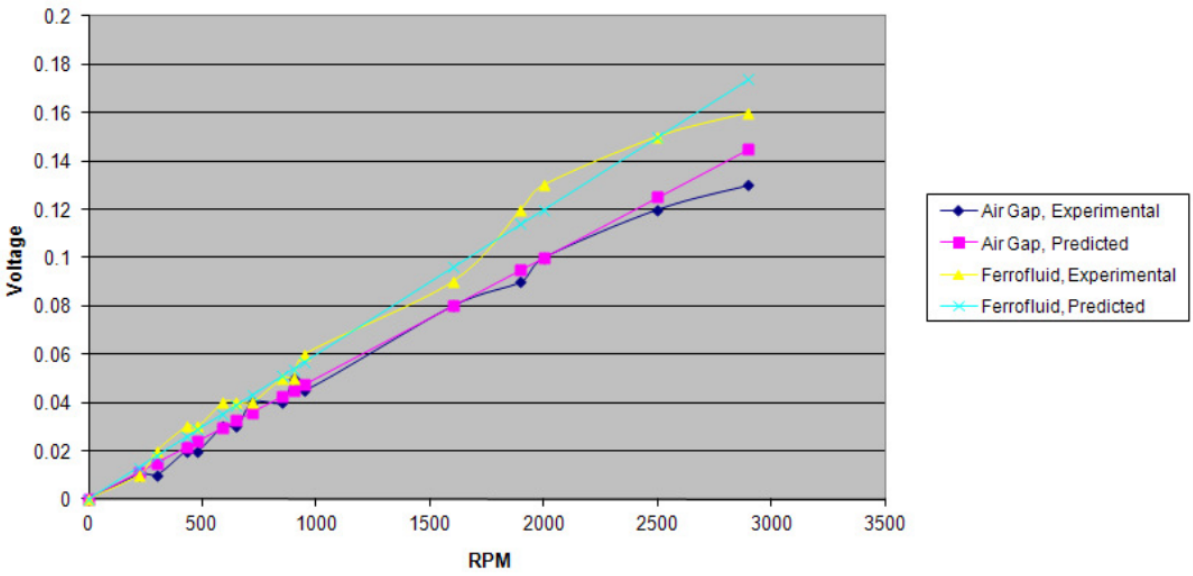

Figure 5.15: Experimental results of Andy Judge showing comparing voltage output with an air-gap and a ferrofluid-gap and a comparison with predicted values [156].

5.4.3 Zeng *et al.* "Asynchronous Machine with Ferrofluid in Gap: Modelling, Simulation, and Analysis"

In a more recent paper from 2020, Zeng *et al.* investigate the ferrofluid-gap concept for an asynchronous induction motor with the intention of increasing efficiency [157].

A 1D magnetic analysis is given to show that an increased air-gap permeability would improve machine performance.

A 'frictional model' is presented which is again based on laminar Taylor-Couette flow with no consideration of turbulence or interactions between the magnetic fields and the ferrofluid.

An FEM analysis is presented for a realistic geometrical depiction of an induction motor. However, as before, the non-linearity of the ferrofluid B-H curve and magnetic saturation are not accounted for. A single constant relative permeability of 2 is assigned to the entire air-gap region to represent ferrofluid. It appears that only an open-load condition is investigated in their FEA analysis.

Some experimental results are briefly mentioned with little information on the electrical machine specification or ferrofluid properties. Again, the experiment is performed with a motor, and no comparison is made between their modelling methods and the experimental data.

5.4.4 Mateev *et al.* "Modelling of low-speed magnetic gear with viscose ferrofluid"

Mateev *et al.* investigate the application of a ferrofluid-gap to a magnetic gear, where the air-gap region next to the low-speed rotor is filled with ferrofluid and sealed from the air-gap next to the high-speed rotor [158].

Although the non-linear magnetic properties of ferrofluid are discussed, the ferrofluid-gap is represented with a constant value of relative permeability in the range of 2 to 10 in their FEM simulations.

Although the ferrofluid-gap is assumed to be completely filled with no air present, they assume that the Kelvin body force contributes towards drag within the magnetic gear. However, as discussed in Section 5.3.4, according to ferrohydrodynamic theory the

Kelvin body force is counteracted by the magnetic pressure gradient within the ferrofluid, invalidating this assumption.

In their model, there is no consideration of magnetoviscous effects.

There is no comparison between their computational model of magnetic gear performance and their experimental results.

They report a 4% increase in magnetic torque due to the ferrofluid-gap from their experimental results, and that with increasing speed the additional frictional drag from the ferrofluid surpassed the increase in magnetic torque.

5.4.5 Ferrofluid Cooling of Electrical Machines

A company named Grind Tech markets a ferrofluid product called ‘Statorade’ intended for use in direct-drive outer-rotor PM motor air-gaps for electric bikes [159]. The concept is to improve the heat transfer from the stator to the outer casing of the motor via the rotor due to a partially filled ferrofluid-gap. It is claimed that since the air-gap is only partially filled with ferrofluid there is a negligible loss of efficiency due to drag.

In separate studies Karimi-Moghaddam *et al.* and Zhang *et al.* investigate the use of temperature-sensitive ferrofluid for enhanced cooling of electrical machine end windings [160], [161]. Due to the passive convection effect which is driven by an appreciable temperature gradient and the end winding leakage flux, it is found that submersion of the end windings with ferrofluid has the potential to improve heat transfer. Zhang *et al.* find that the ferrofluid cooling has improved performance in comparison to a non-magnetic oil with similar properties.

Rietz *et al.* conducted exploratory experimentation of jet impingement cooling of end windings using ferrofluid [162]. Based on a simplified experimental set-up, they find that the cooling performance increases with increasing flux density in the vicinity of the end windings. The dynamics involved are highly complex due to the alternating magnetic field and the free surfaces of the ferrofluid jet which will be subject to Kelvin body forces. Further work is required to understand the potential of ferrofluid in this application.

There is a significant amount of interest in utilising ferrofluid as a heat exchanging medium for electrical machines, it is already used in other applications such as

loudspeaker coils and for transformer cooling to great effect. It may be possible to combine the ferrofluid-gap concept with a cooling strategy for electrical machines. However, the use of temperature-sensitive magnetic fluids (TSMFs) in the air-gap region may reduce the potential for PM material mass reduction due to their relatively low saturation magnetisation in comparison to iron oxide based ferrofluids.

5.4.6 Opportunities for Further Research of Ferrofluid-Gaps

Following is a summary of opportunities for novel research of ferrofluid-gaps which are addressed in the following chapters of this thesis:

- Magnetic modelling of electrical machine performance with realistic electrical machine geometries and ferrofluid-gap properties.
- Investigation into the influence of the rotating and non-uniform magnetic field within the air-gap region on the drag of a ferrofluid-gap.
- Detailed investigation of the thermal behaviour of an electrical machine with a ferrofluid-gap.
- Experimental investigation into the ferrofluid-gap concept with a test-rig set-up that allows for a separate analysis of the magnetic and mechanical influence of the ferrofluid.
- A comparison between ferrofluid-gap modelling methods and experimental results, providing validation of analysis methodologies that can be applied to arbitrary electrical machine topologies.
- Utilisation of ferrofluid-gap modelling techniques in a feasibility study of the concept applied to multi-megawatt rated DD WTGs.

Although several issues have been identified in the discussed research articles, they demonstrate that a ferrofluid-gap has the potential to improve electrical machine performance.

5.5 Conclusion

In this Chapter an unconventional approach for reducing air-gap reluctance was introduced. By flooding the air-gap region of an electrical machine with ferrofluid, making it a ‘ferrofluid-gap’, the magnetic permeability of the region can be increased.

Since direct-drive (DD) wind turbine generators (WTGs) are very large and operate at a relatively low rotational speeds the loss in efficiency due to ferrofluid-gap drag may be acceptable.

In Section 5.1, the concept of a ferrofluid-gap was introduced and it was explained that for DD WTGs, a significant reduction in PM material may be possible without unacceptably compromising efficiency due to drag losses.

In Section 5.2, an overview of ferrofluid was provided and it was highlighted that its unique properties make it especially suited for use in the air-gap region of electrical machines.

In Section 5.3, it was explained how ferrofluid-gap magnetic and mechanical behaviour can be modelled according to theoretical predictions and prior experimental works.

In Section 5.4, previous work in which the application of ferrofluid to electrical machines was discussed and opportunities for further research were highlighted.

The following chapters of this thesis will explore the opportunities for further research of the ferrofluid-gap concept as highlighted in Section 5.4.6.

Chapter 6: Design and Fabrication of a Ferrofluid-Gap Test Rig

As detailed in Chapter 5, Section 5.4, prior experimental work on the ferrofluid-gap concept leaves several gaps in knowledge that can be clarified through further experimentation:

- In each study insufficient detail is provided on the experimental set-up and the properties of the tested ferrofluid, there is a lack of detailed comparison between theoretically predicted and experimentally observed impacts of the ferrofluid-gap on electrical machine performance. Therefore, theoretically predicted ferrofluid-gap behaviour remains unvalidated by experimentation.
- Comparison of induction motor efficiency with and without a ferrofluid-gap does not allow for the magnetic (increased air-gap region magnetic permeability) and mechanical behaviour (increased viscous drag) to be distinguished from the experimental results. The efficiency of a ferrofluid-gap motor depends on both the ferrofluid-gap magnetic and mechanical behaviour, this obscures direct measurement of either effect.
- The use of PMs means that the magnetic field strength cannot be modulated, therefore the ferrofluid-gap behaviour can only be evaluated at a single magnetic field strength (assuming constant air-gap clearance). In addition, any influence of the magnetic field on ferrofluid-gap drag cannot be readily determined from experimentation since the rotor field is always present.

This chapter details the design and fabrication of a novel ferrofluid-gap test rig, a picture of the test rig rotor and stator is provided in Figure 6.1.

In the following section the concept and design of the test rig are explained. Section 6.2 details the fabrication of the test rig and the overall experimental testing set-up. In Section 6.3 a summary is provided of the different ferrofluids that were tested.

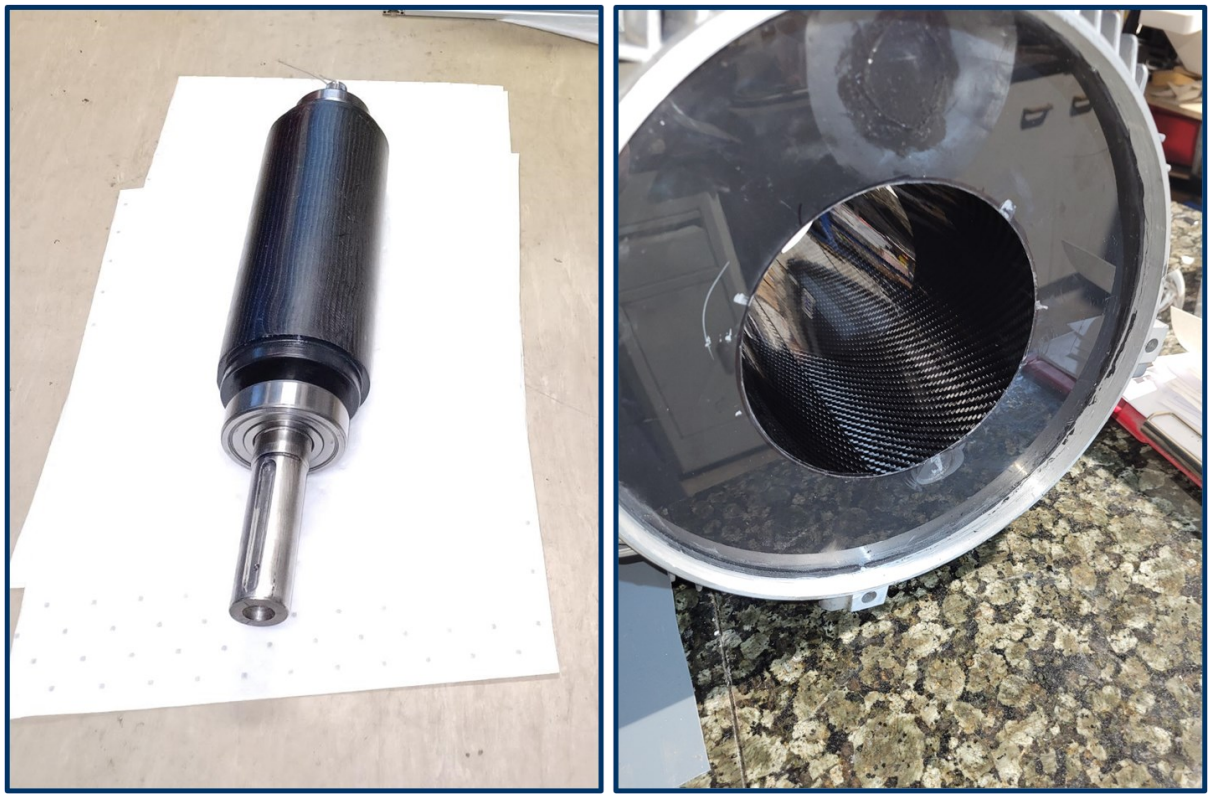

Figure 6.1: Picture of the ferrofluid-gap test rig rotor (left) and stator (right).

6.1 Design of a Ferrofluid-Gap Test Rig

It is important to understand that the objective behind the test rig is not to produce a high-performance machine but rather a device that can produce novel experimental data that characterises the magnetic and mechanical behaviour of ferrofluid-gaps over a large range of conditions. The key aims of experimental testing are as follows:

- Evaluate whether the magnetic properties of a ferrofluid-gap are influenced by fluid dynamics, namely turbulence and shear rate. As explained in Chapter 5, Section 5.3.3, it is expected that the fluid dynamics will have no impact on the magnetic performance of the ferrofluid-gap.
- Evaluate whether the impact of a ferrofluid-gap on electrical machine performance can be accurately modelled according to theoretical predictions. As explained in Chapter 5, Section 5.3.3, it is expected that the ferrofluid-gap will have homogeneous magnetic properties.
- Evaluate how the non-uniform and time-varying magnetic field within the air-gap region influences the ferrofluid-gap drag. As explained in Chapter 5, Section 5.3.4, it should be possible to model the ferrofluid-gap fluid dynamics

using the standard Navier-Stokes equations, however it is expected that the magnetic field will increase the ferrofluid viscosity.

- Produce high-quality ferrofluid-gap experimental test data over a large range of magnetic and fluid dynamic conditions. As highlighted in Chapter 5, Section 5.4, prior experimental results examining ferrofluid-gap behaviour in a generator have significant uncertainty.

The test rig takes the form of a synchronous generator that is driven on a test bed by a motor. This set-up allows for separate investigation of ferrofluid-gap magnetic and mechanical behaviour since the electrical output of the generator is not influenced by the mechanical drag of the ferrofluid-gap assuming that it is held at a constant speed by the motor. It was decided that the test rig's rotor field would be provided by a DC excited rotor winding, this has several advantages compared to PMs:

- The rotor field winding current can be modulated, allowing for experimentation over a range of rotor winding magnetomotive force (MMF) magnitudes.
- The rotor winding current can be turned ON/OFF during operation allowing for the detection of any abrupt changes in torque due to the influence of the rotor field on ferrofluid-gap drag.
- The lack of PMs simplifies the disassembly and cleaning of the test rig between tests with different ferrofluids.

6.1.1 Scaling the Test Rig Geometry

The test rig was designed such that ferrofluid-gap behaviour could be investigated in similar fluid dynamic conditions to what would be expected in multi-megawatt scale DD WTGs. It was desired to scale the fluid properties directly, so that a ferrofluid of any kinematic viscosity (υ) could be tested in scaled conditions:

$$\upsilon = \eta/\rho \tag{6.1}$$

where η is dynamic viscosity and ρ is fluid density. It is convenient to characterise the ferrofluid-gap flow as a Taylor-Couette (TC) flow, as is common practice in the analysis of radial-flux electrical machines [68]. In a surface mounted PM machine, the spacing between the rotor poles and stator slot openings render the rotor and stator to be non-cylindrical, however if a ferrofluid-gap were to be implemented it would be beneficial

to fill the spaces between the rotor poles and to utilise stator slot wedges in order to minimize unwanted magnetic leakage: this would result in an air-gap topology closely resembling a TC system. It was therefore decided to design the test rig such that it resembles a TC apparatus with a smooth and cylindrical rotor profile and stator bore. This topology also simplifies the sealing of ferrofluid within the air-gap region as radial shaft seals can be implemented at each end. An idealised test-rig geometry also simplifies comparison between the experimental results and computational fluid dynamics (CFD) simulations, for this reason it was also decided to avoid any skewing of the stator slots or rotor poles.

Although DD WTGs operate at a low rotational speed (ω), their large rotor radius (r_{r}) and air-gap clearance (h_{g}) could result in appreciable turbulence of a fluid in the air-gap region. This can be demonstrated by considering the Reynolds number for TC flow:

$$\mathrm{Re} = \frac{\omega r_{\mathrm{r}} h_{\mathrm{g}}}{\nu} \tag{6.2}$$

However, the onset of turbulence in a TC flow depends not only on the Reynolds number but also on the radius ratio $(\Gamma_{\mathrm{r,s}})$, which in the case of an inner-rotor electrical machine is the ratio between the rotor radius, and the stator inner radius (r_{s}):

$$\Gamma_{\mathrm{r,s}} = \frac{r_{\mathrm{r}}}{r_{\mathrm{s}}} \tag{6.3}$$

As discussed in Chapter 3, since the radius ratio of DD WTGs is very close to unity (~0.998), the standard Taylor correlations for turbulence are not applicable. The 'Energy Gradient Method' proposed by Dou *et al.* was therefore utilised for scaling the test rig flow to that of multi-megawatt scale DD WTGs since it is applicable for all radius ratios [69].

This was achieved by considering the maximum value of the dimensionless K parameter from the energy gradient method, which is located at the rotor periphery:

$$K_{\max} = \mathrm{Re}\frac{r_{\mathrm{r}}}{2(r_{\mathrm{r}} + r_{\mathrm{s}})}\left(1 - \frac{h_{\mathrm{g}}}{r_{\mathrm{s}}}\right)^2\left(2 - \frac{h_{\mathrm{g}}}{r_{\mathrm{s}}}\right)^2 \tag{6.4}$$

and the critical value of K which denotes the onset of turbulence, which according to an empirical fit provided by Li *et al.* can be estimated as [110]:

$$K_{\mathrm{crit}} = 365.7 \exp\left(\frac{-h_{\mathrm{g}}}{0.047 r_{\mathrm{s}}}\right) + 42.5 \tag{6.5}$$

When K_{max} surpasses K_{crit} the flow becomes turbulent, therefore the ratio $K_{\mathrm{max}}/K_{\mathrm{crit}}$ represents the extent of turbulence. Since direct scaling of fluid properties was desired, the ratio was decomposed into a component that represents the contribution due to geometry and velocity (K_{geo}), and the contribution from the fluid properties, i.e. the kinematic viscosity:

$$\frac{K_{\mathrm{max}}}{K_{\mathrm{crit}}} = \frac{K_{\mathrm{geo}}}{\mathcal{V}} \tag{6.6}$$

The test rig ferrofluid-gap turbulence could then be scaled against multi-megawatt DD WTGs according to K_{geo} by utilising the sizing equations introduced in Chapter 2, Section 2.1.3.

Figure 6.2 shows how K_{geo} varies for a range of DD WTGs input powers with an upper and lower bound calculated according to the range of parameters provided in Table 6.1.

Table 6.1: Range of wind turbine parameters.

Parameter	Symbol	Range of Values	Unit
Blade swept radius	r_{Swept}	$25 - 200$	m
Generator aspect ratio	Γ_{gen}	$0.15 - 0.30$	–
Rated average electromagnetic shear stress	$\bar{\sigma}_t$	$40 - 100$	kPa
Aerodynamic power extraction efficiency	ζ_{aero}	$0.4 - 0.5$	–
Rated wind speed	$v_{\mathrm{wind,rated}}$	$10 - 12$	m/s
Tip speed ratio	Γ_{TSR}	$6 - 10$	–
Air-gap clearance factor	C_{hg}	$0.00075 - 0.00125$	–

Several designs from literature are included for comparison [13], [17], [22], [27], [43], [78], [79]. It is important to note that this derivation of K_{geo} is based on inner-rotor TC flow and that outer-rotor topologies are popular for DD WTGs, however since inner-rotor TC flow is more turbulent for a given geometry and rotational speed the assumption provides an upper bound for the extent of turbulence. As indicated by the referenced DD WTG designs, K_{geo} does not tend to increase rapidly with P_{shaft}:

- As P_{shaft} increases designers tend to increase the electromagnetic shear stress ($\bar{\sigma}_t$) to limit the DD WTG size.
- As P_{shaft} increases some designers decrease the air-gap clearance factor (C_{hg}) to minimise the amount of PM material required.
- As the wind turbine swept radius (r_{swept}) increases the angular velocity (ω) tends to decrease since it is constrained by the maximum allowable blade tip speed ($v_{\text{tip,max}}$).

Initially, it was decided to target a maximum test rig K_{geo} value of $2 \times 10^{-4}\ \text{m}^2/\text{s}$ since this surpasses all the referenced designs with a significant margin for error.

In Figure 6.3 K_{geo} is plotted for a range of rotor radii and air-gap clearances suitable for a small-scale test rig assuming a rotational speed of 1500 RPM. A rotational speed of 1500 RPM was chosen as a conservative estimate taking into consideration that the ferrofluid needs to be sealed within the air-gap region and to avoid strict requirements for rotor balancing. The air-gap clearance required to achieve the target K_{geo} of $2 \times 10^{-4}\ \text{m}^2/\text{s}$ can be seen to decrease rapidly as the rotor radius increases, indicating that the rotor radius should be at least 30 mm, otherwise an impractically large rotor winding magnetomotive force (MMF) would be required to achieve appreciable air-gap flux densities (B_{g}).

Ferrofluid-gap shear rate is given by the tangential velocity of the rotor interface at the air-gap region divided by the air-gap clearance:

$$\dot{\gamma} = \frac{\omega r_{\text{r}}}{h_{\text{g}}} \tag{6.7}$$

It is relatively low in DD WTGs due to the large value of h_{g} and the low tangential velocities, the largest value of the referenced designs is $\sim 785\ \text{s}^{-1}$ [22]. It is not difficult to achieve larger values of $\dot{\gamma}$ in a small-scale test rig since h_{g} is smaller and larger tangential velocities are straightforward to obtain.

In a TC flow, when the ratio of hydrodynamic axial length (l_h) to h_{g}, known as the TC aspect ratio ($\Gamma_{\text{TC}} = l_h/h_{\text{g}}$), is sufficiently large ($\Gamma_{\text{TC}} > \sim 40$) the influence of end-effects becomes negligible [163]. Therefore, since end-effects should be negligible in full-

scale DD WTGs ($\Gamma_{TC} \approx 200$) it was ensured that the test rig $\Gamma_{TC} > 40$ rather than attempting to scale it directly.

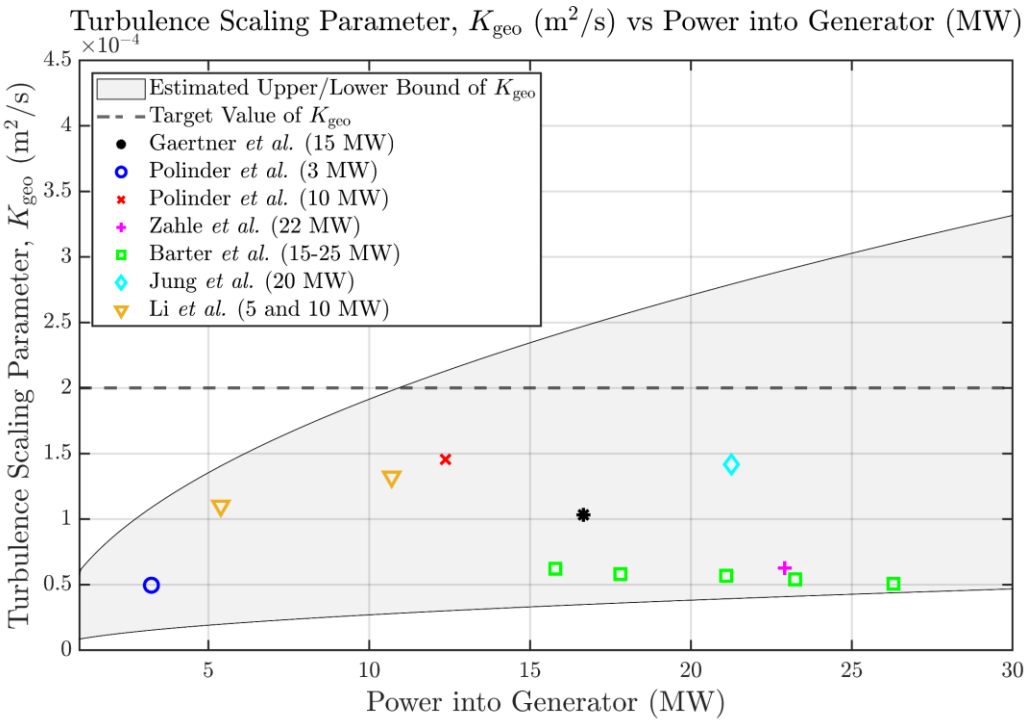

Figure 6.2: Contribution to ferrofluid-gap turbulence from geometry and velocity (K_{geo}) vs wind turbine shaft power (P_{shaft}), range estimated according to parameters in Table 1 and designs referenced from literature [13], [17], [22], [27], [43], [78], [79]. Target value of test rig K_{geo} is indicated with a dashed line.

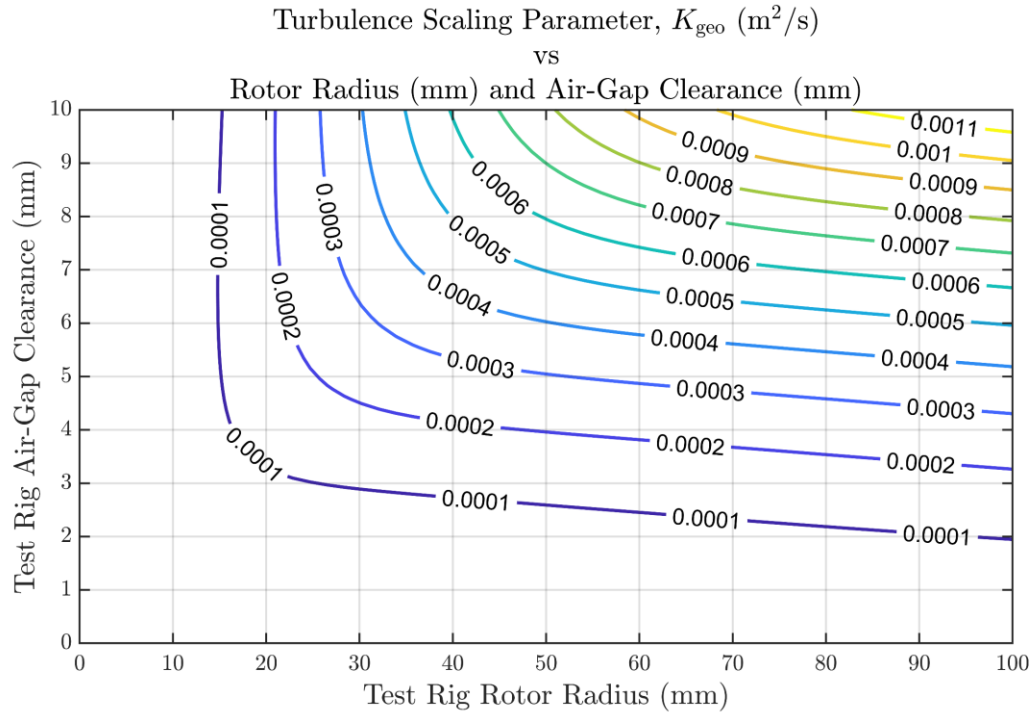

Figure 6.3: Contribution to ferrofluid-gap turbulence from geometry and velocity (K_{geo}) at a rotational speed of 1500 RPM as a function of test rig geometry: air-gap clearance (h_g) and rotor radius (r_r).

6.1.2 Ensuring Feasibility of the Test Rig Design

The next step was to ensure that an appropriate air-gap flux density could be achieved with the DC excited rotor field winding. To achieve the desired value of K_{geo} it is clear that h_{g} needs to be quite large compared to what is typical for electrical machines of a similar size.

It was decided that a two-pole topology would be implemented as this maximises the amount of space available for the rotor winding and simplifies construction. The electrical frequency of multi-megawatt scale DD WTGs is typically quite low, on the order of ~15-25 Hz, which can be achieved by a two-pole design in the speed range of ~900-1500 RPM.

Since the maximum achievable saturation magnetisation of iron oxide based ferrofluid is relatively low (~0.15 T) compared to typical air-gap flux densities (~1.0 T) it was decided that the test rig only needed to be capable of fully saturating any tested ferrofluid: this would allow for full testing of a ferrofluid-gap magnetisation (M) curve. As explained in Chapter 5, Section 5.3.5, it is expected that the magnetic field will increase the viscosity of the ferrofluid due to the additional component of rotational viscosity, this effect does not increase significantly once the ferrofluid is magnetically saturated. Testing at relatively low flux densities is also advantageous since the ferrofluid-gap will have a very significant impact on the electrical output of the test rig: allowing for clear comparison against the baseline case of a conventional air-gap.

It is important to consider that K_{geo} depends on the test rig's 'hydrodynamic gap' and that the effective 'magnetic air-gap' ($g_{\mathrm{eff,TR}}$) of the test rig will be larger due to the material that is placed on the outer/inner layer of the rotor/stator to produce the smooth and cylindrical TC topology. An allowance was therefore made for additional material (h_{extra}) when considering the test rig's 'magnetic air-gap':

$$g_{\mathrm{eff,TR}} = h_{\mathrm{g}} + h_{\mathrm{extra}} \tag{6.8}$$

The air-gap flux density of the test rig can be estimated based on a basic 1D magnetic circuit analysis in which iron reluctance, slotting, and magnetic leakage are neglected:

$$B_g = \frac{\mu_0 \mathcal{F}_{\mathrm{RW}}}{2 g_{\mathrm{eff,TR}}} \tag{6.9}$$

where μ_0 is the permeability of free space, and $\mathcal{F}_{\mathrm{RW}}$ is the MMF from the rotor winding:

$$\mathcal{F}_{\mathrm{RW}} = N_{\mathrm{RW}} I_{\mathrm{RW}} \tag{6.10}$$

where N_{RW} is the number of rotor winding turns, and I_{RW} is the rotor winding current. The maximum flux density in the rotor core ($B_{\max}$) was estimated by considering the ratio of pole face width (w_{pole}) to the minimum rotor core width (w_{core}):

$$B_{\max} = \frac{w_{\mathrm{pole}}}{w_{\mathrm{core}}} B_g \tag{6.11}$$

To avoid overheating of the test rig components and to ensure that the ferrofluid-gap temperature would not deviate significantly during testing, the maximum current density of the rotor field winding was estimated and limited to $\sim 4\ \mathrm{A/mm^2}$:

$$J_{\mathrm{RW}} = \frac{\mathcal{F}_{\mathrm{RW}}}{C_{\mathrm{fill}} A_{\mathrm{cond}}} \tag{6.12}$$

where C_{fill} is a slot fill factor for the rotor winding and A_{cond} is the cross-sectional area of one rotor slot, estimated as:

$$A_{\mathrm{cond}} = 0.5\pi(r_2^2 - r_1^2) - w_{\mathrm{core}}(r_2 - r_1) \tag{6.13}$$

$$r_2 = r_r - w_{\mathrm{tip}} \tag{6.14}$$

$$w_{\mathrm{tip}} = 0.5\left(1 - \frac{w_{\mathrm{core}}}{w_{\mathrm{pole}}}\right) w_{\mathrm{core}} \tag{6.15}$$

$$w_{\mathrm{pole}} = \theta_{\mathrm{arc}} r_r \tag{6.16}$$

$$r_1 = r_{\mathrm{shaft}} + 0.5 w_{\mathrm{core}} \tag{6.17}$$

where r_1 and r_2 is the inner and outer radius of the slot respectively, w_{tip} is the width of the pole tips, r_{shaft} is the radius of the rotor shaft, w_{pole} is the pole face width, and θ_{arc} is the arc angle of the pole face. An annotated diagram of the rotor core is provided in Figure 6.4.

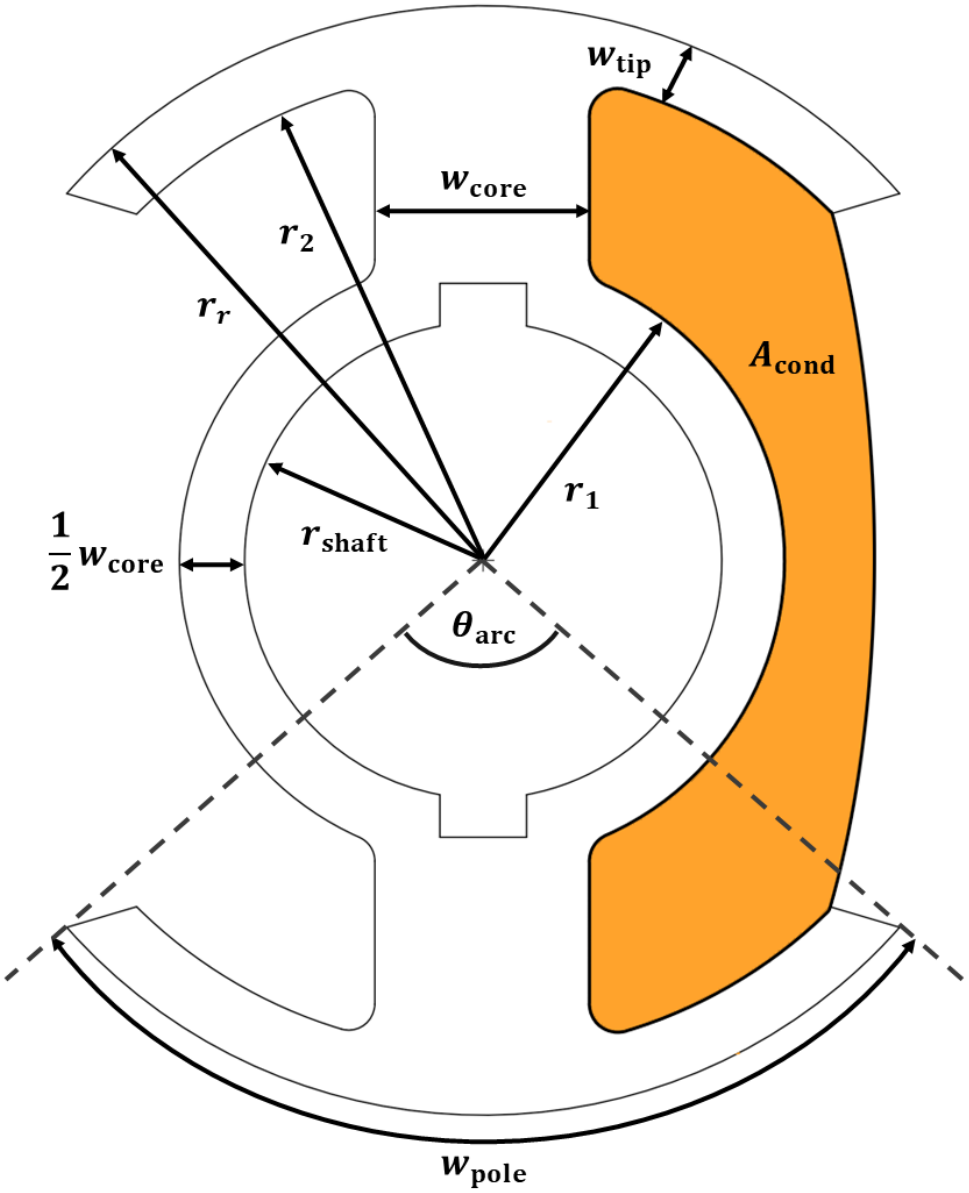

Figure 6.4: Annotated diagram of test rig rotor core geometry.

In Figure 6.5 the current density required to achieve a target test rig air-gap flux density of 0.3 T for the target K_{geo} of $2 \times 10^{-4}\ \mathrm{m}^2/s$ at a rotational speed of 1500 RPM is plotted for a range of rotor radii and slot fill factors according to the values provided in Table 6.2. For rotor radii greater than ~60 mm it appears that the target air-gap flux density can be achieved within the threshold for current density $(4\ \mathrm{A/mm}^2)$ for fill factors as low as ~0.3. It was therefore determined to be feasible that the target level of turbulence and air-gap flux density could be achieved in a machine with a rotor radius of ~60 mm without significant heating of the ferrofluid or magnetic saturation of

the rotor iron. As the test rig was developed further, finite element method (FEM) simulations were utilised to evaluate and refine the design.

Table 6.2: Test rig parameters for feasibility study.

Parameter	Symbol	Value	Units
Target turbulence at 1500 RPM	K_{geo}	2×10^{-4}	m^2/s
Target air-gap flux density	B_{g}	0.3	T
Maximum iron flux density	B_{max}	1.6	T
Rotor shaft radius	r_{shaft}	21	mm
Allowance for air-gap material	h_{extra}	2	mm
Rotor pole arc angle	θ_{arc}	$\pi/2$	rad

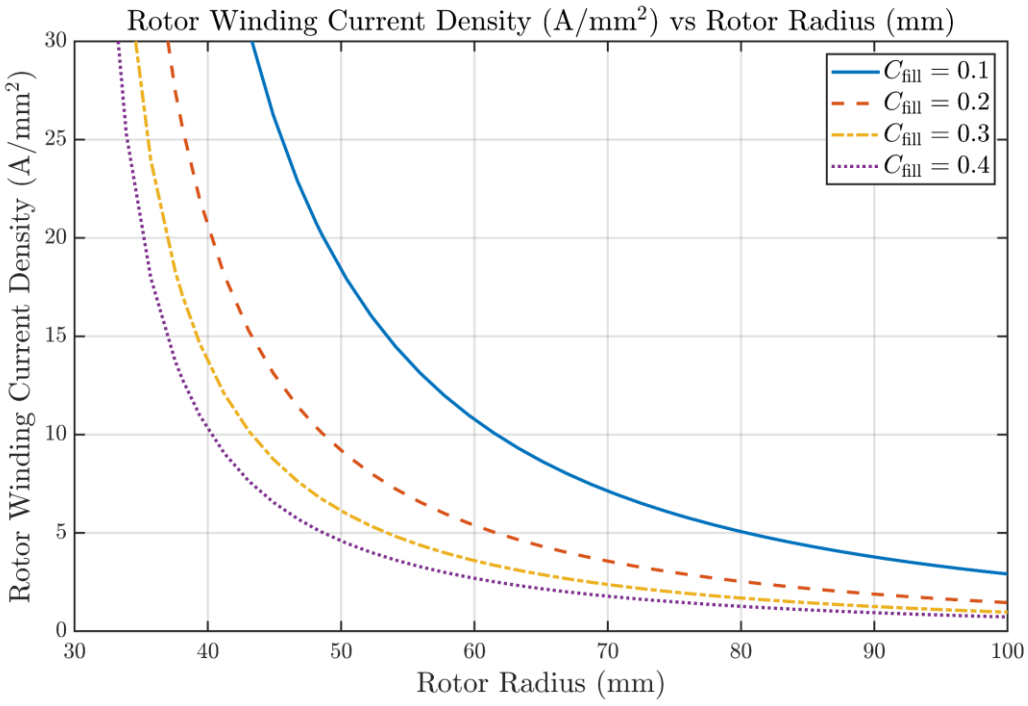

Figure 6.5: Current density of rotor winding (J_{RW}) vs rotor radius (r_r) for a range of rotor slot fill factors (C_{fill}) at a target K_{geo} of 2×10^{-4} m^2/s for a rotational speed of 1500 RPM.

6.2 Ferrofluid-Gap Test Rig Fabrication

The following section will discuss the fabrication of the ferrofluid-gap test rig which was undertaken by Fountain Design Ltd [164]. Rather than constructing the test rig completely from scratch it was decided to instead modify an off-the-shelf totally enclosed fan-cooled (TEFC) 2-pole 18.5 kW induction motor. This power rating was selected since the stator bore was large enough to accommodate the desired test rig rotor geometry, yet the machine still had a convenient weight and size.

The original squirrel cage rotor core was removed from the rotor shaft and a custom 2-pole rotor core was attached in its place. For the rotor winding, 600 turns of 1 mm diameter copper conductor were wound around the core. Excitation was provided to the rotor winding via slip rings that were attached to the non-drive end of the shaft. The terminals of the rotor winding were routed to the slip rings via keyways that were added to the shaft. The rotor core was cast in epoxy, machined to be cylindrical, wrapped with a 0.25 mm thick carbon fibre sheet, and finished with a file to produce a secure, smooth, and cylindrical rotor. In Figure 6.6 the key steps of rotor fabrication are pictured.

The stator was also cast in epoxy, a 139 mm outer diameter PVC tube was used along with custom end plates to produce an internal mould for the epoxy, the tube was cut away after the epoxy had set. A layer of 0.25 mm carbon fibre sheet was added to the inside of the stator bore, resulting in a smooth inner surface. Two fluid ports were added to allow for filling/draining of the air-gap region with ferrofluid. The air-gap region was sealed on either end of the core using radial shaft seals which were seated in purpose-built grooves and secured using silicone sealant. In Figure 6.7 the key steps of stator modification and final assembly of the test rig are pictured.

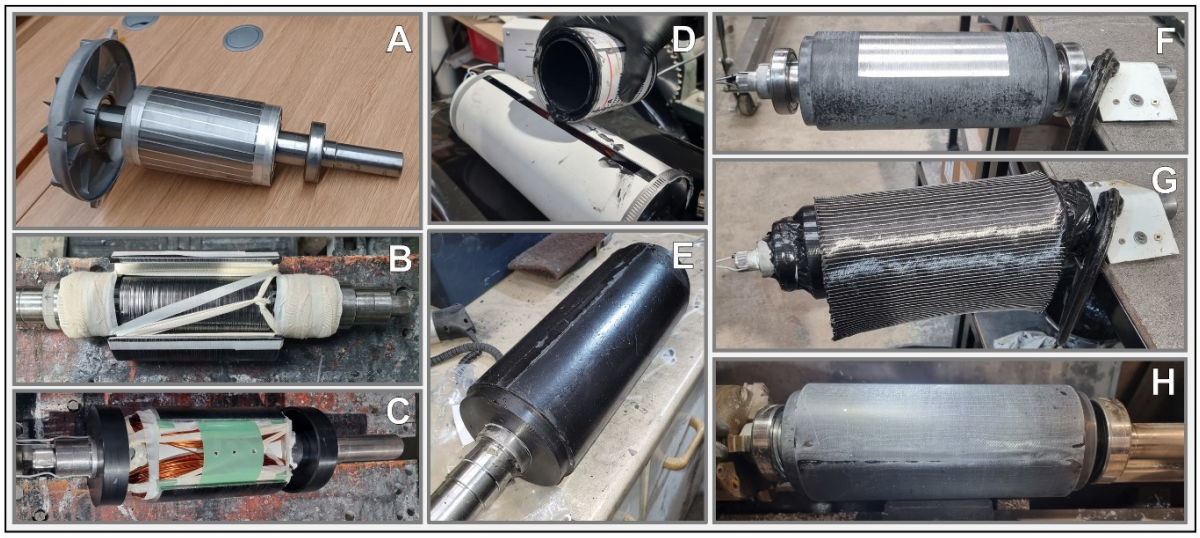

Figure 6.6: Key steps in fabrication of the test rig rotor: (A) The original off-the-shelf induction motor rotor prior to any modifications. (B) Original rotor core removed and custom 2-pole rotor core attached to the shaft. (C) Rotor core wound with 600 turns of 1 mm diameter copper conductor. (D) Rotor cast in epoxy. (E) Rotor after epoxy had set and mould removed. (F) Rotor after being machined. (G) Rotor being wrapped with a 0.25 mm thick carbon fibre sheet. (H) Completed test rig rotor.

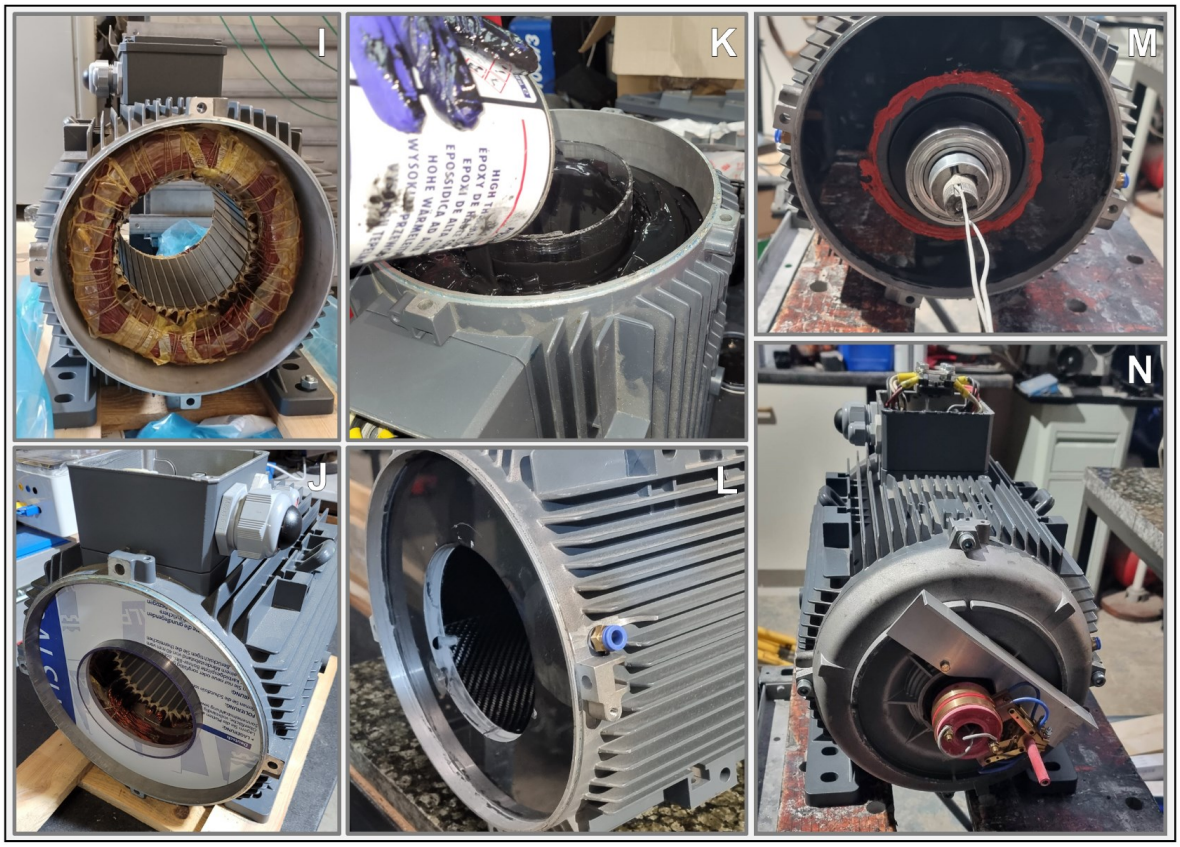

Figure 6.7: Key steps in fabrication of the stator and final assembly of the test rig: (I) The original off-the-shelf stator. (J) Internal mould placed within the stator. (K) The stator cast in epoxy. (L) The stator after having inner bore wrapped with 0.25 mm carbon fibre sheet and with filling/draining ports added. (M) Rotor placed into stator, each end of air-gap sealed with a radial lip seal and silicone sealant. (N) Final assembly of test rig, non-drive end pictured showing the slip rings for rotor winding excitation.

6.2.1 The Full Experimental Test Set-Up

Once completed the test rig was connected to a drive motor on a test bed via a torque transducer that measured both torque and speed. The drive motor was powered by a variable speed drive which provided closed-loop speed control according to feedback provided by an encoder attached to the motor. Excitation was provided to the rotor winding with an adjustable DC power supply and the excitation voltage was externally monitored and logged during testing. A thermocouple was positioned within one of the test rig's filling ports to provide an estimate of ferrofluid-gap temperature, while another measured ambient temperature. The voltage output of the generator was measured using voltage probes and an oscilloscope. The current output was measured using a current sensor and an oscilloscope. All data streams were synchronised and logged using a custom LabVIEW program on a PC. A block diagram and photos of the overall test set-up is provided in Figure 6.8 and Figure 6.9 respectively. The specification of each component is provided in Table 6.3.

Table 6.3: Components used in the full experimental set-up.

Component	Brand	Product
Inverter Drive	Parker	690+ series AC Drive
Induction Motor	AmTecs	AM2 180L4
Torque Transducer	Sensor Technology	TorqSense SGR521
DC Power Supply	RS Pro	RS-6005P
Load Bank	Cressall	AC30
DAQ Device	National Instruments	cDAQ-9174
Oscilloscope	Keysight	InfiniiVision DSOZ2002A
Thermocouple	Omega	5TC Series
Current Sensor	Rohde and Schwarz	HZO-50

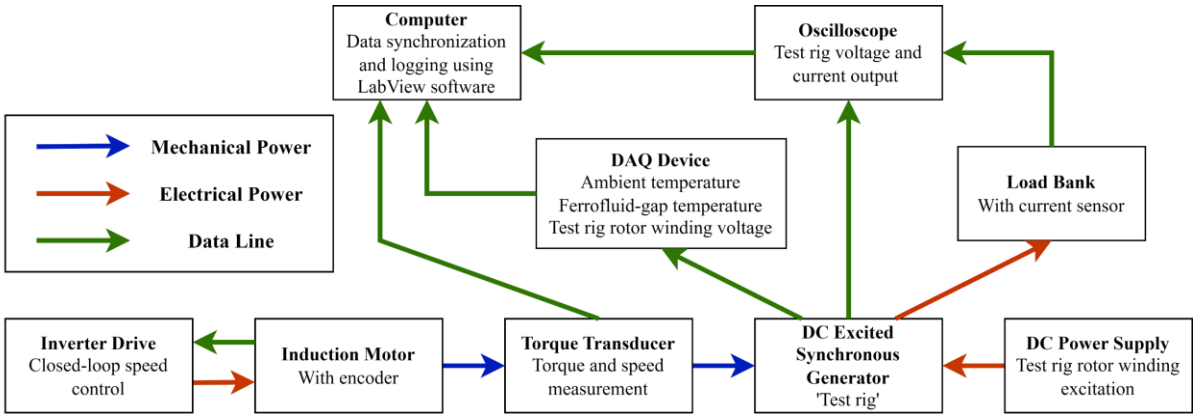

Figure 6.8: Block diagram of the overall experimental test set-up.

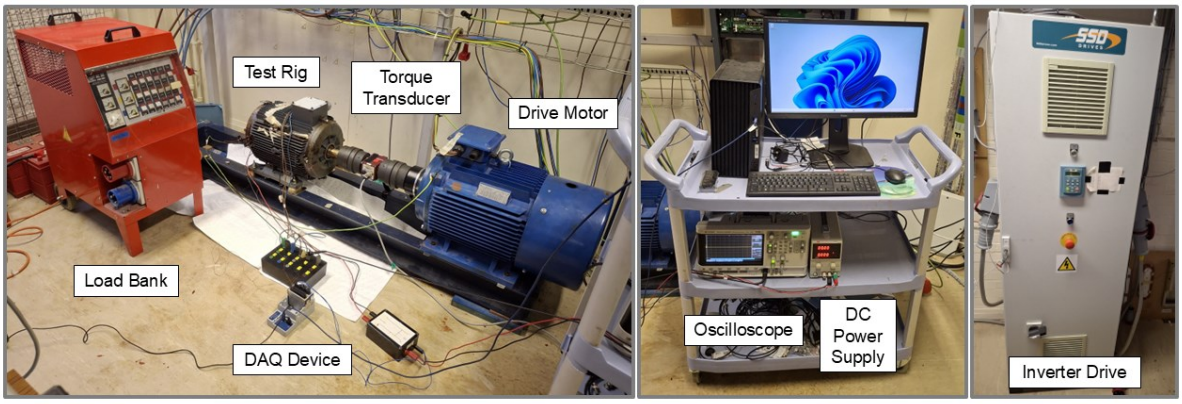

Figure 6.9: Photos of the overall experimental test set-up in open load conditions.

6.2.2 Detailed Test Rig Specifications

A FARO arm was used to obtain precision measurements of the test-rig geometry before and after the fabrication process [165]. A 3D scan was taken of one of the stator teeth to ensure that the geometry was represented accurately in simulations, this is shown in Figure 6.10. In Table 6.4 detailed specifications are provided for the test rig.

Table 6.4: Detailed test rig specifications.

Description	Symbol	Value	Units
Rotor outer radius	$r_{\mathrm{r,tot}}$	64.46	mm
Rotor core outer radius	$r_{\mathrm{r,mag}}$	64.0	mm
Stator inner radius	$r_{\mathrm{s,tot}}$	69.25	mm
Stator core inner radius	$r_{\mathrm{s,mag}}$	70.43	mm
Hydrodynamic air-gap	h_{g}	4.79	mm
Effective magnetic air-gap	$g_{\mathrm{eff,TR}}$	6.43	mm
Magnetic core length	l_c	180.8	mm
Hydrodynamic core length	l_h	283.0	mm
Tooth tip width	w_{TT}	13.91	mm
Tooth width	w_{tooth}	9.56	mm
Slot height	h_{slot}	30	mm
Number of slots	N_{slot}	36	–
Rotor winding turns	N_{RW}	600	–
Pole face arc angle	θ_{arc}	1.676	rad
TC aspect ratio	Γ_{TC}	59	–
K_{geo} at 1500 RPM	K_{geo}	2.99×10^{-4}	m^2/s
Shear rate at 1500 RPM	$\dot{\gamma}$	2114	s^{-1}
Stator winding turns per phase (2 parallel branches of 12)	N_s	24	–
Winding layout	AAAAAAC'C'C'C'C'C'BBBBBBA'A'A'A'A'A'CCCCCCB'B'B'B'B'B'		

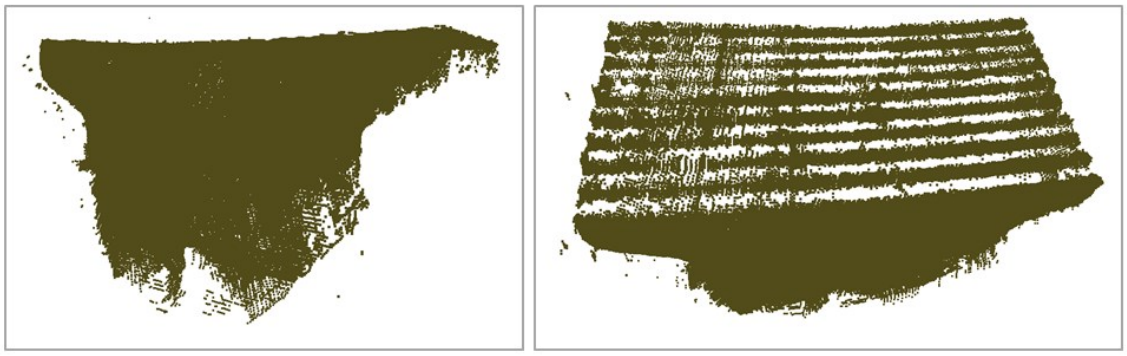

Figure 6.10: 3D scan of a test rig stator tooth.

6.2.3 Test Rig Commissioning

Once the full experimental test set-up was assembled the next step was to perform initial commissioning of the test rig to ensure that its performance matched expectations.

6.2.3.1 Air-Gap Flux Density

2D finite element method (FEM) magnetic simulations of the test rig were conducted in COMSOL Multiphysics 6.1. An image is provided of the simulation domain in Figure 6.11. The accuracy of the simulation method was validated by comparing the air-gap flux density obtained from the simulation with that measured with a Hirst Magnetic Instruments GM08 Gaussmeter at a rotor MMF of 1500 A. As shown in Figure 6.12 there is very good agreement between the experimental measurement and the simulation results.

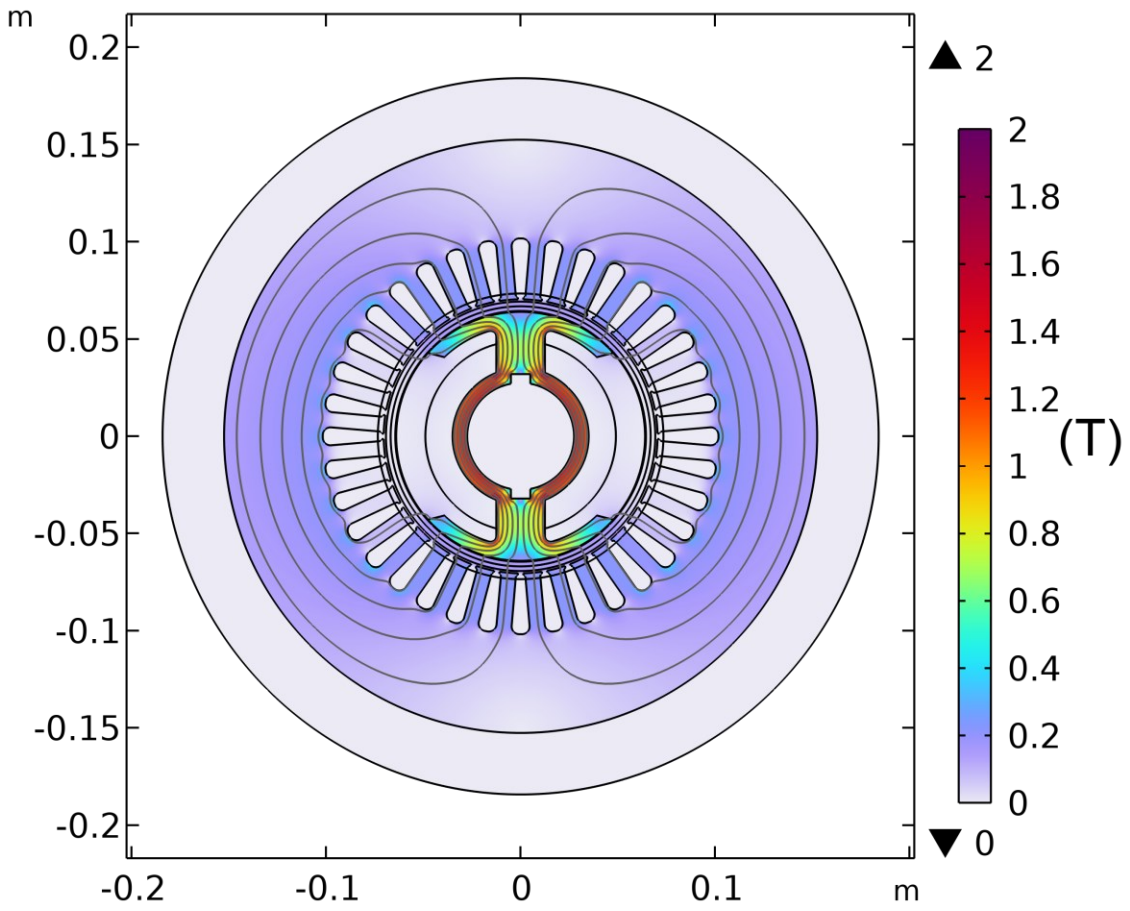

Figure 6.11: Image of a finite element method (FEM) simulation of the test rig with a rotor winding magnetomotive force (MMF) of 1500 A.

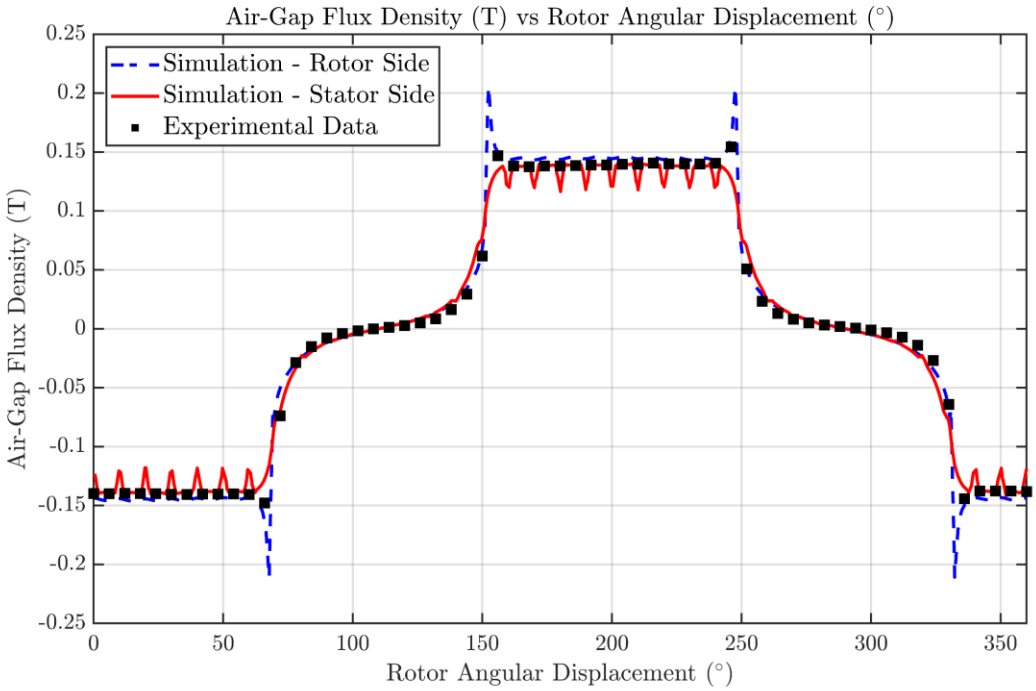

Figure 6.12: Comparison of test rig air-gap flux density with a rotor winding magnetomotive force (MMF) of 1500 A obtained via measurement with a gaussmeter and FEM (finite element method) simulation.

6.2.3.2 Shaft Alignment

The quality of the shaft alignment in the experimental set-up was assessed by examining the frequency spectrum of the torque measured at a constant speed of 1510 RPM. Figure 6.13 shows an example of a measurement indicating good alignment and a smooth drivetrain. There are well defined peaks of torque corresponding to multiples of the rotational frequency, the higher order torque harmonics are significantly smaller than the fundamental indicating that the drive motor and test rig are in good alignment [166].

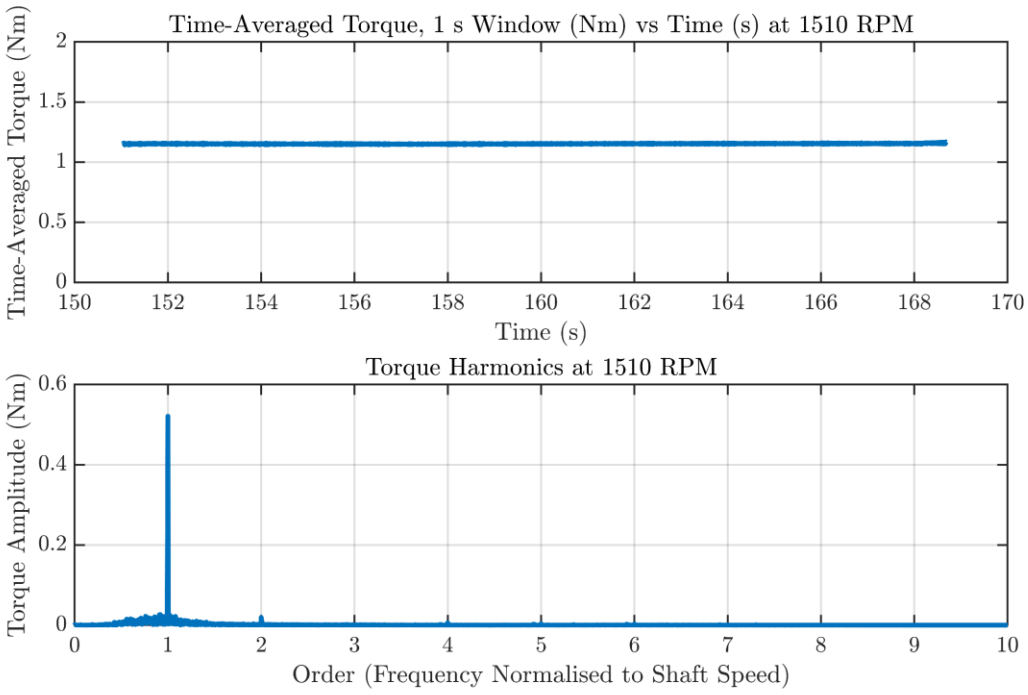

Figure 6.13: Time-averaged torque (1 s window) and torque harmonics measured by the torque transducer at a test rig rotational speed of 1510 RPM.

6.3 Tested Ferrofluids

The behaviour of three different ferrofluids was investigated in the experimental testing, their key properties are summarised in Table 6.5. For each ferrofluid specimen, the magnetisation curve and viscosity at various temperatures were measured directly, additional detail is provided in Appendix G.

Two of the ferrofluids were supplied by FerroTec [141]:

- FerroTec EFH1 Ferrofluid: EFH1 ferrofluid can be purchased ‘off-the-shelf’, it was therefore the first ferrofluid to be used in the test rig since procurement was

straightforward. It has a very low viscosity since the carrier fluid is a light hydrocarbon oil, this results in significant turbulence of the test rig's ferrofluid-gap.

- A custom ferrofluid was ordered from FerroTec, it was specified to have the same concentration of iron oxide nanoparticles as EFH1, however they were suspended in a mineral oil carrier fluid with a much larger viscosity. This allowed for a comparison of ferrofluid-gap behaviour for different intensities of turbulence while maintaining the same shear rate. It was also of interest to compare how viscosity influenced the ferrofluid-gap behaviour in the case of a partially filled gap.

As mentioned in Chapter 5, a ferrofluid sample was also synthesised in-house following the chemical co-precipitation method outlined in Appendix E. Although it was not feasible to produce a large sample of ferrofluid with the same quality as an industrial supplier it was of interest to investigate how the quality of the ferrofluid would influence the ferrofluid-gap behaviour. The 'In-House' ferrofluid arguably falls outside the standard definition of a ferrofluid since the average nanoparticle diameter is much larger than the typical range of ~5-15 nm. The specific magnetisation of the In-House ferrofluid nanoparticles is also relatively low due to significant oxidation during the synthesis process.

Table 6.5: Summary of tested ferrofluid properties.

Ferrofluid property	Symbol	Units	EFH1	Custom	In-House
Magnetic volume fraction	ϕ_{M}	–	0.077	0.077	0.043
Hydrodynamic volume fraction	ϕ_{H}	–	0.21**	0.21**	0.052**
Specific magnetisation of the ferrofluid particles.	ψ_M	$\mathrm{emu/g}$	86.53	86.53	15.82
Average particle magnetic diameter	d_M	nm	10	10	62.5
Saturation magnetisation	M_s	T	0.043**	0.042	0.0047
Density	ρ_{FF}	$\mathrm{kg/m^3}$	1206*	1233	959
Dynamic Viscosity at $35^{\circ}\mathrm{C}$	η_{FF}	$\mathrm{Pa.s}$	0.0063	0.195	0.128***

*Estimated based on a surfactant thickness of 2 nm.

**Average value of the four EFH1 samples.

***Measured at a shear rate of 200 1/s.

6.4 Conclusion

In this chapter, the design and fabrication of a novel ferrofluid-gap test rig were detailed.

In Section 6.1, the concept and design of the test rig were discussed. As highlighted in Chapter 5, Section 5.4, the theoretically predicted magnetic and mechanical behaviour of a ferrofluid-gap had not been experimentally validated in prior works. It was decided to construct a test rig in the form of a DC excited synchronous generator, this allows for independent measurement of the ferrofluid-gap magnetic and mechanical behaviour. By utilising a rotor winding, as opposed to permanent magnets, the strength of the rotor field can be modulated using a DC power supply. This allows for testing over a larger range of experimental conditions and facilitates an evaluation of how the magnetic field within the ferrofluid-gap influences the mechanical drag.

Since the ferrofluid-gap application of interest for this thesis is multi-megawatt scale direct-drive (DD) wind turbine generators (WTGs) the test rig geometry was scaled such that the extent of turbulence and shear rate in the ferrofluid-gap would surpass what would be expected in full scale machines. This resulted in a design with an unusually large air-gap clearance in comparison to its size. The geometry of the test rig was also idealised, taking the form of a Taylor-Couette apparatus, to simplify sealing of the ferrofluid and the comparison between the experimentally evaluated ferrofluid-gap drag and computational fluid dynamics (CFD) simulations.

In Section 6.2, the fabrication of the test rig is detailed, and the full experimental test set-up was explained. Key steps were detailed regarding the commissioning of the test rig. It was demonstrated that the 2D magnetic simulations of the test rig agreed with direct measurements of the air-gap flux density. It was shown that good alignment was achieved between the test rig, torque transducer, and drive motor on the test bed such that torque could be measured accurately.

In Section 6.3, the three different ferrofluids used in the experimental testing were introduced and their key properties summarised. Additional detail is provided in Appendix G.

Chapter 7: Experimental Validation of Ferrofluid-Gap Behaviour

This chapter details the various experimental investigations that were carried out using the ferrofluid-gap test rig introduced in Chapter 6. The objective behind the test rig was to validate the predicted magnetic and mechanical behaviour of ferrofluid-gaps, as detailed in Chapter 5.

The chapter is structured around each research question that was investigated using the ferrofluid-gap test-rig, for example:

- Are the ferrofluid-gap magnetic properties influenced by the fluid dynamic conditions, i.e. turbulence and shear rate?
- Does the magnetic field influence the ferrofluid-gap drag? If so, can this effect be predicted?

To answer such questions, distinct experimental methodologies were employed, and a variety of results were obtained. The experimental results were then compared with predictions obtained from magnetic, computational fluid dynamics (CFD), and multi-physics simulations. To present the results clearly, each section will be introduced with the key research question, the experimental methodology will then be detailed, the experimental results will be presented, and a discussion will follow in which the results are compared against the predicted ferrofluid-gap behaviour obtained from the corresponding modelling/simulation method.

In Section 7.1, the results for a ‘full’ ferrofluid-gap are presented, i.e. where the entire air-gap region was filled with ferrofluid. In Section 7.2, results are presented for cases in which the air-gap region was only partially filled with ferrofluid.

7.1 Full Ferrofluid-Gaps

The following section will detail the various experimental investigations that were conducted with a ‘full’ ferrofluid-gap.

7.1.1 Ferrofluid-Gap Magnetic Behaviour in Open-Load Conditions

In the following section the experimental methodology and the results for the test rig open load voltage output are presented. By comparing the open load voltage output of the test rig with an air- and a ferrofluid-gap key questions regarding ferrofluid-gap behaviour can be answered:

- Are the ferrofluid-gap magnetic properties influenced by the fluid dynamic conditions, i.e. turbulence and shear rate?
- Can the electrical machine performance with a ferrofluid-gap be predicted accurately?

7.1.1.1 Methodology and Baseline Measurements

First, the methodology for measuring the open load voltage output of the test rig is explained by presenting baseline measurements, i.e. measurements with an air-gap, of the test rig performance.

For each speed and rotor magnetomotive force (MMF) tested, it was ensured that a sufficient number of voltage waveforms were sampled to eliminate random error and provide an RMS voltage ($\mathcal{V}_{\mathrm{RMS}}$) value that was representative of the average rotational speed (ω). In Figure 7.1 an example of $\mathcal{V}_{\mathrm{RMS}}$ convergence is provided: the change in the mean value of $\mathcal{V}_{\mathrm{RMS}}$ obtained for a speed of 302 RPM and a rotor winding MMF of 1260 A is plotted against the number of samples considered.

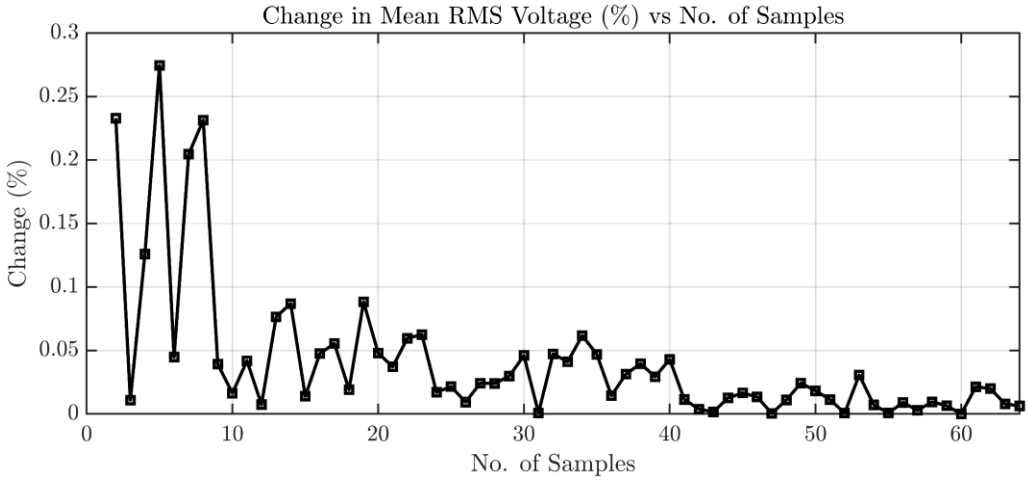

Figure 7.1: Change RMS Voltage measurement vs number of voltage waveform samples, rotational speed of 302 RPM and rotor winding magnetomotive force (MMF) of 1260 A.

Since the test rig is an iron-cored synchronous generator, a small voltage is produced in the absence of rotor winding excitation due to the residual magnetisation of the iron cores. While the influence of residual magnetisation is negligible at relatively large values of rotor winding MMF, steps were taken to minimise its impact on the experimental results to ensure that the influence of a ferrofluid-gap on the test rig performance could be reliably investigated for low values of rotor winding MMF.

To keep the impact of residual magnetisation consistent between baseline and ferrofluid-gap tests a 'zeroing' procedure was performed at the start of each test run. First, the polarity of the rotor excitation was reversed, and a current of 4 A was injected into the rotor winding by the DC power supply. The test rig was then driven by the drive motor in open-load conditions for one minute. The DC power supply was then switched off, and the polarity was reversed back to the original configuration. Then, starting from a rotor winding current of 0 A, the open-load voltage output was monitored at a rotational speed of 1208 RPM, and the current was increased gradually in increments of 1 mA. For a small rotor winding current, typically ~30 mA, a minimum magnitude of voltage output would be found: this was taken as the 'zero point' of the rotor winding MMF. Following IEEE guidelines, for each test run measurements of the test rig electrical output were taken at progressively increasing excitations from the zero point [167].

For each value of rotor MMF, a voltage-speed constant was obtained and normalised according to the rotor winding current:

$$Z_{VAI} = \frac{1}{I_{\mathrm{RW}}}\left(\frac{d\mathcal{V}_{\mathrm{RMS}}}{d\omega}\right)_{fit} \tag{7.1}$$

Where I_{RW} is the rotor winding current and $\left(\frac{d\mathcal{V}_{\mathrm{RMS}}}{d\omega}\right)_{fit}$ represents the slope of the linear least-squares fit of RMS line-to-neutral voltage versus rotational speed.

In Figure 7.2 Z_{VAI} is plotted for the baseline case of an air-gap over a range of rotor winding MMF values. A comparison is made between the trend of Z_{VAI} with and without the zeroing procedure. It is shown that the zeroing procedure results in a more consistent value of Z_{VAI} over the range of tested rotor winding MMF. The uncertainty in Z_{VAI} is represented by 95% confidence intervals of the linear regression fit.

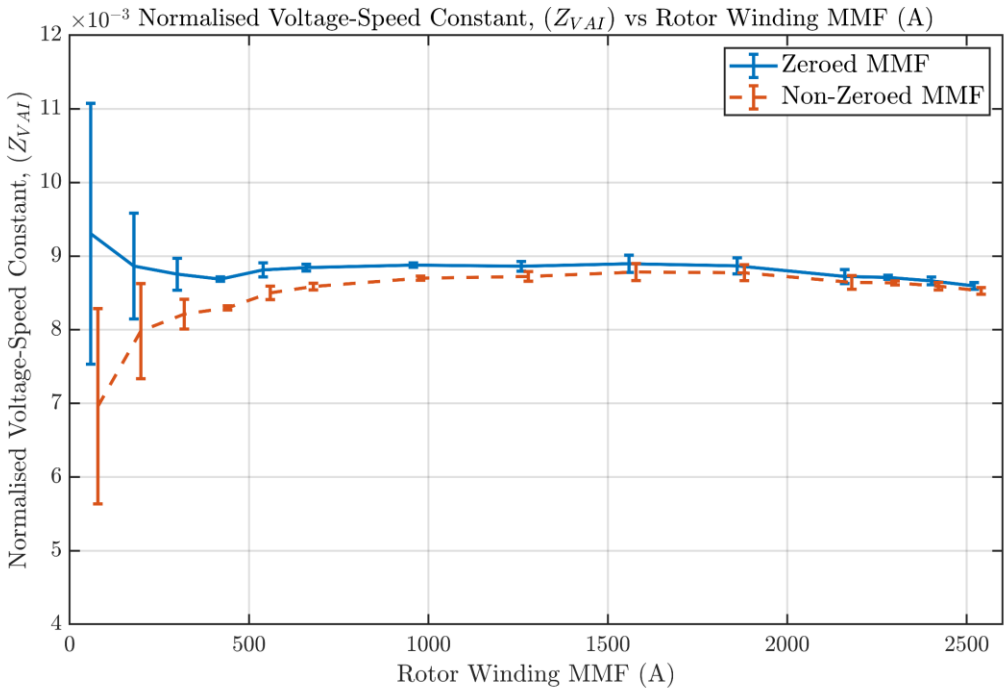

Figure 7.2: Open-load air-gap normalised voltage-speed constant (Z_{VAI}) plotted over a range of rotor winding magnetomotive force (MMF). Results are compared for when the MMF zeroing procedure is and is not followed.

In Figure 7.3 the trend of RMS voltage vs rotational speed and the voltage waveform is compared for a rotor winding MMF of 59 and 1861 A. At low values of rotor winding MMF, the measured data exhibits greater scatter due to the low output voltage of the test rig, making the measurement more sensitive to noise and residual magnetisation of the iron cores. In addition, at low excitation levels, the output current of the power supply is closer to its resolution limit, introducing additional uncertainty in the magnitude of the rotor winding current. The relatively large uncertainty in Z_{VAI} at low levels of rotor winding excitation can also be observed in Figure 7.2.

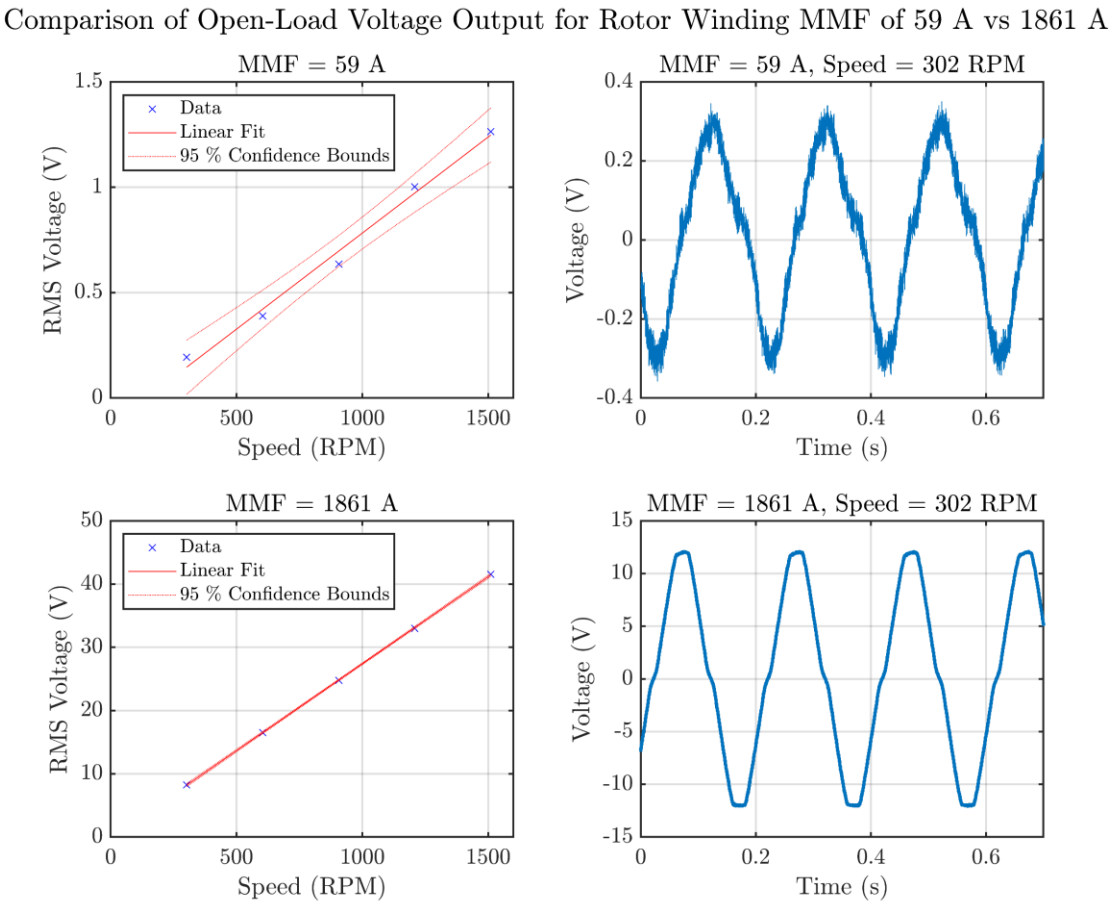

Figure 7.3: Comparison of open-load voltage output for a rotor winding magnetomotive force (MMF) of 59 A and 1861 A.

The open load saturation curve was obtained by measuring the RMS line-to-neutral voltage output at a constant speed of 906 RPM over a range of rotor excitations as shown in Figure 7.4. The voltage output can be seen to deviate from a linear trend once the rotor MMF exceeds ~2160 A (rotor current of ~3.6 A), which equates to a rotor winding current density of ~4.58 A/mm^2, indicating that the test rig's rotor core begins to magnetically saturate at a rotor excitation slightly larger than estimated in the initial design phase as detailed in Chapter 6, Section 6.1.2. Note that the saturation of the rotor core can also be observed in Figure 7.2 for rotor MMF values greater than 2000 A.

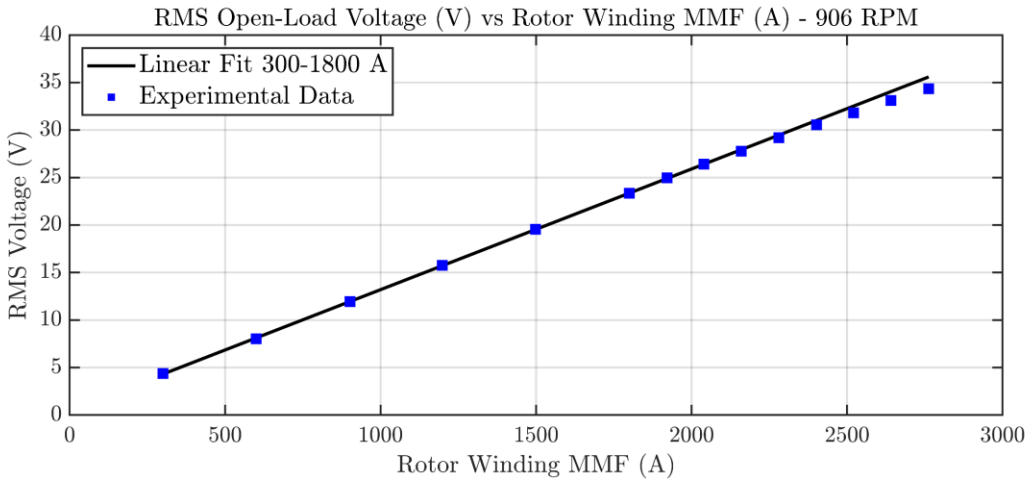

Figure 7.4: RMS open-load voltage vs rotor winding magnetomotive force (MMF). A linear fit is extrapolated from rotor winding MMF values of 300-1800 A.

7.1.1.2 Open-Load Voltage Output with Ferrofluid-Gaps

The open-load line-to-neutral voltage output was measured for a range of rotor winding MMF magnitudes and rotational speeds with the various ferrofluid-gaps. The experimental methodology was the same as described for the baseline air-gap measurements in which the zeroing procedure was followed.

In Figure 7.5 the RMS value of the open load voltage output is plotted for various rotational speeds and MMF values for EFH1, Custom, and In-House ferrofluid. In all cases, a ferrofluid-gap results in a higher voltage output compared to an air-gap. The relationship between RMS voltage and speed was observed to be linear for each of the ferrofluid-gaps.

Figure 7.6 shows the coefficient of determination (R^2) of the linear fit of RMS voltage versus speed for an air-gap and for each ferrofluid-gap over a range of rotor winding MMF values. For all cases there is an extremely good fit between the linear fit and the experimental data for rotor winding MMF magnitudes greater than ~300 A, suggesting that the magnetic behaviour of each ferrofluid was not influenced by the rotational speed of the test rig. The reduction in R^2 observed for MMF values less than ~300 A can be attributed to the low voltage output of the test rig as highlighted in Figure 7.3, there is no evidence that the ferrofluid-gap magnetic properties were influenced by the rotational speed for rotor MMF less than ~300 A.

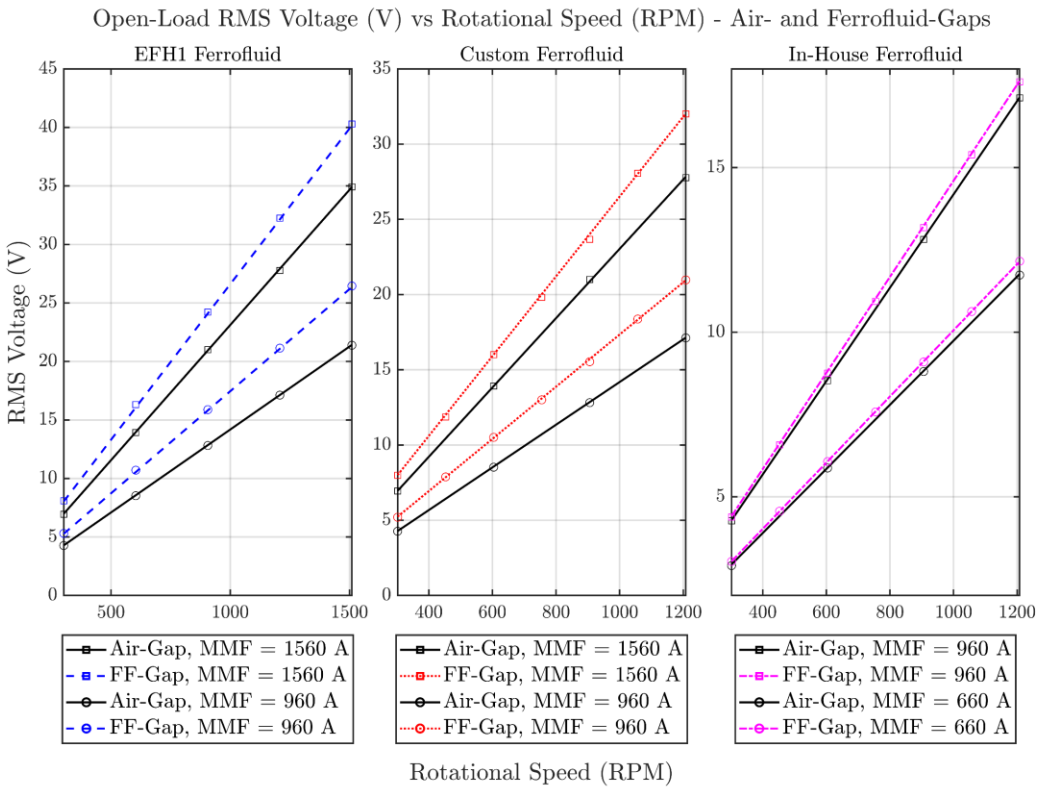

Figure 7.5: RMS open-load voltage output of each ferrofluid-gap compared against an air-gap for the same values of rotor winding magnetomotive force (MMF).

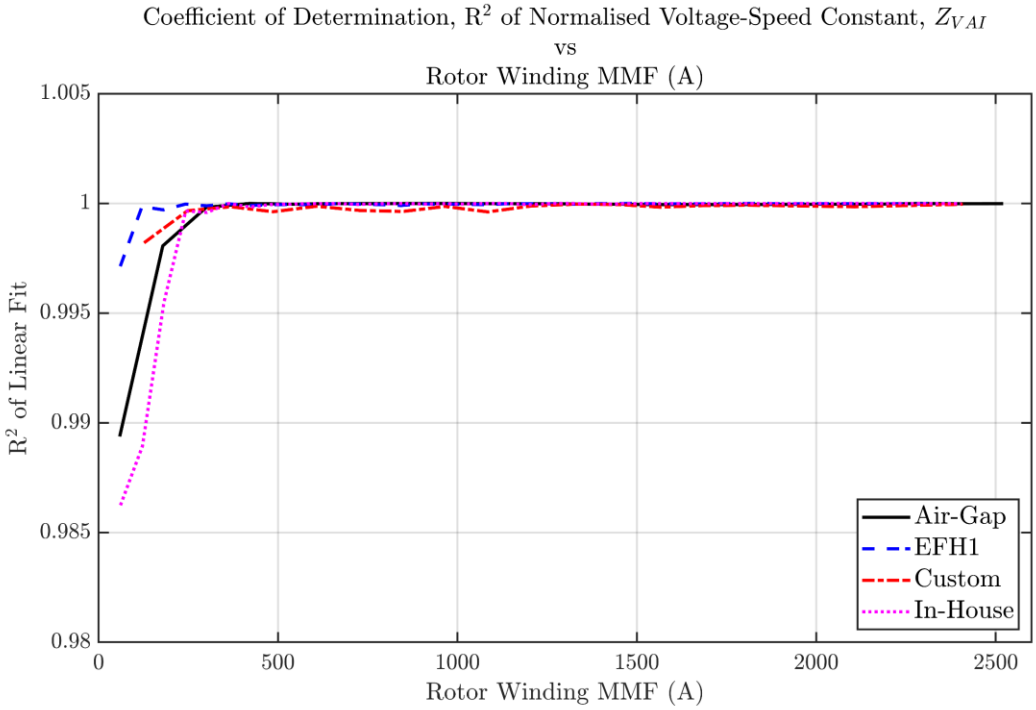

Figure 7.6: Coefficient of determination (R^2) of normalised voltage-speed constant (Z_{VAI}) obtained for each ferrofluid and an air-gap plotted over a range of rotor winding magnetomotive force (MMF).

In Figure 7.7 the line-to-neutral open load voltage harmonics are presented for the baseline air-gap and for a EFH1 ferrofluid-gap for a range of speeds and a rotor winding MMF of 300 and 1860 A. The harmonic amplitudes are normalised with respect to the fundamental harmonic for each speed and rotor MMF value. There is no significant indication that the rotational speed influenced the harmonics of the ferrofluid-gap open load voltage output. Similar variation in the normalised harmonic amplitudes is observed for both the air-gap and the EFH1 ferrofluid gap.

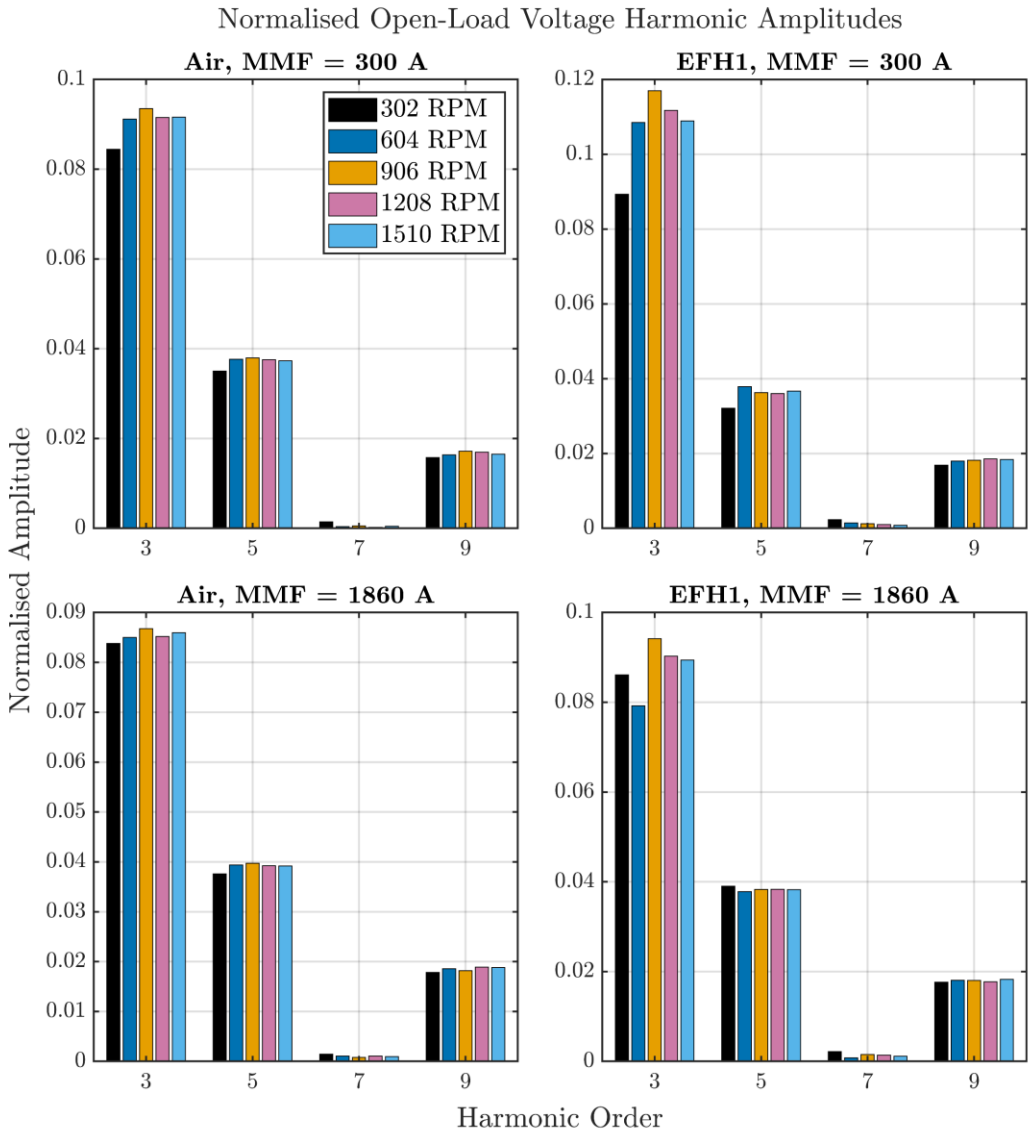

Figure 7.7: Normalised open-load voltage harmonic amplitudes with an air-gap and a EFH1 ferrofluid-gap for a range of rotational speeds. The harmonic amplitudes are normalised with respect to the fundamental harmonic amplitude for each rotational speed and rotor winding magnetomotive force (MMF) value.

In Figure 7.8 Z_{VAI} is plotted for a range of rotor excitations for the baseline case of an air-gap, and for each tested ferrofluid. The ferrofluid-gap experimental data shows a decreasing trend of Z_{VAI} with increasing rotor MMF, attributed to magnetic saturation of the ferrofluid.

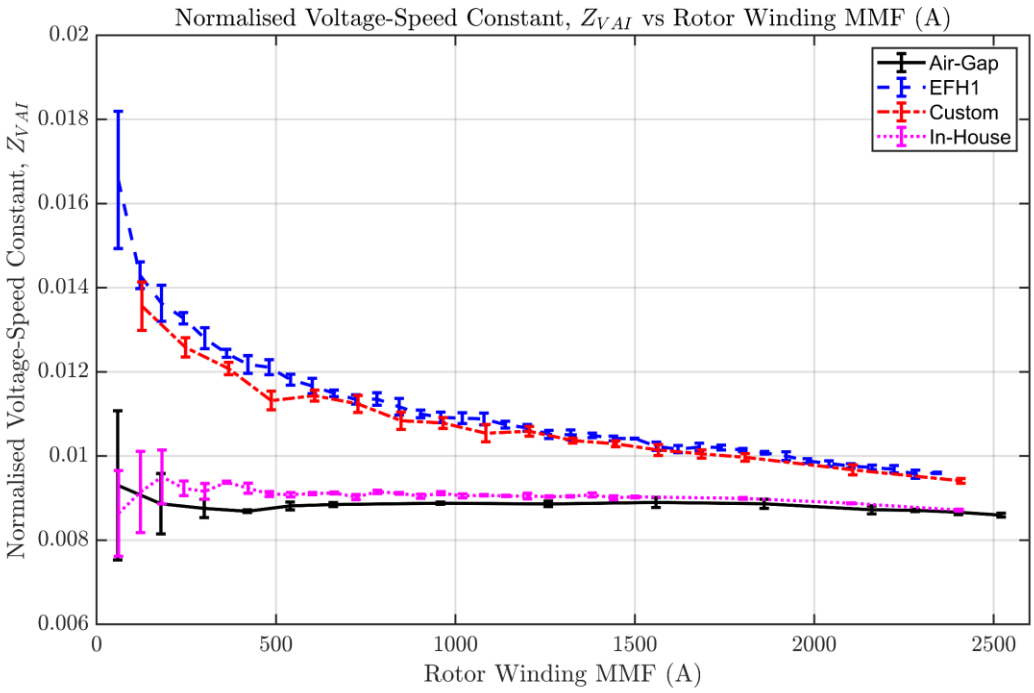

Figure 7.8: Normalised voltage-speed constant (Z_{VAI}) plotted for a range of rotor winding magnetomotive force (MMF) for an air-gap and each tested ferrofluid-gap.

7.1.1.3 Comparison with Simulation

In the following section, the influence of the various ferrofluid-gaps on the open load voltage output of the test rig is compared against FEM simulation results.

In the FEM simulations, the ferrofluid-gap is assigned a BH curve corresponding to the vibrating sample magnetometry (VSM) measurements of the samples as provided in Appendix G. The magnetic properties of the ferrofluid-gap region are assumed to be homogeneous.

Iron reluctance is neglected in the simulations by assigning the iron components a very large relative permeability of 1×10^7.

In Figure 7.9 the increase in RMS open load voltage output due to each ferrofluid gap is compared for the experimental data and the simulation results.

The experimentally observed increase in open load voltage was obtained by comparing the values of Z_{VAI} obtained for the ferrofluid-gaps and the baseline case of an air-gap. The uncertainty is represented as the summation of the baseline and ferrofluid-gap uncertainty in Z_{VAI}.

There is very good agreement between the experimental data and the FEM simulation results. The simulations predict a slightly larger increase in voltage output, this could be attributed to the neglect of iron reluctance in the simulations.

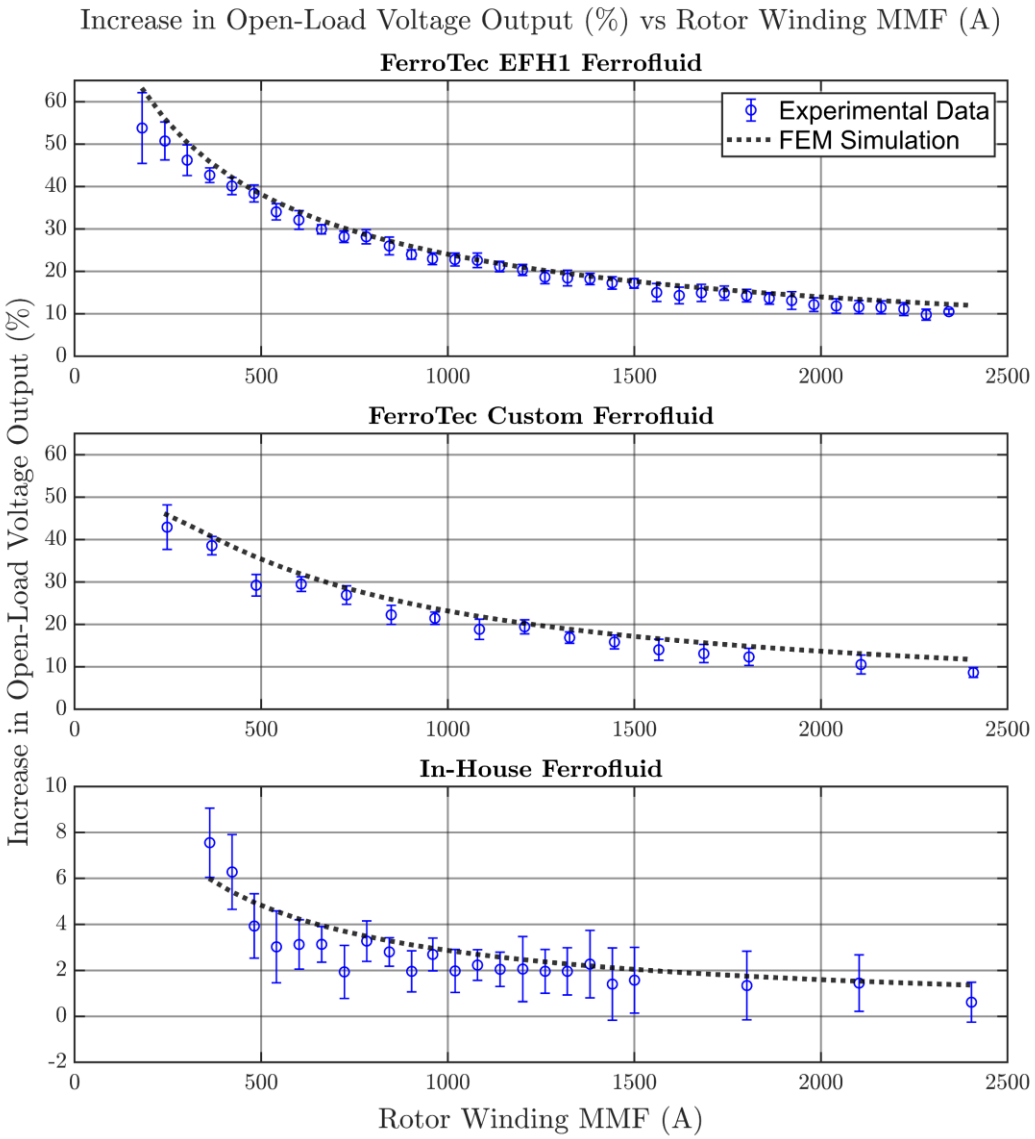

Figure 7.9: Comparison between the experimentally measured and simulated estimate for the increase in open-load voltage with each ferrofluid-gap compared to an air-gap.

In Figure 7.10 the influence of the ferrofluid-gap on the line-to-neutral open load voltage waveform is compared for experimental data and FEM simulations. The

experimental data is normalised against the experimental baseline measurements, and the FEM simulation is normalised against the baseline simulation data. The FEM simulations are observed to predict the influence of the ferrofluid-gap on the open load voltage output with reasonable accuracy.

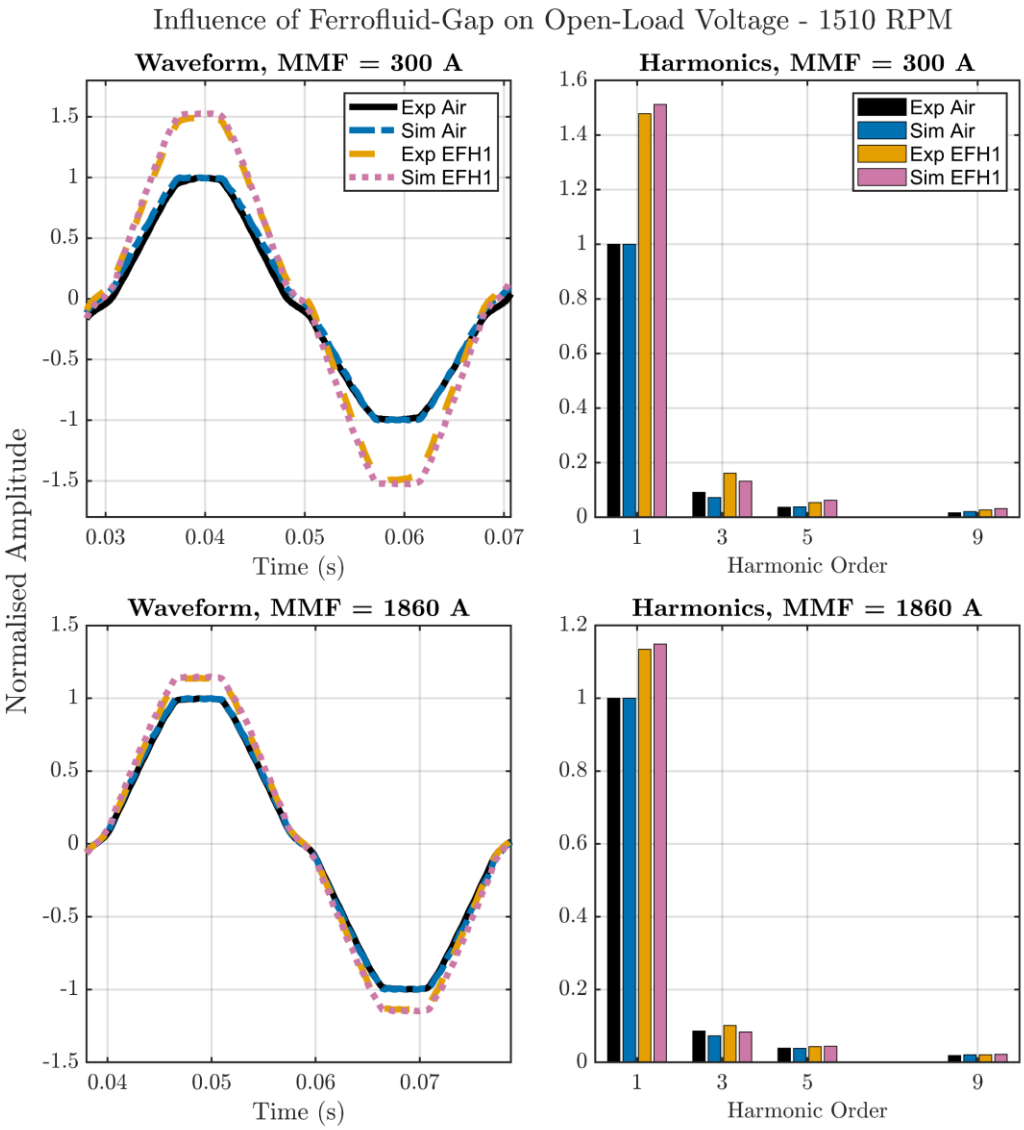

Figure 7.10: Comparison between the experimentally measured and simulated change in the open-load line-to-neutral voltage waveform of the test rig due to a EFH1 ferrofluid-gap compared to an air-gap. Data is presented for a rotational speed of 1510 RPM and a rotor winding magnetomotive force of 300 and 1860 A.

7.1.1.4 Summary of Ferrofluid-Gap Behaviour in Open-Load Conditions

To summarise the investigation of ferrofluid-gap behaviour in open-load conditions we can return to the key research questions:

- Are the ferrofluid-gap magnetic properties influenced by the fluid dynamic conditions, i.e. turbulence and shear rate?

As demonstrated in Section 7.1.1.2, the trend of open-load voltage output vs rotational speed was observed to be linear with the various ferrofluid-gaps. There was no indication that the rotational speed of the test rig influenced the impact that the various ferrofluid-gaps had on the open-load output voltage of the test rig up to a rotational speed of 1510 RPM.

Secondly:

- Can the electrical machine performance with a ferrofluid-gap be predicted accurately?

As demonstrated in Section 7.1.1.3, the increase in the test rig open-load voltage output due to a ferrofluid-gap was predicted accurately by the FEM simulations. The ferrofluid-gap was assigned a *BH* curve corresponding to the VSM measurements presented in Appendix G, and it was assumed that the ferrofluid-gap magnetic properties were homogeneous.

7.1.2 Influence of Magnetic Field on Ferrofluid-Gap Drag

In the following section it is investigated whether the magnetic field within the air-gap region influences the ferrofluid-gap drag. The key research question is:

- Does the magnetic field influence the ferrofluid-gap drag? If so, can this effect be predicted?

In short, the following experimental methodology is based on measuring and comparing how torque changes in response to excitation of the rotor windings in open-load conditions with an air- and ferrofluid-gap.

This investigation required very precise measurements of torque, involving the use of a torque transducer with an unusually low torque rating (8.5 Nm) and sensitivity ($\pm$0.0085 Nm) in comparison to the size and mass of the drive motor and test rig.

A novel test procedure was developed for this investigation as explained in the following section.

7.1.2.1 Open-Load Magnetic Torque

In open load conditions a small amount of torque is produced due to excitation of the rotor windings due to iron losses, residual magnetisation, and unbalanced magnetic pull (UMP) within the test rig, this will be referred to as the ‘open load magnetic torque’. The magnitude and behaviour of the open load magnetic torque must be taken into consideration such that the influence of the magnetic field on the ferrofluid-gap drag can be evaluated, this required baseline measurements for the case of a conventional air-gap.

Precise measurement of torque on a drive train of this size is challenging since there is a considerable amount of friction acting on the drivetrain, the magnitude of friction torque acting on the drive train is unsteady and difficult to predict since it depends on the operating conditions of the various bearings and seals in both the test rig and the drive motor.

It is therefore impractical to produce a precise measurement of the absolute value of torque since the frictional drag component will introduce significant error. This is especially problematic since the test rig had to be stripped down and rebuilt between different tests. Such an approach also requires very consistent zeroing of the torque transducer measurements which can be challenging.

However, the test rig was designed to circumvent this issue.

Since the test rig rotor utilises a DC excited coil to generate the rotor field (as opposed to permanent magnets) the ‘open load magnetic torque’ can be measured with precision by measuring the change in torque that occurs due to repeated cycling of the rotor winding excitation, i.e. turning the power supply ON/OFF.

In Figure 7.11 the time averaged torque history is shown for a test run in which the rotor coil excitation is repeatedly cycled ON/OFF at a test rig rotational speed of 1208 RPM. Clear trapezoidal peaks of torque are observed corresponding to changes in the rotor winding excitation. By measuring the magnitude of this change in torque the open load magnetic torque can be evaluated.

By repeating this measurement several times the random error can be reduced, allowing for precise measurement. Figure 7.12 compares the probability density of the torque data with a normal probability density function (PDF) using both a histogram and a quantile–quantile (QQ) plot. The distribution of the measured torque is shown to be well approximated by a normal PDF.

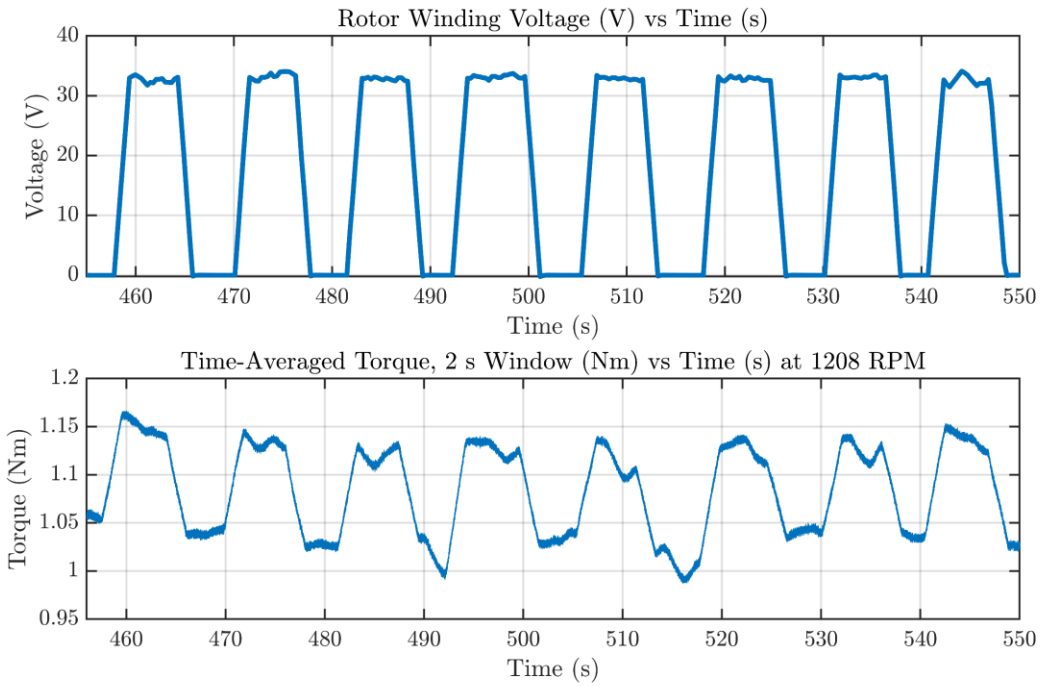

Figure 7.11: Example of torque variation due to excitation of the rotor windings.

The random error of the torque measurements was therefore represented by the standard error of the mean:

$$\Lambda_{\text{rand}} = \frac{\text{SD}}{\sqrt{N_{\text{rep}}}} \tag{7.2}$$

where SD is the standard deviation of the measurements and N_{rep} is the number of measurements.

The total measurement uncertainty was obtained by combining the torque transducer measurement uncertainty ($\pm$ 0.0085 Nm) with the random error:

$$\Lambda_{\text{tot}} = \sqrt{\Lambda_{\text{trans}}^2 + \Lambda_{\text{rand}}^2} \tag{7.3}$$

As shown in Figure 7.13, the total uncertainty is very close to the specified torque transducer accuracy, confirming that the measurement precision is primarily limited by the sensor accuracy rather than random variability in the test procedure.

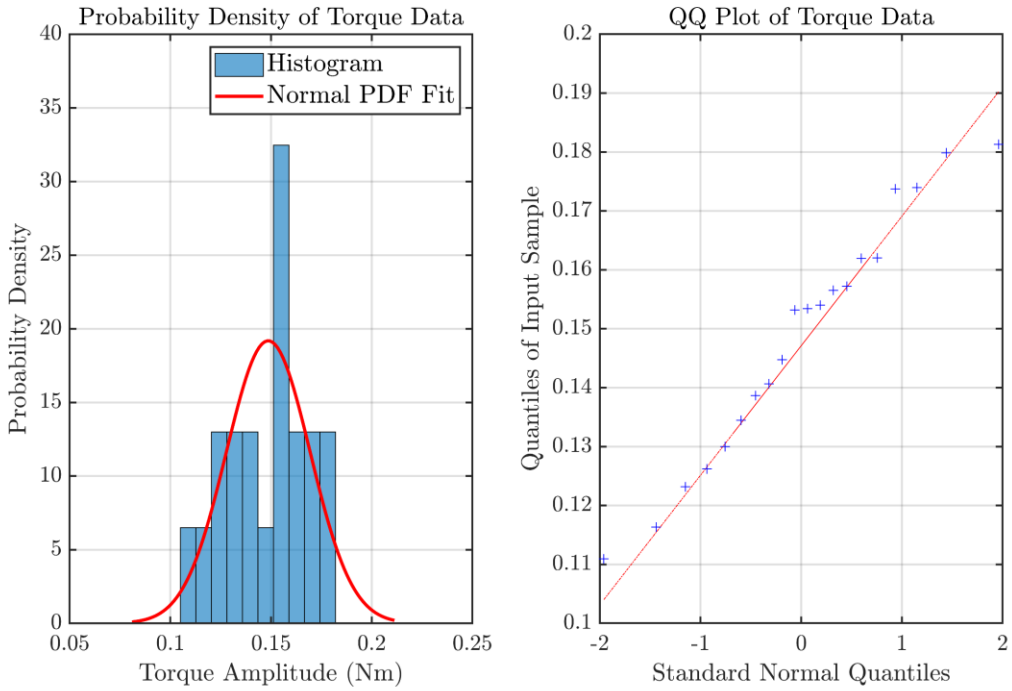

Figure 7.12: Probability density and a quantile-quantile plot of measurements of torque variation at a rotational speed of 1208 RPM and an excited rotor winding magnetomotive force (MMF) of 2400 A.

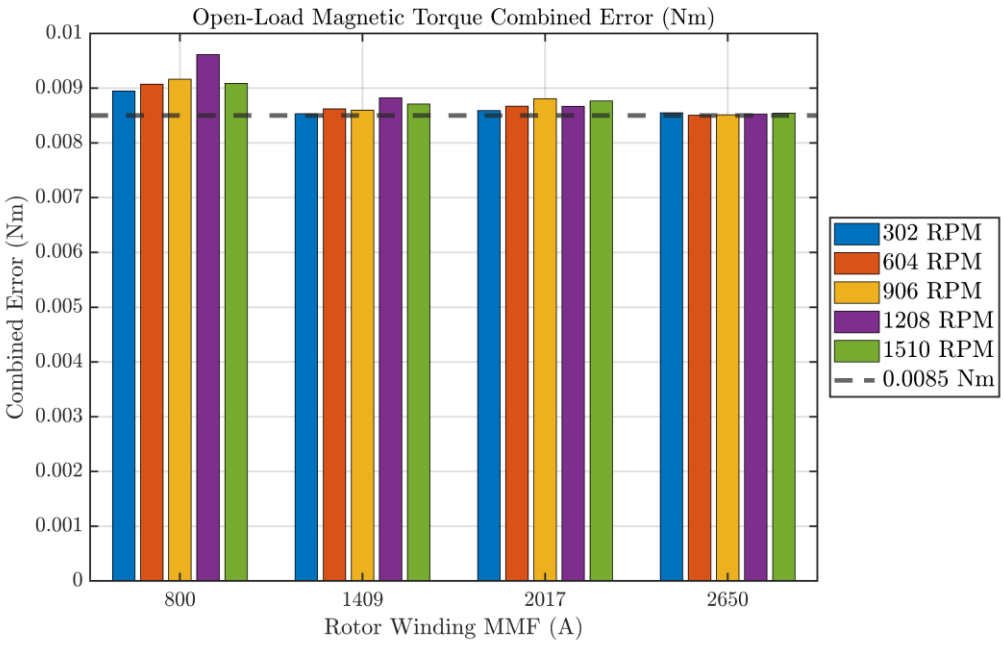

Figure 7.13: Combined error in the measurement of open-load magnetic torque for various rotational speeds and values of rotor winding magnetomotive force (MMF). The torque transducer measurement error (± 0.0085 Nm) is included for comparison.

The magnitude of the open-load magnetic torque corresponds to the magnetic flux produced by the rotor winding MMF. When a ferrofluid-gap is present, the magnetic flux will have a larger magnitude for a given value of rotor winding MMF. Therefore, it is not appropriate to estimate the magnitude of the open load magnetic torque according to the rotor MMF when performing tests with ferrofluid-gaps. Instead, the open-load magnetic torque was correlated with the RMS open-load voltage output of the test rig. This allows for an estimation of the open-load magnetic torque when a ferrofluid-gap is present.

Essentially, it is assumed that the RMS voltage output is proportional to the flux produced by the rotor winding MMF. This approach neglects any change in the spatial distribution of flux within the test rig due to a ferrofluid-gap. However, this is assumed to have a negligible influence in comparison to the measurement uncertainty of the torque transducer.

For each rotor winding MMF value, a second-order polynomial was fitted to the RMS open-load voltage as a function of rotational speed. The resulting fits were then used to construct a piecewise linearly interpolated surface, as shown in Figure 7.14 along with the experimentally obtained data points.

It can be observed that there is a non-zero magnitude of torque predicted for a rotational speed of 0 RPM. In Figure 7.15 the open load magnetic torque measured at standstill is presented for a range of relative rotor-stator positions. The torque magnitude varies according to the relative positioning of the rotor and stator, however it was consistently measured to act in the same direction. It was therefore assumed that unbalanced magnetic pull (UMP), together with residual magnetisation of the iron cores, was responsible for the non-zero open-load magnetic torque observed at standstill. The magnitude of this torque was found to be consistent for different test runs, including those conducted before and after complete disassembly and reassembly of the experimental set-up.

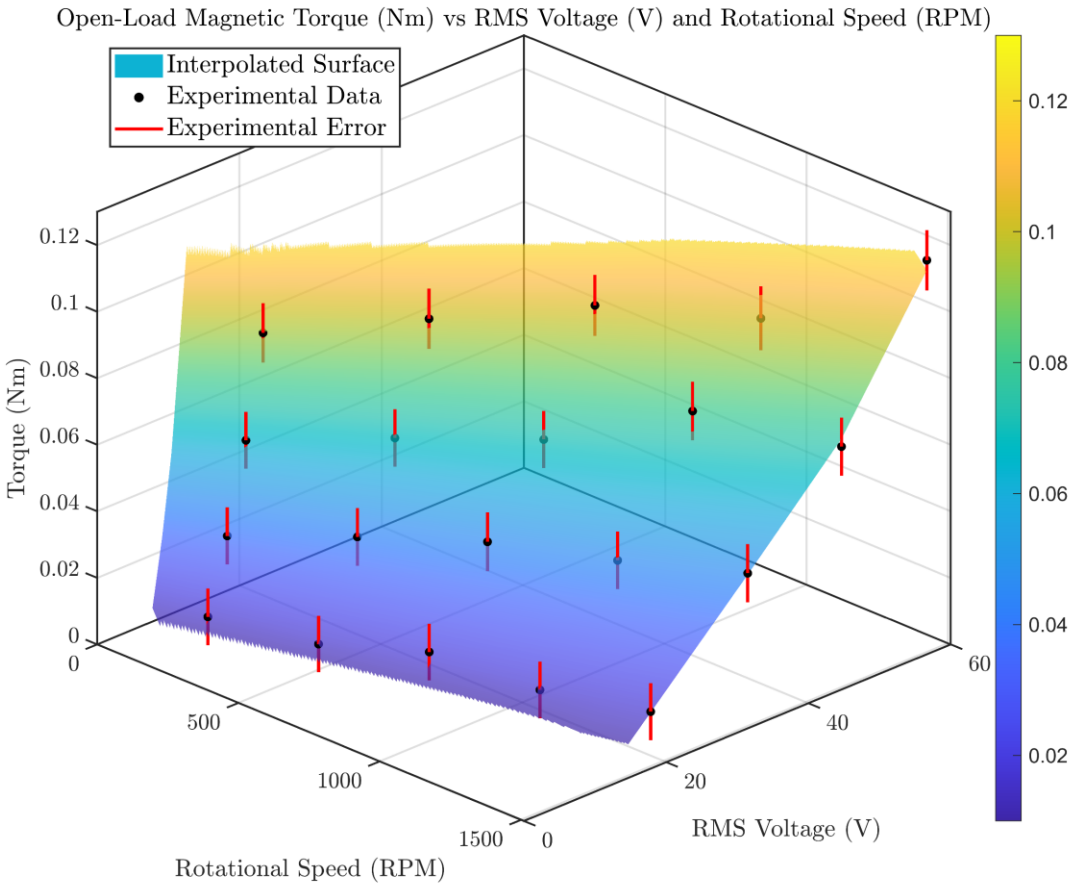

Figure 7.14: Surface plot of open-load magnetic torque (Nm) as a function of line-to-neutral RMS voltage output (V) and rotational speed (RPM).

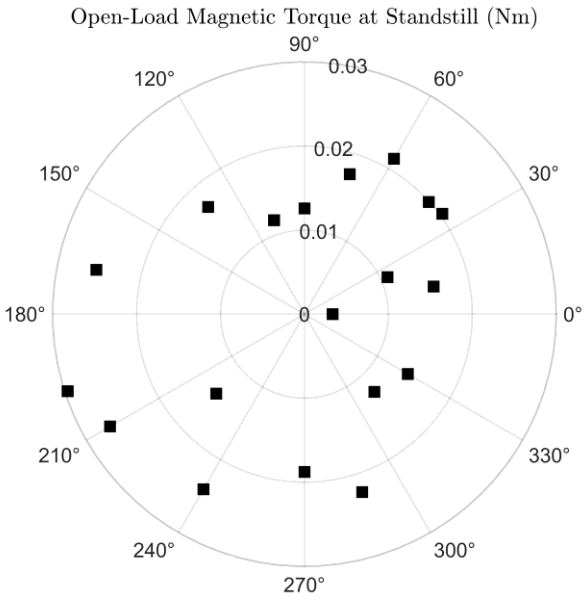

Figure 7.15: Open-load magnetic torque (Nm) measured at standstill over a range of rotor-stator relative positions (°).

7.1.2.2 Ferrofluid-Gap Open-Load Magnetic Torque

The influence of the magnetic field on the ferrofluid-gap drag was investigated by following the same procedure by which the open-load magnetic torque was obtained. In Figure 7.16 the torque history of a test with a Custom ferrofluid-gap is provided in which the DC power supply is cycled ON/OFF for various speeds, resulting in a rotor winding MMF that alternates between 0 A and 2400 A. The trapezoidal spikes in torque correspond to when the DC power supply is cycled between ON/OFF.

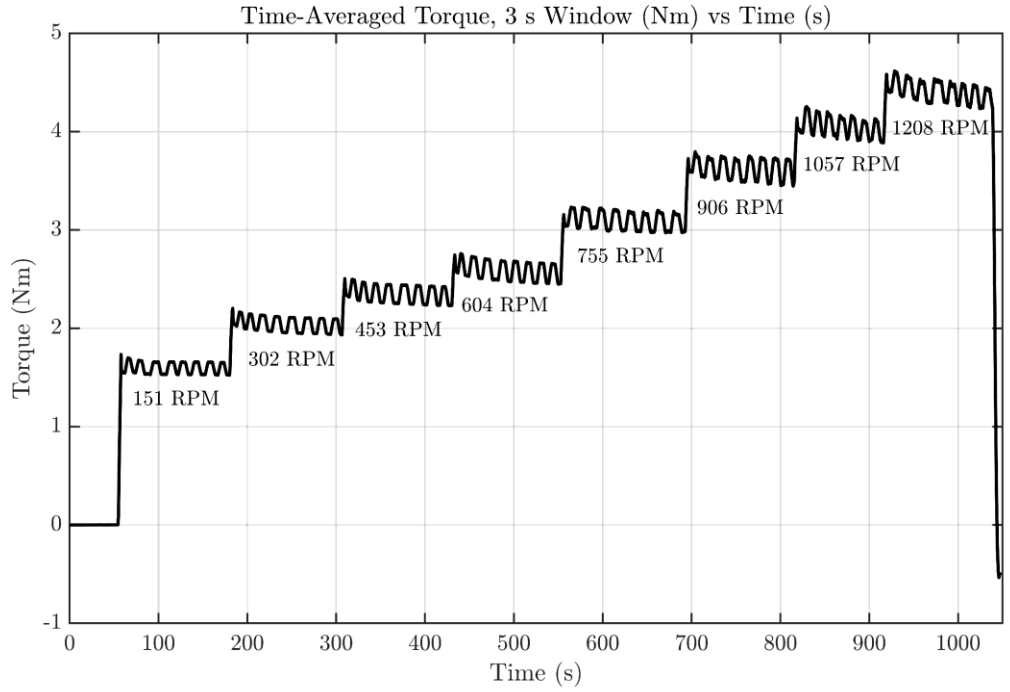

Figure 7.16: Example of time-averaged torque history (3 s window) during a test run with a Custom ferrofluid-gap.

The amplitude of each of the torque spikes was extracted from the data, and the baseline open load magnetic torque determined from the interpolation model, as shown in Figure 7.14, was subtracted to give an estimate of the increase in ferrofluid-gap drag due to the magnetic field. The uncertainty of this measurement was taken to be the summation of the error of the baseline open-load magnetic torque measurements ($\Lambda_{\mathrm{tot,air}}$) and that of the ferrofluid-gap measurements ($\Lambda_{\mathrm{tot,FF}}$):

$$\Lambda_{\mathrm{comp}} = \Lambda_{\mathrm{tot,FF}} + \Lambda_{\mathrm{tot,air}} \tag{7.4}$$

The ferrofluid temperature for each test was monitored via a thermocouple positioned in the filling port of the test rig. Since the viscosity of each ferrofluid is sensitive to

temperature, as detailed in Appendix G, an effort was made to maintain similar ferrofluid-gap temperatures between the different test runs. According to the measurements obtained from the thermocouple positioned within the test rig's filling port, the ferrofluid temperature was observed to vary by up to $7.5^{\circ}\mathrm{C}$ between the lowest and largest value measured in the tests. As shown in Appendix G, the viscosity of the EFH1 ferrofluid is the least sensitive to temperature, with a $25 - 32.5^{\circ}\mathrm{C}$ temperature range resulting in a ~16% variation in the viscosity. The Custom and In-House ferrofluid are more sensitive, with the same temperature range resulting in a viscosity variation of ~32% and ~25% respectively.

In Figure 7.17 the increase in drag found for each ferrofluid is plotted against rotational speed. Since the change in ferrofluid-gap drag due to the influence of the magnetic field was relatively small there is considerable uncertainty in the results, especially for the low viscosity EFH1 ferrofluid. However, it can be observed that the amplitude of the torque variations generally increases with speed. The amplitude of the torque variations also appears to increase nonlinearly with increasing rotor winding MMF.

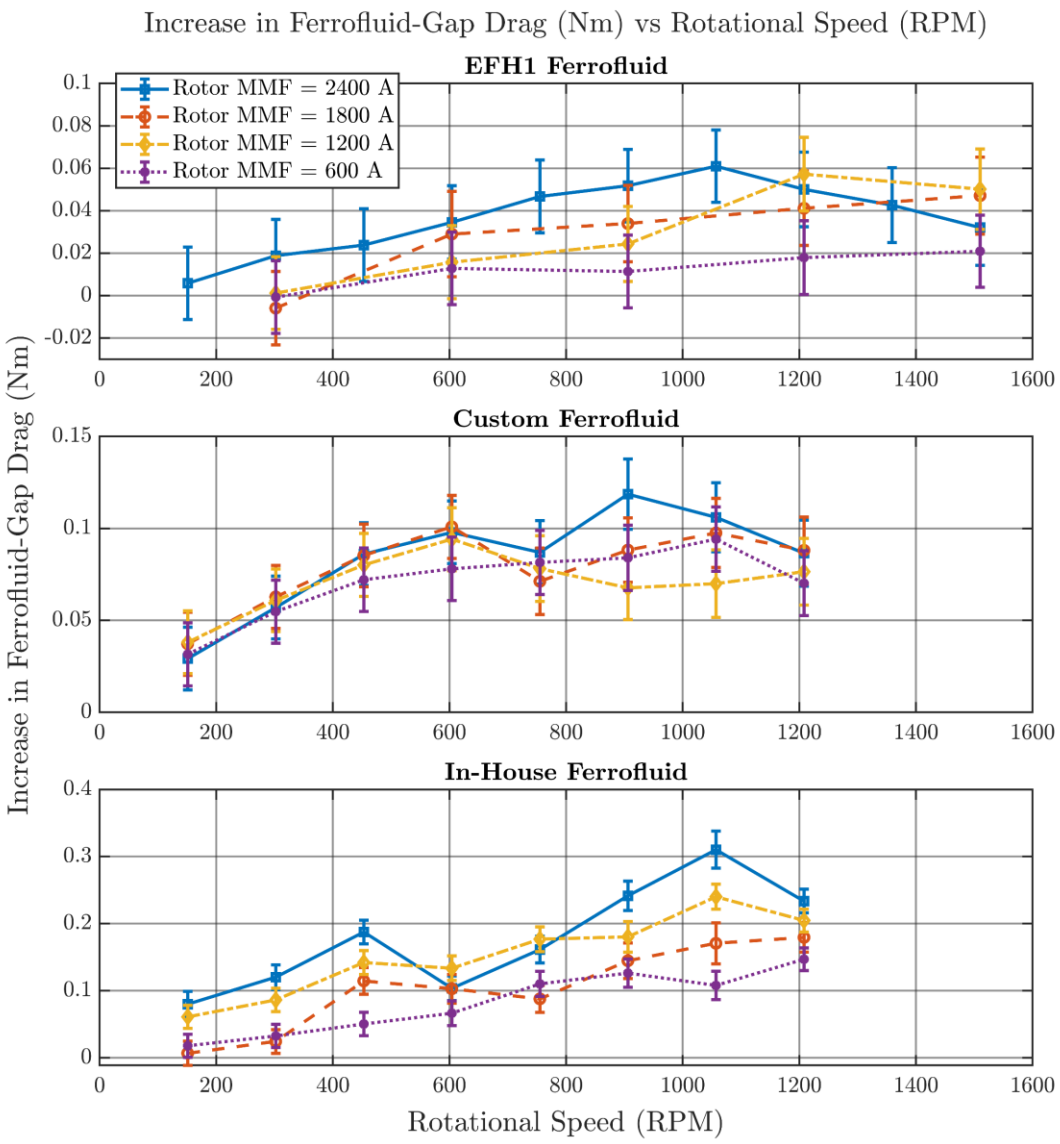

Figure 7.17: Experimentally obtained measurements for the increase in ferrofluid-gap drag due to the test rig magnetic field in open-load conditions for a range of rotor winding magnetomotive force (MMF) and rotational speeds (RPM).

7.1.2.3 Relative Increase in Ferrofluid-Gap Drag

For a better understanding of how the magnetic field influences the ferrofluid-gap drag the relative increase in drag, i.e. the increase in ferrofluid-gap drag due to the magnetic field in comparison to the absolute value of ferrofluid-gap drag in the absence of a magnetic field, was determined.

To quantify the relative change in ferrofluid-gap drag due to the magnetic field, the absolute value of ferrofluid-gap drag in the absence of a magnetic field had to be

determined. This was achieved using a combination of experimental results, CFD simulations, and analytical calculations.

As discussed in Section 7.1.2.1, the frictional drag within the test rig obscures the direct measurement of ferrofluid-gap drag. However, during open-load testing with an air-gap (including the ferrofluid-gap seals) it was observed that the frictional drag did not change significantly with rotational speed. Therefore, a value can be obtained experimentally for the change in the ferrofluid-gap drag due to the rotational speed with respect to a non-zero rotational speed reference point. For example, in Figure 7.16 the average torque measured with no rotor excitation can be obtained for each rotational speed. The change in torque with respect to a reference rotational speed of 151 RPM can then be calculated.

To estimate how the absolute value of ferrofluid-gap drag varies with speed, a value had to be determined for the reference rotational speed. The experimentally measured change in drag could then be added to this value to obtain an estimate for the total ferrofluid-gap drag in the absence of a magnetic field.

Since the Custom and In-House ferrofluid had a relatively large viscosity the ferrofluid-gap flow was expected to be laminar at low rotational speeds, the resulting torque due to ferrofluid-gap drag could therefore be approximated analytically:

$$\mathcal{T}_{\mathrm{drag}} = 4\pi\eta_{\mathrm{FF}}\omega l_h \left(\frac{r_{\mathrm{r,tot}}^2 r_{\mathrm{s,tot}}^2}{r_{\mathrm{s,tot}}^2 - r_{\mathrm{r,tot}}^2} \right) \tag{7.5}$$

where η_{FF} is the ferrofluid dynamic viscosity, ω is the test rig rotational speed, l_h is the test rig hydrodynamic core length, $r_{\mathrm{r,tot}}$ is the test rig rotor outer radius, and $r_{\mathrm{s,tot}}$ is the test rig stator inner radius.

The EFH1 ferrofluid had a relatively low viscosity, resulting in a transition to turbulent flow at relatively low rotational speeds. Therefore, computational fluid dynamics (CFD) simulations were performed such that the drag due to the turbulent EFH1 ferrofluid flow could be estimated. A large eddy simulation (LES) method was selected such that the unsteady nature of the flow could be captured, the LES method also facilitated the ferrohydrodynamic multi-physics simulations of EFH1 ferrofluid-gap flow which are detailed in Section 7.1.2.5. In Appendix H, the set-up of the CFD simulations is detailed.

The analytical calculations and CFD simulations of the ferrofluid-gap drag could then be validated against the experimental data by comparing the increase in drag with respect to the same reference speed. In Figure 7.18 the increase in drag vs speed is compared between experimentation and calculation/simulation for the various ferrofluids. The estimate of the total ferrofluid-gap drag is also provided.

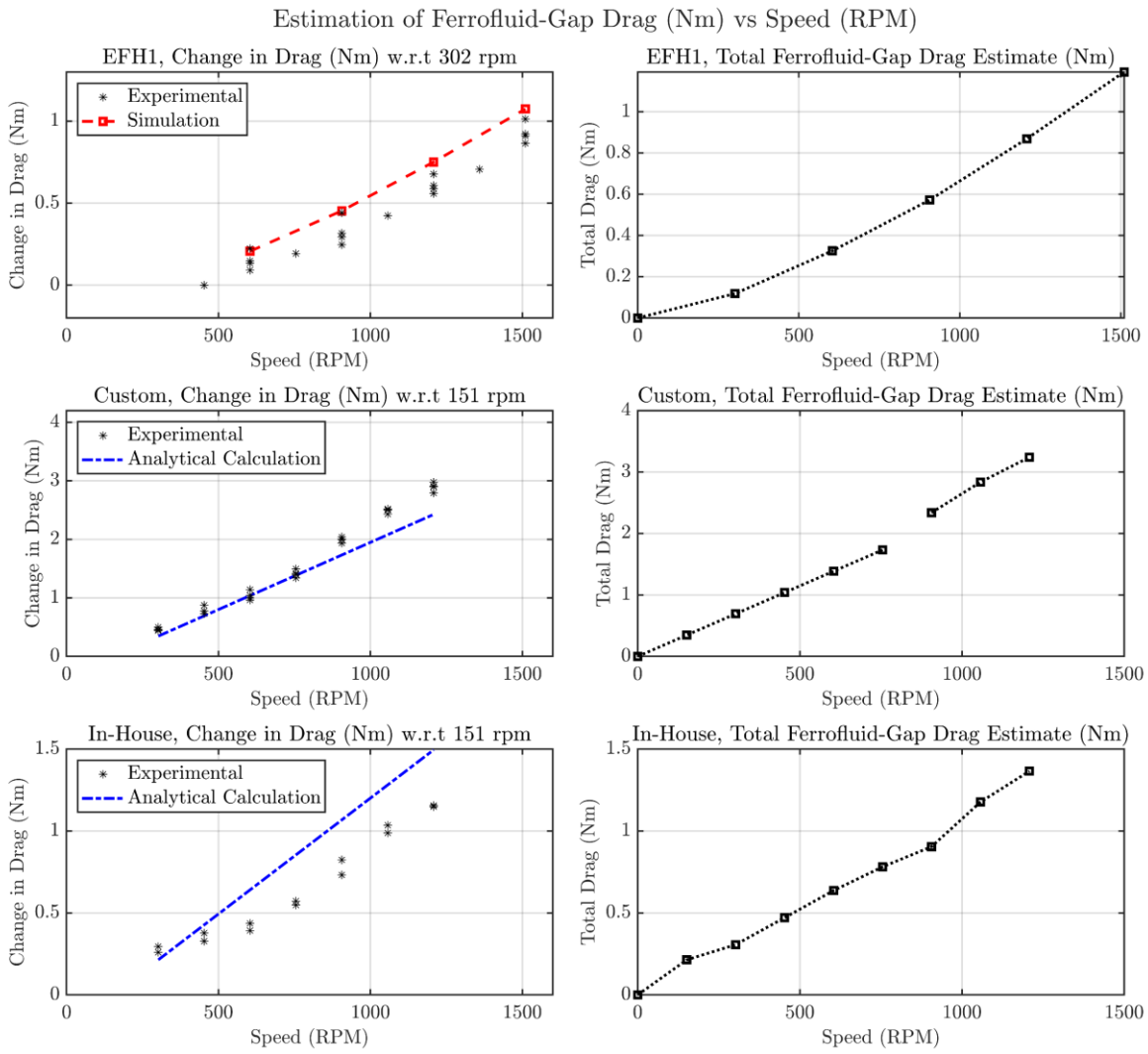

Figure 7.18: Estimation of ferrofluid-gap drag in the absence of a magnetic field. On the LHS the change in drag with respect to (w.r.t) a relatively low rotational speed is compared for experimental measurements and either simulation or analytical calculations. On the RHS an estimate for the total ferrofluid-gap drag is provided.

For the simulations and analytical calculations, the ferrofluid viscosity was specified according to the average temperature measured by the thermocouple during the tests. It was found that a good agreement would be achieved assuming that the average ferrofluid temperature was $5^{\circ}\mathrm{C}$ larger than that measured by the thermocouple.

Reasonable agreement was observed between the CFD simulations of EFH1 ferrofluid-gap drag and the experimental data. The analytical calculation of Custom ferrofluid-gap drag agreed well with the experimental data for speeds less than 755 RPM, the disagreement at larger speeds can be attributed to a transition to turbulent flow. The analytical calculation of In-House ferrofluid-gap drag had reasonable agreement for speeds less than 453 RPM, the disagreement at larger speeds can be attributed to a combination of shear thinning behaviour, as demonstrated in Appendix G, and a transition to turbulent flow.

In Figure 7.19 the relative increase in ferrofluid-gap drag due to the magnetic field is estimated by comparing the experimentally obtained values for the increase in drag due to a magnetic field, as in Figure 7.17, with the estimated absolute values of ferrofluid-gap drag in the absence of a magnetic field, as in Figure 7.18.

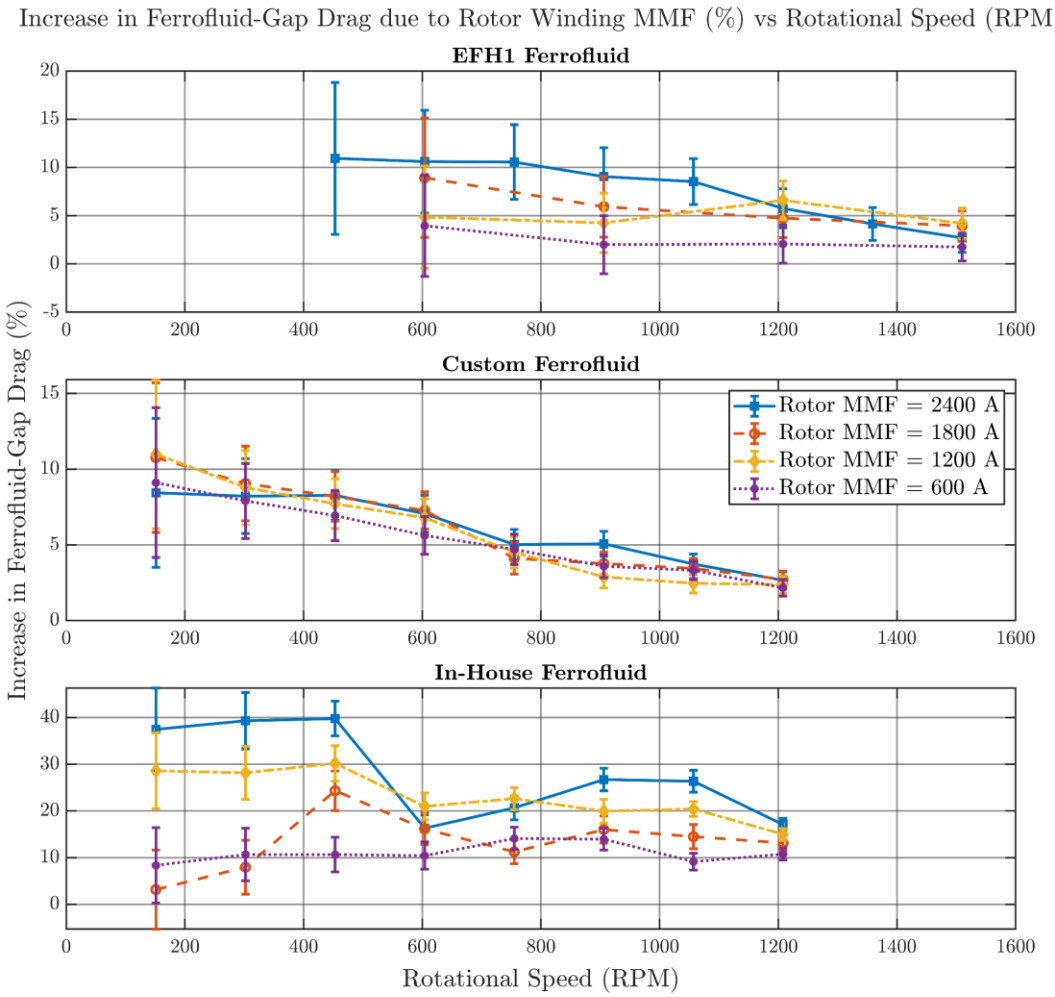

Figure 7.19: Experimentally measured increase in ferrofluid-gap drag due various values of rotor winding magnetomotive force (MMF) over a range of rotational speeds (RPM).

The increase in ferrofluid-gap drag due to the magnetic field was observed to decrease with increasing speed for each ferrofluid. The EFH1 and Custom Ferrofluid showed similar behaviour with a maximum increase of ~10% which decreased to ~3% as the rotational speed increased. As discussed in Chapter 5, Section 5.3.5, magnetoviscous effects due to particle chain formation are suppressed as shear rate is increased, this may explain the trend observed in the experimental data. However, an increase in drag would still be expected to occur for large shear rates due to the additional component of rotational viscosity.

The In-House ferrofluid displayed a larger change in drag due to the magnetic field in comparison to the EFH1 and Custom ferrofluid despite having a much lower saturation magnetisation (~10% the saturation magnetisation of the other ferrofluids). The In-House ferrofluid had much larger particles than the other ferrofluids (average diameter of 62.5 nm compared to 10 nm) and contained particles with diameters as large as 1000 nm. As explained in Chapter 5, Section 5.3.5, larger magnetic particles are more susceptible to chain formation when exposed to a magnetic field, this can result in a significant increase in viscosity. A comparison between the In-House and the EFH1 and Custom ferrofluid highlights the importance of ferrofluid quality in relation to the ferrofluid-gap performance. It is demonstrated that ferrofluids with appropriately sized ferrofluid particles (5-15 nm) exhibit less of an increase in ferrofluid-gap drag due to a magnetic field despite having a much larger saturation magnetisation.

Due to the sensitivity of the measurements and the variation in ferrofluid temperature during testing there is considerable uncertainty in the results, however it has been determined that the magnetic field increased the EFH1 and Custom ferrofluid-gap drag on the order of ~3-10% in relative terms. In the following sections this result is compared against theoretical predictions, and it is demonstrated that an increase of this magnitude can be expected.

7.1.2.4 Analytical Estimate for Ferrofluid-Gap Drag Increase

In the following section the observed change in EFH1 and Custom ferrofluid-gap drag due to the magnetic field is compared with an analytical estimate based on the increase in rotational viscosity. Recall the equation for the additional component of rotational viscosity:

$$\eta_{\mathrm{rot}} = \frac{3}{2}\phi_{\mathrm{H}}\eta_{\mathrm{FF},0}\frac{\xi - \tanh\xi}{\xi + \tanh\xi} < \sin^2\beta_\theta > \tag{7.6}$$

where ϕ_{H} is the hydrodynamic volume fraction, $\eta_{\mathrm{FF},0}$ is the dynamic viscosity of ferrofluid in the absence of a magnetic field, β_θ is the angle between the axis of vorticity and field direction (< ... > denotes the spatial average), and ξ is the Langevin parameter:

$$\xi = \frac{\mu_0 m H}{k_B T} \tag{7.7}$$

where m is the magnetic moment of the colloid, H is the magnetic field strength, and T is the temperature in Kelvin.

Approximating the flow as laminar and taking into consideration that the magnetic flux in the air-gap region will be mostly radial in direction such that $< \sin^2\beta_\theta > \approx 1$, the change in drag can be estimated according to the additional rotational viscosity component:

$$\Delta\eta = \frac{\eta_{\mathrm{rot}} + \eta_{\mathrm{FF},0}}{\eta_{\mathrm{FF},0}} = 1 + \frac{3}{2}\phi_{\mathrm{H}}\frac{\xi - \tanh\xi}{\xi + \tanh\xi} \tag{7.8}$$

Only a portion of the ferrofluid-gap is exposed to a significant magnetic field strength, a factor is therefore defined which considers the ratio of the ferrofluid-gap volume above the poles to the total ferrofluid-gap volume:

$$\Gamma_{\mathrm{FF,rotvis}} = \frac{l_c}{l_h}\frac{w_{\mathrm{pole}}}{\tau_{\mathrm{pole}}} \tag{7.9}$$

where l_c is the magnetic core length, l_h is the hydrodynamic length, and τ_{pole} is the pole pitch, and w_{pole} is the pole face width. Note that the ratio $w_{\mathrm{pole}}/\tau_{\mathrm{pole}}$ corresponds to the magnet width factor ($C_{\mathrm{PM,w}}$) introduced in Chapter 2, Section 2.1.3.

The relative increase in drag can then be estimated according to:

$$\Delta\mathcal{T}_{\mathrm{drag}} = \Gamma_{\mathrm{FF,rotvis}}\Delta\eta \tag{7.10}$$

The hydrodynamic volume fraction (ϕ_{H}) can be approximated by assuming a surfactant thickness of 2 nm as explained in Chapter 5, Section 5.2.4. The magnetic field strength can be obtained from either FEM simulations, or a magnetic circuit model of the electrical machine.

In Figure 7.20 the increase in ferrofluid-gap drag predicted for an EFH1 and Custom ferrofluid-gap is plotted for a range of rotor winding MMF values. The experimentally tested rotor winding MMF values are highlighted with black markers and text.

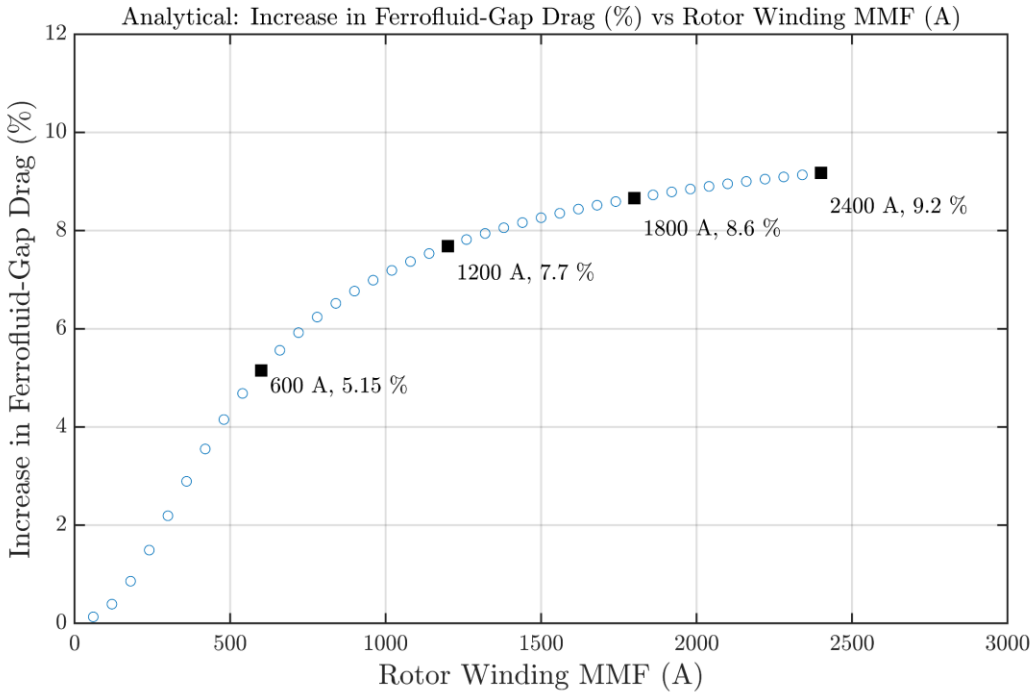

Figure 7.20: Analytical estimate for the increase in ferrofluid-gap drag due the rotor winding magnetomotive force (MMF). The experimentally investigated values of rotor winding MMF are highlighted.

The analytical prediction corresponds reasonably well to the experimentally obtained values presented in Figure 7.19. An experimentally obtained ferrofluid-drag increase of ~3-10% was obtained for EFH1 and Custom ferrofluid due to a rotor winding MMF of 2400 A, the analytical estimate predicts an increase of 9.2%.

According to Eq. 7.6, the rotational viscosity does not increase linearly with magnetic field strength, therefore the predicted change in ferrofluid-gap does not increase significantly beyond a rotor winding MMF of 1200 A. A similar trend can be observed in the experimental results.

As discussed in Chapter 5, Section 5.3.5, it is theorised that there is no rotational viscosity if the colloids are sufficiently small for Néel relaxation. The average colloid magnetic diameter of the EFH1 and Custom ferrofluid is 10 nm, which for a magnetite ferrofluid nanoparticle should be sufficiently small for Néel relaxation. However, it is likely that a portion of the ferrofluid nanoparticles are sufficiently large such that

Brownian relaxation occurs, and rotational viscosity takes place. Such an estimate is therefore prone to overestimating the increase in ferrofluid-gap drag due to the magnetic field, however it appears to work well as a convenient and conservative estimate. If the particle size distribution of the ferrofluid sample is known, then the estimate could be refined further by considering the percentage of ferrofluid particles in the sample that experience Brownian relaxation.

7.1.2.5 Multiphysics Simulation of Ferrofluid-Gap Drag

The analytical estimate for the increase in ferrofluid-gap drag due to the magnetic field presented in the previous section assumes laminar flow such that the angle between the axis of vorticity and the direction of the magnetic field (β_θ) is equal to 90° such that $< \sin^2 \beta_\theta > \approx 1$. However, for turbulent ferrofluid-gap flow this assumption is no longer valid due to the formation of vortices with varying orientations relative to the magnetic field, which leads to local fluctuations in β_θ. It can therefore be hypothesised that the value of $< \sin^2 \beta_\theta >$ decreases relative to that in laminar flow.

To obtain a more refined estimate of the change in ferrofluid-gap drag induced by the magnetic field, multi-physics simulations of ferrohydrodynamic flow within the ferrofluid-gap region were performed in COMSOL Multiphysics 6.1.

This was achieved by combining the FEM magnetic simulations of the test rig with the LES CFD simulations of the EFH1 ferrofluid-gap flow.

As discussed in Chapter 5, Section 5.3.3, and supported by the experimental results presented in Section 7.1.1.2 of this chapter, it is valid to assume that the fluid dynamic conditions of the ferrofluid-gap have no influence on the magnetic field within the test rig. Consequently, a one-way coupling approach was adopted: the results of the magnetic simulation were used to inform the LES simulation, while the LES results did not affect the magnetic field solution. This assumption significantly reduces the computational cost of the simulation compared to a fully coupled (two-way) approach.

The viscosity of EFH1 ferrofluid was specified to be a function of the local magnetic field strength in the radial direction and the angle (β_θ) between the magnetic field vector and the axis of vorticity in the flow:

$$\eta_{\mathrm{FF}} = \eta_{\mathrm{FF},0}\left[1 + \mathrm{ramp}(t)\left(\frac{3}{2}\phi_{\mathrm{H}}\frac{\xi - \tanh\xi}{\xi + \tanh\xi}\sin^2\beta_\theta\right)\right] \tag{7.11}$$

where $\mathrm{ramp}(t)$ is a ramping function implemented in COMSOL to ensure numerical stability and provide a valid initialisation condition for the CFD simulation. The coupling between the magnetic and CFD models was gradually introduced: the value of $\mathrm{ramp}(t)$ was initially zero and smoothly increased to one over a period of 0.14 seconds.

As with the analytical approach in the previous section the hydrodynamic volume fraction (ϕ_{H}) was approximated by assuming a surfactant thickness of 2 nm.

In Figure 7.21 a snapshot is provided for the ferrohydrodynamic multi-physics simulation of a EFH1 ferrofluid-gap at a rotational speed of 1510 RPM and a rotor winding MMF of 1800 A in open-load conditions. A coloured plot of ferrofluid-gap dynamic viscosity is overlaid on a greyscale plot of the flux density magnitude within the test rig. The dynamic viscosity of the ferrofluid can be observed to increase above the pole faces due to the magnetic field developed by the rotor winding MMF. For a EFH1 ferrofluid-gap at 1510 RPM the flow is highly turbulent, therefore the value of β_θ varies throughout the ferrofluid-gap, this results in a non-uniform increase in the dynamic viscosity above the rotor poles as indicated by the variation in colour within the ferrofluid-gap region.

It was not feasible to simulate the entire ferrofluid-gap region due to the computational cost required, i.e. a 3D magnetic simulation coupled to a full-scale 3D CFD simulation. Therefore, a factor must be applied to the simulation results to account for the end-spaces in which the ferrofluid-gap is not exposed to a significant magnetic field strength:

$$\Gamma_{\mathrm{FF,rotvis}} = \frac{l_c}{l_h} \tag{7.12}$$

In Figure 7.22 the torque due to the ferrofluid-gap drag is plotted against time for a simulation in which there was no magnetic field, and for a rotor winding MMF of 1800A for rotational speeds of 604 and 1510 RPM. In both cases an increase in torque was observed due to the additional rotational viscosity of the ferrofluid above the pole faces. By averaging the torque after the flow reached a fully developed state a relative increase of 4.3% and 6.1% was obtained for a rotational speed of 604 and 1510 RPM respectively.

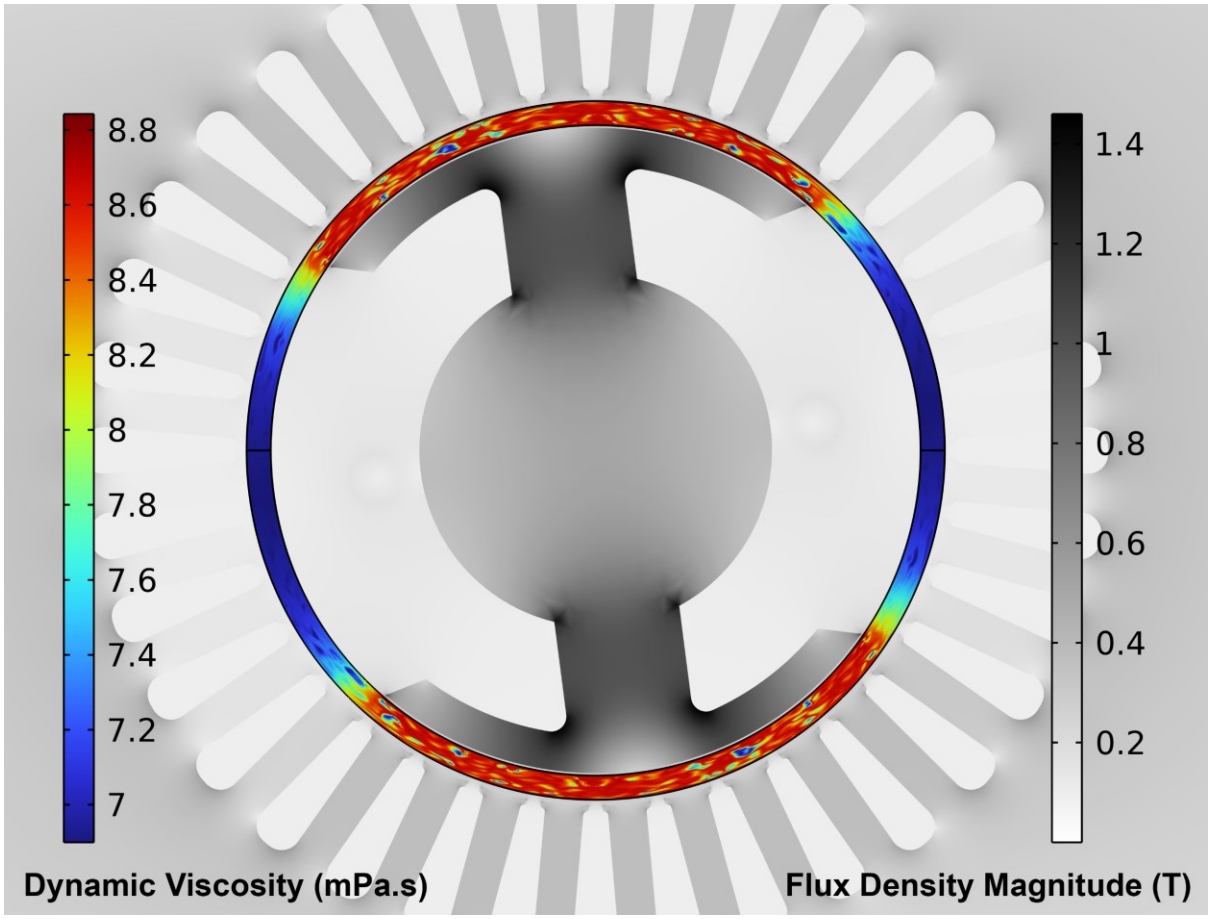

Figure 7.21: Plot of ferrofluid-gap dynamic viscosity (mPa.s) overlaid on a plot of test rig flux density magnitude (T) obtained from COMSOL Multiphysics 6.1.

The computationally expensive ferrohydrodynamic simulations therefore predict a reduced increase in drag due to the magnetic field in comparison to the analytical method: 4.3% and 6.1% compared to 8.6% for the analytical method. However, despite the complexity of the simulation method it is subject to the same uncertainties regarding the properties of the ferrofluid, particularly the particle size distribution and the thickness of the stabilising layer.

The analytical approach therefore appears to be a reasonable approximation for the initial design stage of a ferrofluid-gap electrical machine, facilitating a fast approximation of the ferrofluid-gap drag. In the later stages of design, it may then be appropriate to conduct a ferrohydrodynamic simulation of the ferrofluid-gap flow for a more refined estimate.

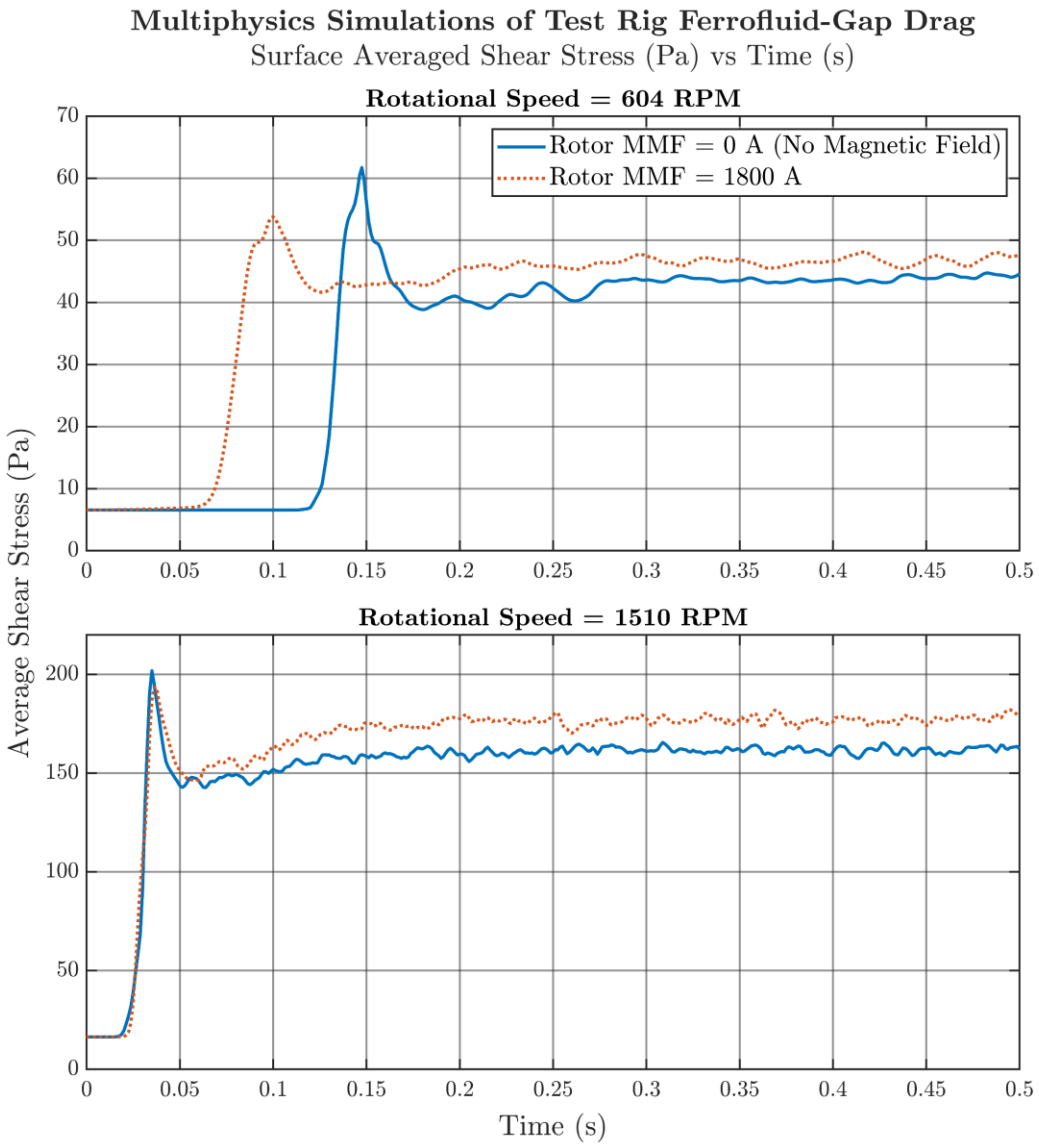

Figure 7.22: Comparison of surface-averaged shear stress (Pa) obtained from multi-physics simulations of EFH1 ferrofluid-gap flow for a rotor winding magnetomotive force (MMF) of 0 and 1800 A at rotational speeds of 604 and 1510 RPM.

7.1.2.6 Summary of Ferrofluid-Gap Drag

To summarise the investigation of how the magnetic field influences the ferrofluid-gap drag we return to the key research question:

- Does the magnetic field influence the ferrofluid-gap drag? If so, can this effect be predicted?

Based on a novel experimental methodology, it has been demonstrated that the magnetic field does indeed increase the ferrofluid-gap drag. Although the measurement uncertainty was considerable due to the sensitivity of the set-up, a

relative increase in the range of ~3-10% was observed for the EFH1 and Custom ferrofluid-gaps, while a larger increase of ~10-40% was recorded for the In-House ferrofluid.

Although the In-House ferrofluid had a significantly lower saturation magnetisation compared to the EFH1 and Custom ferrofluid (~10%), a larger increase in drag was observed due to the significantly larger size of the ferrofluid particles in the sample. This highlights how the quality of the ferrofluid synthesis impacts the ferrofluid-gap performance.

The experimental results were compared with an analytical prediction in which the increased drag was attributed to an additional component of rotational viscosity. The analytical results were in good agreement with the experimental data and explained the observed convergence of ferrofluid-gap drag increase for rotor winding MMF values above 1200 A.

Ferrohydrodynamic simulations of the EFH1 ferrofluid-gap flow were conducted in COMSOL Multiphysics 6.1. The simulated increase in ferrofluid-gap drag due to the magnetic field also corresponded well with the experimentally obtained values.

For improved experimental quantification of the magnetic contribution to ferrofluid-gap drag, future work could investigate ferrofluids with higher magnetic volume fractions. A larger increase in viscosity would be expected, thereby providing a clearer measurement of the change in drag.

Since the viscosity of the ferrofluids was temperature sensitive, variations in the ferrofluid-gap temperature during testing introduced further uncertainty into the measurements. A maximum temperature variation of $7.5^{\circ}\mathrm{C}$ was measured according to the thermocouple placed in the filling port of the test rig.

In conclusion, the magnetic field does influence the ferrofluid-gap drag. A reasonable approximation of this effect can be obtained using the analytical model described in Section 7.1.2.4, while a more detailed estimate can be obtained through ferrohydrodynamic simulations described in Section 7.1.2.5, albeit at significantly higher computational cost.

7.1.3 Full Ferrofluid-Gap in Loaded Conditions

In the following section the ferrofluid-gap behaviour in loaded conditions is investigated. The key research question is:

- How does a ferrofluid-gap influence electrical machine performance in loaded conditions? Can its influence be predicted with finite element method (FEM) simulations?

In the following section the influence of a ferrofluid-gap on the magnetising inductance of the test rig is investigated in stationary conditions. The impact of a ferrofluid-gap on the performance of the test rig in loaded conditions is then detailed in Section 7.1.3.2.

7.1.3.1 Influence on Armature Inductance

As detailed in Chapter 5, Section 5.3.3, and supported by the experimental results presented in Section 7.1.1.2, it is valid to assume that the fluid dynamic conditions of the ferrofluid-gap have no influence on the magnetic field within the test rig. Therefore, the single-phase inductance was compared for an air- and ferrofluid-gap over a range of relative rotor-stator positions and rotor winding excitations in stationary conditions using a Wayne Kerr 3260B LCR meter. The torque transducer was used to measure the relative rotor-stator position during the measurements.

In Figure 7.23, the single-phase inductance is plotted for a range of rotor-stator positions for an air-gap and with a EFH1 ferrofluid-gap, the displacements of 0° and 90° correspond to the d- and q-axis respectively.

For a rotor winding MMF of 120 A the ferrofluid-gap can be seen to increase the d-axis inductance significantly since the ferrofluid-gap relative permeability is relatively large due to the low magnetic flux density. When the rotor winding MMF is increased the single-phase inductance of the ferrofluid-gap is observed to be similar to that of the air-gap since the ferrofluid is magnetically saturated. Due to the saliency of the rotor core, the ferrofluid-gap has little impact on the q-axis inductance.

The difference in air- and ferrofluid-gap q-axis inductance, and d-axis inductance at large values of rotor winding MMF, can be explained by an increase in end winding inductance due to the proximity of unsaturated ferrofluid.

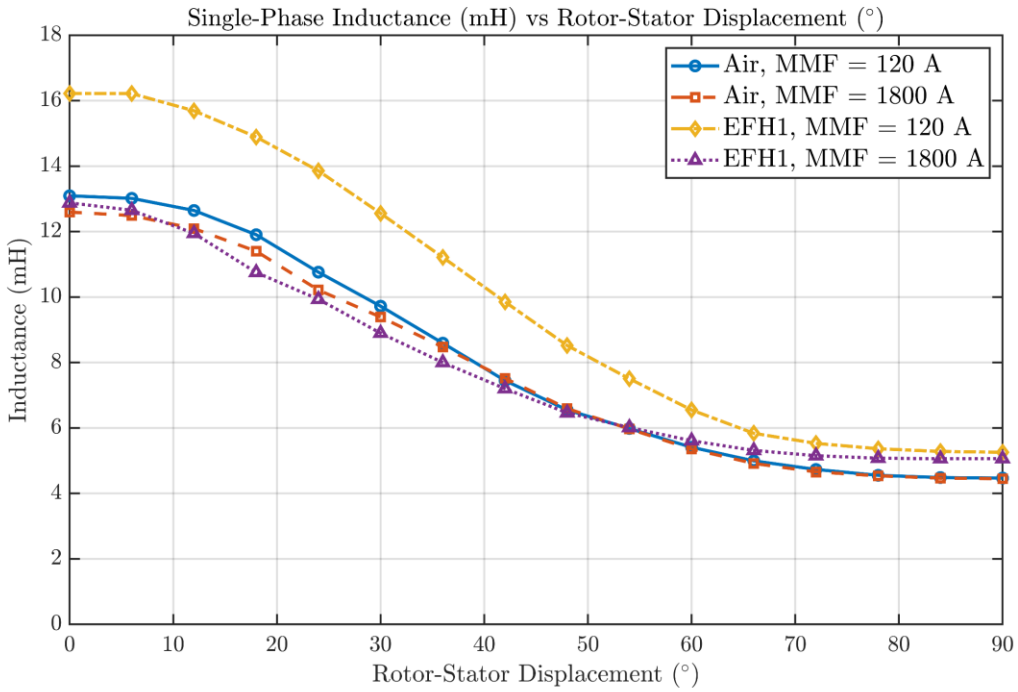

Figure 7.23: Single-phase inductance of the test rig armature windings at standstill with an EFH1 ferrofluid-gap and an air-gap for a rotor winding magnetomotive force (MMF) of 120 A and 1800 A over a range of rotor-stator relative positions.

In Figure 7.24 the experimentally measured d- and q-axis single-phase inductance is plotted for a range of rotor winding MMF magnitudes.

The influence of the ferrofluid-gap on the test-rig magnetising inductance was investigated using FEM. To account for the dependence of the ferrofluid-gap's magnetic behaviour on the rotor field two simulations were conducted for each data point: a simulation with just the rotor field, and a simulation with the rotor and single-phase excited stator field. The single-phase inductance was then estimated by subtracting the simulation results with just a rotor field from the simulation with both a rotor and stator field.

In Figure 7.25 the d-axis single-phase inductance obtained via FEM simulation is plotted for a range of rotor winding MMF values. As with the experimental results the d-axis inductance with a ferrofluid-gap can be observed to converge towards the value with an air-gap. Since it was a 2D simulation in which end winding inductance is neglected, the inductance value is observed to fully approach the air-gap value with no offset.

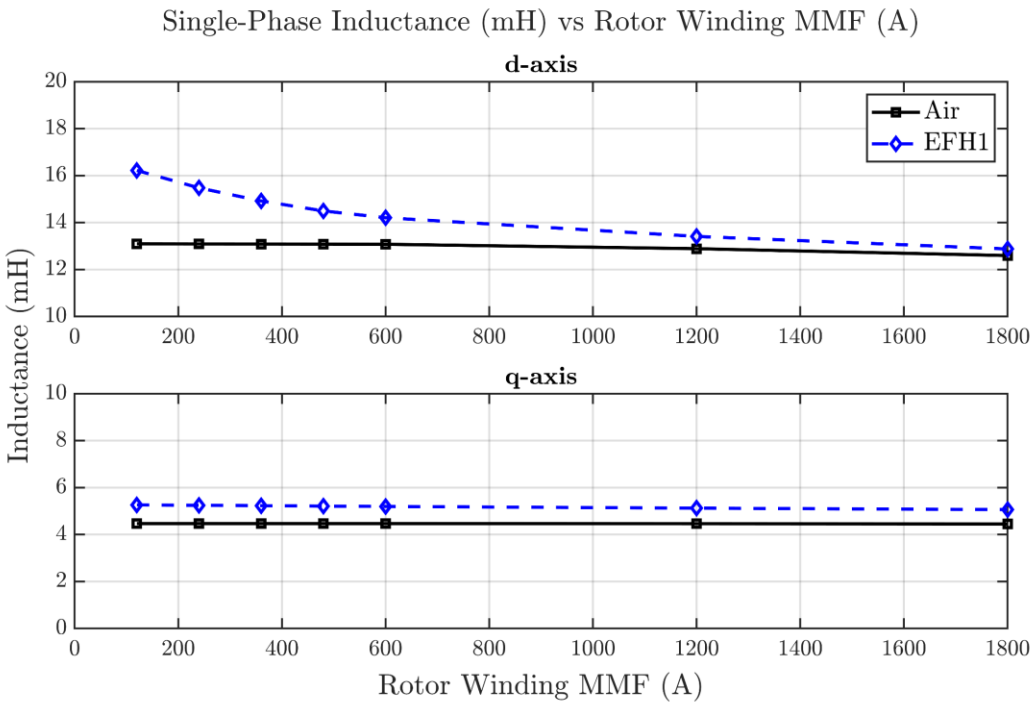

Figure 7.24: d- and q-axis single-phase inductance of the test rig armature windings with an air-gap and a EFH1 ferrofluid-gap at standstill over a range of rotor winding magnetomotive force (MMF).

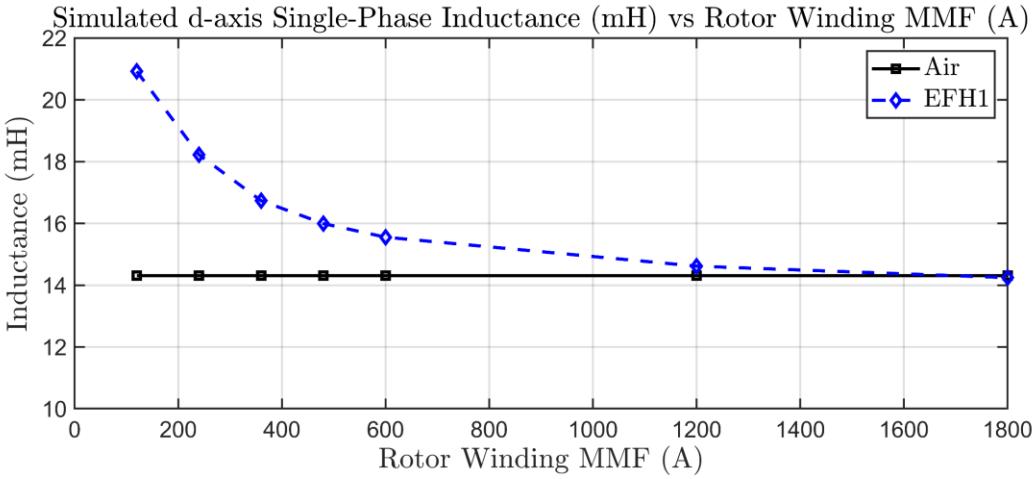

Figure 7.25: d-axis single-phase inductance of the test rig armature windings for an air-gap and a EFH1 ferrofluid-gap over a range of rotor winding magnetomotive force (MMF) obtained from finite element method (FEM) simulation.

7.1.3.2 Terminal Voltage and Torque Output

The on-load behaviour of the test-rig was evaluated by connecting its terminals to a Cressall AC30 load bank. The line-to-neutral terminal voltage and torque were measured for various rotor excitations and loads.

As shown in Figure 7.26, the on-load torque was measured via the same method as the open-load torque; by injecting current into the rotor winding and then detecting the

change in torque, this allowed the electromagnetic torque to be measured independently of the drivetrain friction. However, the measurement also included iron losses, unbalanced magnetic pull, and the increase in ferrofluid-gap drag due to the magnetic field.

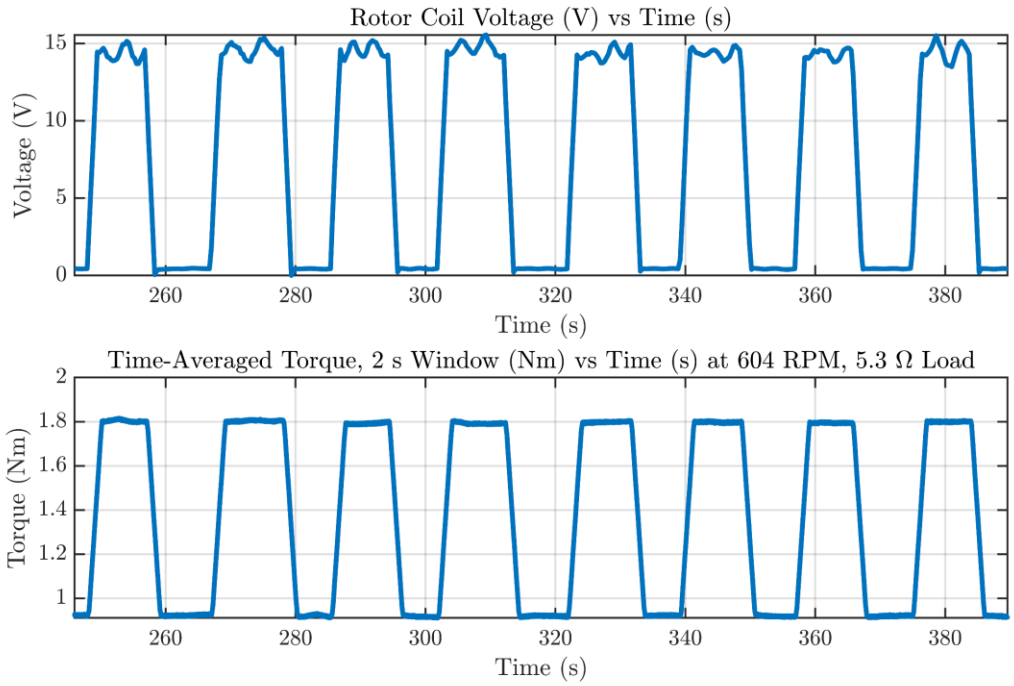

Figure 7.26: Example of torque variation due to excitation of the rotor windings with a 5.3 Ω load.

In Figure 7.27 the RMS terminal voltage and torque measured with a load of 5.3 Ω is compared for an EFH1 and Custom ferrofluid-gap and the baseline case of an air-gap. In both cases, the ferrofluid-gap is observed to result in a larger terminal voltage and torque in comparison to the baseline case of an air-gap. The Custom ferrofluid-gap was observed to produce slightly less terminal voltage than the EFH1 ferrofluid-gap, however the measured torque is larger, this can be explained by the larger increase in ferrofluid-gap drag due to the magnetic field.

An estimate for the electromagnetic torque developed by the test-rig with an air- and ferrofluid-gap can be obtained from FEM simulation using Arkkio's method [168]:

$$\mathcal{T}_E = \frac{n_{\text{sec}} l}{(r_{out} - r_{in})} \int_S \sigma_t r_A dS \tag{7.13}$$

where n_{sec} is the number of simulated sectors that make up a full machine (required due to periodic boundary conditions), σ is the local Maxwell shear stress, S is the

cross-sectional area of the air-gap region, r_A is the distance from the rotation centre, r_{out} and r_{in} are the outer and inner radius of the air-gap region respectively.

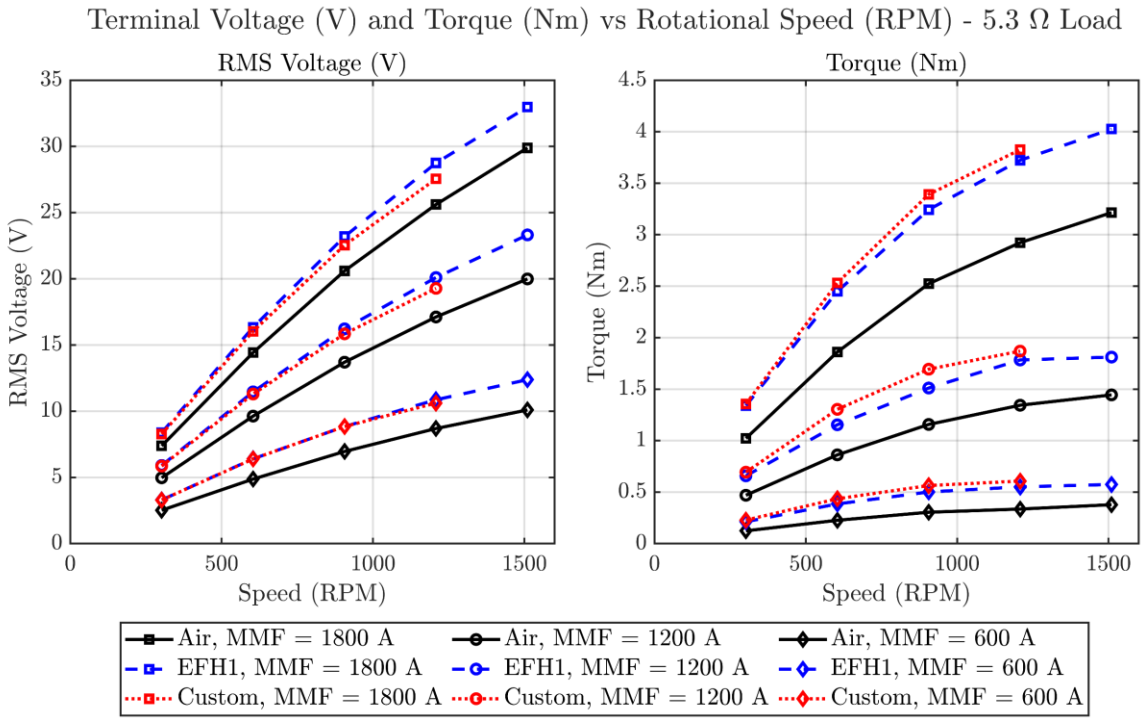

Figure 7.27: Terminal voltage (V) and torque (Nm) output of the test rig with a 5.3 Ω load for an air-gap, EFH1 ferrofluid-gap, and Custom ferrofluid-gap over a range of rotational speeds (RPM) and rotor winding magnetomotive force (MMF).

With a ferrofluid-gap care must be taken to calculate the electromagnetic shear stress appropriately, for example in COMSOL Multiphysics 6.1 the default equation for the local value of electromagnetic shear stress in the air-gap is specified as:

$$\sigma_t = \frac{B_r B_t}{\mu_0} \tag{7.14}$$

where the subscripts r and t refer to the radial and tangential directions respectively (with respect to a cylindrical coordinate system).

However, to avoid an overestimate of the Maxwell shear stress it must be calculated as follows [169]:

$$\sigma_t = B_r H_t \tag{7.15}$$

These terms are equivalent when $\mu_{rg} = 1$ since:

$$H_t = \frac{B_t}{\mu_0 \mu_{rg}} \tag{7.16}$$

However, when $\mu_{rg} > 1$ they are no longer equivalent hence Eq. (7.15) must be used.

In Figure 7.28 the increase in terminal voltage and torque due to a EFH1 ferrofluid-gap with a 5.3 Ω resistive load predicted from FEM simulations is compared with the experimental data.

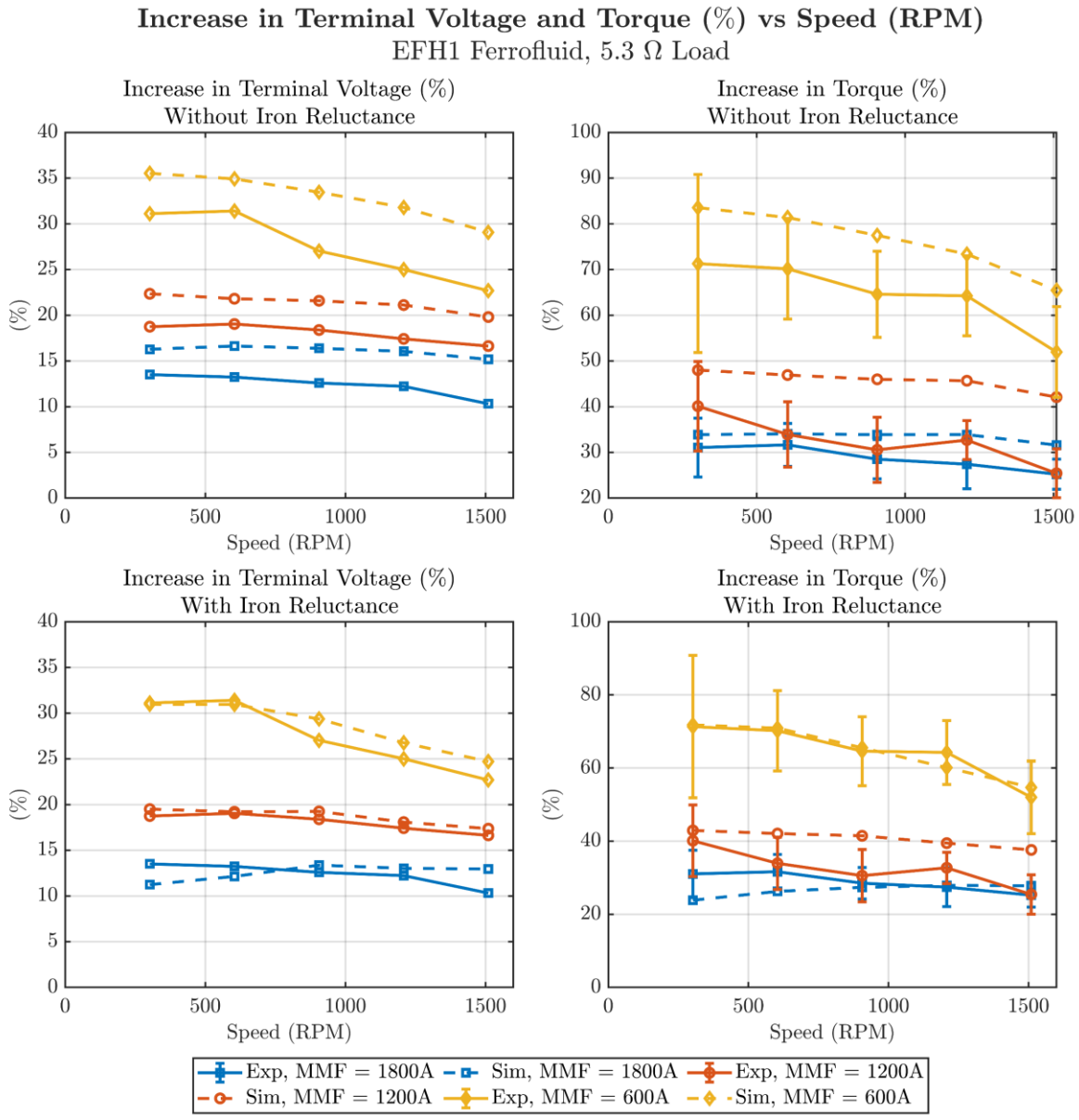

Figure 7.28: Comparison between the increase in terminal voltage and torque measured experimentally with an EFH1 ferrofluid-gap compared to an air-gap and estimated from finite element method (FEM) simulations over a range of rotational speeds (RPM) and for various values of rotor winding magnetomotive force (MMF). A comparison is made where iron reluctance is neglected in the simulation and when it is approximated.

It was found that the FEM simulations would overestimate the increase in voltage and torque if the reluctance of the steel components were neglected in the simulations. However, if the rotor iron reluctance was modelled according to the nonlinear BH curve

for CR4 mild steel, good agreement was obtained between the experimental results and the FEM simulations.

Figure 7.29 illustrates that the increase in torque is significantly overestimated if the incorrect formulation for the ferrofluid-gap electromagnetic shear stress is used, Eq. (7.14), and that an accurate estimate can be achieved by using Eq. (7.15).

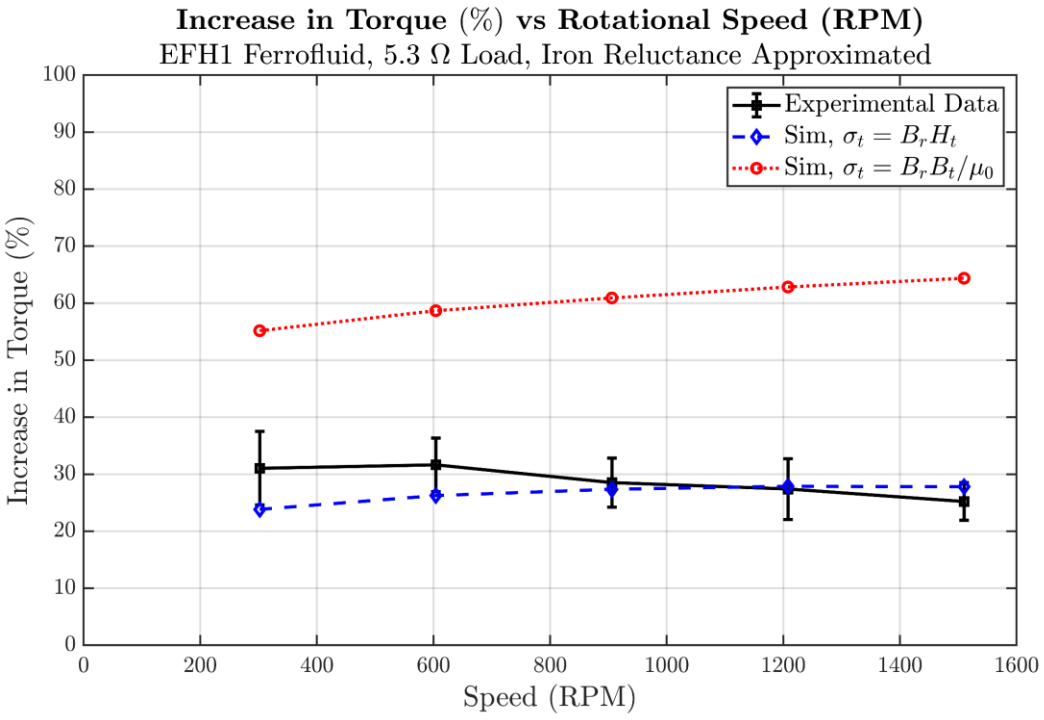

Figure 7.29: A comparison between the experimentally measured increase in torque with an EFH1 ferrofluid-gap compared to an air-gap and estimated from finite element method (FEM) simulations. It is highlighted that an incorrect formulation for Maxwell shear stress leads to an overestimation of the increase in torque due to a ferrofluid-gap.

7.1.3.3 Summary of Full Ferrofluid-Gap in Loaded Conditions

To summarise the investigation of how a ferrofluid-gap influences electrical machine performance in loaded conditions we return to the key research question:

- How does a ferrofluid-gap influence electrical machine performance in loaded conditions? Can its influence be predicted with finite element method (FEM) simulations?

In Section 7.1.3.1, the influence of a ferrofluid-gap on magnetising inductance was investigated. It was demonstrated that once the ferrofluid-gap above the pole faces becomes magnetically saturated due to the rotor field its effective relative permeability with respect to the d-axis magnetising inductance is the same as air ($\mu_r = 1$).

In Section 7.1.3.2, the increase in terminal voltage and torque due to a ferrofluid-gap was determined experimentally and compared with FEM simulations. When iron reluctance was neglected the simulation results were found to overestimate the experimentally obtained values. However, when the iron reluctance was approximated good agreement was demonstrated. It was highlighted that care should be taken to calculate the electromagnetic shear stress within the ferrofluid-gap appropriately, by calculating the Maxwell shear stress according to the radial component of magnetic flux density (B_r) and tangential component of magnetic field strength (H_t) it was shown that the increase in torque due to a ferrofluid-gap can be well approximated with FEM simulations.

To conclude, a ferrofluid-gap does indeed influence electrical machine performance in loaded conditions resulting in an increase in terminal voltage and torque. This can be approximated well with FEM simulations by assigning the ferrofluid-gap a BH curve corresponding to VSM measurements as presented in Appendix G and treating the ferrofluid-gap as a magnetically homogeneous region.

7.2 Results and Discussion for Partially Filled Ferrofluid-Gaps

The following section will present the results and discussion for partially filled ferrofluid-gaps, in which the air-gap region contains both air and ferrofluid. The key research question addressed is:

- Can a partially filled ferrofluid-gap improve the electromagnetic performance of an electrical machine? If so, how is its behaviour influenced by magnetic field strength and rotational speed?

It is important to note that the test rig was scaled such that the turbulence and shear rate of a fully filled ferrofluid-gap exceeds what can be expected in multi-megawatt scale DD WTGs. The behaviour of a partially filled ferrofluid-gap is more complex, particularly due to the magnetic forces acting on the ferrofluid-air interfaces, as described in Chapter 5, Section 5.3.4. Consequently, the experimental set-up does not directly replicate the conditions expected in multi-megawatt DD WTGs. Nevertheless, an investigation into the behaviour of partially filled ferrofluid-gaps is valuable, given the limited prior experimental work in this area.

7.2.1 Partially Filled Ferrofluid-Gap Voltage Output

The open load voltage output was measured for a range of rotor winding MMF magnitudes and ferrofluid-gap fill factors $(C_{\text{fill,FF}})$: defined as the ratio of the volume of ferrofluid in the air-gap region (V_{FF}) to the total volume of the air-gap region (V_g):

$$C_{\text{fill,FF}} = \frac{V_{\text{FF}}}{V_g} \tag{7.17}$$

In Figure 7.30 the increase in voltage output is plotted for various speeds, fill factors, and rotor winding MMF magnitudes for EFH1 ferrofluid, a similar plot is given in Figure 7.31 for Custom ferrofluid. In each plot a reference line is included which approximates the expected performance assuming that the ferrofluid has a uniform distribution within the air-gap region, it was obtained by multiplying the corresponding performance of a full ferrofluid-gap by $C_{\text{fill,FF}}$.

For each ferrofluid it can be observed that the experimentally obtained increase in voltage output generally surpasses the isotropic estimate, suggesting that the ferrofluid tends to be retained above the rotor poles by the magnetic field. As the rotor winding MMF is increased the tendency of ferrofluid to remain above the poles becomes more pronounced. There is a distinct difference in the increase in voltage output due to the partially filled ferrofluid-gap when comparing a relatively low rotational speed of 302 RPM to the higher rotational speeds for both ferrofluids. This suggests that as the rotational speed increases the ferrofluid is displaced from the region above the poles.

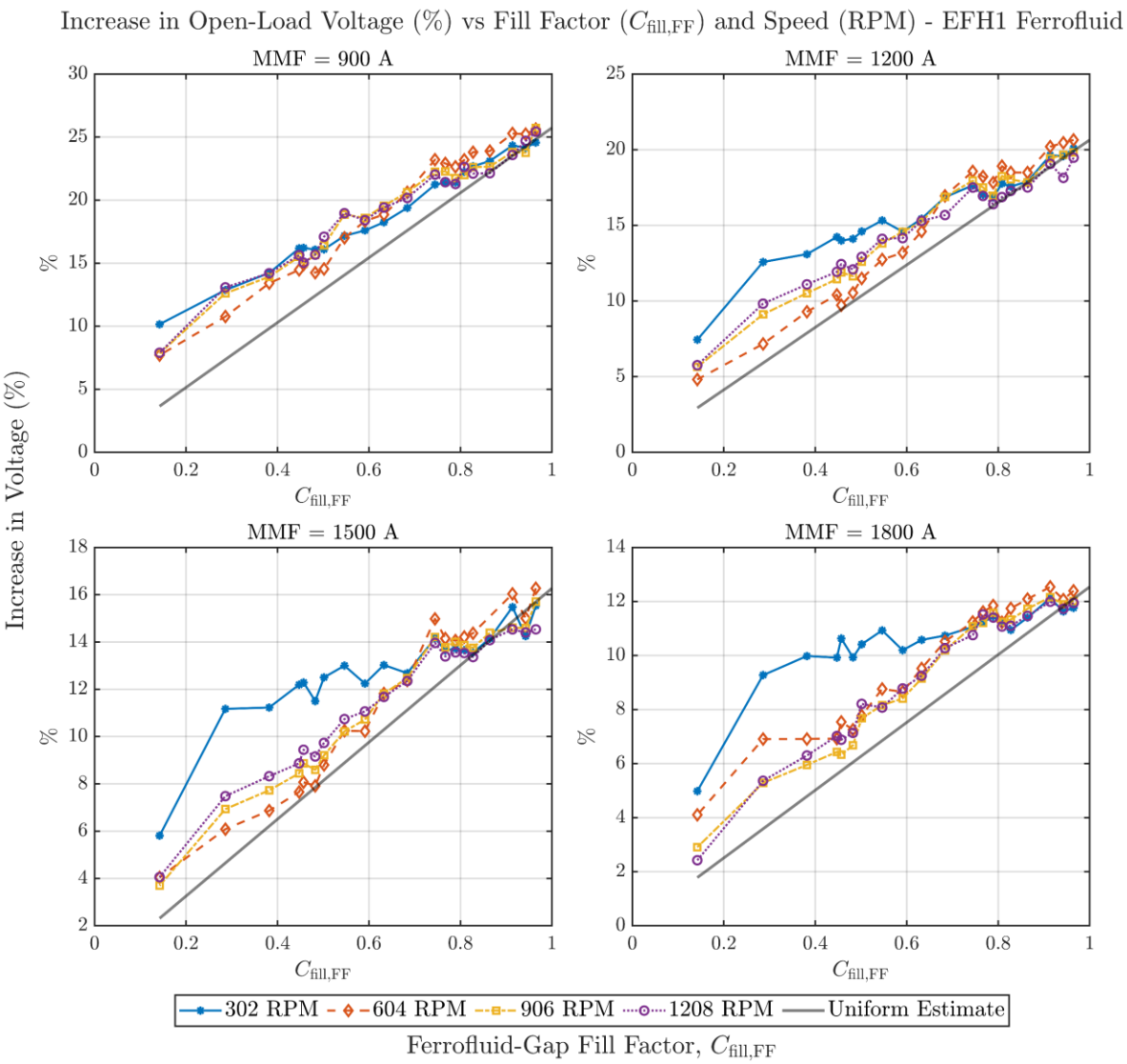

Figure 7.30: Increase in open-load voltage with a partially filled EFH1 ferrofluid-gap compared to an air-gap for a variety of rotational speeds (RPM), ferrofluid-gap fill factors ($C_{\text{fill,FF}}$), and rotor winding magnetomotive force (MMF) values.

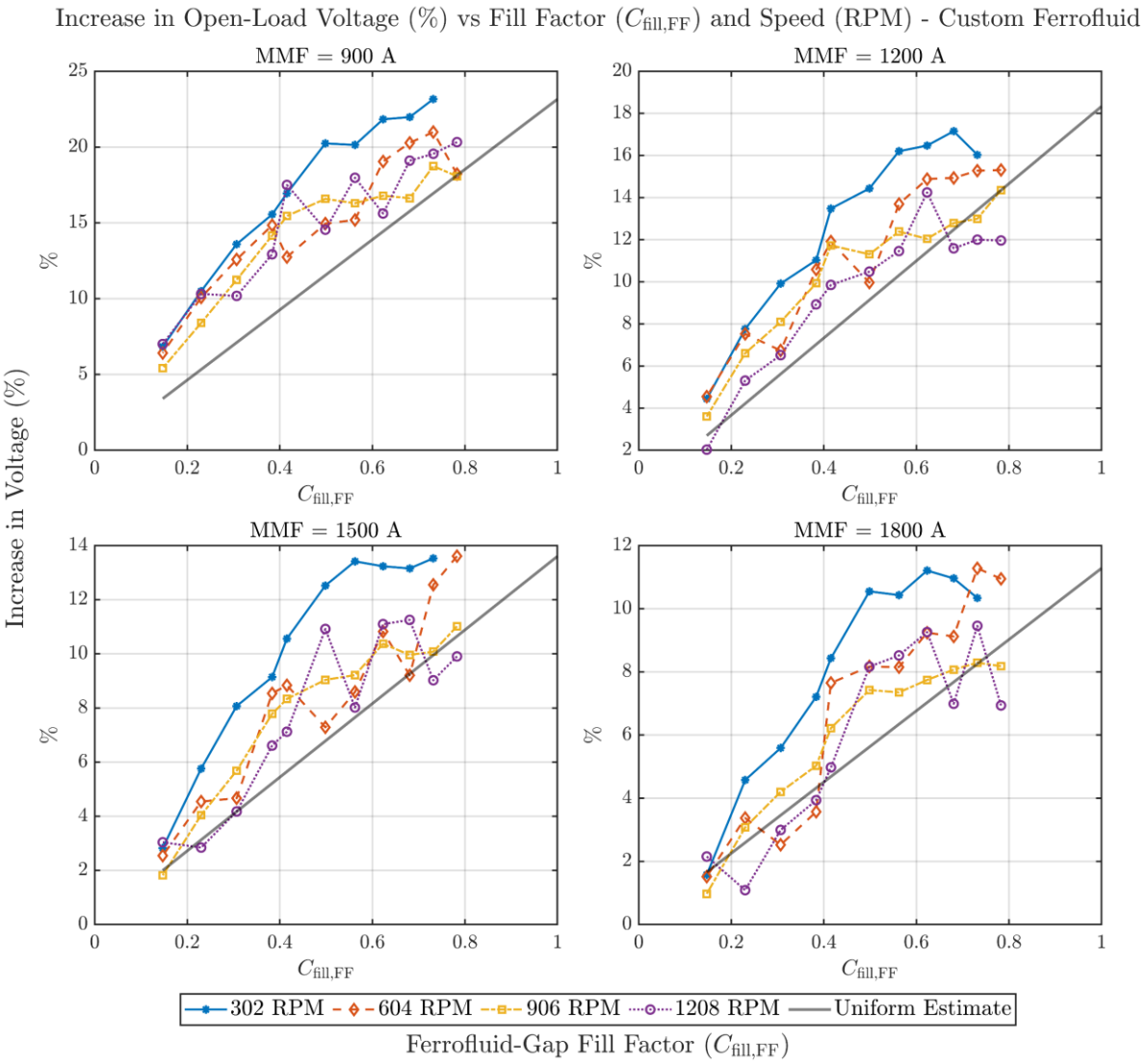

Figure 7.31: Increase in open-load voltage with a partially filled Custom ferrofluid-gap compared to an air-gap for a variety of rotational speeds (RPM), ferrofluid-gap fill factors ($C_{\text{fill,FF}}$), and rotor winding magnetomotive force (MMF) values.

Since the EFH1 and Custom ferrofluids have very similar saturation magnetisations and densities, a comparison of their performance provides insight into the influence of viscosity in partially filled ferrofluid-gaps. It appears that the low viscosity EFH1 ferrofluid performs better for low values of $C_{\text{fill,FF}}$, however for larger values of $C_{\text{fill,FF}}$ the relatively high viscosity Custom ferrofluid appears to maintain performance similar to a full ferrofluid-gap until $C_{\text{fill,FF}}$ falls below ~0.5, below which the performance decreases rapidly. In Figure 7.32 a direct comparison is given between EFH1 and Custom ferrofluid for a rotor MMF of 1800 A at a rotational speed of 302 RPM for various fill factors.

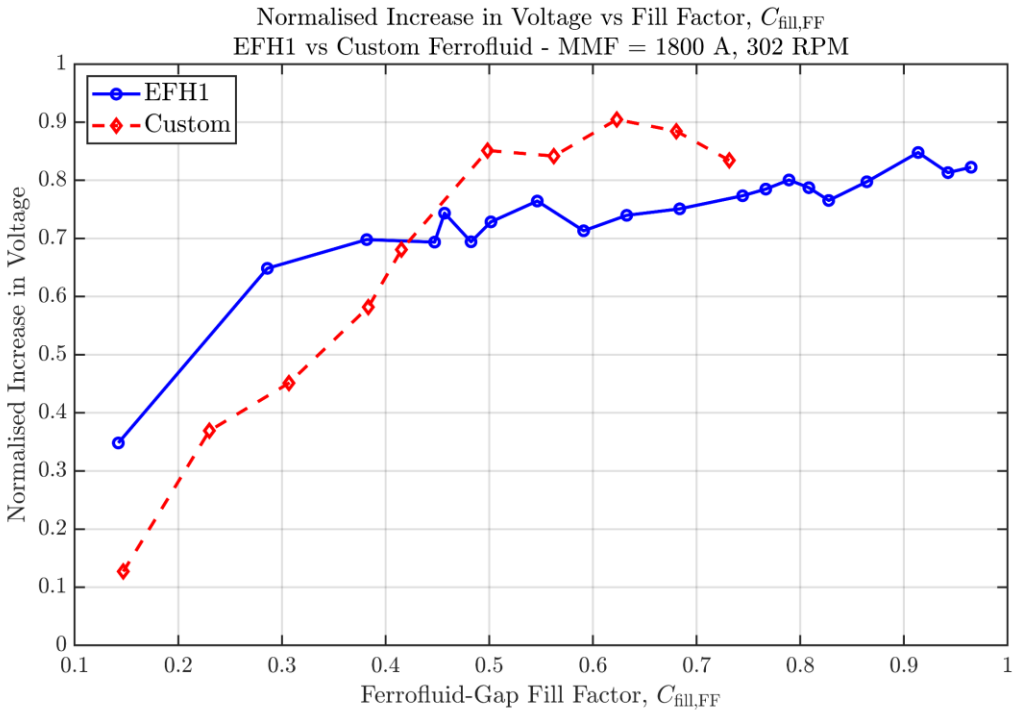

Figure 7.32: Comparison between the normalised increase in voltage due to a partially filled EFH1 and Custom ferrofluid-gap compared to an air-gap for a range of ferrofluid-gap fill factors ($C_{\text{fill,FF}}$) at a rotational speed of 302 RPM and a rotor winding magnetomotive force (MMF) of 1800 A. The increase in voltage is normalised with respect to the increase obtained with a full ferrofluid-gap.

In Figure 7.33 and Figure 7.34 the influence of rotational speed on the performance of a partially filled ferrofluid-gap with $C_{\text{fill,FF}} = 0.38$ is investigated in detail for EFH1 and Custom ferrofluid respectively. For EFH1 ferrofluid the performance is observed to steadily decrease with increasing speed before reaching a steady value. For Custom ferrofluid the performance appears to remain somewhat consistent over the tested range of speeds.

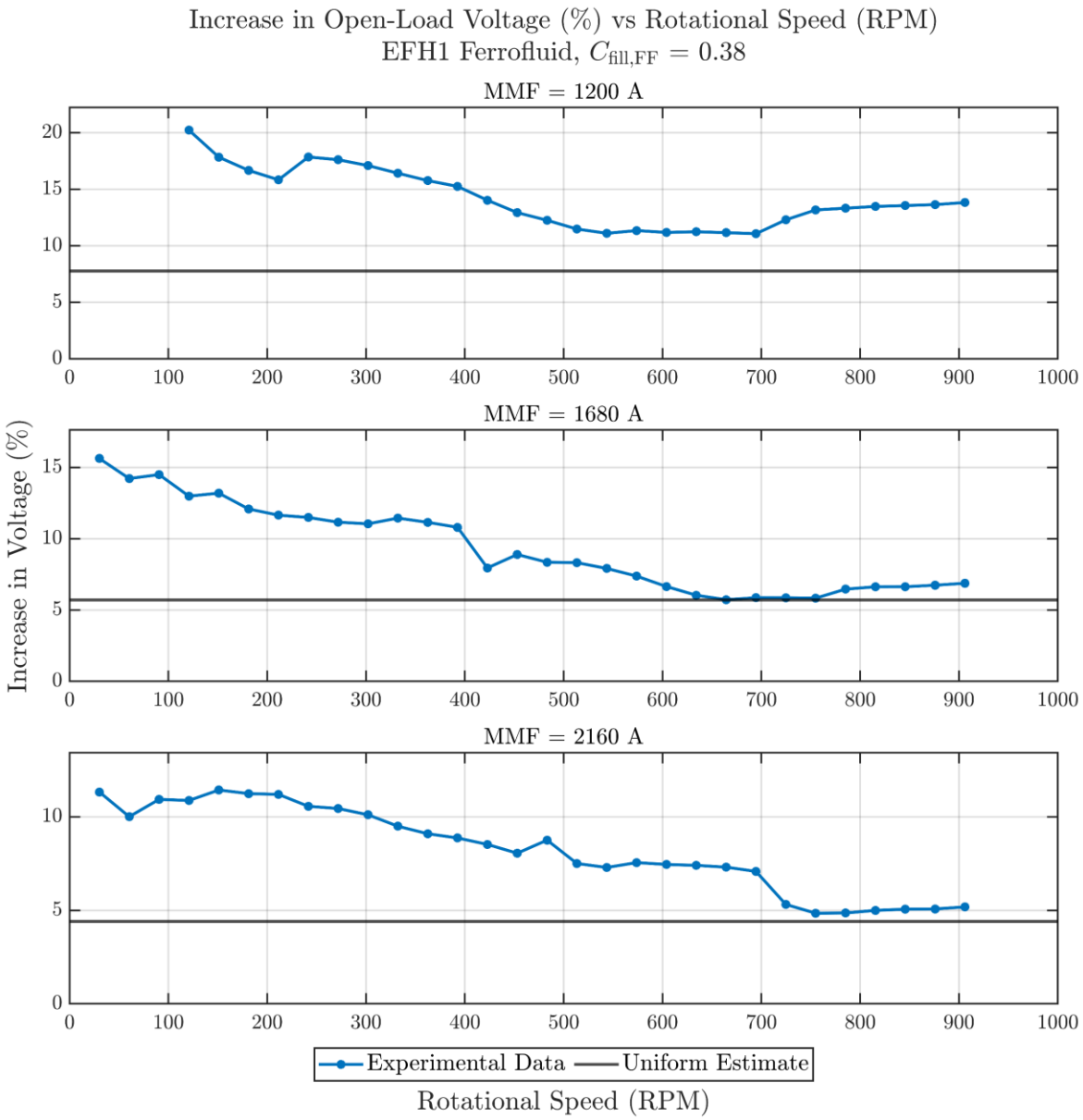

Figure 7.33: Increase in open-load voltage for a partially filled EFH1 ferrofluid-gap with a fill factor of ($C_{\text{fill,FF}}$) 0.38 compared to an air-gap over a range of rotational speeds (RPM) and rotor winding magnetomotive force (MMF) values.

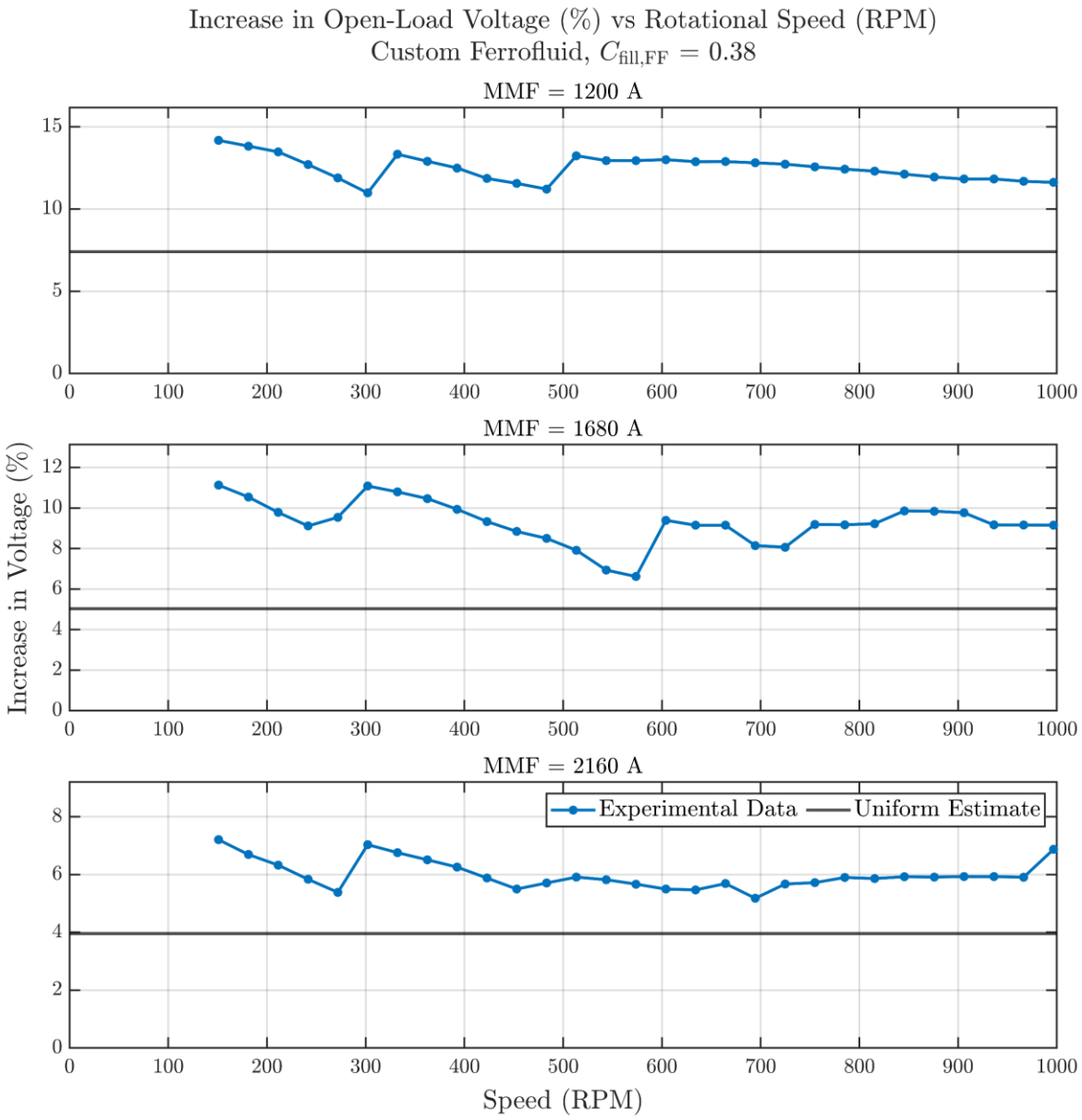

Figure 7.34: Increase in open-load voltage for a partially filled Custom ferrofluid-gap with a fill factor of ($C_{\mathrm{fill,FF}}$) 0.38 compared to an air-gap over a range of rotational speeds (RPM) and rotor winding magnetomotive force (MMF) values.

The difference in the EFH1 and Custom ferrofluid behaviour is highlighted in Figure 7.35, in which the performance is compared over a range of rotational speeds for a rotor winding MMF of 2160 A and $C_{\mathrm{fill,FF}} = 0.38$.

In Figure 7.36 the increase in voltage output due to a partially filled EFH1 ferrofluid-gap with $C_{\mathrm{fill,FF}} = 0.38$ in loaded conditions is investigated for a range of rotational speeds and a rotor winding MMF of 1200 and 1800 A. The observed behaviour is similar to that in open load conditions, with decreasing performance with speed and improved ferrofluid retention above the poles with increasing rotor winding MMF.

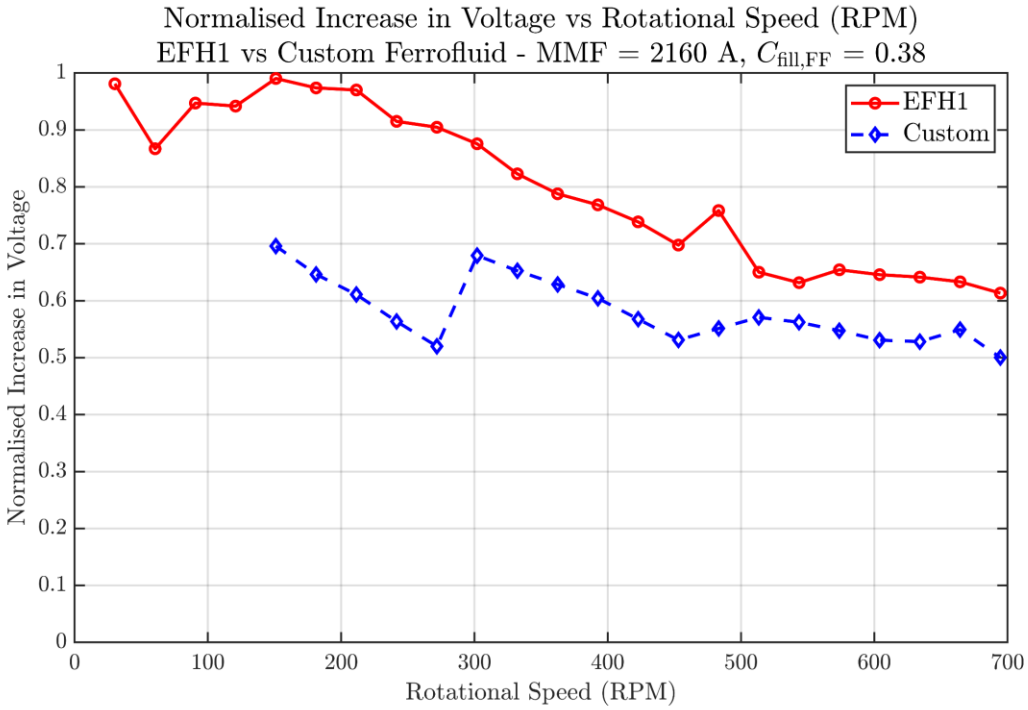

Figure 7.35: Comparison between the normalised increase in voltage due to a partially filled EFH1 and Custom ferrofluid-gap compared to an air-gap for a ferrofluid-gap fill factors ($C_{\text{fill,FF}}$) of 0.38 over a range of rotational speeds (RPM) with a rotor winding magnetomotive force (MMF) of 2160 A. The increase in voltage is normalised with respect to the increase obtained with a full ferrofluid-gap.

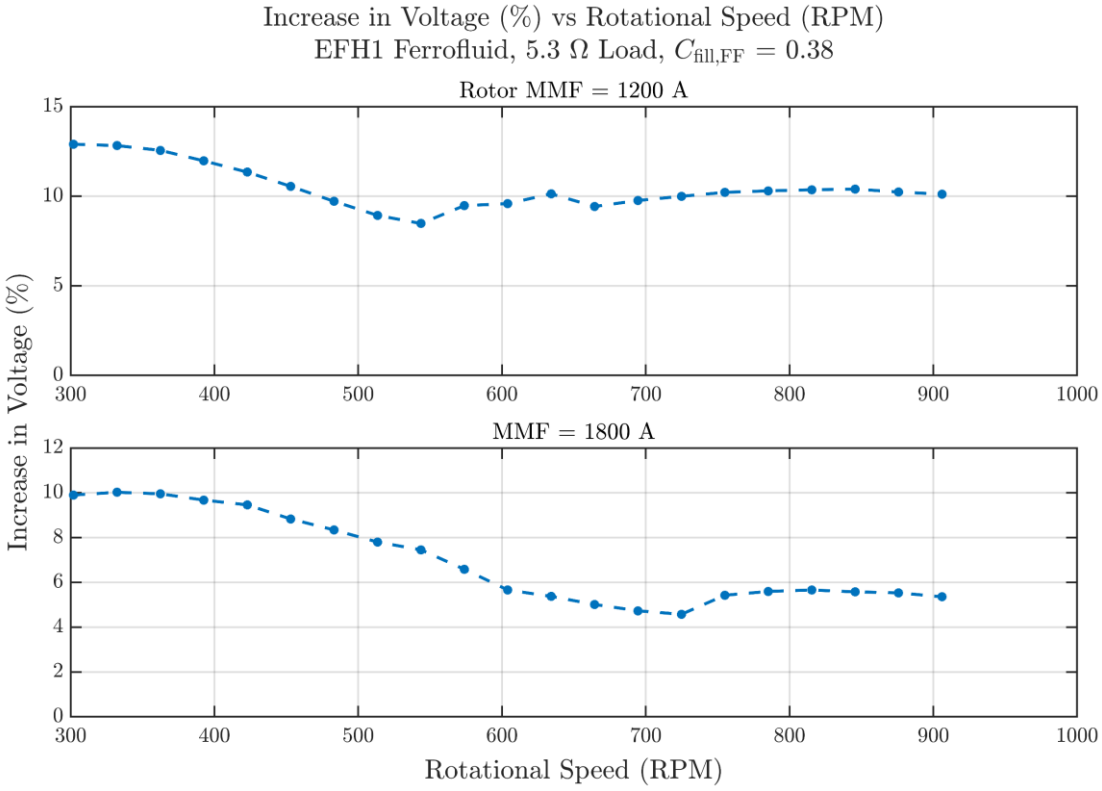

Figure 7.36: Increase in terminal voltage (%) with a partially filled EFH1 ferrofluid-gap compared to an air-gap with a load of 5.3 Ω over a range of rotational speeds (RPM) and a rotor winding magnetomotive force (MMF) of 1200 and 1800 A.

7.2.2 Partially Filled Ferrofluid-Gap Open Load Torque

The influence of the rotor winding MMF on partially filled ferrofluid-gap drag was investigated for a ferrofluid fill factor ($C_{\mathrm{fill,FF}}$) of 0.38 for EFH1 and Custom ferrofluid. The methodology was the same as described in Section 7.1.2.1, in which the rotor winding MMF is cycled between ON/OFF.

The observed change in torque was very significant as shown in Figure 7.37, where time histories of torque are provided for EFH1 and Custom ferrofluid where a rotor winding MMF of 2400 A is cycled ON/OFF.

In Figure 7.38 the change in torque due to the magnetic field is provided for a range of rotational speeds and rotor winding MMFs for both EFH1 and Custom ferrofluid.

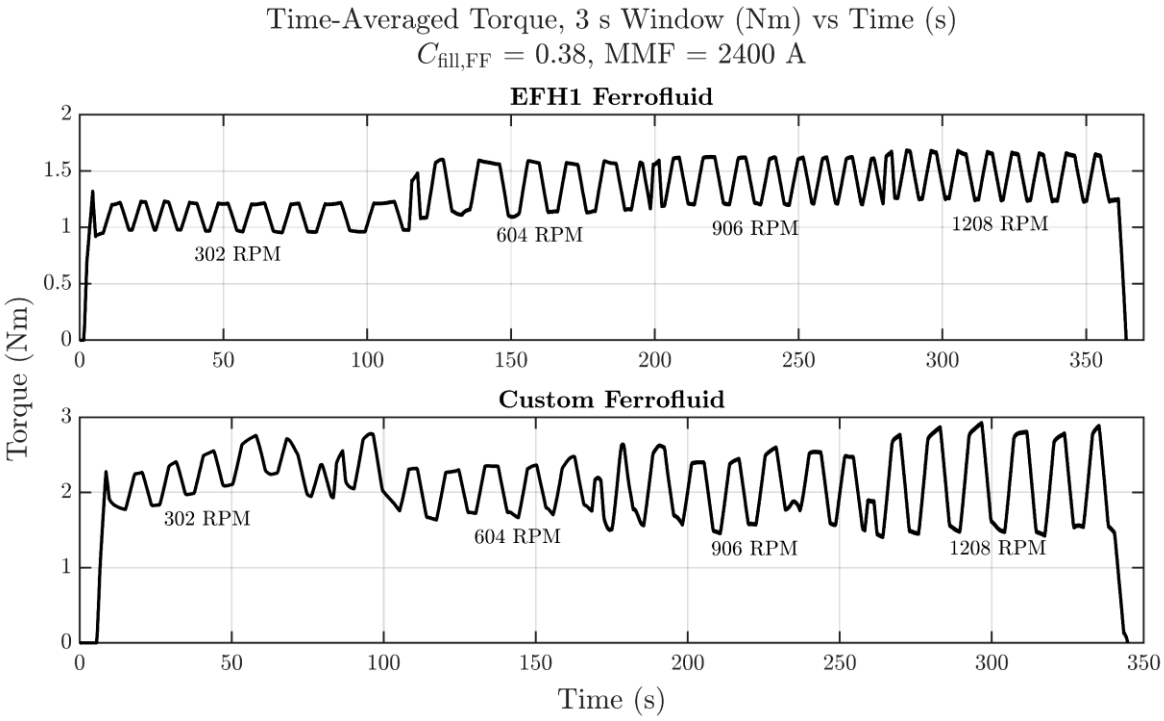

Figure 7.37: Examples of time averaged torque history (3 s window) during test runs with a partially filled EFH1 and Custom ferrofluid-gap with $C_{\mathrm{fill,FF}} = 0.38$ and an excited rotor winding magnetomotive force (MMF) of 2400 A.

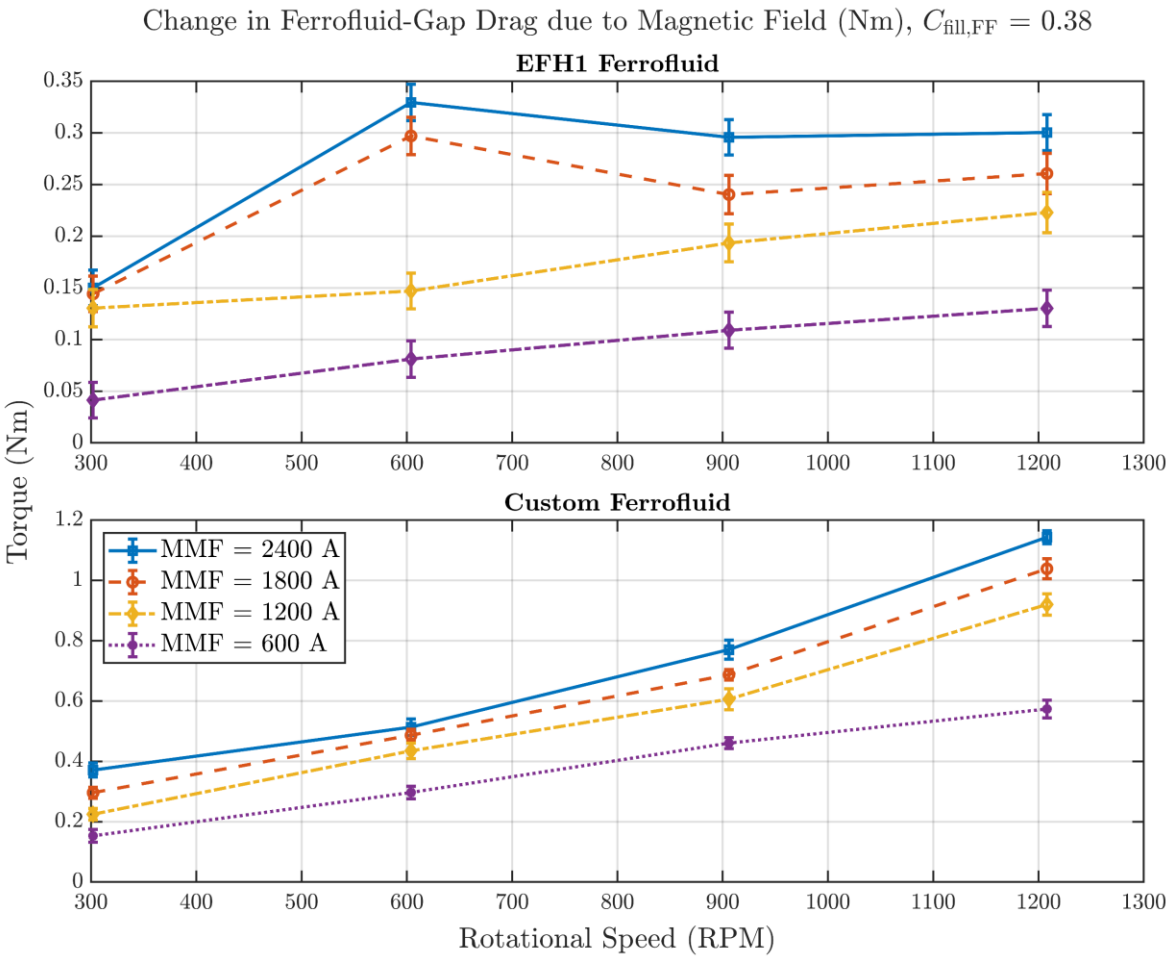

Figure 7.38: Experimentally obtained measurements for the increase in torque resulting from excitation of the rotor windings with a partially filled EFH1 and Custom ferrofluid-gap with $C_{\text{fill,FF}} = 0.38$ over a range of rotational speed (RPM) and for various excited rotor winding magnetomotive force (MMF) values.

The change in partially filled ferrofluid-gap drag is much larger than that of full ferrofluid-gap for a given value of rotor winding MMF. The dynamics of such a system are very complex and require further investigation to better understand. In fact, understanding the windage losses resulting from partially filling an air-gap with non-magnetic fluid is an active area of research [170]. However, based on the observed tendency of the ferrofluid to remain above the rotor pole faces, two mechanisms are proposed for the increase in drag:

- The magnetic field increases the viscous drag losses due to increased shearing of the ferrofluid. Since the ferrofluid is attracted to above the rotor pole faces, there are more regions in which the ferrofluid is in contact with both the rotor and stator boundaries, resulting in an increase in shear stress due to the ferrofluid viscosity.

- The ferrofluid is attracted to above the rotor poles and is essentially 'dragged' along with the rotation of the rotor by the magnetic forces acting on the ferrofluid-air interfaces. This results in an increase in torque due to the rotor winding MMF.

The total increase in partially-filled ferrofluid-gap is likely a combination of both mechanisms, however it is interesting to note that the increase in drag observed with the Custom ferrofluid is much larger than the EFH1 ferrofluid. Since both ferrofluids have a similar saturation magnetisation and density, but different viscosities, this indicates that an increase in viscous drag may play a significant role in the increased drag due to the rotor winding MMF.

The change in torque due to the Custom ferrofluid also appears to increase linearly with rotational speed, whereas the change due to the EFH1 ferrofluid appears to be nonlinear. This may be related to the behaviour observed in Figure 7.35 in which the normalised increase in voltage due to the partially-filled EFH1 ferrofluid-gap decreases with increasing speed, whereas the increase remains relatively consistent for the partially-filled Custom ferrofluid-gap over the examined range of rotational speed.

7.2.3 Summary of Partially Filled Ferrofluid-Gap Testing

To summarise the investigation into the behaviour of partially filled ferrofluid-gaps we return to the key research question:

- Can a partially filled ferrofluid-gap improve the electromagnetic performance of an electrical machine? If so, how is its behaviour influenced by magnetic field strength and rotational speed?

In Section 7.2.1, the electromagnetic performance of the test rig with partially filled ferrofluid-gaps with various ratios of ferrofluid and air was investigated in open load conditions. It was demonstrated that the increase in performance compared to the baseline case of a conventional air-gap generally exceeded what would be expected if the ferrofluid had a uniform distribution within the air-gap region, especially for low rotational speeds and relatively large values of rotor winding MMF. For a ferrofluid-gap fill factor ($C_{\mathrm{fill,FF}}$) of 0.38, it was also demonstrated that a performance improvement can be obtained in loaded conditions.

In Section 7.2.2, the influence of the magnetic field on the partially-filled ferrofluid-gap drag was investigated. The magnetic field was observed to increase the drag significantly in comparison to a full ferrofluid-gap.

To conclude, a partially-filled gap can indeed improve electromagnetic performance, the ferrofluid has a tendency to remain above the rotor pole faces at considerable rotational speeds.

It is important to note that the test rig was not designed specifically for partially-filled ferrofluid-gaps, therefore it is not possible to directly translate the observed behaviour to what would be expected in direct-drive (DD) wind turbine generators (WTGs). In particular:

- The proportion of the air-gap region in which there is a significant magnetic field strength is an important parameter, in the test rig the volume above the pole faces accounts for ~34% of the total hydrodynamic volume of the air-gap region whereas in a DD WTG a value of ~70-80% would be expected.
- The magnitude of the magnetic flux density above the rotor pole faces influences the extent of ferrofluid retention. As detailed in Chapter 6, Section 6.1.2, the test rig air-gap flux density is significantly lower than what would be expected in a DD WTG.

In the following chapter it will be discussed how a partially filled ferrofluid-gap design could alleviate some of the practical issues associated with implementing ferrofluid-gaps in electrical machines. The concept may merit further experimental research with a purpose-built test rig that is scaled appropriately.

7.3 Conclusion

In conclusion, this chapter has detailed the experimental work carried out with the ferrofluid-gap test rig, introduced in Chapter 6, that was constructed to validate the theoretical predictions of ferrofluid-gap magnetic and mechanical behaviour as described in Chapter 5, Section 5.3.

Other published experimental investigations of ferrofluid-gap behaviour prior to this thesis have demonstrated that a ferrofluid-gap has the potential to improve the electromagnetic performance of electrical machines. However, in this work, for the first

time the theoretically predicted magnetic and mechanical behaviour of a ferrofluid-gap has been directly validated through experimentation.

To summarise the key findings:

- It has been experimentally validated that the ferrofluid-gap magnetic performance is unaffected by turbulence or shear rate exceeding what can be expected in multi-megawatt scale direct-drive (DD) wind turbine generators (WTGs).
- It has been demonstrated that a ferrofluid-gap can be modelled effectively by treating it as a homogeneous material and assigning it a *BH* curve corresponding to vibrating sample magnetometry (VSM) measurements.
- It has been demonstrated that the magnetic field within the ferrofluid-gap region will result in an increase in ferrofluid-gap drag, even for highly turbulent ferrofluid-gap flow.
- The increase in ferrofluid-gap drag due to a magnetic field can be approximated by considering the increase in viscosity resulting from the additional component of rotational viscosity.
- The increase in ferrofluid-gap drag due to a magnetic field can be approximated using ferrohydrodynamic multi-physics simulation in which a one-way coupling is specified between a FEM magnetic simulation and the local viscosity of the ferrofluid in a CFD simulation.
- In loaded conditions the increase in electromagnetic torque can be calculated according to the electromagnetic shear stress in the ferrofluid-gap.
- In a partially filled ferrofluid-gap, the ferrofluid tends to remain above the pole faces at significant rotational speeds.
- In a partially filled ferrofluid-gap, the magnetic field has a significant impact on the ferrofluid-gap drag, resulting in a larger increase than in a full ferrofluid-gap.

Although the test rig was designed with DD WTGs as the application of interest, the objective behind the experimental methodology was to validate the fundamental behaviour of a ferrofluid-gap, rather than to evaluate its performance for a specific set-up. These findings are therefore not limited to the application of ferrofluid-gaps to DD WTGs; this work provides experimental validation of analysis methods that can be

applied or adapted to the application of ferrofluid-gaps for arbitrary electrical machine topologies.

The experimental work could be further reinforced by evaluating the performance of a ferrofluid-gap with a larger magnetic volume fraction than what was presented in this thesis. This would be particularly beneficial for the evaluation of how the ferrofluid-gap drag is influenced by the magnetic field within the machine since the effect would be more pronounced and easier to measure.

It has been demonstrated that a partially filled ferrofluid-gap can enhance magnetic performance at considerable rotational speeds due to the tendency of the ferrofluid to remain above the pole faces. However, the test rig was not scaled such that the conditions of a partially filled gap matched those of multi-megawatt scale DD WTGs. Nevertheless, the experimental results presented in this chapter for partially filled ferrofluid-gaps are a unique contribution to literature.

In the following chapter it is discussed how a partially filled ferrofluid-gap may alleviate some of the practical challenges associated with implementing ferrofluid-gap in electrical machines, particularly in relation to the sealing and pressure regulation of the ferrofluid-gap. It is therefore an interesting topic for further research.

Chapter 8: Assessment of Ferrofluid-Gaps for Direct-Drive Wind Turbine Generators

In this chapter it is assessed whether a ferrofluid-gap could positively influence the performance and cost of multi-megawatt scale direct-drive (DD) wind turbine generators (WTGs).

To provide an in-depth understanding of how a ferrofluid-gap influences the performance of a DD WTG the analysis will first be based upon simplified assumptions, and additional complexity will be progressively introduced in each section of this chapter.

In the following section it is explained how the key material properties of a ferrofluid-gap can be estimated for a range of magnetic volume fractions (ϕ_{M}) according to the selection of a suitable mineral oil carrier fluid. In Section 8.2, a detailed magnetic analysis is provided for ferrofluid-gaps in DD WTGs. In Section 8.3, the magnitude of ferrofluid-gap drag in DD WTGs is estimated and the impact on generator efficiency is discussed. In Section 8.4, the influence of a ferrofluid-gap on the thermal performance of DD WTGs is investigated. In Section 8.5, the main practical challenges associated with implementing ferrofluid-gaps in DD WTGs are discussed. In Section 8.6 the overall feasibility of ferrofluid-gaps for DD WTGs is discussed.

8.1 Specification of Ferrofluid-Gap Material Properties

Prior works concerned with the analysis of ferrofluid-gaps in electrical machines tend to examine a specific set of ferrofluid properties, however as discussed in Chapter 5, the material properties of ferrofluid are significantly influenced by the magnetic volume fraction (ϕ_{M}). For instance, increasing the magnetic volume fraction of a ferrofluid will increase its saturation magnetisation: improving the potential for permanent magnet (PM) mass reduction. However, the viscosity will also increase nonlinearly: increasing the loss in generator efficiency due to ferrofluid-gap drag. It is therefore important to examine the impact of a ferrofluid-gap for a range of magnetic volume fraction such

that the trade-off between PM mass savings and efficiency losses in DD WTGs can be examined.

To specify the properties of a ferrofluid for use in the air-gap region of an electrical machine the first step is to select an appropriate carrier fluid. Mineral oil is a suitable candidate for several reasons:

- It has a low vapour pressure: it will not evaporate during operation.
- It has a high boiling point: it can withstand the elevated temperatures within DD WTGs.
- It is not electrically conductive: it will not increase the risk of short circuits or experience eddy current losses.
- It can have a relatively low viscosity: the ferrofluid-gap drag will be relatively low.
- It has a history of being used effectively for ferrofluids [171].

ISO VG 10 viscosity class mineral oil is a suitable choice since it has a reasonably low viscosity while retaining a sufficiently high flash point ($> 170^{\circ}\mathrm{C}$), such oils are characterised as having a kinematic viscosity of ~10 mm^2/s at $40^{\circ}\mathrm{C}$ [172].

The viscosity of mineral oil is very sensitive to temperature, with the kinematic viscosity of ISO VG 10 mineral oils typically dropping to ~2.5 mm^2/s at $100^{\circ}\mathrm{C}$. If a specific mineral oil is selected, then the relationship between viscosity and temperature should be fitted with an appropriate function. Otherwise, if the viscosity is known for only 2 different temperatures, as is typical in mineral oil datasheets, the temperature dependence of kinematic viscosity can be approximated using the ASTM D341 standard in which the two viscosity values are fitted to the Walther equation:

$$\log_{10}(\log_{10}(\nu_0 + 0.7)) = a_1 - b_1 \log_{10}(T) \tag{8.1}$$

Where ν_0 is the kinematic viscosity, T is the temperature in Kelvin, a_1 and b_1 are fitted parameters. The dynamic viscosity can be found according to the carrier fluid density:

$$\eta_0 = \frac{\nu_0}{\rho_0} \tag{8.2}$$

Once the carrier fluid properties are known, the ferrofluid properties can be determined using the various equations detailed in Chapter 5. In Table 8.1 the relevant equations and assumed material properties are summarised for convenience.

This approach facilitates an appropriate specification of ferrofluid-gap properties according to the magnetic volume fraction. Justification for the assumed material properties is provided in Chapter 5.

Table 8.1: Summary of assumed ferrofluid properties and relevant equations.

Parameter	Symbol	Value/Equation	Unit
Carrier fluid kinematic viscosity	ν_0	Eq. (8.1) where $a_1 = 10.1475, b_1 = 4.0609$	$\mathrm{m^2/s}$
Carrier fluid density	ρ_0	840	$\mathrm{kg/m^3}$
Carrier fluid dynamic viscosity	η_0	$\eta_0 = \frac{\nu_0}{\rho_0}$	$\mathrm{Pa.s}$
Carrier fluid thermal conductivity	k_0	0.1	$\mathrm{W/m.K}$
Carrier fluid specific heat capacity	$c_{p,0}$	2082	$\mathrm{J/kg.K}$
Magnetite heat capacity	$c_{p,\mathrm{M}}$	670	$\mathrm{J/kg.K}$
Nominal nanoparticle magnetic radius	r_{M}	5	nm
Nominal nanoparticle surfactant thickness	t_{stab}	2	nm
Nanoparticle specific magnetisation	ψ_M	86.53	emu/g
Magnetite density	ρ_{M}	5150	$\mathrm{kg/m^3}$
Nanoparticle magnetic volume	V_{M}	$V_{\mathrm{M}} = \frac{4}{3}\pi r_{\mathrm{M}}^3$	$\mathrm{m^3}$
Nanoparticle hydrodynamic volume	$\mathrm{V_H}$	$\mathrm{V_H} = \frac{4}{3}\pi(r_{\mathrm{M}} + t_{\mathrm{stab}})^3$	$\mathrm{m^3}$
Nanoparticle magnetic moment	m	$m = \psi_{\mathrm{M}}\rho_{\mathrm{M}}V_{\mathrm{M}}$	$\mathrm{A.m^2}$
Nanoparticle spontaneous magnetisation	M_d	$M_d = \psi_{\mathrm{M}}\rho_{\mathrm{M}}$	$\mathrm{A/m}$
Langevin parameter	ξ	$\xi = \frac{\mu_0 m H}{k_B T}$	–
Langevin function	$\mathcal{L}(\xi)$	$\mathcal{L}(\xi) = \coth(\xi) - \frac{1}{\xi}$	–
Ferrofluid saturation magnetisation	M_s	$M_s = M_d\phi_{\mathrm{M}}$	$\mathrm{A/m}$
Ferrofluid magnetisation	M_{FF}	$M_{\mathrm{FF}} = M_S\mathcal{L}(\xi)$	$\mathrm{A/m}$
Ferrofluid hydrodynamic volume fraction	ϕ_{H}	$\phi_{\mathrm{H}} = \frac{V_{\mathrm{C}}}{V_{\mathrm{M}}}\phi_{\mathrm{M}}$	–

Parameter	Symbol	Value/Equation	Unit
Ferrofluid dynamic viscosity	η_{FF}	$\eta_{\mathrm{FF}} = \eta_{\mathrm{rel}}\eta_0$ $\eta_{\mathrm{rel}} = \left\{\exp\left(\frac{2.5\phi_{\mathrm{H}}}{1-\phi_{\mathrm{H}}}\right) + \frac{A_{\mathrm{vis}}\phi_{\mathrm{H}}^2}{1-A_{\mathrm{vis}}\phi_{\mathrm{H}}^2\phi_{\mathrm{M}}}\right\}$	$\mathrm{Pa.\,s}$
Ferrofluid density	ρ_{FF}	$\rho_{\mathrm{FF}} = (1-\phi_M)\rho_0 + \phi_{\mathrm{M}}\rho_{\mathrm{M}}$	$\mathrm{kg/m^3}$
Ferrofluid thermal conductivity	k_{FF}	$k_{\mathrm{FF}} = \frac{1+2\beta_k\phi_{\mathrm{M}}}{1-\beta_k\phi_{\mathrm{M}}}k_0$ $\beta_k = \frac{k_M - k_0}{k_M + 2k_0}$	$\mathrm{W/m.\,K}$
Ferrofluid specific heat capacity	$c_{p,\mathrm{FF}}$	$c_{p,\mathrm{FF}} = \frac{(1-\phi_{\mathrm{M}})\rho_0 c_{p,0} + \phi_{\mathrm{M}}\rho_{\mathrm{M}}c_{p,\mathrm{M}}}{(1-\phi_{\mathrm{M}})\rho_0 + \phi_{\mathrm{M}}\rho_{\mathrm{M}}}$	$\mathrm{J/kg.\,K}$

8.2 A Magnetic Analysis of Ferrofluid-Gaps for Direct-Drive Wind Turbine Generators

The following section details a magnetic analysis of the ferrofluid-gap concept applied to surface mounted PM DD WTGs in which the ferrofluid-gap magnetic properties are appropriately specified.

As discussed in Chapter 5, Section 5.4, prior works which attempt to model the impact of a ferrofluid-gap on electrical machine magnetic performance assume unrealistically large constant values of relative permeability for the ferrofluid-gap.

In Chapter 7, it was experimentally validated that the ferrofluid-gap magnetic behaviour is not influenced by the shear rate or turbulence expected in DD WTGs.

An FEA analysis was conducted with COMSOL Multiphysics 6.1 for a pole-pair of a 3 MW DD PM WTG topology with full-pitch armature windings based on the work of Polinder *et al.* [173], [22]. An integer slot design was chosen for simplicity, since only a single pole pair needs to be simulated with periodic boundary conditions applied. In contrast, fractional-slot designs require a larger simulation domain since the greatest common divisor (GCD) of the number of stator slots and poles is larger.

Parameters of the generator model, unless otherwise specified, are provided in Table 8.2. It is assumed that a material with $\mu_r = 1$ is placed within the magnet spacing and the slot openings such that the ferrofluid is confined to the air-gap region to minimise any increase in inter-pole or slot magnetic leakage.

Table 8.2: Key parameters of the 3 MW integer-slot direct-drive wind turbine generator.

Parameter	Symbol	Value	Units
Air-gap diameter	D_{g}	5	m
Core length	l_{core}	1	m
Number of poles	N_{pole}	160	–
Number of slots	N_{slot}	480	–
Air-gap clearance	h_{g}	5	mm
Slot pitch	τ_{slot}	32.7	mm
Slot width	w_{slot}	14.7	mm
Tooth width	w_{tooth}	18.0	mm
Slot opening width	w_{SO}	10	mm
Slot height	h_{slot}	80	mm
Rotor yoke thickness	h_{RY}	40	mm
Stator yoke thickness	h_{SY}	40	mm
Pole pitch	τ_{pole}	98.2	mm
Magnet width	w_{PM}	68.74	mm
Magnet remanent flux density	B_{rem}	1.2	T
Magnet relative permeability	$\mu_{r.\mathrm{PM}}$	1.05	–
Iron relative permeability (assumed negligible)	$u_{r,\mathrm{iron}}$	1×10^7	–

8.2.1 Inter-Pole Magnetic Leakage with a Ferrofluid-Gap

First, the influence of a ferrofluid-gap on inter-pole magnetic leakage was investigated. If ferrofluid-gaps increase inter-pole magnetic leakage, then the potential for magnetic performance enhancement would be reduced.

Two cutlines were defined for post-processing of the FEA results as shown in Figure 8.1. Cutline B was placed slightly below the top of the slots to avoid concentrations in magnetic flux density around the slot corners.

The integral of the normal component of flux density $B_{\perp}$ crossing cutline A equals the flux that crosses the air-gap region and is linked with the armature windings Φ_{linked} in addition to rotor pole-pole leakage flux Φ_{leak} from a single PM:

$$\Phi_{\mathrm{tot}} = \Phi_{\mathrm{linked}} + \Phi_{\mathrm{leak}} = \int_{l_{\mathrm{A,start}}}^{l_{\mathrm{A,end}}} |B_{\perp}|\, dl_{\mathrm{A}} \tag{8.3}$$

where l_{A} is the length of cutline A, $l_{\mathrm{A,start}}$ is the start of cutline A, and $l_{\mathrm{A,end}}$ is the end of cutline A.

The integral of $B_{\perp}$ crossing cutline B will equal twice the total flux that crosses the air-gap region and links with the armature windings:

$$\Phi_{\text{linked}} = \frac{1}{2}\int_{l_{\text{B,start}}}^{l_{\text{B,end}}} |B_{\perp}|\, dl_{\text{B}} \tag{8.4}$$

where l_{B} is the length of cutline B, $l_{\text{B,start}}$ is the start of cutline B, and $l_{\text{B,end}}$ is the end of cutline B.

A 'leakage efficiency' ζ_{leak} can be calculated which characterises the ratio of flux linked with the armature windings compared to the total flux produced by one PM (rotor pole to rotor yoke leakage is neglected):

$$\zeta_{\text{leak}} = \frac{\Phi_{\text{linked}}}{\Phi_{\text{tot}}} \tag{8.5}$$

In Figure 8.2 ζ_{leak} is presented for an air- and ferrofluid-gap with ϕ_{M} = 0.2 for a range of magnet width factors ($C_{\text{PM,w}}$) and air-gap clearance factors (C_{hg}), it was found to be very similar with less than a 1.7% difference throughout the investigated range. This similarity was found to be consistent for the full range of rotor pole-stator tooth positions.

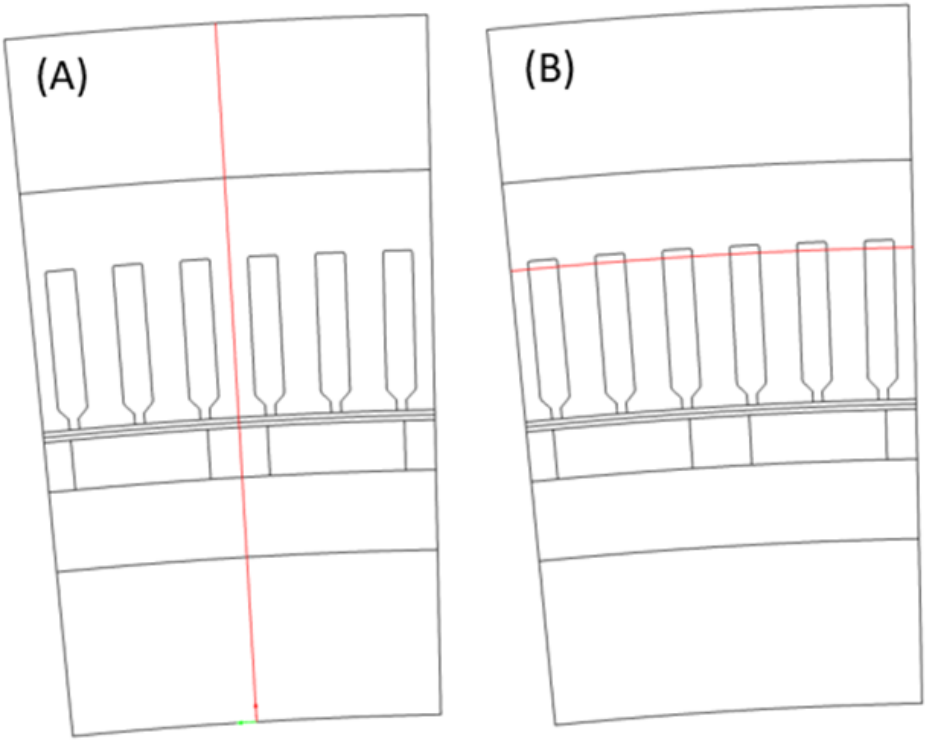

Figure 8.1: Positioning of cutline A (LHS) and cutline B (RHS).

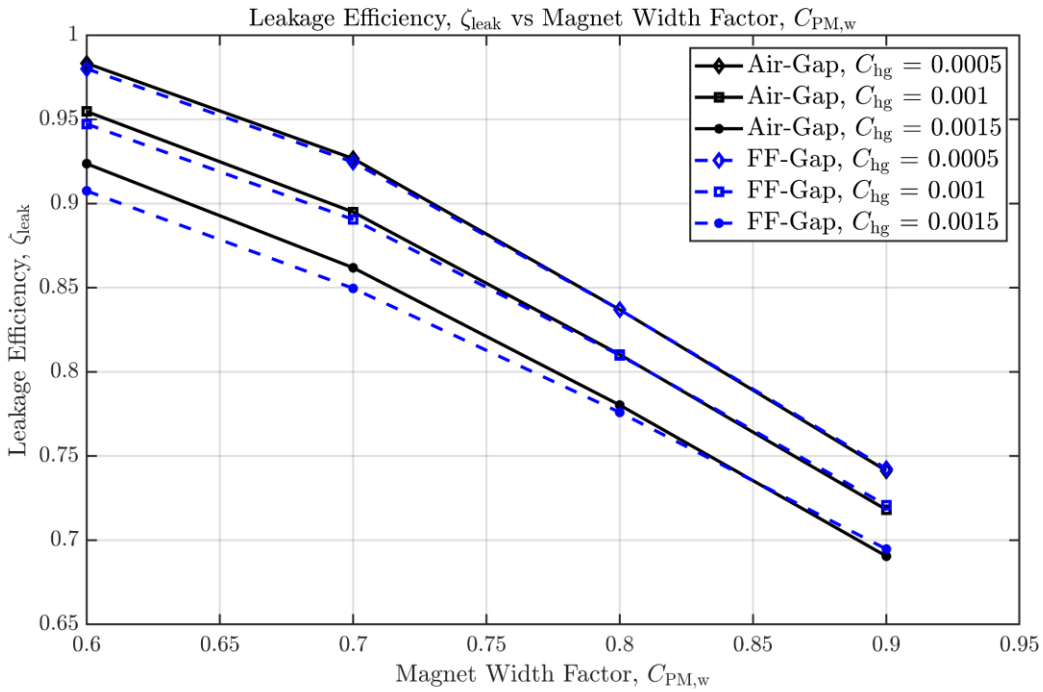

Figure 8.2: Leakage efficiency (ζ_{leak}) for air- and ferrofluid-gap with a magnetic volume fraction (ϕ_{M}) of 0.2 compared for a range of magnet width factors ($C_{\mathrm{PM,w}}$) and air-gap clearance factors (C_{hg}).

8.2.2 An Open-Load Analysis

Since ζ_{leak} is very similar for air- and ferrofluid-gaps a 1D magnetic circuit analysis can be used to calculate the relative effect of a ferrofluid-gap on PM flux compared to a conventional air-gap in an open-load condition:

$$\Delta\Phi_{\%} = \left(\frac{\Phi_{\mathrm{FG}} - \Phi_{\mathrm{AG}}}{\Phi_{\mathrm{AG}}}\right) 100 \tag{8.6}$$

where Φ_{FG} is the PM flux with a ferrofluid-gap and Φ_{AG} the PM flux with an air-gap.

For an estimate of Φ_{FG} an iterative approach is required to account for the non-linear magnetic properties of the ferrofluid.

First an estimate is made of the flux density in the air-gap region (B_{g}). it is convenient to estimate B_{g} as the flux density resulting from a conventional air-gap (this can be achieved using Eq. (2.14) to (2.19) presented in Chapter 2, Section 2.1.4).

The magnetic field strength in the air-gap region (H_{g}) can then be obtained according to the ferrofluid *BH* curve (this can be generated according to the Eq. (5.24) to (5.30) presented in Chapter 5, Section 5.3.1).

A value for Φ_{FG} can then be obtained by considering the magnetomotive force (MMF) drop in the ferrofluid-gap region:

$$\Phi_{\mathrm{FG}} = \frac{\mathcal{F}_{\mathrm{PM}} - C_{\mathrm{carter}} h_{\mathrm{g}} H_{\mathrm{g}}}{\mathcal{R}_{\mathrm{PM}}} \tag{8.7}$$

Where $\mathcal{F}_{PM}$ is the MMF of one PM, $\mathcal{R}_{PM}$ is the PM reluctance, and C_{carter} is the Carter factor.

A new value for B_{g} can then be obtained:

$$B_{\mathrm{g,new}} = \frac{\Phi_{\mathrm{FG}}}{A_{\mathrm{PM}}} \tag{8.8}$$

where A_{PM} is the cross-sectional area of the PM.

The process is then repeated by finding the corresponding value of $H_{\mathrm{g,new}}$ according to the ferrofluid-gap *BH* curve and repeating the procedure until the value of $B_{\mathrm{g,new}}$ converges to a steady value.

In Figure 8.3 the increase in magnetic flux linked with the armature windings due to a ferrofluid-gap with ϕ_{M} = 0.2 is plotted for a range of air-gap clearance factors (C_{hg}). The 1D magnetic circuit and FEM modelling approach are observed to provide similar results.

In Figure 8.4 the potential reduction in PM mass due to a ferrofluid-gap predicted by the 1D magnetic circuit model is plotted for a range of ϕ_{M} for various values of B_g. It is observed that for $\phi_{\mathrm{M}} = 0.2$, greater than a 10% reduction in the PM mass may be possible.

In Figure 8.5 the increase in flux crossing the air-gap region due to a ferrofluid-gap with ϕ_{M} = 0.2 predicted by a 1D magnetic circuit method and FEM is compared for a range of magnet height factors for both the 3 MW integer slot machine, and a fractional-slot machine corresponding to the IEA 15 MW reference design [13]. It is shown that the 1D magnetic circuit method provides a reasonable approximation for both machine topologies.

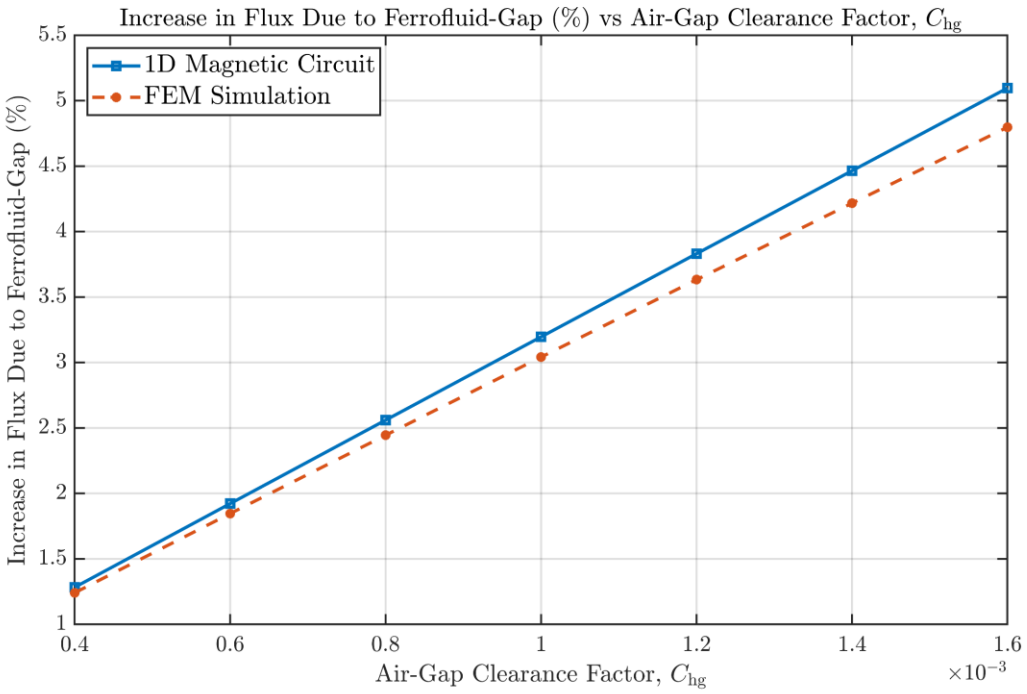

Figure 8.3: Increase in magnetic flux (%) due to a ferrofluid-gap with a magnetic volume fraction (ϕ_M) of 0.2 in comparison to an air-gap for a range of air-gap clearance factors (C_{hg}). Results from the 1D magnetic circuit model and the finite element method (FEM) simulation are compared.

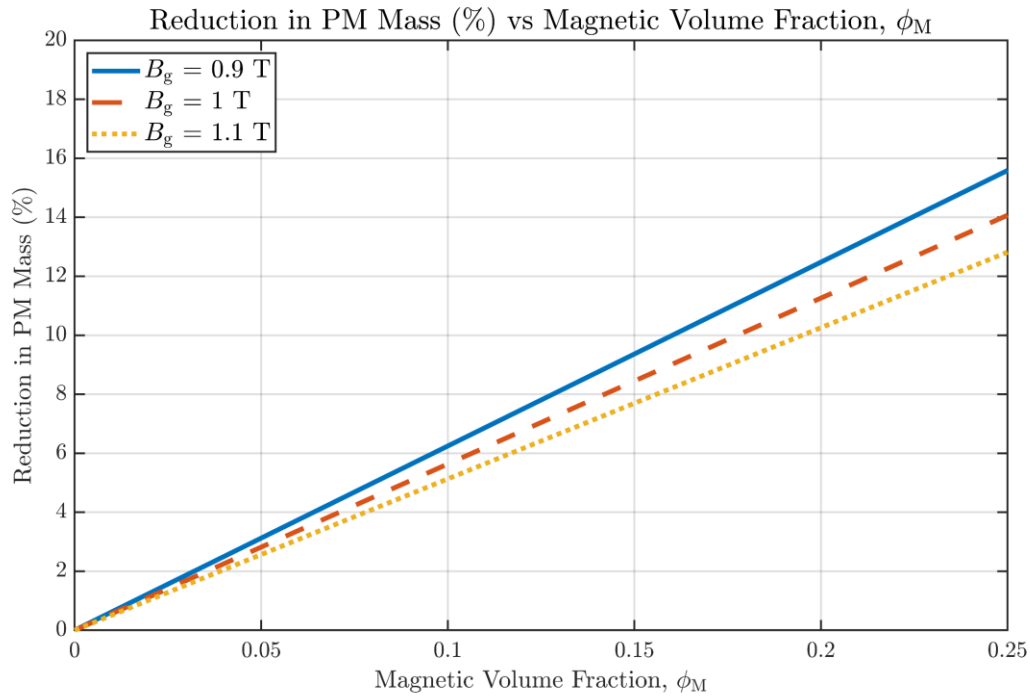

Figure 8.4: Reduction in permanent magnet (PM) mass for a range of magnetic volume fractions (ϕ_M) based on an open-load condition. Various air-gap magnetic flux densities (B_g) are compared.

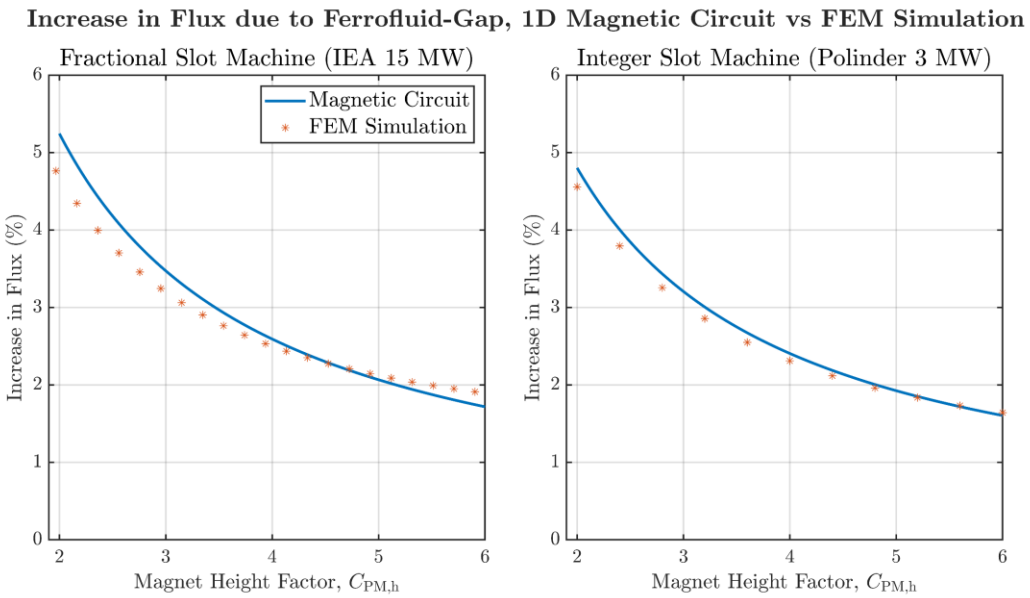

Figure 8.5: Increase in magnetic flux (%) due to a ferrofluid-gap with a magnetic volume fraction (ϕ_M) of 0.2 compared to an air-gap calculated for a range of magnet height factors ($C_{PM,h}$) estimated from a 1D magnetic circuit model and finite element method (FEM) simulations. Results are presented for a fractional slot and an integer slot direct-drive (DD) wind turbine generator (WTG) [13], [22].

8.2.3 Additional Sources of Magnetic Circuit Reluctance

In the previous sections the magnetic circuit of the DD WTG was idealised such that the magnetic behaviour of the ferrofluid-gap could be evaluated independently. However, there are additional sources of magnetic reluctance to consider.

Magnetic saturation of the stator yoke, teeth, and rotor yoke will reduce the flux enhancing potential of a ferrofluid-gap. If the electrical steel is significantly saturated, then the increase in flux due to the ferrofluid-gap may be rendered negligible.

In Figure 8.6 the improvement in flux due to a ferrofluid-gap is plotted for a range of tooth widths with a non-linear *BH* curve assigned to the electrical steel components in the FEM analysis. The COMSOL Multiphysics 6.1 ‘soft iron’ material properties were used in this analysis. It is demonstrated that significant saturation in the electrical steel components will negate the magnetic benefits of a ferrofluid-gap.

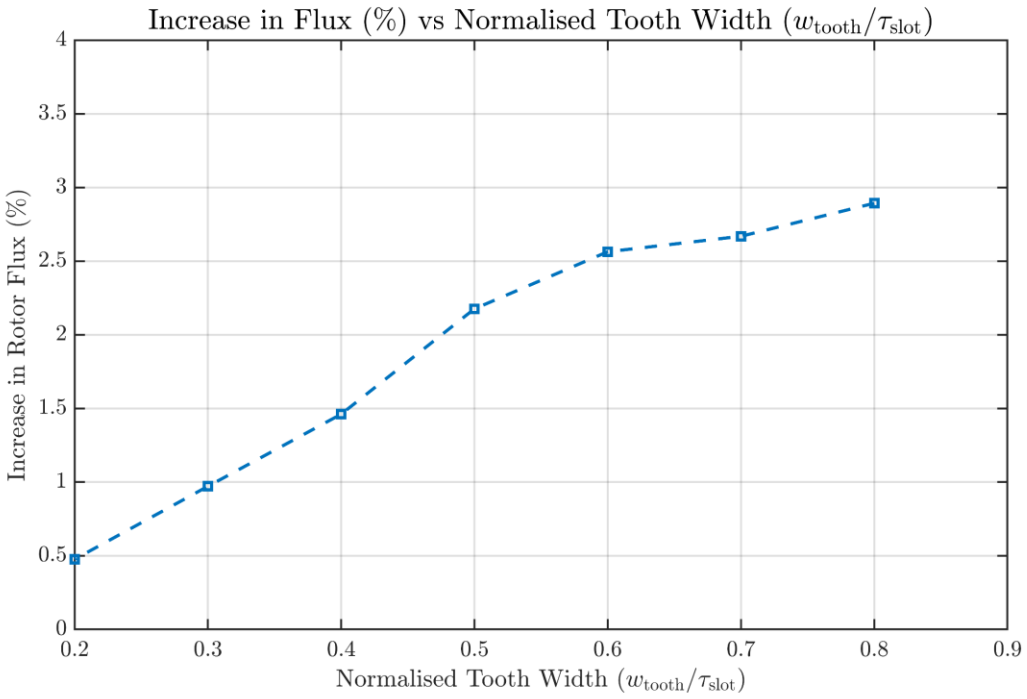

Figure 8.6: Increase in magnetic flux (%) due to a ferrofluid-gap with a magnetic volume fraction (ϕ_{M}) of 0.2 compared to an air-gap calculated for a range of normalised tooth width to slot pitch ratios ($w_{\text{tooth}}/\tau_{\text{slot}}$). Obtained from finite element method (FEM) simulations with iron reluctance included.

The PM coating and the magnet glue will result in an additional component of reluctance in the magnetic circuit, reducing the impact of a ferrofluid-gap. Eq. (5.5) and Eq. (5.6) from Chapter 5, Section 5.1.1, can be modified to incorporate the magnet glue and coating reluctance:

$$B_{\text{g}} = \frac{B_{\text{rem}} h_{\text{PM}}}{\mu_{r,\text{PM}} \left(\frac{h_{\text{g}}}{\mu_{r,\text{g}}} + \frac{h_{\text{PM}}}{\mu_{r,\text{PM}}} + t_{\text{glue}} + t_{\text{coat}} \right)} \tag{8.9}$$

$$h_{\text{PM}} = \frac{\mu_{r,\text{PM}} B_{\text{g}} \left(\frac{h_{\text{g}}}{\mu_{r,\text{g}}} + t_{\text{glue}} + t_{\text{coat}} \right)}{\left(B_{\text{rem}} - B_{\text{g}} \right)} \tag{8.10}$$

The implication is that a ferrofluid-gap will have more of an impact with increasing air-gap size assuming that the magnet reinforcement and glue thickness remain constant. In Figure 8.7 the percentage reduction in PM mass possible for a ferrofluid gap with $\phi_{\text{M}} = 0.2$, $B_{\text{g}} = 1\,T$, and $B_{\text{rem}} = 1.2\,T$, is presented for a range of air-gap clearances assuming a magnet glue and reinforcement thickness of 0.1 mm and 0.5 mm respectively. In this case it is shown that the magnet glue and coating significantly hinder the potential to reduce the PM mass for air-gap clearances below ~4 mm.

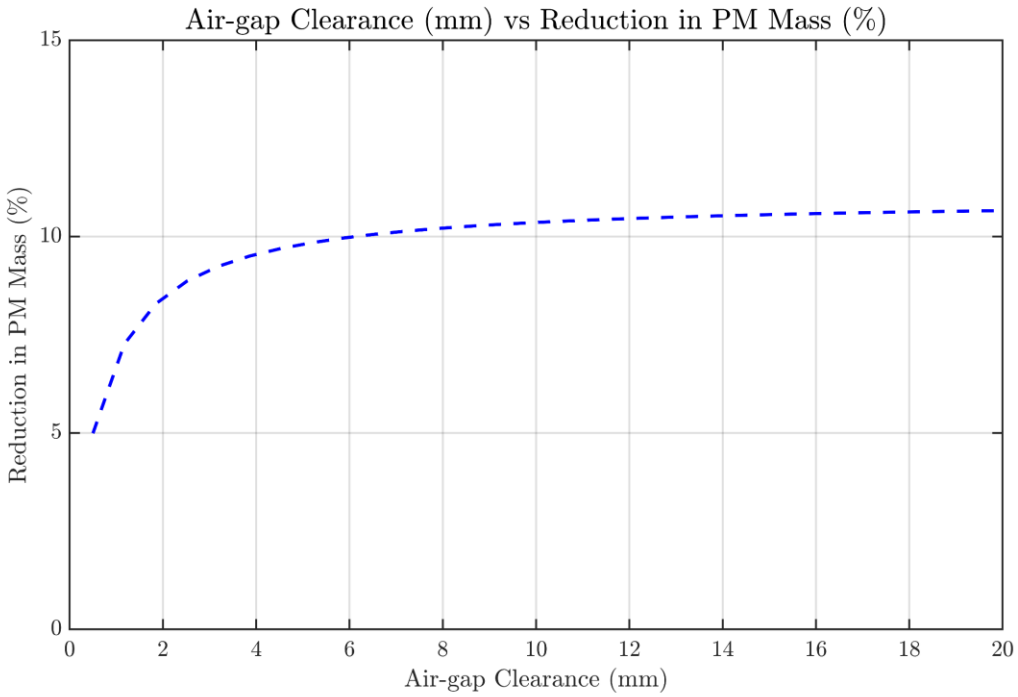

Figure 8.7: Potential reduction in permanent magnet (PM) mass (%) achievable with a ferrofluid-gap with a magnet volume fraction (ϕ_{M}) of 0.2 for a range of air-gap clearance values assuming a magnet glue and reinforcement thickness of 0.1 mm and 0.5 mm respectively.

8.2.4 Influence on Electromagnetic Torque

The electromagnetic torque $\mathcal{T}_E$ developed by the machine with an armature winding RMS current density of 3 A/mm^2 was calculated for an air- and ferrofluid-gap using FEM and Arkkio's method as detailed in Chapter 7, Section 7.1.3.2 [168]:

The average electromagnetic shear stress was calculated as:

$$\bar{\sigma}_t = \frac{\mathcal{T}_E}{2\pi r_r^2 l_c} \tag{8.11}$$

In Figure 8.8 $\bar{\sigma}_t$ developed for various magnet height factors ($C_{\mathrm{PM,h}}$) is presented for an air- and ferrofluid-gap with ϕ_{M} = 0.2. The presented value of $\bar{\sigma}_t$ is an average taken over the full range of rotor pole-stator tooth positions such that the influence of cogging torque is eliminated. It appears that the PM mass can be reduced by ~14% to achieve the same $\bar{\sigma}_t$ as a conventional air-gap. In this case the load angle was specified to be 90° and the iron reluctance was neglected.

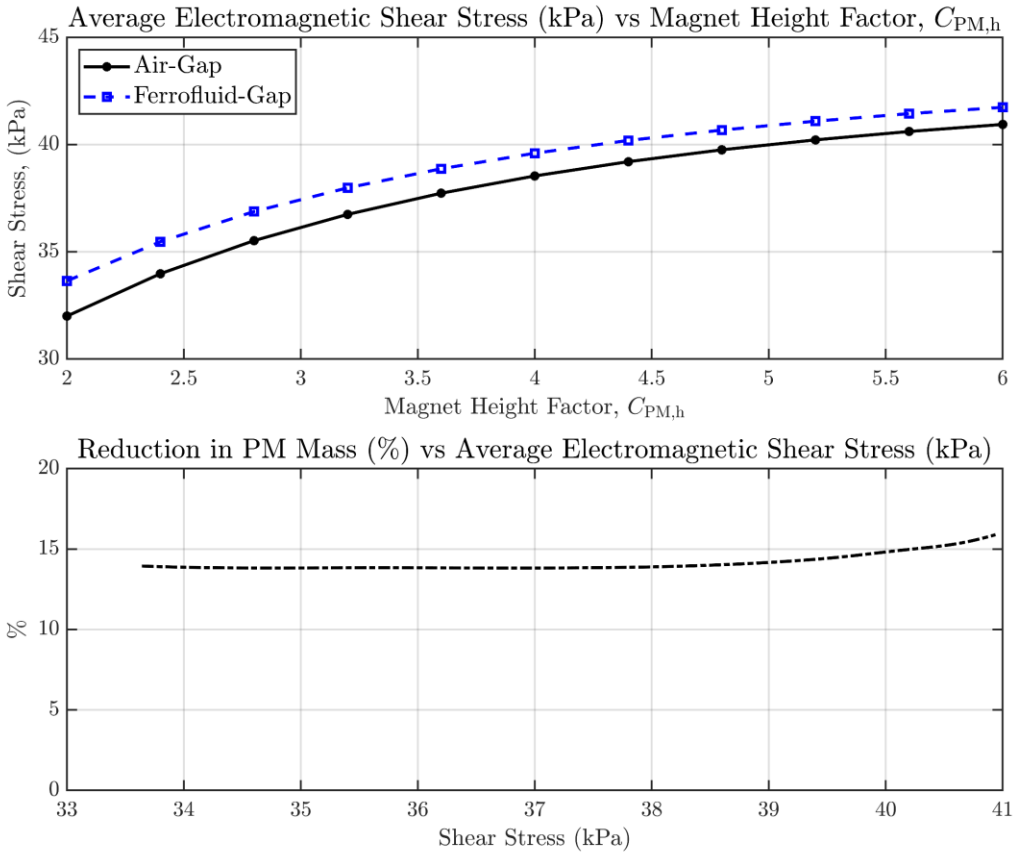

Figure 8.8: Average electromagnetic shear stress (kPa) developed for an air- and ferrofluid-gap with a magnetic volume fraction (ϕ_M) of 0.2 for a range of magnet heights obtained from finite element method (FEM) simulations. The potential reduction in permanent magnet (PM) mass due to the ferrofluid-gap is plotted.

8.2.5 Impact of Armature Reaction

The stator field can influence the extent of saturation in the electrical steel components, potentially influencing the effectiveness of the ferrofluid-gap. In Figure 8.9 the increase in torque due to a ferrofluid gap with ϕ_M = 0.2 is plotted for a range of load angles where the electrical steel is assigned a non-linear BH curve and when it is assumed to have a large linear permeability of 1×10^7.

As the load angle is increased the increase in torque due to the ferrofluid-gap can be seen to decrease when the electrical steel is assigned a non-linear BH curve, this is due to increased saturation of the stator teeth in the d-axis of the machine. In comparison, if linear magnetic properties are assumed, the load angle is observed to have no impact on the increase in torque due to the ferrofluid-gap.

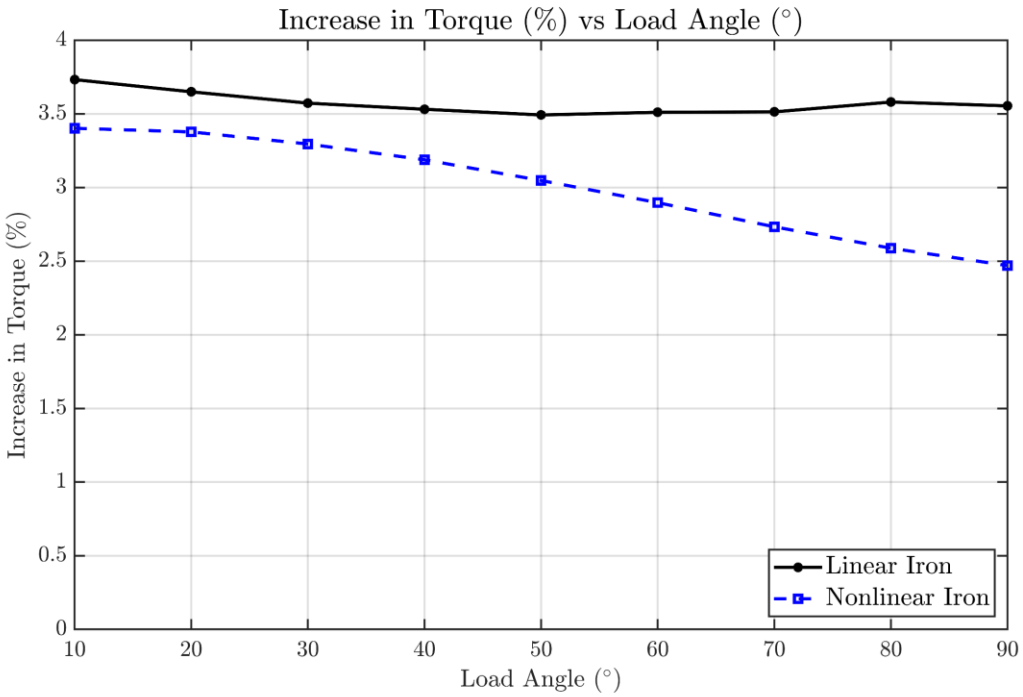

Figure 8.9: Increase in electromagnetic torque (%) due to a ferrofluid-gap with a magnetic volume fraction (ϕ_M) of 0.2 plotted over a range of load angles (°) for linear and nonlinear iron permeability. Results are obtained from finite element method (FEM) simulations.

8.2.6 Summary of Magnetic Analysis

In summary of the magnetic analysis:

- It was demonstrated that a ferrofluid-gap has little impact on inter-pole magnetic leakage assuming that the magnet spacing is filled with a material with $\mu_r = 1$.
- Since the inter-pole magnetic leakage is similar for an air- and ferrofluid-gap, the impact of a ferrofluid-gap on the magnetic performance of DD WTGs can be approximated well using a 1D magnetic circuit.
- Although the relative increase in magnetic flux due to a ferrofluid-gap is relatively small, this can result in a significant saving in PM mass.
- Significant magnetic saturation of the electrical steel components will reduce the flux enhancing capabilities of a ferrofluid-gap.
- Additional sources of reluctance, such as magnet glue and reinforcement can reduce the flux enhancing capabilities of a ferrofluid-gap, the impact is reduced with increasing air-gap clearance.
- A ferrofluid-gap is shown to increase torque in loaded conditions, however armature reaction can influence the saturation of the electrical machine components and should be considered when performing a detailed analysis.

8.3 Ferrofluid-Gap Drag and Impact on Efficiency

The following section will discuss the extent of ferrofluid-gap drag, and consequently the reduction efficiency that results due to the implementation of ferrofluid-gaps in PM DD WTGs.

8.3.1 Calculation of Ferrofluid-Gap Drag

As discussed in Chapter 6, Section 6.1.1, it is assumed that the magnet spacings and slot openings are filled with a non-magnetic material, approximating an idealised Taylor-Couette (TC) flow geometry.

For laminar flow, the torque resulting from ferrofluid-gap viscous drag in the absence of a magnetic field can be calculated as:

$$\mathcal{T}_{\text{drag}} = 4\pi\eta_{\text{FF},0}\omega l_c\left(\frac{r_r^2 r_s^2}{r_s^2 - r_r^2}\right) \tag{8.12}$$

where $\eta_{\text{FF},0}$ is the ferrofluid dynamic viscosity in the absence of an external magnetic field.

To estimate the drag for turbulent ferrofluid-gap flow computational fluid dynamics (CFD) simulations were carried out using the large eddy simulation (LES) method for inner-rotor TC flow with a radius ratio of 0.998, this equates to an air-gap clearance equaling 1/1000$^{\text{th}}$ the air-gap diameter.

As discussed in Chapter 3, Section 3.3.3.1, thin-gap TC flow is linearly stable, however it is reasonable to expect that in DD WTGs the flow will experience significant perturbations that will induce turbulence. In each simulation the flow was initially perturbed from a laminar initial condition by applying a Gaussian pulse to the tangential velocity of the rotor wall, this raised the tangential velocity by 250% and then lowered it back to the initial value over a period of 0.1 seconds. If the turbulence was sustained after the perturbation, then a turbulent flow state was assumed for the DD WTG ferrofluid-gap. For relatively low Reynolds numbers (Re) the flow would quickly decay back to a laminar state.

The non-dimensional torque coefficient was determined over a range of Re [174]:

$$C_{\mathcal{T}} = \frac{\mathcal{T}_{\text{drag}}}{0.5\pi\rho_{FF} l_c \omega^2 r_r^4} \tag{8.13}$$

where ρ_{FF} is the ferrofluid density.

This approach allows for a correlation between the drag predicted with the CFD simulations and a ferrofluid-gap with arbitrary fluid properties and WTGs with arbitrary scale, assuming that the air-gap clearance is equal to 1/1000th of the air-gap diameter.

In Figure 8.10 the trend of $C_{\mathcal{T}}$ vs Re is plotted based on an analytical calculation of laminar flow and from results obtained from the CFD simulations. A transition to turbulent flow was observed to occur at a Reynolds number of ~1000.

For turbulent flow, the drag can be estimated by first calculating the Reynolds number, determining the associated value of $C_{\mathcal{T}}$, and then rearranging Eq. (8.13) to solve for $\mathcal{T}_{\mathrm{drag}}$:

$$C_{\mathcal{T}} = 0.005015 \quad 800 \leq \mathrm{Re} < 1578 \tag{8.14}$$

$$C_{\mathcal{T}} = 0.0874\mathrm{Re}^{-0.3882} \quad 1578 \leq \mathrm{Re} \leq 20{,}000 \tag{8.15}$$

To facilitate a fast computation of $C_{\mathcal{T}}$ for a given set of ferrofluid properties and WTG parameters a constant value of $C_{\mathcal{T}}$ is assumed for the transitional flow regime. For developed flow, C_{τ} is calculated according to a power law fit of the CFD data. This approach results in a conservative estimate of C_{τ}.

As demonstrated in Chapter 7, Section 7.1.2, the magnetic field increases the ferrofluid-gap drag and can be approximated reasonably well with an analytical method without the need for computationally expensive multi-physics simulations. The influence of the magnetic field on the ferrofluid-gap drag is therefore accounted for by multiplying the predicted drag by a correction factor which approximates the additional rotational viscosity of the ferrofluid above the poles:

$$C_{\mathrm{rot,vis}} = 1 + \frac{3}{2} C_{\mathrm{PM,w}} \phi_{\mathrm{H}} \frac{\xi - \tanh \xi}{\xi + \tanh \xi} \tag{8.16}$$

where $C_{\mathrm{PM,w}}$ is the magnet width factor, and ξ is the Langevin parameter.

The WTG power loss due to the ferrofluid-gap drag can therefore be estimated as:

$$P_{\mathrm{drag}} = C_{\mathrm{rot,vis}} \mathcal{T}_{\mathrm{drag}} \omega \tag{8.17}$$

As discussed in Chapter 3, Section 3.3.3.1, determining the flow state of outer-rotor TC flow is challenging due to the lack of centrifugal instability. Perturbations such as

non-uniformity and displacement of the air-gap due to external loading and manufacturing tolerances have the potential to induce subcritical turbulence which can result in increased drag. Because the onset and persistence of such turbulence depend on case-specific details, the associated drag is difficult to generalise. A practical approach is to define bounds: the laminar solution provides a lower limit, Eq. (8.12), while the drag scaling of inner-rotor TC with equivalent geometry serves as an upper bound.

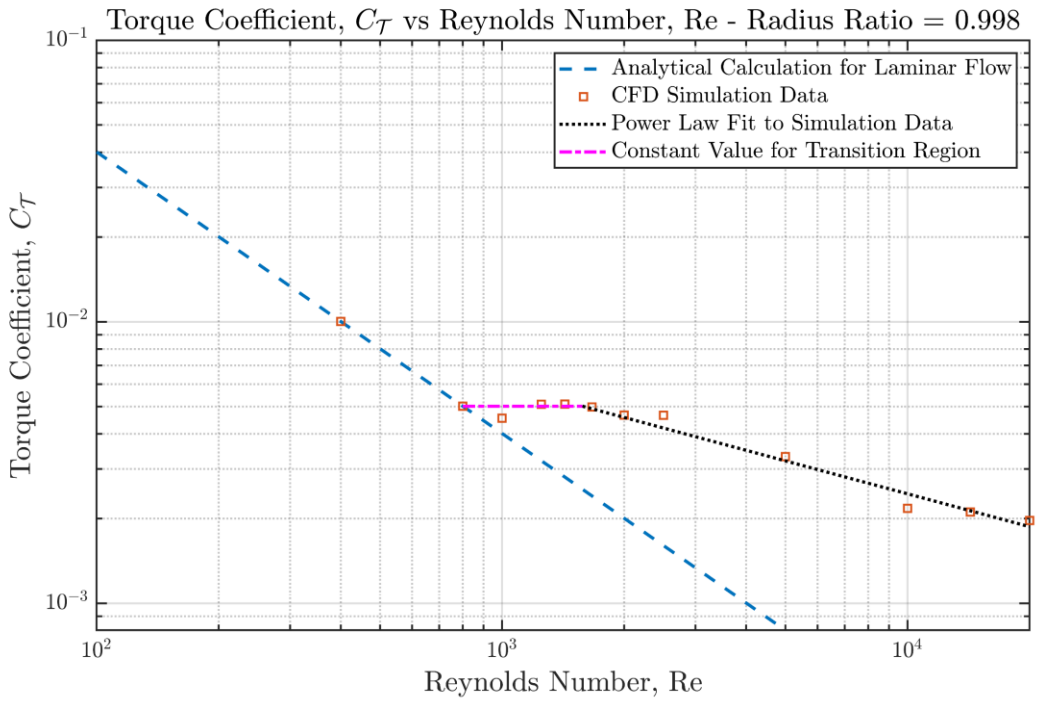

Figure 8.10: Torque coefficient ($C_\mathcal{T}$) vs Reynolds number (Re) for a Taylor-Couette (TC) flow with a radius ratio of 0.998. The blue dashed line represents an analytical calculation for laminar flow, the orange squares are data points obtained from computational fluid dynamics (CFD) simulations, the black dotted line is a power law fit of the simulation data, and the pink dashed line is a constant value approximated for the region of laminar-turbulent transition.

8.3.2 Impact of Ferrofluid-Gap Drag on Efficiency

In the following section the impact of ferrofluid-gap drag on DD WTG efficiency is explored. First, the impact of ferrofluid-gap drag on the efficiency of the example 15 MW machine introduced in Chapter 2 is examined.

In Figure 8.11 the loss in efficiency at rated speed is calculated for a range of magnetic volume fractions assuming a ferrofluid-gap temperature of $100^{\circ}\mathrm{C}$. A lower- and upper-bound estimate of efficiency loss is included which corresponds to laminar and turbulent flow conditions respectively. As the magnetic volume fraction is increased

the loss in efficiency is observed to increase significantly due to the increased viscosity of the ferrofluid. However, even with a large magnetic volume fraction of 0.2 and an assumption of turbulent flow the loss in efficiency reaches a peak of only 0.11%.

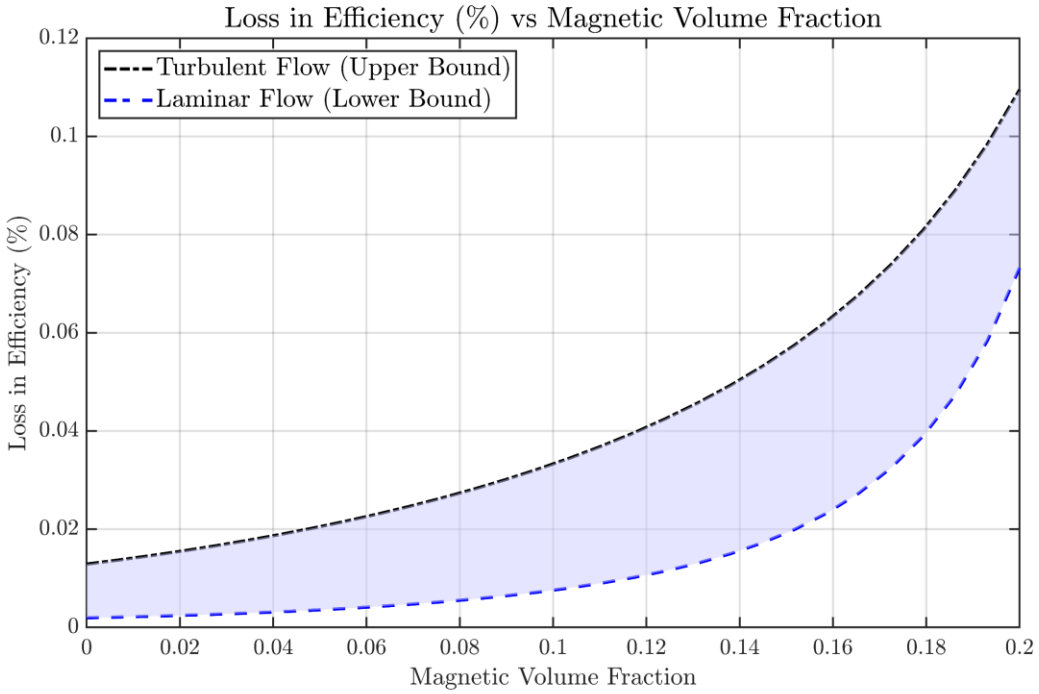

Figure 8.11: Loss in efficiency (%) of the example 15 MW direct-drive (DD) wind turbine generator (WTG) resulting from ferrofluid-gap drag at rated speed and a temperature of $100^{\circ}\mathrm{C}$ for a range of magnetic volume fraction (ϕ_{M}). An upper- and lower-bound estimate is provided assuming turbulent and laminar flow respectively.

As discussed in Section 8.1, the viscosity of a mineral oil based ferrofluid is sensitive to temperature. DD WTGs can take several hours to reach a steady state temperature, and if operating below rated conditions the component temperatures may remain relatively low. Therefore, the ferrofluid-gap temperature can be expected to vary significantly during the operational lifetime of a DD WTG. In Figure 8.12 the loss in efficiency of the example 15 MW machine at rated speed is investigated for temperatures ranging between $20 - 100^{\circ}\mathrm{C}$ for a range of magnetic volume fractions. The loss in efficiency is observed to increase significantly with increasing magnetic volume fraction, reaching a peak of ~0.6% for a magnetic volume fraction of 0.2 at a temperature of $20^{\circ}\mathrm{C}$, compared to a peak of only ~0.16% for a magnetic volume fraction of 0.15 at $20^{\circ}\mathrm{C}$.

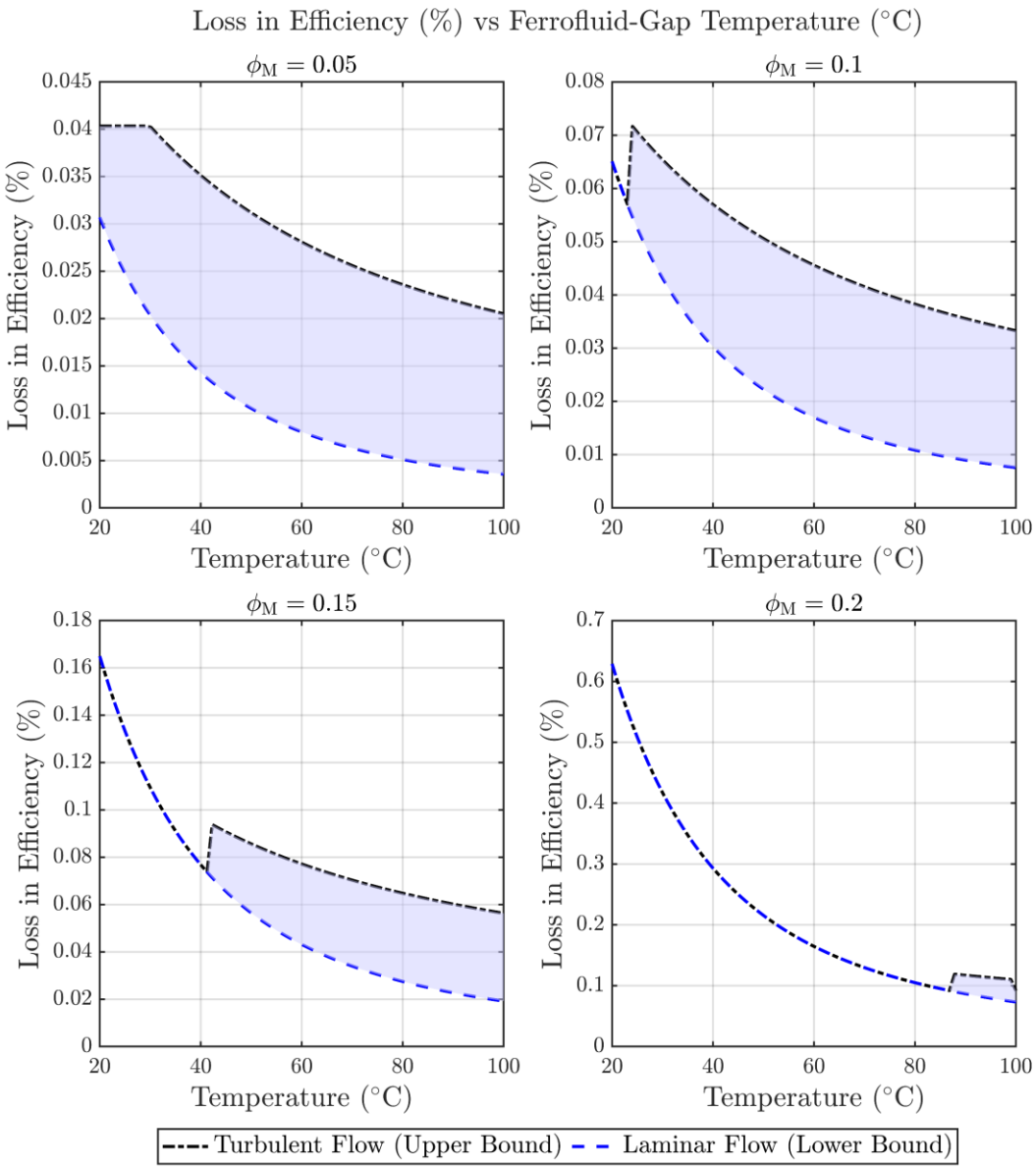

Figure 8.12: Loss in efficiency (%) of the example 15 MW direct-drive (DD) wind turbine generator (WTG) resulting from ferrofluid-gap drag at rated speed for various magnetic volume fractions (ϕ_M) and a range of ferrofluid temperatures (°C).

In Figure 8.13 an upper bound estimate for the loss in efficiency at rated speed is investigated for a range of wind turbine power capacities for a ferrofluid temperature of 100°C. The geometry and speed of the various WTG topologies under study were obtained using the sizing equations introduced in Chapter 2, Section 2.1.3, subject to the input parameters presented in Table 2.1.

For magnetic volume fractions of 0.15 and lower the loss in efficiency is observed to remain relatively consistent for power capacities greater than ~5 MW. For a magnetic

volume fraction of 0.2 the loss in efficiency is observed to decrease significantly with increasing power capacity up to a rating of ~8 MW.

This can be explained due to the onset of turbulence. As highlighted in Chapter 5, Section 5.1.2, for laminar flow the loss in efficiency is observed to decrease with increasing power capacity due to a reduced shear rate resulting from an increased air-gap clearance and reduced rotational speed. However, for turbulent flow, the reduction in shear rate is offset by an increase in Reynolds number which results in a relatively consistent trend of efficiency loss vs power capacity.

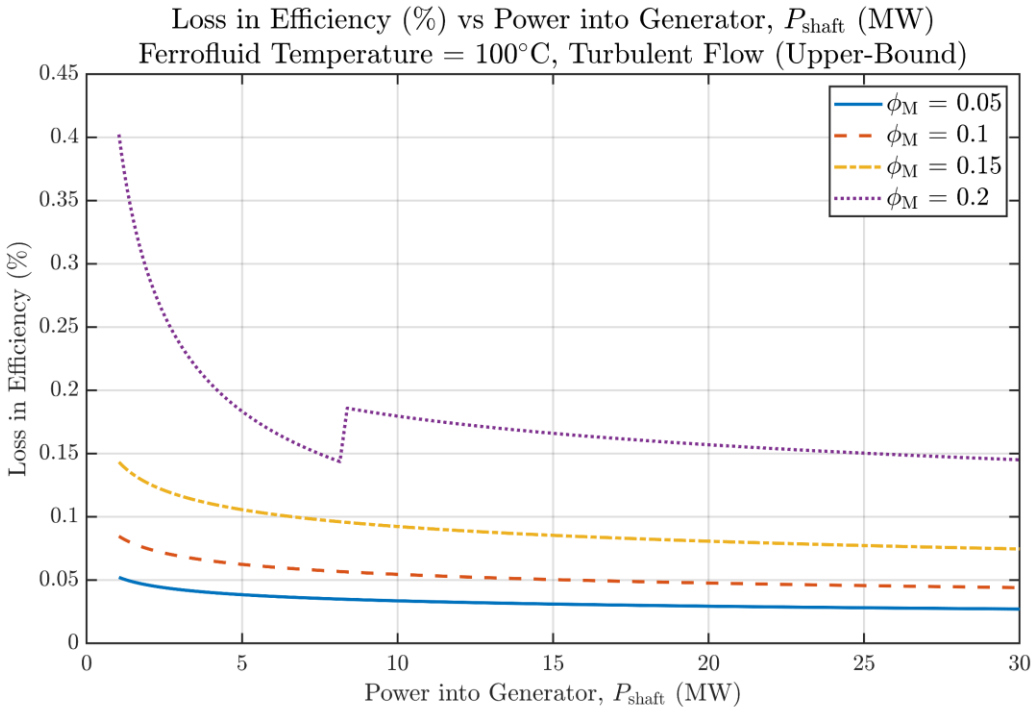

Figure 8.13: Loss in efficiency (%) resulting from ferrofluid-gap drag at rated speed for various direct-drive (DD) wind turbine generator (WTG) designs obtained from scaling equations subject to a range of input powers (P_{shaft}). Turbulent flow is assumed at a ferrofluid temperature of 100°C for various magnetic volume fractions (ϕ_{M}).

8.3.3 Reduction in PM Mass vs Energy Yield

In the following section a fundamental question regarding the performance of ferrofluid-gaps in DD WTGs is addressed:

- “Does the cost saved in PM material exceed the loss in WTG lifetime revenue due to the reduction in efficiency resulting from ferrofluid-gap drag?”

As detailed in Section 8.2.2, the magnetic performance of a ferrofluid-gap can be compared against a conventional air-gap with reasonable accuracy with the use of a 1D magnetic circuit model since the inter-pole magnetic leakage is very similar.

As highlighted in Chapter 7, Section 7.1.3.1, the ferrofluid-gap should have little impact on the magnetising inductance of the machine since it is saturated in the d-axis. Although it will be unsaturated in the q-axis this increase in permeability will be offset by the relative permeability of the PMs in the d-axis. It is therefore assumed that for surface mounted PM WTGs, the common approximation that the d- and q-axis magnetising inductance is comparable still applies: $L_{m,\mathrm{d}} \approx L_{m,\mathrm{q}}$.

To obtain a first approximation of the PM mass reduction, magnetic saturation of the electrical steel components and the impact of the ferrofluid-gap on the thermal performance of the machine are neglected.

Following the design procedure presented in Chapter 2, the impact of a ferrofluid-gap on the performance of the example 15 MW machine was evaluated over a range of magnetic volume fractions. In Figure 8.14 the reduction in PM mass and the loss in annual energy yield are plotted for a range of magnetic volume fractions and for a range of constant ferrofluid-gap temperatures. It was found that the temperature of the ferrofluid-gap has a very significant impact on the additional loss in annual energy yield as the magnetic volume fraction increases beyond a value of ~0.12.

To compare the cost reduction in the PM material with the loss in lifetime revenue several assumptions must be made regarding the PM material cost, the cost of energy, the discount rate, and the production-based availability factor. Such assumptions are open to interpretation due to the volatility of rare-earth PM material costs (as discussed in Chapter 2, Section 2.2.1) and the region and energy market in which the wind turbine is assumed to operate.

For an appropriate comparison of PM material cost savings and the loss in lifetime revenue the costs must be compared on a net present value (NPV) basis. Since PM costs are an upfront capital cost, no discount factor is applied. However, a discount rate is applied in the calculation of lifetime revenue:

$$\Pi_{\mathrm{Rev}} = \mathrm{AEP}\frac{\zeta_{\mathrm{av}} C_{\mathrm{MWh}} t_{\mathrm{life}}}{(1+i_{\mathrm{DR}})^{t_{\mathrm{life}}}} \tag{8.18}$$

where AEP is the annual energy production, ζ_{av} is the production-based availability factor, C_{MWh} is the price per MWh of energy produced, t_{life} is the wind turbine lifetime in years, and i_{DR} is the discount rate.

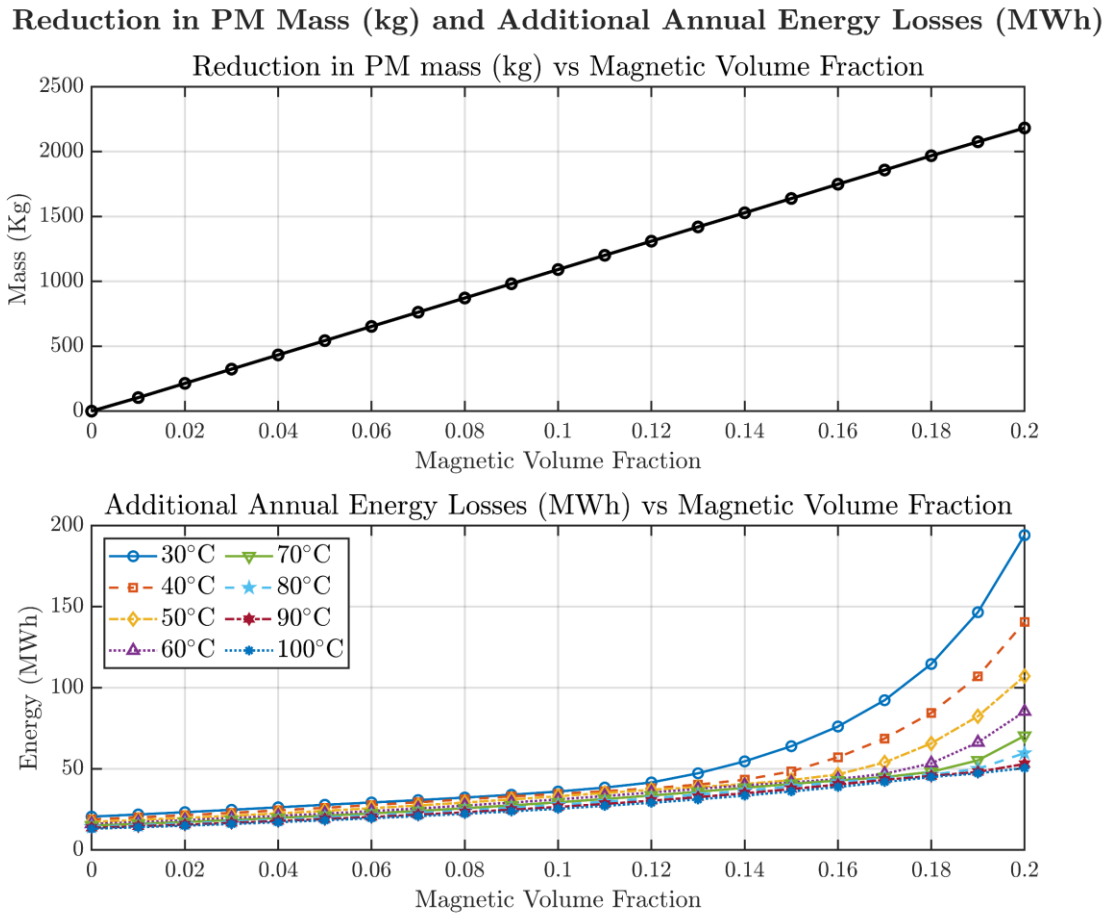

Figure 8.14: Reduction in permanent magnet (PM) mass (kg) due to a ferrofluid-gap in the example 15 MW direct-drive (DD) wind turbine generator (WTG) for a range of magnetic volume fractions (ϕ_{M}), and the additional annual energy losses (MWh) due to ferrofluid-gap drag for a range of ϕ_{M} and ferrofluid temperatures (°C).

In Figure 8.15 the PM material cost saving is compared with the loss in revenue assuming a 25-year lifetime. The following assumptions are made:

- The cost of the NeFeB 52H PMs utilised in the example 15 MW machine is assumed to be 29,130 $/tonne [42].
- The cost of energy is assumed to be 152.7 $/MWh which corresponds to the UK's contracts for difference allocation round 7 strike price [175].
- A discount rate of 7% is assumed which is regarded as reasonable for offshore wind projects [176], [177].
- A production-based availability factor of 94% is assumed [178].

Based on these assumptions, the PM material cost reduction can exceed the additional loss in revenue for magnetic volume fractions greater than ~0.05. However, the peak cost saving is relatively modest with a saving of only ~$30,000 assuming the ferrofluid has a very high magnetic volume fraction of 0.2. The optimal ferrofluid-gap magnetic volume fraction is observed to depend on the assumed temperature, for relatively low ferrofluid temperatures increasing the magnetic volume fraction can negatively impact the net cost saving due to the increased ferrofluid-gap drag. Considering that the example 15 MW machine has an air-gap volume of 0.678 m^3, a ferrofluid unit cost of less than $44.2 per litre would be required to break even. Replacement of the ferrofluid during the wind turbine's lifetime and other associated costs would further decrease this value.

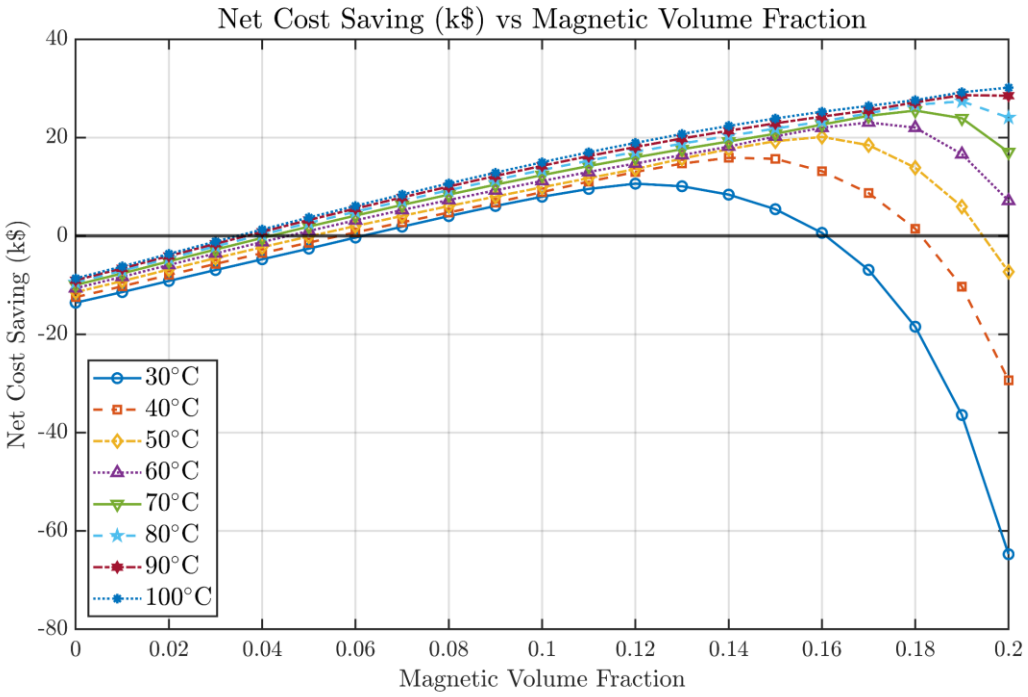

Figure 8.15: The net cost saving taking into account the reduction in permanent magnet (PM) mass and the reduced efficiency of the example 15 MW direct-drive (DD) wind turbine generator (WTG) due to a ferrofluid-gap for a range of magnetic volume fraction (ϕ_{M}) and various ferrofluid-gap temperatures (°C). Assumed magnet cost of $29,130 per tonne and cost of energy of 152.7 $/MWh.

Due to the volatility of rare-earth magnet prices and the cost of energy, the potential cost saving can change significantly if different, yet still reasonable, assumptions are made regarding the PM cost and the cost of energy. In Figure 8.16 the net cost saving is presented assuming:

- The magnet price is doubled to $58,260 due to a spike in cost (which is not unreasonable as detailed in Chapter 2, Section 2.2.1).

- The cost of energy is assumed to be 80.9 $/MWh which corresponds to the UK's contracts for difference round 3 strike price (inflation-adjusted for 2025) [179].
- As before a discount rate of 7% and a production-based availability factor of 94% is assumed.

Based on these assumptions, it could be concluded that the reduction in magnet costs comfortably exceeds the additional loss in revenue for magnetic volume fractions greater than ~0.01. A peak cost saving of ~$100,000 is obtained assuming that the ferrofluid has a magnetic volume fraction of 0.2. A ferrofluid cost of $147.5 per litre would be required to break even. As before, replacement of the ferrofluid during the wind turbine's lifetime and other associated costs would further decrease this value.

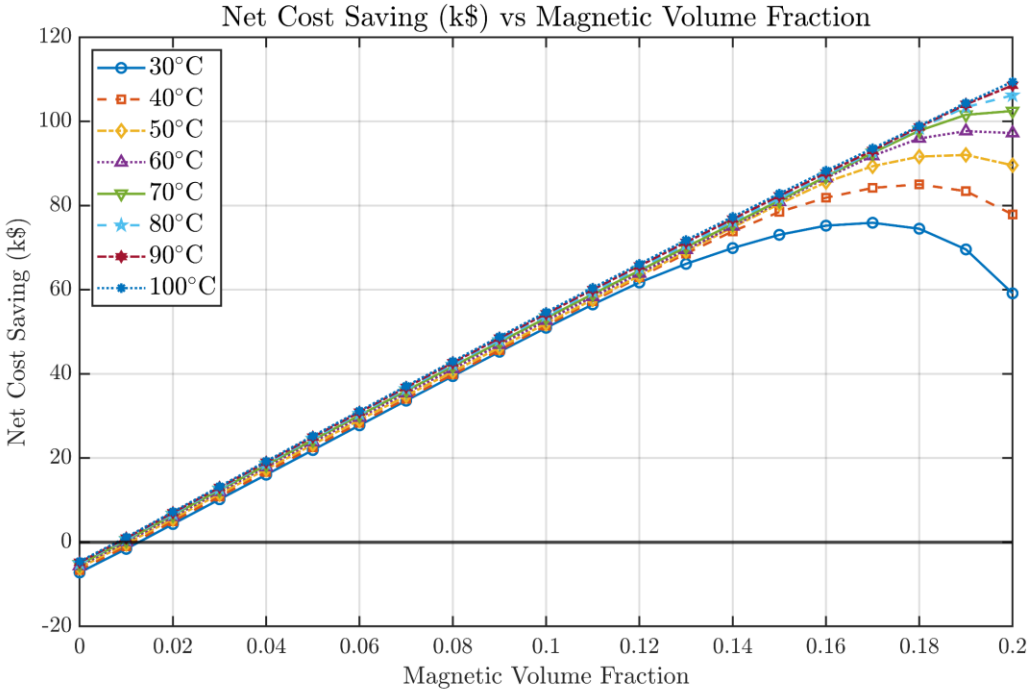

Figure 8.16: The net cost saving taking into account the reduction in permanent magnet (PM) mass and the reduced efficiency of the example 15 MW direct-drive (DD) wind turbine generator (WTG) due to a ferrofluid-gap for a range of magnetic volume fraction (ϕ_M) and various ferrofluid-gap temperatures (°C). Assumed magnet cost of $58,260 per tonne and cost of energy of 80.9 $/MWh.

8.3.4 Summary of Ferrofluid-Gap Drag and Efficiency Impact

It appears that the reduction in PM cost has the potential to exceed the loss of revenue due to the decreased WTG efficiency over a 25-year wind turbine lifetime. However, it has been demonstrated that the PM material cost saving can be relatively modest, leaving a small budget to cover the cost of the ferrofluid and other costs associated

with implementing a ferrofluid-gap into a DD WTG. In the next section, the impact of ferrofluid-gaps on the thermal performance of DD WTGs is investigated and the potential for enhanced cooling with a ferrofluid-gap is explored.

As a first approximation a constant value of ferrofluid-gap temperature has been assumed which has demonstrated that the temperature of a ferrofluid-gap has a significant impact on the loss in revenue. However, the impact of ferrofluid-gap temperature on the WTG efficiency is further complicated by taking into consideration that the temperature of the generator components will vary significantly during operation depending on the power output and ambient temperature [180]. Due to their significant thermal mass, the generator component temperatures depend on the time history of the power output. Correlations of output power vs component temperature are therefore subject to significant variance [181], [182].

An improved estimate of cumulative ferrofluid-gap drag losses could be achieved through a time-stepping approach in which the performance of the WTG is assessed over the course of a year subject to varying wind speeds and ambient temperatures. However, at this stage the impact of a ferrofluid-gap on the thermal performance of the DD WTG should first be understood, this is covered in the following section.

8.4 Thermal Performance with a Ferrofluid-Gap

In the following section the thermal model introduced in Chapter 3 is utilised to investigate the impact of a ferrofluid-gap on the thermal performance of DD WTGs.

A ferrofluid-gap will result in a significantly reduced thermal resistance between the air-gap region and the rotor/stator due to a much larger convective heat transfer coefficient in comparison to a conventional air-gap. This will have a significant impact on the thermal performance of a DD WTG. The convection coefficient into the ferrofluid-gap can be estimated from the ferrofluid material properties following the same approach as in Chapter 3, Section 3.3.3.1. In Figure 8.17 the heat transfer coefficient into a ferrofluid-gap and an air-gap are compared for a temperature of $100^{\circ}\mathrm{C}$.

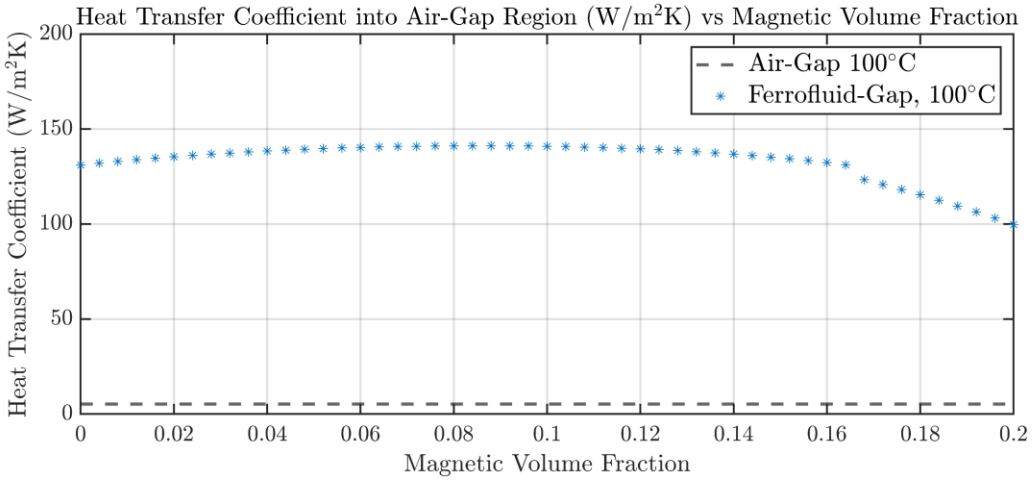

Figure 8.17: Heat transfer coefficient into the air-gap region ($\bar{\alpha}_{\mathrm{g}}$) for a ferrofluid-gap at a temperature of $100^{\circ}\mathrm{C}$ for a range of magnetic volume fractions (ϕ_{M}). A comparison is made with an air-gap.

8.4.1 Ferrofluid-Gap with No Circulation

First, the case of a ferrofluid-gap which is sealed on either end of the core with no circulation via a heat exchanger is considered.

In the thermal model it is assumed that the frictional losses in the ferrofluid-gap, as calculated by Eq. (8.17), are distributed homogeneously within the air-gap region.

The presence of material in the magnet spacing is accounted for by calculating the heat transfer area between the PMs and the air-gap according to the magnet width, as opposed to the pole pitch as detailed in Chapter 3, Section 3.3.3.1.

As in Chapter 3, the peak WTG component temperatures are evaluated for steady-state conditions at rated wind speed assuming an ambient temperature (T_{∞}) of $40°\mathrm{C}$, a cooling duct inlet temperature ($T_{\mathrm{duct,in}}$) of $50°\mathrm{C}$, and an internal air temperature (T_{int}) of $55°\mathrm{C}$.

The peak magnet, coil, and end winding temperatures are presented for the example 15 MW machine for a range of armature current loadings for an air-cooled strategy in Figure 8.18. The temperatures obtained for an air-gap are compared to a ferrofluid-gap with a magnetic volume fraction of 0.1. For the inner-rotor topology there is a negligible difference in the coil and end winding temperatures, however the magnet temperature was found to be reduced within the operational range of current loading. In contrast, for the outer-rotor topology a reduction in the coil and end winding

temperatures is observed, extending the maximum specific current loading by ~8%. However, a significant increase in the magnet temperature can be observed.

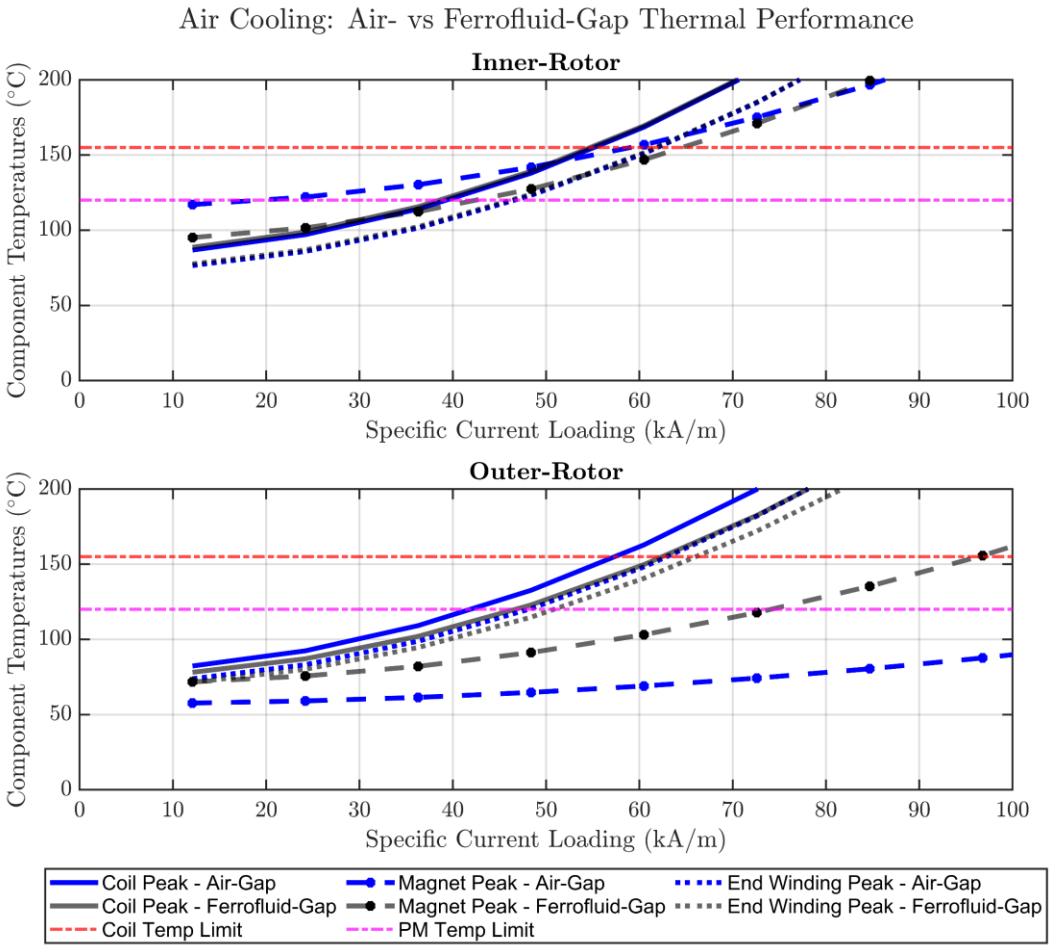

Figure 8.18: Comparison between the thermal performance of the example 15 MW direct-drive (DD) wind turbine generator (WTG) with an air-gap and a ferrofluid-gap with a magnetic volume fraction (ϕ_M) of 0.1 with a forced-air cooling strategy.

In Figure 8.19, a similar plot is presented for the liquid cooled strategy applied to the example 15 MW machine. A similar trend is observed between the impact of the ferrofluid-gap on the inner- vs outer-rotor topology, however there is less of a reduction in coil and end winding temperatures for the outer-rotor machine, leading to a negligible increase in the maximum current loading.

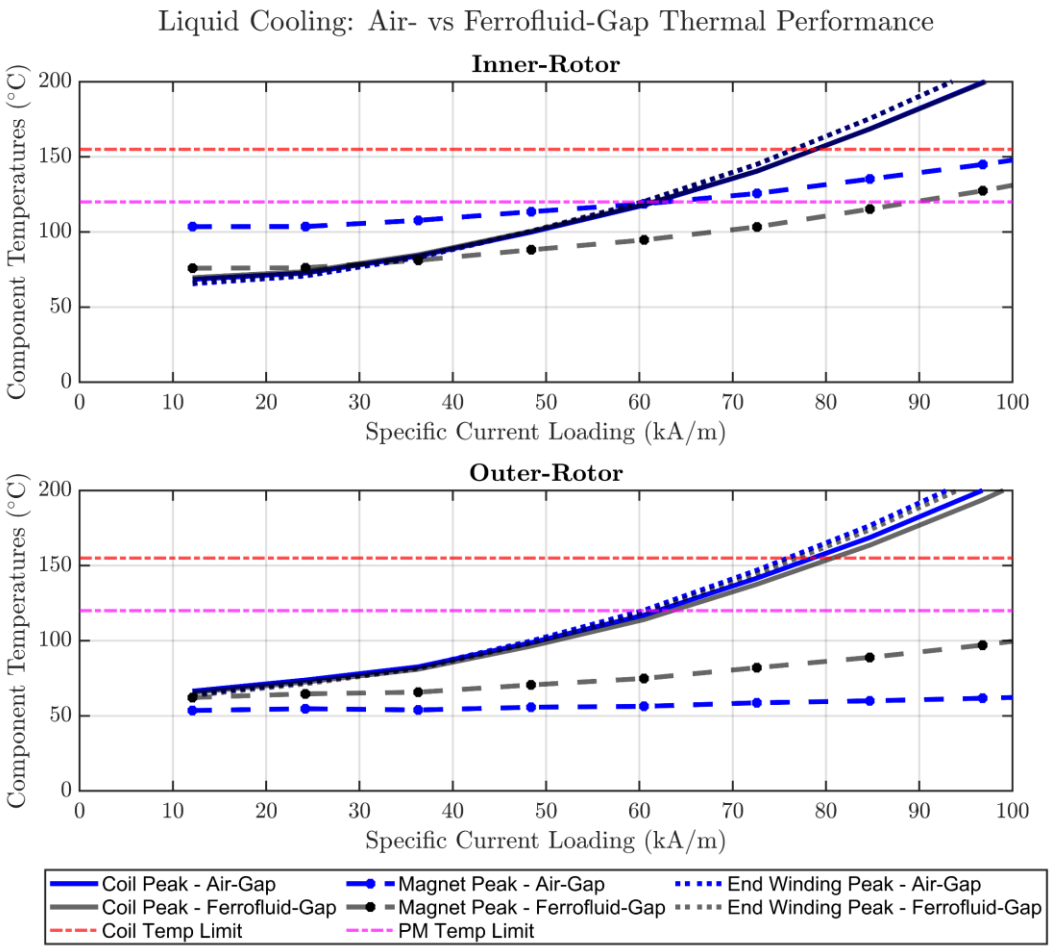

Figure 8.19: Comparison between the thermal performance of the example 15 MW direct-drive (DD) wind turbine generator (WTG) with an air-gap and a ferrofluid-gap with a magnetic volume fraction (ϕ_{M}) of 0.1 with a liquid cooling strategy.

By implementing a ferrofluid-gap in the inner-rotor machine, the heat transfer resistance between the magnets and the cooling vents is reduced, allowing for a reduction in the magnet temperature. Since the heat transfer resistance is assumed to be significant between the rotor and the internal air there is little difference in the coil and end winding temperatures.

Although the ferrofluid-gap was found to decrease the magnet temperature for the inner-rotor topology it is important to note that in this comparison the air-gap is assumed to be unventilated. By ventilating the air-gap, as discussed in Chapter 3, Section 3.5.5, it would be possible to reduce the PM temperature.

In the case of the outer-rotor machine it is assumed that there is significant heat transfer between the rotor structure and the external air flow. Therefore, the enhanced heat transfer between the rotor and stator due to the ferrofluid-gap results in a

significant increase in heat flow between the coils and the rotor resulting in a decrease in the coil and end winding temperatures. Consequently, the magnet temperature is increased due to the additional heat flow from the stator. Although the ferrofluid-gap increases the current loading capacity of the outer-rotor machine, the increase in PM temperature is significant. This would result in a reduced PM remanent flux density and potentially require the use of a more expensive grade of PM, significantly increasing the PM material costs.

8.4.2 Ferrofluid-Gap for Enhanced Cooling

Since the heat transfer coefficient into the air-gap region is significantly increased by implementing a ferrofluid-gap there is the potential to enhance the cooling performance of DD WTGs, possibly allowing for an increased current loading capacity or reduced PM temperatures. These additional benefits may help to offset the costs and difficulties associated with implementing a ferrofluid-gap in DD WTGs.

To achieve this the ferrofluid needs to be circulated through the air-gap region and cooled via a heat exchanger. In an actively cooled machine, such as the air- and liquid-cooled designs detailed in Chapter 3, an effective method may be to utilise the cooling ducts as an intermediate stage heat exchanger: the heat absorbed by the ferrofluid could be exchanged to the coolant flow and ultimately expelled to the ambient air via the external heat exchanger. This would prevent the need for an additional ferrofluid heat exchanger circuit, reducing the system complexity and the volume of ferrofluid required in the design.

Since the convection coefficient into the ferrofluid-gap region is already significant due to the movement of the rotor, and the specific heat capacity of ferrofluid is relatively high, the required flow rate of the ferrofluid cooling circuit may be very low since it only needs to be sufficient to prevent a large temperature rise of the ferrofluid between the inlet and outlet of the ferrofluid-gap.

Such as in Chapter 3, Section 3.5.5, an estimate of the required flow rate and axial velocity of the ferrofluid through the air-gap region is considered by assigning the ferrofluid-gap as a constant temperature source in the LPTN model and assuming fully developed flow and constant heat flux boundary conditions for the rotor and stator surfaces. The net heat transfer rate into the ferrofluid-gap is obtained and the temperature rise is calculated with consideration of the ferrofluid-gap drag losses:

$$\Delta T_{\mathrm{FF,axial}} = \frac{\dot{Q}_{\mathrm{FF}} + P_{\mathrm{drag}}}{\rho_{\mathrm{FF}} c_{p,\mathrm{FF}} \dot{V}_{\mathrm{FF,axial}}} \tag{8.19}$$

where $\dot{Q}_{\mathrm{FF}}$ is the net heat flux into the ferrofluid-gap, ρ_{FF} is the ferrofluid density, $c_{p,\mathrm{FF}}$ is the ferrofluid specific heat capacity, and $\dot{V}_{\mathrm{FF,axial}}$ is the volumetric flow rate of ferrofluid in the axial direction.

In Figure 8.20, the temperature rise of the ferrofluid flow with a magnetic volume fraction of 0.1 is plotted for a range of axial flow velocities based on the air-cooled inner-rotor 15 MW example machine with a specific current loading of 60 kA/m for various ferrofluid inlet temperatures. Due to the large specific heat capacity of the ferrofluid the temperature rise can be limited to less than $5^{\circ}\mathrm{C}$ with an axial velocity of only ~0.05 m/s. Comparing this axial velocity to the tangential velocity of the rotor results in a rotation ratio of ~80, indicating that the resulting flow is dominated by the rotation of the rotor, it was therefore deemed reasonable that the convection coefficient was solely determined based on the rotational flow.

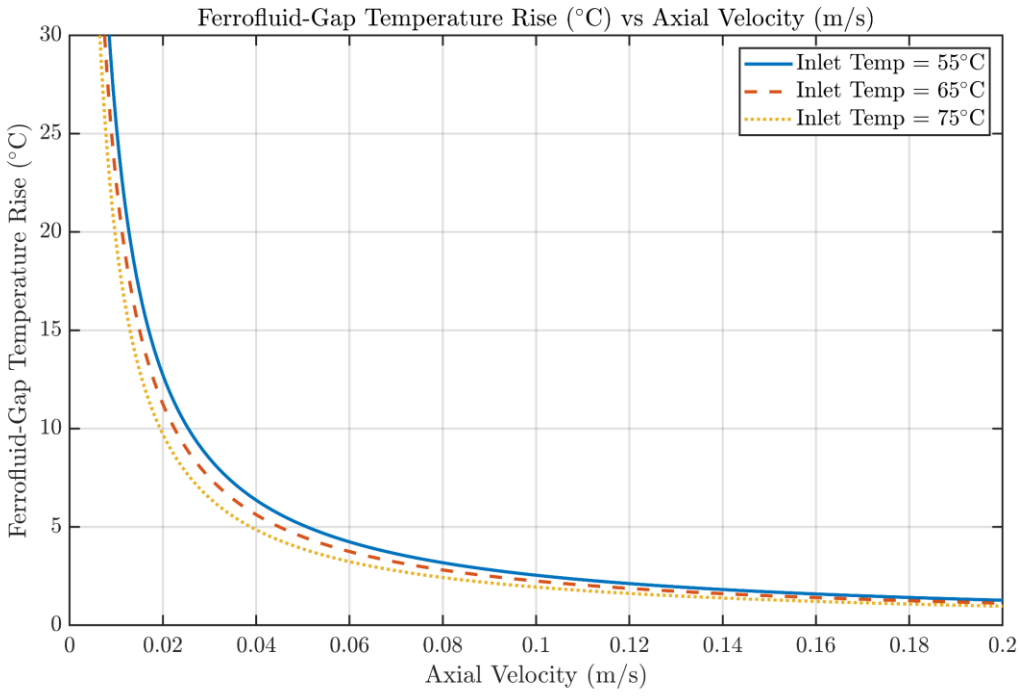

Figure 8.20: Temperature rise of ferrofluid flow through the air-gap region of the air-cooled example inner-rotor 15 MW machine with a specific current loading of 60 kA/m plotted for a range of axial velocities (m/s) and a variety of inlet temperatures (°C).

To find the pressure and power required to drive the flow, the influence of rotation on the axial pressure drop should be considered. First the axial Reynolds number is calculated:

$$\mathrm{Re}_{\mathrm{FF,axial}} = \frac{\rho_{\mathrm{FF}} v_{\mathrm{FF,axial}} D_{h,\mathrm{g}}}{\eta_{\mathrm{FF}}} \tag{8.20}$$

where D_h is the hydraulic diameter of the ferrofluid-gap region ($D_{h,\mathrm{g}} = 2h_{\mathrm{g}}$).

The friction factor is first calculated assuming a stationary rotor, since the axial Reynolds number is relatively low (less than 2000) the flow is assumed to be laminar and the friction factor can be calculated as [183]:

$$\varsigma_{\mathrm{FF,axial}} = \frac{96}{\mathrm{Re}_{\mathrm{FF,axial}}} \tag{8.21}$$

According to the work of Yamada, a correction factor can be applied to the friction factor which takes into consideration the influence of the rotational flow [183]:

$$C_{\mathrm{rot}} = \left[1 + \left(\frac{7}{8}\right)^2 \left(\frac{\mathrm{Re}_{\mathrm{g}}}{\mathrm{Re}_{\mathrm{FF,axial}}}\right)^2\right]^{0.38} \tag{8.22}$$

where Re_{g} is the Reynolds number of the ferrofluid-gap Taylor-Couette flow.

The pressure required to drive the axial flow can then be found:

$$\Delta p_{\mathrm{FF,axial}} = C_{\mathrm{rot}} \varsigma_{\mathrm{FF,axial}} \frac{l_c \rho_{\mathrm{FF}} v_{\mathrm{FF,axial}}^2}{2 D_{h,\mathrm{g}}} \tag{8.23}$$

The required power to drive the flow (neglecting pump efficiency) is given by:

$$P_{\mathrm{FF,axial}} = \dot{V}_{\mathrm{FF,axial}} \Delta p_{\mathrm{FF,axial}} \tag{8.24}$$

In Figure 8.21 the ferrofluid temperature rise is plotted against the pressure and power required to drive the ferrofluid flow based on the example liquid cooled outer-rotor 15 MW machine. It appears that circulating the ferrofluid through the air-gap region requires relatively little pressure and power, suggesting that such a strategy may allow for efficient cooling.

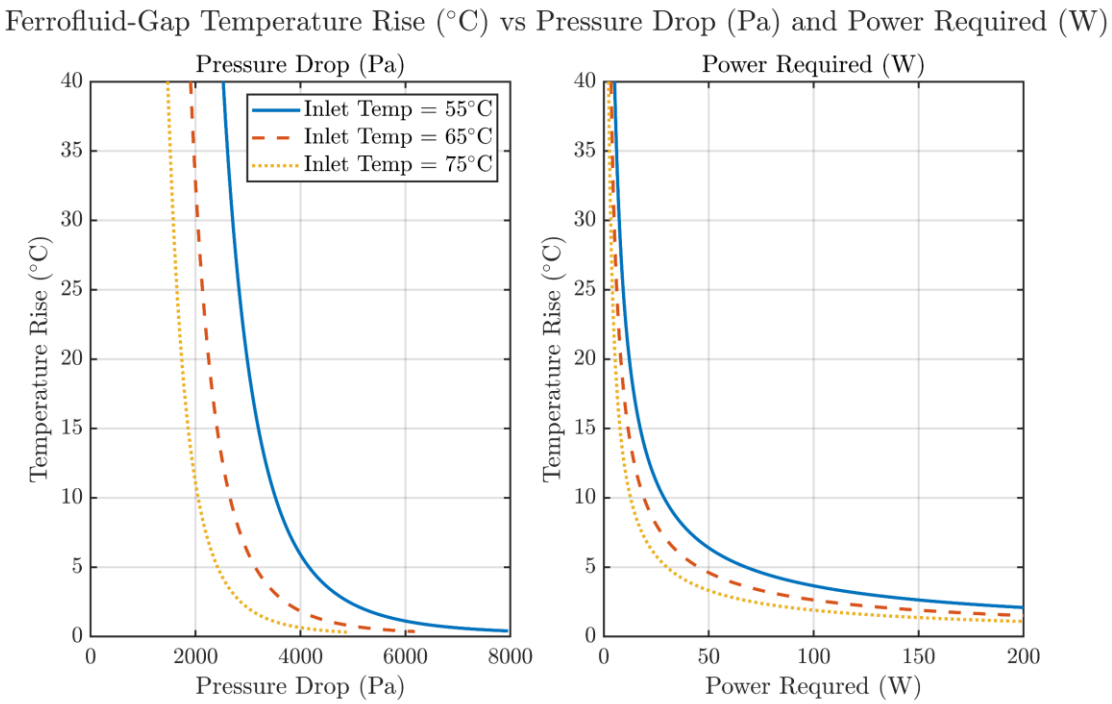

Figure 8.21: Ferrofluid axial temperature rise (℃) as a function of pressure drop (Pa) and idealised power required (W) to drive the axial ferrofluid flow for a variety of inlet temperatures.

For a first approximation of how a ferrofluid-gap cooling circuit could impact WTG performance it is assumed that all the heat absorbed by the ferrofluid-gap is transferred into the cooling duct flow by recirculating the ferrofluid back to the air-gap inlet in proximity to the cooling ducts.

Even if the additional pressure drops and practical difficulties associated with recirculating the ferrofluid are disregarded two crucial constraints remain regarding the ferrofluid-gap cooling performance:

- The cooling fluid in the coolant ducts must be at a lower temperature than the ferrofluid to facilitate heat transfer.
- The temperature rise between the inlet and outlet of the coolant duct will be increased due to the additional heat transferred from the ferrofluid.

It is therefore assumed that the ferrofluid-gap inlet temperature must exceed the coolant duct outlet temperature:

$$T_{\mathrm{FF,in}} > T_{\mathrm{duct,out}} \tag{8.25}$$

The temperature rise of the coolant flow is calculated by taking into consideration the heat flux into both the coolant flow and the ferrofluid-gap, in additional to the frictional losses in both the ferrofluid-gap and the cooling duct:

$$\Delta T_{\mathrm{cool}} = \frac{\dot{Q}_{\mathrm{duct}} + \dot{Q}_{\mathrm{FF}} + P_{\mathrm{drag}} + P_{\mathrm{cool}}}{\rho_{\mathrm{cool}} c_{\mathrm{p,cool}} \dot{V}_{\mathrm{cool}}} \tag{8.26}$$

where $\dot{Q}_{\mathrm{duct}}$ is the heat flux into the coolant flow, P_{cool} is the frictional loss in the coolant duct, ρ_{cool} is the density of the coolant, $c_{\mathrm{p,cool}}$ is the specific heat capacity of the coolant, and $\dot{V}_{\mathrm{cool}}$ is the volumetric flow rate of the coolant.

The temperature of the stator components is estimated by adding the coolant flow temperature rise to the values obtained from the LPTN model, the rotor components are estimated by adding the ferrofluid-gap temperature rise.

As before, the peak WTG component temperatures are evaluated for steady-state conditions at rated wind speed assuming an ambient temperature (T_{∞}) of $40^{\circ}\mathrm{C}$, a cooling duct inlet temperature ($T_{\mathrm{duct,in}}$) of $50^{\circ}\mathrm{C}$, and an internal air temperature (T_{int}) of $55^{\circ}\mathrm{C}$. The ferrofluid-gap flow rate is adjusted such that the temperature rise does not exceed $5^{\circ}\mathrm{C}$.

In Figure 8.22 and Figure 8.23, an idealised prediction of the WTG performance is presented for the air- and liquid-cooled example 15 MW WTG designs respectively assuming that the ferrofluid-gap inlet temperature is equal to the coolant duct outlet temperature. The performance of identical WTG designs with an unventilated air-gap is provided for comparison:

- For the inner-rotor WTG topologies it is found that a significant reduction in the PM temperature can be achieved by circulating the ferrofluid through the air-gap region compared to an unventilated air-gap.
- For the outer-rotor WTG topologies it is found that the PM temperature is comparable to the case of an unventilated air-gap.
- In the air-cooled WTGs, the maximum specific current loading is increased due to the additional heat transfer from the ferrofluid, extending it by ~24% and ~19% in the case of the inner- and outer-rotor WTG respectively.

- For the liquid cooled WTGs, a significant reduction in the peak coil temperature is achieved, however the peak end-winding temperature is reduced only slightly, limiting the increase in the maximum specific current loading.
- For the liquid cooled WTGs, the ferrofluid inlet temperature can be maintained at a low value for high levels of current loading due to the low temperature rise of the liquid coolant. For the air-cooled design the inlet temperature is observed to increase with increased current loading due to the significant temperature rise of the cooling air, resulting in higher PM temperatures.

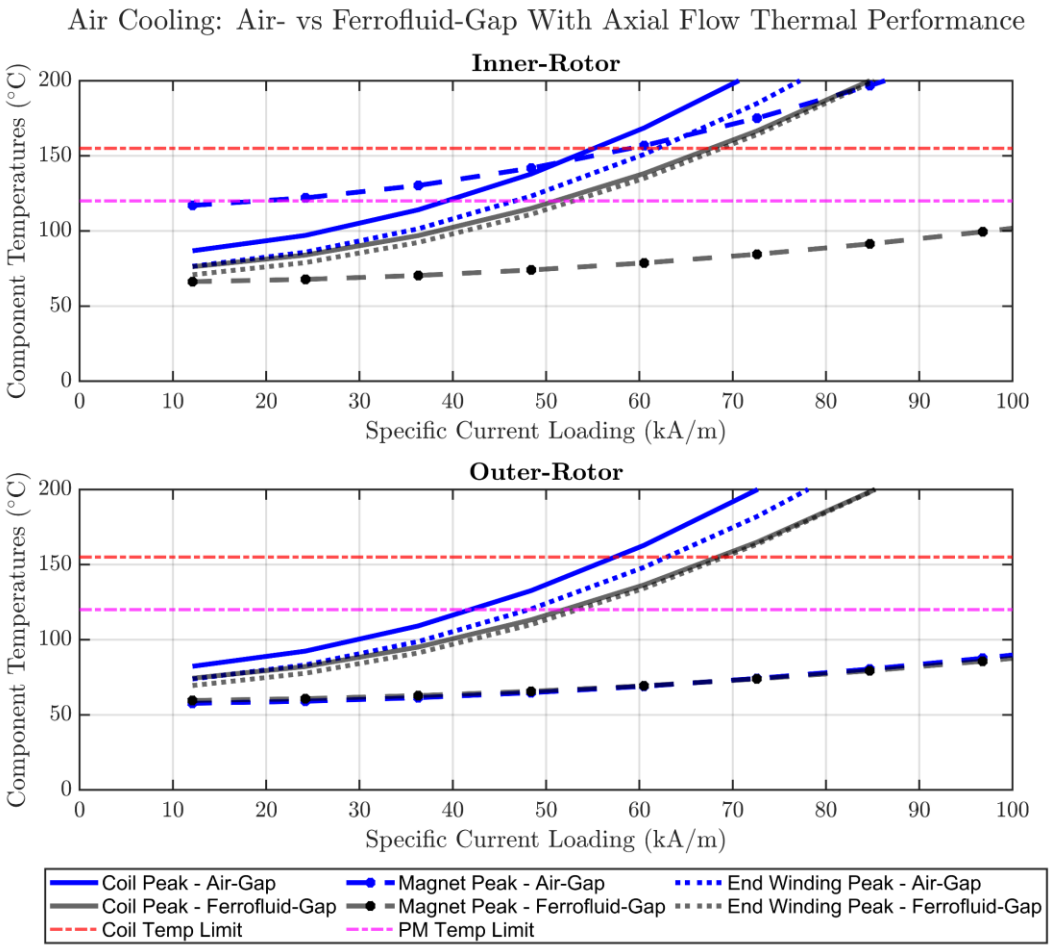

Figure 8.22: Comparison between the thermal performance of the example 15 MW direct-drive (DD) wind turbine generator (WTG) with an air-gap and an axial ferrofluid-gap flow with a magnetic volume fraction (ϕ_{M}) of 0.1 with a forced-air cooling strategy.

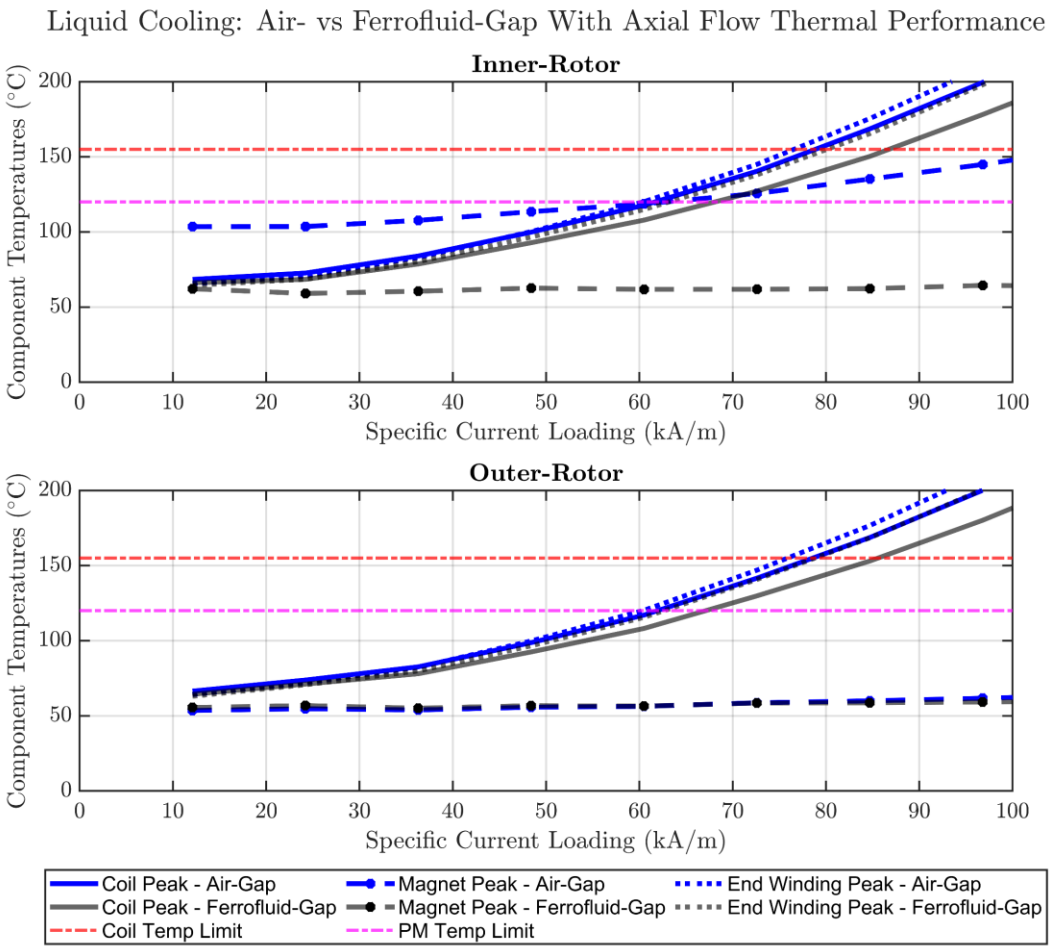

Figure 8.23: Comparison between the thermal performance of the example 15 MW direct-drive (DD) wind turbine generator (WTG) with an air-gap and an axial ferrofluid-gap flow with a magnetic volume fraction (ϕ_M) of 0.1 with a liquid cooling strategy.

In the presented results an idealised ferrofluid-gap inlet temperature has been assumed which is equal to the coolant duct outlet temperature. To allow for effective heat transfer between the ferrofluid and the coolant flow it would likely need to be increased such that there is an adequate temperature gradient between the ferrofluid and the coolant flow. It is important to note therefore that even if the ferrofluid is circulated through the air-gap region, the PM temperature would likely be elevated in comparison to an outer-rotor WTG topology with an unventilated air-gap.

8.4.3 Summary of Thermal Performance

In summary, it was found that a ferrofluid-gap can result in reduced PM temperatures compared to an unventilated air-gap for inner-rotor WTG topologies, however it can be argued that a similar reduction in PM temperature could be achieved by ventilating the air-gap as discussed in Chapter 3, Section 3.5.5.

For outer-rotor WTG topologies in which the external surface of the rotor is exposed to the ambient air flow it was found that the armature winding and end-winding temperatures could be reduced, however the PM temperature would be significantly increased in comparison to an unventilated air-gap. The elevated PM temperature would result in a reduced PM remanent flux density and potentially require a more expensive grade of PM, increasing the PM material cost of the machine and negating the benefits of increasing the magnetic permeability in the air-gap region.

Based on an idealised approach it was found that circulating the ferrofluid through the air-gap and exchanging the absorbed heat via the cooling ducts has the potential to improve the thermal performance of both the inner- and outer-rotor WTG topologies: significantly increasing the current loading capacity of the air-cooled designs, allowing for a large reduction in PM temperature for the inner-rotor topologies, and potentially allowing for a similar PM temperature in the outer-rotor topologies in comparison to an unventilated air-gap. For the liquid cooled designs, it was found that the current loading capacity was limited by the end-winding temperature.

The design of a ferrofluid-gap cooling circuit could be taken a step further by incorporating end-winding cooling and direct cooling of the stator windings by flowing the ferrofluid through the slots. This may lead to a significant increase in the current loading capacity of the machine. However, it can be argued that similar performance benefits could be achieved by flowing liquid coolant through the slots via slot jackets or hollow conductors without the need for fluid in the air-gap region.

It is important to note that to prevent elevated PM temperatures in comparison to an air-gap the ferrofluid-gap must be maintained at a relatively low temperature, this results in an increased viscosity and therefore ferrofluid-gap drag. As demonstrated in Section 8.3.3, this has a significant impact on the loss in revenue, especially for large magnetic volume fractions.

It was demonstrated that circulating the ferrofluid through the air-gap region requires relatively little pressure and power, however the additional losses associated with the recirculation path have not been considered. To provide an idealised estimate of performance it was assumed that the heat is transferred efficiently to the cooling ducts, however further work in this area could investigate the heat transfer surface area, flow rate, and temperature gradient required to cool the ferrofluid. As highlighted in Chapter

3, Section 3.5.4, a liquid-to-liquid heat exchanger requires significantly less heat transfer surface area than a liquid-to-air heat exchanger, a ferrofluid-gap cooling system may therefore be more feasible in liquid cooled DD WTGs.

The ferrofluid-gap pumping source has not been specified. Implementation of a conventional pump would likely be impractical as it would be difficult to provide a uniform flow of ferrofluid through the air-gap region. Further work could investigate the use of temperature-sensitive magnetic fluids (TSMFs), utilising the thermomagnetic convection effect as discussed in Chapter 5, Section 5.2.10. Another possibility would be to utilise the rotor end faces as a centrifugal pump.

Liquid cooling of the air-gap region is not necessarily limited to ferrofluids, a non-magnetic mineral oil could also be utilised. It is interesting to note that in prior works, flooding the air-gap region is often disregarded as a viable option due to the reduction in efficiency due to the viscous losses [57]. However as demonstrated in Section 8.3.2, viscous losses can have a minor impact on WTG efficiency assuming a low viscosity mineral oil is utilised.

8.5 Practical Challenges of Ferrofluid-Gaps for DD WTGs

It has been demonstrated that, from a performance standpoint, a ferrofluid-gap has the potential to reduce PM material costs and improve the thermal performance of DD WTGs without excessively reducing the lifetime revenue of the wind turbine due to the ferrofluid-gap drag losses. However, to assess the overall feasibility of ferrofluid-gaps for DD WTGs various practical issues associated with their implementation must be considered.

The levelized cost of energy (LCOE) of offshore wind turbines is heavily dependent on their reliability and availability, as explained in Chapter 2, Section 2.2.3, this can be represented by the production-based availability factor. To illustrate the importance of wind turbine availability the loss in lifetime revenue of the example 15 MW WTG is plotted against the availability factor in Figure 8.24 assuming a baseline production-based availability factor of 0.94.

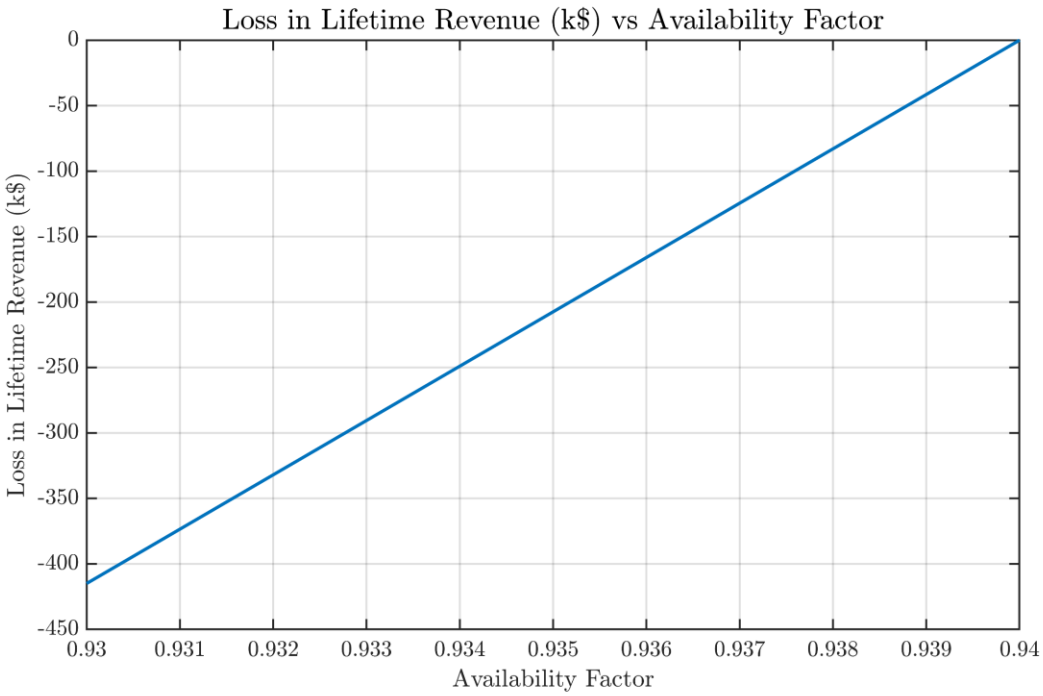

Figure 8.24: Loss in lifetime revenue (k$) of the example 15 MW direct-drive (DD) wind turbine generator (WTG) plotted against the production-based availability factor (ζ_{av}).

A slight reduction in the availability factor due to the implementation of a ferrofluid-gap would certainly offset the PM material cost savings, even before any additional costs associated with the repair or replacement of components are considered. For a ferrofluid-gap to be feasible for DD WTGs, it must not reduce reliability in comparison to a conventional air-gap. Practical implementation of a reliable ferrofluid-gap is challenging for several reasons, in the following section key issues are considered.

8.5.1 Pressure and Volume Regulation

As discussed in Chapter 4, thermal expansion and mechanical strain of the DD WTG structure result in a variation in air-gap clearance during operation. Although other sources of air-gap deformation, such as displacement of the shaft due to external loading, will not result in a significant change in the net volume of the air-gap region they would introduce pressure variations which would make sealing of the ferrofluid difficult.

A ferrofluid-gap would therefore require some form of pressure and volume regulation. This could be achieved by implementing a hydraulic accumulator which would compensate for changes in the air-gap volume and buffer variations in pressure [184].

A partially-filled ferrofluid-gap could be advantageous in this regard, rather than requiring an accumulator there would be extra space for the ferrofluid to move into when the air-gap volume is decreased, potentially allowing for a simpler system and making sealing easier.

8.5.2 Sealing the Ferrofluid

Arguably the largest challenge in implementing a ferrofluid-gap is sealing the ferrofluid within the air-gap region in a cost-effective, reliable, and efficient manner.

In the following section, various approaches for sealing the ferrofluid are discussed.

8.5.2.1 Conventional Seals

One approach would be to seal the ferrofluid-gap at either end of the core with a conventional dynamic seal. However, this is problematic for several reasons:

- The air-gap diameter of a 15 MW DD WTG is on the order of ~10 m. Such a seal is not readily available due to the extremely large size required.
- The large contact area may lead to significant drag and an increased probability of leakage.
- The long-term reliability of such a seal is questionable, although it is reasonable to assume it would need to be replaced during the ~25-year operational lifespan of a wind turbine.

Alternatively, the seal could be implemented at the shaft, which has some benefits:

- Seals of this size already exist, such as for a low-speed shaft (LSS) into a wind turbine gearbox and for the main bearings.
- The contact area and velocity of the seal interface are reduced, leading to decreased drag and probability of leakage.

However, there are additional issues:

- Significantly more ferrofluid would be required in the machine as the end-spaces would need to be filled, increasing the overall cost of the ferrofluid significantly.
- Filling the end-spacings of the machine would increase the total drag losses, further decreasing efficiency.

- The machine structures would need to be modified to accommodate the sealing of the fluid. The structures usually have arms/spokes with hollow areas, these would need to be covered to contain the ferrofluid. The machine structures would also have to be extended to fully enclose the ferrofluid.
- There would be no access to the inside of the generator which would be problematic for maintenance.
- As before the long-term reliability of such a seal is questionable and it would likely require replacement or servicing during the lifetime of the wind turbine.

8.5.2.2 Magnetic Sealing of Ferrofluid-Gaps

Due to ferrofluid's magnetic properties a magnetic seal may be possible. Ferrofluid has been used to great effect as a magnetic seal in a variety of applications [126], [185]. The main advantages would be a lack of mechanical wear and comparatively low drag compared to a conventional seal, offering a potential solution for reliable ferrofluid-gap sealing.

The general concept is that the ferrofluid is held in place by a magnetic field, a sketch is provided in Figure 8.25. The burst pressure of a ferrofluid seal can be approximated as being equal to the magnetic pressure in the sealing region [144]:

$$\Delta p_{\mathrm{burst}} = \mu_0 \bar{M} H \tag{8.27}$$

If the ferrofluid is magnetically saturated, then $\bar{M} = M_s$. The maximum pressure capacity of a single-stage seal is typically stated to be ~1 Bar.

The gap dimensions of ferrofluid seals are typically much smaller than what would be required for a multi-megawatt scale DD WTGs, Parmar *et al.* regard a clearance of 0.7 mm as 'large' [186]. It is often stated that as the sealing gap clearance is increased, the sealing capacity is reduced significantly, however the explanation given for this is that the flux density in the gap decreases due to increased reluctance of the magnetic circuit. Although the air-gap clearance of a DD WTG is much larger than what is typically observed in ferrofluid seals, if a large magnetic flux density can be maintained then a sealing capacity of ~1 Bar could still be achieved in theory.

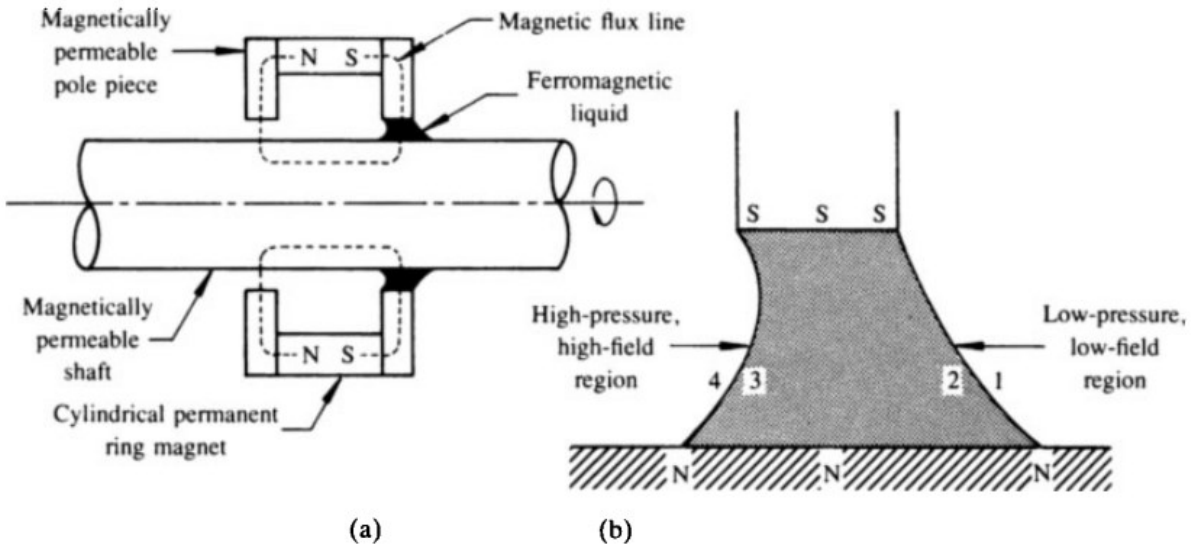

Figure 8.25: (a) Components of a ferrofluid rotary shaft seal. (b) Sketch of ferrofluid-air boundaries at the sealing interface [144].

8.5.2.3 Specification of a Magnetic Seal

In the following section the requirements of a magnetic seal for a ferrofluid-gap for multi-megawatt scale DD WTGs are considered. In the following calculations the IEA 15 MW DD WTG is used as a reference [13].

High tangential velocities (> 20 m/s) can compromise ferrofluid seals due to centrifugal forces, however the tangential velocities expected in DD WTGs are within a reasonable range (~5 m/s at the air-gap, ~3 m/s at the shaft for the IEA 15 MW design) [185]. To illustrate that the pressure due to centrifugal forces is negligible, we can consider co-rotating TC flow and integrate the centrifugal body force over the width of the gap to provide a conservative estimate of the pressure difference between the rotor and stator boundaries:

$$\Delta p_\omega = \int_{r_r}^{r_s} \rho_{\mathrm{FF}} \omega^2 r_r dr = 0.5 \rho_{\mathrm{FF}} \omega^2 (r_s^2 - r_r^2) = 0.5 \rho_{\mathrm{FF}} \omega^2 \left(2 r_r h_{\mathrm{g}} + h_{\mathrm{g}}^2\right) \tag{8.28}$$

Assuming that $\rho_{\mathrm{FF}} = 1000\ \mathrm{kg/m^3}$, $\omega = 0.792\ \mathrm{rad/s}$, $r_{\mathrm{r}} = 5.08\ \mathrm{m}$, and $h_{\mathrm{g}} = 0.01016\ \mathrm{m}$, this conservative estimate results in a pressure difference of only ~32.4 Pa.

If a low vapour pressure carrier fluid is utilised, such as mineral oil, then the ferrofluid-gap may not require pressurisation to prevent cavitation. To assess the risk of cavitation, the cavitation number can be considered which represents the ratio of the local absolute pressure to the kinetic energy per unit volume in a flow:

$$\mathrm{Ca} = \frac{p_{\min} - p_{\mathrm{vap}}}{0.5\rho_{\mathrm{FF}}\omega^2 r_r^2} \tag{8.29}$$

where p_{vap} is the vapour pressure of the ferrofluid, and $p_{\min}$ is the minimum pressure within the flow, given by:

$$p_{\min} = p_{\mathrm{atm}} - \Delta p_{\omega} \tag{8.30}$$

where p_{atm} is atmospheric pressure. Assuming that $p_{\mathrm{vap}} = 10\ \mathrm{Pa}$ (corresponding to ISO VG 10 mineral oil), and that $\rho_{\mathrm{FF}} = 1000\ \mathrm{kg/m^3}$, then $\mathrm{Ca} \approx 12.5$ which far exceeds 1. This indicates that there is little risk of cavitation and that the ferrofluid-gap does not require external pressurisation.

Due to the large scale of DD WTGs, the dominant source of pressure acting on the seal would be the hydrostatic pressure due to the weight of the ferrofluid:

$$p_h = \rho_{FF} g h \tag{8.31}$$

where g is the acceleration due to gravity, and h is the vertical distance between the bottom of the seal and the top of the ferrofluid-gap.

If the ferrofluid is sealed on either end of the air-gap then the maximum hydrostatic pressure can be calculated assuming that the air-gap diameter (D_{g}) approximates h ($h \approx D_{\mathrm{g}}$). Alternatively, if a seal were to be implemented at the shaft $h \approx r_{\mathrm{shaft}} + r_{\mathrm{r}}$.

In Figure 8.26 the magnetic flux density required in the magnetic sealing gap of the example 15 MW machine is plotted against magnetic volume fraction. Increasing the magnetic volume fraction increases the saturation magnetisation of the ferrofluid, which as per Eq. (8.27) reduces the magnetic flux density required per unit of pressure capacity. However, the ferrofluid density also increases which results in an increased hydrostatic pressure acting on the seal. It is demonstrated that for a 15 MW DD WTG, a magnetic seal necessitates the use of a highly concentrated ferrofluid-gap such that the required flux density is achievable, however even with a very high magnetic volume fraction of 0.2 a seal at each end of the air-gap would require a flux density of at least 1.9 T, or for the case of a seal at the shaft 1.5 T.

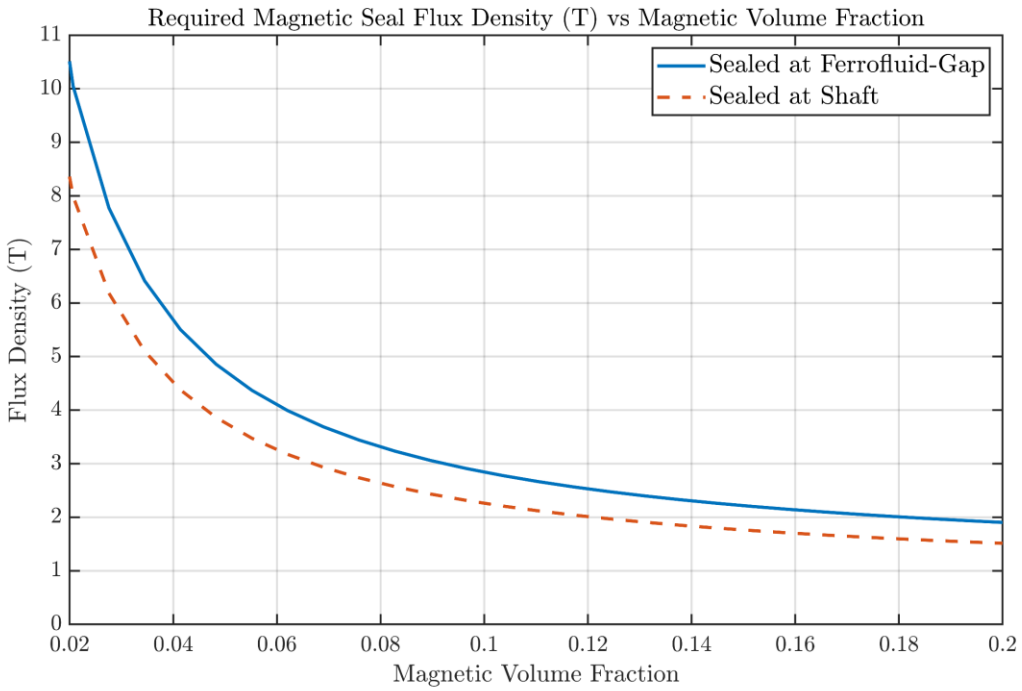

Figure 8.26: Estimate for magnetic flux density (T) required in the sealing interface of a magnetic seal applied to the IEA 15 MW reference direct-drive (DD) wind turbine generator (WTG) [13].

In Figure 8.27 the magnetic flux density required in the magnetic seal is plotted against air-gap diameter for a magnetic volume fraction of 0.2. For this plot it is assumed that the diameter of the shaft scales according to the ratio of the IEA 15 MW machine shaft diameter to air-gap radius (60%). Since the hydrostatic pressure increases according to the size of the WTG it becomes increasingly difficult to implement a magnetic seal as the power capacity is increased.

If the air-gap clearance scales in directly proportion to the air-gap diameter ($h_g \approx 0.001 D_r$) then the PM material required for the magnetic seal will increase rapidly with increasing air-gap diameter. As the air-gap diameter is increased both h_g and B_g will increase linearly, therefore the amount of PM required in the magnetic seal will increase rapidly.

As the gap clearance increases the extent of magnetic flux fringing in the gap will also increase, requiring increasingly wide pole faces such that a large flux density can be achieved in the sealing gap: further compounding the requirement for PM material with increasing WTG diameter.

Deflection of the air-gap introduces additional difficulty: a sufficient magnetic seal flux density would need to be maintained in the event of an extreme air-gap deflection, further increasing the PM material required in the seal.

A ferrofluid-gap magnetic seal may therefore only be economically feasible for relatively small machines such that the required PM material in the seal does not offset the reduction in the PM mass due to the increased permeability of the air-gap region. It is conceivable that for a relatively small machine in which the hydrostatic pressure is low that less expensive grades of PM could be used in the magnetic seal design, such as ferrite magnets.

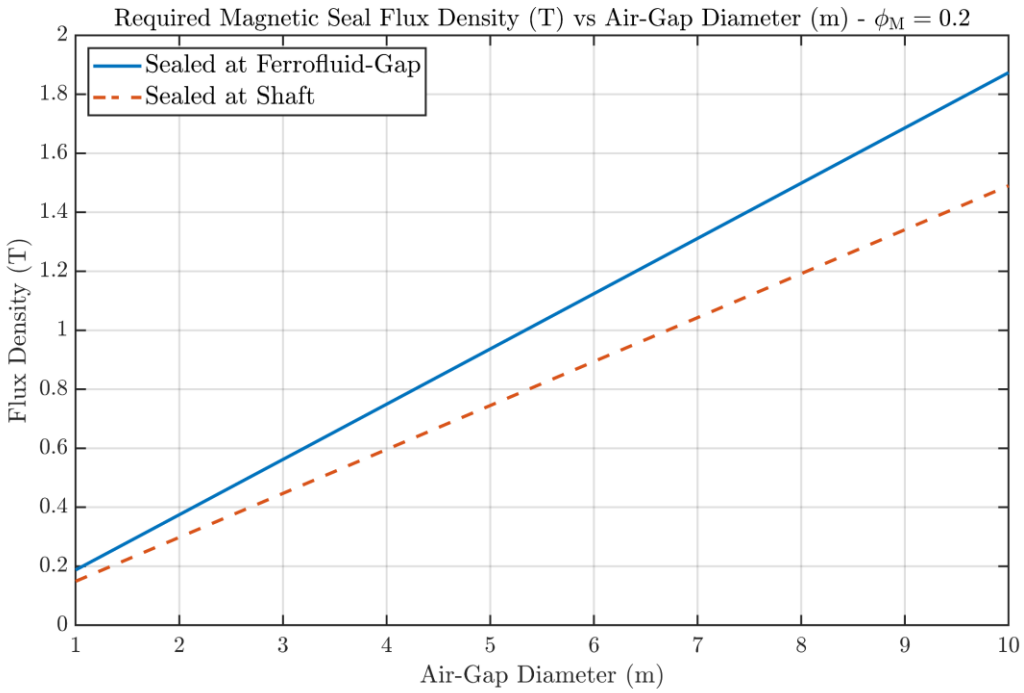

Figure 8.27: Estimate for magnetic flux density (T) required in the sealing interface of a magnetic seal plotted as a function of air-gap diameter (m).

8.5.2.4 Sealing a Partially Filled Ferrofluid-Gap

A partially filled ferrofluid-gap may be advantageous in terms of sealing.

For a totally filled ferrofluid-gap, the magnetic force acts only at the ferrofluid-air interface at the seal and the PMs within the machine do not contribute towards sealing of the ferrofluid. However, if the ferrofluid-gap is partially filled, and the ferrofluid is retained above the poles the internal PMs will help to contain the ferrofluid within the machine due to the ferrofluid-air interfaces within the air-gap region. An illustration of the concept is provided in Figure 8.28.

If the ferrofluid above each pole is separated by a boundary of air, then the hydrostatic pressure could be reduced significantly allowing for a less expensive magnetic seal.

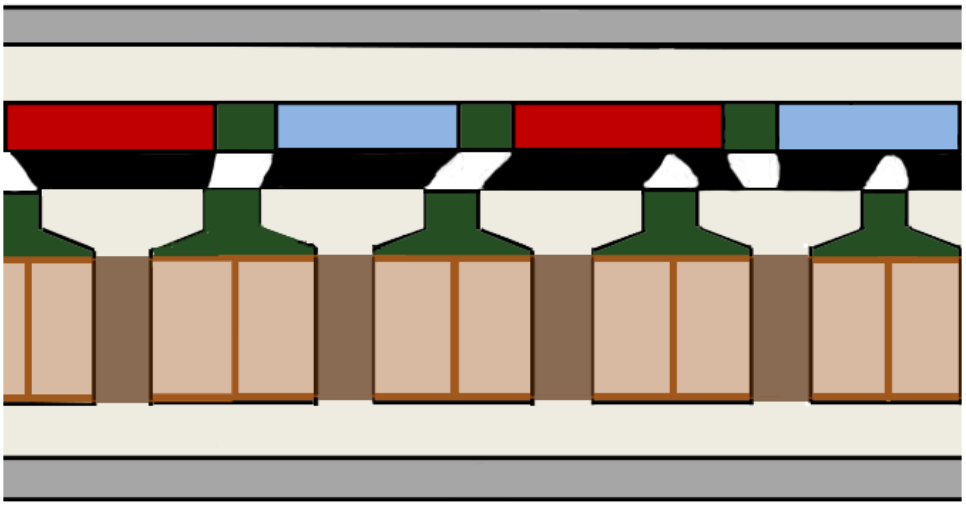

Figure 8.28: Illustration of a partially-filled ferrofluid-gap in the IEA 15 MW reference wind turbine generator design [13].

8.5.3 Ferrofluid-Gap Longevity and Cost

During WTG operation, the ferrofluid-gap experiences continuous shear and a time-varying magnetic field, both of which act to suppress particle chain formation and the development of concentration gradients. This dynamic environment is therefore beneficial for maintaining colloidal stability within the ferrofluid-gap.

However, in the event of a wind turbine fault, the ferrofluid-gap would be exposed to a static magnetic field without shearing for an extended period, increasing the risk of particle sedimentation.

As discussed in Chapter 5, Section 5.3.5, the presence of large magnetic particles in the ferrofluid act as nucleation sites for chain formation, this can compromise the colloidal stability of the ferrofluid-gap. If sedimentation occurs, then a risk of abrasion is introduced.

To ensure the longevity of the ferrofluid-gap and to minimise the risk of wear on the wind turbine components, particularly the PMs, a high quality of ferrofluid is required. As discussed in Section 8.3.3, according to an optimistic estimate of DD WTG PM mass reduction, a ferrofluid unit cost of less than $147.5 per litre with a magnetic volume fraction of 0.2 would be required to break even, this is before additional costs

associated with the implementation of the ferrofluid-gap are taken into account, or replacement of the ferrofluid during the wind turbine lifetime of 25 years.

As discussed in Chapter 5, Section 5.2.9, the raw materials required to synthesise iron oxide based ferrofluid are relatively low-cost and abundant. It is conceivable that a low unit cost can be achieved through high volume production, however significant progress is required in this area for the concept to be economically feasible for DD WTGs.

8.6 Discussion

According to the preceding analysis it can be concluded that the potential benefits of a ferrofluid-gap are outweighed by the costs and difficulties associated with their implementation in multi-megawatt scale DD WTGs:

- The air-gap flux density of DD WTGs is relatively high (~1 T), since the ferrofluid-gap is highly saturated the potential for PM mass reduction is modest: approximately a 10% reduction for a large magnetic volume fraction of 0.2.
- It was found that the cost savings in PM material can exceed the loss in revenue due to the reduced efficiency of the DD WTGs, however a relatively small budget is left to cover the cost of the ferrofluid and other expenses associated with implementing and maintaining the ferrofluid-gap.
- Significant saturation of the electrical steel in the WTG magnetic circuit reduces the potential for PM mass savings. Designing the magnetic circuit to accommodate the potential benefits of a ferrofluid-gap may place unacceptable constraints on the WTG design, e.g. necessitating wider stator teeth than an air-gap machine.
- The practical issues associated with sealing the ferrofluid are very challenging. A magnetic seal appears to be uneconomical for multi-megawatt scale DD WTGs machines, and a conventional seal would likely lead to an unacceptable reduction in wind turbine availability.
- A magnetic seal may be feasible for DD WTGs of a relatively small scale in which the air-gap clearance is relatively small, however as discussed in Section 8.2.3 the magnet glue and reinforcement reduce the potential for PM mass reduction in such machines.

- In certain conditions the ferrofluid-gap can improve the thermal performance of DD WTGs, however it can be argued that similar improvements can be achieved through alternative strategies which are less complicated.

It is worth noting that other concepts have been investigated in which fluid is introduced into the air-gap region of DD WTGs. For instance Bang *et al.* investigated the concept of a buoyant rotor structure in which the air-gap region is filled with fluid [187]. Implementing a ferrofluid-gap in conjunction with such a concept may help to offset the associated practical difficulties.

In Chapter 7, Section 7.3, it was highlighted that the experimental results obtained from the ferrofluid-gap test rig can be applied to arbitrary electrical machine topologies. Similarly, the methodology laid out in this chapter can be adapted for the analysis of different types of electrical machines.

As discussed in Chapter 5, Section 5.4, prior works which investigate the ferrofluid-gap concept for electrical machines model the magnetic and mechanical behaviour incorrectly, therefore the work laid out in this chapter provides a useful resource that can support future analysis of the ferrofluid-gap concept applied to different applications.

8.7 Conclusion

The impact of implementing mineral oil based ferrofluid-gaps in multi-megawatt scale surface mounted permanent magnet (PM) direct-drive (DD) wind turbine generators (WTGs) has been assessed in terms of magnetic performance, WTG efficiency, thermal performance, and the practical difficulties associated with implementing the system.

In Section 8.2, a magnetic analysis was conducted of ferrofluid-gaps for DD WTG topologies, unlike previous work regarding ferrofluid-gaps for electrical machines the ferrofluid-gap magnetic properties were assigned appropriate values according to the magnetic volume fraction and the nonlinearity of the ferrofluid *BH* curve was considered. It was demonstrated that a ferrofluid-gap has the potential to reduce the PM material requirements of DD WTGs due to the increased permeability of the air-gap region.

In Section 8.3, the reduction in WTG efficiency due to a ferrofluid-gap was investigated considering turbulence and the increased viscosity of the ferrofluid due to the magnetic field within the air-gap region. The loss in revenue resulting from the reduction in WTG efficiency was compared with the cost savings associated with the reduction in PM material requirements, and it was shown that the cost saved in PM material can exceed the loss in revenue due to the reduction in efficiency.

In Section 8.4, the impact of a ferrofluid-gap on the thermal performance of a WTG was assessed:

It was demonstrated that if the ferrofluid is contained within the air-gap region with no circulation the PM temperature of an inner-rotor WTG topology can be reduced in comparison to an unventilated air-gap, however for an outer-rotor topology in which the external rotor surface is exposed to the external air-flow the PM temperature was shown to increase significantly in comparison to an unventilated air-gap.

Implementation of a ferrofluid coolant loop was considered, it was demonstrated that an improvement in thermal performance is possible assuming that the ferrofluid is circulated via the WTG cooling system. However, the limitations of such a system were highlighted, and it was argued that similar performance enhancements can be achieved through less complex methods.

In Section 8.5, key practical issues associated with implementing a ferrofluid-gap in DD WTGs were discussed. It was shown that a small reduction in WTG availability due to the implementation of a ferrofluid-gap would offset the potential benefits, necessitating that the implementation of a ferrofluid-gap does not reduce wind turbine reliability in comparison to a conventional air-gap.

The issue of sealing the ferrofluid within the generator was discussed and it was highlighted that conventional approaches would likely reduce the WTG availability by an unacceptable extent. Implementation of a magnetic seal was considered, and it was highlighted that due to the significant hydrostatic pressure of the ferrofluid it would be an uneconomical approach for multi-megawatt scale WTGs.

The practical issues of ferrofluid-gap pressure regulation and sedimentation were discussed, and it was highlighted that a low unit cost of high quality ferrofluid would be required for a net cost saving to be achieved with a ferrofluid-gap.

Chapter 9: Conclusion

This thesis investigated the concept of flooding the air-gap region of permanent magnet (PM) direct-drive (DD) wind turbine generators (WTGs) with magnetically permeable ferrofluid such that the requirement for PM material can be reduced. Throughout the thesis the concept is referred to as a ‘ferrofluid-gap’. Following a summary of each chapter is provided, the key research questions are discussed, the contributions to knowledge from this work are highlighted, and the opportunities for further work are discussed.

9.1 Chapter Summaries

In Chapter 2, a design procedure was presented for a multi-megawatt scale surface mounted PM DD WTGs with fractional-slot concentrated windings (FSCWs). This design procedure was utilised throughout the thesis to numerically quantify the impact of various design variations on the performance of multi-megawatt scale DD WTGs. Detailing the design procedure at the beginning of the thesis also served as a review of the various multidisciplinary aspects of DD WTG design. The various objectives behind the design of multi-megawatt scale DD WTGs were discussed and it was highlighted that reducing the rare-earth PM material requirements can result in significant cost savings. Based on an example 15 MW DD WTG design various approaches for reducing the PM material requirements were highlighted, motivating the following chapters in this thesis.

In Chapter 3, a refined lumped parameter thermal network (LPTN) modelling method for multi-megawatt scale DD WTGs was introduced. Recent developments in distributed loss modelling were incorporated into the model, improving the estimation of peak component temperatures and the accuracy of multi-dimensional heat flows. To improve the flexibility of the thermal model the convection coefficients were derived from empirical relationships, drawing analogy to simplified geometries. Both a forced air- and a liquid-cooling strategy were investigated for inner- and outer-rotor DD WTG topologies, and a design procedure for both an air-to-air and a liquid-to-air external heat exchanger was provided. It was demonstrated that a liquid-cooling strategy can allow for more efficient and higher performance cooling than an air-cooling strategy. It was shown that an outer-rotor WTG topology can result in improved cooling,

particularly of the PMs, assuming that the external WTG structure is exposed to the ambient air flow. A comparison of air-to-air and liquid-to-air heat exchanger performance highlighted that the required power consumption of both approaches is relatively modest compared to the WTG power capacity, however a liquid-to-air heat exchanger requires significantly less volume to operate effectively.

In Chapter 4, a review of air-gap clearance dimensioning for multi-megawatt scale DD WTGs was provided and it was highlighted that further research in this area would be very beneficial. For the case of a 15 MW surface mounted PM DD WTG, it was demonstrated that the minimum air-gap clearance is primary constrained by the extent of air-gap non-uniformity and the risk of rotor-stator contact, as opposed to the armature inductance, armature reaction, or the risk of PM demagnetisation. Opportunities to improve models of air-gap stability based on the concept of magnetic stiffness were highlighted, it was emphasised that the spatial distribution of air-gap non-uniformity has a significant impact on the extent of the corresponding mechanical deformation of the WTG structure. An analytical model was introduced for determining the wavenumber and frequency of air-gap radial Maxwell stress harmonics that result from high-order air-gap non-uniformity. This model was validated through a full-scale finite element method (FEM) simulation of a 15 MW DD WTG. It was shown that high-order air-gap non-uniformities can result in low-wavenumber stress harmonics which are particularly problematic for WTG vibration.

In Chapter 5, an overview of ferrofluid was provided with a particular focus towards its application in ferrofluid-gaps for electrical machines. It demonstrated how the key magnetic and mechanical properties of ferrofluid can be determined according to the carrier fluid properties and the magnetic volume fraction. The theoretically predicted magnetic and mechanical behaviour of a ferrofluid-gap was explained. A review was provided of previous research concerned with the application of ferrofluid in electrical machines and the opportunities for further research in this area were highlighted.

In Chapter 6, the design and fabrication of a novel ferrofluid-gap test rig were detailed. A DC excited wound-rotor synchronous machine with an unusually large air-gap clearance and an idealised rotor/stator geometry was constructed such that the fundamental magnetic and mechanical behaviour of ferrofluid in the air-gap region of electrical machines could be characterised. The test rig was scaled such that the

ferrofluid-gap shear rate and turbulence surpassed what is expected in multi-megawatt scale DD WTGs.

Chapter 7 detailed the various experimental investigations that were conducted with the ferrofluid-gap test rig. It was demonstrated that the shear rate and turbulence of the ferrofluid-gap had no discernible impact on its magnetic behaviour. It was demonstrated that the magnetic performance of a ferrofluid-gap can be accurately simulated in open-load and loaded conditions by simply assigning the ferrofluid-gap region the appropriate magnetic properties obtained from vibrating sample magnetometry (VSM) lab tests and treating the ferrofluid-gap as a homogeneous magnetic material. The influence of the magnetic field on ferrofluid-gap drag was investigated; it was demonstrated that the increased drag due to the magnetic field can be estimated with an analytical approach. A multi-physics ferrohydrodynamic simulation of the test-rig ferrofluid-gap drag was also compared with the experimental results, showing good agreement. The behaviour of a partially-filled ferrofluid-gap was also investigated, it was demonstrated that the magnetic field within the air-gap region can retain the ferrofluid above the poles at significant rotational speeds.

Chapter 8 presents an assessment of the feasibility of ferrofluid-gaps for multi-megawatt scale PM DD WTGs. The analysis presented in Chapter 8 was supported by the various design tools presented in the previous chapters and the experimental validation of ferrofluid-gap magnetic and mechanical behaviour. The magnetic performance of ferrofluid-gaps in PM DD WTGs was investigated through a combination of FEM simulations and analytical magnetic circuit analysis. It was shown that a ferrofluid-gap can allow for an appreciable reduction in PM material despite its relatively low saturation magnetisation. It was demonstrated that the WTG efficiency loss resulting from ferrofluid-gap drag can be relatively modest, and that the cost saved in PM material can exceed the additional loss in revenue over an assumed 25-year wind turbine lifetime. The impact of a ferrofluid-gap on the thermal performance of DD WTGs was investigated, it is found that it may allow for a reduction in PM temperatures for inner-rotor WTGs in comparison to an unventilated air-gap, however it would significantly increase the PM temperature of outer-rotor WTGs. The concept of circulating the ferrofluid through the air-gap region was investigated, it was demonstrated that there is potential for enhanced cooling. Practical issues related to the implementation of ferrofluid-gaps in multi-megawatt scale DD WTGs were

discussed. It was highlighted that there can be no allowance for compromising WTG reliability due to a ferrofluid-gap. The issue of sealing the ferrofluid within the WTG was discussed, it was determined that a conventional seal would likely result in an unacceptable reduction in reliability. The concept of a wear-free magnetic seal was discussed, and it was shown that it is likely uneconomical for large WTGs due to the significant hydrostatic pressure of the ferrofluid.

9.2 Discussion and Conclusions

In the introduction, the fundamental research question underlying this thesis was stated as:

- If the air-gap region of permanent magnet (PM) direct-drive (DD) wind turbine generators (WTG) is flooded with ferrofluid can a reduction in PM material be achieved without unacceptably compromising WTG performance?

Answering this question required a comprehensive multi-physics approach encompassing magnetic, electrical, thermal, fluid dynamic, chemical, and structural analysis supported by extensive experimental investigation.

It has been demonstrated that, in principle, a ferrofluid-gap can indeed enable a reduction in PM magnet material requirements without unacceptably compromising WTG performance, it was shown that:

- Despite its relatively low saturation magnetisation, a ferrofluid-gap can allow for an appreciable reduction in PM material.
- The WTG efficiency loss resulting from the ferrofluid-gap drag can be relatively modest, and the cost saved in PM material can exceed the additional loss in lifetime revenue.
- A ferrofluid-gap can enhance the thermal performance of a PM DD WTG; by circulating the ferrofluid through the air-gap region enhanced cooling is also possible.

Nevertheless, several factors limit the practicality of implementing a ferrofluid-gap in multi-megawatt scale DD WTGs:

- To allow for a reasonable reduction in PM mass due to a ferrofluid-gap magnetic saturation of the electrical steel components must be minimised, constraining the possible design space of DD WTG magnetic circuits.

- Although a ferrofluid-gap can enhance cooling, this can arguably be achieved by more practical methods such as direct liquid cooling of the armature windings.
- A small reduction in WTG reliability would negate the PM magnet material cost savings. Maintaining the same reliability as a conventional air-gap WTG would be very difficult, particularly due to the difficulties associated with sealing the ferrofluid within the machine.
- The cost of the ferrofluid and the other expenses associated with the implementation and maintenance of a ferrofluid-gap would have to be very low to allow for a net cost saving over the lifetime of a wind turbine.

It is therefore reasonable to conclude that the adoption of a ferrofluid-gap is not recommended for multi-megawatt scale DD WTGs.

It can be argued that such a conclusion could have been reached without going into the level of detail provided in this thesis. However, as discussed in Chapter 5, Section 5.4, prior to this thesis the concept of ferrofluid-gaps for electrical machines was underdeveloped both in terms of experimental analysis and theoretical treatment. Although the application of focus in this thesis was direct-drive (DD) wind turbine generators (WTGs), the experimental results and analysis methodologies presented in this work are broadly applicable and can be adapted to investigate alternative machine topologies in which the ferrofluid-gap concept may offer greater potential.

9.3 Further Work

In the following section, recommendations are made on how the work presented in this thesis could be taken further.

In Chapter 3, Section 3.3.3.1, it was highlighted that for very thin-gap Taylor-Couette (TC) flow, the Taylor criterion is no longer strictly appropriate, and the behaviour of the flow is analogous to plane Couette flow. In this case the flow is linearly stable, however turbulence can be initiated and sustained if the flow is perturbed. It was therefore assumed that non-uniformity of the air-gap and external loading would likely result in turbulent flow in DD WTG air-gaps. The standard Taylor-Couette Nusselt number correlations for inner-rotor TC flow were therefore used to approximate the air-gap convective heat transfer coefficient. Further research into the flow state expected

within DD WTG air-gaps would be useful for informing appropriate values of the air-gap convective heat transfer coefficient.

In Chapter 3, two specific cooling strategies were investigated and compared, however there are a variety of strategies that could be implemented in DD WTGs. Adapting the thermal model to represent additional cooling strategies would facilitate a quantitative comparison of their performance.

In Chapter 4 the air-gap dimensioning of DD WTGs was discussed, and insights were presented regarding air-gap stability modelling and vibration induced by high-order air-gap non-uniformity. Further research into air-gap dimensioning would be beneficial for improving the understanding of DD WTG design and may lead to innovations that could reduce PM material requirements.

In Chapter 7, experimental investigations with the ferrofluid-gap test rig are detailed. Three different ferrofluids were tested, however experimentation with additional ferrofluids would be useful. Experimentation with a ferrofluid with a relatively large magnetic volume fraction would help to clarify how the magnetic field influences the ferrofluid-gap drag since a more pronounced effect would be expected, this would reduce the uncertainty in the results.

Experimental results were presented for partially-filled ferrofluid-gaps, it was demonstrated that the ferrofluid was retained above the pole faces at significant rotational speeds. However, as discussed in Chapter 7, Section 7.2.3, the test rig was not designed such that the behaviour of the partially-filled ferrofluid-gap represented what could be expected in multi-megawatt scale DD WTGs. As highlighted in Chapter 8, Section 8.5, a partially filled ferrofluid-gap may alleviate some of the practical challenges, particularly sealing of the ferrofluid and regulation of the volume and pressure. Further experimental investigation into the partially-filled ferrofluid-gap concept would be an interesting topic for future research.

In Chapter 8, the feasibility of ferrofluid-gaps for DD WTGs was assessed. However, the experimental results presented in this thesis and the various analysis frameworks that were utilised can be applied or adapted to other electrical machine topologies. Although it was concluded that ferrofluid-gaps are not practical for DD WTGs, they may be more beneficial for other electrical machine designs and applications.

References

[1] T. Hale *et al.*, “Assessing the rapidly-emerging landscape of net zero targets,” *Clim. Policy*, vol. 22, no. 1, pp. 18–29, 2022, doi: 10.1080/14693062.2021.2013155.

[2] International Energy Agency, “Net Zero by 2050: A Roadmap for the Global Energy Sector,” 2021. [Online]. Available: https://www.iea.org/reports/net-zero-by-2050

[3] ORE Catapult, “An innovator’s guide to The Offshore Wind Market,” 2018. [Online]. Available: https://ore.catapult.org.uk/app/uploads/2018/10/OREC01_7468-SME-Report-2-Offshore-Wind-Market-SP.pdf

[4] H. Díaz and C. Guedes Soares, “Review of the current status, technology and future trends of offshore wind farms,” *Ocean Eng.*, vol. 209, no. April, p. 107381, 2020, doi: 10.1016/j.oceaneng.2020.107381.

[5] A. McCoy *et al.*, “Offshore Wind Market Report: 2024 Edition,” Golden, CO (United States), Aug. 2024. doi: 10.2172/2434294.

[6] M. Shields, P. Beiter, J. Nunemaker, A. Cooperman, and P. Duffy, “Impacts of turbine and plant upsizing on the levelized cost of energy for offshore wind,” *Appl. Energy*, vol. 298, p. 117189, 2021, doi: 10.1016/j.apenergy.2021.117189.

[7] A. R. Nejad *et al.*, “Wind turbine drivetrains: State-of-the-art technologies and future development trends,” *Wind Energy Sci.*, vol. 7, no. 1, pp. 387–411, 2022, doi: 10.5194/wes-7-387-2022.

[8] J. Carroll, A. McDonald, D. McMillan, T. Stehly, C. Mone, and B. Maples, “Cost of energy for offshore wind turbines with different drive train types,” in *European Wind Energy Association Annual Conference and Exhibition 2015, EWEA 2015 - Scientific Proceedings*, 2015, p. 9.

[9] Arup, “Ports for offshore wind: A review of the net-zero opportunity for ports in Scotland,” 2020. [Online]. Available: https://www.crownestatescotland.com/resources/documents/ports-for-offshore-wind-a-review-of-the-net-zero-opportunity-for-ports-in-scotland

[10] M. Hannon, T. Eva, J. Dixon, D. McMillan, and M. Collu, “Offshore wind, ready to float? Global and UK trends in the floating offshore wind market,” 2019. doi: 10.17868/69501.

[11] “GE unveils nacelle of massive Haliade-X wind turbine.” https://www.windpowerengineering.com/ge-unveils-nacelle-of-massive-haliade-x-wind-turbine/ (accessed Oct. 29, 2025).

[12] J. M. D. Coey, “Perspective and Prospects for Rare Earth Permanent Magnets,” *Engineering*, vol. 6, no. 2, pp. 119–131, 2020, doi: 10.1016/j.eng.2018.11.034.

[13] E. Gaertner *et al.*, “Definition of the IEA Wind 15-Megawatt Offshore Reference Wind Turbine Technical Report,” 2020. [Online]. Available: www.nrel.gov/publications.

[14] C. Y. Hsiao, S. N. Yeh, and J. C. Hwang, “Design of high performance permanent-magnet synchronous wind generators,” *Energies*, vol. 7, no. 11, pp. 7105–7124, 2014, doi: 10.3390/en7117105.

[15] C. Scherer and A. M. Figueiredo Neto, “Ferrofluids: Properties and Applications,” *Brazilian J. Phys.*, vol. 35, no. 3A, 2005.

[16] “Ferrotec Global - Ferrofluid | Ferrotec Global.” https://www.ferrotec-global.com/tech_2_1.php (accessed Oct. 29, 2025).

[17] F. Zahle *et al.*, “Definition of the IEA Wind 22-Megawatt Offshore Reference Wind Turbine,” 2024. doi: 10.11581/DTU.00000317.

[18] A. Grauers, “Design of Direct-driven Permanent-magnet Generators for Wind Turbines,” Chalmers University of Technology, 1996.

[19] L. Sethuraman and K. Dykes, “GeneratorSE : A Sizing Tool for Variable-Speed Wind Turbine Generators,” 2017. [Online]. Available: www.nrel.gov/publications.

[20] A. Hebala, W. A. M. Ghoneim, and H. A. Ashour, “Detailed Design Procedures for PMSG Direct-Driven by Wind Turbines,” *J. Electr. Eng. Technol.*, vol. 14, no. 1, pp. 251–263, Jan. 2019, doi:

10.1007/s42835-018-00010-y.

[21] K. Jahani, R. G. Langlois, and F. F. Afagh, “Structural dynamics of offshore Wind Turbines: A review,” *Ocean Engineering*, vol. 251. 2022. doi: 10.1016/j.oceaneng.2022.111136.

[22] H. Polinder, F. F. A. Van Der Pijl, G. J. De Vilder, and P. J. Tavner, “Comparison of direct-drive and geared generator concepts for wind turbines,” *IEEE Trans. Energy Convers.*, vol. 21, no. 3, pp. 725–733, Sep. 2006, doi: 10.1109/TEC.2006.875476.

[23] D. K. Kana Padinharu, G. J. Li, Z. Q. Zhu, P. Wang, R. Clark, and Z. Azar, “Comparison of direct-drive Vernier wind generators for potential use at ≥10 MW power level,” *IET Electr. Power Appl.*, 2024, doi: 10.1049/elp2.12477.

[24] M. O. L. Hansen, *Aerodynamics of wind turbines: Third edition*. 2015. doi: 10.4324/9781315769981.

[25] A. Zavvos, A. McDonald, and M. Mueller, “Optimisation tools for large permanent magnet generators for direct drive wind turbines,” *IET Renew. Power Gener.*, vol. 7, no. 2, pp. 163–171, 2013, doi: 10.1049/iet-rpg.2012.0135.

[26] A. S. McDonald, “Structural analysis of low speed, high torque electrical generators for direct drive renewable energy converters,” The University of Edinburgh, 2008. [Online]. Available: http://hdl.handle.net/1842/12608

[27] H. Polinder, D. Bang, R. P. J. O. M. Van Rooij, A. S. McDonald, and M. A. Mueller, “10 MW wind turbine direct-drive generator design with pitch or active speed stall control,” in *Proceedings of IEEE International Electric Machines and Drives Conference, IEMDC 2007*, 2007, vol. 2, pp. 1390–1395. doi: 10.1109/IEMDC.2007.383632.

[28] P. Ponomarev, Y. Alexandrova, I. Petrov, P. Lindh, E. Lomonova, and J. Pyrhonen, “Inductance calculation of tooth-coil permanent-magnet synchronous machines,” *IEEE Trans. Ind. Electron.*, vol. 61, no. 11, pp. 5966–5973, 2014, doi: 10.1109/TIE.2014.2304933.

[29] D. Hanselman, *Brushless permanent magnet motor design*. 2003. [Online]. Available: http://digitalcommons.library.umaine.edu/fac_monographs/231/

[30] G. W. Carter, *The Electromagnetic Field in its Engineering Aspects*, vol. 5, no. 56. Longmans, 1954.

[31] H. Vu Xuan, D. Lahaye, H. Polinder, and J. A. Ferreira, “Influence of stator slotting on the performance of permanent-magnet machines with concentrated windings,” *IEEE Trans. Magn.*, vol. 49, no. 2, pp. 929–938, 2013, doi: 10.1109/TMAG.2012.2212025.

[32] L. Zhu, S. Z. Jiang, Z. Q. Zhu, and C. C. Chan, “Comparison of analytical models for predicting cogging torque in surface-mounted PM machines,” *19th Int. Conf. Electr. Mach. ICEM 2010*, pp. 1–6, 2010, doi: 10.1109/ICELMACH.2010.5607822.

[33] R. Scott Semken *et al.*, “Direct-drive permanent magnet generators for high-power wind turbines: Benefits and limiting factors,” *IET Renew. Power Gener.*, vol. 6, no. 1, pp. 1–8, Jan. 2012, doi: 10.1049/iet-rpg.2010.0191.

[34] H. Polinder, S. W. H. De Haan, M. R. Dubois, and J. G. Slootweg, “Basic operation principles and electrical conversion systems of wind turbines,” *EPE J. (European Power Electron. Drives Journal)*, vol. 15, no. 4, pp. 43–50, 2005, doi: 10.1080/09398368.2005.11463604.

[35] A. Grauer and S. Landström, “The Rectifiers Influence on the Size of Direct-driven Generators,” in *1999 European Wind Energy Conference, 1-5 March 1999, Nice, France*, 1999, pp. 829–832. [Online]. Available: https://www.researchgate.net/publication/2466342

[36] H. Li, Z. Chen, and H. Polinder, “‘Integrated Wind Turbine Design’ 019945 (SES6) RESEARCH REPORT on MODELS for NUMERICAL EVALUATION of VARIABLE SPEED DIFFERENT WIND GENERATOR SYSTEMS (Deliverable No.: D 1B2.b.2).”

[37] C. Ciriani, H. A. Khan, K. Mansour, M. Olivo, and A. Tessarolo, “Simple and Accurate Computation of Rotor Eddy-Current Losses in Surface-Mounted Permanent Magnet Machines Accounting for Magnet Circumferential Segmentation,” *IEEE Access*, vol. 12, pp. 36810–36824, 2024, doi: 10.1109/ACCESS.2024.3374214.

[38] S. Ruoho, T. Santa-Nokki, J. Kolehmainen, and A. Arkkio, “Modeling magnet length in 2-D finite-

element analysis of electric machines," *IEEE Trans. Magn.*, vol. 45, no. 8, pp. 3114–3120, Aug. 2009, doi: 10.1109/TMAG.2009.2018621.

[39] I. Rudden, G. J. Li, Z. Q. Zhu, A. Duke, and R. Clark, "Analysis of MW-Level Offshore Wind Turbine Generators with Dual Star–Delta Fractional-Slot Windings," *Energies* , vol. 17, no. 12, 2024, doi: 10.3390/en17122958.

[40] Y. Feng, P. J. Tavner, and H. Long, "Early experiences with UK round 1 offshore wind farms," *Proc. Inst. Civ. Eng. Energy*, vol. 163, no. 4, pp. 167–181, 2010, doi: 10.1680/ener.2010.163.4.167.

[41] J. Pyrhönen, J. Nerg, P. Kurronen, J. Puranen, and M. Haavisto, "Permanent magnet technology in wind power generators," *19th Int. Conf. Electr. Mach. ICEM 2010*, 2010, doi: 10.1109/ICELMACH.2010.5608312.

[42] "Rare Earth Magnets price today | Historical Rare Earth Price Charts | SMM Metal Market." https://www.metal.com/price/Rare-Earth/Rare-Earth-Magnets (accessed Jun. 04, 2025).

[43] G. E. Barter, L. Sethuraman, P. Bortolotti, J. Keller, and D. A. Torrey, "Beyond 15 MW: A cost of energy perspective on the next generation of drivetrain technologies for offshore wind turbines," *Appl. Energy*, vol. 344, no. April, p. 121272, 2023, doi: 10.1016/j.apenergy.2023.121272.

[44] "Neodymium Rare Earth - Price - Chart - Historical Data - News." https://tradingeconomics.com/commodity/neodymium (accessed Jul. 04, 2025).

[45] A. S. McDonald, M. A. Mueller, and H. Polinder, "Structural mass in direct-drive permanent magnet electrical generators," in *IET Renewable Power Generation*, 2008, vol. 2, no. 1, pp. 3–15. doi: 10.1049/iet-rpg:20070071.

[46] A. M. Kazemi Amiri, K. Tartt, and A. McDonald, "Identifying path ahead for tackling future challenges in direct-drive permanent magnet wind turbine generator's electro-mechanical design and manufacturing," *Forsch. im Ingenieurwesen/Engineering Res.*, vol. 89, no. 1, 2025, doi: 10.1007/s10010-025-00792-4.

[47] R. Williams *et al.*, "2023 Global Offshore Wind Report," 2023. [Online]. Available: https://gwec.net

[48] A. S. Escalera Mendoza, D. Todd Griffth, C. Qin, E. Loth, and N. Johnson, "Rapid approach for structural design of the tower and monopile for a series of 25 MW offshore turbines," in *Journal of Physics: Conference Series*, Jun. 2022, vol. 2265, no. 3. doi: 10.1088/1742-6596/2265/3/032030.

[49] A. B. Abrahamsen *et al.*, "Comparison of Levelized Cost of Energy of Superconducting Direct Drive Generators for a 10-MW Offshore Wind Turbine," *IEEE Trans. Appl. Supercond.*, vol. 28, no. 4, pp. 1–5, 2018, doi: 10.1109/TASC.2018.2810294.

[50] L. Sethuraman, V. Venugopal, A. Zavvos, and M. Mueller, "Structural integrity of a direct-drive generator for a floating wind turbine," *Renew. Energy*, vol. 63, pp. 597–616, Mar. 2014, doi: 10.1016/j.renene.2013.10.024.

[51] "Wind turbine SG 21-276 DD hits 21.5 MW in Denmark." https://www.rinnovabili.net/business/energy/wind-turbine-sg-21-276-dd-hits-21-5-mw-in-denmark/ (accessed Jun. 07, 2025).

[52] E. Spooner, P. Gordon, J. R. Bumby, and C. D. French, "Lightweight ironless-stator PM generators for direct-drive wind turbines," *IEE Proc. Electr. Power Appl.*, vol. 152, no. 1, pp. 17–26, 2005, doi: 10.1049/ip-epa:20041084.

[53] N. A. Bhuiyan and A. McDonald, "Optimization of Offshore Direct Drive Wind Turbine Generators With Consideration of Permanent Magnet Grade and Temperature," *IEEE Trans. Energy Convers.*, vol. 34, no. 2, pp. 1105–1114, 2019, doi: 10.1109/TEC.2018.2879442.

[54] I. Rudden, G.-J. Li, Z.-Q. Zhu, A. Duke, and R. Clark, "An Investigation into the Saliency Ratio of Fractional-Slot Concentrated-Winding Generators for Offshore Wind Power," *Energies*, vol. 18, no. 8, p. 2057, Apr. 2025, doi: 10.3390/en18082057.

[55] A. Boglietti, A. Cavagnino, D. Staton, M. Shanel, M. Mueller, and C. Mejuto, "Evolution and

modern approaches for thermal analysis of electrical machines," *IEEE Trans. Ind. Electron.*, vol. 56, no. 3, pp. 871–882, 2009, doi: 10.1109/TIE.2008.2011622.

[56] I. Boldea, *Synchronous Generators (Electric Generators Handbook)*. 2006.

[57] P. Taras, R. Nilifard, Z. Q. Zhu, and Z. Azar, "Cooling Techniques in Direct-Drive Generators for Wind Power Application," *Energies*, vol. 15, no. 16, 2022, doi: 10.3390/en15165986.

[58] "Wind Turbine Cooling Systems | Heatex." https://www.heatex.com/applications/wind-turbine-cooling/ (accessed Oct. 30, 2025).

[59] M. Polikarpova, P. Ponomarev, P. Röyttä, S. Semken, Y. Alexandrova, and J. Pyrhönen, "Direct liquid cooling for an outer-rotor directdrive permanent-magnet synchronous generator for wind farm applications," *IET Electr. Power Appl.*, vol. 9, no. 8, pp. 523–532, Sep. 2015, doi: 10.1049/iet-epa.2014.0342.

[60] G. Mottershead, S. Bomben, I. Kerszenbaum, and G. Klempner, *Handbook of Large Hydro Generators*. 2020. doi: 10.1002/9781119524205.

[61] G. Bywaters *et al.*, "Northern Power NW 1500 Direct-Drive Generator: April 12, 2001 - September 30, 2006," 2007. [Online]. Available: https://www.nrel.gov/docs/fy08osti/40177.pdf%0Ahttp://www.osti.gov/servlets/purl/920936-3pMsQr/

[62] R. Iracheta-Cortez and R. Sanchez-Carvajal, "Thermal Analysis for Designing Wind Turbines based on RF-PMSGs," *Proc. IEEE Cent. Am. Panama Conv. CONCAPAN*, no. 2024, 2024, doi: 10.1109/CONCAPAN63470.2024.10933841.

[63] D. Liang, Z. Qiang Zhu, R. Nilifard, Z. Azar, N. Madani, and J. Brix Christensen, "Novel Lumped-Parameter Thermal Modeling - Part II: Thermal Models for Cylindrical Components and Application to Electrical Machines," *IEEE Trans. Transp. Electrif.*, vol. 11, no. 1, pp. 3956–3969, 2025, doi: 10.1109/TTE.2024.3449646.

[64] D. Liang, Z. Qiang Zhu, R. Nilifard, Z. Azar, N. Madani, and J. Brix Christensen, "Novel Lumped-Parameter Thermal Modeling - Part I: Thermal Models for Cuboidal Components," *IEEE Trans. Transp. Electrif.*, vol. 11, no. 1, pp. 3942–3955, 2025, doi: 10.1109/TTE.2024.3449637.

[65] G. Kylander, "Thermal modelling of small cage induction motors," Chalmers University of Technology.

[66] M. Polikarpova, P. Röyttä, J. Alexandrova, S. Semken, J. Nerg, and J. Pyrhönen, "Thermal design and analysis of a direct-water cooled direct drive permanent magnet synchronous generator for high-power wind turbine application," *Proc. - 2012 20th Int. Conf. Electr. Mach. ICEM 2012*, pp. 1488–1495, 2012, doi: 10.1109/ICElMach.2012.6350075.

[67] D. A. Staton and A. Cavagnino, "Convection heat transfer and flow calculations suitable for electric machines thermal models," *IEEE Trans. Ind. Electron.*, vol. 55, no. 10, pp. 3509–3516, 2008, doi: 10.1109/TIE.2008.922604.

[68] S. Grossmann, D. Lohse, and C. Sun, "High-Reynolds Number Taylor-Couette Turbulence," *Annu. Rev. Fluid Mech.*, vol. 48, pp. 53–80, Jan. 2016, doi: 10.1146/annurev-fluid-122414-034353.

[69] H.-S. Dou, B. C. Khoo, and K. S. Yeo, "Instability of Taylor-Couette flow between concentric rotating cylinders," *Int. J. Therm. Sci.*, vol. 47, no. 11, pp. 1422–1435, Nov. 2008, doi: 10.1016/j.ijthermalsci.2007.12.012.

[70] H.-S. Dou, "Physics of flow instability and turbulent transition in shear flows," *Int. J. Phys. Sci.*, vol. 6, no. 6, pp. 1411–1425, 2011.

[71] M. Fénot, Y. Bertin, E. Dorignac, and G. Lalizel, "A review of heat transfer between concentric rotating cylinders with or without axial flow," *International Journal of Thermal Sciences*, vol. 50, no. 7. Elsevier Masson SAS, pp. 1138–1155, 2011. doi: 10.1016/j.ijthermalsci.2011.02.013.

[72] T. L. Bergman, A. S. Lavine, F. P. Incropera, and P. D. David, *Fundamentals of Heat and Mass Transfer*. John Wiley & Sons, 2006.

[73] D. Staton, A. Boglietti, and A. Cavagnino, "Solving the more difficult aspects of electric motor thermal analysis in small and medium size industrial induction motors," *IEEE Transactions on*

Energy Conversion, vol. 20, no. 3. pp. 620–628, Sep. 2005. doi: 10.1109/TEC.2005.847979.

[74] P. Liang, F. Chai, K. Shen, and W. Liu, “Thermal design and optimization of a water-cooling permanent magnet synchronous in-wheel motor,” in *2019 22nd International Conference on Electrical Machines and Systems (ICEMS)*, Aug. 2019, pp. 1–6. doi: 10.1109/ICEMS.2019.8922510.

[75] P. Shams Ghahfarokhi *et al.*, “Steady-State Thermal Modeling of Salient Pole Synchronous Generator,” *Energies*, vol. 15, no. 24, Dec. 2022, doi: 10.3390/en15249460.

[76] A. I. Zografos, W. A. Martin, and J. E. Sunderland, “Equations of properties as a function of temperature for seven fluids,” *Comput. Methods Appl. Mech. Eng.*, vol. 61, no. 2, pp. 177–187, 1987, doi: 10.1016/0045-7825(87)90003-X.

[77] W. M. Kays and A. L. London, *Compact heat exchangers. Third Edition.* Scientific International, 1984.

[78] H. Li, Z. Chen, and H. Polinder, “Optimization of multibrid permanent-magnet wind generator systems,” *IEEE Trans. Energy Convers.*, vol. 24, no. 1, pp. 82–92, 2009, doi: 10.1109/TEC.2008.2005279.

[79] S. W. Jung, D. Kang, K. Palanimuthu, Y. H. Joo, and S. Y. Jung, “Design of 20 MW direct-drive permanent magnet synchronous generators for wind turbines based on constrained many-objective optimization,” *Wind Energy*, 2024, doi: 10.1002/we.2916.

[80] L. Sethuraman, Y. Xing, V. Venugopal, Z. Gao, M. Mueller, and T. Moan, “A 5 MW direct-drive generator for floating spar-buoy wind turbine: Drive-train dynamics,” *Proc. Inst. Mech. Eng. Part C J. Mech. Eng. Sci.*, vol. 231, no. 4, pp. 744–763, Feb. 2017, doi: 10.1177/0954406215623306.

[81] M. Bichan, A. Jack, and P. Jaen-Sola, “Establishing the Importance of Operating Temperature in the Structural Integrity of Large-Scale Direct-Drive Wind Turbine Generators,” *Machines*, vol. 11, no. 8, p. 780, Jul. 2023, doi: 10.3390/machines11080780.

[82] A. Baseer, Y. He, R. Schelenz, A. Kari, B. Roscher, and G. Jacobs, “Comparison of a Direct Drive Wind Turbine with and without LSS-Coupling Regarding Air Gap Displacement,” in *Journal of Physics: Conference Series*, Sep. 2020, vol. 1618, no. 5. doi: 10.1088/1742-6596/1618/5/052004.

[83] A. Zavvos, A. McDonald, and M. Mueller, “Optimisation tools for large permanent magnet generators for direct drive wind turbines,” *IET Renew. Power Gener.*, vol. 7, no. 2, pp. 163–171, Mar. 2013, doi: 10.1049/iet-rpg.2012.0135.

[84] P. Jaen-Sola, E. Oterkus, and A. S. McDonald, “Parametric lightweight design of a direct-drive wind turbine electrical generator supporting structure for minimising dynamic response,” *Ships Offshore Struct.*, vol. 16, no. S1, pp. 266–274, 2021, doi: 10.1080/17445302.2021.1927356.

[85] P. Jaen-Sola, A. S. McDonald, and E. Oterkus, “Dynamic structural design of offshore direct-drive wind turbine electrical generators,” *Ocean Eng.*, vol. 161, pp. 1–19, Aug. 2018, doi: 10.1016/j.oceaneng.2018.04.074.

[86] T. Hartkopf, M. Hofmann, and S. Jockel, “Direct-drive generators for Megawatt wind turbines,” in *European Wind Energy Conference, Dublin Ireland*, 1997, pp. 668–671.

[87] M. Ghods, Z. Tabarniarami, J. Faiz, and M. A. Bazrafshan, “Turn-to-turn and phase-to-phase short circuit fault detection of wind turbine permanent magnet generator based on equivalent magnetic network modelling by wavelet transform approach,” *IET Electr. Power Appl.*, vol. 18, no. 9, pp. 1005–1020, 2024, doi: 10.1049/elp2.12452.

[88] T. Sebastian and G. Slemon, “Transient torque and short circuit capabilities of variable speed permanent magnet motors,” *IEEE Trans. Magn.*, vol. 23, no. 5, pp. 3619–3621, 1987, doi: 10.1109/TMAG.1987.1065207.

[89] I. D. Chasiotis and Y. L. Karnavas, “A generic multi-criteria design approach toward high power density and fault-tolerant low-speed PMSM for pod applications,” *IEEE Trans. Transp. Electrif.*, vol. 5, no. 2, pp. 356–370, 2019, doi: 10.1109/TTE.2019.2894995.

[90] D. Palani, Z. Azar, A. Thomas, Z. Q. Zhu, and D. Gladwin, “Modeling technique for large permanent magnet generators accounting for manufacturing tolerances and limitations,” 2016.

doi: 10.1109/ICELMACH.2016.7732565.

[91] H. C. Dirani, A. Merkhouf, A. M. Giroux, B. Kedjar, and K. Al-Haddad, “Impact of real air-gap nonuniformity on the electromagnetic forces of a large hydro-generator,” *IEEE Trans. Ind. Electron.*, vol. 65, no. 11, pp. 8464–8475, 2018, doi: 10.1109/TIE.2018.2814021.

[92] H. Emanuel, M. Schellschmidt, S. Wachtel, and S. Adloff, “Power quality measurements of wind energy converters with full-scale converter according to IEC 61400-21,” *2009 10th Int. Conf. Electr. Power Qual. Util. EPQU’09*, pp. 1–7, 2009, doi: 10.1109/EPQU.2009.5318814.

[93] H. Ehya, I. Sadeghi, and J. Faiz, “Online condition monitoring of large synchronous generator under eccentricity fault,” in *Proceedings of the 2017 12th IEEE Conference on Industrial Electronics and Applications, ICIEA 2017*, 2017, vol. 2018-Febru, pp. 19–24. doi: 10.1109/ICIEA.2017.8282807.

[94] C. Patsios, A. Chaniotis, E. Tsampouris, and A. Kladas, “Particular electromagnetic field computation for permanent magnet generator wind turbine analysis,” *IEEE Trans. Magn.*, vol. 46, no. 8, pp. 2751–2754, 2010, doi: 10.1109/TMAG.2010.2043345.

[95] J. N. Stander, G. Venter, and M. J. Kamper, “Review of direct-drive radial flux wind turbine generator mechanical design,” *Wind Energy*, vol. 15, no. 3. John Wiley and Sons Ltd, pp. 459–472, 2012. doi: 10.1002/we.484.

[96] T. Burton, N. Jenkins, D. Sharpe, and E. Bossanyi, *Wind Energy Handbook*, vol. 1, no. 1. Wiley, 2011. doi: 10.1002/9781119992714.

[97] “Hexagon hybrid technology drives wind energy innovation at Siemens Gamesa | Hexagon.” https://hexagon.com/company/newsroom/press-releases/2021/hybrid-technology-wind-energy-innovation (accessed Aug. 19, 2025).

[98] P. Jaen Sola and A. S. McDonald, “A comparative study of methods for modelling the structural stiffness of generator components,” *IET Conf. Publ.*, vol. 2016, no. CP684, pp. 1–7, 2016, doi: 10.1049/cp.2016.0314.

[99] A. McDonald and P. Jaen-Sola, “A Stiffness Approach for Coupling Structural and Magnetic Models for the Sustainable Design, Optimisation and Real-Time Structural Integrity Assessment of Radial Flux Permanent Magnet Generators for Direct-Drive Wind Turbines,” *Sustain.* , vol. 16, no. 6, 2024, doi: 10.3390/su16062393.

[100] P. Jaen-Sola and A. S. Mcdonald, “Structural Analysis and Characterization of Radial Flux PM Generators for Direct-Drive Wind Turbines,” in *3rd Renewable Power Generation Conference (RPG 2014)*, 2014, p. 6.

[101] Y. K. Chin, P. Kanninen, P. Maki-Ontto, R. Sakki, and H. Lendenmann, “Phenomenon of magnetic force in permanent magnet wind turbine generators,” *Proc. - 12th Int. Conf. Electr. Mach. Syst. ICEMS 2009*, pp. 1–6, 2009, doi: 10.1109/ICEMS.2009.5382708.

[102] B. Cassoret, J. P. Lecointe, and J. F. Brudny, *Power Electronics and Motor Drives*. CRC Press, 2018. doi: 10.1201/9781315218410.

[103] K. Mostafa, “Direct Drive Wind Turbines : The Effect of Unbalanced Magnetic Pull on Permanent Magnet Generators and Bearing Arrangements Kaswar Mostafa Thesis submitted towards the degree of The University of Edinburgh,” 2018, [Online]. Available: https://era.ed.ac.uk/handle/1842/31360

[104] M. Valavi, A. Nysveen, R. Nilssen, and T. Rolvag, “Slot harmonic effect on magnetic forces and vibration in low-speed permanent-magnet machine with concentrated windings,” *IEEE Trans. Ind. Appl.*, vol. 50, no. 5, pp. 3304–3313, Sep. 2014, doi: 10.1109/TIA.2014.2309717.

[105] C. L. Klop, “ModHVDC Forces and vibrations in a Modular HVDC Generator,” 2022. [Online]. Available: http://resolver.tudelft.nl/uuid:f8fdcfb6-c05a-4a1f-873b-26f7c8409d68

[106] M. Valavi, A. Nysveen, R. Nilssen, R. D. Lorenz, and T. Rølvåg, “Influence of pole and slot combinations on magnetic forces and vibration in low-speed PM wind generators,” *IEEE Trans. Magn.*, vol. 50, no. 5, 2014, doi: 10.1109/TMAG.2013.2293124.

[107] T. Decker *et al.*, “Experimental Validation of a Structure-Borne Sound Model of a Direct Drive Wind Turbine Generator,” *Forsch. im Ingenieurwesen/Engineering Res.*, vol. 87, no. 1, pp. 3–

12, Mar. 2023, doi: 10.1007/s10010-023-00612-7.

[108] M. Valavi, J. Le Besnerais, and A. Nysveen, “An Investigation of Zeroth-Order Radial Magnetic Forces in Low-Speed Surface-Mounted Permanent Magnet Machines,” *IEEE Trans. Magn.*, vol. 52, no. 8, Aug. 2016, doi: 10.1109/TMAG.2016.2553642.

[109] H. Fang, D. Li, R. Qu, and P. Yan, “Modulation Effect of Slotted Structure on Vibration Response in Electrical Machines,” *IEEE Trans. Ind. Electron.*, vol. 66, no. 4, pp. 2998–3007, 2019, doi: 10.1109/TIE.2018.2847639.

[110] Y. Li, Z. Jiao, T. Yu, and Y. Shang, “Viscous loss analysis of the flooded electro-hydrostatic actuator motor under laminar and turbulent flow states,” *MPDI Process.*, vol. 8, no. 8, Aug. 2020, doi: 10.3390/PR8080975.

[111] D. S. Bolintineanu, G. S. Grest, J. B. Lechman, F. Pierce, S. J. Plimpton, and P. R. Schunk, “Particle dynamics modeling methods for colloid suspensions,” *Comput. Part. Mech.*, vol. 1, no. 3, pp. 321–356, 2014, doi: 10.1007/s40571-014-0007-6.

[112] K. R. Schumacher, J. J. Riley, and B. A. Finlayson, “Homogeneous turbulence in ferrofluids with a steady magnetic field,” *J. Fluid Mech.*, vol. 599, pp. 1–28, Mar. 2008, doi: 10.1017/S0022112007009640.

[113] W. Brenig, “Brownian Motion: Langevin Equation,” *Stat. Theory Heat*, pp. 69–72, 1989, doi: 10.1007/978-3-642-74685-7_14.

[114] S. Genc and B. Derin, “Synthesis and rheology of ferrofluids: A review,” *Curr. Opin. Chem. Eng.*, vol. 3, no. 3, pp. 118–124, 2014, doi: 10.1016/j.coche.2013.12.006.

[115] L. Vékás, “Magnetic Fluids: From fundamental properties of matter to magnetic materials and applications.” 2021. [Online]. Available: https://magnetism.eu/esm/2021/slides/slides-vekas.pdf

[116] D. Utami *et al.*, “Material characterization of a magnetorheological fluid subjected to long-term operation in damper,” *Materials (Basel).*, vol. 11, no. 11, 2018, doi: 10.3390/ma11112195.

[117] S. P. Schwaminger, D. Bauer, P. Fraga-García, F. E. Wagner, and S. Berensmeier, “Oxidation of magnetite nanoparticles: impact on surface and crystal properties,” *CrystEngComm*, vol. 19, no. 2, pp. 246–255, 2017, doi: 10.1039/c6ce02421a.

[118] M. Darbandi *et al.*, “Nanoscale size effect on surface spin canting in iron oxide nanoparticles synthesized by the microemulsion method,” *J. Phys. D. Appl. Phys.*, vol. 45, no. 19, May 2012, doi: 10.1088/0022-3727/45/19/195001.

[119] M. P. Morales *et al.*, “Surface and internal spin canting in γ-Fe2O3 nanoparticles,” *Chem. Mater.*, vol. 11, no. 11, pp. 3058–3064, 1999, doi: 10.1021/cm991018f.

[120] R. Frison *et al.*, “Magnetite-maghemite nanoparticles in the 5-15 nm range: Correlating the core-shell composition and the surface structure to the magnetic properties. A total scattering study.,” *Chem. Mater.*, vol. 25, no. 23, pp. 4820–4827, Dec. 2013, doi: 10.1021/cm403360f.

[121] C. Graf *et al.*, “Local Magnetic and Electronic Structure of the Surface Region of Postsynthesis Oxidized Iron Oxide Nanoparticles for Magnetic Resonance Imaging,” *J. Phys. Chem. C*, vol. 119, no. 33, pp. 19404–19414, Aug. 2015, doi: 10.1021/jp512023z.

[122] D. Susan-Resiga and L. Vékás, “Ferrofluid-based magnetorheological fluids: tuning the properties by varying the composition at two hierarchical levels,” *Rheol. Acta*, vol. 55, no. 7, pp. 581–595, 2016, doi: 10.1007/s00397-016-0931-x.

[123] G. D. Scott and D. M. Kilgour, “The density of random close packing of spheres,” *J. Phys. D. Appl. Phys.*, vol. 2, no. 6, pp. 863–866, 1969, doi: 10.1088/0022-3727/2/6/311.

[124] A. O. Ivanov and A. Zubarev, “Chain formation and phase separation in ferrofluids: The influence on viscous properties,” *Materials (Basel).*, vol. 13, no. 18, pp. 1–26, 2020, doi: 10.3390/ma13183956.

[125] M. Raşa, D. Bica, A. Philipse, and L. Vékás, “Dilution series approach for investigation of microstructural properties and particle interactions in high-quality magnetic fluids,” *Eur. Phys. J. E*, vol. 7, no. 3, pp. 209–220, 2002, doi: 10.1140/epje/i200101129.

[126] D. Susan-Resiga and L. Vékás, “From high magnetization ferrofluids to nano-micro composite

magnetorheological fluids: Properties and applications," *Rom. Reports Phys.*, vol. 70, no. 1, pp. 1–29, 2018.

[127] T. S. Chow, "Viscosities of concentrated dispersions," *Phys. Rev. E*, vol. 48, no. 3, pp. 1977–1983, 1993, doi: 10.1103/PhysRevE.48.1977.

[128] S. Vinod and J. Philip, "Thermal and rheological properties of magnetic nanofluids: Recent advances and future directions," *Adv. Colloid Interface Sci.*, vol. 307, no. June, p. 102729, 2022, doi: 10.1016/j.cis.2022.102729.

[129] C. N. Marin, I. Malaescu, and P. C. Fannin, "Theoretical evaluation of the heating rate of ferrofluids," *J. Therm. Anal. Calorim.*, vol. 119, no. 2, pp. 1199–1203, 2015, doi: 10.1007/s10973-014-4224-2.

[130] C. E. Botez and Z. Mussslewhite, "Evidence of Individual Superspin Relaxation in Diluted Fe3O4/Hexane Ferrofluids," *Materials (Basel).*, vol. 16, no. 13, 2023, doi: 10.3390/ma16134850.

[131] M. Lahonian, "Diffusion of Magnetic Nanoparticles Within a Biological Tissue During Magnetic Fluid Hyperthermia," in *Hyperthermia*, vol. 11, no. tourism, InTech, 2013, p. 13. doi: 10.5772/52305.

[132] S. S. Papell, "US3215572A - Low viscosity magnetic fluid obtained by the colloidal suspension of magnetic particles," 1963

[133] W. Huang and X. Wang, "Ferrofluids lubrication: A status report," *Lubr. Sci.*, vol. 28, no. 1, pp. 3–26, Jan. 2016, doi: 10.1002/ls.1291.

[134] S. Odenbach, *Ferrofluids: Magnetically Controllable Fluids and Their Applications*, 1st ed., vol. 594. Berlin, Heidelberg: Springer Berlin Heidelberg, 2002. doi: 10.1007/3-540-45646-5.

[135] "Liquisort Separation – LHS." https://www.lhs.uk.com/product/liquisort-separation/ (accessed Nov. 06, 2025).

[136] L. Göpfert *et al.*, "Enabling continuous flow manufacturing of magnetic nanoparticles with a millifluidic system," *J. Magn. Magn. Mater.*, vol. 563, no. July, 2022, doi: 10.1016/j.jmmm.2022.169985.

[137] P. T. Phong, P. H. Nam, D. H. Manh, and I. J. Lee, "Mn0.5Zn0.5Fe2O4 nanoparticles with high intrinsic loss power for hyperthermia therapy," *J. Magn. Magn. Mater.*, vol. 433, pp. 76–83, 2017, doi: 10.1016/j.jmmm.2017.03.001.

[138] M. S. Pattanaik, V. B. Varma, S. K. Cheekati, V. Chaudhary, and R. V. Ramanujan, "Optimal ferrofluids for magnetic cooling devices," *Sci. Rep.*, vol. 11, no. 1, pp. 1–19, 2021, doi: 10.1038/s41598-021-03514-2.

[139] Y. Iwamoto, H. Yamaguchi, and X. D. Niu, "Magnetically-driven heat transport device using a binary temperature-sensitive magnetic fluid," *J. Magn. Magn. Mater.*, vol. 323, no. 10, pp. 1378–1383, 2011, doi: 10.1016/j.jmmm.2010.11.050.

[140] M. Darbandi *et al.*, "Nanoscale size effect on surface spin canting in iron oxide nanoparticles synthesized by the microemulsion method," *J. Phys. D. Appl. Phys.*, vol. 45, no. 19, 2012, doi: 10.1088/0022-3727/45/19/195001.

[141] FerroTec, "FERROFLUID." https://www.ferrotec.com/products-technologies/ferrofluids/ (accessed Nov. 08, 2025).

[142] L. Blaney, "Magnetite (Fe3O4): Properties, Synthesis, and Applications," *Lehigh Rev.*, vol. 15, 2007, [Online]. Available: https://api.semanticscholar.org/CorpusID:92689666

[143] T. Upadhyay, R. Upadhyay, R. Mehta, V. Aswal, and P. Goyal, "Characterization of a temperature-sensitive magnetic fluid," *Phys. Rev. B - Condens. Matter Mater. Phys.*, vol. 55, no. 9, pp. 5585–5588, 1997, doi: 10.1103/PhysRevB.55.5585.

[144] R. E. Rosensweig, *Ferrohydrodynamics*. Dover Publications, 2014. [Online]. Available: https://app.knovel.com/hotlink/toc/id:kpF0000008/ferrohydrodynamics/ferrohydrodynamics

[145] W. Boon, "Concentration profiles of ferrofluids in magnetic fields," Utrecht University, 2018.

[146] S. Taketomi, "Motion of Ferrite Particles under a High Gradient Magnetic Field in a Magnetic Fluid Shaft Seal," *Jpn. J. Appl. Phys.*, vol. 19, no. 10, p. 1929, 1980.

[147] M. I. Shliomis, “How a rotating magnetic field causes ferrofluid to rotate,” *Phys. Rev. Fluids*, vol. 6, no. 4, pp. 1–20, 2021, doi: 10.1103/PhysRevFluids.6.043701.

[148] S. Odenbach and S. Thurm, “Magnetoviscous Effects in Ferrofluids,” vol. 71, Berlin, Heidelberg: Springer Berlin Heidelberg, 2002, pp. 185–201. doi: 10.1007/3-540-45646-5_10.

[149] S. Odenbach, “Magnetoviscous and viscoelastic effects in ferrofluids,” *Int. J. Mod. Phys. B*, vol. 14, no. 16, pp. 1615–1631, 2000, doi: 10.1142/S0217979200001692.

[150] S. Odenbach, “Transport phenomena in magnetic fluids in cylindrical geometry,” no. July, 2000, pp. 156–170. doi: 10.1007/3-540-45549-3_10.

[151] L. Sun *et al.*, “Magnetic lubricants: Preparation, physical mechanism, and application,” *Friction*, vol. 13, no. 7, p. 9441010, 2025, doi: 10.26599/frict.2025.9441010.

[152] S. Miyake and S. Takahashi, “Sliding bearing lubricated with ferromagnetic fluid,” *ASLE Trans.*, vol. 28, no. 4, pp. 461–466, 1985, doi: 10.1080/05698198508981643.

[153] A. M. Van Silfhout, H. Engelkamp, and B. H. Erné, “Colloidal Stability of Aqueous Ferrofluids at 10 T,” *J. Phys. Chem. Lett.*, vol. 11, no. 15, pp. 5908–5912, 2020, doi: 10.1021/acs.jpclett.0c01804.

[154] A. Veneruso, “Submersible motor with ferrofluid gap, US20100164303A1,” 2010 [Online]. Available: https://patents.google.com/patent/US20100164303A1/en

[155] A. Nethe, T. Scholz, and H. D. Stahlmann, “Improving the efficiency of electric machines using ferrofluids,” *J. Phys. Condens. Matter*, vol. 18, no. 38, Sep. 2006, doi: 10.1088/0953-8984/18/38/S31.

[156] A. Judge, “Air-Gap Elimination in Permanent Magnet Machines,” WORCESTER POLYTECHNIC INSTITUTE, 2012. [Online]. Available: https://digital.wpi.edu/concern/etds/rx913q00j?locale=en

[157] G. Zeng *et al.*, “Asynchronous machine with ferrofluid in gap: Modeling, simulation, and analysis,” *IEEE Trans. Magn.*, vol. 56, no. 1, Jan. 2020, doi: 10.1109/TMAG.2019.2948614.

[158] V. Mateev and I. Marinova, “Modelling of low-speed magnetic gear with viscose ferrofluid,” *COMPEL - Int. J. Comput. Math. Electr. Electron. Eng.*, vol. 41, no. 5, pp. 1956–1970, 2022, doi: 10.1108/COMPEL-07-2021-0233.

[159] J. Lemire-elmore, “A Proposal for the Use of Statorade Ferrofluid on BionX Hub Motors,” 2018. [Online]. Available: https://ebikes.ca/documents/BionX_Statorade_Study.pdf

[160] G. Karimi-Moghaddam, R. D. Gould, S. Bhattacharya, and D. D. Tremelling, “Thermomagnetic liquid cooling: A novel electric machine thermal management solution,” *2014 IEEE Energy Convers. Congr. Expo. ECCE 2014*, pp. 1482–1489, 2014, doi: 10.1109/ECCE.2014.6953594.

[161] W. Zhang, G. J. Li, B. Ren, Y. C. Chong, and M. Michon, “Investigation of Ferrofluid Cooling for High Power Density Permanent Magnet Machines,” *IEEE Trans. Magn.*, vol. 59, no. 1, 2023, doi: 10.1109/TMAG.2022.3224787.

[162] M. Rietz, Q. Shu, H. El Bahi, J. Raisin, R. Kneer, and H. Askarizadeh, “Direct Cooling of Stator End-Windings Using Ferrofluids: An Exploratory Experimental Study on Flow Dynamics and Heat Transfer,” *IEEE Trans. Magn.*, vol. 61, no. 7, pp. 1–10, 2025, doi: 10.1109/TMAG.2025.3564337.

[163] J. A. Cole, “Taylor-vortex instability and annulus-length effects,” *J. Fluid Mech.*, vol. 75, no. 1, pp. 1–15, May 1976, doi: 10.1017/S0022112076000098.

[164] “Fountain Design Ltd.” https://www.fountaindesign.co.uk/ (accessed Nov. 08, 2025).

[165] FARO, “FARO.” https://www.faro.com/en/Products/Hardware/Quantum-FaroArms

[166] J. Mais, “Spectrum Analysis-The key features of analyzing spectra,” 2002. [Online]. Available: https://cdn.skfmediahub.skf.com/api/public/0901d1968024acef/

[167] IEEE, “IEEE Guide for Test Procedures for Synchronous Machines Including Acceptance and Performance Testing and Parameter Determination for Dynamic Analysis,” vol. 2019. IEEE, Piscataway, NJ, USA, pp. 1–246, Nov. 07, 2019. doi: 10.1109/IEEESTD.2020.9050934.

[168] A. Arkkio, “Analysis of Induction Motors Based on the Numerical Solution of the Magnetic Field and Circuit Equations.,” Helsinki University of Technology, 1987. [Online]. Available: https://aaltodoc.aalto.fi/items/1bcfc3de-f81e-4e23-8eaa-7e7f0ebdd187

[169] S. Odenbach, *Colloidal Magnetic Fluids*, vol. 763. Berlin, Heidelberg: Springer Berlin Heidelberg, 2009. doi: 10.1007/978-3-540-85387-9.

[170] S. Zhang *et al.*, “Experimental Investigation of Windage Loss Impacts on Electrical Machine with Oil Jet Cooling,” *2024 27th Int. Conf. Electr. Mach. Syst. ICEMS 2024*, pp. 3381–3386, 2024, doi: 10.23919/ICEMS60997.2024.10921444.

[171] M. Rajňák *et al.*, “Comparison of physical properties of ferrofluids based on mineral transformer oil and bio-degradable gas-to-liquid oil,” *J. Magn. Magn. Mater.*, vol. 589, no. October 2023, 2024, doi: 10.1016/j.jmmm.2023.171628.

[172] “Hydra Oil ISO VG 10 – Maxoline.” https://maxoline.com/shop-default-page/lubricating-oils/industrial-oils/hydra-oil-iso-vg-10/ (accessed Nov. 09, 2025).

[173] COMSOL, “COMSOL Multiphysics® v. 6.1.” Stockholm, Sweden. [Online]. Available: www.comsol.com

[174] S. Dong, “Direct numerical simulation of turbulent Taylor - Couette flow,” *J. Fluid Mech.*, vol. 587, pp. 373–393, Sep. 2007, doi: 10.1017/S0022112007007367.

[175] Department for Energy Security and Net Zero, “Contracts for Difference Strike Prices for CfD Allocation Round 7,” 2025. [Online]. Available: https://assets.publishing.service.gov.uk/media/6880d6f8f47abf78ca1d3550/cfd-ar7-administrative-strike-prices-methodology-note.pdf

[176] C. Kost, S. Shammugam, V. Fluri, D. Peper, A. D. Memar, and T. Schlegel, “Levelized Cost of Electricity- Renewable Energy Technologies July 2024,” 2024. [Online]. Available: https://www.ise.fraunhofer.de/en/publications/studies/cost-of-electricity.html

[177] T. Freyman and T. Tran, “Renewable energy discount rate survey results -2017,” 2018. [Online]. Available: https://www.grantthornton.co.uk/globalassets/1.-member-firms/united-kingdom/pdf/documents/renewable-energy-discount-rate-survey-results-2018.pdf

[178] D. Sumner and A. Yardley, “System Performance, Availability and Reliability Trend Analysis – SPARTA: Portfolio Review 2020/21,” 2019. [Online]. Available: https://cms.ore.catapult.org.uk/wp-content/uploads/2022/06/SPARTA-Review-2021-Final.pdf

[179] S. Virley, B. Beals, and J. Dennis, “Blown away: CfD Round 3 delivers record low price for offshore wind,” 2019. [Online]. Available: https://assets.kpmg.com/content/dam/kpmgsites/uk/pdf/2019/09/kpmg-blown-away.pdf

[180] R. Liang *et al.*, “Determination of thermal and thermo-mechanical stresses in stator insulation of wind turbine generator based on online monitoring temperatures,” *Proc. 2016 IEEE Int. Conf. Dielectr. ICD 2016*, vol. 2, pp. 1183–1186, 2016, doi: 10.1109/ICD.2016.7547829.

[181] Y. A. Feliciano, C. A. Trinchet Varela, J. A. Vargas Guativas, L. L. Lorente-Leyva, and D. H. Peluffo-Ordóñez, “Evaluation of working temperature in wind turbine bearings by simulation of lubricant level,” *Int. J. Des. Nat. Ecodynamics*, vol. 16, no. 1, pp. 99–104, 2021, doi: 10.18280/ijdne.160113.

[182] X. Wang, Q. C. Zhao, X. B. Yang, and B. Zeng, “Analysis of long-term temperature monitoring of multiple wind turbines,” *Meas. Control (United Kingdom)*, vol. 54, no. 5–6, pp. 627–640, 2021, doi: 10.1177/00202940211013061.

[183] Y. Yamada, “Resistance of a Flow through an Annulus with an Inner Rotating Cylinder,” *Bull. JSME*, vol. 5, no. 18, pp. 302–310, 1962, doi: 10.1299/jsme1958.5.302.

[184] G. K. Costa and N. Sepehri, “Hydraulic accumulators in energy efficient circuits,” *Front. Mech. Eng.*, vol. 9, no. July, pp. 1–11, 2023, doi: 10.3389/fmech.2023.1163293.

[185] D. Li, Y. Li, Z. Li, and Y. Wang, “Theory analyses and applications of magnetic fluids in sealing,” *Friction*, vol. 11, no. 10. Tsinghua University, pp. 1771–1793, Oct. 01, 2023. doi: 10.1007/s40544-022-0676-8.

[186] S. Parmar, V. Ramani, R. V. Upadhyay, and K. Parekh, “Design and development of large radial

clearance static and dynamic magnetic fluid seal," *Vacuum*, vol. 156, no. August, pp. 325–333, 2018, doi: 10.1016/j.vacuum.2018.07.055.

[187] D. J. Bang, J. A. Ferreira, H. Polinder, and S. S. Hong, "Structural mass minimization of large direct-drive wind generators using a buoyant rotor structure," *2010 IEEE Energy Convers. Congr. Expo. ECCE 2010 - Proc.*, pp. 3561–3568, 2010, doi: 10.1109/ECCE.2010.5617705.

[188] Arnold Magnetic Technologies, "Neodymium Iron Boron Magnet Catalog," 2021. [Online]. Available: https://www.arnoldmagnetics.com/wp-content/uploads/2019/06/Arnold-Neo-Catalog.pdf

[189] D. Pirrò and M. Quadrio, "Direct numerical simulation of turbulent Taylor-Couette flow," *Eur. J. Mech. B/Fluids*, vol. 27, no. 5, pp. 552–566, Sep. 2008, doi: 10.1016/j.euromechflu.2007.10.005.

[190] Y. Bazilevs and I. Akkerman, "Large eddy simulation of turbulent Taylor-Couette flow using isogeometric analysis and the residual-based variational multiscale method," *J. Comput. Phys.*, vol. 229, no. 9, pp. 3402–3414, 2010, doi: 10.1016/j.jcp.2010.01.008.

Appendix A: Armature Current Calculation

The following section will detail the derivation of the armature current equation.

It is assumed that reactive power is supplied by the power converter such that the magnitude of the open-load EMF ($|E_p|$) is equal to that of the terminal voltage ($|\mathcal{V}_s|$).

The resistive voltage drop is neglected in the calculation of stator current, but is considered in Chapter 2, Section 2.1.6 using an iterative approach.

According to a voltage balance:

$$E_p = \mathcal{V}_s + jI_sX_S$$

The current contains a real and a reactive component:

$$E_p = \mathcal{V}_s + jX_S(I_{\mathrm{s,real}} + jI_{\mathrm{s,img}})$$

This can be expanded to give:

$$E_p = \mathcal{V}_s + jI_{\mathrm{s,real}}X_s - I_{\mathrm{s,img}}X_s$$

Therefore:

$$|E_p|^2 - (I_{real}X_s)^2 = \left(\mathcal{V}_s - I_{\mathrm{s,img}}X_s\right)^2$$

Take the square root of both sides:

$$\sqrt{|E_p|^2 - (I_{real}X_s)^2} = |\mathcal{V}_s - I_{\mathrm{s,img}}X_s|$$

Hence:

$$|I_{\mathrm{s,img}}X_s| = |\mathcal{V}_s| - \sqrt{E_p^2 - I_{\mathrm{s,real}}X_s^2}$$

Rearranging for $I_{\mathrm{s,img}}$:

$$I_{\mathrm{s,img}} = \frac{I_{\mathrm{s,img}}X_s}{X_s} = \frac{|\mathcal{V}_s| - \sqrt{E_p^2 - I_{\mathrm{s,real}}X_s^2}}{X_s}$$

Consider that:

$$I_s = \sqrt{I_{\mathrm{s,real}}^2 + I_{\mathrm{s,img}}^2}$$

Therefore:

$$I_s = \sqrt{\left(I_{\text{s,real}}\right)^2 + \left(\frac{|\mathcal{V}_s| - \sqrt{E_p^2 - I_{\text{s,real}} X_s^2}}{X_s}\right)^2}$$

Consider that:

$$I_{\text{s,real}} = \frac{P_E}{E_p N_{\text{phase}}}$$

$$X_s = \omega_e L_s$$

$$\left|E_p\right| = |\mathcal{V}_s|$$

Therefore:

$$I_s = \sqrt{\left(\frac{P_E}{E_p N_{\text{phase}}}\right)^2 + \left(\frac{E_p - \sqrt{E_p^2 - (\omega_e L_s)^2 \left(\frac{P_E}{E_p N_{\text{phase}}}\right)^2}}{(\omega_e L_s)}\right)^2}$$

Appendix B: Magnet Losses

Eddy current losses in the PMs were estimated based on the fully analytical method from Ciriani e. al. [37].

The method was implemented as a MATLAB function that facilitated a fast estimation of PM losses in a 12-10 slot-pole combination machine based on the generator geometry, and electrical parameters:

$$P_{\mathrm{PM}} = f\left(h_{\mathrm{PM}}, h_{\mathrm{g}}, \tau_{\mathrm{pole}}, \widehat{I_s}, \omega_e, N_{\mathrm{TC}}, l_c, n_{\mathrm{seg,C}}, \kappa\right)$$

where h_{PM} is the magnet height, h_{g} is the air-gap clearance, τ_{pole} is the pole pitch, $\widehat{I_s}$ is the peak current amplitude, ω_e is the electrical frequency in rad/s, N_{TC} is the number of turns per coil, l_c is core length, $n_{\mathrm{seg,C}}$ is the total number of circumferential magnet segmentations in the machine (including the pole spacing between neighbouring magnets), κ is the magnet's electrical conductivity.

While the influence of circumferential segmentations is included within the method, the influence of axial segmentation was accounted for using a correction factor [38]:

$$C_{\mathrm{axial}} = \frac{3}{4}\frac{l_{\mathrm{PM}}^2}{w_{\mathrm{PM}}^2 + l_{\mathrm{PM}}^2}$$

where l_{PM} is the axial length of a magnet segment, w_{PM} is the width of a magnet segment.

Appendix C: Magnet Grades

Magnet prices were obtained from [42]. Properties were obtained from [188].

Magnet Grade	Max Temp (°C)	Remanent flux density at max temp (T)	Average price ($/kg)
NdFeB N35 (Ce)	80	1.13	17.45
NdFeB N38 (Ce)	80	1.18	18.07
NdFeB N40 (Ce)	80	1.2	18.68
NdFeB N42 (Ce)	80	1.23	19.29
NdFeB N45 (Ce)	80	1.26	19.91
NdFeB N48 (Ce)	80	1.31	20.52
NdFeB N50 (Ce)	80	1.33	22.37
NdFeB N52 (Ce)	80	1.36	22.98
NdFeB N55 (Ce)	80	1.4	25.44
NdFeB 35M	100	1.1	22.98
NdFeB 38M	100	1.14	23.35
NdFeB 40M	100	1.16	23.72
NdFeB 42M	100	1.2	23.96
NdFeB 45M	100	1.23	24.33
NdFeB 48M	100	1.27	24.33
NdFeB 50M	100	1.30	25.56
NdFeB 52M	100	1.32	26.18
NdFeB 33H	120	1.05	21.14
NdFeB 35H	120	1.08	22.37
NdFeB 38H	120	1.11	22.98
NdFeB 40H	120	1.13	24.21
NdFeB 42H	120	1.15	25.44
NdFeB 45H	120	1.2	26.67
NdFeB 48H	120	1.22	27.28
NdFeB 50H	120	1.26	28.51
NdFeB 52H	120	1.28	29.13
NdFeB 30SH (Ce)	150	0.95	26.05
NdFeB 33SH (Ce)	150	1	26.67
NdFeB 35SH (Ce)	150	1.02	27.28
NdFeB 38SH (Ce)	150	1.07	28.51
NdFeB 40SH (Ce)	150	1.09	29.74
NdFeB 45SH (Ce)	150	1.14	30.97
NdFeB 48SH (Ce)	150	1.19	32.20

NdFeB 50SH	150	1.21	35.27
NdFeB 52SH	150	1.24	36.50
NdFeB 54SH	150	1.26	37.48
NdFeB 35UH	180	1.00	35.88
NdFeB 38UH	180	1.02	36.5
NdFeB 40UH	180	1.03	37.11
NdFeB 42UH	180	1.06	37.73

Appendix D: Thermal Resistances

Detailed Thermal Resistance Values
$R_{01,\text{Inner-Rotor}} = \frac{1}{\bar{\alpha}_{\text{ext}} \tau_{\text{slot}} l_c} \quad R_{01,\text{Outer-Rotor}} = \frac{1}{\bar{\alpha}_{\text{int}} \tau_{\text{slot}} l_c}$
$R_{02} = \frac{h_{\text{ss}}}{k_{\text{Fe,s}} \tau_{\text{slot}} l_c} + \frac{t_{\text{tol}}}{k_{\text{air}} \tau_{\text{slot}} l_c}$
$R_{03} = \frac{h_{\text{duct,wall}}}{k_{\text{Fe,s}} \tau_{\text{slot}} l_c}$
$R_{04} = \frac{1}{\bar{\alpha}_{\text{cool}} \tau_{\text{slot}} l_c}$
$R_{05} = \frac{1}{\bar{\alpha}_{\text{cool}} w_{\text{tooth}} l_c}$
$R_{06} = \frac{1}{\bar{\alpha}_{\text{cool}} w_{\text{slot}} l_c}$
$R_{07} = \frac{h_{\text{duct,wall}}}{k_{\text{Fe,s}} w_{\text{tooth}} l_c} + \frac{t_{\text{tol}}}{k_{\text{air}} w_{\text{tooth}} l_c}$
$R_{08} = \frac{h_{\text{duct,wall}}}{k_{\text{Fe,s}} w_{\text{slot}} l_c} + \frac{t_{\text{tol}}}{k_{\text{air}} w_{\text{slot}} l_c}$
$R_{09} = \frac{h_{\text{SY}}}{2 k_{\text{Fe,e}} w_{\text{tooth}} l_c}$
$R_{10} = \frac{h_{\text{SY}}}{2 k_{\text{Fe,e}} w_{\text{slot}} l_c}$
$R_{11} = \frac{w_{\text{tooth}}}{2 k_{\text{Fe,e}} h_{\text{SY}} l_c}$
$R_{12} = \frac{w_{\text{slot}}}{2 k_{\text{Fe,e}} h_{\text{SY}} l_c}$
$R_{13} = \frac{h_{\text{slot}}}{2 k_{\text{Fe,e}} w_{\text{tooth}} l_c}$
$R_{14} = \frac{h_{\text{TT,1}}}{k_{\text{Fe,e}} (w_{\text{tooth}} + w_{\text{TT}}) l_c} + \frac{h_{\text{TT,2}}}{2 k_{\text{Fe,e}} w_{\text{TT}} l_c}$
$R_{15} = \frac{1}{\bar{\alpha}_{\text{g}} w_{\text{TT}} l_c}$
$R_{16} = \frac{t_{\text{SL}}}{k_{\text{SL}} w_{\text{coil}} l_c}$

$$R_{17} = \frac{h_{\mathrm{coil}}}{2k_{\mathrm{coil,eq}} w_{\mathrm{coil}} l_c}$$
$$R_{18} = \frac{h_{\mathrm{TT},1}}{k_{\mathrm{SW}}(w_{\mathrm{slot}} + w_{\mathrm{SO}}) l_c} + \frac{h_{\mathrm{TT},2}}{2k_{\mathrm{SW}} w_{\mathrm{SO}} l_c}$$
$$R_{19} = \frac{1}{\bar{\alpha}_{\mathrm{g}} w_{\mathrm{SO}} l_c}$$
$$R_{20} = \frac{w_{\mathrm{tooth}}}{2k_{\mathrm{Fe,e}} h_{\mathrm{slot}} l_c}$$
$$R_{21} = \frac{t_{\mathrm{SL}}}{k_{\mathrm{SL}} h_{\mathrm{coil}} l_c}$$
$$R_{22} = \frac{w_{\mathrm{coil}}}{2k_{\mathrm{coil,eq}} h_{\mathrm{coil}} l_c}$$
$$R_{23} = 2R_{21}$$
$$R_{24} = \frac{0.5w_{\mathrm{tooth}} + 1.5w_{\mathrm{TT}}}{k_{\mathrm{Fe,e}}\left(h_{\mathrm{TT},1} + h_{\mathrm{TT},2}\right) l_c}$$
$$R_{25} = \frac{0.5w_{\mathrm{slot}} + 1.5w_{\mathrm{SO}}}{k_{\mathrm{SW}}\left(h_{\mathrm{TT},1} + h_{\mathrm{TT},2}\right) l_c}$$
$$R_{26} = \frac{1}{\bar{\alpha}_{\mathrm{g}} \tau_{\mathrm{pole}} l_c}$$
$$R_{27} = \frac{t_{\mathrm{coat}}}{k_{\mathrm{coat}} w_{\mathrm{PM}} l_c}$$
$$R_{28} = \frac{h_{\mathrm{PM}}}{2k_{\mathrm{PM}} w_{\mathrm{PM}} l_c}$$
$$R_{29} = \frac{t_{\mathrm{glue}}}{k_{\mathrm{glue}} w_{\mathrm{PM}} l_c}$$
$$R_{30} = \frac{h_{\mathrm{RY}}}{k_{\mathrm{Fe,e}} \tau_{\mathrm{pole}} l_c}$$
$$R_{31} = \frac{h_{\mathrm{RS}}}{k_{\mathrm{Fe,s}} \tau_{\mathrm{pole}} l_c} + \frac{t_{\mathrm{tol}}}{k_{\mathrm{air}} \tau_{\mathrm{pole}} l_c}$$
$$R_{32,Inner-Rotor} = \frac{1}{\bar{\alpha}_{\mathrm{int}} \tau_{\mathrm{pole}} l_c} \qquad R_{32,Outer-Rotor} = \frac{1}{\bar{\alpha}_{\mathrm{ext}} \tau_{\mathrm{pole}} l_c}$$
$$R_{33} = \frac{l_c}{2k_{\mathrm{Cu}} w_{\mathrm{coil}} h_{\mathrm{coil}} C_{\mathrm{fill}}}$$
$$R_{46} = \frac{\pi(0.5w_{\mathrm{tooth}} + 0.25w_{\mathrm{slot}})}{2k_{\mathrm{Cu}} w_{\mathrm{coil}} h_{\mathrm{coil}} C_{\mathrm{fill}}}$$

$$R_{47} = \frac{\ln\left(\frac{0.25w_{slot} + 0.5w_{\text{tooth}}}{0.25w_{\text{slot}} + 0.5w_{\text{tooth}} - 0.5w_{\text{coil}}}\right)}{\pi h_{\text{coil}} k_{\text{coil,eq}}}$$
$$R_{48} = \frac{\ln\left(\frac{0.25w_{\text{slot}} + 0.5w_{\text{tooth}} + 0.5w_{\text{coil}}}{0.25w_{\text{slot}} + 0.5w_{\text{tooth}}}\right)}{\pi h_{\text{coil}} k_{\text{coil,eq}}}$$
$$R_{49} = \frac{1}{\bar{\alpha}_{\text{EW}}(0.25w_{\text{slot}} + 0.5w_{\text{tooth}} - 0.5w_{\text{coil}})\pi h_{\text{coil}}}$$
$$R_{50} = \frac{1}{\bar{\alpha}_{\text{EW}}(0.25w_{\text{slot}} + 0.5w_{\text{tooth}} + 0.5w_{\text{coil}})\pi h_{\text{coil}}}$$
$$R_{51} = \frac{h_{\text{coil}}}{0.125\pi w_{\text{coil}}(2w_{\text{tooth}} + w_{\text{slot}})k_{\text{coil,eq}}}$$
$$R_{52} = \frac{1}{\bar{\alpha}_{\text{EW}} 0.25\pi w_{\text{coil}}(2w_{\text{tooth}} + w_{\text{slot}})}$$

Simplified Thermal Resistance Values
$$R_{55} = \frac{(R_{01} + R_{02} + R_{03} + R_{04})}{N_{\text{slot}}}$$
$$R_{56} = \frac{(R_{05} + R_{07} + R_{09})}{N_{\text{slot}}}$$
$$R_{57} = \frac{(R_{06} + R_{08} + R_{10})}{N_{\text{slot}}}$$
$$R_{58} = \frac{0.5(R_{11} + R_{12})}{N_{\text{slot}}}$$
$$R_{59} = \frac{(R_{09} + R_{13})}{N_{\text{slot}}}$$
$$R_{60} = \frac{(R_{10} + 0.5(R_{16} + R_{17}))}{N_{\text{slot}}}$$
$$R_{61} = \frac{0.5(R_{20} + R_{21} + 2R_{22})}{N_{\text{slot}}}$$
$$R_{62} = \frac{R_{13} + R_{14}}{N_{\text{slot}}}$$
$$R_{63} = \frac{(R_{18} + 0.5(R_{16} + R_{17}))}{N_{\text{slot}}}$$
$$R_{64} = \frac{0.5(R_{24} + R_{25})}{N_{\text{slot}}}$$
$$R_{65} = \frac{(R_{14} + R_{15})}{N_{\text{slot}}}$$

$$R_{66} = \frac{(R_{18} + R_{19})}{N_{\text{slot}}}$$
$$R_{67} = \frac{0.25R_{33}}{N_{\text{slot}}}$$
$$R_{68} = \frac{(R_{26} + R_{27})}{N_{\text{pole}}}$$
$$R_{69} = \frac{R_{28}}{N_{\text{pole}}}$$
$$R_{70} = \frac{R_{28} + R_{29} + R_{30} + R_{31} + R_{32}}{N_{\text{pole}}}$$
$$R_{83} = \frac{0.5R_{46}}{2N_{\text{slot}}}$$
$$R_{84a} = R_{47} + R_{49}$$
$$R_{84b} = R_{48} + R_{50}$$
$$R_{84c} = R_{84a} // R_{84b}$$
$$R_{84d} = 0.5(R_{51} + R_{52})$$
$$R_{84} = \frac{(R_{80c} // R_{84d})}{2N_{\text{slot}}}$$

Compensation Thermal Resistance Values
Stator Yoke Above Tooth
$$R_{34} = \sum_{m,n=odd} \frac{64}{w_{\text{tooth}} l_{\text{c}} h_{\text{SY}} \left(k_{\text{Fe,e}} \alpha_{m,\text{b}}^2 + k_{\text{Fe,e}} \beta_{n,\text{b}}^2\right) n^2 m^2 \pi^4}$$ $$- \sum_{m,n=odd} \frac{16}{w_{\text{tooth}} l_{\text{core}} h_{\text{SY}} \left(k_{\text{Fe,e}} \alpha_{m,\text{b}}^2 + k_{\text{Fe,e}} \beta_{n,\text{b}}^2\right) mn\pi^2} \sin\left(\frac{m\pi}{2}\right) \sin\left(\frac{n\pi}{2}\right)$$
$$R_{35} = \sum_{m,n=odd} \frac{16}{w_{\text{tooth}} l_{\text{core}} h_{\text{SY}} \left(k_{\text{Fe,e}} \alpha_{m,\text{b}}^2 + k_{\text{Fe,e}} \beta_{n,\text{b}}^2\right) mn\pi^2} \sin\left(\frac{m\pi}{2}\right) \sin\left(\frac{n\pi}{2}\right)$$ $$- 0.5R_{09} // 0.5R_{11}$$
$$\alpha_{m,\text{b}} = \frac{m\pi}{w_{\text{tooth}}} \quad \beta_{n,\text{b}} = \frac{n\pi}{h_{\text{SY}}}$$
$$R_{71} = \frac{R_{34}}{N_{\text{slot}}}$$

$$R_{72} = \frac{R_{35}}{N_{\text{slot}}}$$

Stator Yoke Above Slot

$$R_{36} = \sum_{m,n=odd} \frac{64}{w_{\text{slot}} l_c h_{\text{SY}} \left(k_{\text{Fe,e}} \alpha_{m,\text{c}}^2 + k_{\text{Fe,e}} \beta_{n,\text{c}}^2\right) n^2 m^2 \pi^4}$$

$$- \sum_{m,n=odd} \frac{16}{w_{\text{slot}} l_c h_{\text{SY}} \left(k_{\text{Fe,e}} \alpha_{m,\text{c}}^2 + k_{\text{Fe,e}} \beta_{n,\text{c}}^2\right) mn\pi^2} \sin\left(\frac{m\pi}{2}\right) \sin\left(\frac{n\pi}{2}\right)$$

$$R_{37} = \sum_{m,n=odd} \frac{16}{w_{\text{slot}} l_c h_{\text{SY}} \left(k_{\text{Fe,e}} \alpha_{m,\text{c}}^2 + k_{\text{Fe,e}} \beta_{n,\text{c}}^2\right) mn\pi^2} \sin\left(\frac{m\pi}{2}\right) \sin\left(\frac{n\pi}{2}\right) - 0.5R_{10} // 0.5R_{12}$$

$$\alpha_{m,\text{c}} = \frac{m\pi}{w_{\text{slot}}} \quad \beta_{n,\text{c}} = \frac{n\pi}{h_{\text{SY}}}$$

$$R_{73} = \frac{R_{36}}{N_{\text{slot}}}$$

$$R_{74} = \frac{R_{37}}{N_{\text{slot}}}$$

Tooth Next to Slot

$$R_{38} = \sum_{m,n=odd} \frac{64}{w_{\text{tooth}} l_c h_{\text{slot}} \left(k_{\text{Fe,e}} \alpha_{m,\text{d}}^2 + k_{\text{Fe,e}} \beta_{m,\text{d}}^2\right) n^2 m^2 \pi^4}$$

$$- \sum_{m,n=odd} \frac{16}{w_{\text{tooth}} l_c h_{\text{slot}} \left(k_{\text{Fe,e}} \alpha_{m,\text{d}}^2 + k_{\text{Fe,e}} \beta_{m,\text{d}}^2\right) mn\pi^2} \sin\left(\frac{m\pi}{2}\right) \sin\left(\frac{n\pi}{2}\right)$$

$$R_{39} = \sum_{m,n=odd} \frac{16}{w_{\text{tooth}} l_c h_{\text{slot}} \left(k_{\text{Fe,e}} \alpha_{m,\text{d}}^2 + k_{\text{Fe,e}} \beta_{m,\text{d}}^2\right) mn\pi^2} \sin\left(\frac{m\pi}{2}\right) \sin\left(\frac{n\pi}{2}\right) - 0.5R_{13} // 0.5R_{20}$$

$$\alpha_{m,\text{d}} = \frac{m\pi}{w_{\text{tooth}}}, \qquad \beta_{m,\text{d}} = \frac{n\pi}{h_{\text{slot}}}$$

$$R_{75} = \frac{R_{38}}{N_{\text{slot}}}$$

$$R_{76} = \frac{R_{39}}{N_{\text{slot}}}$$

Coil

$$R_{77} = \left(\sum_{m,n,p=odd} \frac{512}{2w_{\text{coil}} h_{\text{coil}} l_c \left(k_{\text{coil,eq}} \alpha_{m,\text{e}}^2 + k_{\text{coil,eq}} \beta_{n,\text{e}}^2 + C_{\text{fill}} k_{\text{Cu}} \gamma_{n,\text{e}}^2\right) m^2 n^2 p^2 \pi^3} - \sum_{m,n,p=odd} \frac{64}{2w_{\text{coil}} h_{\text{coil}} l_c \left(k_{\text{coil,eq}} \alpha_{m,\text{e}}^2 + k_{\text{coil,eq}} \beta_{n,\text{e}}^2 + C_{\text{fill}} k_{\text{Cu}} \gamma_{n,\text{e}}^2\right) mnp\pi^3} \sin\left(\frac{m\pi}{2}\right) \sin\left(\frac{n\pi}{2}\right) \sin\left(\frac{p\pi}{2}\right) \right) / N_{\text{slot}}$$

$$R_{78} = \left(\sum_{m,n,p=odd} \frac{64}{2w_{\text{coil}} h_{\text{coil}} l_c \left(k_{\text{coil,eq}} \alpha_{m,\text{e}}^2 + k_{\text{coil,eq}} \beta_{n,\text{e}}^2 + C_{\text{fill}} k_{\text{Cu}} \gamma_{n,\text{e}}^2\right) mnp\pi^3} \sin\left(\frac{m\pi}{2}\right) \sin\left(\frac{n\pi}{2}\right) \sin\left(\frac{p\pi}{2}\right) - R_{22} // 0.25R_{17} // 0.25R_{33} \right) / N_{\text{slot}}$$

$$\alpha_{m,\text{e}} = \frac{m\pi}{2w_{\text{coil}}} \quad \beta_{n,\text{e}} = \frac{n\pi}{h_{\text{coil}}} \quad \gamma_{p,\text{e}} = \frac{p\pi}{l_{\text{core}}}$$

Tooth Tip

$$R_{42} = \sum_{m,n=odd} \frac{64}{l_c (0.5w_{\text{tooth}} + 1.5w_{\text{TT}}) \left(h_{\text{TT},1} + h_{\text{TT},2}\right) \left(k_{\text{Fe,e}} \alpha_{m,\text{f}}^2 + k_{\text{Fe,e}} \beta_{m,\text{f}}^2\right) m^2 n^2 \pi^4} - \sum_{m,n=odd} \frac{16}{l_c (0.5w_{\text{tooth}} + 1.5w_{\text{TT}}) \left(h_{\text{TT},1} + h_{\text{TT},2}\right) \left(k_{\text{Fe,e}} \alpha_{m,\text{f}}^2 + k_{\text{Fe,e}} \beta_{m,\text{f}}^2\right) mn\pi^2} \sin\left(\frac{m\pi}{2}\right) \sin\left(\frac{n\pi}{2}\right)$$

$$R_{43} = \sum_{m,n=odd} \frac{16}{l_c (0.5w_{\text{tooth}} + 1.5w_{\text{TT}}) \left(h_{\text{TT},1} + h_{\text{TT},2}\right) \left(k_{\text{Fe,e}} \alpha_{m,\text{f}}^2 + k_{\text{Fe,e}} \beta_{m,\text{f}}^2\right) mn\pi^2} \sin\left(\frac{m\pi}{2}\right) \sin\left(\frac{n\pi}{2}\right) - 0.5R_{14} // 0.5R_{24}$$

$$\alpha_{m,\text{f}} = \frac{m\pi}{(0.5w_{\text{tooth}} + 1.5w_{\text{TT}})} \quad \beta_{n,\text{f}} = \frac{n\pi}{\left(h_{\text{TT},1} + h_{\text{TT},2}\right)}$$

$$R_{79} = \frac{R_{42}}{N_{\text{slot}}}$$

$$R_{80} = \frac{R_{43}}{N_{\text{slot}}}$$

Magnet

$R_{44} = -\frac{h_{\mathrm{PM}}}{24 k_{\mathrm{PM}} w_{\mathrm{PM}} l_c}$
$R_{45} = -\frac{h_{PM}}{8 k_{\mathrm{PM}} w_{PM} l_c}$
$R_{81} = \frac{R_{42}}{N_{\mathrm{pole}}}$
$R_{82} = \frac{R_{43}}{N_{\mathrm{pole}}}$

End Windings

R_{53}

$$= \sum_{m,n,p=odd} \frac{512}{\pi(0.25 w_{\mathrm{slot}} + 0.5 w_{\mathrm{tooth}}) w_{\mathrm{coil}} h_{\mathrm{coil}} \left(k_{\mathrm{coil,eq}} \alpha_{m,\mathrm{j}}^2 + k_{\mathrm{coil,eq}} \beta_{m,\mathrm{j}}^2 + C_{\mathrm{fill}} k_{\mathrm{Cu}} \gamma_{p,\mathrm{j}}^2\right) m^2 n^2 p^2 \pi^3}$$

$$- \sum_{m,n,p=odd} \frac{64}{\pi(0.25 w_{\mathrm{slot}} + 0.5 w_{\mathrm{tooth}}) w_{\mathrm{coil}} h_{\mathrm{coil}} \left(k_{\mathrm{coil,eq}} \alpha_{m,\mathrm{j}}^2 + k_{\mathrm{coil,eq}} \beta_{m,\mathrm{j}}^2 + C_{\mathrm{fill}} k_{\mathrm{Cu}} \gamma_{p,\mathrm{j}}^2\right) mnp\pi^3} \sin\left(\frac{m\pi}{2}\right) \sin\left(\frac{n\pi}{2}\right) \sin\left(\frac{p\pi}{2}\right)$$

R_{54}

$$= \sum_{m,n,p=odd} \frac{64}{\pi(0.25 w_{\mathrm{slot}} + 0.5 w_{\mathrm{tooth}}) w_{\mathrm{coil}} h_{\mathrm{coil}} \left(k_{\mathrm{coil,eq}} \alpha_{m,\mathrm{j}}^2 + k_{\mathrm{coil,eq}} \beta_{m,\mathrm{j}}^2 + C_{\mathrm{fill}} k_{\mathrm{Cu}} \gamma_{p,\mathrm{j}}^2\right) mnp\pi^3} \sin\left(\frac{m\pi}{2}\right) \sin\left(\frac{n\pi}{2}\right) \sin\left(\frac{p\pi}{2}\right)$$

$$- 0.5 R_{46} // R_{84c} // R_{84d}$$

$$\alpha_{m,\mathrm{j}} = \frac{m\pi}{w_{\mathrm{coil}}} \quad \beta_{n,\mathrm{j}} = \frac{p\pi}{h_{\mathrm{coil}}} \quad \gamma_{p,\mathrm{j}} = \frac{n}{(0.5 w_{\mathrm{tooth}} + 0.25 w_{\mathrm{slot}})}$$

$$R_{81} = \frac{R_{53}}{2 N_{\mathrm{slot}}}$$

$$R_{82} = \frac{R_{54}}{2 N_{\mathrm{slot}}}$$

Appendix E: In-House Ferrofluid Synthesis

Following is the protocol used to synthesis the In-House ferrofluid samples.

Chemicals Involved	Equipment Required
• Anhydrous $FeCl_3$ • Potassium Iodide • Iodine • Nitrogen • 25% Ammonia Solution • Magnetite • Oleic Acid • Dilute Hydrochloric Acid • Isopropanol • Mineral Oil	• Beakers • Filters • Filters • Funnels • Wash Bottle • Desk Mounted Stirrer • pH Meter • Dropping Funnel • Nitrogen Line • Strong Magnet • Stir Rods • Drying Bowl • Tissue Paper

Method:

1. Dissolve 19.46 g (0.119 mol) of anhydrous $FeCl_3$ in 150.0 ml of distilled water to prepare aqueous solution A.

2. Dissolve 6.584 g (0.0396 mol) of potassium iodide in 50.0 ml of distilled water to prepare aqueous solution B.

3. Mix solutions A and B together at room temperature, stir, and allow to reach equilibrium for one hour. We will call this solution C.

4. Filter out the precipitate of iodine, wash with distilled water, and add the distilled water used for washing into the filtrate (filtered solution C).

5. Set up solution C with a desk mounted stirrer (non-magnetic), a pH meter, a nitrogen line for bubbling the solution, and a dropping funnel positioned above.

6. With the dropping funnel closed, add 25% ammonia solution to the funnel – ready to be added to solution C when the funnel is opened.

7. Turn on the stirrer so that there is good mixing but no risk of spillage, take note of the settings for future reference. Begin bubbling nitrogen through solution C, again at a rate that does not risk spillage.

8. Gradually add the ammonia solution dropwise into solution C using the dropping funnel over the course of 20 minutes. Complete precipitation of the magnetite (Fe3O4) should be achieved at a pH of 9-11. At this point stop adding ammonia to solution C. Leave stirring for 15 minutes.

9. Add 12 g of Oleic Acid into a beaker, add 16 ml of distilled water, and then 8 ml of the ammonia solution, mix, this should create ammonium oleate soap. We will call this solution D.

10. Ensure that solution C has a pH of at least 10. Add solution D to solution C, use distilled water to ensure that all of solution D leaves its beaker. Let it stir for 20 minutes.

11. Ensuring that the dropping funnel is empty and closed, add dilute hydrochloric acid in preparation for adding to the solution C.

12. Slowly add the dilute hydrochloric acid dropwise to solution C until the pH of the solution drops to 6-7. When the solution pH drops below 7 a colour change might be observed in the foam (grey to white) and the magnetite should separate from the solution.

13. The dropping funnel, stirrer, pH meter, and nitrogen line can now be removed from solution C.

14. The magnetite precipitate now must be separated from the rest of solution C, this can be done with the help of a magnet as the magnetite is ferromagnetic. By keeping the magnetite within the beaker using the magnet, the excess liquid can be transferred out for disposal.

15. The magnetite now must be washed. Add distilled water to the magnetite and stir. Like before, use the magnet to keep the magnetite within the beaker while removing the water. Repeat 3 times.

16. Repeat the same process using Isopropanol, 3 times as before. The Isopropanol should look clear by the 3rd time.

17. Transfer the magnetite into a clean beaker. Remove as much isopropanol from the magnetite as possible with the help of the magnet. Add the desired quantity of mineral oil to the magnetite in the beaker. Stir with a glass rod, the magnetite should disperse within the mineral oil resulting in ferrofluid.

18. Over time the isopropanol will separate from the ferrofluid and rise to the top of the beaker. This can be removed with a syringe. Over time the remaining isopropanol will evaporate if the ferrofluid is left unsealed.

This protocol results in a small sample of ferrofluid, for the ‘In-House’ ferrofluid used in the experimental testing a larger quantity was made by scaling up the quantities by a factor of 10. This is not recommended for a quality synthesis, however that was not the objective for the test.

Appendix F: Nondimensionalisation of Navier-Stokes Equation

The ferrohydrodynamic Navier-Stokes equation is as follows:

$$\rho\frac{\mathrm{D}\boldsymbol{v}}{\mathrm{D}t} = -\boldsymbol{\nabla}(p + p_s + p_M) + \mu_0 M\boldsymbol{\nabla}\boldsymbol{H} + \eta\boldsymbol{\nabla}^2\boldsymbol{v} + \rho\boldsymbol{g}$$

It can be nondimensionalised by considering the following scaling parameters:

Scaling Parameter	Description	Primary Dimensions
h_g	Characteristic length: air-gap clearance	L
v_r	Characteristic speed: rotor peripheral speed	Lt^{-1}
f	Characteristic frequency	t^{-1}
$p_0 - p_\infty$	Reference pressure difference	$mL^{-1}t^{-2}$
g	Gravitational acceleration	Lt^{-2}
M_s	Characteristic magnetisation: ferrofluid saturation magnetisation	AL^{-1}
H_g	Characteristic magnetic field strength density: ferrofluid-gap magnetic field strength	$mt^{-2}A^{-1}$

where L is length, t is time, m is mass, A is ampere, p_0 is the ferrofluid pressure, and p_∞ is atmospheric pressure. Note that ampere (A) is not a fundamental unit, however it cancels out later in the derivation.

Nondimensional variables can then be defined and rearranged with respect to the dimensional variables:

Nondimensional Variables	Rearranged
$t^* = ft$	$t = \frac{t^*}{f}$
$x^* = x/h_\mathrm{g}$	$x = x^* h_\mathrm{g}$
$\boldsymbol{v}^* = \boldsymbol{v}/v_r$	$\boldsymbol{v} = \boldsymbol{v}^* v_r$

$p^* = \frac{p - p_\infty}{p_0 - p_\infty}$	$p = p_\infty + (p_0 - p_\infty)p^*$
$\boldsymbol{g}^* = \boldsymbol{g}/\lvert\boldsymbol{g}\rvert$	$\boldsymbol{g} = \boldsymbol{g}^*\lvert\boldsymbol{g}\rvert$
$\boldsymbol{\nabla}^* = h_\mathrm{g}\boldsymbol{\nabla}$	$\boldsymbol{\nabla} = \boldsymbol{\nabla}^*/h_\mathrm{g}$
$\boldsymbol{M}^* = \boldsymbol{M}/\lvert M_s\rvert$	$\boldsymbol{M} = \boldsymbol{M}^*\lvert M_s\rvert$
$\boldsymbol{H}^* = \boldsymbol{H}/\lvert H_\mathbf{g}\rvert$	$\boldsymbol{H} = \boldsymbol{H}^*\lvert H_\mathrm{g}\rvert$

Now, substituting into the ferrohydrodynamic Navier-Stokes equation:

$$\rho v_r f\frac{\partial \boldsymbol{v}^*}{\partial t^*} + \frac{\rho v_r^2}{h_\mathrm{g}}(\boldsymbol{v}^*\cdot\boldsymbol{\nabla}^*)\boldsymbol{v}^* = -\frac{p_0 - p_\infty}{h_\mathrm{g}}\boldsymbol{\nabla}^* p^* + \rho\lvert g\rvert\boldsymbol{g}^* + \frac{\eta v_r}{h_\mathrm{g}^2}\boldsymbol{\nabla}^{*2}\boldsymbol{v}^* + \frac{\mu_0 M_s H_\mathrm{g}}{h_\mathrm{g}}\boldsymbol{M}^*\boldsymbol{\nabla}^*\boldsymbol{H}^*$$

Each term in the above equation has the dimensions $mL^{-2}t^{-2}$, we can non-dimensionalise the equation by multiplying every term by the constant $h_\mathrm{g}/\rho v_r^2$ which has the inverse dimensions $m^{-1}L^{-2}t^{-2}$ such that the dimensions cancel:

$$\frac{f h_g}{v_r}\frac{\partial \boldsymbol{v}^*}{\partial t^*} + (\boldsymbol{v}^*\cdot\boldsymbol{\nabla}^*)\boldsymbol{v}^* = -\frac{p_0 - p_\infty}{\rho v_r^2}\boldsymbol{\nabla}^* p^* + \frac{\lvert\boldsymbol{g}\rvert h_g}{v_r^2}\boldsymbol{g}^* + \frac{\eta}{\rho v_r h_g}\boldsymbol{\nabla}^{*2}\boldsymbol{v}^* + \frac{\mu_0 M_s H_g}{\rho v_r^2}\boldsymbol{M}^*\boldsymbol{\nabla}^*\boldsymbol{H}^*$$

This can also be written as:

$$[\mathrm{St}]\frac{\partial \boldsymbol{v}^*}{\partial t^*} + (\boldsymbol{v}^*\cdot\boldsymbol{\nabla}^*)\boldsymbol{v}^* = -[\mathrm{Eu}]\boldsymbol{\nabla}^* p^* + \left[\frac{1}{\mathrm{Fr}^2}\right]\boldsymbol{g}^* + \left[\frac{1}{\mathrm{Re}}\right]\boldsymbol{\nabla}^{*2}\boldsymbol{v}^* + [\mathrm{Mn}]\boldsymbol{M}^*\boldsymbol{\nabla}^*\boldsymbol{H}^*$$

Where St is the Strouhal number, Eu is the Euler number, Fr is the Froude number, Re is the Reynolds number, and Mn is a dimensionless number that characterises the ratio of magnetic force to inertial force in the ferrofluid-gap:

$$[\mathrm{Mn}] = \frac{\mu_0 M_s H_g}{\rho v_r^2}$$

Mn quantifies the relative importance of magnetic body forces to inertial forces in the ferrofluid. A small Mn indicates that inertial effects dominate over the Kelvin body force. In the context of a ferrofluid-gap, this means that the magnetic force becomes progressively less significant as the rotor's tangential velocity, and therefore the inertial forces in the flow, increases.

Appendix G: Ferrofluid Characterisation

EFH 1 Ferrofluid

For each specimen of EFH1 ferrofluid used in the experiments, specific BH curves were obtained by FerroTec with vibrating sample magnetometry (VSM).

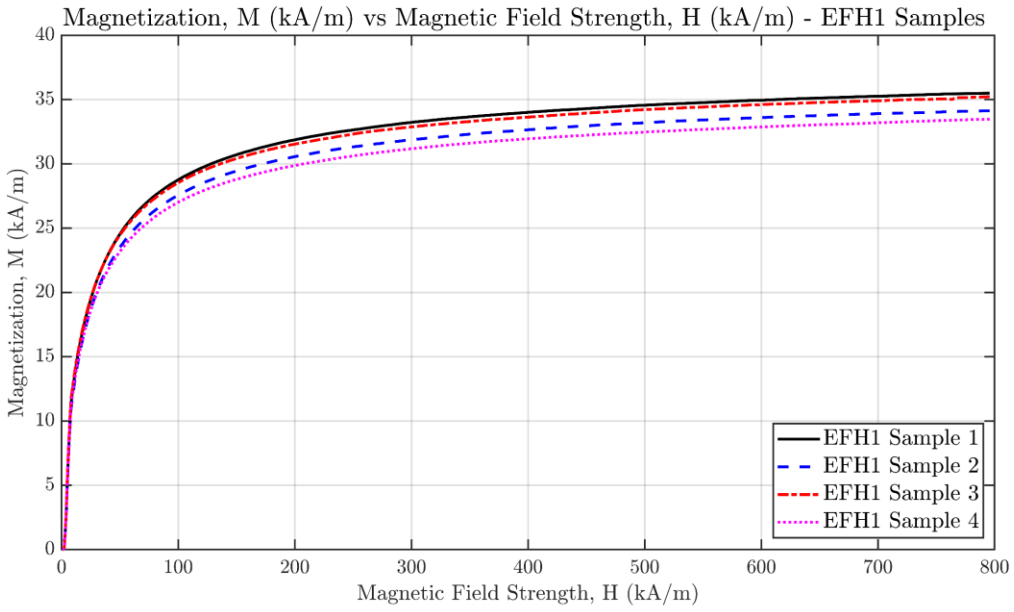

The viscosity of EFH1 ferrofluid was measured using a rheometer, for a range of temperatures. It was observed to display Newtonian behaviour.

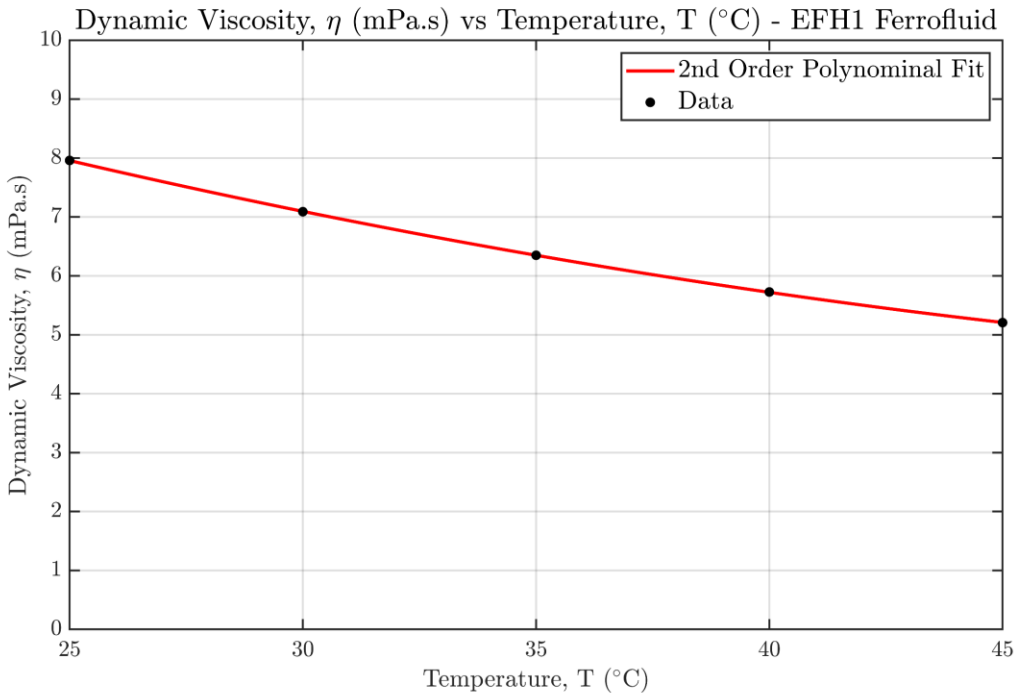

FerroTec Custom Ferrofluid

The BH curve of the FerroTec Custom ferrofluid was provided by FerroTec for the specific specimen used in the experiments:

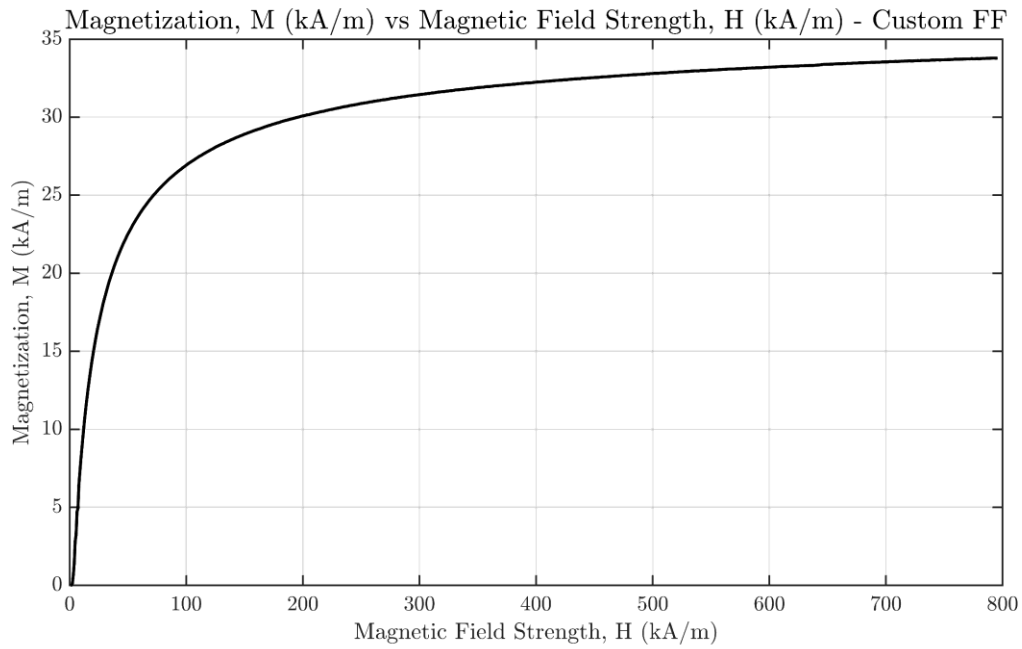

The viscosity was also measured by FerroTec with a rheometer for a range of temperatures:

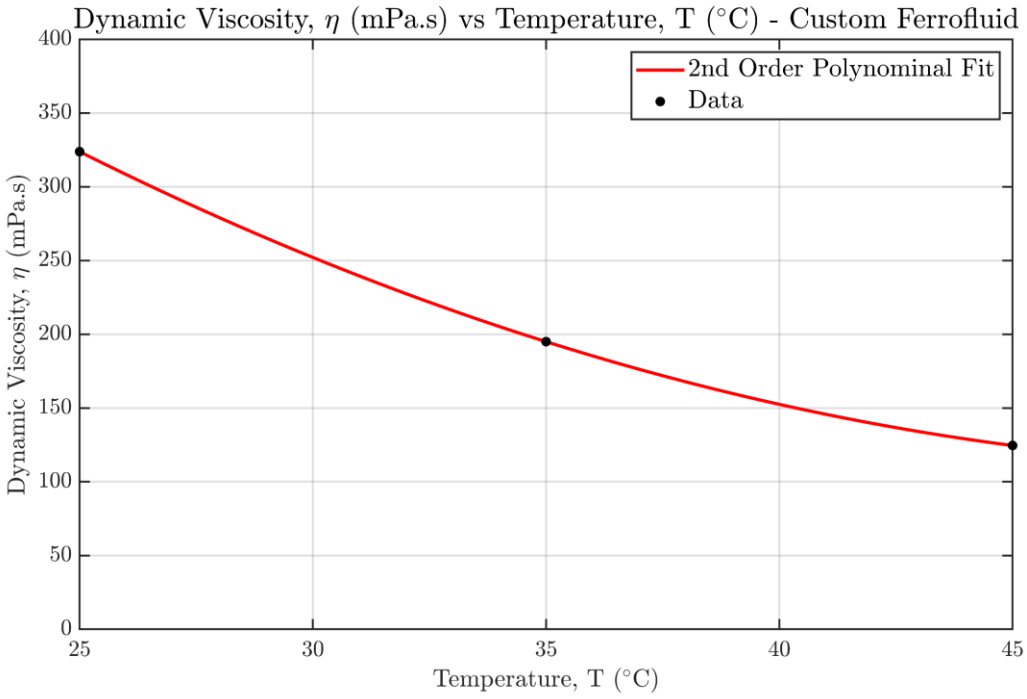

In-House Synthesised Ferrofluid

The BH curve of the In-House synthesised ferrofluid was measured by FerroTec, it was found to be unstable due to an increasing value of magnetisation with time at a constant magnetic field strength, indicating that the sample was not colloidally stable:

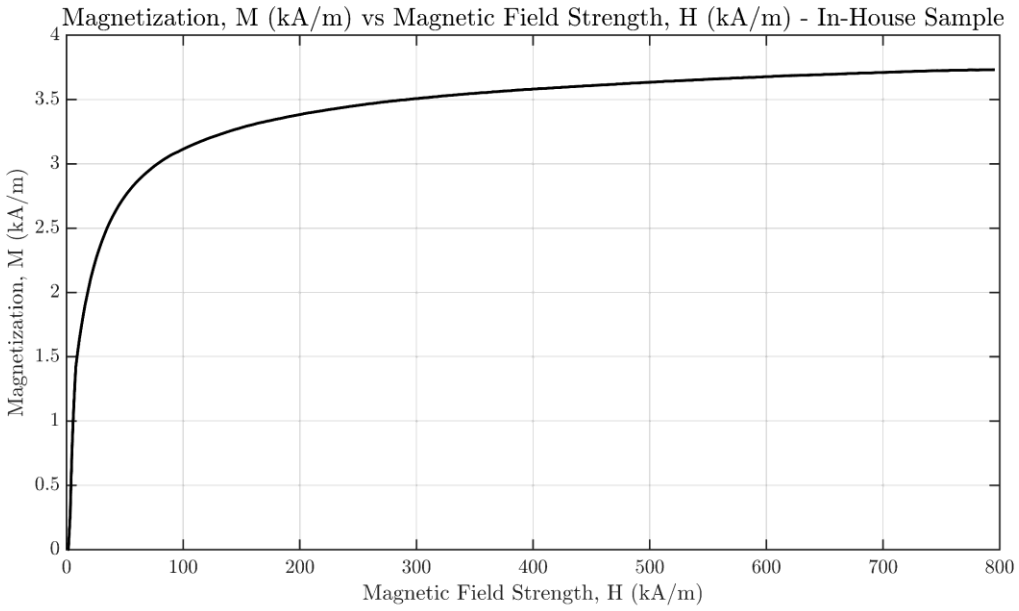

The magnetic volume fraction was estimated by measuring the magnetisation curve of the dry particles. The magnetic volume fraction of the ferrofluid could then be estimated by comparing the measurement with the magnetisation curve of the ferrofluid sample for the same value of magnetic field strength in the saturation region:

$$\phi_M = \frac{M_{\mathrm{s,liquid}}}{M_{\mathrm{s,particle}}} = \frac{M_{\mathrm{s,liquid}}}{\psi_{\mathrm{M}}\rho_{\mathrm{M}}}$$

where $M_{\mathrm{s,liquid}}$ is the saturation magnetisation of the ferrofluid, $M_{\mathrm{s,particle}}$ is the saturation magnetisation of the particles, ψ_{M} is the specific magnetisation of the particles (emu/g), and ρ_{M} is the density of the particles (kg/m^3).

The particle magnetisation was measured with a vibrating sample magnetometer (VSM).

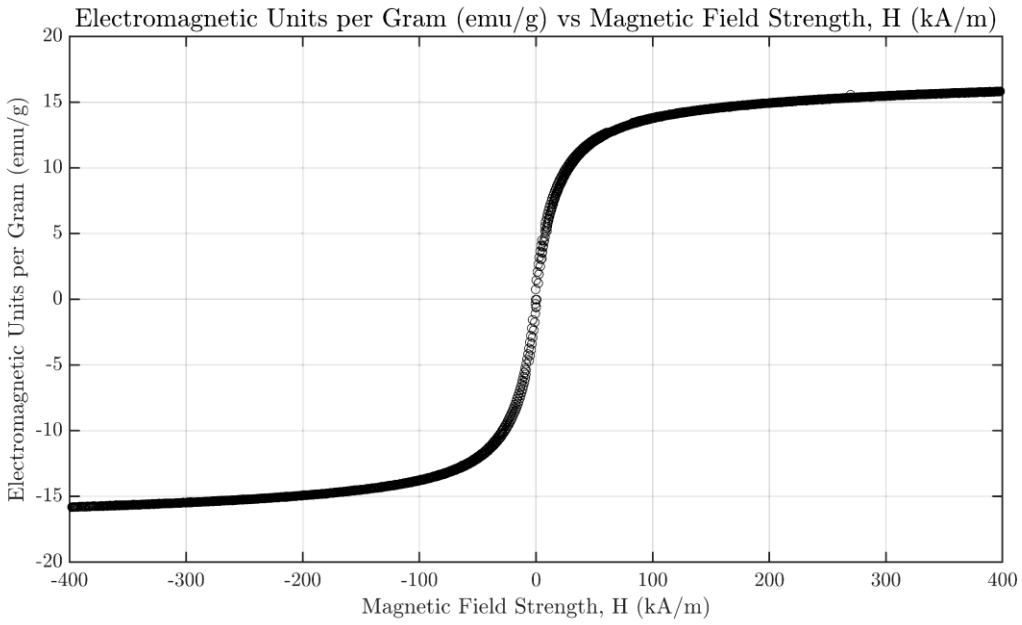

The particle size distribution of the In-House synthesised ferrofluid was determined from transmission electron microscopy (TEM) images of dried particle samples. Due to the wide range of particle sizes observed, multiple magnification levels were used. To account for the varying sampling areas, particle counts were weighted according to the field of view of each image.

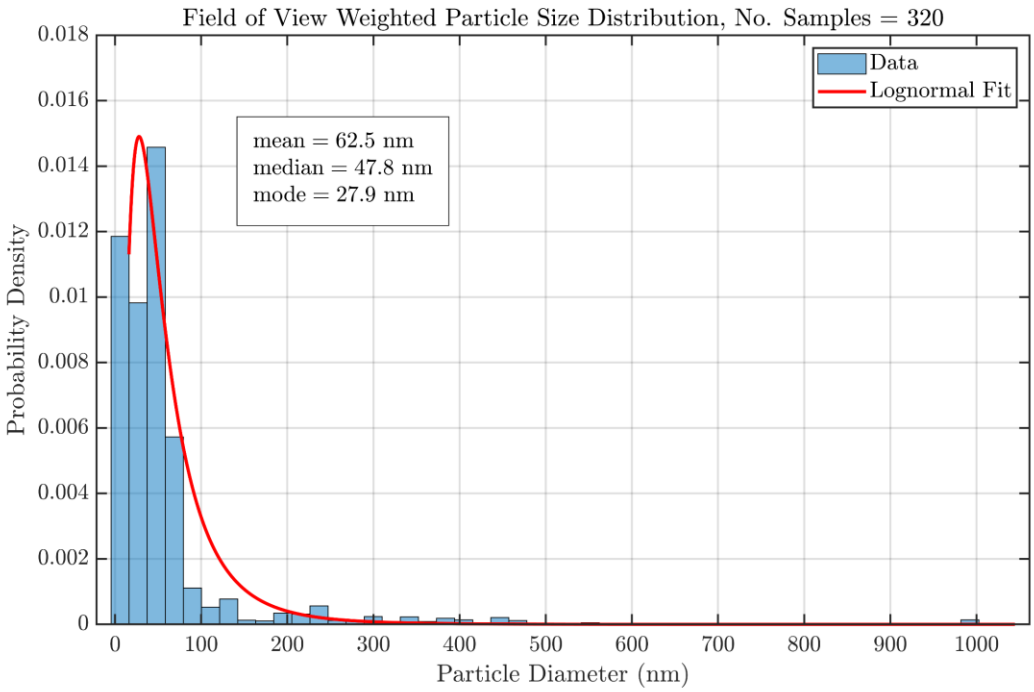

The viscosity was measured with a rheometer for a range of temperatures. Significant non-Newtonian shear thinning behaviour was observed. The high-shear viscosity was estimated according to a Cross Model fit of the viscosity data for each temperature:

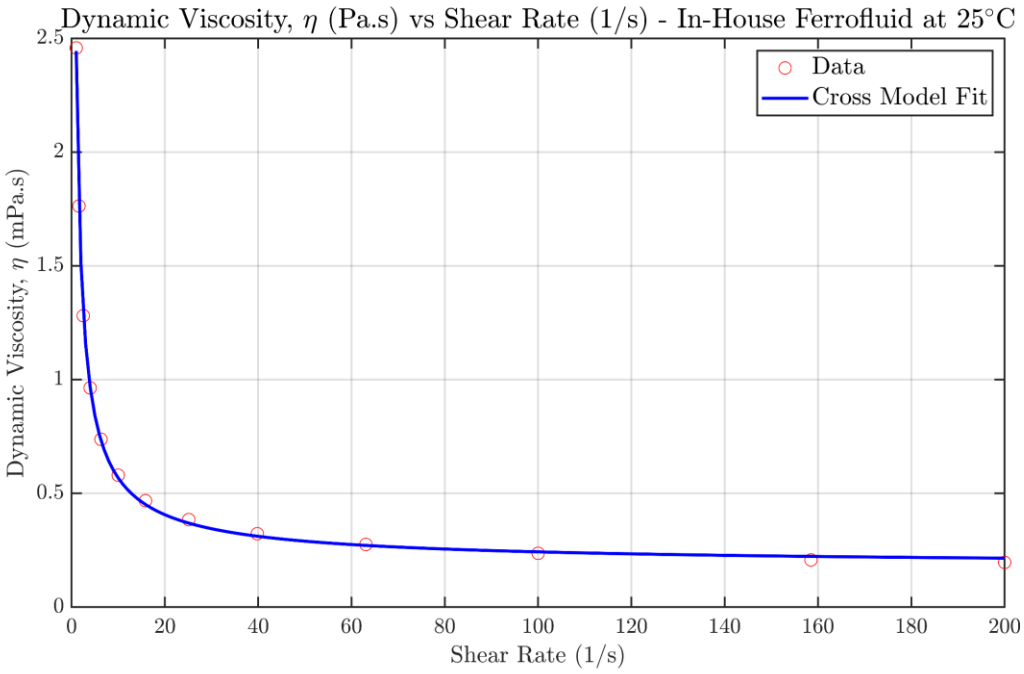

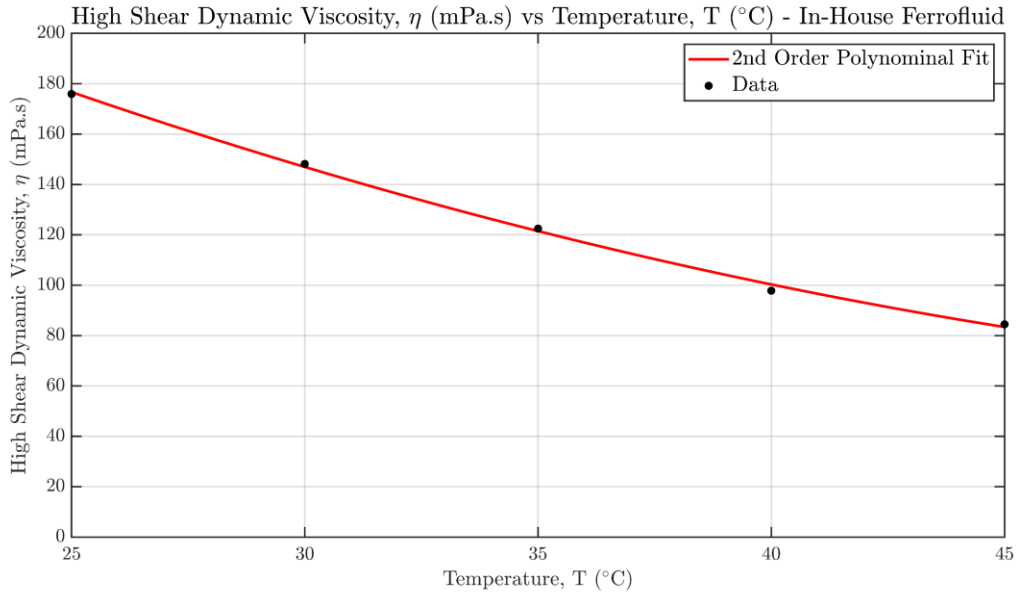

Appendix H: Large Eddy Simulation Method

Large eddy simulations (LES) were conducted using COMSOL Multiphysics's Smagorinsky interface. The Smagorinsky parameter (C_s) was set to 0.13.

The CFD domain was periodic in both the axial and azimuthal directions, with no-slip boundary conditions specified for the walls representing the rotor and stator boundaries. The stator and the rotor wall were specified as a stationary and a moving wall respectively. The size of the domain in the axial and azimuthal directions was specified according to the work of Pirrò *et al.* [189]. In which the azimuthal arc angle (θ_{azi}) and axial length of the domain (L_{axial}) is given by:

$$\theta_{\mathrm{azi}} = \frac{5\pi h_{\mathrm{g}}}{r_r + \frac{h_{\mathrm{g}}}{2}}$$

$$L_{\mathrm{axial}} = 2.5 h_{\mathrm{g}}$$

A mapped mesh was constructed. Such as in the work of Bazilevs *et al.* the number of mesh elements was defined according to a parameter p as $32p \times 8p \times 16p$ in the azimuthal, radial, and axial dimensions respectively [190]. Mesh refinement studies were conducted by increasing p in integer steps. A boundary layer mesh applied to the rotor and stator walls with a total thickness equal to 10% of the gap width, the thickness of the first layer (δ_w) was specified according to:

$$\delta_w = 0.1 h_{\mathrm{g}} \frac{(1-G)}{(1-G^N)}$$

where G is the growth factor, and N is the number of boundary layer elements.

The LES method was compared against the work of Dong who presents experimentally validated direct numerical simulation (DNS) results for a large gap TC flow at large Reynolds numbers [174]. For a Reynolds number of 8000, the LES result was found to be within 5% of the result of Dong.

Simulations were run for a sufficient number of timesteps such that a steady value of surface-averaged rotor wall shear stress was achieved.

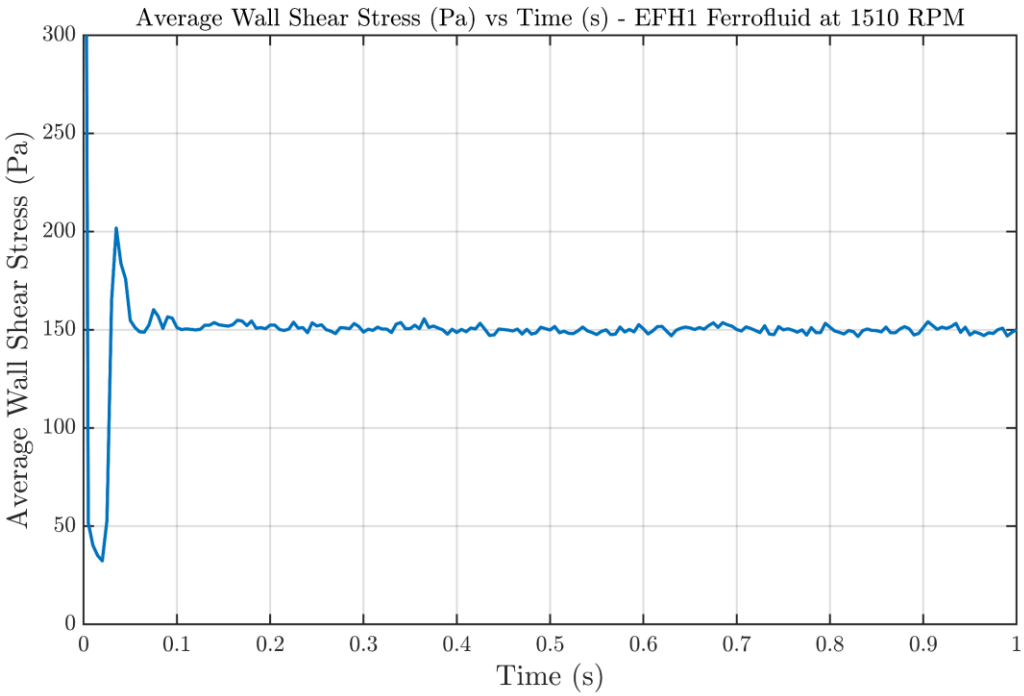

By increasing p and adjusting N such that the wall resolution value was verified to be less than 1 according to COMSOL's post-processing tools. A good trade-off between accuracy and computational cost was achieved for $p = 3$. Below the normalised surface-averaged rotor wall shear stress of EFH1 ferrofluid at a rotational speed of 1510 RPM is compared for different values of p, in this case a value of 3 was found to provide a good balance between accuracy and computational cost.

When applying the LES method to different geometries the mesh refinement study was conducted at the maximum rotational speed investigated, the same mesh was then used for lower rotational speeds.